Lecture Notes in Civil Engineering

B. Kondraivendhan
C. D. Modhera
Vasant Matsagar *Editors*

Sustainable Building Materials and Construction

Select Proceedings of ICSBMC 2021

Springer

Lecture Notes in Civil Engineering

Volume 222

Lecture Notes in Civil Engineering (LNCE) publishes the latest developments in Civil Engineering - quickly, informally and in top quality. Though original research reported in proceedings and post-proceedings represents the core of LNCE, edited volumes of exceptionally high quality and interest may also be considered for publication. Volumes published in LNCE embrace all aspects and subfields of, as well as new challenges in, Civil Engineering. Topics in the series include:

- Construction and Structural Mechanics
- Building Materials
- Concrete, Steel and Timber Structures
- Geotechnical Engineering
- Earthquake Engineering
- Coastal Engineering
- Ocean and Offshore Engineering; Ships and Floating Structures
- Hydraulics, Hydrology and Water Resources Engineering
- Environmental Engineering and Sustainability
- Structural Health and Monitoring
- Surveying and Geographical Information Systems
- Indoor Environments
- Transportation and Traffic
- Risk Analysis
- Safety and Security

To submit a proposal or request further information, please contact the appropriate Springer Editor:

– Pierpaolo Riva at pierpaolo.riva@springer.com (Europe and Americas);
– Swati Meherishi at swati.meherishi@springer.com (Asia - except China, and Australia, New Zealand);
– Wayne Hu at wayne.hu@springer.com (China).

All books in the series now indexed by Scopus and EI Compendex database!

More information about this series at https://link.springer.com/bookseries/15087

B. Kondraivendhan · C. D. Modhera ·
Vasant Matsagar
Editors

Sustainable Building Materials and Construction

Select Proceedings of ICSBMC 2021

Springer

Editors
B. Kondraivendhan
Department of Civil Engineering
Sardar Vallabhbhai National Institute of Technology
Surat, Gujarat, India

C. D. Modhera
Department of Civil Engineering
Sardar Vallabhbhai National Institute of Technology
Surat, Gujarat, India

Vasant Matsagar
Department of Civil Engineering,
Indian Institute of Technology Delhi
New Delhi, Delhi, India

ISSN 2366-2557 ISSN 2366-2565 (electronic)
Lecture Notes in Civil Engineering
ISBN 978-981-16-8495-1 ISBN 978-981-16-8496-8 (eBook)
https://doi.org/10.1007/978-981-16-8496-8

Contents

About the Editors

Dr. B. Kondraivendhan is currently an assistant Professor at Department of Civil Engineering, Sardar Vallabhbhai National Institute of Technology, Surat. He obtained his B.E. (Civil) from Alagappa Chettiyar Government College of Engineering and Technology, Karaikudi, and M.E. (Structural Engineering) from Annamalai University, Chidambaram, and Ph.D. from Indian Institute of Technology Delhi, New Delhi. He was a visiting Student of university of Dundee, Scotland, UK. He also had Post Doctoral experience from Nanyang Technological University (NTU), Singapore. His major areas of research interest includes pore structure characterization and modeling, rebar corrosion, alternative binders in concrete preparation, repair and rehabilitation of concrete structures. He has published more than 27 papers in respected international journals and conferences. At present he is acting as a member secretary of Indian Concrete Institute (ICI) Surat center. Currently he is one of the main review members of the *Indian Concrete Journal*.

Dr. C. D. Modhera is currently Professor (HAG) at Department of Civil Engineering, Sardar Vallabhbhai National Institute of Technology. Surat. He obtained his B.E. (Civil) and M.E. (Structural Engineering) from Sardar Vallabhbhai National Institute of Technology. Surat, and Ph.D. from Indian Institute of Technology Bombay. His major area of research interest includes special concrete and its relevant application in the field; rebar corrosion, alternative binders in concrete preparation and repair and rehabilitation of concrete structures as well as earthquake engineering. He has published more than 150 papers in respected international journals and conferences. At present he is acting as a chairman of Indian Concrete Institute (ICI) Surat center. He was former Dean (Planning and Development) and Head of the Department of Applied Mechanics.

Dr. Vasant Matsagar is currently Professor and incumbent Dogra Chair at Department of Civil Engineering, Indian Institute of Technology (IIT) Delhi. He obtained his Ph.D. degree from Indian Institute of Technology (IIT) Bombay. He also has post-doctoral research experience from Lawrence Technological University (LTU) USA. His major area of research interest includes multi-hazard protection of structures,

earthquake, wind, blast and fire engineering, offshore structures, fiber-reinforced polymer (FRP) composites, finite element analysis in structural engineering. He has published more than 250 papers in reputed international journals and conferences. He received Humboldt Research Fellowship in the year of 2019 and is Fellow of Indian National Academy of Engineering (INAE), Institution of Engineers (India), Indian Society of Earthquake Technology (ISET), and Coalition for Disaster Resilient Infrastructure (CDRI). At present, he is serving as an Editor-in-Chief for the *Indian Society of Earthquake Technology* (ISET) Journal and *Indian Concrete Journal*.

Effect of High Temperature on the Calcinated Clay-Limestone Cement Concrete (LC^3)

S. M. Gunjal and B. Kondraivendhan

Abstract In cement manufacturing, a lot of CO_2 emitted into the atmosphere creates a global warming problem. To solve this problem partly, calcined clay-limestone cement concrete can be used. The impact of high temperature on calcinated clay-limestone cement concrete (LC^3) is studied in this paper. LC^3 is innovative ternary mixed cement made from a mixture of 30% low-grade calcined clay, 15% limestone, and gypsum 5 percent, along with 50% cement clinkers. That means 50% of cement clinkers are replaced by supplementary cementitious materials which is advantageous for reducing carbon dioxide (CO_2) emissions during cement manufacturing. In the present study, M25 grade concrete are prepared by calcined clay-limestone cement. After 28 days, prepared samples were subjected to 100, 200, 400, 600, and 800 °C temperature. The surface texture and compressive strength (CS) tests were performed on the cubes of size 100 × 100 × 100 mm^3. The result displays that the CS after 200 °C decreases rapidly, and after '400 °C,' major losses take place. Once the temperature touched 400 °C, minute visible cracks began to appear on all the grades of cube surface. All test results were compared with concrete prepared by ordinary Portland cement (OPC).

Keywords Elevated temperature · Calcinated clay · Heating · Color change · Compressive strength

1 Introduction

Concrete typically exhibits good fire resistance properties also have a wide range of uses in buildings and other constructed infrastructures. Where fire safety is an absolute priority, developed countries need much concrete in their construction [4].

S. M. Gunjal (✉) · B. Kondraivendhan
Department of Civil Engineering, S.V.N.I.T, Surat 395007, India

S. M. Gunjal
Department of Structural Engineering, Sanjivani College of Engineering, S.P.P.U, Kopargaon, Maharashtra 423603, India

B. Kondraivendhan et al. (eds.), *Sustainable Building Materials and Construction*,
Lecture Notes in Civil Engineering 222,
https://doi.org/10.1007/978-981-16-8496-8_1

Calcinated clay-limestone concrete (LC^3) is an innovative type of cement concrete that has been shown to have high later-age strength [13]. The development of LC^3 cement concrete can provide a workable, tough, and commercial alternative to the concrete industry [2]. Scrivener [13] discovered that future cement such as LC^3 contributes to the decrease of CO_2 release related to the creation of cement. At temperatures of 10, 20, 40, and 60 °C found that, although the major variation in the Ca/Si ratio and Al content, the water content decreases as the temperature rises and the evolution of the water content between plain cement and LC^3 was very similar [3]. For the rising temperature (250, 500, 750, and 950 °C), limonite concrete has the maximum Young modulus, density, smallest absorption percent, and maximum value of compressive strength [11]. Spewing water for 30 min or more over elevated temperature (200–800 °C), concrete was more severe of compressive and split tensile strength loss due to natural cooling [8]. Sancak et al. [12] prepared both lightweight concrete and normal weight concrete subjected to high temperature (20, 100, 400, 800, 1000 °C) curing. The authors found that the compressive strength and weight loss are more in normal-weight concrete compared to lightweight concrete. Using two cooling methods, viz freezing at normal temperature and sprinkle water over higher temperature, concrete-containing palm oil fuel ash reported that it has a higher compressive strength than normal concrete [6].

The aim of this research is to prepare limestone calcined cement concrete (LC^3). The prepared LC^3 concrete is compared with normal concrete at temperatures of 100, 200, 400, 600, and 800 °C. The physical and chemical changes under these temperatures such as weight loss, surface structure, and compressive strength of 100 × 100 × 100 mm^3 size of cubes have been observed.

2 Material

In the preparation of LC^3, ground calcined clay, 53 grade of ordinary Portland cement (OPC) confirming IS 12269-2013, ground limestone powder, and imported gypsum have been used. Table 1 gives the chemical study of all of these materials using XRF techniques. Fineness modulus (FM) of sand of 2.55 was used as a fine aggregate. Basalt-crushed stone aggregates of nominal scale 20 and 12.5 mm were used as a coarse aggregate in the proportion of 70:30 verifying IS 383–1970. The specific gravity of calcined clay is reported as 2.6. The materials used for the preparation of the LC^3 system contain finer particles as compared to OPC.

2.1 Mix Design of Concrete System

The objective of this study is to evaluate compressive strength of concrete prepared by OPC and LC^3 at elevated temperature. IS 10262:2009 was used to design for M25 grade of concrete mix with w/c of 0.5 and cement content of 380 kg of concrete per

Table 1 Oxides constituent of materials

Chemical oxide (%)	Al_2O_3	SiO_2	K_2O	CaO	TiO_2	Na_2O	MgO	P_2O_5	SO3	Fe_2O_3	Loss of ignition
Calcined clay	44.32	53.75	0.004	0.483	1.707	0.447	0.19	0.078	0.03	0.415	0.30
OPC	3.6	22.07	0.7	63.25	0.007	0.3	1.08	0.008	–	4.69	1.140
Limestone powder	2.15	11.42	0.82	44.82	0.11	0.13	2.10	0.03	0.18	1.97	36.14
Gypsum	0.62	2.77	0.04	32.53	0.04	0.008	1.25	0.03	38.72	0.58	22.95

Table 2 Mix design of M25 grade of concrete

Sr. no	Grade	Mix Id	W/C	Cement kg/m^3	Aggregate (Fine) kg/m^3	Aggregate (Coarse) kg/m^3		Slump (mm)
						12.5 mm	20 mm	
1	M25	M25-OPC	0.50	OPC-380	756.00	340.20	793.80	100
		M25-LC^3	0.50	LC^3-380	756.00	340.20	793.80	85

cubic meter. The filled concrete cubes were kept 24 h at surrounding temperature after that cube was placed in water at 28 days. To monitor the temperature effect on compressive strength, the concrete cubes were subjected to temperatures of 100, 200, 400, 600, and 800 °C for 3 h. The detail of the mix design of M25 grade of concrete was given in Table 2.

2.2 Heating Details

The concrete cubes of 100 mm × 100 mm × 100 mm size were heated to high temperatures at the age of 28 days. As illustrated in Fig. 1, an automatic electric furnace was used. The furnace was rated at 1200 °C and had a temperature controller attached to it. The specimens were subjected to a stable state after being exposed to the highest temperatures of 100, 200, 400, 600, and 800 °C [10]

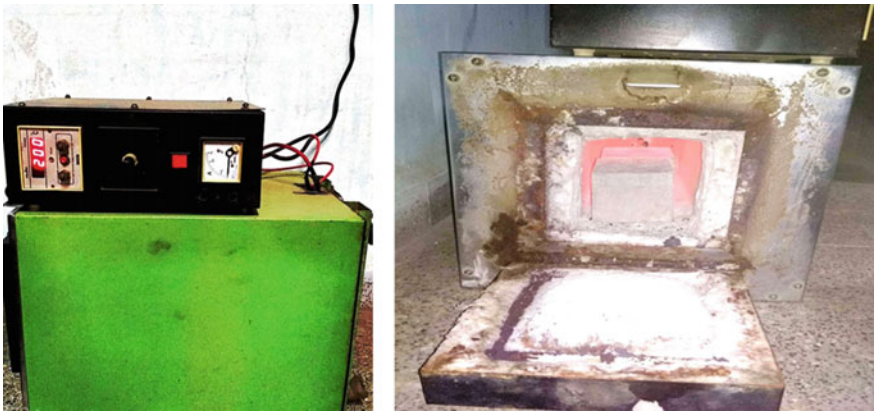

Fig. 1 Automatic electric furnace used for 100–800 °C temperature

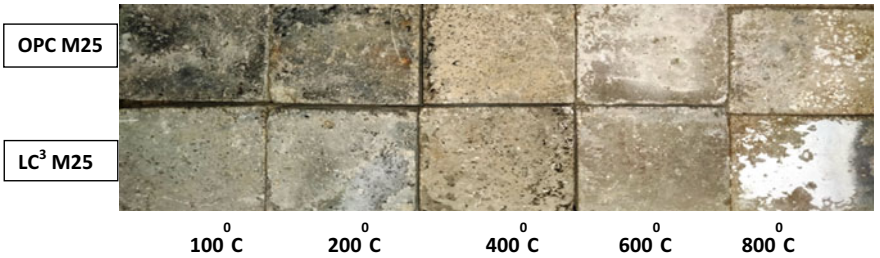

Fig. 2 M25 grade of concrete surface cube after elevated temperature

3 Results and Discussion

3.1 Shape of Cracks and Color Changes of Cubes

Cracks appeared on M25-OPC and M25-LC^3 concrete cubes as the temperature increased from 100 to 800 °C, as illustrated in Fig. 2. M25 grade of concrete, prepared with OPC and LC^3 cement, were subjected to a temperature of 200 °C, and no visible changes on the concrete cubes surface were observed. When the temperature reached 400 °C, noticeable minute cracks appeared on the M25-OPC concrete surface cubes. At 600 °C, the concrete cube molds turned a whitish color, a hairline crack appeared, and the concrete became a whitish-gray color after reaching 800 °C. However, as compared to M25-LC^3 at 400 and 600 °C, the color of concrete cubes and visualization of crack pattern observation was slightly less which is because of pozzolanic behavior, compactness, and strength of LC^3 materials at later age. Temperature changes cause chemical changes, degradation, and the appearance of cracks, voids, and penetrating paste to shrinkage. When the temperature was raised to 800 °C, the color of the concrete cube changed to a light creamy color, and the cracks became deeper and wider. However, the M25 grade of OPC has more deep and wide cracks than the LC^3 grade. In normal concrete, same trends were observed by the study of [1].

3.2 Compressive Strength

Figure 3 illustrates the CS of concrete for M25 grade at elevated temperatures under normal cooling. At normal temperature (27 °C), the CS of M25-OPC concrete cubes was 26.12 MPa, and after 100 °C, it was 24.11 MPa similarly, for 200 °C to 800 °C was 20.02 MPa, 16.98 MPa, 12.66 MPa and 9.15 MPa, respectively. As the temperature was increased, the compressive strength decreased. The percentage decrease for M25-OPC concrete for 100 °C was 7.69% and for 200 °C, 400 °C, 600 °C, and 800 °C was 23.12%, 34.99%, 51.53%, and 64.96%, respectively. The percentage

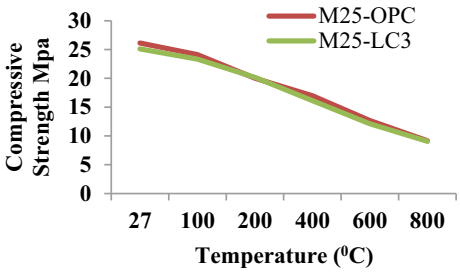

Fig. 3 Compressive strength of M25 grade of concrete cube at high temperature

decrease for M25 -LC^3 concrete for 100 °C was 7.08% and for 200 °C, 400 °C, 600 °C, and 800 °C was 19.71%, 35.80%, 51.77%, and 63.91%, respectively.

When the temperature was above 100 °C, the compressive strength reduced by a small fraction due to evaporation of freely available moisture [7]. At temperatures over 200 °C, dehydration such as the leakage of chemically binding water from the C–S–H becomes evident which may cause strength loss at that temperature [5]. At around 400–600 °C, calcium hydroxide, essential mixtures in cement paste, dissociates, causing concrete to shrink and a greater reduction in strength (Mehmet [9]. The decomposition of $Ca(OH)_2$ and C–S–H gel caused the strength losses to increase significantly when the temperature reached 800 °C. Compressive strength after 200 °C decreases rapidly after 400 °C and major loss take places [4].

When the temperature increases, the percentage reduction in compressive strength of M25-LC^3 concrete was less than M25-OPC grade of concrete. This can be clarified with the consideration of compactness and pozzolanic behavior of LC^3 material and the synergetic reaction between calcined clay and calcium carbonate (limestone). This reaction leads to carbo aluminate hydrates which fills the space and contribute to the development of strength in LC^3 concrete [13].

4 Conclusions

- M25-OPC concrete cubes display a more crack pattern when the temperature increases from 100 to 800 °C. Similarly, the color of the concrete cube changed to light creamy as the temperature increased to 800 °C and cracks were deep and broad in comparison with M25-LC^3 concrete cubes.
- M25-LC^3 concrete cubes have more resistance to temperature than M25-OPC concrete cubes, regarding compressive strength as temperature increases. This can be compactness and pozzolanic behavior of LC^3 material and the synergetic reaction between calcined clay and limestone. It shows that LC^3 concrete has good capability to performance at higher temperature.

References

1. Arioz O (2007) Effects of elevated temperatures on properties of concrete. Fire Saf J 42(8):516–522. https://doi.org/10.1016/j.firesaf.2007.01.003
2. Avet F, Scrivener K (2018) Investigation of the calcined kaolinite content on the hydration of Limestone Calcined Clay Cement (LC3). Cem Concr Res 107:124–135. https://doi.org/10.1016/j.cemconres.2018.02.016
3. Avet F, Scrivener K (2020) Effect of temperature on the water content of C-A-S-H in plain Portland and blended cements. Cem Concr Res 136:1–6. https://doi.org/10.1016/j.cemconres.2020.106124
4. Caetano et al (2019) Effect of the high temperatures on the microstructure and compressive strength of high strength fibre concretes. Constr Build Mater 199: 717–736. https://doi.org/10.1016/j.conbuildmat.2018.12.074
5. Haridharan MK, Natarajan C, Chen SE (2017) Evaluation of residual strength and durability aspect of concrete cube exposed to elevated temperature. J Sustain Cement-Based Mater 6(4):231–253. https://doi.org/10.1080/21650373.2016.1230898
6. Ismail M, Elgelany Ismail M, Muhammad B (2011) Influence of elevated temperatures on physical and compressive strength properties of concrete containing palm oil fuel ash. Constr Build Mater 25(5):2358–2364. https://doi.org/10.1016/j.conbuildmat.2010.11.034
7. Isteita M, Xi Y (2017) The effect of temperature variation on chloride penetration in concrete. Constr Build Mater 156:73–82. https://doi.org/10.1016/j.conbuildmat.2017.08.139
8. Kodur V, Khaliq W (2011) Effect of temperature on thermal properties of different types of high-strength concrete. J Mater Civ Eng 23(6):793–801
9. Mehmet Canbaz (2014) The effect of high temperature on reactive powder concrete. Constr Build Mater 70: 508–513. https://doi.org/10.1016/j.conbuildmat.2014.07.097
10. Nadeem A, Memon SA, Lo TY (2014) The performance of fly ash and Metakaolin concrete at elevated temperatures. Constr Build Mater 62:67–76. https://doi.org/10.1016/j.conbuildmat.2014.02.073
11. Sakr K, El-Hakim E (2005) Effect of high temperature or fire on heavy weight concrete properties. Cem Concr Res 35(3):590–596. https://doi.org/10.1016/j.cemconres.2004.05.023
12. Sancak E, Dursun Sari Y, Simsek O (2008) Effects of elevated temperature on compressive strength and weight loss of the light-weight concrete with silica fume and superplasticizer. Cement Concr Compos 30(8):715–721. https://doi.org/10.1016/j.cemconcomp.2008.01.004
13. Scrivener KL (2014) Options for the future of cement. Indian Concrete J 88(7): 11–21. http://www.lc3.ch/wp-content/uploads/2014/09/0851_ICJ_Article.pdf

Prediction of Compressive Strength of Fly Ash-Based Geopolymer Concrete Using AI Approach

Mandha Sandhya and G. Mallikarjuna Rao

Abstract The present paper describes the application of artificial neural networks (ANN) as one of the artificial intelligence (AI) approaches for predicting the compressive strength of fly ash-based geopolymer concrete. In the proposed model, amount of fly ash, alkaline solution (combination of sodium hydroxide and sodium silicate solution), coarse aggregate content, fine aggregate content, molarity, water content, superplasticizer, curing time, temperature and age was considered as the ten input parameters, while the compressive strength was the output parameter. Modelling has been carried out using MATLAB, and training and validation processes are carried out for the corresponding mix proportions. Model performance was observed by changing the number of neurons in the hidden layers. The performance of this model was evaluated using a set of three metrics, including correlation coefficient (R), mean absolute error (MAE) and root mean square error (RMSE). With the less amount of data, by changing the neurons, best results could be obtained. The predicted results are near agreement with the experimental results, and ANN acts as a promising tool for the prediction of compressive strength with tiny errors.

Keywords Geopolymer concrete · Fly ash · Artificial intelligence · Artificial neural networks

1 Introduction

The term artificial intelligence (AI) was invented by John McCarthy to designate the development of human thinking as a mechanical operation of symbols was started in the 1940s. Artificial intelligence (AI) denotes the replication of human intelligence in machines that are involuntary to deliberate like humans and mimic their actions [4].

M. Sandhya (✉) · G. Mallikarjuna Rao
Department of Civil Engineering, Vardhaman College of Engineering, Hyderabad, Telangana, India

G. Mallikarjuna Rao
e-mail: mallikarjuna@vardhaman.org

B. Kondraivendhan et al. (eds.), *Sustainable Building Materials and Construction*,
Lecture Notes in Civil Engineering 222,
https://doi.org/10.1007/978-981-16-8496-8_2

In the civil engineering field, several problems, particularly in engineering design, were influenced by various uncertainties which could be resolved not only in need of mathematics, physics and mechanics calculations but also depend on the experience of practitioners [13]. This knowledge and involvement are inconsistently incomplete and indefinite, and they cannot be fingered by outmoded procedures. However, artificial intelligence has its peculiar pre-eminence [14]. It can resolve composite complications to the levels of specialists by means of replicate specialists. All in all, artificial intelligence has a comprehensive claim projection in the practice of civil engineering [11]. In this study, prediction of compressive strength of fly ash-based geopolymer concrete is carried out. Various soft computing artificial intelligence techniques are used for prediction, among those, all artificial neural networks are used widely due to its less complexity and higher agreement between input and output variables [3]. Artificial neural networks are algorithms pretending the functioning of human brains [12] in which inputs are converted to outputs in a neural network [9].

The incentive for the growth of neural network knowledge curtailed from the yearning to develop an artificial system that could accomplish "intelligent" tasks analogous to those performed by the human brain. The new field in computing incorporates that it stores the information as patterns and problems can be resolved by using those patterns [2]. ANNs perform best when they do not generalize beyond the extreme values of the data used for standardization [8]. Finding compressive strength was a time-consuming process, and the need for raw materials in the laboratory is more and cost efficient. By considering all these problems, researchers focus on soft computing techniques, which will perform by saving time, materials and money [6]. ANN is used as a strong prediction tool with less computational error.

2 Artificial Neural Network Architecture

Model parameters are accustomed in a model standardization phase called "training" or "learning" to diminish the error between the actual measured outputs and those predicted by ANN for a precise data set (the training set) [10]. In this study, feed forward backpropagation network system was used in ANN, in which the errors were proliferated backwards by regulating the neurons [5].

Assuming that the network has the inputs (X_1, X_2, X_3,…, X_n) connected with the K-th neuron to the hidden neuron by adjusting weights (W_{k1},W_{k2},W_{k3},…,W_{kn}), where O_k is the output neuron, the summing junction is used to sum all the weights connected with the neuron K, and the total task was completed by using activation function [7].

$$u_k = \sum_{i=1}^{n} X_j W_{jk} + b_k$$

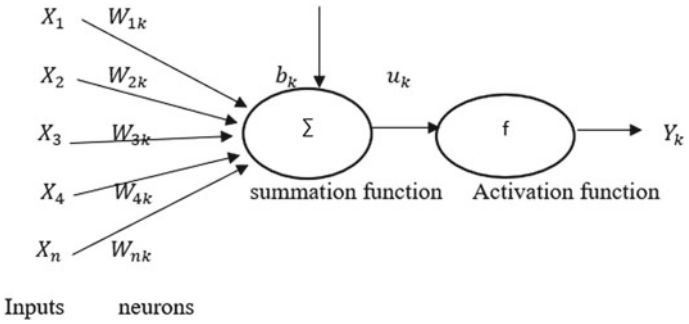

Fig. 1 Artificial neuron diagram

where f is the transfer function, b_j is the bias factor for the weighted input K-th neuron, and the out function can be written as follows:

$$O_k = f(u_k) = f\left(\sum_{i=1}^{n} X_j W_{jk} + b_k\right)$$

Figure 1 represents the weights, outputs and inputs of an artificial neuron.

Various algorithms that can be instigated in artificial neural network are Levenberg–Marquardt backpropagation algorithm, BFGS quasi-Newton backpropagation algorithm, Powell-Beale conjugate gradient backpropagation algorithm, Powell conjugate gradient backpropagation algorithm, Polak–Ribiere conjugate gradient backpropagation algorithm and one step secant backpropagation algorithm (Azar 2013). In this study, Levenberg–Marquardt backpropagation algorithm is used due to its speed and efficiency.

2.1 Neural Network System Methodology

The simple elements function in parallel with neural expert system [1]. These simple essential elements act as biological neurons. The information was relocated between these neurons. Figure 2 characterizes the artificial neuron development with the inspiration of biological neuron.

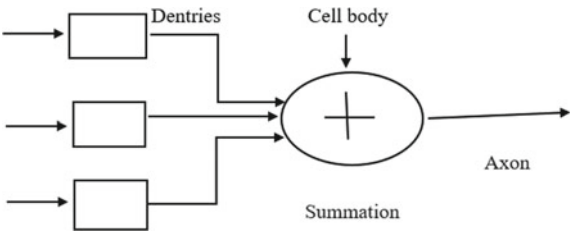

Fig. 2 Development of artificial neuron with the inspiration of biological neuron

The connection between the elements was used for the determination of network function.

Similarly, the modelling should be involved in three stages. Those are training, testing and implementation. In training stage, the given input data should be trained by adjusting neurons to get a specific target output data. While in the training process, the network should be trained in a manner to give the output with less predicting error, and the layers should be created in between input and output to make the neuron clustering. With this, the weights are adjusted in between layers trained perfectly to give the desired specific output.

2.1.1 Data Collection

For this study, about 50 experimental mix values of fly ash-based geopolymer concrete were collected by referring to previous literatures. For this, specific input parameters were fixed in a way to get the better-predicted output. The data can be divided into three parts: about 60% of data is used for training, 20% is used for validation, and remaining 20% is used for prediction. Most of the data was used for training because to train the network very well so that the neurons and the layers adjusted weights and learn from that data. MATLAB tool was used for the complete modelling.

The number of input and output variables and the range of variables used in this study are represented in Table 1.

2.1.2 Development of Neural Network Model

Neural network model was developed by arranging neurons in the hidden layer. The neural network model was developed by changing the number of neurons in the hidden layer, and the performance of the model was observed by changing the number of neurons in the hidden layer. Total eight neural network models were developed for the above represented data. The first network model ANN-I was developed by using only one hidden layer and arranged one neuron in the layer. The second neural network model ANN-II was developed by using two neurons in the hidden layer. Third network model ANN-III was developed by using three neurons in the hidden layer. Fourth neural network model ANN-IV was developed by using four neurons in the hidden layer. Fifth model ANN-V was developed by using five neurons in the layer. Sixth neural network model ANN-VI was developed by using six neurons in the hidden layer, and seventh model ANN-VII was developed by using seven neurons in the hidden layer. Finally, seven neural network model was developed by using eight neurons in the hidden layer. Table 2 represents the variables used for all the eight models (Figs. 3, 4, 5, 6, 7, 8 and 9).

Table 1 Mix values of fly ash-based GPC

	Input variables										Output variables
S .NO	Fly ash (kg/m^3)	Fine aggregate (kg/m^3)	Coarse aggregate (kg/m^3)	Alkaline solution (kg/m^3)	Molarity	Water (l/m^3)	Super plasticizer (kg/m^3)	Time (Hr)	Temperature (^{o} C)	Age (days)	Compressive strength (MPa)
1	408	554	1294	154.5	14	16.5	0	24	60	3	42
2	408	647	1201	144	12	14.3	6.1	24	60	7	40
3	408	554	1294	144	14	20.7	6.1	24	60	21	65
–	–	–	–	–	–	–	–	–	–	–	–
–	–	–	–	–	–	–	–	–	–	–	–
–	–	–	–	–	–	–	–	–	–	–	–
48	408	647	1201	144	14	17.6	6.1	24	60	7	43
49	408	647	1201	160	8	14.3	6.1	24	60	7	75
50	408	554	1294	144	14	0	6.1	24	90	90	89
Max	408	554	1201	144	8	0	0	4	30	3	17
Min	476	647	1294	168	14	20.7	8.2	48	90	90	89

Table 2 Usage of various variables in ANN model

Variables	Values
Number of input neurons	10
Number of output neurons	01
Rate of learning	0.01
Momentum coefficient	0.1
Epochs	1000

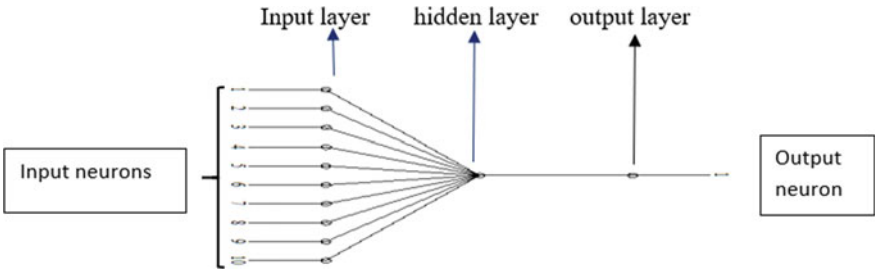

Fig. 3 ANN-I architecture

Fig. 4 ANN-II architecture

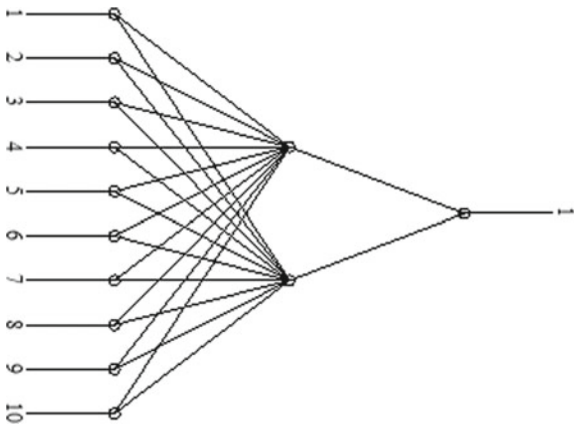

For the above models, each input neurons is connected with every neuron in the hidden layer. Trial and error method was used in the application of changing neurons in the hidden layer. The best neuron adopting technique was observed in this study to minimize the error and to obtain the speedy convergence.

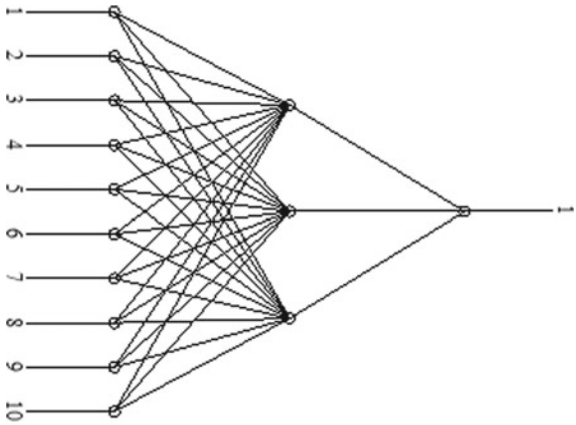

Fig. 5 ANN-III architecture

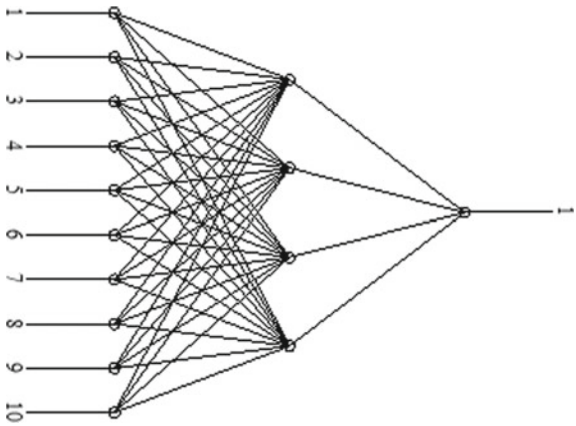

Fig. 6 ANN-IV architecture

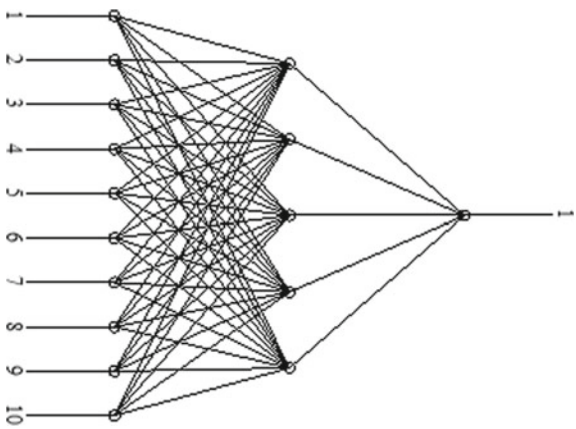

Fig. 7 ANN-V architecture

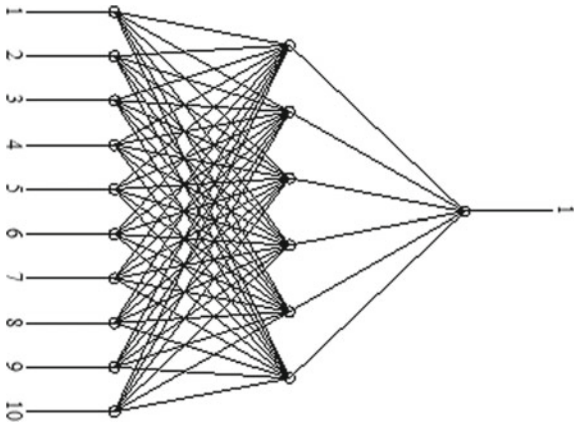

Fig. 8 ANN-VI architecture

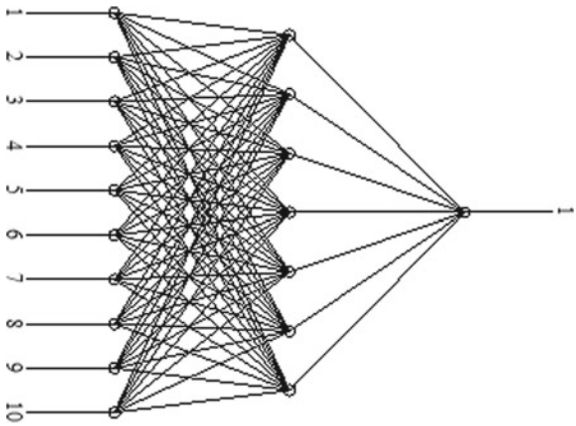

Fig. 9 ANN-VII architecture

3 Results and Discussion

The input parameters were selected in a manner that they contain all relevant information to get the target output. Training, validation and prediction processes are carried out. The three metrics correlation coefficient (R^2), mean absolute percentage error (MAPE) and root mean square error (RMSE) were used to validate the performance of ANN. Equations 1, 2 and 3 are used to calculate these three metrics.

$$R^2 = \left(\frac{\sum_{i=1}^{n} (M_i - N_i)2}{\sum_{i=1}^{n} N_i^2} \right) \tag{1}$$

$$\text{MAPE} = \frac{1}{n} \sum_{i=1}^{n} \left| \frac{M_i - N_i}{M_i} \right| \times 100 \tag{2}$$

$$\text{RMSE} = \sqrt{\frac{1}{n}\sum_{i=1}^{n}(M_i - N_i)^2} \tag{3}$$

where n = no. of data sets used in training and testing phase.
M_i = actual strength values.
N_i = predicted strength values.

As the calculations of numerical parameters of ANN-I to ANN-VII are represented in Table 3, Figs. 10, 11, 12, 13, 14, 15 and 16 characterize the regression curves of ANN-I to ANN-VII models.

Table 3 Numerical calculations of ANN-I to ANN-VII models

Models	R^2		MAPE		RMSE	
	Training	Testing	Training	Testing	Training	Testing
ANN-I	0.67	0.59	7.852	8.102	7.909	8.366
ANN-II	0.79	0.71	6.001	7.236	6.332	7.529
ANN-III	0.86	0.83	4.352	4.623	4.418	4.731
ANN-IV	0.91	0.89	1.093	1.996	1.119	2.001
ANN-V	0.97	0.94	0.619	0.997	0.782	0.998
ANN-VI	0.87	0.83	4.464	4.795	4.547	5.019
ANN-VII	0.79	0.75	6.000	6.751	6.253	6.985

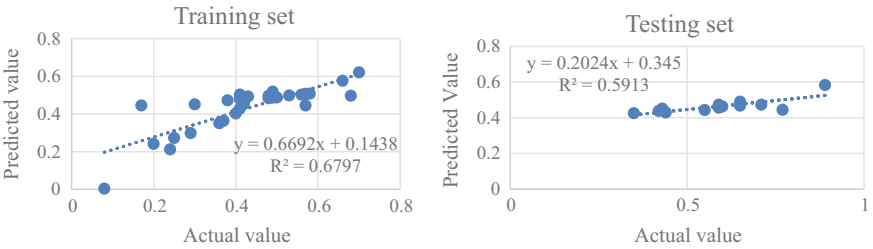

Fig. 10 Characterization of regression curves of ANN-I model

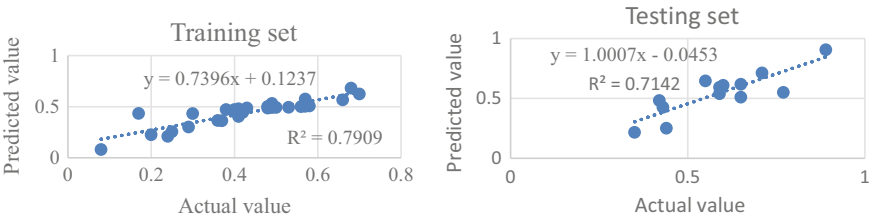

Fig. 11 Characterization of regression curves of ANN-II model

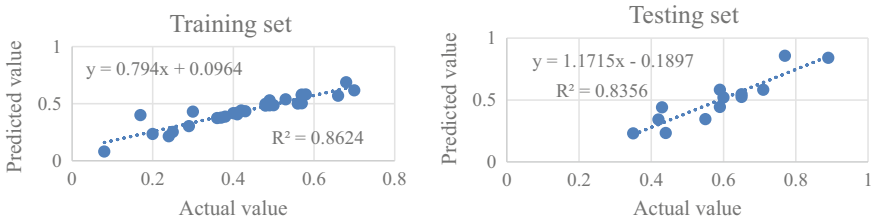

Fig. 12 Characterization of regression curves of ANN-III model

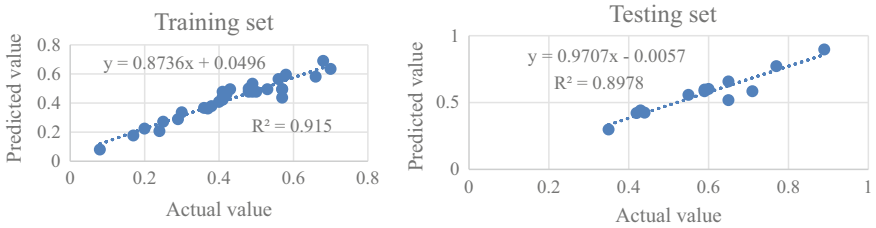

Fig. 13 Characterization of regression curves of ANN-IV model

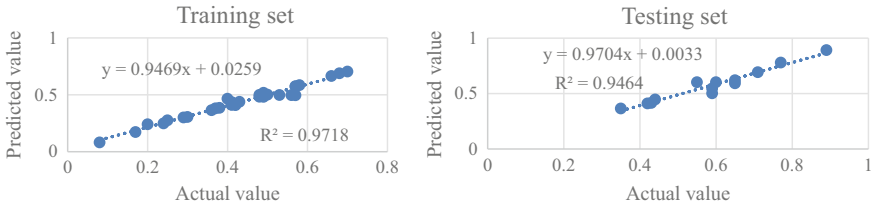

Fig. 14 Characterization of regression curves of ANN-V model

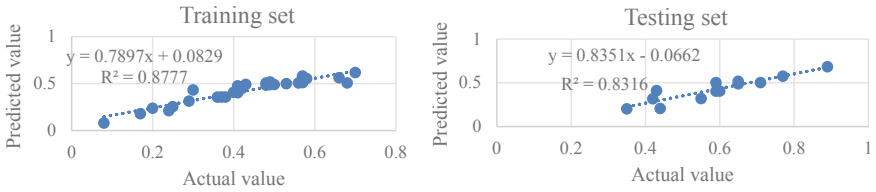

Fig. 15 Characterization of regression curves of ANN-VI model

ANN-V model shows the best performance with the R^2 value of 0.97 and 0.94 in the training and testing phases. This model predicts the compressive strength with very less error. Also, it exhibits the best correlation coefficient value and lesser value of MAPE and RMSE values. It is observed that the half the number of neurons used as that of input neurons signifies the best result; in this study, 10-5-1 architecture

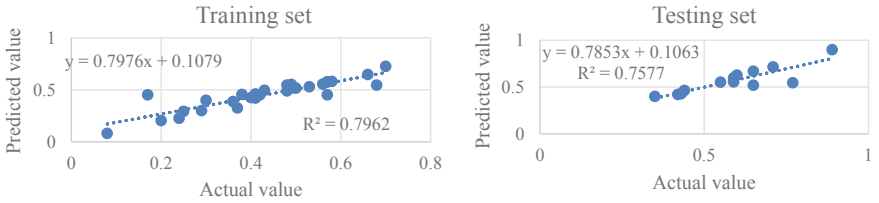

Fig. 16 Characterization of regression curves of ANN-VII model

gives the best result. The prediction accuracy of ANN-V was good, and above 90% accuracy is shown by this model. From this study, it is observed that not only training process but also change in the number of neurons in the hidden layer affects the performance of ANN model.

4 Conclusions

This study is an effective approach for the prediction of compressive strength of fly ash-based geopolymer concrete. The models prepared in this study are based on the number of neurons in hidden layer. For the less experimental data, using less termination epochs and changing the number of neurons in the hidden layer observed the best prediction accuracy in the models. As half the number of neurons used with respect to number of input neurons displays a good result, ANN-V model shows best compatibility in between input and output neurons. The obtained error in this model was very less and indicates that there is a good convergence between layers, and the weights are adjusted very well. From this study, it was concluded that ANN shows better performance in the prediction due to the nonlinear relationship between the input and output variables, and change in the performance was observed by changing the number of neurons in hidden layers. In order to go with costly experimental investigation, ANN acts as a strong prediction tool and shows the better accuracy with the minimum amount of data.

References

1. Bahrammirzaee A (2010) A comparative survey of artificial intelligence applications in finance: artificial neural networks, expert system and hybrid intelligent systems. Neural Comput Appl 19(8):1165–1195
2. Cousins KC, Robey D (2005) Human agency in a wireless world: patterns of technology use in nomadic computing environments. Inf Organ 15(2):151–180
3. Dao DV, Ly HB, Vu HLT, Le TT, Pham BT (2020) Investigation and optimization of the C-ANN structure in predicting the compressive strength of foamed concrete. Materials 13(5):1072
4. Favro T (2018) Generation robot: a century of science fiction, fact, and speculation. Simon and Schuster

5. Ilin R, Kozma R, Werbos PJ (2008) Beyond feedforward models trained by backpropagation: a practical training tool for a more efficient universal approximator. IEEE Trans Neural Netw 19(6):929–937
6. Liu Y, Farnsworth M, Tiwari A (2017) A review of optimisation techniques used in the composite recycling area: state-of-the-art and steps towards a research agenda. J Clean Prod 140:1775–1781
7. Meesaraganda LP, Saha P, Tarafder N (2019) Artificial Neural Network for strength prediction of fibers' self-compacting concrete. In*: Soft computing for problem solving*. Springer, Singapore, pp 15–24
8. Minns AW, Hall MJ (1996) Artificial neural networks as rainfall-runoff models. Hydrol Sci J 41(3):399–417
9. Okayama Y (1991) A primitive study of a fire detection method controlled by artificial neural net. Fire Saf J 17(6):535–553
10. Prasad R, Deo RC, Li Y, Maraseni T (2018) Ensemble committee-based data intelligent approach for generating soil moisture forecasts with multivariate hydro-meteorological predictors. Soil Tillage Res 181:63–81
11. Shokri M, Tavakoli K (2019) A review on the artificial neural network approach to analysis and prediction of seismic damage in infrastructure. Int J Hydromechatronics 2(4):178–196
12. Trad A, Kalpić D (2017) A neural networks portable and agnostic implementation environment for business transformation projects the basic structure. In: 2017 IEEE international conference on Computational Intelligence and Virtual Environments for Measurement Systems and Applications (CIVEMSA). IEEE, pp 153–158
13. Vesilind PA (2010) Engineering peace and justice: the responsibility of engineers to society. Springer Science & Business Media
14. Zavadskas EK, Antucheviciene J, Vilutiene T, Adeli H (2018) Sustainable decision-making in civil engineering, construction and building technology. Sustainability 10(1):14

Experimental Investigation on Development of Compressive Strength of High-Strength Geopolymer Concrete Containing M-Sand

Gaurav Jagad, C. D. Modhera, and Dhaval Patel

Abstract The serious issue related to more consumption of cement-based concrete because of the CO_2 emission, while manufacturing of the cement. The Portland cement manufacturing causes the emissions of pollutants in atmosphere. By use of industrial by products in construction industry will reduce these harmful effects. The incorporation of Ground Granulated Blast Furnace Slag (GGBS) in construction field is the best suitable solution to utilize waste as a binder. Also, the demand of river sand is so high and the resources of natural river sand going to over and become costly and finally become expensive and rare. Because of these illegal excavations of river sand have occur and natural resources will be destroyed. To overcome this issue in eco-friendly aspect, in this research, the incorporation of manufactured sand instead of river sand can be the better solution in construction industry. The ultimate objective of this study is to incorporate the locally available material in high-strength geopolymer concrete like GGBS as a binder and manufactured sand as a fine aggregate.

Keywords High-strength geopolymer concrete · Manufactured sand · Ground granulated blast furnace slag

1 Introduction

Geopolymer concrete is considered very strong in nature and can withstand harsh conditions and existing temperatures. Compared with steel fiber, GGBS in low-calcium geopolymer concrete exhibits particularly high-pressure resistance and toughness [1]. Facts have proved that, compared with Portland cement concrete, low-calcium fly ash-based geopolymer concrete is extremely cost-effective and eliminates greenhouse gases harmful to sustainable development. Concrete is the main constructing material which is the second highest consumption by human after the water and the main component of concrete is Portland cement. In a new aspect,

G. Jagad (✉) · C. D. Modhera · D. Patel
Sardar Vallabhbhai National Institute of Technology, Surat, India

B. Kondraivendhan et al. (eds.), *Sustainable Building Materials and Construction*,
Lecture Notes in Civil Engineering 222,
https://doi.org/10.1007/978-981-16-8496-8_3

the biggest risk facing humans on earth today is global warming and environmental pollution. Cement production refers to the production of pollution caused by carbon dioxide emissions during the production process. To reduce construction costs, improve construction efficiency and increase the compressive strength of concrete, the industrial waste can be converted into usable building materials [2]. Every ton of cement produced will produce a ton of carbon dioxide, which will pollute the environment [3]. Therefore, the use of geopolymer concrete is best suitable solution for eco-friendly concrete.

Concrete is made of natural sand as fine aggregate. Due to the depletion of natural resources, the scarcity of natural sand, and due to environmental considerations, concrete manufacturers have to seek suitable alternative for fine aggregates [3]. One such alternative is "Manufactured sand," and it is made by sieving natural stone powder or crushed granite stone to adapt to the particle size of natural sand, to be used as fine aggregate [4].

The objectives of the present research study are to find the feasibility study on high-strength geopolymer concrete made with M-sand as fine aggregate. To determine the workability of wet concrete, the slump cone test was carried out and after that concrete has placed in 15 cm × 15 cm × 15 cm cube mold for 24 h. After 24 h, concrete demolding of cast concrete carried out and placed ambient curing for 7 days.

2 Experimental

2.1 Material and Mix Proportions

2.1.1 GGBS

GGBS is created by the method of quenching, which is the method of sudden ion slag cooling from a blast furnace using water or flux. A glassy, granular substance is obtained at the end of the process, and then dried and grinded into fine powder. GGBS is a form of off-white cement. It's often referred to as slag cement by the United Kingdom which it has used in Europe, United States and Asia. GGBS is a binding material which is used mainly in ready-mix concrete with a ratio of 30–70% to create an eco-friendly concrete [5]. GGBS used as the main binder material in this article and the chemical composition of GGBS in Table 3.

2.1.2 Alkaline Solution

For the geopolymerization process, alkaline solution plays main role. The combination of NaOH and Na_2SiO_3 was used as an alkaline solution. The sodium silicate (Na_2SiO_3) solution was purchased from Sadguru Chemicals, Veraval, Rajkot.

Table 1 Chemical composition of GGBS

Particulars	(SiO_2)	(Al_2O_3)	(Fe_2O_3)	(CaO)	(MgO)	(K_2O)	(Na_2O)	(TiO_2)
GGBS	32.19	8.59	2.8	38.09	5.5	0.4	0.26	8.89

Table 2 Properties of an aggregate

Size	Specific gravity	Impact value
20 mm	2.75	20%
10 mm	2.65	24%

Table 3 Sieve analysis of river sand and manufactured

Sieve size	10 mm	4.75 mm	2.36 mm	1.18 mm	600 micron	300 micron	150 micron	75 micron	Pan
River sand	100	99.8	93.3	55.95	33.8	11.9	5.7	0	0
M sand	100	100	97.8	90.7	70.4	16.95	12.2	0.5	0

2.1.3 Aggregate

Coarse Aggregate

Aggregates that were locally available has been used for the experiment work. Properties of aggregate are mentioned in following Table 4.

Fine Aggregate (River Sand and Manufactured Sand)

M-sand is nothing but artificial sand made by crushing rocks or granite for construction purposes. The physical and mineralogical properties of M-sand are different from those of natural river sand. Nowadays, due to environmental degradation, natural sand sources (such as river sand, pit sand, stream sand, sea sand and other sand used as concrete aggregates) have become scarce and depleted. The driving need for alternative aggregates in construction has given the source to M Sand. Sieve analysis and physical properties of both sand tabulated as in Tables 1 and 2, respectively (Tables 3 and 4).

Table 4 Physical properties of river sand and manufactured sand

	Fineness modulus	Specific gravity	Water absorption (%)	Loose density (kg/m^3)	Rodded density (kg/m^3)	Grading zone	Voids (%)	Moisture content (%)
River Sand	2.8	2.66	1.8	1.7	1.83	Zone II	36.09	1.9
M Sand	2.9	2.536	5.544	1.71	1.84	Zone II	32.57	0.15

3 Experimental Program

Concrete mix was prepared using GGBS as a binder and alkaline liquid. Alkaline solution has been prepared one day before casting. A solution with a Na_2O/SiO_2 ratio by mass of approximately 2 (say, $Na_2O = 14.7\%$, $SiO_2 = 29.4\%$, and water $= 55.9\%$) is recommended. Sodium hydroxide with 98% purity, in pellet form, was used. The concentration of NaOH in terms of molarity was 16M. In this study river sand as well as M-sand used as a fine aggregate content and as a coarse aggregate 20 mm as well as 10 mm sized aggregates were used. The wet mix was then placed in a mold and vibrated on a table vibrator. The mix proportions of geopolymer concrete as given in following Table 5.

3.1 Methodology

The ratio of Na_2SiO_3 to NaOH has taken as 3, in terms of Molarity concern 16M concentration has been selected. Binder to solution ratio taken as 0.5. River sand has completely eliminated by manufactured sand. GGBS used as a main binder content and 1% plasticizer used for better workability. Ambient curing for 24 h and then after demolding and applied only free air curing for cast concrete specimens [6] (Figs. 1, 2, 3, 4, 5 and 6).

Table 5 Mix proportion

Constituent	GGBS	Sand	Coarse aggregate	NaOH solution	Na_2siO_3	Extra water	SP
Quantity (kg/m^3)	480	625	1216	59	175	92.21	4.8

Fig. 1 NaOH flex

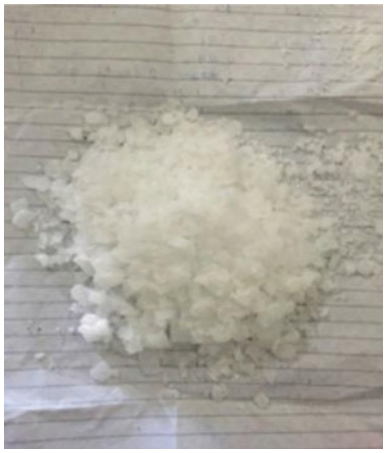

Fig. 2 Na_2SiO_3 solution

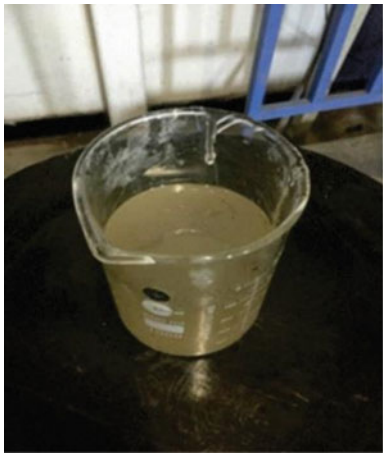

Fig. 3 Alkaline solution

Fig. 4 Machine mixing

Fig. 5 Measuring slump

4 Results and Discussion

The workability and compressive strength of high-strength geopolymer concrete have been carried out and the results shown in Figs. 5 and 6 as under.

Fig. 6 Compression test

- Workability of high-strength geopolymer concrete containing river sand is high as compared to high-strength manufactured sand concrete because the moisture content is already present in the river sand, and manufactured sand is free from moisture. Moreover, the river sand particles are rounded and manufactured sand particles are angular, and these angular shape particles make concrete denser.
- While using manufactured sand in concrete workability has been decreased. This issue can be overcome by incorporating superplasticizer content more than 1.5% or 2% in wet concrete mix.
- In compressive strength of both concrete seems good but as compared to river sand, manufactured concrete gave higher strength because of the angular particles of manufactured sand the bonding between subsequent particles is good (Figs. 7 and 8).

5 Conclusions

From the experimental study and investigations performed, the following conclusions were made,

- The improvement of compressive strength in M-sand concrete is approximately 10% at 7 days. So, it can be noted that the M-sand is the best alternative as a natural sand.
- The wet concrete mix of M-sand has low workability, because its particle shape is angular, which can be compensated by adding superplasticizer to the mixture.

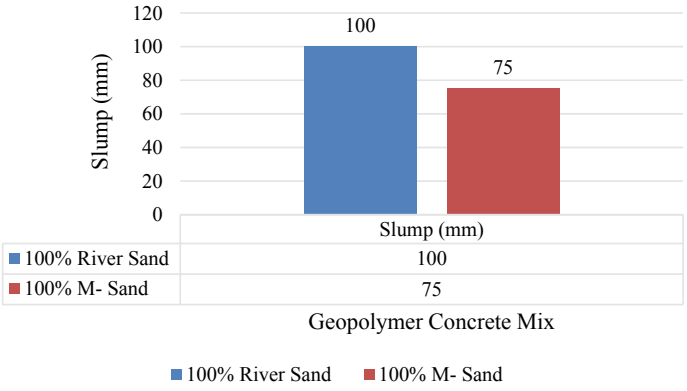

Fig. 7 Slump test results

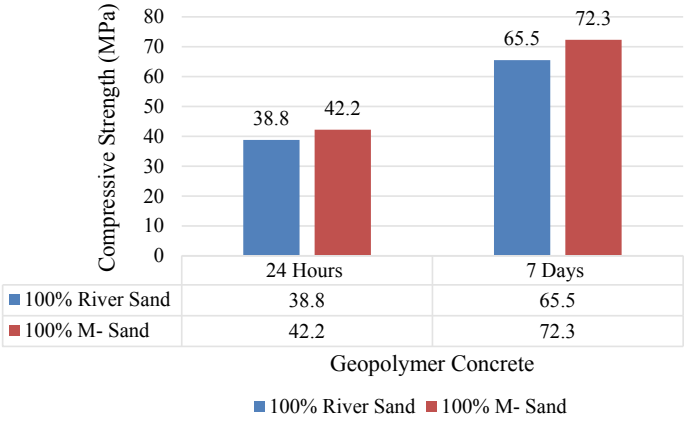

Fig. 8 Compression test results

- The water requirement of M-sand geopolymer concrete is high because of free moisture of M-sand is almost zero as compared to river sand.

References

1. Sashidar C et al (2015) Fresh and strength properties of self compacting geopolymer concrete using manufactured sand. Int J Chemtech Res 8(7): 183–190. ISSN: 0974-4290
2. Gomathi J, Doraikannan J (2016) Study on geopolymer concrete using manufactured sand. Int J Adv Res Trends Eng Technol (IJARTET)
3. Janani R, Revathi A (2015) Experimental study of geopolymer concrete with manufactured sand. Int J Sci Eng Technol Res (IJSETR) 4(4)
4. Abdul Aleem MI, Arumairaj PD (2013) Pollution free geopolymer concrete with m-sand

5. Nagajothi S, Elavenil S (2016) Strength assessment of geopolymer concrete using m-sand. Int J Chem Sci 14(S1): 115–126. ISSN 0972-768X
6. Topark-Ngarm P, Chindaprasirt P, Sata V (2014) Setting Time, strength, and bond of high-calcium fly ash geopolymer concrete. https://doi.org/10.1061/(ASCE)MT.1943-5533.0001157. © 2014 American Society of Civil Engineers

Experimental Study on the Performance of Manufactured Sand Over Natural Sand-Based Cement Mortar

Suraj D. Bhosale, Atul K. Desai, and Dhaval Patel

Abstract In the current construction industry, due to rapid changes in construction activities, the availability of natural sand has been exhausted. In addition, it may be necessary to transport high-quality sand from long distances, which increases construction costs. Therefore, it is inevitable to use alternative materials for fine aggregates, including recycled aggregates, artificial sand, and crushed stone powder. This article presents an experimental analysis on the effect of replacement of natural sand with manufactured sand (M-sand). The 1:2, 1:3, and 1:6 proportions are considered for mortar cube test. The use of variable river sand cement mortars substitute natural sand with M-sand at levels 20, 40, 60, 80, and 100% is typical cement mortar. Cube mold casted cured at ambient temperature and compressive strength measured, after 3 days, 7 days, and 28 days, Mortar cube measuring 70.7 × 70.7 × 70.7 mm was casted. In different stages of the replacement, the strength and toughness of natural sand and cements from M-sand were extracted. The compression strength of cement mortar improves with an increase in M-sand up to 80%. The strength and durability of cement mortar using natural sand and M-sand as fine aggregates in different substitution levels were evaluated and compared. Prism tests have shown that replacing the M-sand by 40–60% shows higher compressive strength. It was found that the water absorption rate increases as the replacement rate of M-sand increases. Therefore, M-sand is recommended as an alternative to natural river sand for up to 80% of cement mortar.

Keywords Manufactured sand · Compressive strength · Water absorption

1 Introduction

Masonry walls are used in nearly every form of built building worldwide because of its low cost, increased sound and heat separation, simple visibility, accessible local material, and professional workmanship [1]. Masonry is made up of two parts: the unit

S. D. Bhosale (✉) · A. K. Desai · D. Patel
Department of Civil Engineering, S.V. National Institute of Technology, Surat, India

B. Kondraivendhan et al. (eds.), *Sustainable Building Materials and Construction*,
Lecture Notes in Civil Engineering 222,
https://doi.org/10.1007/978-981-16-8496-8_4

Table 1 Property of cement

Material	Fineness	Standard consistency	Initial and final setting time	Specific gravity	Compressive strength (7 day and 28 days)
PPC Cement	3%	31%	150 min and 215 min	3.16	36.38 and 54.2 MPa

Note Physical and chemical properties were determined to be in line with IS 1489 (Part 1):1991 (Reaffirmed 2005) standards

and the mortar. Masonry is one of the oldest and most popular structure material [2]. Unreinforced masonry infill walls are typically used in reinforced concrete frame structures in earthquake-prone countries such as the United States, India, Turkey, and others. Infill walls can increase the structural efficiency by improving the lateral strength and stiffness of the structural framework up to a certain level of seismic load on which undesirable damage would occur [3]. Importance of masonry walls has been increased as it enhances the structural performance during lateral loading at the time of earthquake. The researcher gained attention toward mortar and brick [4]. The role of non-structural members in seismic design and structural performance is now well accepted by researchers and practicing engineers [5].

2 Material

2.1 Cement

Portland pozzolana cement (PPC) is used for this experiment. It can meet the consumer needs for higher strength mortar and is found very useful for reducing carbon footprint in manufacturing of cement (Tables 1 and 2).

2.2 Fine Aggregate

Either natural or M-sand aggregates. Grading is the job must be done coherent. The structure, absorption properties, and humidity must be monitored closely. The powder composition is contributed by particles smaller than 125 microns help in void feeling. To avoid segregation, a certain degree of fineness must be achieved.

Table 2 Chemical properties of cement

Chemical composition		CaO	SiO_2	Al_2O_3	Fe_2O_3	MgO	So_3	Loss on ignition	Na_2O	Ki_2O
Cement (% by weight)	Test result %	62.1	19.8	4.8	4.9	1.8	2.4	2.5	0.28	0.75
	IS-12269–2004					< 6	< 3	< 4		

Table 3 Property of fine aggregate

Material	Fineness	Water absorption (%)	Moisture contain (%)	Specific gravity	Bulk density loose	Bulk density rodded	Void ratio	Zone
River Sand	2.80	1.7	1.8	2.67	1.72	1.85	37.52	II
M-sand	2.87	5.32	0.2	2.54	1.74	1.86	32.40	II

2.3 Manufactured Sand

Manufactured sand is made by grinding hard granite stone and is used as a replacement for river sand in building or for other related items. Materials of adequate power, form, and consistency should be used. Manufactured sand (M-sand) has a particle size of less than 4.75 mm. It is manufactured sand that conforms to IS: 383-1970. Zone II has been confirmed by sieve analysis. Relevant gravity, water absorption, and fineness modulus of fine aggregate are measured in compliance with IS: 2386-1975 (Table 3).

2.4 Fly Ash Bricks

Bricks are a form of construction material that is made up of mixture of mud, fly ash, and other material in proper composition. Because of its appeals and superior features such as high-pressure resistance, toughness, excellent protection against fire, good thermal, and sound insulation, the bricks are widely used for construction, structural engineering, and landscape design. The physical properties are inspected by IS 3495(part 1):1992 (Table 4).

Table 4 Property of fly ash bricks

Water absorption	Presence of salts	Hardness	Size	Compressive strength
16%	12% deposit observe on surface	No impression was seen	254*178*102 Locally available	19.56 Mpa

3 Mix Procedure and Test Conducted

3.1 Casting of Specimen

3.1.1 Mortar Cubes

Cement mortar was prepaid by combining cement, water, and replacing natural sand with M-sand at various stages of substitution, including 20%, 40%, 60%, 80%, and 100%. For the mortar analysis, three mortar mixes were chosen: 1:2, 1:3, and 1:6. Molds with dimensions of 70.7 mm × 70.7 mm × 70.7 mm were used as shown in Fig. 1, resulting in a cross-sectional area of 5000mm^2. The compressive strength of mortars is determined after 3 days, 7 days, and 28 days of curing, and few tested sample are shown in Fig. 2.

Fig. 1 Mortar cube after demolding

Fig. 2 Failure pattern of mortar cube in compression

3.1.2 Masonry Prism

The specimen must be at least 40 cm tall and have a height to thickness ratio (h/t) of at least 2, but not more than 5, according to IS 1905-1987(2002). The specimen's height should be at least twice its thickness, or at least 15 inches, according to ASTM E447-1997. The overall height should be five times the thickness. The specimen was estimated to be based on both the code requirements and the brick size 102 mm × 178 mm × 550 mm. Five burned clay bricks make up the stack bonded masonry prism. As shown in Fig. 4, bricks are placed on top of the other with proper vertical orientation using cement mortar as a binding agsent. Figure 5 represents testing setup, and moreover, Fig. 6 shows failure pattern of bricks (Fig. 3).

Fig. 3 Brick compression test

Fig. 4 Brick prism stag casted

Fig. 5 Compression test on brick prism

Fig. 6 Failure pattern of brick prism

4 Results and Discussions

4.1 Compressive Strength of Mortars

Below Fig. 7 shows the compressive strength of the mortar cube with three different ratios 1: 2, 1:3, and 1:6 which clearly shows that 60% and 80% replacement of river sand with manufacturing sand enhances the compressive strength of mortar cube in 1:2 and 1:3 mortar ratio, respectively. Brick failure pattern of 1:2 mortar ratio is

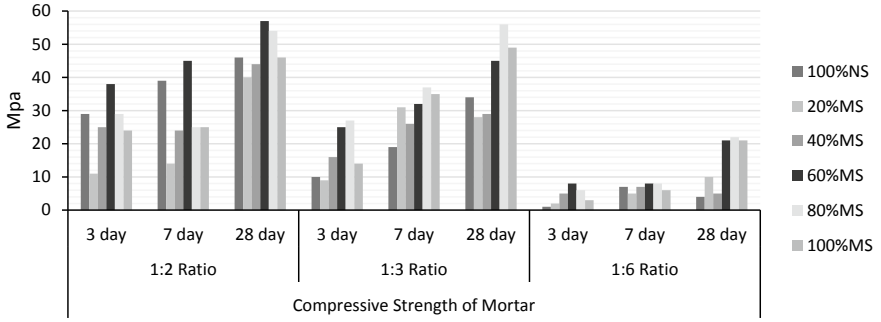

Fig. 7 Comparison of compressive strength of mortar cube of partial replaces M-sand (20, 40, 60, and 80, 100%) with natural sand for 1:2, 1:3, 1:6 ratio

shown in Fig. 6 which clearly indicates the crushing failure of brick in compression. It was also observed that in 1:3 mortar ratio the crack was propagated through a brick and mortar joint. Moreover, in 1:6 mortar ratio, brick mortar joint failure has been observed. It shows the different type failure according to strength of mortar and bricks.

5 Conclusions

Workability of manufacturing sand used in mortar is marginally lesser than river sand as its shape is angular and water absorption is more. It was also found that partial replacement of natural sand with the manufacturing sand up to 60% to 80% gives good results. When brick mortar joint is strong, brick-crushing, failure has been observed; however, when mortar joint is weak, crack propagating through brick and mortar joint is noted.

References

1. Kaushik HB, Rai DC, Jain SK (2007) Stress-strain characteristics of clay brick masonry under uniaxial compression. J Mater Civ Eng 19(9):728–739. https://doi.org/10.1061/(ASCE)0899-1561(2007)19:9(728)
2. Abdulla KF, Cunningham LS, Gillie M (2017) Simulating masonry wall behaviour using a simplified micro-model approach. Eng Struct 151:349–365. https://doi.org/10.1016/j.engstruct.2017.08.021
3. Stavridis A, Koutromanos I, Shing PB (2012) Shake-table tests of a three-story reinforced concrete frame with masonry infill walls. Earthquake Eng Struct Dynam 41(6):1089–1108. https://doi.org/10.1002/eqe.1174
4. Bhosale SD, Desai AK (2019) Simulation of Masonry wall using concrete damage plasticity model. Int J Innov Technol Exploring Eng 8(9S3): 1241–1244. https://doi.org/10.35940/ijitee.i3274.0789s319

5. Sousa L, Monteiro R (2018) Seismic retrofit options for non-structural building partition walls: impact on loss estimation and cost-benefit analysis. Eng Struct 161:8–27. https://doi.org/10.1016/j.engstruct.2018.01.028

Fresh and Hardened Properties of Pozzolanic Binary Blend Self-compacting Concrete

V. Renuka, B. Sravani, and B. Harsh Vignesh Singh

Abstract Due to its revolutionary design, self-compacting concrete (SCC) had a significant influence on the concrete building industry. The method of achieving SCC either contributes to greater shrinkage or alter the concrete's mechanical properties. As a result, blended pozzolanic materials are needed for making SCC in order to improve its properties. This study reports on experimental work conducted to study the influence of using rice husk ash (RHA) and metakaolin (MK) as partial replacement materials for SCC. Tests are conducted on fresh and hardened binary blend SCC. With the addition of powder, the induced SCC's flow and segregation resistance improved at a fresh stage. After seven days of curing, it is noticed that adding up to 20% blends improved the strength of SCC. If SCC is rendered with a mixture of RHA and MK, 20% cement replacement is recommended as the ideal standard.

Keywords Self-compacting concrete · Supplementary cementitious materials

1 Introduction

Usage of SCMs is becoming more common, owing to their ability to improve the concrete properties and also to lower the quantity of cement needed [1, 2]. Supplementary cementitious materials (SCMs) like fly ash, ground granulated blast furnace slag, silica fume, calcined clay, RHA, and MK with 15–25, 30–45, 5–10, 10–35, 10–20, and 5–15%, respectively, by the mass of cement, and also, many other materials were used in SCC production as binary or ternary cementitious blends, yielding positive results at the recommended dosage level [3]. As a result, increase in the replacement level with one pozzolanic material may alter the properties of SCC.

V. Renuka (✉)
Department of Civil Engineering, NIT Warangal, Warangal 506004, India

B. Sravani · B. Harsh Vignesh Singh
Department of Civil Engineering, Vardhaman College of Engineering, Shamshabad, Hyderabad 501218, India

B. Kondraivendhan et al. (eds.), *Sustainable Building Materials and Construction*,
Lecture Notes in Civil Engineering 222,
https://doi.org/10.1007/978-981-16-8496-8_5

In order to produce SCC, high powder content and the use of viscosity modifying agents are necessary. The high powder content causes a lot of shrinkage, whereas the viscosity modifying agents have an effect on the concrete's mechanical properties. To address these issues, several studies have been carried out using industrial waste or natural pozzolanic materials to determine the appropriate partial substitute for cement in SCC processing.

There are drawbacks of utilizing a single pozzolanic material in making SCC as a result, there is a need among researchers to determine fresh and hardened properties of pozzolanic binary blend SCC. The purpose of the study is to investigate how binary blended pozzolanic materials (RHA and MK) affect the SCC properties and to identify whether binary blend materials could be used in the production of SCC.

2 Materials and Methodology

2.1 Materials

ASTM Type I cement was used in this experiment; RHA and MK were obtained from Hyderabad.

Table 1 shows the chemical analysis of OPC, RHA, and MK used for laboratory work and found that RHA and MK are pozzolanic materials. Table 2 shows bulk density, specific gravity, fineness of materials. Table 3 shows SC, IST, FST values of the cement, RHA, MK, and Cement + RHA + MK. Fine aggregate chosen to a down size of 4.75 mm which is obtained from the nearby source conforming to grading

Table 1 Chemical analysis—OPC, RHA, MK

Material	SiO_2	CaO	Al_2O_3	Fe_2O_3	SO_3	MgO	LOI
OPC	18.42	70.10	4.68	2.75	–	–	3.40
RHA	85.30	4.10	0.90	0.45	1.25	0.12	2.25
MK	52.80	0.43	40.68	0.88	–	–	1.70

Table 2 Bulk density, specific gravity, fineness of the materials

Materials	Bulk density kg/m^3	Specific gravity g/cm^3	Fineness %
OPC	1495	3.32	5
RHA	472	2.15	6
MK	655	2.50	7
Fine aggregate	1475	2.65	2.8
Coarse aggregate	1650	6.52	6.5

Table 3 SC, IST, FST—Cement + RHA + MK

S. No	Mix Type	Mix ID	Materials			SC (%)	IST (min)	FST (max)
			OPC	RHA	MK			
1	Control Mix	SCC-00	100	–	–	30.60	132	240
2	10(RHA + MK)	SCC-10	90	6.7	3.3	34.00	130	236
3	20(RHA + MK)	SCC-20	80	13.4	6.6	39.00	128	245
4	30(RHA + MK)	SCC-30	70	20.0	10.0	38.62	142	268
5	40(RHA + MK)	SCC-40	60	26.7	13.3	45.50	156	296

Requirement: SC-Standard consistency = 25 to 35%, IST-Initial setting time = 30 min (minimum), FST-Final setting time = 600 min (maximum).

Zone III as per ASTM standard. Coarse aggregate chosen to a down size of 12.5 mm crushed granite stones are used confirming to the requirements of ASTMC33 [4]. Super plasticizer Chryso Optima 100 was used in this study in the view of BS EN 934-2 [5] and ASTM C494 [6] as Type A.

2.2 Mix Design

DOE mix design for M 40 normal concrete is followed and then converted to SCC mix using the method of trial. Cement, RHA, and MK are the binder materials used. Quantity of cement, fine aggregate, and coarse aggregate is taken as 480 kg/m^3, 880 kg/m^3, and 680 kg/m^3, respectively. Water-cement ratio is considered as 0.40, and super plasticizer dosage varied for subsequent mixes. A 2:1 proportion of RHA and MK was used to make the blend. RHA can substitute cement up to 20% in SCC production, whereas MK can only substitute cement up to 10%, according to previous studies [1].

2.3 Tests on Fresh Binary Blend SCC—Slump Flow + T_{500} (Filling Ability), Passing Ability (L-box Method), Segregation Resistance

As per EFNARC [7], tests were conducted as shown in Fig. 1. FA-filling ability (slump flow + T_{500}) measures a concrete's mean diameter and time reaching 500 mm diameter of the concrete after releasing an inverted slump cone, PA-passing ability (L-box method)that represents the ability of concrete to pass obstacles following

Fig. 1 FA (slump flow + T_{500}), PA (L-box method) conducted on pozzolanic binary blend SCC

EFNARC and SR-segregation ratio which is the ratio of concrete quantity poured on 5 mm sieve (350 mm dia) to the amount of workable paste.

2.4 Tests on Hardened Binary Blend SCC

Density test was performed conforming to BS EN 12390-7 [8]; compressive strength test was carried out based on BS EN 12390-3 [9]; split tensile strength test was conducted in view of BS EN 12390-6 [10], and UPV test was carried in view with the specifications of BS EN 12504-4 [11] at different curing ages.

3 Results and Discussion

3.1 Binary Blend SCC-Fresh Properties

Increase of powder blend improved FA, PA, and SR values at the fresh stage. Table 4 displays the flow properties of binary bend SCC. The lower SR indicates improved segregation resistance which is believed to be due to blended powder used. It can be said that if a significant volume of powder is used; SCC can be made without the use of VMA.

Table 4 Flow properties of binary blend SCC

S. No	Mix ID	Flow properties measured			
		FA		PA	SR
		AV	T_{500}	H_2/H_1	W_a/W_c
1	SCC-00	660	3	0.82	4.35
2	SCC-10	675	4	0.83	3.28
3	SCC-20	680	4	0.83	2.26
4	SCC-30	683	4	0.84	1.95
5	SCC-40	685	5	0.85	0.82

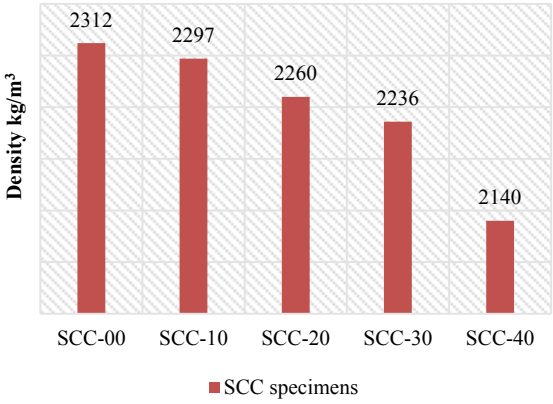

Fig. 2 Density of SCC specimens

3.2 Binary Blend SCC-Hardened Properties

Density-The density of the SCC specimens is depicted in Fig. 2. It can be noted that SCC-00, SCC-10, SCC-20, and SCC-30 could be used to make regular weight concrete, whereas SCC-40 is less than lower limit and used for low density (lightweight) concrete.

Compressive strength-From Fig. 3, it is noticed that compressive strength increased at an early age when cement is replaced with a blend of pozzolanic materials by 10–20% since MK is the reason that improved the powder's initial setting time which resulted in improved early strength whereas the substitution levels of 30 and 40% lessen compressive strength at an early age. At 28, 56, and 90 days, SCC specimens with cement replacement have lower compressive strength values than SCC-00. However, at 150 and 180 days, binary blend SCC specimens have a similar range of compressive strength values.

Split tensile strength-Fig. 4 shows that SCC-10 and SCC-20 displayed an improvement in split tensile strength early in the curing process, which is thought to be attributed to the action of MK added to blends. In SCC-30 and SCC-40, higher RHA

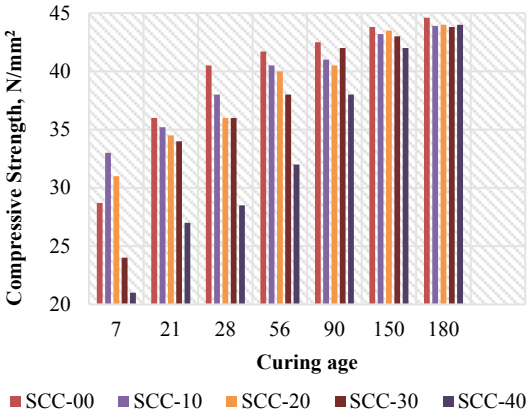

Fig. 3 Compressive strength

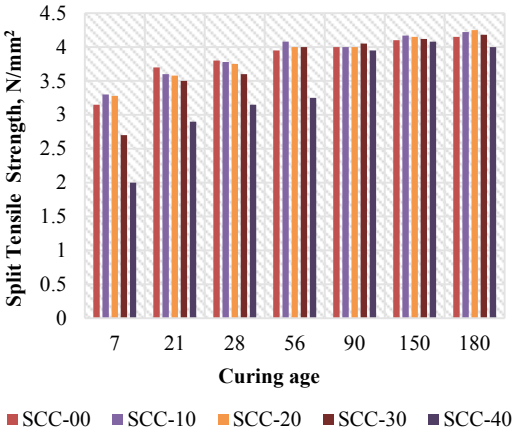

Fig. 4 Split tensile strength

content suppressed early split tensile strength progress; however, normal strength improvement was noticed at a later age.

Ultrasonic Pulse Velocity (UPV)-UPV results are shown in Fig. 5. UPV is used to determine concrete strength without causing damage to its structure. The findings reveal that as the curing age increases, UPV value also increases. SCC-10 and SCC-20 have outstanding concrete quality at seven days, whereas the rest of the specimens had decent concrete quality. With the exception of SCC-40, which has average concrete quality, all of the specimens at 21 and 28 days had excellent concrete quality and found to be outstanding at 56, 90, 150, and 180 days.

Fig. 5 UPV values

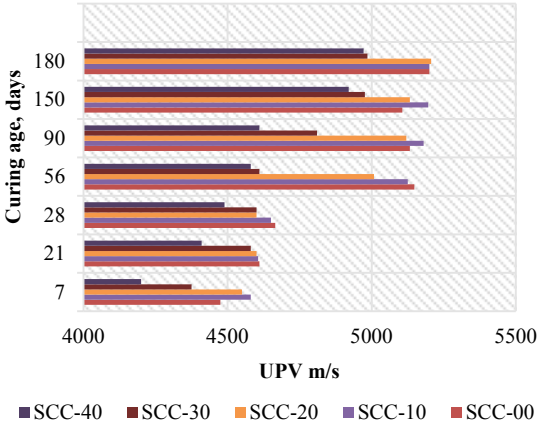

4 Conclusions

This paper highlights about the binary blend SCC made with RHA and MK in order to study their potential as a partial replacement for cement in making SCC. The following conclusions have been reached:

- Based on their chemical compositions, RHA and MK were observed to be pozzolanic and so may be utilized as SCMs in making SCC.
- Binary blend SCC have filling ability, passing ability, and segregation ratio ranging from 660 to 685 mm, 0.82 to 0.85 mm, and 0.82–4.35%. The normal consistency ranges from 30 to 65.20%. This binary blend SCC can be used in congested reinforced concrete components without segregation or bleeding. It can be noted that super plasticizer Chryso Optima 100 improved the performance of cementitious material.
- When up to 20% of the cement is replaced with RHA and MK at the hardened stage, early and later strength enhancement is observed in binary blend SCC. If SCC is rendered with a mixture of RHA and MK, 20% cement replacement is recommended as the ideal standard.
- A 2:1 proportion of RHA and MK is used to make a blend. From this study, it can be noted that further addition of MK may increase mechanical strength and enhances long term strength.

References

1. Kannan V (2018) Strength and durability performance of self compacting concrete containing self-combusted rice husk ash and metakaolin. Constr Build Mater 160:169–179

2. Pongsakon Promsawat BGN (2020) Properties of self-compacting concrete prepared with ternary Portland cement-high volume fly ash-calcium carbonate blends. Case Stud Constr Mater 13
3. Anhad Singh Gill RS (2017) Strength and micro-structural properties of self-compacting concrete containing metakaolin and rice husk ash. Constr Build Mater 157:51–64
4. ASTMC33 (2018) Standard specification for concrete aggregates. ASTM International, West Conshohocken, PA
5. BSEN934-2 (2009) Admixtures for concrete, mortar and grout. British Standards Institution
6. ASTMC494 (2019) Standard specification for chemical admixtures for concrete. s.l.:ASTM International
7. EFNARC (2005) EFNARC, specification and guidelines for self-compacting concrete
8. BSEN 12390-7 (2019) Testing hardened concrete Part 7: density of hardened concrete. British Standard
9. BSEN12390-3 (2019) Testing hardened concrete. Part-3 Compressive strength of test specimens. BSI
10. BSEN12390-6 (2009) Testing hardened concrete—Part 6: tensile splitting strength. BSI
11. BSEN12504-4 (2019) Testing concrete—determination of ultrasonic pulse velocity. BSI

Properties of Binary Admixtures and Recycled Coarse Aggregate Mixed Self-compacting Concrete

Anjali Singh, P. K. Mehta, and Rakesh Kumar

Abstract This study presents the results of the inclusion of binary admixtures [Fly Ash (FA) + Silica Fume (SF)] and Recycled Coarse Aggregate (RCA) in Self-Compacting Concrete (SCC). First, SCC mixes were prepared by replacing parts of 43-grade Ordinary Portland Cement (OPC) with different combinations of FA + SF to find their optimum replacement level (25%). Then, another set of SCC mixes was prepared by replacing parts of Natural coarse aggregate (NCA) with RCA (0–100%) to obtain the optimum level (25%), maintaining the optimum level of ternary blend obtained previously. The green, hardened, and microstructural properties of all SCC mixes were determined. On inclusion of binary admixtures at optimum OPC replacement level [FA(15%) + SF(10%)] with NCA, both the fresh properties and compressive strength increase. On inclusion of RCA at optimum level (25%) along with the ternary blend at the optimum level, the fresh properties of SCC increase up to a certain limit (25%), and thereafter, these decrease with an increase in RCA content. At the optimum ternary blend level, the compressive strength is increased significantly. At optimum ternary blend and RCA levels, the compressive strength is improved further. Further, in all the above mixes, the microstructure is improved.

Keywords Recycled Coarse Aggregate · Self-Compacting Concrete · Ternary blend

A. Singh (✉) · P. K. Mehta · R. Kumar
Civil Engineering Department, Motilal Nehru National Institute of Technology, Allahabad, Prayagraj, UP, India

P. K. Mehta
e-mail: pradeep11@mnnit.ac.in

R. Kumar
e-mail: rkpat@mnnit.ac.in

B. Kondraivendhan et al. (eds.), *Sustainable Building Materials and Construction*,
Lecture Notes in Civil Engineering 222,
https://doi.org/10.1007/978-981-16-8496-8_6

1 Introduction

Generally, SCC is made with different combinations of fine and coarse aggregates and by replacing a part of OPC with suitable pozzolanic material(s). The use of binary admixtures and RCA, obtained from refuse and construction debris, may also be advantageous for SCC. An increase of FA content in SCC mixes improves the rheological properties of high-performance SCC [1]. Mechanical and transport properties of SCC are improved by blending the silica nanoparticles and SF [2]. Medium strength concrete may be made using the same cement content and effective w/c ratio as conventional concrete, but by replacing 25% of NCA by RCA, almost the same mechanical properties can be achieved [3]. The SCC can be made using low/high volume FA and RCA, and the results indicate that the carbonation resistance of SCC decreases by increasing the RCA content [4].

In this study, the effect of binary admixtures (FA + SF) and RCA mixed SCC is investigated. Total 11 SCC mixes cubes were prepared with a constant w/b (0.43) and total powder content of 465 kg/m^3. First, the SCC mixes cubes were prepared by replacing part of OPC by binary admixtures (FA + SF) in varying proportions (0–25%), and the resulting mixes are designated as M1[FA(00%) + SF(25%)], M2[FA(05%) + SF(20%)], M3[FA(10%) + SF(15%)], M4[FA(15%) + SF(10%)], M5[FA(20%) + SF(05%)], and M6[FA(25%) + SF(00%)].

Another set of SCC mixes was prepared by replacing part of NCA with RCA (0–100%), maintaining the optimum level of ternary blend obtained previously, and the corresponding mixes are designated as M7[FA(15%) + SF(10%) + RCA(00%)], M8[FA(15%) + SF(10%) + RCA(25%)], M9[FA(15%) + SF(10%) + RCA(50%)], M10[FA(15%) + SF(10%) + RCA(75%)] and M11[FA(15%) + SF(10%) + RCA(100%)].

2 Methodology

2.1 Materials

A 43-grade OPC (Brand-Prism) conforming to IS: 8112-1989; fine aggregate and NCA (10 mm & 20 mm) conforming to IS: 383-1987; class F-FA (gray color) confirming to IS: 3812-2000; SF (dark gray color) conforming to IS: 15388-2003; polycarboxylic-ether-based superplasticizer was used; tap fresh potable water for curing of SCC mixes. The sieve analysis results and images of both NCA and RCA of sizes 10 and 20 mm are included in Figs. 1 and 2, respectively.

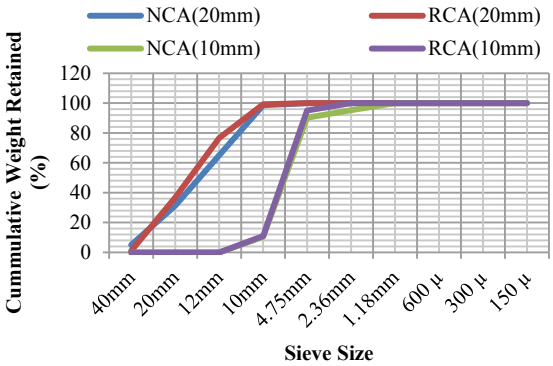

Fig. 1 NCA and RCA

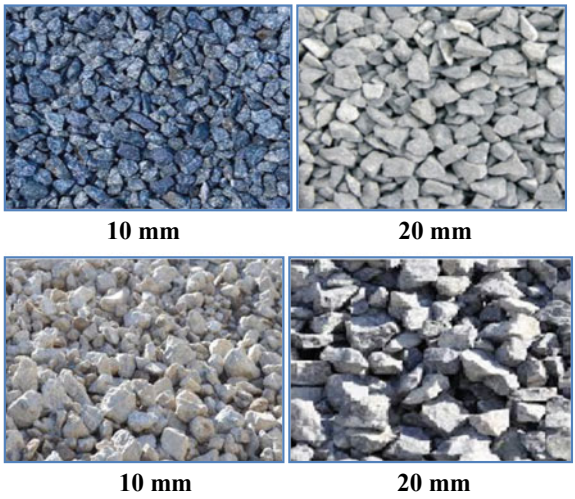

Fig. 2 Images of NCA and RCA

2.2 Tests on SCC Mixes

2.2.1 Properties of SCC Mixes in the Green State

The different workability parameters of SCC made with binary admixtures (0–25%) and RCA (0–100%) in the green state are determined as per EFNARC-2005 guidelines. The filling ability was measured with the help of slump flow, T-50 time (Sec), V-funnel, and U-box. The passing ability of different mixtures was determined using L-box and J-ring tests.

2.2.2 Properties of SCC Mixes in the Hardened State

The compressive strength of SCC mixes cubes containing binary admixtures (0–25%) and RCA (0–100%) was measured at 7 and 28 days per the provisions of IS: 516-1959.

2.2.3 Micro-Structural Analysis

X-ray Diffraction Analysis (XRD)

The micrographs were obtained by X-ray transmission (Xpert pro, Panalytical, USA). The XRD analysis was accompanied by the determination of the mineralogical constitution of mixes designated as M4 and M8 (Range of 2Θ from 0 to 100°).

Scanning Electron Microscopy Analysis (SEM)

The influence of binary admixtures and RCA on the concrete microstructure could be investigated by SEM, which visually presented the porosities, micro-cracks, and possible interactions between the aggregates and the mortar.

3 Results and Discussion

3.1 Properties of SCC Mixes in the Green State

For the first set of mixes containing binary admixtures and NCA, the slump flow increases up to optimum binary admixtures' content [FA(15%) + SF(10%)] (M4), and thereafter, it decreases, while T-50 time, V-funnel, L-box ratio, U-box, and J-ring values continue to decrease. For the second set of mixes containing binary admixtures at optimum level (25%) and increasing RCA content, the slump flow increases up to the optimum level of NCA by RCA (25%) (M8), and after that it decreases, while T-50 time, V-funnel, L-box, U-box, and J-ring values decrease up to optimum RCA level (M8), and after that these increase with the RCA content. The results are presented in Figs. 3, 4, and 5.

3.2 Property of SCC Mixes in the Hardened State

The compressive strength of SCC mixes was determined for 100 mm sizes of cubes after 7 and 28 days of water curing, and its variation is presented in Fig. 6. On

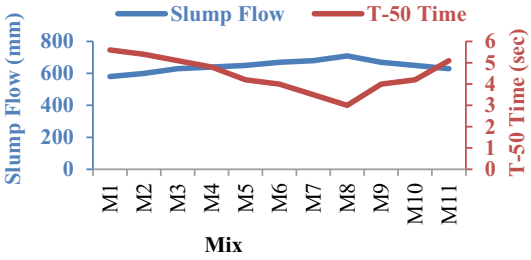

Fig. 3 Slump flow and T-50 time

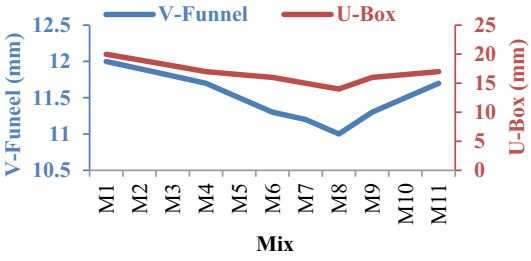

Fig. 4 V-funnel and U-box

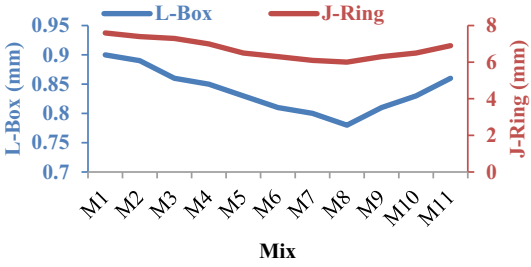

Fig. 5 L-box and J-ring

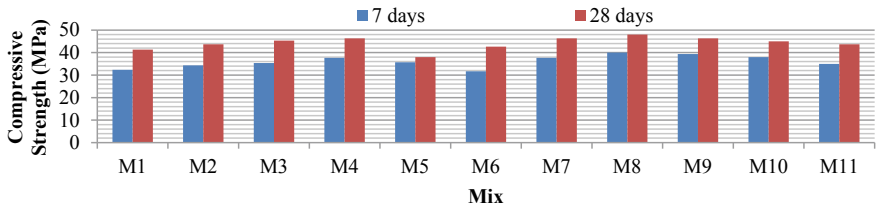

Fig. 6 Compressive strength of SCC mixes

using binary admixtures in SCC at optimum level [FA(15%) + SF(10%)], the mix (M4) shows a higher compressive strength (18.94%) in comparison to the control mix (CM—concrete containing 25% FA and NCA), at 7 days, and it increases by 8.60% at 28 days. At optimum binary admixtures' level [FA(15%) + SF(10%)] and optimum RCA level (25%), the gain in compressive strength of the SCC mix (M8)

is 26.30 and 12.49%, in comparison to the CM at 7 and 28 days, respectively. The results are shown in Fig. 6.

3.3 Micro-Structural Analysis

3.3.1 X-ray Diffraction Analysis (XRD)

Figure 7 shows the XRD analysis of CM (SCC containing 25% FA) at 28 days. Figure 8 shows the same for SCC mix containing binary admixtures at optimum level [FA(15%) + SF(10%)] (M4) at 28 days, while Fig. 9 shows for SCC mix containing both binary admixtures and RCA at their optimum levels (M8) at 28 days.

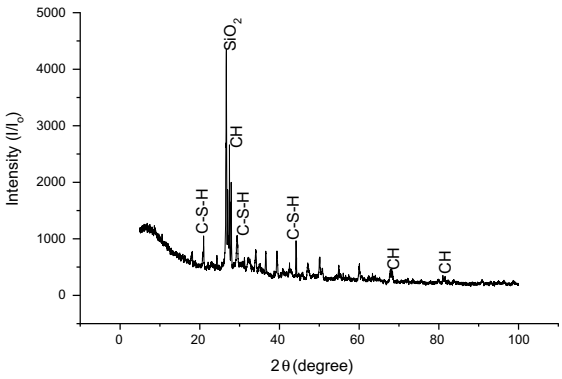

Fig. 7 XRD of CM

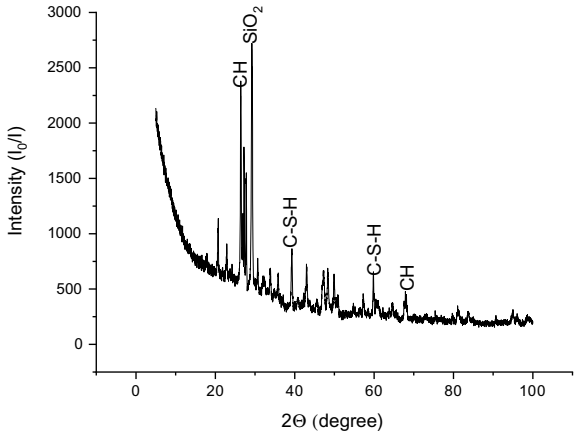

Fig. 8 XRD of M4

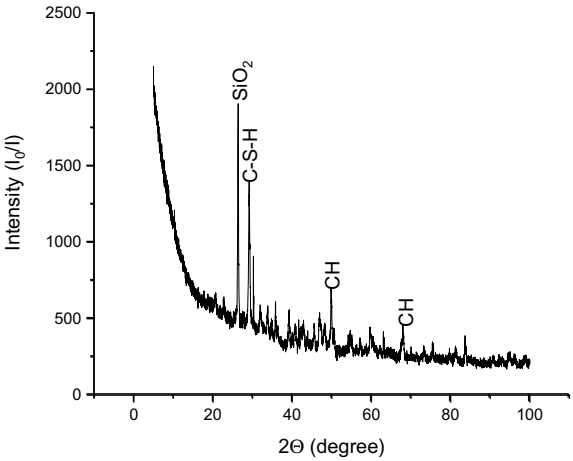

Fig. 9 XRD of M8

3.3.2 Scanning Electron Microscopy Analysis (SEM)

Figures 10, 11, and 12 show the SEM images of SCC mixes CM, M4, and M8, respectively.

It is observed from the above micrographs that more quantity of C–S–H gel and less quantity of CH crystals are present in the M4 mix, while less C–S–H gel and fewer CH crystals are present in the M8 mix in comparison to the CM. The chemical reaction of binary admixtures leads to the construction of additional C–S–H gel and reduction of CH in comparison to a single admixture. Further, the microstructure becomes more dense and uniform due to CH crystals being consumed by binary admixtures; in combination, to construct additional C–S–H gel, this is the main reason for the increase in strength for the M4 mix. In the case of the M8 mix, the

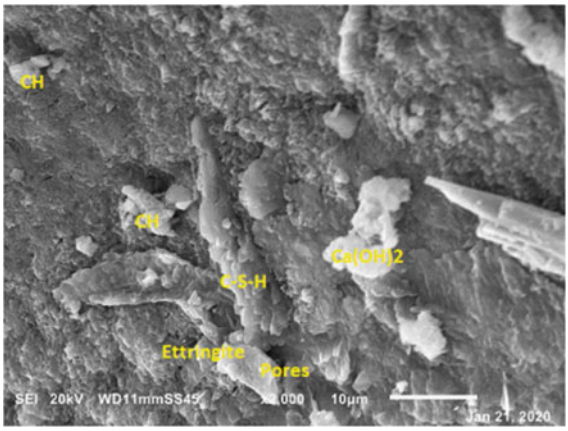

Fig. 10 SEM of CM

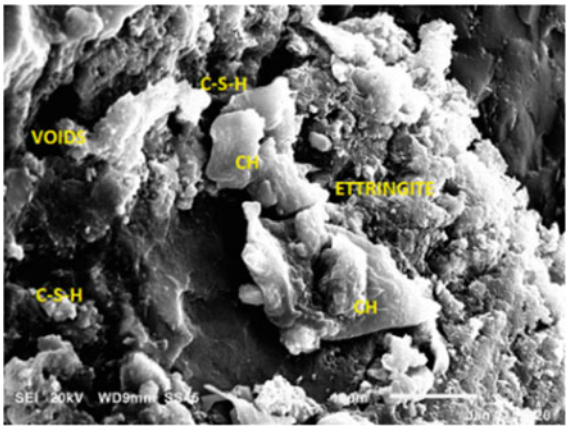

Fig. 11 SEM of M4

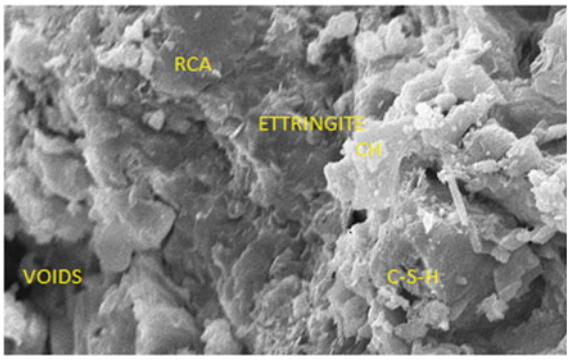

Fig. 12 SEM of M8

silica present in the RCA and a film of old cement present on the surface of the RCA help in gain of strength as compared to both CM and M4.

4 Conclusions

It is concluded from this study that binary admixtures (FA + SF) can be used beneficially for part replacement of OPC in SCC, the optimum level being 25% [FA(15%) + SF(10%)]. On using the binary admixtures, properties of SCC mixes in green and hardened state increase up to the optimum replacement level (M4), and thereafter, these decrease. The optimum replacement level of NCA by RCA is 25%. On inclusion of both binary admixtures and RCA at their optimum levels (25% each), both the fresh and hardened properties increase up to a certain limit (M8), and thereafter, these decrease with an increase in RCA content. The compressive strength of both M4 (concrete containing binary admixtures at optimum levels and NCA) and

M8 (concrete containing binary admixtures and RCA at optimum levels) mixes are higher than the CM, the gain being more in M8 concrete. The microstructure of both M4 and M8 concretes becomes more dense and uniform in comparison to the CM.

References

1. Khayat KH, Guizani Z (1997) Use of viscosity-modifying admixture to enhance stability of fluid concrete. ACI Mater J 94(4): 332–341
2. Ozawa K, Maekawa K, Kunishima M, Okamura H (1989) Performance of concrete based on the durability design of concrete structures. In: Proceedings of the second East Asia-Pacific conference on structural engineering and construction
3. Etxeberria M, Vazquez EA, Barra M (2007) Influence of amount of recycled coarse aggregates and production progress on properties of recycled aggregate concrete. Cem Concr Res 37: 735–742
4. Navdeep Singh ME, Singh SP (2016) Carbonation resistance and microstructural analysis of low and high volume fly ash self compacting concrete containing recycled concrete aggregates. Constr Build Mater 127: 828–842

Use of Mineral Admixtures and M-sand for Sustainable Concrete

Deep Tripathi, Rakesh Kumar, P. K. Mehta, and Amrendra Singh

Abstract The findings of an experimental programme to explore the properties of self-compacting concrete (SCC) containing dual admixtures are presented in this paper. Three different SCC mixes (grade-M25) were prepared using: (i) ordinary portland cement (OPC) and natural fine aggregate (NFA) (M-1); (ii) OPC, dual admixtures [fly ash (FA) + Metakaolin (MK)] and NFA (M-2); (iii) OPC, dual admixtures, NFA and manufactured sand (M-sand) (M-3). The properties of the various mixes are compared in both fresh and hardened states. The optimal level of OPC substitution by binary admixtures is 25% [FA(15%) + MK(10%)]. The NFA was partially replaced by M-sand after finding the optimal dose of binary admixture (FA + MK), and the optimum dose was 50%. All specimens were cured in tap water for 90 days and tested.

Keywords Mineral admixtures · M-sand · Self-compacting concrete

1 Introduction

The use of pozzolanic materials in SCC reduces the amount of cement used. This also aids in the reduction of carbon dioxide emissions because the production of the cement is not environmental friendly. Further, FA or some other pozzolana is industrial by-products and needs proper disposal or stabilisation. The strength of SCC containing mineral admixtures is more than the normal SCC [1]. Gaywala

D. Tripathi (✉) · R. Kumar · P. K. Mehta · A. Singh
Civil Engineering Department, NIT Allahabad, Prayagraj, UP, India
e-mail: deep@mnnit.ac.in

R. Kumar
e-mail: rkpat@mnnit.ac.in

P. K. Mehta
e-mail: pradeep11@mnnit.ac.in

A. Singh
e-mail: amrendra@mnnit.ac.in

B. Kondraivendhan et al. (eds.), *Sustainable Building Materials and Construction*,
Lecture Notes in Civil Engineering 222,
https://doi.org/10.1007/978-981-16-8496-8_7

et al. [2] stated that SCC's strength parameters were maximum at 15% replacement level of OPC with FA. 50–60% FA can be included in SCC to improve workability parameters with a substantial increase in compressive strength up to 180 days [3].

The NFA is a key component of concrete, but it is becoming increasingly costlier and scarce due to a lot of factors. Sand quarrying is also becoming increasingly difficult due to environmental concerns. As a result, a low-cost alternative is required, which can be found in the form of M-sand. As a fine aggregate material, the NFA is the most popular option. It is mined from riverbeds, with severe environmental effects. M-sand is rock that has been crushed to the desired grain size distribution. SCC has been successfully prepared using M-sand as a filler material. Its use improves the hardened properties and reduces the environmental impact too [4]. For the same paste composition, the compressive strength of M-sand mixed concrete is more than that containing NFA only [5]. The use of M-sand containing no more than 13% stone powder content has been reported to be advantageous for the long-term split tensile strength of M-sand concrete [6].

2 Methodology

2.1 Material and Their Properties

For this research, a 43 grade OPC (Brand-MP Birla), conforming to IS: 8112-1989, was used. Rounded NFA falling in Zone II of IS: 383-1970 was used. M-sand was procured from Jhansi, UP, and it also satisfied the requirements of Zone II. The coarse aggregates of size 10 and 20 mm were used, satisfying the requirements of IS 383-1970. The fly ash (class-F; colour-grey; specific gravity-2.13), satisfying the requirements of IS 3812-2000, was purchased from NTPC-Unchahar (UP). Metakaolin used in this study was procured from Gujarat. A superplasticizer, MasterRheobuild @875, was used for maintaining the fresh properties as per the requirements. Table 1 presents the constituents of OPC and mineral admixtures.

Table 1 Chemical compositions of OPC and mineral admixtures

Chemical composition (%)	OPC	FA	MK
Silicon dioxide (SiO_2)	20.05	59.51	51.46
Calcium oxide (CaO)	62.95	5.0	36.05
Aluminium oxide (Al_2O_3)	5.28	20.34	2.21
Iron oxide (Fe_2O_3)	4.01	5.89	0.81
Magnesium oxide (MgO)	1.50	1.50	0.18
Potassium oxide (K_2O)	0.95	1.92	0.28
Sodium oxide (Na_2O)	0.24	0.61	0.74
Loss of ignition	3.12	0.35	0.96

2.2 Mix Proportioning and Casting

M25 grade SCC mix was prepared in this study, using 43 grade OPC, satisfying the requirements of EFNARC, 2005. The quantities of different materials in one cubic metre of SCC at water/binder ratio-0.44 were binder content-450 kg; sand-890 kg; coarse aggregate-750 kg; superplastisizer-6.75 kg. The optimum replacement level of OPC by binary admixtures is 25% (15%FA + 10%MK) [7]. It is reported that 50% of NFA can be replaced by M-sand [8]. In this experiment, M-sand and FA + MK were used to partially replace NFA and OPC, respectively, in the preparation of SCC. After finalising the mix proportions, three different SCC mixes (M25) (M-1, M-2, M-3) were prepared. For the determination of compressive, split tensile and flexural strengths, cubes (100 mm), cylinders (100 × 200 mm) and beams (100 × 100 × 500 mm) were cast. Both the fresh and hardened properties of the SCCs (M-1, M-2, M-3) made using the following were investigated: (i) OPC and NFA, (M-1); (ii) OPC, dual admixtures (15%FA + 10%MK) and NFA, (M-2); (iii) OPC, (15%FA + 10%MK), NFA and M-sand, (M-3).

3 Results and Discussion

The results of the study are presented herein.

3.1 Fresh Properties of Concrete

Table 2 lists the workability characteristics of all mixes. It was found that the workability of the different SCCs increased with the FA content and decreased with the increase in MK content. The flowability of SCCs slightly decreased as M-sand content was increased, but it was within the EFNARC limits.

Table 2 Workability parameters of SCCs

Tests	Results			EFNARC limits	
	M-1 type	M-2 type	M-3 type	Min	Max
Slump flow (mm)	670	690	685	650	800
T_{50} time (s)	4.5	3.0	3.2	2	5
V- funnel (s)	11.5	10	10.5	6	12
L-box (h_2/h_1)	0.85	0.94	0.90	0.8	1.0
U-box (h_2-h_1) (mm)	29	20	21	0	30
J-ring (mm)	9.5	6	6.5	0	10

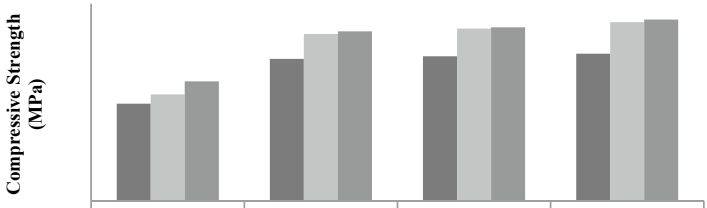

	7 days	28 days	56 days	90 days
M-1 type	24.67	36	36.67	37.33
M-2 type	27	42.33	43.67	45.33
M-3 type	30.33	43	44	46

Fig. 1 Compressive strength of the specimens

3.2 Hardened Properties of Concrete

3.2.1 Compressive Strength

According to IS:516-1959, concrete cubes' compressive strength was determined. The results are shown in Fig. 1.

It is found that the gain in compressive strengths of M-2 concrete over M-1, M-3 over M-1 and M-3 over M-2 concrete is in the range of 9–22, 19–24, 2–12%, respectively, upto 90 days of tap water curing. The gain in strength of M-sand mixed concrete may be due to its perfect grading and its cubical shape. The same pattern has been observed by a number of other scholars.

3.2.2 Split Tensile Strength

Cylinders (100 mm × 200 mm) were used to calculate the split tensile strength of all three specimens, as per the provisions of IS: 5816-999. The results are presented in Fig. 2.

It is found that the gain in split tensile strength of M-2 concrete over M-1, M-3 over M-1 and M-3 over M-2 concrete is in the range of 19–23, 40–47, 9–18%, respectively, upto 90 days of curing.

3.2.3 Flexural Strength

Beams (100 mm × 100 mm × 500 mm) were cast to assess the flexural strength of all SCCs, as per the provisions of IS: 516-1959. The results are presented in Fig. 3.

It is observed that the gain in flexure strength of M-2 concrete over M-1, M-3 over M-1 and M-3 over M-2 concrete is in the range of 8–27, 27–47, 13–21%, respectively, upto 90 days of curing.

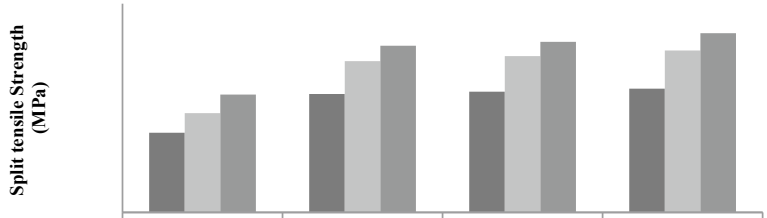

	7 days	28 days	56 days	90 days
M-1 type	2.67	3.97	4.05	4.15
M-2 type	3.33	5.07	5.24	5.43
M-3 type	3.95	5.59	5.72	6.01

Fig. 2 Split tensile strength of the specimens

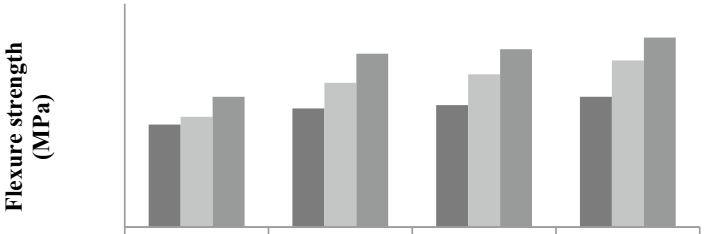

	7 days	28 days	56 days	90 days
M-1 type	3.67	4.25	4.37	4.67
M-2 type	3.95	5.17	5.47	5.97
M-3 type	4.67	6.21	6.37	6.79

Fig. 3 Flexure strength of the specimens

4 Conclusions

The following conclusions can be derived from the experimental research.

- The workability of the SCC mixes increases on increasing the FA content and decreases with increase in MK content; the flowability of SCCs decreases slightly as M-sand content increases but was within the EFNARC limits.
- The compressive, split tensile and flexural strengths of the SCC containing optimum dual mineral admixtures, and NFA (M-2) is higher than the normal SCC (M-1), and the increment lies in the range of 9–22, 19–23 and 8–27%, respectively.
- The compressive, split tensile and flexure strengths of the SCC containing optimum dual admixtures, and optimum M-sand (M-3) is higher than the SCC containing optimum dual admixtures and NFA (M-2), and the increment lies in the range of 2–12, 9–18 and 13–21%, respectively.

- Upto 90 days, all strength parameters of mineral admixtures and M-sand mixed SCC were higher in comparison with the SCC containing OPC only.

References

1. Duan P et al (2016) Influence of partial replacement of fly ash by metakaolin on mechanical properties and microstructure of fly ash geopolymer paste exposed to sulfate attack. Ceram Int 42(2):3504–3517
2. Gaywala et al (2011) Self compacting concrete: a concrete of next decade. J Eng Res Stud 2(4)
3. Khatib JM (2008) Performance of self-compacting concrete containing fly ash. Constr Build Mater 22:1963–1971
4. Matos De et al (2019) Ecological, fresh state and long-term mechanical properties of high-volume fly ash high-performance self-compacting concrete. Constr Build Mater 203:282–293
5. Nanthagopalan P, Santhanam M (2011) Fresh and hardened properties of self compacting concrete produced with manufactured sand. Cement Concrete Compos 33:353–358
6. Zhao S et al (2017) Experimental study on tensile strength development of concrete with manufactured sand. Constr Build Mater 138:247–253
7. Tripathi D et al (2019) Optimum dose of binary admixture in self compacting concrete. Int J Innovat Explor Eng 9:103–108
8. Tripathi D et al (2020) An experimental study on the properties of SCC with manufactured sand. J Ind Chem Soc 97(10a):1673–1677

A Study on Geopolymer Concrete

T. Yeswanth Sai, K. Athira, and V. Sairam

Abstract Cement free concrete is an emerging field in modern construction industry. This technology is highly recommended due to the reduction in greenhouse gas emission. In the last few decades, the environmental CO_2 footprint is increasing day by day due to the high consumption of cement. To overcome this issue, the other pozzolanic materials are incorporated instead of cement. Geopolymer concrete is an innovative construction material that utilizes fly ash as one ingredient. Geopolymer concrete also reduces global emission of CO_2 by approximately 2.1 billion tonnes per year. It can also be referred to as cement-free concrete. It is also known as greener construction technology. The fly ash is non-binding material, and it is activated by an alkaline solution to produce the binding material. The main objective is to achieve the sustainable fly ash-based geopolymer concrete and to carry out the mechanical properties like compressive strength, split tensile strength and flexural strength and durability properties when exposed to acid, sulphates, chlorides and water absorption for M30 grade at 7, 14, 21 and 28 days.

Keywords Geopolymer concrete · Compressive strength · Water absorption · Durability

1 Introduction

1.1 Materials Used and Mix Proportioning

The materials used in geopolymer concrete are low calcium fly ash (source or base material) or class F fly ash, fine aggregate passing through 4.75 mm sieve of zone 2, coarse aggregate of size 20 mm. The properties of geopolymer concrete are designed in comparison with M30 grade nominal concrete. The specific gravity of fine and coarse aggregates is 2.71 and 2.73, respectively. The chemical composition of fly

T. Yeswanth Sai · K. Athira · V. Sairam (✉)
School of Civil Engineering, Vellore Institute of Technology, Vellore, India
e-mail: vsairam@vit.ac.in

B. Kondraivendhan et al. (eds.), *Sustainable Building Materials and Construction*,
Lecture Notes in Civil Engineering 222,
https://doi.org/10.1007/978-981-16-8496-8_8

Table 1 Chemical composition of class F fly ash

SiO_2	Al_2O_3	Fe_2O_3	MgO	SO_3	Na_2O	CaO	LOI
57.30%	27.13%	8.06%	2.13%	1.06%	0.73%	0.03%	1.60%

Table 2 Mix proportioning of concrete

Mix	Cement	Water (L)	Fine aggregate (kg/m^3)	Coarse aggregate (kg/m^3)	Admixture	Class-F fly ash
OPC (M1)	438 kg/m^3	197	685	1079	125 ml/1 bag of cement	0
GPC (M2)	0	27.55	619.06	1149.68	NaOH- 19.95 kg/m^3 and Na_2Sio_3- 118.25 kg/m^3	475 kg/m^3

ash is given in Table 1. The alkali activators used are sodium hydroxide (NaOH) and sodium silicate (Na_2SiO_3). The mix proportioning of the control mix (M1) and geopolymer concrete (M2) is given in Table 2. The mix design was done in accordance with [1]

2 Methodology

2.1 Synthesis and Tests

The sodium hydroxide solution and the sodium silicate solution were mixed to prepare the alkaline activator solution to enhance the reaction between source material and the activator [2]. The geopolymer concrete is casted by adopting the conventional technique used in the manufacture of portland cement concrete as per IS: 516 [3]. The workability of the fresh concrete was taken as 100 mm slump [4]. The geopolymer concrete takes 2–3 days to get harden. Normal water curing has been adopted for both nominal as well as geopolymer concrete [5]. For strength tests, the demoulded specimens were cured in water for 7, 14, 21 and 28 days. For durability, the demoulded cubes were cured in sodium sulphate for 7, 14, 21 and 28 days. Similarly, the demoulded cylinders are cured in sodium chloride and beams in sulphuric acid. The compressive, split tensile and flexure strength test on hardened fly-ash-based geopolymer concrete were performed on standard compression testing machine and universal testing machine, respectively, for the water cured specimens in accordance with IS:516 [3]. The prolonged curing enhances the polymerization process and results in higher compressive strength.

3 Results and Discussion

Mechanical and durability properties of geopolymer concrete: After curing of 7, 14, 21 and 28 days, the compressive, tensile and flexure strength developed are shown in Tables 3, 4 and 5. The strength gain percentage of geopolymer concrete as compared to nominal concrete mix is shown in Figs. 1, 2 and 3. Compressive strength at early curing period shows 17% increment in strength, whereas at the later stage of curing shows only 8.2% increment in compressive strength. It shows a parabolic trend in strength gain. Similarly, tensile strength shows 32.82% of enhancement at 7th day strength and 24.93% at 28th day but there is a sudden drop in strength gain at 14th day curing in the comparative study which is better than nominal concrete. Flexural strength shows maximum strength gain at 14th day curing, whilst early strength gain shows 21.7%, 28th day flexural strength gives only 13.18% strength gain as compared to the nominal M30 concrete mix (Table 6).

Compressive strength (N/mm²) and water absorption (sulphate solution): Cubes were cured in sulphate solutions for 7, 14, 21 and 28 days. Compressive strength and water absorption were found and compared with nominal concrete.

Table 3 Compressive strength (N/mm^2)

Number of curing days	Compressive strength (N/mm^2)	
	OPC (M1)	GPC (M2)
7	20.73	24.29
14	24.14	28.59
21	26.95	31.84
28	34.07	36.88

Table 4 Tensile strength (N/mm^2)

Number of curing days	Tensile strength (N/mm^2)	
	OPC (M1)	GPC (M2)
7	1.98	2.63
14	2.87	3.43
21	3.06	4.00
28	3.77	4.71

Table 5 Flexural strength (N/mm^2)

Number of curing days	Flexure strength (N/mm^2)	
	OPC (M1)	GPC (M2)
7	2.07	2.52
14	2.43	3.24
21	3.46	4.08
28	4.55	5.15

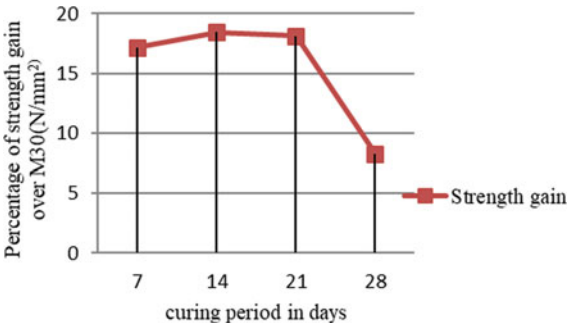

Fig. 1 Compressive strength (N/mm^2) gain pattern of geopolymer concrete compared to M30 concrete mix

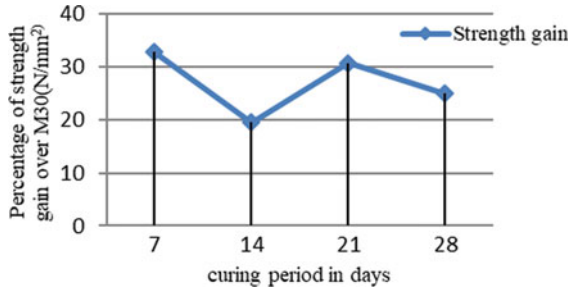

Fig. 2 Tensile strength (N/mm^2) gain pattern of geopolymer concrete compared to M30 concrete mix

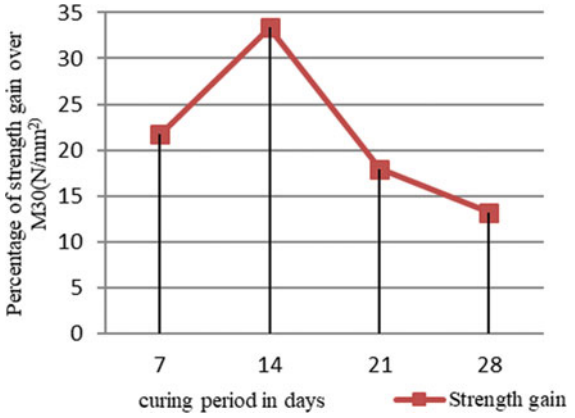

Fig. 3 Flexural strength (N/mm^2) gain pattern of geopolymer concrete compared to M30 concrete mix

Table 6 Compressive strength (N/mm^2) and water absorption (sulphate solution)

Days	Compressive strength (N/mm^2)		Water absorption (%)	
	OPC (M1)	GPC (M2)	OPC (M1)	GPC (M2)
7	24.80	28.60	0.985	0.755
14	29.83	33.46	1.535	0.935
21	35.46	38.89	1.880	1.285
28	40.10	44.02	2.290	1.410

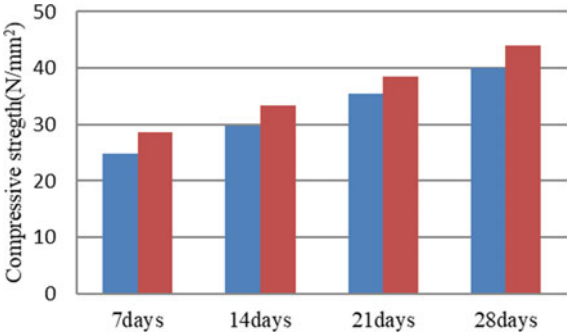

Fig. 4 Compressive strength (N/mm^2) versus curing in days

Percentage increases in compressive strength for 7, 14, 21 and 28 days are 15.3%, 12.1%, 9.6% and 9.7%, respectively. Maximum percentage increment is observed after 7 days curing. This might be due to the higher rate of early strength gain and capacity to resist sulphate attacking geopolymer concrete. But in the later stage of curing, the pattern of increment is more or less constant (Fig. 4).

Split tensile strength (N/mm^2) and water absorption (chloride solution): The resistance to chloride attack is also a major concern of offshore, coastal and chemically prone structures. The OPC and GPC cylinders were cured in sodium chloride solution for 7, 14, 21 and 28 days. After the curing periods, the specimens were tested for split tensile strength and water absorption. Table 7 and Fig. 6 represent the test results. There was a sharp increase of 26% in split tensile strength of control mix at 28 days. The geopolymer attained a sharp increase in split tensile strength after 21 days about 38%. The water absorption rate increased drastically at 14 days testing for both OPC and GPC mixes about 115% and 212%, respectively. But the overall water absorption of GPC mix was lower than OPC mix by about 30% at 28 days (Fig. 5).

Flexural strength (N/mm^2) and water absorption (sulphuric acid solution): The acidic environment condition was created with the help of sulphuric acid. The flexural strength of the GPC mix increased 41% with respect to OPC mix at 28 days. The rate of water absorption test showed a decrease at 28 days of curing to about 13% (Fig. 6).

Table 7 Split tensile strength (N/mm^2) and water absorption (chloride solution)

Days	Split tensile strength (N/mm^2)		Water absorption (%)	
	OPC (M1)	GPC (M2)	OPC (M1)	GPC (M2)
7	1.93	2.56	0.9	0.449
14	2.07	2.86	1.94	1.402
21	3.01	3.96	2.03	1.490
28	3.82	4.02	2.40	1.671

Table 8 Flexural strength (N/mm^2) and water absorption (sulphuric acid solution)

Days	Flexural strength (N/mm^2)		Water absorption (%)	
	OPC (M1)	GPC (M2)	OPC (M1)	GPC (M2)
7	3.89	4.38	1.08	0.75
14	4.08	5.48	1.4	0.86
21	4.44	6.58	2.27	1.78
28	4.83	6.83	2.60	2.26

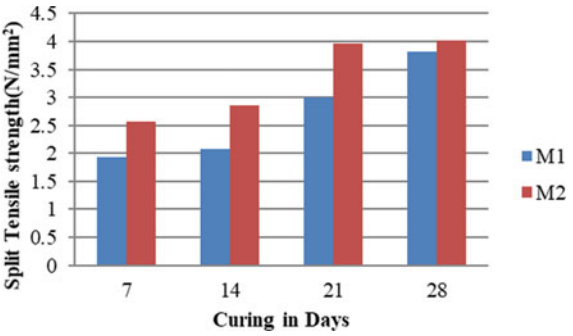

Fig. 5 Split tensile strength (N/mm^2) versus curing in days

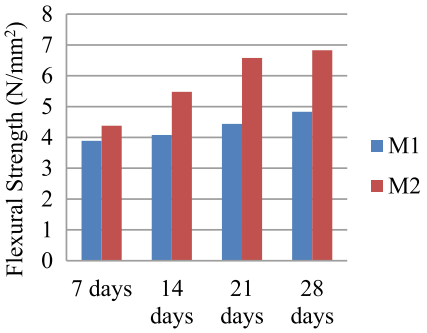

Fig. 6 Flexural strength (N/mm^2) versus curing in days

Water absorption (%): The water absorption rate is gently decreasing in geopolymer concrete as the curing period proceeds. After 28th day curing in sulphate solution, water absorption dropped to 38.42%. This indicates a reduction in porosity. The water absorption shows maximum decrease in the chloride and sulphuric acid solution at the early stages of curing (Fig. 7).

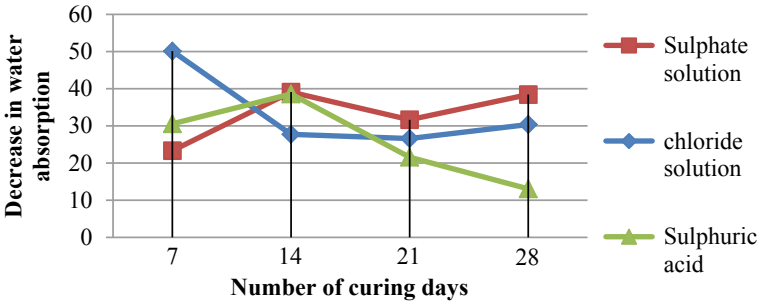

Fig. 7 Water absorption (%)

4 Conclusions

- Geopolymer has competitive compression, tension and flexural strength when compared to conventional concrete. Compressive strength gain is maximum at 7th day curing, whereas flexural strength gain is at 14th day curing. Split tensile strength shows a sudden drop at 14th day curing and shows maximum strength gain at 7th day curing. All the cases show a drop in strength gain in the later stage of curing compared to the initial strength gain patterns.
- Compressive strength can be increased by increasing the concentration of sodium hydroxide.
- Fly ash-based geopolymer concrete has excellent durability, and it is suitable for many structural applications. Resistance to sulphate attack is better than nominal concrete in every curing stage on an average of 11.73% in terms of compressive strength. Similarly, average enhancement of resistance to chloride attack in terms of split tensile strength is 26.9% and acid attack in terms of flexural strength is 34.1%.
- The water absorption results show that the porosity of geopolymer concrete is less as fly ash is finer than OPC, and results in less water absorption are the control concrete. The drop in water absorption indicates reduction in porosity.
- To overcome the delay in setting due to sodium silicate gel, heat curing is recommended.

References

1. Nataraja MC, Das L (2010) Concrete mix proportioning as per IS 10262: 2009–Comparison with IS 10262:1982 and ACI 211.1-91. Ind Concrete J 64–70
2. Xu H, Van Deventer JS (2000) Ab initio calculations on the five-membered alumino-silicate framework rings model: implications for dissolution in alkaline solutions. Comput Chem 24(3–4):391–404
3. IS: 516 (1959) Method of tests for strength of concrete. Bureau of Indian Standards 1991–07

4. Lodge JP Jr (1988) Methods of air sampling and analysis. CRC Press
5. Indian Standards Institution (1965) Code of practice for plain and reinforced concrete: IS. Indian Standards Institution

Comparison of Different Numerical Models Developed for FE Simulation of Concrete-Filled Steel Tubular Composite Columns

Dishant R. Prajapati and Devang R. Panchal

Abstract The steel–concrete composite structures become more popular because it possesses different structural benefits at a time. This study aims to compare five different nonlinear numerical models for confined concrete and mild steel to simulate the experimental results with finite element analysis. The nonlinear analysis of CFST composite slender column is carried out for square shape having L/D ratio as 13. A numerical model which will have the best match with experimental results will be considered for the further analysis of composite columns having different L/D ratio and shapes. Also, the numerical and experimental elastic axial resistance is compared with the different country codes. The nonlinear finite element analysis will be carried out in Abaqus software.

Keywords Composite column · Numerical model · Concrete simulation

1 Introduction

A steel–concrete composite structural element is taking place rapidly in commercial projects due to its excellent performance under various loading conditions. Initially, the concrete-filled steel tube is being used in some industries with the only purpose to protect concrete by external steel tube from many harmful chemicals and gases, no structural advantage of composite action is being considered.

The main objective of the study is to compare five different numerical models for confined concrete to perform nonlinear analysis to opt best-suited numerical model for the proposed work and to compare the axial resistance using different country codes. The reason behind this is that the nonlinear behavior depends on several parameters such as boundary condition, type of loading, grade of the steel and concrete and wall thickness of the steel tube. Also, the interaction between steel and concrete plays a vital role in the simulation of the composite column; it is not feasible to rely on single numerical properties. It becomes very essential that the

D. R. Prajapati (✉) · D. R. Panchal
The Maharaja Sayajirao University of Baroda, Vadodara, Gujarat, India
e-mail: drprajapati-appmech@msubaroda.ac.in

B. Kondraivendhan et al. (eds.), *Sustainable Building Materials and Construction*,
Lecture Notes in Civil Engineering 222,
https://doi.org/10.1007/978-981-16-8496-8_9

best model which agrees with the experimental results should opt among the five numerical models.

2 Comparison of Different Numerical Models

Following are the five different numerical models developed for finite element simulation,

2.1 Numerical Model 1 Used by Han et al. [1]

For nonlinear analysis, they have modified the stress–strain relationship for the confined concrete presented in Han et al. [13]. The damage plasticity model used in Abaqus for simulation is described below:

$$y = 2x - x^2 (x \leq 1) \tag{1}$$

$$y = \frac{x}{\beta_0 (x-1)^n + x} \; (x > 1) \tag{2}$$

where x = Є/Є$_0$, $y = \sigma/\sigma_0$, $\sigma_0 = f_c'$(N/mm^2), Є$_0$ = Є$_c$ + 800 $\xi^{0.2} \times 10^{-6}$, Є$_c$ = (1300 + 12.5 f'c) × 10^{-6}.

$n = 1.6 + 1.5$ x, $\beta_0 = \frac{(f_c')^{0.1}}{1.2\sqrt{1+\xi}}$, $\xi = \frac{A_s f_y}{A_c f_c'}$ = Confinement factor.

Here, f_c' = characteristic compressive strength of the concrete. For steel tube, an elasto-plastic nonlinear stress–strain relationship model consists of five stages was used. A detailed explanation is given in [1].

2.2 Numerical Model 2 Used by Han et al. [2]

The numerical model showing stress–strain relation of the confined concrete developed in five stages. They have used the nonlinear model developed by Tao et al. (1998). A detailed expression is given as follows:

$$\sigma = \sigma_0 \left[A.\left(\frac{\varepsilon}{\varepsilon_0}\right) - B.\left(\frac{\varepsilon}{\varepsilon_0}\right)^2 \right] \text{ for } \varepsilon \leq \varepsilon_0, \tag{3}$$

$$\sigma = \sigma_0 \left(\frac{\varepsilon}{\varepsilon_0}\right).\frac{1}{\beta.\left(\frac{\varepsilon}{\varepsilon_0} - 1\right)^{\eta} + \frac{\varepsilon}{\varepsilon_0}} \text{ for } \varepsilon > \varepsilon_0 \tag{4}$$

$$\sigma_0 = f_{ck}.\left[1.194 + 0.25.\left(\frac{13}{f_{ck}}\right)^{0.45}.\left(-0.07845.\xi^2 + 0.5789.\xi\right)\right] \tag{5}$$

$$\varepsilon_0 = \varepsilon_{cc} + 0.95\left[1400 + 800.\left(\frac{f_{ck} - 20}{20}\right)^{0.45}\right].\xi^2,\ \varepsilon_{cc} = 1300 + 14.93.f_{ck}$$

$$\eta = 1.60 + 1.5.\left(\frac{\varepsilon_0}{\varepsilon}\right),\ A = 2.0 - k,\ B = 1.0 - k,\ k = 0.1.\xi^{0.745}$$

$$\beta = \frac{0.75.f_{ck}^{0.1}}{\sqrt{1+\xi}} \text{ for } \xi \le 3.0,\ \beta = \frac{0.75.f_{ck}^{0.1}}{\sqrt{1+\xi}(\xi-2)^2} \text{for } \xi > 3.0$$

For material modeling of the steel, the same stress–strain relationship is used which was used in Model 1.

2.3 Numerical Model 3 Developed by Tao et al. [3]

A series of test performed has been compared with A damage plasticity model was used to define a nonlinear property of the confined concrete. The stress–strain relationship has been developed as follows:

$$\frac{\sigma}{f_c'} = \frac{A.X + B.X^2}{1 + (A-2)X + (B+1)X^2} \text{ for } 0 < \varepsilon \le \varepsilon_{c0},$$
$$X = \frac{\varepsilon}{\varepsilon_{c0}},\ A = \frac{E_C\varepsilon_{c0}}{f_c'},\ B = \frac{(A-1)^2}{0.55} - 1,\ \frac{\varepsilon_{cc}}{\varepsilon_{c0}} = e^k, \tag{6}$$

$$f_B = \frac{0.25\left(1 + 0.027f_y\right).e^{\frac{-0.02\sqrt{B^2+D^2}}{t}}}{1 + 1.6.e^{-10}.\left(f_c'\right)^{4.8}} \tag{7}$$

The ascending curve can be described as,

$$\varepsilon_{c0} = 0.00076 + \sqrt{\left(0.626f_c' - 4.33\right).10^{-7}},$$
$$k = \left(2.9224 - 0.00367f_c'\right)\left(\frac{f_B}{f_c'}\right)^{0.3124+0.002f_c'}$$

The descending curve can be developed as,

$$f_B = f_r + \left(f_c' - f_r\right)\exp\left[-\frac{\varepsilon - \varepsilon_{cc}}{\alpha}\right]^{\beta} \text{for } \varepsilon \ge \varepsilon_{cc}, \tag{8}$$

where f_r = Residual stress can be calculated as $0.1f_c'$ for rectangular sections.

Parameter $\alpha = 0.005 + 0.0075\xi_c$ and β will be considered as 0.92 for rectangular columns.

The model can be expressed as follows,

For steel tubes, $\sigma = E_s\varepsilon \ldots (0 \le \varepsilon < \varepsilon_y)$, $\sigma = f_y \ldots . (\varepsilon_y \le \varepsilon < \varepsilon_p)$ $\sigma = f_u - (f_u - f_y)\left[\frac{\varepsilon_u - \varepsilon_{cc}}{\varepsilon_u - \varepsilon_p}\right]^p \ldots (\varepsilon_p \le \varepsilon < \varepsilon_u)$, $\sigma = f_u \ldots (\varepsilon \ge \varepsilon_u)$ $p = E_p\left[\frac{\varepsilon_u - \varepsilon_p}{f_u - f_y}\right]$	$\varepsilon_p = 15\varepsilon_y \ldots f_y \le 300$ Mpa $\varepsilon_p = \left[15 - 0.018(f_y - 300)\right]\varepsilon_y \ldots$ 300 Mpa $\le f_y \le$ 800 Mpa $\varepsilon_u = 100\varepsilon_y \ldots f_y \le 300$ Mpa $\varepsilon_u = [100 - 1.15(f_y - 300)]\varepsilon_y \ldots$ 300 Mpa $\le f_y \le$ 800 Mpa

where E_p is the initial modulus of elasticity at the onset of strain hardening and considered as 0.02 E_s.

2.4 Numerical Model 4 Developed by Mander et al. [4]

This numerical function developed by Mander et al. is adopted [4] to predict stress–strain behavior for confined concrete of CFST columns. The model can be developed using following equations,

$$\sigma_0 = \frac{f_c\lambda\left(\frac{\varepsilon_c}{\varepsilon_{c0}}\right)}{\lambda - 1 + \left(\frac{\varepsilon_c}{\varepsilon_{c0}}\right)^{\lambda}}, \tag{9}$$

$$\lambda = \frac{E_c}{E_c - \left(\frac{f_c}{\varepsilon_{c0}}\right)}, \varepsilon_{c0} = 0.002, \text{ for } f_c \le 28 \text{ Mpa}$$

The stress–strain relation can be developed as,

$$\sigma_c = f_c(\varepsilon_{c0} < \varepsilon_c \le 0.005), \sigma_c = \beta_c f_c(\varepsilon_c > 0.005) \tag{10}$$

$$\sigma_c = \beta_c f_c + 100(0.015 - \varepsilon_c)(f_c - \beta_c f_c)(\varepsilon_c > 0.005). \tag{11}$$

where, $\beta_c = 1 \text{for} D/t \le 24$, $\beta_c = (1.5 - D/48.t)$ for $D/t24 < D/t \le 48$

$$\beta_c = 0.5 \text{ for } D/t > 48.$$

For material modeling of the steel, the same stress–strain relationship is used which was used in Model 1.

2.5 Numerical Model 5 Adopted by Liang and Fregomeni [5]

The nonlinear functions used in this analysis for confined concrete are divided into three parts. The ascending part can be obtained as follows,

$$\sigma_c = \frac{f_{cc}^{'}\lambda\left(\frac{\varepsilon_c}{\varepsilon_{cc}^{'}}\right)}{\lambda - 1 + \left(\frac{\varepsilon_c}{\varepsilon_{cc}^{'}}\right)^{\lambda}} \tag{12}$$

$\lambda = \frac{E_c}{E_c - \left(\frac{f_{cc}^{'}}{\varepsilon_{cc}^{'}}\right)}$, $\Upsilon_c = 1.85\ D_c^{-0.135}\quad (0.85 \le \Upsilon_c \le 1.0)$, $f_{cc}^{'} = \Upsilon_c f_c^{'} + k_1\ f_{rp}\varepsilon_{cc}^{'} = \varepsilon_c^{'}\left(1 + k_2\frac{f_{rp}}{\Upsilon_c f_c^{'}}\right)$., The factor k_1 and k_2 can be considered as 4.1 and 20.5, respectively, and $\varepsilon_c^{'} = 0.002$, $f_{rp} = 0.7(\upsilon_e - \upsilon_s)\left(1 + f_{sy}\frac{2t}{D0-2t}\right) for \frac{D}{t} \le 47$.

For detailed explanation, refer (Liang et al. 2009). The rest of the part of the curve can be obtained by following equations,

$$\begin{aligned}\sigma_c &= \beta_c f_{cc}^{'} + \left(\frac{\varepsilon_{cu} - \varepsilon_c}{\varepsilon_{cu} - \varepsilon_{cc}^{'}}\right)\left(f_{cc}^{'} - \beta_c f_{cc}^{'}\right) \quad \text{for } \varepsilon_{cc}^{'} < \varepsilon_c \le \varepsilon_{cu}, \sigma_c \\ &= \beta_c f_{cc}^{'} \quad \text{for } \varepsilon_c > \varepsilon_{cu}\end{aligned} \tag{13}$$

where ε_{cu} is taken as 0.02 and β_c. will be considered as 1.0 for $D/t \le 40$.

The stress–strain relation can be depicted by the following equation proposed by (Liang 2009)

$$\sigma_s = f_{sy}\left(\frac{\varepsilon_s - 0.9\varepsilon_{sy}}{\varepsilon_{st} - 0.9\varepsilon_{sy}}\right)^{\frac{1}{45}} (0.9\varepsilon_{sy} < \varepsilon_s \le \varepsilon_{st}), \tag{14}$$

where ε_{st} is taken as 0.005, σ_s. is the stress in the steel, ε_s. is the strain in the steel, f_{sy} is the yield stress of steel, ε_{sy} is the yield strain of the steel, ε_{su}. and f_{su} are the ultimate strain and stress in steel, respectively.

3 Boundary Condition and Contact Surfaces

The size of the CFST column is considered as 80 × 80 × 4.8 mm wall thickness with 1080 mm length is considered. In this study, at top $u_1 = 0$, $u_2 = 0$ and $u_3 = -15$ are given as this is a displacement control analysis. At the bottom, $u_1 = u_2 = u_3 = 0$ is considered. The contact between an inner surface of the steel and the outer surface of the concrete is connected by surface-to-surface interaction by generating auto contact pair. Also, the mesh size is considered as 10 mm after performing mesh convergence analysis.

Table 1 Material parameters

Cubic compressive strength of concrete f_c	26.6 N/mm^2
Mod. of Elasticity E_c ($5000\sqrt{f_c'}$)	25,787.59 N/mm^2
Poisson's Ratio (steel and conc)	0.3 and 0.2 resp.
Yield strength of steel	360 N/mm^2

4 Material Properties for Analysis

See Table 1.

5 Results and Discussion

1. The comparison of five different nonlinear models in the form of load vs. axial deformation along with experimental results shown in Fig. 1. All the models show almost same results at 15 mm deflection. However, there are some differences at deformation range 0–5 mm.
2. A detailed comparison at the mischievous zone has been carried out, and the load at 1.5 mm and 2.25 mm deformations has been compared for different models with the experimental results as shown in Fig. 2. In this also, model 2 shows the best comparison with experimental results. (Here, M1, M2, M3, M4, M5 are model 1, 2, 3, 4, 5, respectively.)
3. After comparing all five models for confined concrete, model 2 has opted since it shows the best matching when compared with experimental work. Also, the FEA results have shown a similar mode of failure to the experimental model. Numerical model 2 can be utilized for further analysis of the CFST columns.

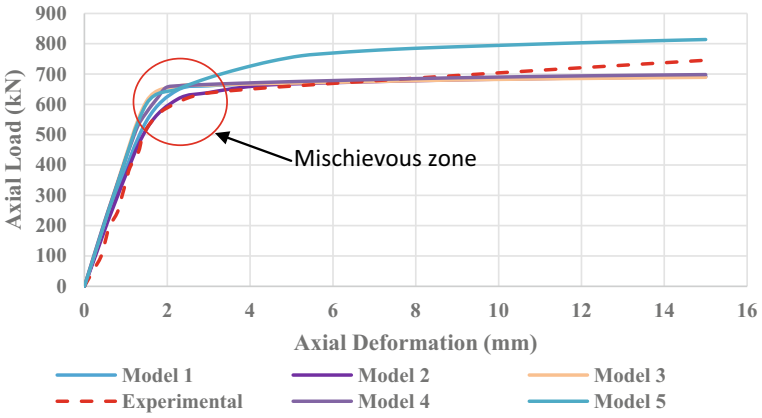

Fig. 1 Axial load versus axial deformation

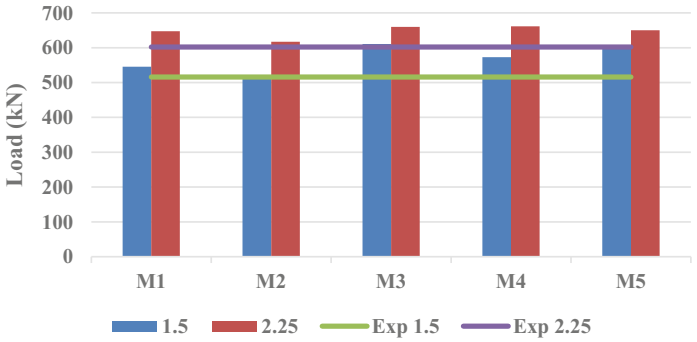

Fig. 2 Axial load at 1.5 mm and 2.5 mm displacement

Table 2 Comparison of axial resistance

S. No.	Analysis type	Max. Compressive resistance (kN)
1	Indian draft code CED38 (13455)	586
2	AISC	631
3	Eurocode	611
4	FE analysis	665
5	Experimental	674

Minimal experimental efforts and a great saving in time can be achieved by only performing the FE analysis.

4. Comparison of different country codes has also been carried out, and the results are tabulated in Table 2 using the draft code CED 38 (13455) of the Indian standards for steel–concrete composite columns; the maximum axial resistance is obtained as 586 kN which is less as compared to other country codes.

References

1. Han L-H, Yao G-H, Tao Z (2007) Performance of concrete-filled thin-walled steel tubes under pure torsion. Thin-Walled Struct 45:24–36
2. Han L-H, Zhao X-L (2001) Tests and mechanics model for concrete-filled SHS stub columns, columns and beam-columns. Steel Compos Struct 1:51–74
3. Tao Z, Wang Z-B, Yu Q (2013) Finite element modeling of concrete-filled steel stub columns under axial compression. J Construct Steel Res 89:121–131
4. Mander JB, Priestley MJ, Park RJJOSE (1988) Theoretical stress-strain model for confined concrete 114:1804–1826
5. Liang QQ, Fragomeni S (2009) Nonlinear analysis of circular concrete-filled steel tubular short columns under axial loading. J Constr Steel Res 65:2186–2196

6. AISC (2010) Load and resistance factor design specification, for structural steel buildings. Chicago, American Institute of Steel Construction (2010).
7. CED 38 (13455) WC Composite Construction in Structural Steel and Concrete – code of practice, Bureau of Indian Standards, New Delhi.
8. Eurocode 4 (2004) Design of composite steel and concrete structures, general rules, and rules for buildings. British Standard Institution, London, ENV 1994-1-1

Fire Exposure Response of Alkali-Activated Concrete Modular Prototype Panels

Ankur Bhogayata and N. K. Arora

Abstract The fire exposure of conventional concrete has been extensively explored to understand the damage scenario in the concrete subjected to direct fire events. However, the conventional concrete's sustainable alternative, namely alkali-activated concrete (AAC), requires rigorous experimental investigations. Since the AAC has emerged as a preferred material for modular or precast structural members, the investigations on the fire resistance and response of AAC as the modular walls and partition may be worth exploring. In the present article, the experimental study of the effects of direct fire on the surfaces of the modular prototype AAC panels has been discussed. The performance criteria of the AAC prototype panels conforming to the IS: 3809-1979 has been evaluated under the varying time durations of fire exposure. The observation values, namely time duration, fire load temperature, the thermal conductivity of panels, mechanical strength before and after fire exposure, and the spalling attributes, were recorded. The test results revealed an encouraging response by the AAC panels under the fire exposure. The AAC panels remained nearly unaffected from any significant surface deterioration, spalling, or cracking even for extended time duration of fire exposure. The panels demonstrated excellent resistance to thermal conductivity also. Similarly, the residual mechanical strength of the panels was found higher than that of the conventional concrete.

Keywords Alkali activated concrete · Fire exposure · Thermal property

1 Introduction

The alkali-activated concrete (AAC) is an emerging concrete-like material with sufficient strength and durability properties. Also, the AAC utilizes waste products of the industries as the major constituents in the mix, and therefore, environmentally, it is

A. Bhogayata (✉)
Marwadi University, Rajkot, Gujarat, India

N. K. Arora
Government Engineering College, Bharuch, Gujarat, India

B. Kondraivendhan et al. (eds.), *Sustainable Building Materials and Construction*,
Lecture Notes in Civil Engineering 222,
https://doi.org/10.1007/978-981-16-8496-8_10

advantageous over the concrete. The present study deals with focusing on the fire resistance offered by the AAC mixes. There have been prototypes of the modular panels of the AAC evaluated under the fire exposure. The researchers have examined that the AAC materials' response, namely geopolymer concretes in terms of bond behavior, effects of exposed fire due to high-velocity impacts, heat transmission, thermal properties, temperature variation, and surface damages, have been explored in the previous studies. Pania et al. [1] have studied the effect of fire on AAC specimens. The study revealed excellent fire resistance by the material at a very high temperature and fire. The aluminum's tertiary chemical binding-silicate chains allowed the release of the inherent water without causing severe damage to the material's microstructure and provided more efficiency over the conventional concrete.

Widodo et al. [2] research revealed the importance of the fine lightweight aggregates in the mortars and composites during the fire exposure. The utilization of the lightweight aggregates in the mixes reduced the thermal conductivity. The present study includes some of the mixes containing the expanded clay aggregates as replacing the conventional aggregates to add the control of the material's thermal conductivity in the post-fire events. In addition, the structural components, namely slabs, columns, and beams, have been investigated for the damage scenario evaluation due to the fire exposure.

Achenbach et al. [3] evaluated the slab and columns for the effect of fire on the elements' cross-section areas by relating the physical and thermal properties of the elements. The work revealed the interesting inter-relationship of the surface damage scenario with the material's density. The work ensured that the thermal properties' uncertainties might be reduced by improving the material properties. This work helped the present study to develop the proper design mix and proportions of the constituents. Monitra et al. [4] worked on the concrete walls subjected to the high-velocity impact on the structural response of the concrete with thermal property changes. The work evaluated the damage caused during the tests for the cracking, spalling, and loss of material and the degree of heat transmission across the wall panel. It was observed that the temperature and fire response were influenced by the type of reinforcement, fibers, and non-fiber concrete mix properties. Sarker et al. [5] evaluated the fly ash-based geopolymer concrete under fire exposure. The study revealed significant details of the modern concrete, namely the material found capable of maintaining the microstructure at the high temperature, and the spalling and cracking of the surface were nearly absent at the temperature up to 1000 °C. The intermolecular bonding of the constituents sustained the fire and effects of temperature excellently. The prototypes prepared in the study have been similarly examined for the possible damage due to the fire exposure and to understand the residual strength mechanism of the AAC material. The test procedure was followed as per the IS:3809-1979 [6] and ACI-216.1-07 [7] guidelines. The relationship of the temperature and duration in the specimens was observed. The damaged surfaces were inspected and assessed for the effect of fire exposure for the spalling, cracking, and loss of material by melting. In addition, the specimens were examined for the strength in compression before and

Table 1 Proportions of the constituents of AAC

Constituent	Content
FA (kg/m^3)	184.55
GGBFS (kg/m^3)	117.44
SF (kg/m^3)	33.56
NaOH molar content (M)	14
NaOH solution (kg/m^3)	49.85
Natural aggregates (kg/m^3)	1973.46

after the fire exposure. The observations were reported and utilized to characterize the AAC blocks subjected to the fire.

2 Experimental

2.1 Material and Mix Proportions

The AAC mixes were prepared with the class F fly ash, grounded granulated blast furnace slag (GGBFS), silica fumes (SF), and the liquid prepared with sodium silicate and sodium hydroxide in the appropriate proportions. The details of the mixture quantities have been listed in Table 1. There were two primary components of the mix, dry constituents, and wet constituents. The dry content comprising the FA, GGBFS, SF, aggregates, and sand was mixed first into the mechanically operated mixer. Then, the liquid was prepared before 24 h of the day of mixing containing sodium silicate and sodium hydroxide. The molar value of the sodium hydroxide liquid was 14 for all the specimens. For the workability of the fresh mix, an appropriate proportion of superplasticizer was also utilized (10% of the weight of the dry constituents).

2.2 Prototype Specimens, Casting, and Testing

The modular wall panel prototypes were prepared with the dimensions of (L × B × T) 450 mm × 450 mm × 100 mm). The specimens were cast with the fresh mix of the AAC at the ambient curing temperature. The GGBFS and SF addition has been observed as the constituents to create enough heat energy to start the chemical process of polymerization of the constituents during the casting stage. The fresh mix's hardening was also observed to be sudden and fast compared to the ordinary concrete mixes.

A total of five prototypes were prepared and tested for fire exposure, as shown in Fig. 1. The tests were performed as per the IS code guidelines and ACI code recommendations. The specimens were allowed for fire exposure for 5 min at the

Fig. 1 Prototype of modular panels

distance of 450 mm between the specimen's surface and the fire source. The thermocouples were attached to all six sides of the specimen to receive the prototype panels' thermal conductivity during and post-test observations. The samples were tested for compressive strength retention after 24 h of the fire test. The compressive strength test results were compared with the test results of the conventional concrete samples of the equivalent strength capacity. The records of temperature transmission, fire load, and time were digitally recorded by the datalogger system, as shown in Fig. 2. The tested samples were utilized for damage detection and observations before compression tests.

Fig. 2 Specimen under fire exposure

3 Results and Discussion

The specimens were tested for 5 min with a continuous fire load. The fire flame's temperature during the test was recorded up to 1200 °C to obtain the heat transfer across the thickness of the specimen, and the temperature readings of the front and back surfaces were continuously recorded in the digital data logger system. The results of the test are shown in Fig. 3.

The graphical presentation compares the results of ordinary cement concrete and AAC. The AAC wall panels performed excellently during all test conditions and showed negligible thermal conductivity. As shown in Fig. 3, the heat transfer between the front and back surfaces was significantly low for the specimens prepared with AAC. The reason behind the low thermal conductivity of AAC may be its denser mix and better intermolecular bonding of the constituents. For a given time of the observation, for AAC samples, the temperature difference between the surfaces was significantly lower than the CC mixes. A similar response has been observed by Sarker et al. [5] during the experimental explorations on fly ash-based concrete. The constituents' fineness, namely fly ash, silica fume, and GGBFS, could produce a denser and more durable mixture by offering a strong adhesion between the gel and the aggregates in the concrete matrix.

The specimens were allowed to maintain the room temperature for 24 h and later with a gentle surface cleaning, utilized for observations for the surface damage scenario. As per the observations, the AAC specimens were found to be intact and free from any significant cracking of the surface even in the extended time of fire exposure. Moreover, there was no significant spalling or loss of the top layer of the wall panel prototype prepared with AAC. On the other hand, the specimens made with the CC mixes showed loss of surface layer and damage in the form of the cracks due to the release of the vapor and water from the mixes during the fire test. The surface loss up to 7 to 10 mm was measured in the case of CC panels, while for the AAC panels, the loss was measured only up to 4 mm. The CC panels showed nearly 12% of surface loss, while the AAC panels showed negligible loss of up to 5% of the total surface area of the panels.

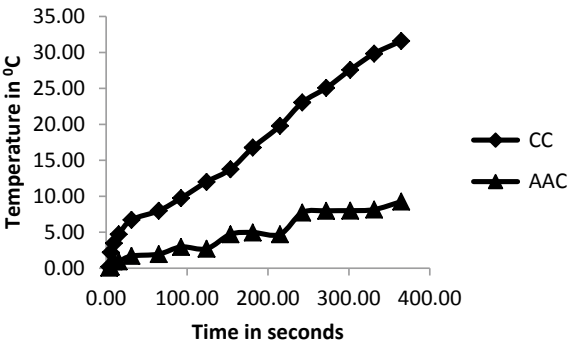

Fig. 3 Comparison of thermal conductivity of CC and AAC panels

Moreover, there was no differential expansion of the AAC panel surfaces observed after the test, and the average crack width was less than 3 mm compared to the CC panels. The compressive strength tests showed that the AAC panels retained the strength up to 67% that of the original strength before the exposure to the fire loads; on the other hand, the CC panels could retain the strength up to 35%. The solid intermolecular bonding in the AAC panels for the constituents supported the resisting capacity of the matrix against the disintegration of the molecular adhesion. The tests, namely fire exposure and compressive strength, established an improved response by the AAC prototype modular panels over the conventional concrete panels.

4 Conclusion

The alkali-activated concrete owing to the fly ash as a significant component resisted the fire exposure damage effectively compared to the conventional concrete. The tests revealed excellent resistance to the panel specimens' thermal conductivity prepared with AAC showed the potential of the use of AAC in the production of modular components for the precast or prefabricated building components, namely wall panels. The AAC was found to retain more than 63% of the strength after the fire exposure, promising excellent strength and durability attributes.

References

1. Panias D, Balomenos E, Sakkas K (2015) The fire resistance of alkali-activated cement-basedconcrete binders. Handbook of alkali-activated cements, mortars and concretes. Woodhead Publishing, pp 423–461
2. Widodo S, Faqih M, Buntara SG (2017) Thermal conductivity and compressive strength of lightweight mortar utilizing Pumice breccia as fine aggregate. Proc Eng 171:768–773
3. Achenbach M, Lahmer T, Morgenthal G (2017) Identification of the thermal properties of concrete for the temperature calculation of concrete slabs and columns subjected to a standard fire—Methodology and proposal for simplified formulations. Fire Saf J 87:80–86
4. Morita T, Beppu M, Suzuki M (2017) An experimental study on the temperature and structural behavior of a concrete wall exposed to fire after a high-velocity impact by a hard projectile. Fire Safety J 91:506–516
5. Sarker PK, Kelly S, Yao Z (2014) Effect of fire exposure on cracking, spalling and residual strength of fly ash geopolymer concrete. Mater Des 63:584–592
6. IS: 3809-1979, Indian standard for fire resistance test of structures
7. ACI-216.1-07 American concrete institute

An Experimental Study on Strength and Durability Properties for Utilization of Rice Husk Ash (RHA) in Geopolymer Concrete

Shalini Annadurai, Kumutha Rathinam, and Vijai Kanagarajan

Abstract Among many environmental issues, carbon dioxide released into the atmosphere takes a serious effect at the time of manufacturing the cement. Cementless binder is an elective material to prevent the earth from global warming. Utilizing pozzolanic-filled industrial waste as source material can decrease the pollution from depravity of environment. Presence of chlorides in the building is the root for causing corrosion in reinforcement and degradation of the reinforced concrete structures. In this paper, tertiary materials such as fly ash, ground-granulated blast-furnace slag, and rice husk ash are employed and activated with 10 Mof NaOH. The results showed that replacement of fly ash by 30% of RHA improves the mechanical properties. Water absorption, sorptivity, and carbonation test are examined to study the durable nature of rice husk ash-based geopolymer concrete. The durability test results exhibit that RHA-based geopolymer concrete enhances the durable properties of concrete by making denser structure by providing strong bonding among the aggregate and paste which resulted in diminishing the water permeability.

Keywords Geopolymer · Rice husk ash · Durability · Interfacial zone · Permeability

1 Introduction

In the world, mankind is benefitted largely by utilizing concrete more and estimated that second priority is given to concrete next to water. The environment faces warming issues at the time of production of cement. Approximately, 1 ton of cement releases 0.95 tons of CO_2 and reaches 6–8% of global warming in the year 2020 as per

S. Annadurai (✉)
Department of Civil Engineering, Sona College of Technology, Salem, Tamil Nadu, India

K. Rathinam
Sri Venkateswara College of Engineering, Sriperumbudur, Tamil Nadu, India

V. Kanagarajan
St. Joseph's College of Engineering, OMR, Chennai, Tamil Nadu, India

B. Kondraivendhan et al. (eds.), *Sustainable Building Materials and Construction*,
Lecture Notes in Civil Engineering 222,
https://doi.org/10.1007/978-981-16-8496-8_11

sustainable development scenario. The letting out of carbon monoxide and carbon dioxide into the atmosphere can be controlled effectively by green concrete called geopolymer concrete. The mechanism of geopolymer in the field of chemistry was identified by the scientist Davidovits in [1], and the zero cement concrete was used majorly in the construction by the Professor B.V. Rangan. The geopolymer will be differentiated as 3D inorganic polymer by adopting a rule: Mn [−(Si−O) z−Al−O] n.w(H_2O), where 'n' is degree of polymerization [2]. This technology removes and replaces the cement by incorporating the different pozzolanic materials such as FA, GGBS, RHA, and metakaolin which are high in silica and alumina content [3]. These resources are mixed with fine aggregate and coarse aggregate and activated by alkaline solutions to achieve the desired strength then allowed for better curing to enhance the speed of polymerization [4]. The strength and durability parameters not only depends on the grading properties but also depends on the source materials used, type of alkaline activator [5] solution which used and curing methods [6, 7] adopted to produce geopolymer concrete. As per the data, the total production of fly ash in the global market is around 780 MT per year, but utilizing the fly ash in concrete is limited to 17–20 percentage only [8].

Partial amount of fly ash [9] was used for the manufacture of Portland pozzolana cement, and the remaining percentage of ash is disposed off either in land or water bodies as a waste material which causes groundwater and soil pollution [10]. Similar to cement, fly ash also becomes shortage nowadays due to extreme usage by the entire construction industry sector being the conventional material. Since 1900s, ground-granulated blast-furnace slag is used as a cementitious matter in concrete due to rich calcium oxide content and developing strength properties of concrete. Rice milling industries produces enormous amount of rice hull and ash was left over during the production of biomass energy. Rice husk ash [11] is also an organic waste and non-bio degradable residue which contains 80–90% of silicon dioxide [12, 13]. Incorporation of RHA in geopolymer concrete increases its corrosion resistance [14]. The literature study revealed that rice husk ash can be used as a cementitious material in geopolymer concrete, enhancing its early age mechanical properties as well as long-term strength properties [15, 16]. The effort has been taken to produce a geopolymer concrete with fly ash, GGBS, rice husk ash and activated with alkaline activator solution. The objective of this experiment is aims to study and compare the mechanical strength and durability properties of rice husk ash-based geopolymer concrete (RHAGPC) with conventional geopolymer concrete (FAGPC).

2 Literature Review

A chemistry Professor [1] found the name geopolymer and identified that geopolymer substances belong to inorganic family. Ganesan et al. [17] assessed the durability characteristics of plain and fiber-reinforced geopolymer concrete (GPC) and its correlation to Portland cement-based conventional concrete (CC). The investigation's results included microstructure-related properties such as water absorption,

Table 1 Chemical oxides of different source materials

Chemical oxides	Present study		
	Fly ash (%)	GGBS (%)	RHA (%)
SiO_2	55.90	41.24	88.64
Al_2O_3	15.23	20.64	1.23
Fe_2O_3	21.78	7.28	1.19
CaO	0.17	25.45	1.09
LoI	0.62	Nil	<6%

apparent porosity, and sorptivity of GPC being lower than in CC and expansion of less steel fiber which improved GPC. VijayaRangan [18] investigated a detailed study on the effect of Geopolymer concrete in environmental protection and concluded that, geopolymer concrete had excellent compressive strength and was suitable for structural applications. Arshad et al. [19] studied on the preparation of geopolymer concrete using Metakaolin (MK) and rice husk ash (RHA) as alternative material for Portland cement. From the observation, it was seen that the major crystal was formed with minor crystals (mullite) which was started to develop at a temperature of 1000 °C [20]. The occurrence of crystalline phase correlated to the mechanical properties of geopolymer concrete.

3 Materials and Properties of GPC

3.1 Source Materials

Class F Fly ash was used in this work which has specific gravity and blain fineness of 2.46 and 2351 cm^2/g, respectively, and it was purchased from Mettur thermal power plant. Ground-granulated blast-furnace slag was received from Quality polytech, Mangalore and it has specific gravity and blain fineness of 3.11 and 4580 cm^2/g, respectively. Rice husk ash was incinerated and bought from locally available rice mill industry, then pulverized in a ball mill for every 60 min. The specific gravity and blain fineness of RHA are 2.13 and 5675 cm^2/g, respectively. Table 1 represents chemical oxides of different source materials and compared with some researchers also.

3.2 Aggregates and Geopolymer Liquids

Locally available Zone-II river sand and locally available 12-mm size of granite stone was taken as fine aggregates and coarse aggregates. The properties of fine and coarse aggregates such as specific gravity, fineness modulus, bulk density are 2.60,

2.60, 1675 kg/m^3, and 2.91, 5.40, 1520 kg/m^{3}was determined as per IS: 2386 (Part III)-1963 [21]. NaOH was available in the form of pellets with 97–98% purity, and Na_2SiO_3 was available in the form of liquid [2]. The Conplast SP 430 superplasticizer was added to the mix. The additional water of 15% of binder materials was added to attain the desired workability. Distilled water was utilized to make the NaOH solution with a concentration of 10 M.

3.3 Mix Proportion

Table 2 specifies the optimized mix proportion for 1 m^{3}of rice husk ash-based geopolymer concrete.

4 Experimental Set up and Results

4.1 Compressive Strength of FAGPC and RHAGPC

The fresh concrete samples were poured in 10 cm × 10 cm × 10 cm cube mold and compaction for each layer was done by compacting steel rod. The concrete was demolded next day and placed in room temperature at 27 ± 2 °C for ambient curing. Table 3 shows the compressive strength result of fly ash and rice husk ash-based geopolymer concrete.

4.2 Tensile and Flexural Strength of FAGPC and RHAGPC

The cylindrical specimen with a size of 15 cm × 30 cm was used to find the maximum failure load at the age of 7 days, 28 days, and 56 days. The testing procedure was followed as per the accordance of IS 516–1959, and all the test specimens were named for further identification. The tensile strength results for 90% replacement of fly ash and 10%, 20%, and 30% replacement of rice husk ash was listed in Table 3. The tensile properties of fly ash and rice husk ash-based geopolymer concrete was found by 10 cm × 10 cm × 50 cm prism in a universal testing machine with a loading capacity of 1000 kN. As per the guidelines in IS 516–1959, modulus of rupture was given to the prism under two-point loading condition. The flexural strength of fly ash and rice husk ash for different mixes at different age of curing was exposed in Table 3.

Table 2 Mix proportion for 1 m^3 of rice husk ash-based geopolymer concrete in kg

Mix Id	% of replacement			Fly Ash	GGBS	RHA	FA	CA	NaOH	Na_2SiO_3	Water	SP
	FA	GGBS	RHA									
GPC-1	90	10	0	354.60	39.40	0	554.40	1294.00	45.10	112.60	59.14	11.83
R10	80	10	10	315.20	39.40	39.40	554.40	1294.00	45.10	112.60	59.14	11.83
R20	70	10	20	275.80	39.40	78.80	554.40	1294.00	45.10	112.60	59.14	11.83
R30	60	10	30	236.40	39.40	118.20	554.40	1294.00	45.10	112.60	59.14	11.83

Table 3 Strength properties of RHA-based GPC

S. No.	Mix Id	Compressive strength in MPa			Split tensile strength in MPa			Flexural strength in MPa		
		7 d	28 d	56 d	7 d	28 d	56 d	7 d	28 d	56 d
1	GPC-1	21.20	31.30	32.32	1.62	2.25	2.64	2.12	3.26	3.42
2	R10	20.19	29.96	30.65	1.53	1.94	2.21	2.28	3.50	3.67
3	R20	17.33	24.46	25.95	2.08	2.39	2.54	2.06	3.17	3.39
4	R30	18.43	28.06	30.33	2.06	2.32	2.49	2.20	3.39	3.62

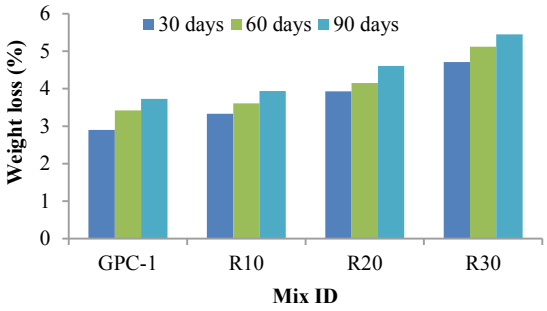

Fig. 1 Weight loss of RHA-based GPC

4.3 Water Absorption of FAGPC and RHAGPC

The porous structure of the geopolymer concrete can be noticed by immersing the specimen of cube with dimension 10 cm × 10 cm × 10 cm in water tank [22]. The weight of the hardened concrete cube was noticed initially then immersed in water tank for 30, 60, and 90 days. The less amount of water absorbed by the geopolymer concrete represents densely packed concrete. After the required time, the loss of strength for each ratio can be analyzed by determining the compressive strength in compressive testing machine. The weight loss of RHA-based GPC at different ages are shown in Fig. 1. The fineness of RHA is very high when compared to other two pozzalonic material. In other hand, RHA contains some unreacted particles in it which was evident from chemical composition of RHA. These two parameters resulted in the increased water absorption capacity of RHA-based geopolymer concrete.

4.4 Sorptivity of FAGPC and RHAGPC

The capillary suction of liquids can be determined by the unidirectional absorption test (or) sorptivity test. As per guidelines of ASTM C 1585-04, the concrete core sample of 100 mm × 50 mm size is placed in a tray with a depth of 3–5 mm. The sorptivity value can be obtained from the following the expression $Q = \mathrm{Ak}\sqrt{t}$ [23].

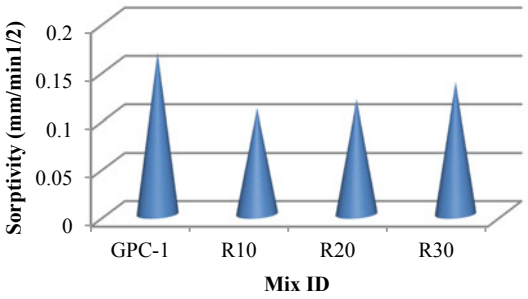

Fig. 2 Sorptivity of RHA based GPC

Figure 2 represents the sorptivity value for GPC 1, R10, R20, and R30 replacement of fly ash and rice husk ash-based geopolymer concrete. The reduction in sorptivity may be due to presence of excessive RHA affecting the structural compatibility by delaying the progress to the denser stage. The capillary suction was enhanced due to it.

4.5 Carbonation of FAGPC and RHAGPC

The concrete structures are mostly deteriorated by the action of corrosion attack in the reinforcement rod attached with the bonding materials. The cubical size of 10-cm test specimen was taken to find the carbonated sample. The specimen was placed in a carbonation chamber by passing carbon dioxide for 1 day. It is one of the simple and easy methods to establish the extent of carbonation on the cube samples. The pH of the sample was found at an age of 0, 3,7,28, and 56 days by water analyzer method. The pH of all mixes before and after carbonation is exposed in Table 4. In OPC concrete, Ca $(OH)_2$ and C–S–H gel assist buffering to ensure pH value greater than 13. Nevertheless, in RHA-based geopolymer concrete, such buffering is not buoyed by the gel. In geopolymer concrete, the carbonation is hypothesised as the reaction of the sodium hydroxide with CO_2 forming sodium carbonate hydrates [24]. This output leads to lesser minimization of pH value, which ranges from 10.58.

Table 4 pH from carbonation test

S. No.	Mix Id	pH (in days)				
		0	3	7	28	56
1	GPC-1	11.43	11.20	11.17	11.10	11.04
2	R10	11.20	10.91	10.86	10.75	10.72
3	R20	11.08	10.82	10.76	10.69	10.61
4	R30	11.03	10.77	10.69	10.61	10.58

5 Conclusions

The test result proves that rice husk ash can be utilized as pozzolanic material to make durable geopolymer concrete with relatively high loss on ignition. The increase in the fineness of RHA resulted in the enriched reactivity and high degree of polymerization. Experimental results on mechanical properties confirm that effective utilization of rice husk ash in the construction field up to 30% of addition with other pozzolanic materials improves the strength characteristics and also enhances the impermeability properties of geopolymer concrete. The test results of durability study also reveal that the production of geopolymer concrete with tri-blended pozzolanic materials resulted in reduced sorptivity and carbonation effect due to more densified structure formation. The durability of concrete structures would be more when incorporating the non-corrosive materials as an additive likes RHA, FA, and GGBS as an alternative to cement. By replacing 30% of RHA with fly ash and GGBS, we can achieve target strength of M_{20} grade concrete. Since, RHA is a waste material, with a maximum percentage, it can be more beneficial in the production of load bearing blocks, bricks, and tiles with low construction cost. By holding the RHA in construction, it shows promising results in diminishing the pollution which softens the environment and also dropping the principal cost of the infrastructure in the country.

References

1. Davidovits J (1988) Geopolymer chemistry and properties. In: Proceedings of the first European conference on soft mineralurgy, France
2. Nanda Kishore G, Gayathri B (2017) Experimental study on rise husk ash and fly ash based geopolymer concrete using M-Sand. In: IOP conference series: materials science and engineering, pp 225
3. Kumar Das S, Mishra J, Patel A (2012) Sulphuric acid resistant ecofriendly concrete from geopolymerisation of blast furnace slag. Ind J Eng Mater Sci 19:357–367
4. Adak D, Sarkar M, Mandal S (2017) Structural performance of nano-silica modified fly-ash based geopolymer concrete. Constr Build Mater 135:430–439
5. Patankar SV, Ghugal YM, Jamkar SS (2014) Mix design of fly ash based geopolymer concrete. Adv Struct Eng 1619–1634
6. Jamkar SS, Ghugal YM, Patankar SV (2013) Effect of fineness of fly ash on flow and compressive strength of geopolymer concrete. Indian Concrete J 87(4):57–61
7. Nath P, Sarker PK, Rangan VB (2015) Early age properties of low-calcium fly ash geopolymer concrete suitable for ambient curing. Proced Eng 125:601–607
8. Hardjito D, Wallah SE et al (2004) On the development of fly ash based geopolymer concrete. ACI Mater J 101:467–472
9. Malhotra VM (1999) Making concrete greener with fly ash. ACI Concrete Int 21(5):61–66
10. Malhotra VM Ramezanianpour AA (1994) Fly Ash in concrete. CANMET Natural Resources, Canada
11. Katroliya A, Tiwari A (2013) The effect of rice husk ash and fly ash used as supplementary cementing material on strength of mortar and concrete. Int J Eng Res Technol 2(12):3696–3706
12. Dara DR, Bhogayata AC (2015) Experimental study of RHA-FA based geopolymer composites. Int J Sci Res Dev 3(4):1615–1617

13. Mehta PK, Malhotra VM (1992) Rice husk ash—a unique supplementary cementing material. In: Abstracts of the CANMET/ACI international symposium on advances in concrete technology, Athens, Greece, 407–430 May 1992
14. Das SK, Mishra J, Mustakim SM (2018) Rice husk ash as a potential source material for geopolymer concrete: a review. Int J Appl Eng Res 13(7):81–84
15. Siddique R, Cachim P (2018) Waste and supplementary cementitious materials in concrete: Characterisation, Properties and Applications, pp 599–621
16. Rangan BV (2008) Mix design and production of fly ash based geopolymer concrete. Ind Concrete J 82(5):7–15
17. Ganesan N, Abraham R, Deepa Raj S (2015) Durability characteristics of steel fibre reinforced geopolymer concrete. Constr Build Mater 93:471–476
18. VijayaRangan B (2014) Geopolymer concrete for environmental protection. Ind Concrete J 88(4):41–59
19. Arshad SE, Aripitri SM, Zainuddin ESM (2015) Geopolymerization of Metakaolin using rice husk ash as silica source with na-based activator. ARPN J Earth Sci 3(3):1–11
20. Das SK, Mishra J, Patel A (2018) A review on rice husk ash based geopolymer concrete. In: Abstracts of the international conference on industrial impacts on environment and sustainable development, Govt. College of Engineering, Keonjhar, Odisha April 2018
21. IS 516 (1959) Method of test for strength of concrete, Reaffirmed 2004, Bureau of Indian standards, New Delhi
22. ASTM Standard C1585 (2006) Standard test method for measurement of rate of absorption of water by hydraulic-cement concretes. ASTM International, West Conshohocken, PA
23. Iyer NR (2020) 1-An overview of cementitious construction materials. New Mater Civil Eng 1–64
24. Kulkarni MS, Mirgal PG et al (2014) Effect of rice husk ash on properties of concrete. J. Civil Eng Environ Technol 1(1): 26–29
25. IS 456 (2000) Indian standard code for plain and reinforced concrete, code of practice, 4th Revision, BIS, New Delhi

Study of Accelerated Carbonation Performance of Concrete Containing Natural Zeolite with the Help of Electrochemical Impedance Spectroscopy

Akshay Ramesh Bura and B. Kondraivendhan

Abstract In this study, an alternate accelerated carbonation technique was investigated using non-destructive testing (electrochemical impedance spectroscopy) on concrete mixes containing natural zeolite. The extent of carbonation in concrete mixtures containing natural zeolite powder and natural zeolite fine aggregates was examined. Alternate accelerated carbonation was introduced by exposing concrete specimens to alternate wetting and drying cycles of 7 days in 0.5 M sodium bicarbonate solution for 90 days. The extent of accelerated carbonation was studied by evaluating compressive strength, carbonation depth and resistance offered by carbonated concrete using the electrochemical impedance spectroscopy technique. Concrete mixes prepared with natural zeolite powder and fine aggregate display higher compressive strength, higher carbonation depth and excellent concrete resistance due to microstructural densification. Prolonged accelerated carbonation confirmed the enhanced compressive strength and extent of carbonation reaction through decreased concrete porosity.

Keywords Carbonation · Natural zeolite · Electrochemical impedance spectroscopy · Carbonation depth · Concrete resistance

1 Introduction

Portland cement (PC)-based concrete is comprehensively used as the primary material for construction in the world. Cement demand in developing countries is growing as a result of fast urbanization [1]. Due to this high demand for cement, the construction industry is a significant source of carbon dioxide (CO_2) emissions in the atmosphere [2]. Therefore, recently, the research focus has been diverted toward an alternative supplementary cementitious material (SCM), resulting in reduced cement usage in concrete. Among the other SCMs, natural zeolite has received significant attention due to its microporous structure and high CO_2 adsorbent property. In recent years,

A. R. Bura (✉) · B. Kondraivendhan
Department of Civil Engineering, Sardar Vallabhbhai National Institute of Technology, Surat, Gujrat 395007, India

B. Kondraivendhan et al. (eds.), *Sustainable Building Materials and Construction*,
Lecture Notes in Civil Engineering 222,
https://doi.org/10.1007/978-981-16-8496-8_12

many research studies have been conducted on the natural carbonation of zeolite concrete and observed that this could be an excellent medium for CO_2 sequestration and cement utilization reduction in concrete [1, 3]. Few researchers have used natural zeolite fine aggregates to replace natural river sand in conventional concrete partially. They have found that natural zeolite aggregates can be an excellent CO_2 adsorption medium when used in the concrete mix [4]. The carbonation process should be artificially increased to accelerate CO_2 sequestration in concrete as the natural carbonation process is not quick and efficient. The accelerated carbonation is usually done by curing specimens in a sealed chamber with a much higher CO_2 concentration than the natural atmosphere (0.04%) [2]. In this study, an innovative alternate technique for accelerated carbonation was implemented using a carbonated water solution (0.5 M sodium bicarbonate solution) instead of a conventional high concentration CO_2 chamber. Recently, electrochemical impedance spectroscopy (EIS) is developing into a widely used non-destructive technique (NDT) for evaluating the electrochemical behavior of complex heterogeneous reinforced concrete systems. Numerous studies have used EIS as an efficient method to provide information on concrete microstructure, corrosion rate and responses at the steel–concrete interface [5].

In this study, the experimental work has been carried out to estimate the extent of carbonation reaction on normal concrete (NC) and zeolite concrete (ZC) specimens exposed to an alternate accelerated carbonation technique. The effect of accelerated carbonation curing on NC and ZC specimens' mechanical properties was evaluated by conducting a compressive strength test. The extent of carbonation reaction progress in the concrete matrix can be assessed by performing carbonation depth measurement and EIS.

2 Experimental Details

2.1 Material Details and Mix Proportion

In this experimental study, two varieties of binders, namely 53 grade ordinary Portland cement (OPC) and OPC with 15% natural zeolite replacement (by binder weight), were used. Coarse aggregates of two sizes, i.e., 20 mm maximum size of aggregate (MSA) and 10 mm MSA and river sand available locally as fine aggregate were used in concrete mix preparation. Thirty percent of fine aggregate content was replaced with fine zeolite aggregates in concrete mixes. The concrete mix proportioning was done by using the DOE method. The extent of carbonation in the concrete depends on its porosity, and porosity further depends on the concrete mix's water-to-binder ratio (w/b). Hence by considering this correlation, the w/b ratio of 0.55 was selected to prepare the concrete mixtures. The concrete mix design for one cubic meter comprises 338.18 kg of OPC, 186 kg of water, 675.30 kg pf river sand,

720.31 kg of 20 mm MSA and 480.21 kg of 10 mm MSA. In the total coarse aggregate content, the proportion of 20 mm MSA and 10 mm MSA aggregate was fixed at 60% and 40%, respectively.

2.2 *Preparation of Specimen and Exposure Condition*

From each concrete mix, cube specimens of 150 mm size were prepared to determine compressive strength. Cylindrical reinforced concrete specimens of 100 mm diameter and 200 mm height with a centrally embedded thermomechanically treated (TMT) steel bar of 12 mm diameter and 250 mm length were prepared for electrochemical measurement test. The TMT steel bar was pickled in 10% sulfuric acid for 15 min, then rinsed in potable water and cleaned with a wire brush to remove any rust present on the surface. Further, the steel bar was masked with insulating tape followed by a two-part epoxy resin coating on the steel bar's particular location to avoid crevice corrosion at places where the surrounding medium of steel bar changes. The cover depth and the exposed length of the steel rebar in the cylindrical specimens are 20 mm and 100 mm, respectively, as represented in Fig. 1. The concrete cubes and cylindrical reinforced concrete specimens were demolded after an initial 24 h of preparation and transferred to the curing tank for 27 days of initial water curing. After completion of initial curing, the cube specimens undergo the compressive strength test, and the cylindrical reinforced concrete specimens were subjected to 14 days of laboratory drying. Subsequently, the epoxy sealer was applied to the top and bottom of the cylindrical specimens. Accelerated carbonation of concrete specimens was carried out using an alternate carbonation technique in which a 0.5 M concentration of sodium bicarbonate ($NaHCO_3$) solution is used as an exposure solution. To accelerate the ingress of carbonate ions in the concrete, the wetting and drying cycle comprises 7 days of wetting followed by 7 days of drying in laboratory conditions.

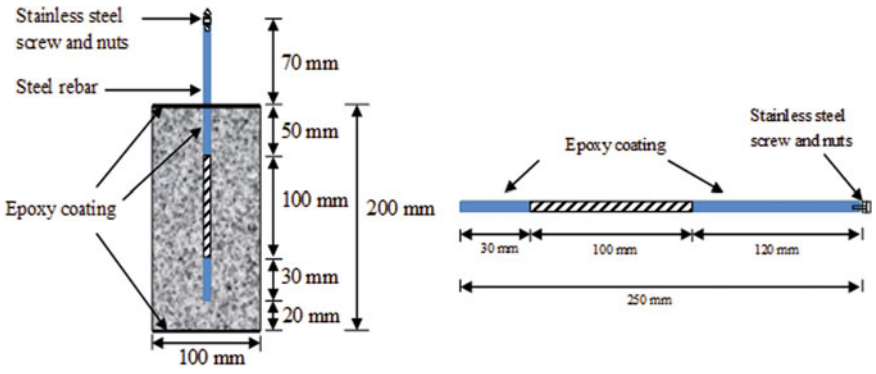

Fig. 1 Schematic diagram of reinforcement steel bar and cylindrical reinforced concrete specimens

Electrochemical measurements were carried out at the start of the exposure and the end of the exposure period of 90 days.

2.3 Carbonation Depth Measurement

After 90 days of accelerated carbonation curing, concrete cube specimens were split into two vertical parts, and freshly fractured surfaces were sprayed with 1% phenolphthalein indicator solution. Phenolphthalein indicator works as a pH indicator and turns uncarbonated concrete to magenta color, whereas the color of fully carbonated concrete remains unchanged. Hence, the carbonation depth of concrete specimens was determined by measuring the distance between the boundary of color change and the concrete surface. In this study, the carbonation depth value reported is the average of three replicate cube specimens.

2.4 Compressive Strength Test

After completion of 0 days and 90 days of accelerated carbonation curing, the NC and ZC specimens were tested in a compression testing machine to determine the compressive strength. These carbonation curing ages were calculated after initial 28 days of normal water curing. For both the concrete mixes, the compressive strength value reported is the average of three replicate cube specimens.

2.5 Electrochemical Impedance Spectroscopy (EIS)

The EIS measurements were carried out on cylindrical reinforced concrete specimens prepared with NC and ZC mixes at the start of accelerated carbonation curing and after 90 days of accelerated carbonation curing. The electrochemical measurements were carried out using a three-electrode system consisting of reinforced steel bar as working electrode (WE), saturated calomel electrode (SCE) as reference electrode (RE) and platinum electrode as an auxiliary electrode (AE). In this study, the EIS measurements were carried using ACM make-Gill AC serial no. 1824 corrosion monitoring instrument in a frequency range of 100–10 MHz, with five points recorded per decade. The sinusoidal wave of amplitude 25 mV RMS was applied. The EIS data was analyzed based on equivalent circuit models using Zman software.

3 Results and Discussion

3.1 Carbonation Depth Measurement

After 90 days of accelerated carbonation curing, 3 and 6 mm carbonation depth values were ascertained in the NC specimens and ZC specimens, respectively. From the results, it is depicted that the concrete containing natural zeolite powder and fine aggregate has greater carbonation depth values as compared to normal concrete. This is attributed to the greater extent of the carbonation reaction in ZC specimens in which calcium hydroxide ($Ca(OH)_2$) reacts with carbonate ions $\left(CO_3^{2-}\right)$ present in carbonated curing water and forms calcium carbonate ($CaCO_3$) [1].

3.2 Compressive Strength

The compressive strength values of NC and ZC specimens exposed to accelerated carbonation curing for 90 days after the initial 28 days of normal water curing are shown in Fig. 2. Each value represented in the figure is the average of three replicate cube specimens of the respective concrete mix. From the results, it is observed that the compressive strength of NC specimens was greater than ZC specimens after the initial 28 days of normal water curing due to a more significant hydration reaction in NC specimens. After 90 days of accelerated carbonation curing, the compressive strength of ZC specimens was greater than that of NC specimens due to the greater extent of carbonation reaction and a higher degree of pozzolanic reaction between $Ca(OH)_2$ and natural zeolite [1].

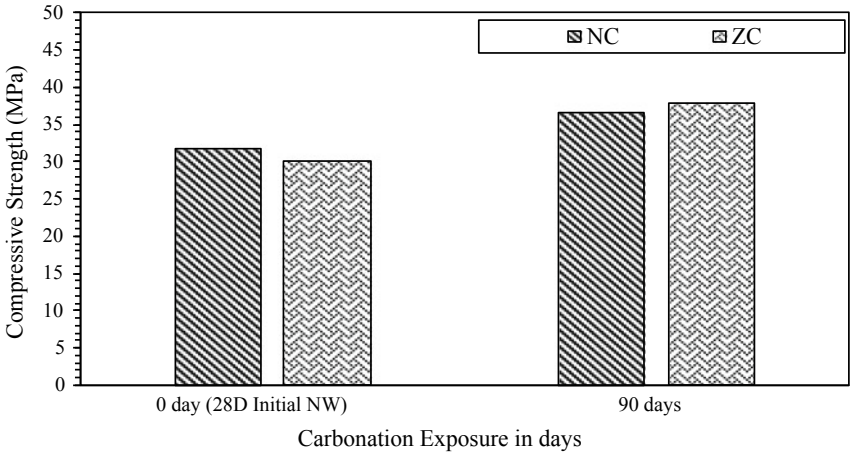

Fig. 2 Compressive strength of NC and ZC specimens

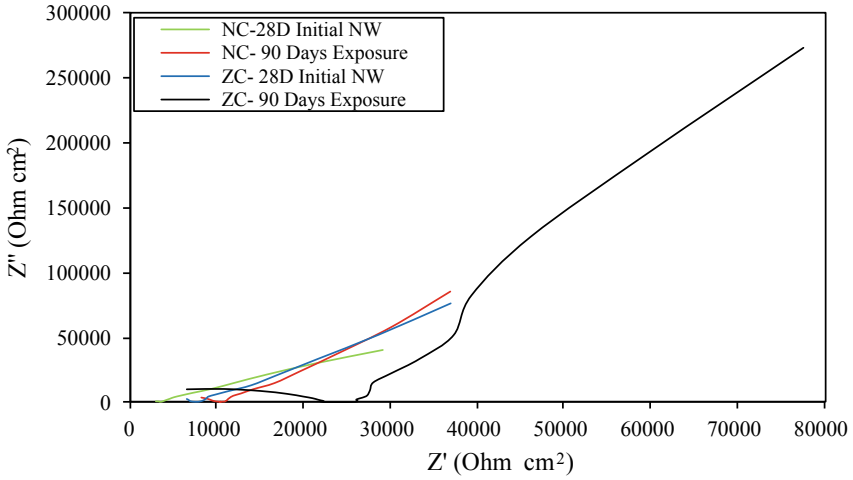

Fig. 3 Nyquist plot for NC and ZC specimens

3.3 Electrochemical Impedance Spectroscopy (EIS)

The electrochemical impedance spectra recorded for cylindrical reinforced concrete specimens prepared with NC and ZC mixes and exposed to accelerated carbonation curing for 90 days are represented in Fig. 3. From the figure, it is observed that in all the four Nyquist plots, two distinct capacitive arcs were depicted, in which the first capacitive arc represents the bulk properties of concrete cover and the second capacitive arc represents the properties of the electrode. Here in this study, we only consider the first capacitive arc representing the bulk properties of concrete. Further, these Nyquist plots were used to determine the resistance offered by concrete cover with the help of equivalent circuit models in Zman software. At the start of accelerated carbonation exposure, the concrete cover resistance in NC and ZC specimens was 60.21 kΩ cm^2 and 207.29 kΩ cm^2, respectively. After 90 days of accelerated carbonation exposure, the concrete cover resistance in NC and ZC specimens was 558.80 kΩ cm^2 and 746.16 kΩ cm^2, respectively. The results show that the ZC specimens show more concrete cover resistance than NC specimens due to the greater extent of $CaCO_3$ precipitation in the concrete pores due to carbonation reaction and a higher degree of pozzolanic reaction between $Ca(OH)_2$ and natural zeolite, which further reduces the porosity of the concrete matrix [1].

4 Conclusion

The following conclusions were reported from the experimental study on the extent of carbonation reaction in normal and zeolite concrete exposed to alternate accelerated carbonation techniques using electrochemical impedance spectroscopy.

- The carbonation depth of NC and ZC specimens after 90 days of accelerated carbonation exposure was 3 mm and 6 mm, respectively. The carbonation depth was greater in ZC specimens than in NC specimens due to a more significant carbonation reaction.
- After 90 days of accelerated carbonation exposure, the ZC specimens exhibited an increment of 26.33% in compressive strength than the compressive strength at the start of the exposure. This increment in compressive strength at the end of 90 days of exposure is due to the greater extent of carbonation reaction and a higher degree of pozzolanic reaction between $Ca(OH)_2$ and natural zeolite.
- The concrete cover resistance in ZC specimens was 746.16 kΩ cm^2 after 90 days of accelerated carbonation exposure. The results show that the ZC specimens demonstrate more concrete cover resistance than NC specimens due to the greater extent of $CaCO_3$ precipitation in concrete pores due to carbonation reaction and a higher degree of pozzolanic reaction between $Ca(OH)_2$ and natural zeolite.

References

1. Ramesh BA, Kondraivendhan B (2020) Effect of accelerated carbonation on the performance of concrete containing natural zeolite. J Mater Civ Eng 32(4):04020037
2. Liu B, Qin J, Shi J, Jiang J, Wu X, He Z (2020) New perspectives on utilization of CO_2 sequestration technologies in cement-based materials. Constr Build Mater 272:121660
3. Ramesh B A, Kondraivendhan B (2020) An Alternative technique for accelerated carbonation of normal concrete. In: IOP conference series: materials science and engineering (IOP Publishing) 829(1):012019
4. Vejmelková E, Koňáková D, Kulovana T, Keppert M, Žumár J, Rovnaníková P, Keršner Z, Sedlmajer M, Černý R (2015) Engineering properties of concrete containing natural zeolite as supplementary cementitious material: Strength, toughness, durability, and hygrothermal performance. Cement Concr Compos 55:259–267
5. Kaur K, Goyal S, Bhattacharjee B, Kumar M (2017) Electrochemical Impedance Spectroscopy to study the carbonation behavior of concrete treated with corrosion inhibitors. J Adv Concr Technol 15(12):738–748

A New EBG Superstrated Rectangular Slotted Microwave Patch Antenna Sensor with Enhanced Gain for Steel Rebar Nondestructive Corrosion Monitoring in Civil Structures

Meghayu Adhvaryu, Piyush N. Patel, and Chetan D. Modhera

Abstract This research introduces the layout and implementation of a slotted rectangular patch antenna device sensor with the enhanced advantage of tracking corrosion on public bodies that does not harm the embedded rebar. The 3.17 GHz frequency resonant rectangular cone is modelled and fitted with an electronic electromagnetic band gap (EBG) with a 2×10 cm^2 opening slot in the centre. The magnitude of the reflection of the coefficient (S11) is calculated with the EBG superstrate included in the test sample at a distance near the field. The oxide layer formed by the process of corrosion above the metal surface creates a change in the strength of the dispersed fields that are detected and measured.

Keywords Corrosion monitoring · Slotted microwave sensor · Reflection coefficient · Signal detection circuit · Superstrated patch

1 Introduction

In the civil structures, rebar is one of the key structural design systems widely used. The erosion rate or corrosion rate decreases the uprightness of the steel and seriously damages the structures because of the natural effect and complicated coatings [1]. Various non-damaging testing techniques have been set up using fibre Bragg grating [2], electrochemical impedance spectroscopy [3], RFID sensors [4] and so on. Fibre Bragg grating (FBG) offers the most elevated affectability for changes in the underlying structure and morphology. Be that as it may, because of the costly establishment and lower fibre capacity, these sensors need greater support and additional shielding [5]. For scanning to locate corrosion strength, a slotted rectangular patch with a

M. Adhvaryu (✉) · P. N. Patel
Sensor Research Laboratory, Department of Electronics Engineering, Sardar Vallabhbhai National Institute of Technology, Surat, Gujarat 395005, India

C. D. Modhera
Department of Civil Engineering, Sardar Vallabhbhai National Institute of Technology, Surat, Gujarat 395005, India
e-mail: cdm@amd.svnit.ac.in

B. Kondraivendhan et al. (eds.), *Sustainable Building Materials and Construction*, Lecture Notes in Civil Engineering 222,
https://doi.org/10.1007/978-981-16-8496-8_13

restricted aperture is used. The theory of sensing, designing and manufacturing of the slotted patch antenna sensor and characterisation is discussed in Sect. 2. The setup of the experiment and the process of sample preparation are discussed in Sect. 3. The findings and data points from the sensor system are analysed in Sect. 4, which coincides with the corrosion phenomenon. Some significant results are illustrated in the concluding segment.

2 Sensor Design and Fabrication

The slotted antenna system will work on classical reflectometry. Magnitude of the reflection coefficient (S_{11}) will be affected by the corrosion which is basically nothing but the oxide layer formation on the steel rebar. As shown in Fig. 1, the flux ($\vec{\vec{E}}_{Tr}$)obtained through slotted patch can be represented as the addition of two field. First is incident flux, and second is reflected flux. Which is experienced as $\vec{\vec{E}}_t + \vec{\vec{E}}_r$. The incident field ($\vec{\vec{E}}_t$)is somewhat adsorbed to the layer of oxide, and the rest portion of the field is thrown back ($\vec{\vec{E}}_r$)through the aperture slot back to the RMPA.

Received power experiences a delay because of the presence of the oxide layer in the form of corrosion,

$$P_r(t - t_d) = 1 \oint_0 E_r(\omega) e^d_{j\omega(t-t)} d\omega \tag{1}$$

It can be observed that oxide layer formation in the form of corrosion affects the wave propagation.

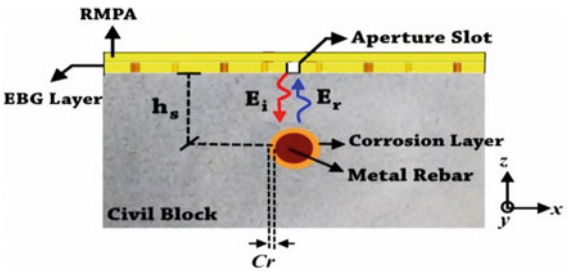

Fig. 1 Sensing mechanism

2.1 Design

For designing an antenna sensor, a slotted microwave patch antenna is taken into account. It is important to sensory system that operating antenna produces minimum or zero interference of other frequency band. By solving the transmission line equation [6], the dimension of the slotted patch antenna which has length 44 mm and width 30 mm was derived. A simulated response of the antenna, frequency band of 3.17 GHz is chosen to be the operating frequency. Operating frequency $f_0 = 3.17$ GHz, relative permittivity of the substrate (R04450B) is $\varepsilon_r = 3.38$, and height of the substrate $h = 1.2$ mm was taken into account. CST MWS v.16 [7] was used to solve geometry of the slotted antenna. Figure 2 shows that the result of simulation coefficient of reflection (S11) is calculated to −29.04 dB at 3.17 GHz, a confident aperture slotted patch increases scanning resolution as well as interference.

An electromagnetic band gap (mushroom EBG) with equidistance metal through is built now to increase the scanning resolution and to work in the 3.17 GHz frequency band. Only a particular RF signal across the path is enabled by the electromagnetic band gap structure. This will decrease disruptive multipath propagation interference. This is also minimised by the phase move. The square EBG base element format of length $L_1 = 9$ mm is shown in Fig. 3a, shown on a substratum with relative permittivity (ε_r) 10.2 and height (h) 1.27 mm, respectively. The locale is determined using Brillouin zones equations for band gap [8] by doling out intermittent limit

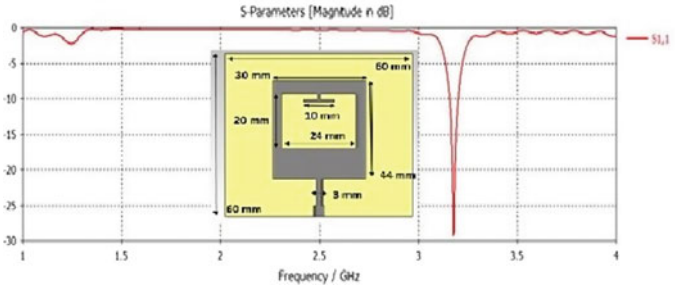

Fig. 2 Simulated plot of S_{11} with slotted RMPA inset schematics

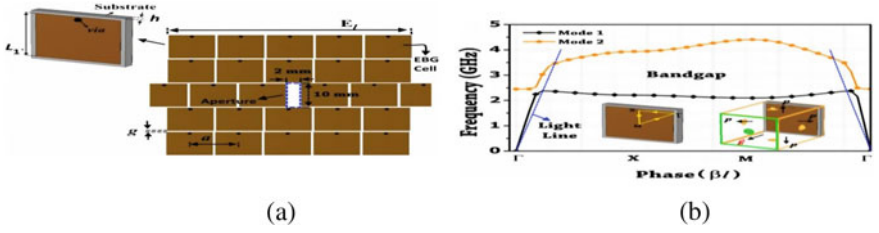

Fig. 3 **a** Simulated 2D dispersion diagram of the EBG unit-cell with periodic boundary conditions, **b** modelled aperture slotted EBG plane with geometrical view

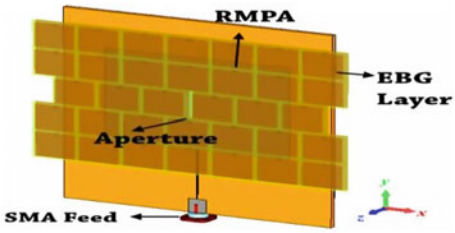

Fig. 4 Modelled EBG superstrated slotted RMPA perspective view

conditions in the xy-heading and cross-over electric field ($\vec{E}$)in the z-course. The two-dimensional scattering profile of the EBG structure is shown in Fig. 3b. Moreover, it is possible to predict stopband recurrence as [9],

$$f_{\text{low}} = \frac{1}{2\pi\sqrt{LC}} \tag{2}$$

$$f_{\text{high}} = \frac{1}{2L_1\sqrt{\varepsilon_{\text{r}}}} \tag{3}$$

where L is the loop, or sometimes referred to as the inductance of the metal circle between two continuous cells, C is the capacitance of the gap or hole between the two coplanar metal plates and the light speed is $C_0 = 3 \times 10^8$ m/s. The parts of the LC are resolved with [20] as.

$$L = uh \tag{4}$$

$$C = \frac{L_1\varepsilon_0(1+\varepsilon_r)}{\pi} \cos\, h^{-1}\left(\frac{2a+g}{g}\right) \tag{5}$$

where $a = 9.0$ mm, g $= 0.5$ mm, $\mu = \mu_0\mu_{\text{r}}$, $\mu_{\text{r}} = 1$, $\mu_0 = 4\pi \times 10^{-7}$ H/m and $\varepsilon_0 = 8.85 \times 10^{-12}$ F/m. As shown in Fig. 3a, an EBG-based superstrate layer with a length of $E_1 = 47$ mm is planned with a gap area of 20 mm^2 at the middle. The proposed EBG layer would permit transmission through the gap from the slotted RMPA, and the high impedance surface of the EBG layer would dispose of the undesirable reflections (Figs. 4 and 5).

2.2 Development and Testing

The RMPA structure is recognised by the use of the RO4450B substrate by means of photolithography measurements. A 50 Ω smaller SMA connector is fastened to

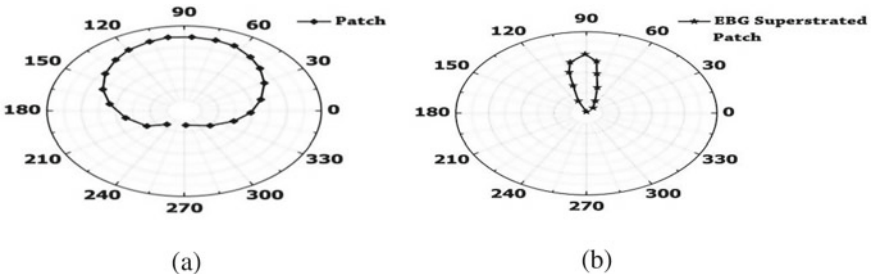

Fig. 5 Polar radiation pattern plot of *xz*-plane for **a** slotted patch, **b** superstrated EBG patch

the microstrip patch feed thread. Using the RO3010 substrate, the superstrate layer that produces a variety of EBG unit-cells is manufactured in line with the material specifics selected in the previous process. Copper wire is used to etch metal via. The N9923A Agilent vector network analyser measures the coefficient of reflection (S11) (VNA). An accurate performance of the VNA is required. For the same purpose, it is tuned with an RF power 0 dBm, a frequency of 5 KHz and 301 focal lengths, also known as sweep points, before recording the information. In Fig. 6, the resonance of the slotted patch is 3.1787 GHz; it coordinates with design simulation result of 3.17 GHz. A minor deviation of 87.5 MHz causes frequency resonance at 3.2575 GHz if an EBG superstrated slotted patch occurs. The change in the frequency is induced by the presence of metal weld spans in the EBG sheet. In addition, the decrease in S_{11} magnitude is a direct consequence of the EBG layer's bound opening space, which limits EM radiation projection.

A further explanation is the band gap recurrence of only creatures from 3.17 GHz onwards. Resonance status, therefore, is affected. However, even under 3.17 GHz, this can be dispensed with by designing an EBG surface with a resonance band gap.

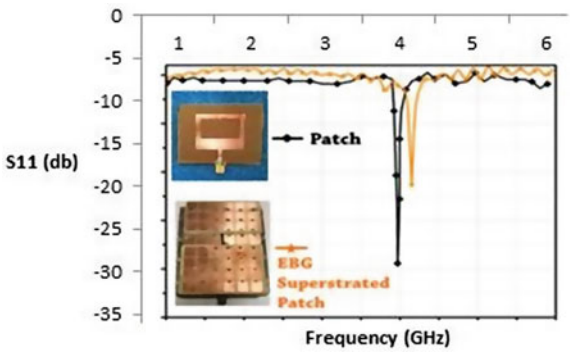

Fig. 6 Patch and EBG superstrated patch S_{11} data comparative graph calculated with inset fabricated images

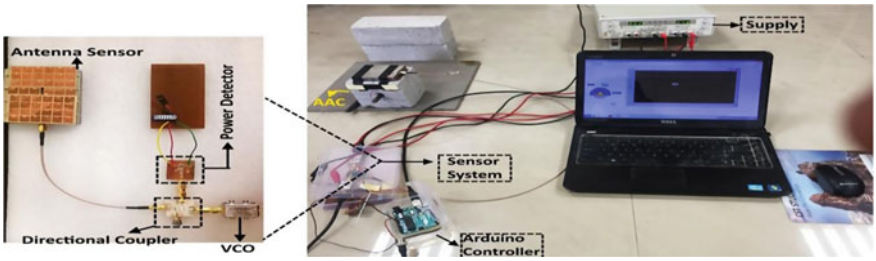

Fig. 7 Image of the corrosion surveillance experimental setup

3 Experimental

3.1 Setup

The detailed arrangement for testing with an EBG ascended slotted patch and detection circuit is shown in Fig. 7. A miniature VCO (ZX95-3800A+) excites the EBG superstrated antenna sensor to provide RF signal. With 4V of tuning voltage, the oscillator generates a resonance of 3.1402 GHz at output power of 4.06 dBm. The detector's yield association port is associated with a LabVIEW operated by Arduino, which enables constant and on-field estimation of the sensor reaction for corrosion observation.

3.2 Sample Preparation

The corrosion cycle creates different chemical oxide reaction over the rebar. It has measuring unit of microns per year (mmpy) and results in the annihilation of the rebar. Using electrochemical reaction, i.e. anodic etching, this wonder is recreated to quicken the corrosion of MUT (Fig. 8).

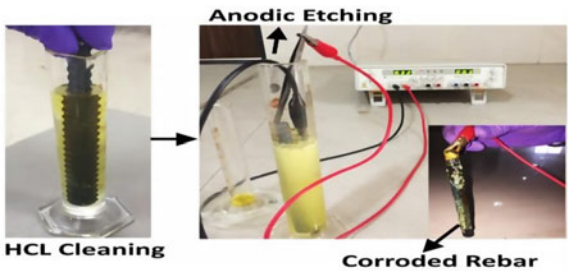

Fig. 8 Picture of rebar sample preparation with pre-cleaning accompanied by anodic etching

4 Results and Discussion

A precast type of solid structural material is a light-weight autoclaved aerated concrete (AAC), which is widely used in prominent civil developments. S11 = −9.1076 dB is found to be the estimated reference RF intensity for blocks with no rebar. As shown in Fig. 9a, the weight reduction occurs again in the rebar due to the increase in corrosion power from −8.2272 to −8.6685 dB. It is perceived from Eq. (6) as

$$P_r = P_t\left(1 - |\Gamma|^2\right) \tag{6}$$

where P_r is the power obtained, P_t communicated power and Γ is the coefficient of reflection. Magnitude of Γ increases as oxide layer is around rebar, it refers to the dielectric.

As electromagnetic flux goes within the layer of oxide and reduced reflection is observed by the sensor. Therefore, in the case of iron rebar without erosion, more reflection measurements occur relative to the reference norm and the power obtained is moderately lower. Then again, the presence of corrosion gives less reflection to a composite medium, and the level of control again moved closer and closer to the reference level. Using the proposed sensor system, the equivalent was tested. The power detection module switches to equivalent DC levels over the RF power from the reception sensor. In Fig. 9b, the plot for the reported yield voltage from the Arduino and LabVIEW interfacing power indicator appears. The instance is affected by corrosion is very well seen; the steady expansion in the weight reduction decreases the intentional voltage levels. For corrosion observing in a concrete block as well, the presentation of the generated sensor is also tried. In this case, due to the presence of rocks and gravel, the signature reaction bend of the sensor is reversed. The magnitude of S11 is 7.5643 dB for the reference test without rebar at first. During the inspection, as rebar appears under the sensor distance, due to the presence of metal and rock, the degree of reflection increases. In any case, when the corrosion starts to structure a

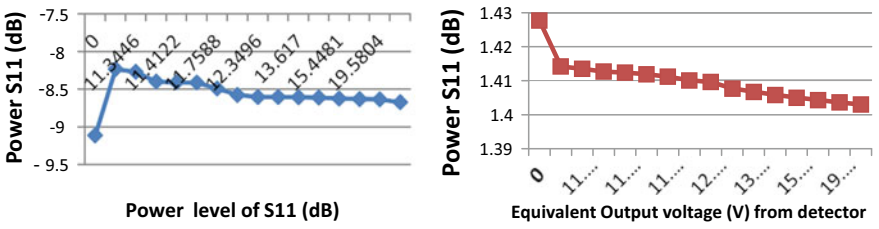

Fig. 9 Measured patch sensor reaction inside the AAC block for rebar corrosion monitoring **a** VNA-registered S_{11}, **b** DC output from single circuit detection

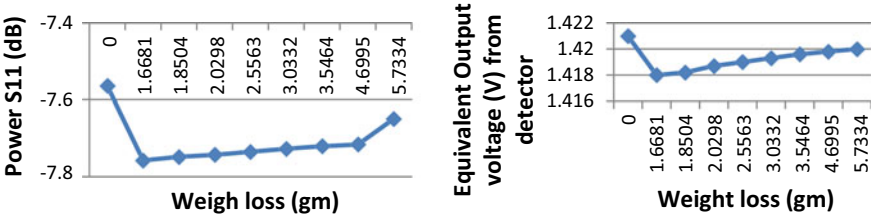

Fig. 10 Measured response of patch sensor put inside concrete block for corrosion monitoring on rebar. **a** VNA-registered S_{11}, **b** equivalent voltage output from single circuit detection

chemical oxide layer over the rebar, S_{11} starts decreases to the initial state. Trademark bend reaction is shown in Fig. 10.

5 Conclusions

For various structural materials, a new EBG mounted slotted patch antenna sensor has been efficiently tested and produced for corrosion monitoring in steel rebar. The results show corrosion layer increases, the weight of rebar decreases. It is possible to further improvise and optimise the aperture sensor for better resolution. The sensor is able to detect the indication of corrosion rate and severity of the same for different structural material.

References

1. Qi X, Gelling VJ (2011) A review of different sensors applied to corrosion detection and monitoring. Recent Pat Corros Sci 1(1):1–7
2. Grattan SKT, Taylor SE, Sun T, Basheer PAM, Grattan KTV (2009) Monitoring of corrosion in structural reinforcing bars: performance comparison using in situ fiber-optic and electric wire strain gauge systems. IEEE Sens J 9(11):1494–1502
3. Barranco V, Jr Feliu SFS (2004) EIS study of the corrosion behaviour of zinc-based coatings on steel in quiescent 3% NaCl solution. Part 1: directly exposed coatings. Corros Sci 46(9):2203–2220
4. Sunny AI, Tian GY, Zhang J, Pal M (2016) Low frequency (LF) RFID sensors and selective transient feature extraction for corrosion characterisation. Sens Actuators, A 241:34–43
5. Islam MA, Kharkovsky S (2017) Detection and monitoring of gap in concrete-based composite structures using microwave dual waveguide sensor. IEEE Sens J 17(4):986–993
6. Damme SV, Franchois A, Zutter DD, Taerwe L (2004) Nondestructive determination of the steel fiber content in concrete slabs with an open-ended coaxial probe. IEEE Trans Geosci Remote Sens 42(11):2511–2521
7. Kharkovsky SN, Akay MF, Hasar UC, Atis CD (2002) Measurement and monitoring of microwave reflection and transmission properties of cement-based specimens. IEEE Trans Instrum Meas 51(6):1210–1218

8. Hyde MW, Havrilla MJ, Bogle AE, Rothwell EJ (2012) Nondestructive material characterization of a free-space-backed magnetic material using a dual-waveguide probe. IEEE Trans Antennas Propag 60(2):1009–1019
9. Sutthaweekul R, Tian GY (2018) Steel corrosion stages characterization using open-ended rectangular waveguide probe. IEEE Sens J 18(3):1054–1062

Life Cycle Carbon Emission Assessment for a Residential Building

Rosaliya Kurian, Kulkarni Kishor Sitaram, and Prasanna Venkatesan Ramani

Abstract The processes of a building construction evolve emissions of greenhouse gases (GHGs) into the atmosphere. The contextual analysis of building processes consolidated four kinds of phases to execute the investigation are materialization, transportation, operational and demolition phases. This paper suggests a building assessment calculation of carbon emissions equivalent ($CO_{2\text{-eq}}$) through life cycle analysis method. As a case study residential apartment building situated in Ernakulum city, India is considered for the estimation of life cycle carbon emissions. Embodied carbon coefficients are extracted from inventory of carbon and energy (ICE) database. The results show selected residential building accounts for about a total carbon emissions equivalent of 0.727 $tCO_{2\text{-eq}}/m^2$. Cement contributes highest $CO_{2\text{-eq}}$. This building assessment method in this study is essential to comprehend point by point carbon emissions profiles to promote low carbon building construction. Main significance of this study is that materials that produce high amount of embodied carbon is identified and should be optimized whilst constructing new buildings. The outcome of this study provides an insight on framework analysis for optimizing carbon emissions in the future.

Keywords Greenhouse gases · Carbon emission · Building assessment

1 Introduction

The weather change brought about by ozone depleting substance outflows has become a major concern over global society. In the next 20 years, every 10 years, the worldwide temperature will keep on intensifying at a speed of 0.2 °C. The 86% of the GHG outflows are due to crude supplies for building materials, handling in plant,

R. Kurian (✉) · K. K. Sitaram · P. V. Ramani
MTech in Construction Technology and Management, Ernakulam, Kerala, India
e-mail: rosaliya.kurian2019@vit.alum.ac.in

K. K. Sitaram
e-mail: kishorsk@cbri.res.in

B. Kondraivendhan et al. (eds.), *Sustainable Building Materials and Construction*,
Lecture Notes in Civil Engineering 222,
https://doi.org/10.1007/978-981-16-8496-8_14

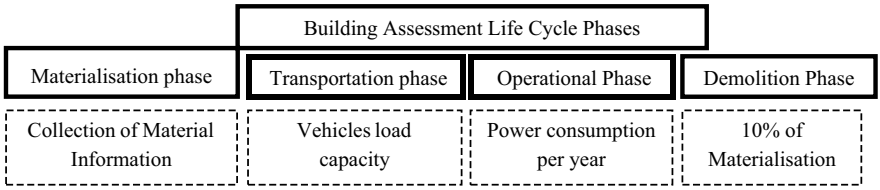

Fig. 1 Building assessment life cycle phases

substitution and transport of the building products. A product emits GHG is called a carbon footprint which can be denoted $CO_{2\text{-eq}}$ [1]. Carbon dioxide equivalent refers to the CO_2, CH_4 and NO_2 as GHG. Life cycle analysis (LCA) is a method to survey natural effects related with the phases of a building materials or reusing [2]. LCA gives an extensive way to deal with environmental assessment. Location of building, transport climate conditions, size of building life, span of the building, methods for materials, manufacturing and construction methods affects the LCA results [3]. The LCA database used step includes collection of information about carbon emissions database from ICE database is developed by university of bath and has their manufacturing characterizes for the processes modelled for the materials.

Low-carbon structures (LCB) are structures that are explicitly designed in view of GHG decrease. So, by definition, a LCB is a structure which produces fundamentally less GHG than conventional structures. To attain a LCB building, it is important to analyze the carbon footprint of construction materials, which material and phase contribute higher $CO_{2\text{-eq}}$ in order to find ways for optimizing the $CO_{2\text{-eq}}$ for sustainable construction [2]. This paper focusses on carbon emissions equivalent of 4 different phases shown in Fig. 1. The carbon emission equivalents evaluated in this study can be useful to figure out the areas of the improvements required and reducing greenhouse gases (GHGs).

2 Case Study of Residential Building

A reinforced cement concrete (RCC) structure which is a (G+2) residential apartment building project which is situated at southern part of India, Ernakulam district in Kerala is taken for the study shown in Fig. 2. The buildup area is about 721 m^2.

2.1 Building Life Cycle Carbon Emissions (LCO_2E)

The life cycle hypothesis emphasis on a structure's LCO_2E into four phases such as the materialization phase (includes acquisition of crude materials, manufacture of construction materials), transportation phase includes loading and unloading of

(a) During construction **(b)** Completed construction

Fig. 2 G+ 2 residential apartment building

materials in vehicles, the operational phase of LCO_2E basically incorporates those created refrigerator, air conditioner, lighting, etc., and the demolition phase (includes structure destruction and reusing thrown away material). Total LCO_2E is calculated using Eq. (1) [4]. Maintenance stage was eliminated due to its lack of realistic data. The embodied carbon coefficient (ECC) is taken from inventory of carbon, and energy is open-source data set which is an optimal asset for carbon configuration.

$$A_{\text{tot}} = A_{\text{con}} + A_{\text{mt}} + A_{\text{ope}} + A_{\text{dem}} \tag{1}$$

where

*A*tot total building carbon emissions (BCO_2E) in $tCO_{2\text{-eq}}$; *A*con total BCO_2E of materialization phase; *A*mt total BCO_2E of transportation phase; *A*ope total BCO_2E of operational phase; *A*dem total BCO_2E of demolition phase.

3 Calculation of LCO_2E

3.1 Materialization Phase

The quantity estimation was collected from bill of quantities (BOQ) sheets. The total BCO_2E of materialization phase is calculated using Eq. (2) [4] and given in Table 1.

$$A_{\text{con}} = \sum B_{\text{mp},i} \times C_{\text{mp},i} \tag{2}$$

*B*mp, *i* quantity of *i*th construction material in kg; *C*mp, *i* ECC of *i*th construction material in kg $CO_{2\text{-eq}}$/kg

Table 1 Building carbon emissions of materialization phase

Construction materials	Material quantity (*B*mp) (kg)	EEC of material *C*mp kg $CO_{2\text{-eq}}$/kg	BCO2E of *A*con (kg $CO_{2\text{-eq}}$)
Cement	68,990.28	0.95	65,540.80
Concrete blocks	112,204.20	0.088	9873.96
Ceramic floor tiles	10,217.30	0.78	7969.49
Red brick	63,912.00	0.24	15,338.88

Therefore, total BCO_2E of materialization phase is *A*con = 98723.1 kg $CO_{2\text{-eq}}$ = 98.723t $CO_{2\text{-eq}}$

3.2 Transportation Phase

The vehicles used for transportation of construction materials are light-duty vehicle (LDV) (Ashok Leyland dost strong), a medium-duty vehicle (MDV) (Eicher Pro 2095XP) having load capacity of 1250 and 8102 kg with fuel efficiency of 8.58 and 4.46 km/l, respectively. The transport distance of the materials is taken as 20 km. ECC of a diesel vehicle is taken as 2.6444 kg $CO_{2\text{-eq}}$/l. Number of trips calculated as quantity of materials divide by load carrying capacity (kg). The total BCO_2E of transportation phase is calculated in Eq. (3), and Table 2 presents the fuel consumption of vehicles for the material transport.

$$A_{\text{mt}} = \sum C_{\text{mt},i} \times F_{\text{C},i} \tag{3}$$

where *C*mt, *i* ECC of engine fuel in kg $CO_{2\text{-eq}}$/l; *F*C, *i* total fuel consumption of *i*th vehicle in litres.

Table 2 Total fuel consumption of vehicles

Construction material (type of vehicle)	Material quantity Bmp (kg)	Number of trips	Total distance (D) km	Fuel consumption FC (lit)
Cement (LDV)	68,990.28	55	1100	128.5
Concrete block (MDV)	112,204.20	14	280	62.7
Ceramic tiles (LDV)	10,217.30	8	160	18.6
Red brick (MDV)	63,912.00	8	160	35.8

Therefore, total BCO_2E during transportation is *A*mt = 245.6 × 2.6444 = 649.46 kg $CO_{2\text{-eq}}$ = 0.649 $tCO_{2\text{-eq}}$

Table 3 Actual power consumption

Bimonthly power consumption (kWh)													
Floors	Jan.	Feb.	Mar.	Apr.	May	Jun.	July	Aug.	Sept.	Oct.	Nov.	Dec.	Total
GF	439		558		549		451		322		419		2738
FF	319		519		529		289		140		360		2156
SF	361		523		551		288		318		351		2392

Yearly, power consumption is obtained as 7286 kWh
Therefore, Aope $= 7286 \times 0.95 \times 60 = 415.302$ $tCO_{2\text{-eq}}$

3.3 Operational Phase

ECC of electricity is taken as 0.95 kg $CO_{2\text{-eq}}$/kWh. The service life of building taken as 60 years substitute to Eq. (4) [4]. The power consumption details of ground floor (GF), first floor (FF) and second floor (SF) are collected from the owners of the building occupants and presented in Table 3.

Total BCO_2E of operational phase is

$$A_{\text{ope}} = E_{\text{c}} \times C_{\text{ele}} \times S_1 \tag{4}$$

where Ec total power consumption in kWh/year, Cele ECC of diesel in kg $CO_{2\text{-eq}}$/kg, Sl is the service life of building.

3.4 Destruction Phase

The total BCO_2E of destruction phase is considered as 10% of total BCO_2E of construction material phase.

Therefore, Adem $= 98.72 \times 0.10 = 9.872$ $tCO_{2\text{-eq}}$.

Therefore, total building carbon emissions (BCO_2E) are 524.54$CO_{2\text{-eq}}$.

The BCO2E per m^2 of building area $= 0.727$ $tCO_{2\text{-eq}}/m^2$.

4 Interpretations and Discussion

The BCO2E of 4 main construction materials at materialization phase is given in Fig. 3

In materialization phase, the cement contributes about 65540.8 kg $CO_{2\text{-eq}}$ around 66.4% whereas red brick contributes about 15338.9 kg $CO_{2\text{-eq}}$ around 15% of total carbon emissions equivalent of 98723.1 kg $CO_{2\text{-eq}}$, respectively. It is clear that embodied carbon coefficient of cement is higher, which contributes to the higher

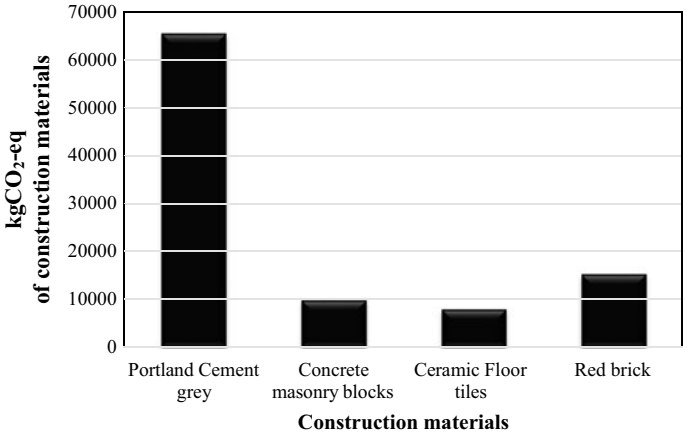

Fig. 3 $CO_{2\text{-eq}}$ analysis of construction materials

carbon emissions equivalent. In transportation phase, for transportation of cement generates around 339.8 kg $CO_{2\text{-eq}}$. So, it is evident that for materialization phase and transportation phase, cement produces more carbon emissions equivalent. In case of concrete masonry blocks, for transporting materials generates carbon emissions of 165.77 kg $CO_{2\text{-eq}}$. The concrete masonry blocks produce 25% of total carbon emissions in transportation phase. The $CO_{2\text{-eq}}$ in transportation stage mainly depends on the total distance covered by vehicle (D), load carrying capacity of vehicle, quantity of construction material, embodied carbon coefficient of engine fuel and consumption of fuel.

The operational phase contributes around 80% of total $CO_{2\text{-eq}}$ of life cycle analysis as show in Fig. 4. The Ernakulam is located in Kerala, the monthly average temperature in June, July, August and September is around 25 °C, and rest of the eight months, the temperature varies from 28 to 30 °C with more than 75% humidity. This creates thermal discomfort to the occupants, and hence, the air conditioner and dehumidifier are extensively used during these eight months. During these months, the electricity

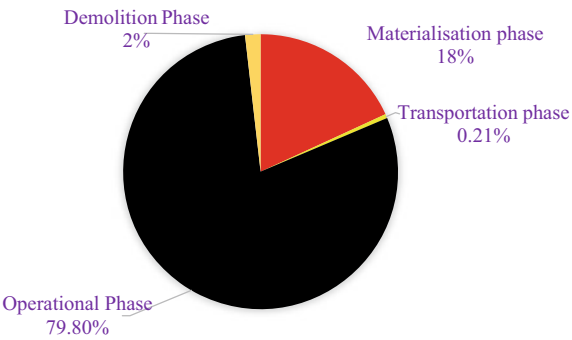

Fig. 4 Contribution of $CO_{2\text{-eq}}$ during 4 phases of LCA

consumption is nearly 1600–1800 kWh. The building LCA results show typical RCC building accounts for about 18, 0.2, 80 and 2% of a total carbon emissions equivalent of 0.727 $tCO_{2\text{-}eq}/m^2$ for materialization, transportation, operational and demolition phases, respectively.

5 Conclusions

The quintessential step of developing a building assessment method of LCA is for carbon building design. According to the above computation results, the larger portion of buildings emissions load is produced during the operational phase accounts for about 79.80% of total $CO_{2\text{-}eq}$. Second largest being the materialization phase accounts for about 18%. Finally, the smallest emissions amongst them are transportation phase about 0.21%. The present study limits to the LCA carbon emissions results obtained from embodied carbon emissions from inventory of carbon and energy database used. It is found that cement and brick contribute more $CO_{2\text{-}eq}$, hence replacing cement with low carbon materials like supplementary cementitious materials and cement concrete blocks with autoclaved aerated concrete block will be an effective way to optimize $CO_{2\text{-}eq}$ for low carbon building construction in sustainable future.

References

1. Peng C, Wu X (2015) Case study of carbon emissions from a building's life cycle based on BIM and Ecotect. Adv Mater Sci Eng 2015:115
2. Yan H et al (2010) Greenhouse gas emissions in building construction: a case study of One Peking in Hong Kong. Build Environ 45(4):949–955
3. Nie Z (2013) Development and application of life cycle assessment in China over the last decade. Int J Life Cycle Assess 18(8):1435–1439
4. Cheng B et al (2020) A BIM-LCA approach for estimating the greenhouse gas emissions of large-scale public buildings: a case study. Sustainability 12(2):685

Lamb Wave Approach for the Structural Health Monitoring

Neeraj Singh, Deep Tripathi, and Bharat Singh Chauhan

Abstract Over the last few decades, as the infrastructural facilities enhanced in modern world, they come with many maintenance problem which comes due to ageing, earthquake, etc., and these maintenance problem are not easy to handle or we can say engineers are not well prepared with these problem. Along with this assessment of building condition immediately after extreme loading such as an earthquake required. These considerations are prompting the development of automated structural health monitoring (SHM) and non-destructive evaluation (NDE) systems, which can provide cost-effective alternative to traditional visual inspection. This SHM system has distinct objectives of health monitoring as to ascertain that damage has occurred or to identify damage, to locate the damage, to determine the severity of damage, to determine remaining useful life of the structure. In this study, the specific objective of work is to determine the presence, location and severity of the crack/damage using lamb wave approach. As a result, we get that damage can be detected using lamb wave and measuring the structural coupled system resistance DC.

Keywords Structural health monitoring · Non-destructive evaluation · Lamb wave

1 Introduction

1.1 Background

Each country's population growth necessitated the development of more civil infrastructure. Infrastructure that is in good working condition can reflect a country's

N. Singh
Department of Civil Engineering, NIT Jamshedpur, Jharkhand, India

D. Tripathi (✉)
Department of Civil Engineering, MNNIT Allahabad, Prayagraj, UP, India

B. S. Chauhan
Central Public Works Department, New Delhi, India

B. Kondraivendhan et al. (eds.), *Sustainable Building Materials and Construction*,
Lecture Notes in Civil Engineering 222,
https://doi.org/10.1007/978-981-16-8496-8_15

wealth. Most civil engineering buildings deteriorate and are damaged as a result of time and natural disasters. In addition, civil engineering infrastructure that collapse cause massive loss of life and property. As a result, structures require some form of maintenance to ensure their integrity and health. However, depending on the structure's importance, ownership, use, danger and hazard, inspection, monitoring and condition monitoring may be required by law. The effectiveness of maintenance and inspection efforts is only as good as their ability to identify problematic accomplishment in a timely manner, which is why continuous, online, real-time and automated systems are being used to complement restricted and intermittent inspection processes. Advanced methods such as SHM and NDE technologies have been proposed as a cost-effective alternative to conventional visual inspection. These are often used to investigate damage caused by challenges, which are identified as changes in the material and geometric properties of these systems, as well as changes in boundary conditions and system connectivity, that have a detrimental effect on their current performance. Damage detection is divided into four levels, as per [3].

1. Determine whether or not damage has occurred or to locate damage.
2. Determine the extent of the damage and its location.
3. Determine the severity of the damage by identifying it, locating it and determining its location (i.e. to quantify it).
4. Determine the structure's remaining useful life by identifying, locating and quantifying damage.

1.2 Literature Review

In general, SHM is a method of providing accurate and timely information regarding the status and performance of a building. It might be a short-term (e.g., repair effectiveness) or long-term (continuous or periodic parameter monitoring) activity. The fact that the properties of both concrete and steel are reliant on a vast number of parameters, many of which are difficult to anticipate in practice, necessitates the employment of SHM. The representative parameters chosen for structural health monitoring can be mechanical, physical or chemical in nature. In general, a typical SHM system consists of three key components: a sensor system, a data processing system (including data acquisition) and a data acquisition system. In general, a typical SHM system includes three major components are sensor system, data processing system (including the data acquisition, transmission and storage) and health evaluation system (including the diagnostic algorithm and information management).

The literature is studied to see which approaches have been used in recent years. However, for many years, numerous scholars have concentrated on questions concerning the properties of cracked buildings. Furthermore, a number of damage detection approaches for engineering structures have been published, the most popular of which is the so-called vibration-based approach for engineering structures [15]. Banan and Hjelmstad [9] also created a static displacement response approach. This method required applying static forces to a structure and measuring

the displacements that resulted. In addition, [8] proposed a method based on static strain measurements. This method has an advantage over the previous one in that strain measurements can be made with greater accuracy than displacement measurements.

Zimmerman and Kaouk [5] developed a method based on the principle of stiffness change produced by damage in later study. The problems of stiffness methodology were explored by Pandey and Biswas [1], who devised the change in flexibility method. This approach is based on the fundamental idea that damage to a structure modifies its flexibility matrix, which can then be utilised to 'detect' damage.

Several other authors, including Shah et al. [2], have described damage detection methods, including a new ultrasonic wave-based method for crack detection in concrete from a single surface. Popovics et al. [13], on the other hand, created a new ultrasonic wave-based method for estimating layer thickness and detecting flaws in concrete. Furthermore, elastic waves are created by plastic deformations (e.g., at the tip of a newly formed crack), and moving dislocations and disbonds are used in the acoustic emission method for structural defect investigation and identification. It requires stress or chemical activity to generate elastic waves and can also be applied to loaded constructions [4], allowing for continuous monitoring. The presence of varied travel pathways from the source to the sensors, on the other hand, poses the most significant challenge to acoustic emission identification. Electrical interference and mechanical ambient noise also decrease the quality of the emission signals [6, 7].

Magneto-optic imaging, on the other hand, is a more advanced form of the process that combines eddy currents with a magnetic field and optical technology to capture an image of the faults [12]. In contrast, an impact source is used to introduce a stress pulse into the probed component during impact echo testing. The wave is reflected by cracks and disbonds as it travels through the structure. The location of cracks or disbonds is determined by measuring and analysing the reflected waves. Although the technology is excellent for detecting huge voids and delaminations, it is insensitive to microscopic cracks (Park et al. 2000a). Furthermore, in the X-ray approach, the test structure is exposed to X-rays, which are subsequently re-captured on film, where the cracks are demarcated as black lines (e.g., Kuzelev et al. [11]). Defects with varying density and/or contrast to the surrounding environment can be found using this method.

1.3 Lamb Wave

The lamb wave was chosen because it can travel long distances with low dispersion and has no higher modes to clog the response waves. The dispersion curves, which are plots of phase and group velocities versus excitation frequency, are the most fundamental technique to explain the propagation of a lamb wave in a given material. The first step in building these curves is to solve the wave equation for the anti-symmetric lamb wave. The lamb wave's group velocity essentially varies by a similar equality to that of a structure's resonant frequency, as $\sqrt{(E/\rho)}$, (where E and ρ are

material properties), so as a wave travels across an area of reduced stiffness, it will slow down. The more energy given to the required driving frequency, the stronger the lamb wave and the more precise the wave speed calculation, and thus the more delicate and reliable the damage detection capacity. Low frequency lamb waves have a more anti-symmetric wave response, whereas higher frequency lamb waves have a more symmetric wave response. The process of detecting waves based on frequency and signal response is known as tuning. The fundamental disadvantage of this method is that it is active, requiring both a power source and a signal generator. Another downside of lamb wave analytical analysis is that it needs the solution of complex equations, which takes time and requires attentiveness when solving.

2 Methodology

The objective of this experiment is to detect damage using a lamb wave method. The following are the procedures for creating damage detection using lamb wave. However, a concrete beam with dimensions of 700 mm × 150 mm × 150 mm and a concrete grade of M25 was used for the experiment. The structure was then purposefully destroyed in order to examine the real-time structural health monitoring issue. PZT was also used near the beam's top. Then, using the resistance DC to plot the graph and calculate damage detection, consider the load to be constant and the frequency to be variable. To identify damage in the beam, the EMI approach was applied.

3 Results and Discussion

The electromechanical admittance Z (unit Siemens or Ω^{-1}) consists of real and imaginary parts, the conductance (G) and sustenance (B), respectively. A conductance plot, i.e. G over a sufficiently wide band of frequency, serves as a diagnosis signature of the structure and is called the conductance signature or simply signature. Since the real part actively interacts with the structure, it is traditionally preferred over the imaginary part in the SHM applications. It is believed that the imaginary part (Sustenance) has very weak interaction with the structure [10]. Therefore, all investigators have so far considered it as redundant and have solely concentrated on the real part (conductance) alone in the SHM applications.

The most important parameter which gave the most fluctuations at instant values is DC resistance. The variation in resistance DC at 10 and 50,000 Hz can be seen in the graphs below. The difference in percentage change in overall values at each frequency was not varying much, but instant variation in the value of resistance DC was maximum among all the parameters. Variation in resistance DC at 10 and 50,000 Hz can be seen in the graphs (Figs. 1 and 2; Table 1).

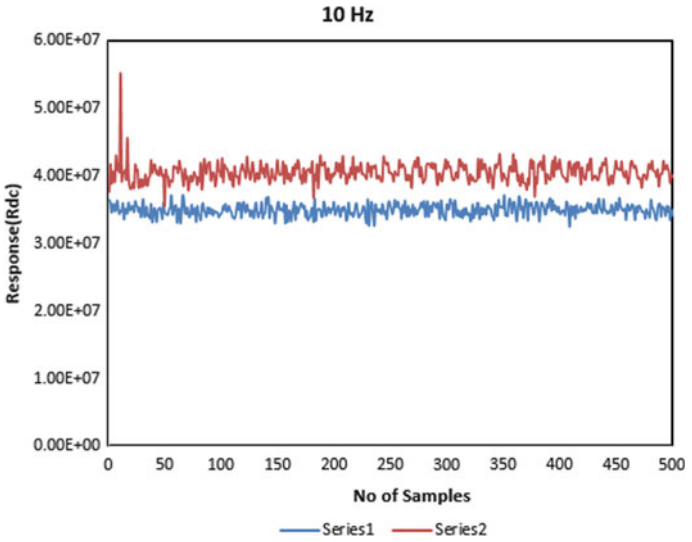

Fig. 1 Resistance DC signature at 10 Hz

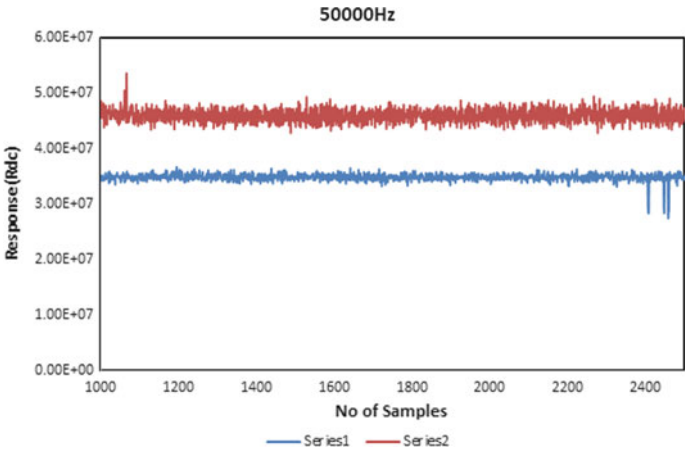

Fig. 2 Resistance DC signature at 50,000 Hz

Table 1 Change in percentage in each parameter at different frequencies

Parameter/frequency (Hz)	10	1000	50,000	100,000
Resistance DC (%)	42.42	30.81	32	31.90

4 Conclusions

The following results were concluded.

- Damage can be detected using lamb wave and measuring the structural coupled system resistance DC.
- Comparative more change in resistance DC was observed at high-frequency range.
- Significant difference change of resistance DC was observed between healthy and damage state. Hence, damage can be clearly identified.
- Resistance DC can be used as indicative parameter for structural health monitoring.
- Location, severity and size of damage is still a matter of research using the lamb waves.

References

1. Pandey AK, Biswas M (1994) Damage detection in structures using changes in flexibility. J Sound Vib 169:3–17
2. Shah A et al (2014) An FEM-BEM interactive coupling for modelling smart structural health monitoring systems. In: 1st international conference on emerging trends in engineering, management and sciences. Peshawar, Pakistan
3. Farrar CR and Jauregui DA (1998) Comparative study of damage identification algorithms applied to a bridge: I. Experiment. Smart Mat Struct 7(5)
4. Boller C (1994) Structural health management of ageing aircraft and other infrastructure. Monogr Struct Heal Monitor
5. Zimmerman DC, Kaouk M (1994) Structural damage detection using a minimum rank update theory. J Vib Acoust 116(2):222–231
6. Park G et al (2000) Impedance-based health monitoring of civil structural components. J Infrastruct Syst 6(4):153–160
7. Kawiecki G (2001) Modal damping measurement for damage detection, June 2001. Smart Mater Struct 10(3):466
8. Sanayei M, Saletnik MJ (1996) Parameter estimation of structures from static strain measurements. I: Formulation. J Struct Eng 122(5)
9. Banan MR, Hjelmstad KD (1994) Parameter estimation of structures from static response. I. Computational aspects. J Struct Eng 120:3243–3258
10. Sun M et al (2010) Smart sensing technologies for structural health monitoring of civil engineering structures. Adv Civ Eng 1–14
11. Kuzelev NR et al (1994) Diagnostics of the state of aircraft parts and assemblies with radionuclide computer tomography. Russ J Non-Destr Test 30(8):614–621
12. Ramuhalli P et al (2002) Multichannel signal processing methods for ultrasonic nondestructive evaluation. In: Sensor array and multichannel signal processing workshop proceedings
13. Popovics S et al (2000) High-frequency ultrasound technique for testing concrete. ACI Struct J 97(1):58–65
14. Giurgiutiu V, Rogers CA (1997) Electro-mechanical (E/M) impedance method for structural health monitoring and non-destructive evaluation. Int Workshop Struct Health Monit Stanford Univ 433–444
15. Wang Y et al (2007) A wireless structural health monitoring system with multithreaded sensing devices: design and validation. Struct Infrastruct Eng 3(2):103–120

Properties of Binary Admixture Mixed SCC Exposed to Sulphate Environment

Amrendra Singh, Rakesh Kumar, P. K. Mehta, and Deep Tripathi

Abstract In this paper, the fresh, hardened and duraility properties self-compacting concrete (SCC) were studied with different variables. The substitution levels of ordinary Portland cement (OPC) by fly ash (FA) were kept as 0, 5, 10, 15, 20 and 25%. Thereafter, for every substitution level of OPC by FA, the OPC was further replaced by different amounts of rice husk ash (RHA) (0–15%). The workability of SCC mix increases with percentage of FA content while a gradual fall in its value was observed as RHA content was increased in the mix. The optimum substitution level of OPC by dual admixtures was obtained at 25% [FA (20%) + RHA (5%)] in terms of fresh and hardened properties. Further, formulae for prediction of different strength parameters are developed for samples exposed to potable water.

Keywords Self-compacting concrete · Ordinary Portland cement · Durability · Hardened property

1 Introduction

Self-compacting concrete is a concrete that can consolidate under its own weight, pass through the spaces between the jam-packed reinforcing bars to entirely fill the formwork, and at the same time maintain its steady composition [1–3]. FA is ordinarily used for SCC. The addition of FA expands functionality and compressive strength of SCC. The SCC containing FA needs less SP to acquire a similar workability containing just OPC, because of round shape and lower water interest of FA particles. The fractional substitution of OPC by FA can essentially improve fresh properties of SCC [4]. RHA is an awesome supplanting for silica fume concerning durability and compressive strength (CS) of SCC due to its high silica content. The examinations uncover that expansion of RHA content increases flow time SCC, especially at lower water/binder (w/b) proportion [5]. Broken up sulphate salts existing in nature or from modern and farming sources go into substance responses with

A. Singh (✉) · R. Kumar · P. K. Mehta · D. Tripathi
MNNIT Allahabad, Prayagraj, India
e-mail: amrendra@mnnit.ac.in

B. Kondraivendhan et al. (eds.), *Sustainable Building Materials and Construction*,
Lecture Notes in Civil Engineering 222,
https://doi.org/10.1007/978-981-16-8496-8_16

concrete based materials causing breaking, spalling and crumbling because of ettringite. Ettringite is an extensive compound and makes an inside tension on the encompassing concrete. This prompts the development of breaks and results in the deficiency of its mechanical properties. In sewers, hydrogen sulphide gas is delivered in the environment above water level because of various synthetic and microbiological responses. This gas responds with oxygen to shape natural sulphure, which is saved on the dividers of the sewerage framework. The option of pozzolanic materials in the concrete settles the free calcium hydroxide during the hydration cycle of the concrete to shape extra cementious material (CSH).The resultant fastener matrix of cement is artificially more safe, by uprightness of its thick tiny pore structure [6]. A few specialists have detailed a more slow pace of sulphate reaction on SCC that contains mineral admixtures [7, 8].

2 Materials and Methods

2.1 Materials

Fourty-three grade OPC acquired from a solitary group was utilized all through this examination. The properties of OPC adjusted the necessities of IS 8112-1989 [9] furthermore, are as per the following: CS at 28 day = 48.67 N/mm^2; final setting time = 480 min; initial setting time = 45 min. The following properties of FA was utilized: class F; specific gravity (SG) = 2.13. The round shaped particles of fly ash go about as rollers inside concrete giving an oil impact. The following properties of RHA was utilized: SG = 2.15; black in colour. The normal stream sand, adjusting to zone II [IS-383-1987] [10], was utilized for making SCC and properties are as per the following: SG = 2.48; bulk modulus (BM) = 1680 kg/m^3; fineness modulus (FM) = 2.462.20 and 10 mm size of coarse aggregate adjusting to IS: 383-1987 [10] were utilized. The properties are: SG = 2.7 and 2.67 for 20 and 10 mm, individually. FM = 7.27 and 6.25 for 20 and 10 mm, separately; BM = 1560 and 1590 kg/m^3 for 20 and 10 mm, individually; water absorption = 1.1 and 1.2% for 20 and 10 mm, individually.

2.2 Methodology

2.2.1 Mix Proportioning

Concrete mix was readied utilizing steady w/b proportion of 0.44 and the substitution levels of OPC by FA were kept as 0, 5, 10, 15, 20 and 25%. Thereafter, for every replacement level of OPC by FA, the OPC was further replaced by different amounts of RHA (0–15%, at an interval of 5%).

2.2.2 Fresh Properties

In this experimental examination, SCC mix was readied utilizing OPC of 43 grade, fulfilling the EFNARC details and BIS draft suggestions [11]. The flowability of SCC mix was found at various substitution levels of OPC by FA and RHA. The filling capacity was assessed by slump flow (expanding slump flow shows a higher filling capacity). The passing capacity was assessed by J-ring (expanding J-ring value shows a more unfortunate passing capacity). The plastic consistency was assessed by flow time (expanding V-funnel time demonstrates a higher plastic viscosity).

2.2.3 Hardened Properties

The CS, split tensile strength (STS) and flexural strength (FS) were determined according to the arrangements contained in IS: 516-1959 [12], IS: 5816-1999 [13] and IS: 516-1959 [12], respectively. The CS, STS and FS were determined after curing the specimen in tap water for 7 and 28 days.

2.2.4 Durability of Concrete

For durability assessment, cubes of RSCC (containing OPC only) and OSCC [(FA (20%) + RHA (5%)] were cast and cured in different concentrations sulphate solutions (SS)(4 and 16 g/l) after 28 days water curing to the measure the durability parameters such as CS and weight change (56, 90 and 180 days).

3 Results and Discussion

3.1 Fresh Properties

The filling height, flow time, blocking ratio, slump flow value and J-ring value of the referral SCC are16mm, 11.5 s, 0.85, 680 and 6 mm, respectively. The change in the filling height, flow time, blocking ratio, slump flow value and J-ring value of optimum SCC formed by partial replacement of OPC by admixtures [FA (20%) + RHA(5%)] are −2.0 mm, −2.1 s, +0.11, +30 mm and −0.5 mm, respectively.

3.2 Hardened Properties

The greatest strength of SCC mix was found at 25% substitution level of OPC (optimum level) by admixtures [(FA (20%) + RHA (5%)].The CS, STS and FS

of optimum SCC (OSCC) at 7 days are 17.69, 12.14 and 16.32%, respectively, more than referral SCC, while at 28 days the above increase is 18.10, 19.50 and 16.64%.

3.3 *Relation Among Compressive, Flexural and Split Tensile Strength of Different SCC*

Linear and exponential relation between CS, STS and FS of different SCC were developed and plotted. The R^2 value for the linear and exponential relation between CS and STS at 7 days is found as 0.926 and 0.905, respectively, it means linear relationship is better than exponential as shown in Fig. 1. The R^2 value for the linear and exponential relation between CS and FS at 7 days is found as 0.916 and 0.922, respectively, it means exponential relationship is better than linear as shown in Fig. 2. The R^2 value for the linear and exponential relation between STS and FS at 7 days is found as 0.850 and 0.876, respectively, it means exponential relationship is better than linear as shown in Fig. 3. The R^2 value for the linear and exponential relation between CS and STS at 28 days is found as 0.918 and 0.911, respectively, it means linear relationship is better than exponential as shown in Fig. 4. The R^2 value for the linear and exponential relation between CS and FS at 28 days is found as 0.839 and 0.847, respectively, it means exponential relationship is better than linear as shown in Fig. 5. The R^2 value for the linear and exponential relation between STS and FS at 28 days is found as 0.694 and 0.706, respectively, it means exponential relationship is better than linear as shown in Fig. 6.

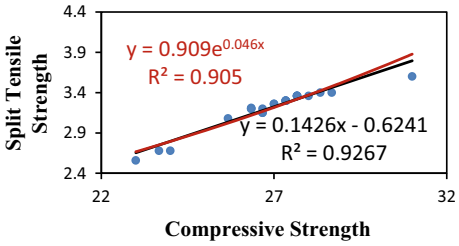

Fig. 1 Relation b/w CS and STS at 7 days

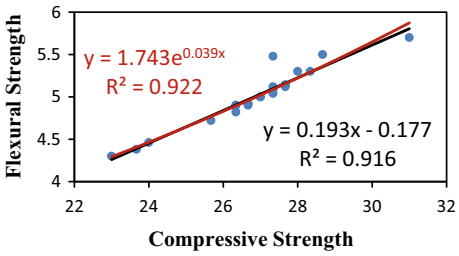

Fig. 2 Relation b/w CS and FS at 7 days

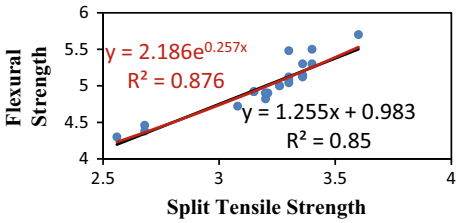

Fig.3 Relation b/w FS and STS at 7 days

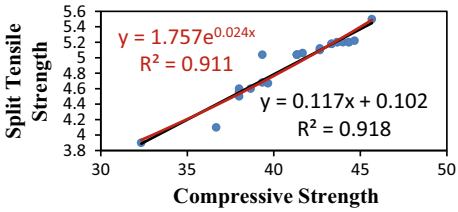

Fig. 4 Relation b/w CS and STS at 28 days

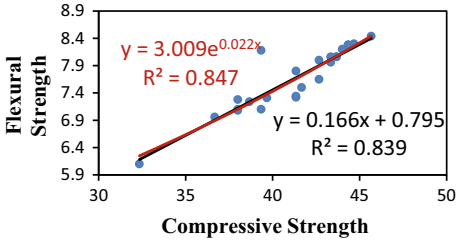

Fig. 5 Relation b/w CS and FS at 28 days

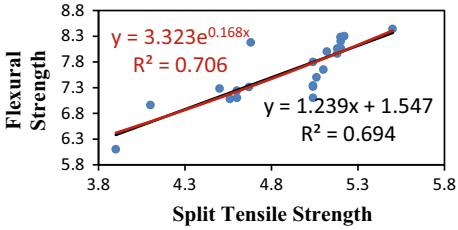

Fig. 6 Relation b/w FS and STS at 28 days

3.4 Durability Properties of Concrete

The important durability parameters considered in this study are included herein.

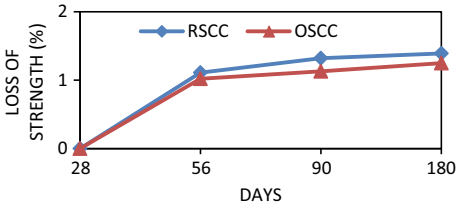

Fig. 7 Loss in CS in SS of 4 g/l

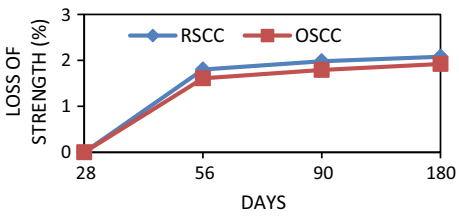

Fig. 8 Loss in CS in SS of 16 g/l

3.4.1 Loss in Compressive Strength

The loss in CS of RSCC after 28, 56, 90 and 180 days exposure in sulphate solution (SS) of 4.0 g/l is 0.00, 1.67, 2.41 and 3.14%, respectively, with respect to those cured in tap water, while for OSCC the respective changes are 0.00, 1.32, 1.98 and 2.59%, respectively. The loss in CS of RSCC after 28, 56, 90 and 180 days exposure in SS of 16 g/l is 0.00, 3.32, 4.83 and 5.50%, respectively, with respect to those cured in tap water, while for OSCC the respective changes are 0.00, 2.60, 3.97 and 4.53%, respectively. A comparable pattern was likewise revealed by Mbessa and Pera [8]. The variation of loss in compressive strength of RSCC and optimized binary admixture SCC specimen with age is shown in Figs. 7 and 8.

3.4.2 Weight Change

The gain in weight of RSCC after 28, 56, 90 and 180 days exposure in sulphate solution of 4.0 g/l is 0.00, 1.11, 1.32 and 1.23%, respectively, with respect to those cured in tap water, while for OSCC the respective changes are 0.00, 1.02, 1.13 and 1.08%, respectively. The gain in weight of RSCC after 28, 56, 90 and 180 days exposure in sulphate solution of 16.0 g/l is 0.00, 1.80, 1.98 and 1.89%, respectively, with respect to those cured in tap water, while for OSCC the respective changes are 0.00, 1.61, 1.79 and 1.70%, respectively. The variation of change in weight of RSCC and optimized binary admixture OSCC specimen with age exposed in sulphate solution of 4 g/l and 16 g/l is shown in Figs. 9 and 10.

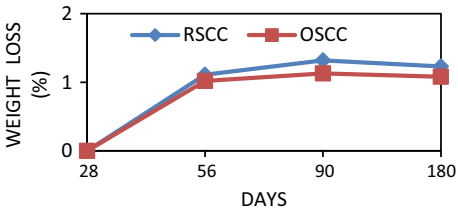

Fig. 9 Change in weight inSS of 4 g/l

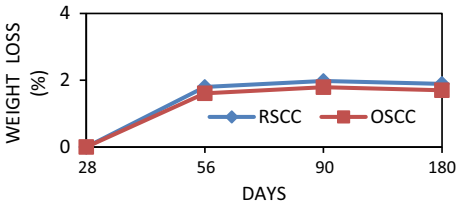

Fig. 10 Changein weight in SS of 16 g/l

4 Conclusions

From the experimental work, the following are observed. The use of RHA increases the cohesion; however, by the use of binary admixtures (FA + RHA) in combination, this negative effect of RHA is minimised. The optimum substitution level of OPC by binary admixtures is 25% [(FA (20%) + RHA (5%)]. The CS, STS and FS of optimum SCC at 28 days are 18.10, 19.50 and 16.64%, respectively, more than the referral SCC. The inclusion of binary admixtures (FA + RHA) is found to improve both the strength and durability of concrete in sulphate environment. Also, the filler effect of FA + RHA may be responsible for improvement in both strength and durability.

References

1. Okamura H, Ouchi M (1998) Self-compacting high performance concrete. Prog Struct Eng Mater 1:378–383
2. The European guidelines for self-compacting concrete, specification, production and use (2005) The self-compacting concrete European Project Group, Norfolk
3. Guidelines for viscosity modifying admixtures for concrete (2006) The European Federation of Specialist Construction Chemicals and Concrete Systems (EFNARC), Norfolk
4. Sukumar B, Nagamani K, Srinivasa Raghavan R (2008) Evaluation of strength at early ages of self-compacting concrete with high volume fly ash. Constr Build Mater 22:1394–1401
5. Siddique R (2011) Properties of self-compacting concrete containing class F fly ash. Mater Des 32:1501–1507
6. Singh A, Kumar R, Mehta PK, Tripathi D (2020) Effect of acidic environment on rice husk ash steel fibre reinforced concrete. Mater Today Proc 27(2):995–1000
7. Nguyen VT, Ye G, van Breugel K, Fraaij ALA, Bui DD (2011) The study of using rice husk ash to produce ultrahigh performance concrete. Constr Build Mater 25:2030–2035

8. Mbessa M, Pera J (2001) Durability of high-strength concrete in ammonium sulfate solution. Cem Concr Res 31(8):1227–1231
9. IS: 8112-1989: Specification for 43 grade ordinary Portland cement. Bureau of Indian standards, New Delhi, India
10. IS: 383-1987: Specification for coarse and fine aggregate from natural sources for concrete. Bureau of Indian Standards, New Delhi, India
11. EFNARC-2002 (2002) Guidelines for self-compacting concrete. London, UK, Association House, pp 32–34
12. IS: 516-1959 In: Methods of tests for strength of concrete
13. IS: 5816-1999. In: Splitting tensile strength of concrete-method of test

Effect of Elevated Temperature on Mechanical Properties of High-Strength Concrete Produced by Adding Fly Ash and Colloidal Nanosilica

V. R. Rathi and C. D. Modhera

Abstract In present study, investigations are done to find the effect of elevated temperature on mechanical and physical properties of high-strength concrete (HSC) incorporating fly ash (FA) as a supplementary cementitious material (SCM) ranging from 10 to 35% b.w.c. along with colloidal nanosilica (CNS) varying from 1 to 5% b.w.c. The specimens were heated in electric furnace at various temperatures from 100 to 800 °C for 2 h. After that, specimens are cooled in furnace for 24 h. Thereafter compressive strength and weight loss, ultrasonic pulse velocity (UPV) is measured. The SEM analysis is carried to study the morphology of concrete at elevated temperature. The result shows that due to addition of CNS along with fly ash, the residual strength at 800 °C remains about 50% of the control mix. Also due to addition of SCM and CNS, the weight loss and compressive strength are reduced, but it is maintained up to 600 °C temperature when compared to control mix. These results were supported by UPV data and scanning electron microscopy (SEM) studies of the various mixes.

Keywords High strength concrete · Elevated temperature · Colloidal nano silica · Scanning electron microscopy

1 Introduction

When concrete is subjected to elevated temperature, its various mechanical properties such as strength, elastic modulus, change in volume are changed abruptly which results in structural instability. So, there is need to take proper care while selecting constituent material to be used in concrete, because when concrete is exposed to

V. R. Rathi (✉)
Department of Civil Engineering, Pravara Rural Engineering College, Loni, Maharashtra 413736, India

C. D. Modhera
Department of Civil Engineering, Sardar Vallabhbhai National Institute of Technology, Surat, Gujarat 395007, India
e-mail: cdm@amd.svnit.ac.in

B. Kondraivendhan et al. (eds.), *Sustainable Building Materials and Construction*,
Lecture Notes in Civil Engineering 222,
https://doi.org/10.1007/978-981-16-8496-8_17

elevated temperature, its behavior depends on material properties such as type of aggregates, bond between the cement paste and aggregate, type of cement, magnitude of temperature, duration of fire, size and shape of structural member, moisture content of concrete; these all affect the performance of concrete exposed to fire [1].

Dehydration and release of chemically bound water from C-S-H is become significant above 110 °C. The dehydration of matrix and thermal expansion of aggregates give rise to thermal stresses; at 300 °C, micro-cracks start (Hertz K. D), and $Ca(OH)_2$ as the most important component of cement paste dissociates at around 530 °C results in shrinkage of concrete. Concrete experiences physical and chemical transformation when subjected to fire and elevated temperature due to its formation process which results in dissociation of its firm bond structure [2]. This change includes evaporation of free water, dehydration of chemical bond water, decomposition of calcium hydroxide and C-S-H, and change in color Hertz [3].

2 Research Methodology

The concrete of M60 grade was first designed without using any mineral admixture by adding cement, sand, and coarse aggregates; thereafter, cement is replaced by various percentage of fly ash along with various percentage of CNS. Then, the specimens are exposed to elevated temperatures for 2 h and cooled up to room temperature to evaluate the effect on mechanical and physical properties of HSC.

3 Materials

For the experimentation work, O.P.C of 53 grade confirming to BIS 12269-1989 along with fly ash and CNS is used. The coarse aggregates of 10 mm size and naturally available river sand are used with fineness modulus of coarse aggregate as 6.78 and that of fine aggregate as 3.45 confirming to Zone II as per BIS 383-1970 with specific gravity 2.60 and 2.77, respectively, are used. The CNS with practical size 5–8 nm with nanosolid is in the range of 15–16%.

4 Test Results and Discussion

The test results presented below are based on the average values of three cubes for each material combination and all percentage of fly ash ranging from 10 to 35% by adding CNS ranging from 1 to 5% in each proportion.

Temperature→	100 °C	200 °C	400 °C	600 °C	800 °C
Average values of % loss in comp. strength	−13.70	−13.72	−21.26	−26.52	−42.64
Average values of % reduction in weight	2.04	3.265	6.27	8.09	10.54
Average values of relative UPV	0.94	0.85	0.663	0.53	0.316

4.1 Discussion on Test Results

As due to increase in temperature, the microstructure of the concrete gets deteriorated which results in decrease in UPV values beyond 600 °C; this decrease in UPV values is observed at higher temperature. This is due to loss of C-S-H gel and increase in air voids as shown in Fig. 2; similarly, from Fig. 1, it is observed that the % reduction in weight is inversely proportional to UPV values as UPV value is more, the reduction in weight is less and vice versa. Also from Fig. 3, it is concluded that as temperature increases, the reduction in weight also increases. From Fig. 4, it is observed that there is decrease in compressive strength proportionally with increase in temperature. Also, it is observed that there is less loss in compressive strength at the addition of 3% CNS for all % replacement of fly ash. Similarly, from Figs. 4, 5 and 6, it is observed that the R^2 values are 0.984 which indicates good relation between % reduction in compressive strength, % reduction in weight, and change in UPV values for 28 days curing.

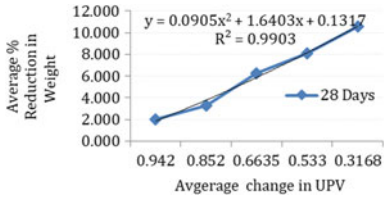

Fig. 1 Relation between change in UPV and % reduction in weight

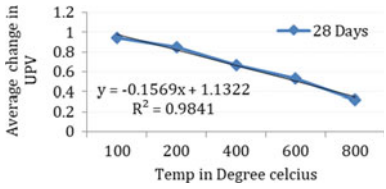

Fig. 2 Relation between temperatures and average change in UPV

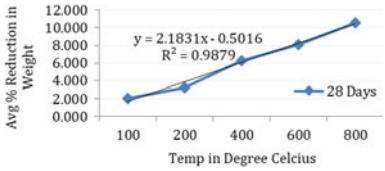

Fig. 3 Relation between temperatures and average % reduction in weight

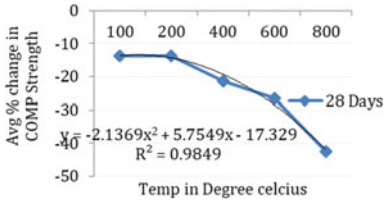

Fig. 4 Relation between temperature and average % change in compressive strength

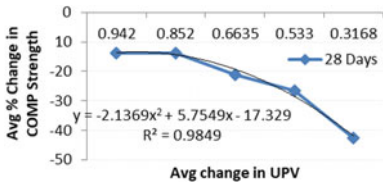

Fig. 5 Relation between average changes in UPV and average % change in compressive strength

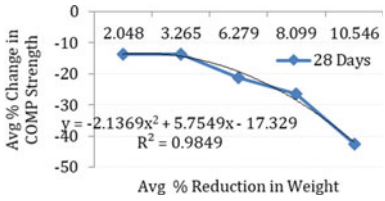

Fig. 6 Relation between average % reductions in weight and average % change in compressive strength

5 Residual Compressive Strength at Elevated Temperature

Various researchers represented the prediction model for calculation of residual strength for concrete subjected to elevated temperature as represented in Table 1. For all the models mentioned in Table 1, **T** = temperature in degree Celsius and $f_{CO} = f_{Ck} = 60$ MPa for various models and given in Table 2.

From the experimental results for CNS added HSC, it is observed that the residual strength of nanoconcrete after 400 °C is good, and it can withstand beyond 400 °C also because at 800 °C temperature also, it has more than 50% residual strength.

It is also observed that the residual strength of CNS added concrete is more than the concrete without CNS. Here, the test results of CNS added concrete do not match with the predicted models mentioned in Table 2 given by various researchers.

Table 1 Models for compressive strength of concrete at elevated temperature [4]

Model no.	Author	Model for compressive strength of concrete at elevated temperature
1	Li and Purkiss [5]	$f_{CT} = f_{CO}$ [0.00165(T/100)^3 − 0.03(T/100)^2 + 0.025(T/100) + 1.002
2	Hertz [3]	$f_{CT} = f_{CO}$ [1/1 + (T/T1) + (T/T2)^2 + (T/T3)^8 + (T/T4)^{64}] Where T1 = 15,000 T2 = 800 T3 = 570 T4 = 100,000
3	Change et al. [6]	$f_{CT} = f_{CO}$ [1.008 + T/450l$_n$ (T/5800)] ≥ 0.0 20 °C < T ≤ 800 °C
4	Bastami and Aslani [2]	$f_{CT} = f_{CO}$ [1.01 − 0.00037 T] ≤ 1.0 20^{0}C < T ≤ 300 °C $f_{CT} = f_{CO}$ [1.0491 − 0.00036 T + 10^{-6} T^2 − 2 * 10^{-9}T^3 300 °C < T ≤ 900 °C 0 T ≥ 1000 °C
5	Ezekiel et al. [4]	$f_{CT} = f_{CO}$ [0.9722/1 + (T/633.835)$^{4.2974}$
6	Mathew and Paul [7]	$f_{CT} = f_{Ck}$ [1.013 − 0.65(T/10000) − 0.51(T/1000)^2 for 28 > T > 600 for 28 > T > 600

Table 2 Residual compressive strength given by various models for M60 grade of concrete (f_{CO} = 60 MPa) in MPa

Model no. →	1	2	3	4	5	6	Experimental results	
Temperature in °C ↓							Without nano	With nano
100	59.91	58.69	57.19	58.38	58.31	55.80	50.95	51.94
200	56.71	55.76	52.56	56.19	57.92	51.75	50.18	51.88
400	43.65	44.93	40.53	56.22	51.24	40.28	47.04	47.28
600	25.60	19.29	25.20	45.66	32.58	26.36	40.23	44.86
800	7.608	3.50	6.635	22.62	15.68	–	30.08	35.28

6 SEM Images

6.1 SEM Analysis

SEM investigation carried out on hardened concrete shows the morphological changes that occur due to elevated temperature. Figure 7 shows micrographs which explain the microstructure characteristics at 100, 200, 400, 600, 800 °C. Figure 7a shows the well-developed hydrated phases exist such as $Ca(OH)_2$ (marked as "CH") which has been mixed with C-S-H (marked as "CSH") and voids marked as ("V"). Similarly when the temperature increases beyond 400 °C, the deformation of $Ca(OH)_2$ and C-S-H gel takes place as shown in Fig. 7d, e; at 400 °C, the transformation of $Ca(OH)_2$ into $CaCO_3$ takes place, and micro-cracks takes place as shown by arrow in Fig. 7c; at the same time due to increase in temperature, the length and

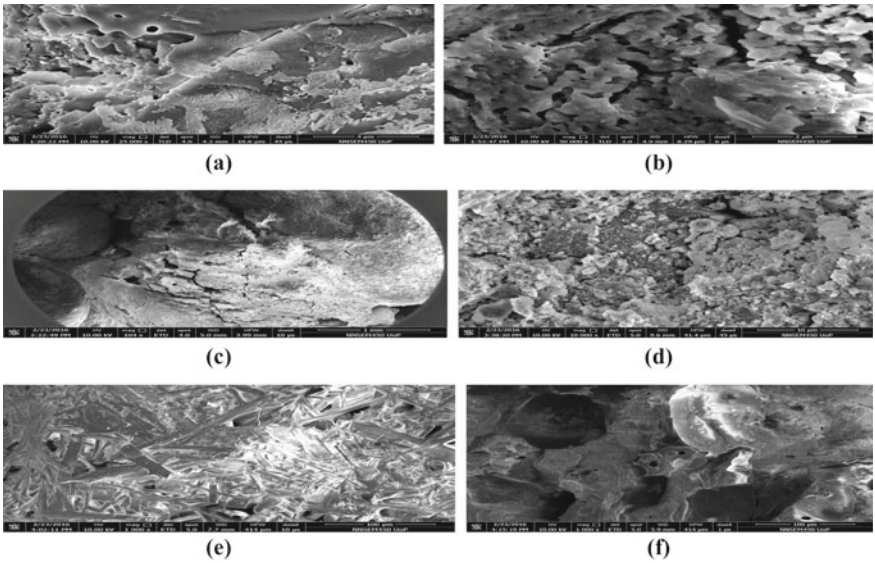

Fig. 7 SEM micrographs showing **a** cracks at aggregate interface at 100 °C, **b** cracks around the anhydrous particles at 200 °C, **c** micro-cracks around the aggregate everywhere at 400 °C, **d** deformation of $Ca(OH)_2$ and C-S-H phase, **e** and **f** declined C-S-H and formation of more pores

width of micro- increase, and thereafter, these micro-cracks turn to voids (Fig. 7f) due to increase in porosity.

7 Conclusions

(1) Up to 20% replacement level of mineral admixture fly ash, the compressive strength is not much affected beyond this strength which reduces rapidly. In present study, HSC with 20% fly ash and 3% addition of CNS gives good residual strength for all temperature.

(2) The addition of 3% CNS along with 20% FA gives more than 50% residual strength at 600 °C temperature, and also, it is observed that though the development of cracks at 400 °C is common in conventional concrete, but CNS added concrete shows good resistance against thermal cracks up to 600 °C.

(3) As R^2 values of all the equations as mentioned above are same 0.9849, it indicates that there is good relation between percentage reduction in weight, compressive strength, and relative ultrasonic pulse velocity (UPV) at various temperatures with addition of nanomaterial

(4) As loss in weight increases, UPV values also increase; similarly, as temperature increases, the relative UPV values also increase.

(5) The loss in weight is consistent up to 600 °C, and it suddenly increases at 800 °C temperature due to release of chemically bound water.
(6) CNS added HSC losses compressive strength significantly at 800 °C temperature having average value of 42.64%, whereas strength reduction at 600 °C temperature is not more compared to 600 °C as it is nearly 1.8 times at 800 °C.
(7) When comparison of models prepared by various researchers is done, it was observed that the residual compressive strength given by CNS added concrete is good beyond 600 °C also up to 800 °C.

References

1. Butcher EG, Pranell AC (1983) In: Designing for fire safety. Wiley, New York
2. Bastami M, Aslani F (2010) Preloaded high temperature constitutive models and relationships for concrete. Scientia Iranica 17(1):11–25
3. Hertz KD (2005) Concrete strength for fire safety design. Mag Concr Res 57(8):445–453
4. Ezekiel S, Xiao RY, Chin CS (2013) Constitutive model for compressive strength and elastic modulus for concrete under elevated temperature. Struc Congr 2013-ASCE, 2916–2925
5. Li long-yuan, Purkis J (2005) Stress-strain constitutive equation of concrete material at elevated temperature. Fire Saf J 40:669–686
6. Change et al (2006) Residual stress-strain for concrete after exposure to high temperature. Cem Concr Res 36:1999–2005
7. Mathew G, Paul MM (2014) Influence of Fly ash and GGBFS in laterized concrete exposed to elevated temperature. J Mater Civ Eng ASCE-2014 26:411–419
8. Nadeem A, Memon SA, Lo TY (2014) The performance of fly ash and Metakaolin Concrete at elevated temperatures. Constr Buil Mater 62:67–76
9. Sreenivasula A, Rao KS (2013) The effect of temperature on mechanical properties of M100 concrete. American J Eng Res 2(4):152–157
10. Demirel B, Kelestemur O (2010) Effect of elevated temperature on the mechanical properties of concrete produced with finely ground pumice and silica fume. Fire Safety J 45:385–391
11. Ren F, Wang JJA, Beverly PDP (2013) Thermal expansion study and micro structural characterization of high-performance concrete. J Mater Civ Eng ASCE-2013 25:1574–1578
12. Fu-Ping C, Kodur VKR, Wang TC (2004) Stress-strain curves for high strength concrete at elevated temperature. J Mater Civ Eng ASCE-2004 16:84–90

Mix Design and Strength Evaluation of Ambient Cured Permeable Alkali-Activated Concrete

Shemal Dave, Irshad Ahmad, and Ankur Bhogayata

Abstract A significant development in the research on the permeable concrete and applications has been noticed in the past decade. On the other hand, a parallel track of research for the sustainable concrete is gaining momentum. It may be an innovative concept of combining the alkali-based binder matrix and a composite with acceptable degree of permeability as a modern construction material for the verities of applications and by limiting the usage of the conventional binders, namely ordinary Portland cement (OPC). However, the development and preparation of a concrete composite demand an accurate mix design for the desirable properties and characteristics. Therefore, the present study has been carried out to obtain the optimum proportions of the alkali-activated permeable concrete (AAPC) constituents with a focus on the preliminary strength properties alongside. The AAPC has been developed by the activation of the industrial waste materials, namely fly ash, silica fumes, and grounded granulated blast furnace slag with the chemical constituents such as sodium silicate and sodium hydroxide in a liquid form. The standard guidelines have been followed in developing AAPC though. The preliminary strength tests have been performed on the specimens. The comparative analysis showed significant improvement in the strength properties of AAPC.

Keywords Alkali activated permeable concrete · Ambient curing · Sustainable development

S. Dave (✉)
Marwadi University, Rajkot, India

I. Ahmad
Muhandesan-E-Nukhba Engineering Consultancy, Kabul, Afghanistan

A. Bhogayata
Civil Engineering Department, Marwadi University, Rajkot, India

B. Kondraivendhan et al. (eds.), *Sustainable Building Materials and Construction*,
Lecture Notes in Civil Engineering 222,
https://doi.org/10.1007/978-981-16-8496-8_18

1 Introduction

The development of permeable concrete immediately gained maximum traction after its first inception. These days, many research scholars are working on the development of better and durable permeable concrete. Generally, development of permeable concrete does not include sand; hence, in this regard, it can be tagged as a sustainable concrete. However, its production requires good amount of conventional cement which has proved to be perilous material for the global environment because of the high carbon footprint during its manufacturing and post-usage [1]. In order to mitigate the environmental damage, many researchers these days are exploring different materials and binders. Alkali-activated concrete (AAC) is emerging as an effective substitute for conventional cement concrete owing to its better strength, durability, and environment-friendly properties. However, the realm of alkali-activated permeable concrete (AAPC) is still the area worth researching as it has huge potential in terms of strength and durability when compared to conventional cement-based permeable concrete. There are very limited researchers who have explored this dimension. For instance, Tho-in et al. [4] have deduced that in order to develop permeable AAC, high-calcium fly ash can be utilized. The team has also concluded that the relationship between density void content and compressive strength void content is similar to that of conventional cement-based permeable concrete. Another team of research fellow Zaetang et al. [6] has used coal ash that is also called fly ash to develop permeable geopolymer concrete. On September 2015, Jo et al. [2] proposed an optimum mix design of fly ash–based geopolymer paste and used it to produce permeable geopolymer concrete (PGC), and compressive strength obtained with this paste ranges between 4.7 and 5.3 MPa using binder to aggregate ratio 1:4 and aggregate size of 4.75–12.5 mm in ambient curing condition.

Sun [3] investigated geopolymer binder to gain its strength; early on 2018, the team has used metakaolin, ground granulated blast furnace, and combination of them for this purpose. PGC produced from that combinations achieved better mechanical properties and water permeability than cement-based pervious concretes at the age of 7 days. Finally, Xu and Shi [5] studied graphene oxide (GO)-modified pervious concrete with fly ash which reveals effect of GO in the hydration of fly ash-enhanced property of PGC. It has been found that GO increases mechanical properties as well as durability to salt scaling resistance of fly ash-based PGC. To deduce, alkali-activated permeable concrete (AAPC) is a very good substitute for Portland cement-based permeable concrete and makes concrete eco-friendlier. In addition to that, it helps to reduce some gaps that exist in OPC-based permeable concrete. For instance, late strength gaining and improper curing concerns cause low strength and less durable permeable concrete. Hence, following study has been conducted to obtain the optimum proportions for the alkali-activated permeable concrete (AAPC) constituents which can not only provide sufficient degree of permeability but also provide desired compressive strength. The mix design of AAPC has been developed considering chemical activation of the industrial waste materials such as fly ash, silica

fumes, and grounded granulated blast furnace slag with the help of alkaline activators such as sodium silicate and sodium hydroxide in a liquid form. The segregating aspect of the present work is the curing of the specimens at the ambient temperature without the usage of an external heating source which is otherwise required to initiate polymerization process.

2 Materials and Methodology

2.1 Paste Materials or Binder

Binder is one of the crucial parts of permeable concrete. The function of paste material is to bind the filler material with each other to produce a material which can resist loads, and the more strength the binder material has, the better compressive strength results can permeable concrete offer. For this experimental work, low calcium Class F Fly ash conforming to the requirements of ASTM C618-08 was used as a main alumino-silicate binder. The FA was acquired from Wanakbori thermal power plant, Gujarat, India. Along with FA, two other pozzolanic binders GGBFS and SF were used to cure the AAC at ambient temperature and to refine the matrix at micro-level. It was observed that the inclusion of GGBFS accelerates the process of polymerization due to the present CaO content which liberates the heat in the presence of water and provides sufficient internal thermal curing. Furthermore, it produces C-S-H gel along with N-S-H/N-A-S-H gel produced by FA which offers better bonding and hence better strength. To initiate polymerization process in pozzolanic binders, sodium-based alkaline solutions were used. A combination of sodium hydroxide (NaOH) in pellet form and sodium silicate (Na_2SiO_3) of A 53 grade ($Na_2O = 14.7\%$, $SiO_2 = 29.4\%$ and $H_2O = 55.9\%$ by mass) was used. The solution was rendered one day prior to casting.

2.1.1 Filler Materials

Different type of aggregate has used as filler material in permeable concrete. It is to be noted that type, size, and gradation of filler affects mechanical, physical, and durability properties of permeable concrete. High compressive strength with satisfactory water permeability can be obtained with dolomite, and good thermal conductivity with reasonable compressive strength can be achieved by coal bottom ash aggregate. Large-size aggregate causes high void content, big pore size, and excellent water infiltration rate but can be resulted in low mechanical properties. On the other hand, small aggregates can reduce rate of permeability in concrete. Ergo, gradation of aggregate is also important as it affects percolation rate. Aggregate used in this study is crushed granite aggregate with size that varies from 2.36 to 12.5 mm.

2.2 Methodology

2.2.1 Mix Design

Aggregate, binder, and activator amount were calculated according to ACI-522R–14. For this experimental work, aggregate fraction was considered as 1:4, alkaline liquid-to-binder ratio = 0.4, alkaline liquid-to-water ratio = 3, molarity of sodium hydroxide = 14 M, sodium silicate-to-hydroxide ratio = 3, and optimum dosage of fly ash (FA), ground granulated blast furnace slag (GGBFS), and silica fume (SF) were considered as 50, 40, and 10%, respectively. Here, it is to be noted that alkaline solution itself is not sufficient to acquire proper workability as it is viscous in nature and has some solid particles. Ergo, fresh mix remains dry and less workable. Therefore, water is needed to gain proper mix and to help binder to cover aggregate uniformly. On the other hand, accuracy must be well thought-out to avoid micro-flow and drain-off of binder from aggregate surface; therefore, water-to-alkali liquid ratio is calculated as per following logic:

Assuming that, water is going to be used instead of alkali solution. Hence, technically proper amount of water for one kilogram of binder would be 400 gm, and the volume of 400 gm water is 400 ml because volume of water is mixed with volume of binder. Volume of 400 gm alkali solution has been found experimentally which turned out to be 265 ml, and it is very low than water to mix with 1 kg binder. Following this idea, maximum amount of water should not be increased than 135 gm for one-kg binder (Fig. 1 and Table 1).

$$\text{Alkaline liquid} - \text{to} - \text{water ratio} = \frac{\mathrm{W_{AL}}}{\mathrm{V_w} - \mathrm{V_{AL}}} = \frac{400}{400 - 265} = 2.962 \cong 3 \quad (1)$$

where

W_{AL} weight of alkaline liquid for one-kg binder
V_w volume of water for same weight of alkali

Fig. 1 Specimen for mechanical strength test and testing setup for permeability test and flexural strength test

Table 1 Mix proportion for ambient cured AAPC

Mix design	Aggregate (kg/m^3)	Binder (kg/m^3)			Activator content (kg/m^3)	Water (kg/m^3)	AL/B	AL/W	NS-to-NH ratio
		Fly ash (50%)	GGBFS (40%)	SF (10%)					
50F40G5SF	1470	181.25	145	36.25	145	48.3	0.4	3	3

V_{AL} volume of alkaline liquid.

3 Results and Discussion

3.1 Mechanical Strengths of AAPC

The compressive, splitting tensile, and flexural strength tests as per guidelines mentioned in IS 516:1959 and IS 5816:1999 were carried out at the age of third, seventh, and twenty-eighth days of casting. The prepared specimens demolded after 24 h and kept at ambient temperature before testing. The results are mentioned in Table 3. According to Table 3, if we assume the twenty-eighth day compressive strength as 100% strength of AAPC, then 83% of total strength was gained after third day, and 98% of its total strength was gained after seventh day of ambient temperature curing. This indicates that early strength which is a major concern on OPC-based pervious concrete can easily be achieved with alkali-activated permeable concrete. On the other hand, due to high void ratio present in PAAC, it is difficult to entrap heat generated by the inclusion of GGBFS. Nonetheless, the results achieved in terms of compressive strength are satisfactory and can be recommended for in situ application (Table 2).

Table 2 Average compressive strength test results

Test	Strength (MPa)		
	Third day	Seventh day	Twenty-eighth day
Compressive strength	18.66	22.16	22.58
Splitting tensile strength	0.98	1.13	1.14
Flexural strength	1.81	2.07	2.08

Table 3 Average dry density and void content

Test	*K*	Dry mass (gm)	Submerged mass (gm)	Density of water (kg/m^3)	Diameter (mm)	Length (mm)	Dry density (kg/m^3)	Void content (%)
Dry density	1,273,240	9589	150	–	150	296.59	1829.04	–
Void content	1,273,240	9589	5844.33	997.033	150	296.59	–	28.36

Table 4 Result of permeability according to falling head method

C/S of specimen (cm^2)	C/S of tube (cm^2)	Length of specimen (cm)	Time (s)	Initial head (cm)	Final head (cm)	Permeability coefficient (cm/s)
78.54	95.033	20	7.83	54.17	28.67	0.59

3.2 Physical Properties of AAPC

To evaluate physical properties of AAPC, dry density, void content, and water permeability were measured. For dry density and void content, guidelines mentioned in ASTM C1754-12 were followed. However, in order to find permeability of AAPC, test setup developed by N. Neithalath et al. was prepared. The results of dry density and void content are mentioned in Table 3. Permeability of AAPC was carried out as per constant head permeability method. The results obtained are mentioned in Table 4.

4 Conclusion

After experimental investigation of physical and mechanical properties of AAPC, following conclusion can be drawn:

- Optimum variation in binder fraction is obtained with 50% fly ash, 40% GGBS, 10% silica fume, and 0.4 alkali-to-binder ratio.
- Being a porous concrete, permeable geopolymer concrete loses the heat, which is required for polymerisation process. Hence, sunlight curing is a significant option for curing.
- Average dry density of PGC is 1830 kg/m^3 with average void content of 29%.
- Average permeability coefficient of 0.591 cm/s is obtained using falling head method and permeameter apparatus.

References

1. Duxson P et al (2007) Geopolymer technology: the current state of the art. J Mater Sci 42(9):2917–2933. https://doi.org/10.1007/s10853-006-0637-z
2. Jo M, Soto L, Arocho M, St John J, Hwang S (2015) Optimum mix design of fly ash geopolymer paste and its use in pervious concrete for removal of fecal coliforms and phosphorus in water. Constr Buil Mater 93:1097–1104. https://doi.org/10.1016/j.conbuildmat.2015.05.034
3. Sun Z, Lin X, Vollpracht A (2018) Pervious concrete made of alkali activated slag and geopolymers. Constr Build Mater 189:797–803. https://doi.org/10.1016/j.conbuildmat.2018.09.067

4. Tho-in et al (2012) Pervious high-calcium fly ash geopolymer concrete. Constr Buil Mater 30:366–371. https://doi.org/10.1016/j.conbuildmat.2011.12.028
5. Xu G, Shi X (2016) Graphene oxide modified pervious concrete with fly ash as sole binder. DEStech Trans Eng Technol Res (ictim). http://dpi-proceedings.com/index.php/dtetr/article/view/5478
6. Zaetang Y et al (2015) Use of coal ash as geopolymer binder and coarse aggregate in pervious concrete. Constr Build Mater 96:289–295. https://doi.org/10.1016/j.conbuildmat.2015.08.076

Outcome of a Magnetic Field on Heat Transfer of Carbon Nanotubes (CNTs)-Suspended Nanofluids by Shooting Type Laplace–Adomian Decomposition Method (LADM)

B. Vennila, N. Nithya, and M. Kabilan

Abstract This paper focuses on the impact of carbon nanotubes (CNTs) on nanofluid flow and heat transfer in the occurrence of a magnetic field. Various parameters' consequences on fluid velocity and temperature have been addressed. To obtain the precise analytic solution for the velocity and temperature distribution, a shooting form Laplace–Adomian decomposition method is used.

Keywords Carbon nanotubes · Magnetic parameter · Solid volume fraction of CNTs

1 Introduction

Single-walled nanotubes (SWNTs) and multi-walled nanotubes (MWNTs) are two types of nanotubes. CNTs are valid nanotechnology: they are substances with a diameter of around a nanometer that can be manipulated physically and chemically in a number of ways. Electronics, materials science, energy storage, chemical engineering and a variety of other areas are all benefit from their use. Choi [1] investigated the value of nanoparticles/carbon nanotubes in developing the thermal conductivity of base fluids. The flow and heat transfer of ordinary nanoparticles and CNT-suspended nanofluids have been studied by several authors.

Using a Navier slip layer, Khan et al. [2] researched the liquid flow and heat transfer of carbon nanotubes beside a smooth plate. For nonlinear differential equations with

B. Vennila (✉) · N. Nithya
Department of Mathematics, School of Basic Sciences, College of Engineering and Technology, SRM Institute of Science and Technology, Kattankulathur 603203, Tamil Nadu, India
e-mail: vennilab@srmist.edu.in

N. Nithya
e-mail: nn7589@srmist.edu.in

M. Kabilan
Department of Computer Science Engineering, School of Computing, College of Engineering and Technology, SRM Institute of Science and Technology, Kattankulathur 603203, Tamil Nadu, India
e-mail: km4463@srmist.edu.in

B. Kondraivendhan et al. (eds.), *Sustainable Building Materials and Construction*,
Lecture Notes in Civil Engineering 222,
https://doi.org/10.1007/978-981-16-8496-8_19

infinity boundary conditions, Sivakumar et al. [3] investigated the shooting form Laplace–Adomian decomposition (LAD) algorithm. In the presence of a magnetic field, Hamad et al. [4] explore an incompressible viscous nanofluid flowing through a semi-infinite vertical stretching sheet.

Emad et al. [5] look at the theoretical analysis of a laminar fluid stream that forms when a smooth surface is stretched in a nanofluid. In the presence of second order slip boundary conditions, Aly et al. [6] inspected peristaltic nanofluid flow in an asymmetric channel. Akbhar et al. [7] used thermal and velocity slip findings to research the flow and heat transfer of carbon nanotubes in an asymmetric path.

For the peristaltic stream of Jeffrey flowing with nanoparticles in an asymmetric tube, Ebaid [8] consider the homotopy perturbation scheme. Kamali et al. [9] investigated numerically the convective heat transfer by multi-walled carbon nanotube (MWCNT) dependent nanofluids in a straight tube under standard wall heat flux provision. Ebaid and Aly [10] analysed the exact model for slip peristaltic flow of nanofluid in detail.

Ebaid and Al Sharif [11] solved the flow and heat transfer of nanofluids balanced with CNTs in the presence of a magnetic field. Tiwari [12] revealed the arithmetic representation for Marangoni convection MHD flow of carbon nanotubes in a porous medium with radiation. The formulae of calculating the effective thermal conductivity of CNTs-based composites using Maxwell theory are given by Xui et al. [13].

Chen et al. [14] established a reliable method for calculating Adomian polynomials for nonlinear operators. Mahalakshmi et al. [15] used the Adomian decomposition technique to analyse the velocity and temperature profiles. The aim of this paper is to look at how magnetic parameters influence velocity and temperature.

2 Formulation of the Problem

The boundary layer equations take the form for the present study is

$$\frac{\partial u}{\partial x} + \frac{\partial v}{\partial y} = 0 \tag{1}$$

$$\rho_{nf}\left(u\frac{\partial u}{\partial x} + v\frac{\partial u}{\partial y}\right) = \mu_{nf}\frac{\partial^2 u}{\partial y^2} - \sigma B_0^2 u \tag{2}$$

$$(\rho C_p)_{nf}\left(u\frac{\partial T}{\partial x} + v\frac{\partial T}{\partial y}\right) = K_{nf}\frac{\partial^2 T}{\partial y^2} \tag{3}$$

Velocity components (u, v) have been considered in the x and y directions, correspondingly, T (local temperature of the liquid), σ(electric conductivity), ρ_{nf}(density of the nanofluid), μ_{nf}(dynamic viscosity of the nanofluid), $(\rho C_p)_{nf}$(heat capacitance) and K_{nf}(thermal conductivity) of the nanofluid and are defined as

$$\rho_{nf} = (1-\phi)_{\rho f} + \phi\rho_s \tag{4}$$

$$\mu_{nf} = \frac{\mu_f}{(1-\phi)^{2.5}} \tag{5}$$

$$(\rho C_p)_{nf} = (1-\phi)(\rho C_p)_f + \phi(\rho C_p)_s \tag{6}$$

$$K_{nf} = K_f \left\{ \frac{Ks + 2Kf - 2\phi(K_f - K_s)}{Ks + 2Kf - 2\phi(K_f - K_s)} \right\} \tag{7}$$

where ϕ is the solid volume fraction of the carbon nanotubes.

Equations (1), (2) and (3) have the boundary conditions.

$$\begin{aligned} &u = u_w(x) = ax,\ \ v = 0,\ T = T_w \text{ at } y = 0 \\ &u \to 0,\ T \to T_\infty \text{ as } y \to 0 \end{aligned} \tag{8}$$

The flow is essentially regulated by the next system of nonlinear differential equations, as seen in ref. [4].

$$f'''(\eta) + \alpha[f(\eta)f''(\eta) - (f'(\eta))^2] - \gamma f'(\eta) = 0 \tag{9}$$

$$\tau\theta''(\eta) + f(\eta)\theta'(\eta) = 0 \tag{10}$$

where

$$\left.\begin{aligned} \alpha &= (1-\phi)^{2.5}[1 - \phi + \phi(\rho_{CNT}/\rho_f)] \\ \gamma &= M(1-\phi)^{2.5} \end{aligned}\right\} \tag{11}$$

$$\tau = \frac{1}{\text{Pr}} \frac{K_{nf}}{K_f} \frac{1}{[1 - \phi + \phi(\rho C_p)_{CNT}/(\rho C_p)_f]} \tag{12}$$

$$\frac{K_{nf}}{K_f} = \frac{1 - \phi + 2\phi\left(\frac{K_{CNT}}{K_{CNT} - K_f}\right)\ln\left(\frac{K_{CNT} + K_f}{2K_f}\right)}{1 - \phi + 2\phi\left(\frac{K_f}{K_{CNT} - K_f}\right)\ln\left(\frac{K_{CNT} + K_f}{2K_f}\right)} \tag{13}$$

The boundaries are as follows:

$$\left.\begin{aligned} &f(0) = 0,\ \ f'(0) = 1,\ \ f'(\infty) = 0 \\ &\theta(0) = 1,\ \ \theta(\infty) = 0 \end{aligned}\right\} \tag{14}$$

Taking Laplace transform on both sides of eqs. (9) and (10) and applying the boundary conditions (14), we get

$$L(f) = \frac{s+p}{s^3-\gamma s} + \frac{\alpha L(f'^2 - ff'')}{s^3-\gamma s} \tag{15}$$

$$L(\theta) = \frac{s+\beta}{\tau s^2} - \frac{L(f\theta')}{\tau s^2} \tag{16}$$

where $f''(0) = p$.

Let

$$f(\mu) = \sum_{n=0}^{\infty} f_n(\mu) \text{ and } \theta(\mu) = \sum_{n=0}^{\infty} \theta_n(\mu) \tag{17}$$

are the solution of eqns. (15) and (16) as well as nonlinear terms ff'' and $f'2$ can be decomposed into Adomian polynomials in the following way:

That is,

$$F(f) = f'^2 = \sum_{n=0}^{\infty} A_n \tag{18}$$

and

$$G(f) = ff'' = \sum_{n=0}^{\infty} B_n \tag{19}$$

The Adomian polynomials of these nonlinear functions are first separated into a tiny number of terms.

$$\left.\begin{array}{l} A_0 = f_0'^2, A_1 = 2f_0'f_1', A_2 = f_1'^2 + 2f_0'f_2' \\ B_0 = u_0u_0'', B_1 = u_1u_0'' + u_0u_1'' \\ B_2 = u_0u_0'' + u_2u_0'' + u_1u_1'' \end{array}\right\} \tag{20}$$

By replacing the Adomian polynomials in Eq. (9), we obtain

$$L(f_0) = \frac{\frac{-p}{\gamma}}{s} + \frac{\frac{p-\sqrt{\gamma}}{2\gamma}}{s+\sqrt{\gamma}} + \frac{\frac{p+\sqrt{\gamma}}{2\gamma}}{s-\sqrt{\gamma}} \tag{21}$$

$$L(f_1) = \frac{-\alpha}{s^3-\gamma s} L(B_0) + \frac{\alpha}{s^3-\gamma s} L(A_0) \tag{22}$$

$$f_0 = l_1 + m_1 e^{-\sqrt{\gamma}\mu} + n_1 e^{\sqrt{\gamma}\mu} \tag{23}$$

$$f_1 = 4m_1n_1\alpha\mu + \frac{2\alpha m_1n_1}{\sqrt{\gamma}} e^{-\sqrt{\gamma}\mu} - \frac{2\alpha m_1n_1}{\sqrt{\gamma}} e^{\sqrt{\gamma}\mu}$$

$$+\frac{\alpha l_1 m_1}{\sqrt{\gamma}}-\frac{\alpha l_1 m_1^3}{4\sqrt{\gamma}}e^{-\sqrt{\gamma}\mu}-\frac{\alpha l_1 m_1}{2}\mu e^{-\sqrt{\gamma}\mu}-\frac{\alpha l_1 m_1}{4\sqrt{\gamma}}e^{\sqrt{\gamma}\mu}$$
$$-\frac{\alpha l_1 n_1}{\sqrt{\gamma}}+\frac{3}{4}\frac{\alpha l_1 n_1}{\sqrt{\gamma}}e^{\sqrt{\gamma}\mu}-\frac{\alpha l_1 n_1}{2}\mu e^{\sqrt{\gamma}\mu}+\frac{\alpha_1 l_1 n_1}{4\sqrt{\gamma}}e^{-\sqrt{\gamma}\mu}$$
$$+l_1 m_1 e^{-\sqrt{\gamma}\mu}+n_1 e^{\sqrt{\gamma}\mu} \tag{24}$$

where

$$l_1=-\frac{p}{\gamma},\ m_1=\frac{p-\sqrt{\gamma}}{2\sqrt{\gamma}},\ n_1=\frac{p+\sqrt{\gamma}}{2\gamma} \tag{25}$$

$$f=P+R+O+\frac{\mu}{1!}[Q-R\sqrt{\gamma}+O\sqrt{\gamma}+P_1+Q_1]$$
$$+\frac{\mu^2}{2!}[R\gamma+O\gamma-P\sqrt{\gamma}+O\sqrt{\gamma}]+\ldots \tag{26}$$

where

$$\left.\begin{aligned}P&=\frac{\alpha l_1 m_1}{\sqrt{\gamma}}-\frac{\alpha n_1 l_1}{\sqrt{\gamma}}+l_1,\ Q=4m_1 n_1\alpha,\ R=\frac{2\alpha m_1 n_1}{\sqrt{\gamma}}+\frac{\alpha n_1 l_1}{4\sqrt{\gamma}}-\frac{\alpha l_1 m_1^3}{4\sqrt{\gamma}}+m_1,\\ O&=\frac{-2m_1 n_1}{\sqrt{\gamma}}-\frac{\alpha l_1 m_1}{4\sqrt{\gamma}}+\frac{3\alpha}{4}\frac{n_1 l_1}{\sqrt{\gamma}}+n_1,\ P_1=\frac{-\alpha l_1 m_1}{2},\ Q_1=\frac{\alpha n_1 l_1}{2}\end{aligned}\right\} \tag{27}$$

the response to Eq. (16) is

$$L(\theta_0)=\frac{s+\beta}{\tau s^2} \tag{28}$$

$$\theta_0=\frac{1}{\tau}+\frac{\beta}{\tau}\mu \tag{29}$$

$$L(\theta_1)=L\left(\frac{f\theta'}{\tau s^2}\right) \tag{30}$$

$$=\frac{l_1\beta}{\tau^2}\frac{1}{s^3}+\frac{m_1\beta}{\tau^2}\frac{1}{s^2(s+\sqrt{\gamma})}+\frac{n_1\beta}{\tau^2 s^2(s-\sqrt{\gamma})} \tag{31}$$

$$\theta=\theta_0+\theta_1$$
$$=\frac{1}{\tau}+\frac{\beta\mu}{\tau}+\left(\frac{l_1\beta}{\tau^2}+\frac{n_1\beta}{\tau^2}+\frac{m_1\beta}{\tau^2}\right)\frac{\mu^2}{2!}$$
$$+\left(\frac{-m_1\beta\sqrt{\gamma}}{\tau^2}+\frac{n_1\beta\sqrt{\gamma}}{\tau^2}\right)\frac{\mu^3}{3!}+\ldots \tag{32}$$

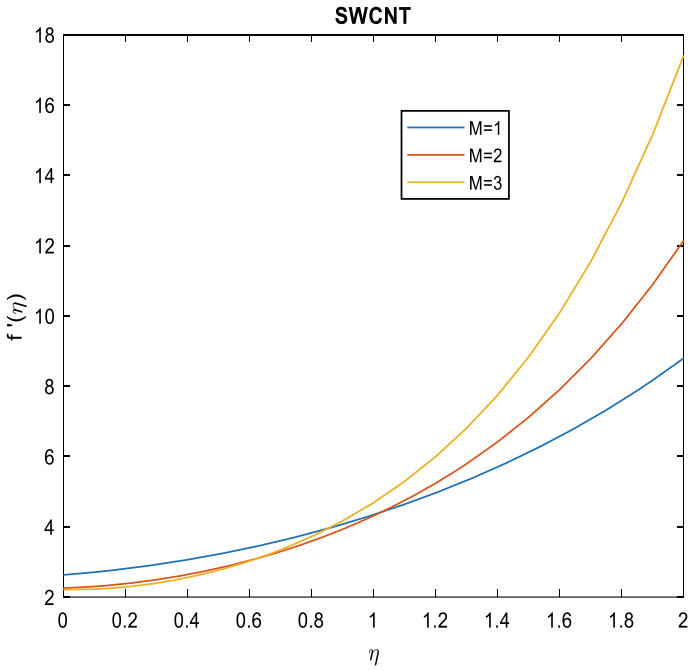

Fig. 1 Velocity profile with different magnetic parameter for SWCNT

3 Results and Discussion

Figures 1 and 2 are depicted to know the control of a magnetic parameter on nanofluid velocity in a single-walled carbon nanotubes and multi-walled carbon nanotubes. It is shown that velocity increases when magnetic parameter increases in both. The velocities of CNTs-suspended nanofluids, on the other hand, are slower than those of normal nanoparticles-suspended nanofluids, as seen in Figs. 1 and 2 of the current report. In visible region of M, it is also observed that the velocity field for SWCNT differs slightly from that of MWCNT. Figure 3 indicates that the temperature profile is declining as the solid volume fraction ϕ grows, suggesting that the temperature profile is decreasing.

4 Conclusions

The Laplace shooting method of Adomian decomposition was used to solve the nonlinear differential equations governing the flow and heat transfer of nanofluids suspended with CNTs in the presence of a magnetic field. The influence of magnetic parameters on fluid velocity and solid volume fraction on heat transfer has been

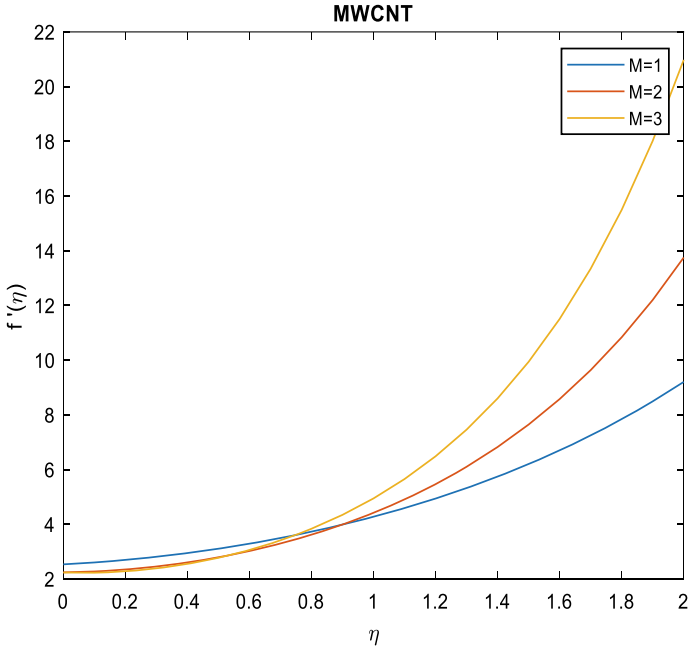

Fig. 2 Velocity profile with different magnetic parameter MWCNT

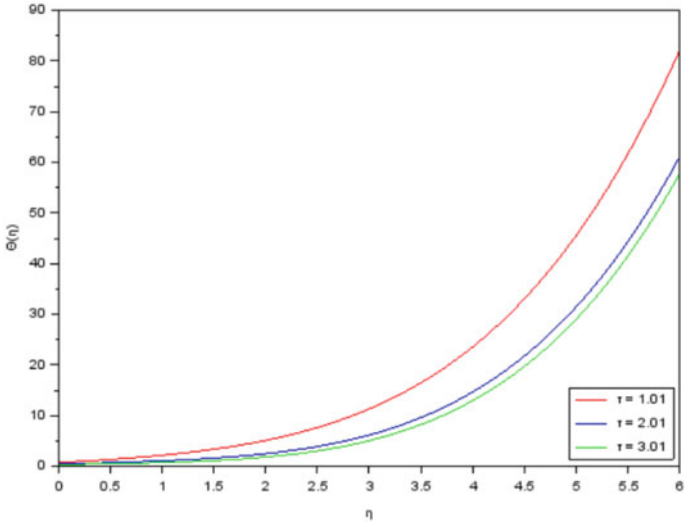

Fig. 3 Temperature profile for various values τ

explored. In this report, the analytical findings indicated that the suspended nanofluids of SWCNTs and MWCNTs have nearly the same velocity. It was also discovered that as the volume fraction of CNTs increases, the heat transfer rates decrease.

References

1. Choi SVS (1995) Developments and applications of non-newtonian flows. In: Siginer DA, Wang HP (eds) vol 66. ASME, New York, p 99
2. Khan WA, Khan ZH, Rahi M (2014) Fluid flow and heat transfer of carbon nanotubes along a flat plate with navier slip boundary. Appl Nanosci 4:633–641
3. Sivakumar TR, Bajju S (2011) A shooting type of laplace—adomian decomposition algorithm for nonlinear differential equations with boundary conditions at infinity. Appl Math Lett 24
4. Hamad MAA (2011) Analytical solution of natural convection flow of a nanofluid over a linearly stretching sheet in the presence of magnetic field. Int Commun Heat Mass Transfer 38(4):487–492
5. Emadh EA, Abdelhalim E (2013) New exact solutions for boundary-layer flow of a nanofluid past a stretching sheet. J Comput Theor Nanosci 10:2591–2594. https://doi.org/10.1166/jctn.2013.3253
6. Aly EH, Ebaid A (2014) Effect of velocity second slip boundary condition on the peristaltic flow of nanofluids in asymmetric channel: exact solution. Abstr Appl Anal. https://doi.org/10.1155/2014/191879
7. Akbar NS et al (2014) Thermal and velocity slip effects on mhd peristaltic flow with carbon nanotubes in an asymmetric channel: application of radiation therapy. Appl Nanosci 4:849–857
8. Ebaid A (2014) Remarks on homotopy perturbation method for the peristaltic flow of jeffery fluid with nano particles in an asymmetric channel. Comput Math Appl 68(3):77–85. https://doi.org/10.1016/j.camwa.2014.05.008
9. Kamali R, Binesh AR (2010) Numerical investigation of heat transfer enhancement using carbon nanotube based non-newtonian nanofluids. Int Commun Heat Mass Transfer 37(8):1153–1157. https://doi.org/10.1016/j.icheatmasstransfer.2010.06.001
10. Ebaid A, Aly EH (2013) Exact analytical solution of the peristaltic nanofluids flow in an asymmetric channel with flexible walls and slip condition: application of cancer treatments. Comput Math Methods Med 2013(825376). https://doi.org/10.1155/2013/825376
11. Ebaid A, Al Sharif MA (2015) 'Application of laplace transform for the exact effect of a magnetic field on heat transfer of carbon nanotubes-suspended nanofluids. Degruyter 70(6). https://doi.org/10.1515/zha-2015-0125
12. Tiwari AK et al (2017) Mathematical model for marangoni convection MHD flow of carbon nanotubes through porous medium. FAETSD J Adv Res Appl Sci 4(7)
13. Xue OZ (2005) Model for thermal conductivity of carbon nanotube based composites. Physica B 368(1–4):302–307. https://doi.org/10.1016/j.physb.2005.07.024
14. Chen V, Lu Z (2004) An algorithm for adomian decomposition method. Appl Math Comput 159(1):221–235
15. Mahalakshmi D, Vennila B (2020) Boundary layer flow of silver and gold nanofluids over a flat plate by Adomian decomposition method. In AIP conference proceedings, vol 2277, p 170002. http://doi.org/10.1063/5.0025571

Utilization of GGBFS and Micro-fine as Partial Replacement of Cement in Mortar with Manufactured and River Sand

Dhaval Patel, C. D. Modhera, and Gaurav B. Jagad

Abstract The compressive strength behavior of cement mortar with ground granulated blast furnace slag (GGBFS) and micro-fine (ultrafine GGBFS) was investigated. The strength characteristics of cement mortar are examined at different replacement level of different supplementary cementitious materials (GGBFS and micro-fine) And also used of manufactured sand with natural river sand of higher percentage of replacement of GGBFS and micro-fine in mortar. GGBFS that is partial replaced with cement was 10–70%, and micro-fine was 5–50% with cement in mortar with standard sand. Different tests on cement like initial-final setting time, consistency, soundness of cement, and compressive strength of mortar were observed for 7 days and 28 days of curing period. From above combination, 40% replacement of GGBFS and 50% replacement of micro-fine give better results compared to cement. Plastering mortar (1:3) is prepared with at 0.5 constant w/c ratio using natural sand as the fine aggregate and replacing it with 20–100% manufactured sand. The cubes were cast and tested on the 7 and 28 days of curing period. In both cases, replacement with 60% manufactured sand has attained higher strength, but 100% replacement manufacture sand also has a better effect than 100% natural river sand. In conclusion, the strength characteristics of manufactured sand were studied, and due to decent bonding properties, manufactured sand exhibits better strength. This study shows that manufactured sand can be used as a replacement for natural river sand in mortar.

Keywords Ground granulated blast furnace slag · Microfine · Manufactured sand · River sand

1 Introduction

Cement clinker processing, which accounts for 5–7% of global anthropogenic carbon dioxide emissions, is the most significant negative environmental effect of concrete [1]. Cement clinker processing, which accounts for around 5–7% of anthropogenic

D. Patel (✉) · C. D. Modhera · G. B. Jagad
Sardar Vallabhbhai National Institute of Technology, Surat, India

B. Kondraivendhan et al. (eds.), *Sustainable Building Materials and Construction*,
Lecture Notes in Civil Engineering 222,
https://doi.org/10.1007/978-981-16-8496-8_20

global CO_2 emissions, is the most significant negative environmental effect of concrete [1]. The use of GGBFS as a cement clinker substitute will boost 380 technical properties such as workability, strength, and durability [2]. GGBFS can effectively minimize pore sizes and accumulated pore volume in concrete [3]. Increased GGBFS replacement results in a denser structure, which prevents capillary water absorption in concrete. River sand is generally used in made of concrete and mortar. Due to excavation of river, high quality of river sand is not available. So, we need to go for alternative of the river sand. Various researchers are already working on the find the alternative waste materials for replace a river sand [4]. Manufactured sand is the best alternative for the river sand which is extracted artificially from quarry. Using of jaw crusher and cone crusher stone is converted into fine particles and its using in concrete as a fine aggregate.

Manufactured sand is prepared artificially, so it has very low moisture content. So, its water absorption capacity is very high than the river sand.

2 Experimental

2.1 Materials Properties

2.1.1 Cement

The cement used was OPC 53 grade, which met the specifications of IS 12269: 2013. The properties are calculated in accordance with applicable IS specifications, and the test results meet the requirements of the code.

2.1.2 Ground Granulated Blast Furnace Slag (GGBFS)

Because of its cost-effectiveness, GGBFS has been used in cement production for a long time. The addition of slag to cement improves the concrete's longevity and decreases its porosity [5]. In this experimental work, SR steel waste GGBFS is used which is processed by SUYOG agency.

2.1.3 Micro-fine (MF)

Micro-fine (ultrafine GGBFS) is actually one type of waste which is found in SR steel industries, and its particle size is very less than GGBFS. Its particle size is varying from 3 to 60 microns. Its chemical properties are shown in Table 1.

Table 1 Chemical properties of cement, GGBS, and micro-fine

Particulars	CaO	SiO_2	Al_2O_3	Fe_2O_3	MgO	Na_2O	K_2O	SO_3
Cement	63	20	6	3	1.5	0.5	0.5	2
GGBS	38.09	32.19	8.59	2.8	5.5	0.26	0.4	8.89
Micro-fine	36.7	35.1	17.58	1.62	7.75	– —	– —	0.65

2.1.4 River Sand

The fine aggregate (natural river sand) that is locally available Nareshwar sand was used in this experimental work. The grade of river sand is Zone II as per sieve analysis. Physical properties of river sand is shown in Table 2.

Table 2 Physical property of fine aggregate

Material	Fineness modulus	Specific gravity	Water absorption (%)	Bulk density loose (kg/m^3)	Bulk density rodded (kg/m^3)	Grading zone	Voids (%)	Moisture content
River sand	2.80	2.66	1.8	1.70	1.83	II	37.12	1.9
M. sand	2.90	2.54	5.54	1.71	1.84	II	32.45	0.15

2.1.5 Manufactured Sand

Manufactured sand (Zone II) is also locally available from Chikhli. The sieve analysis of fine aggregate and manufactured sand is done as per IS 2386: 1963 (Part 1). Also, Physical properties of Manufactured sand is shown in Table 2.

2.2 Methodology for Mortar Cube

Compressive strength of cement mortar for mixes was determined using 70.6 mm × 70.6 mm × 70.6 mm molds for 7 days and 28 days, with (P/4 + 3) percent water of total material weight. The mixing was performed at room temperature (27 ± 2 °C). The cement mortar cubes were made with potable/distilled water. Two minutes were spent compacting fresh cement mortar into the molds.

GGBFS and MF are partially replaced with cement in proportion of 10 to 70% and 5 to 50%, respectively, with the standard sand. Among of that, G4 (40% replacement of GGBFS) and M9 (45% replacement of MF) give good compressive strength compared to cement.

Fig. 1 Testing of mortar cube

Fig. 2 Mortar cube after 28 days of curing

So, that proportion is used to further experimental work. For a water cement ratio of 0.5, mortar cubes were cast in a 1:3 proportion. For a constant w/c ratio of 0.5, the percentage of river sand replaced by manufactured sand was 0% to 100%; at regular interval of 20% cement, mortar cube was casted and tested for compressive test at 7 and 28 days of curing period. Two sets of cubes were casted (Figs. 1 and 2).

3 Results and Discussion

Following graph shows mortar compressive strength for 7 days and 28 days of curing period. The compressive strength is increased up to 40% of replacement of GGBFS with cement. After 40%, it is decreasing gradually with increasing the percentage

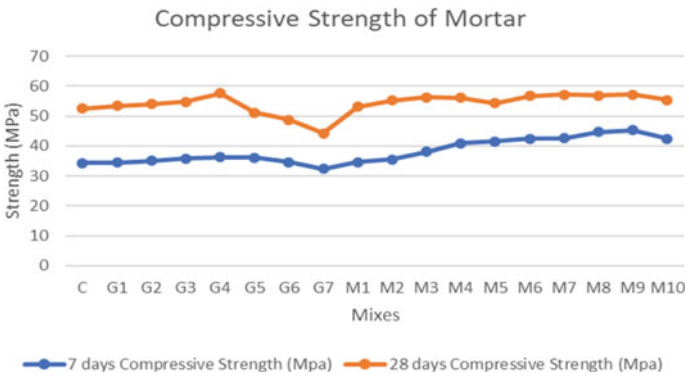

Fig. 3 Compressive of cement mortar after 7 and 28 days of curing with different proportions

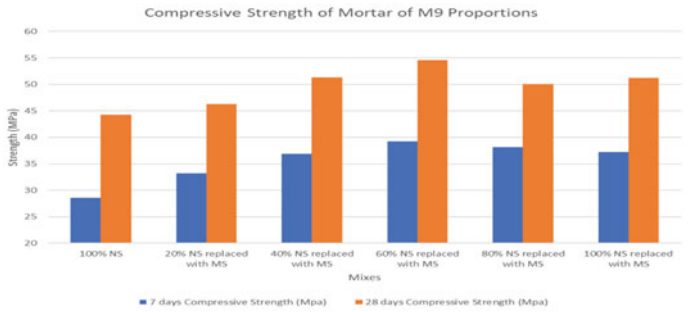

Fig. 4 Compressive strength of mortar with partial replacement of manufactured sand with M9 (45% replacement of micro-fine)

of replacement. The compressive strength is increased up to 45% of replacement of micro-fine with cement. After 45%, it is decreasing gradually with increasing the percentage of replacement. At constant w/c ratio of 0.5, compressive test result is shown in Figs. 4 and 5 with different percentage of replacement of manufactured sand with river sand. The increased compressive strength of mortar made with manufactured sand is primarily due to its improved bonding characteristics. Replacement with 60% manufactured sand achieved higher strength in both cases, but 100% replacement manufactured sand still has a stronger impact than 100% natural river sand (Fig. 3).

4 Conclusions

Consistency of cement and along with GGBFS and MF is found between 28 to 33%. Compressive strength of mortar having GGBFS and micro-fine was found

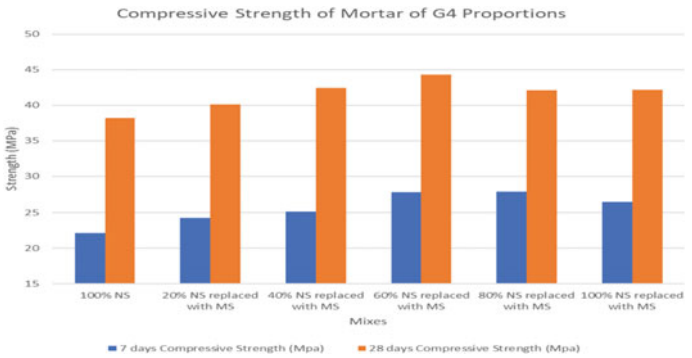

Fig. 5 Compressive strength of mortar with partial replacement of manufactured sand with G4 (40% replacement of GGBFS)

between 44.2 MPa to 57.7 MPa. The compressive strength is increased up to 40% of replacement of GGBFS with cement. After 40%, replacement of GGBFS with cement strength was gradually decreasing. Similarly, in micro-fine, it will give good strength up to 45% replacement with cement. So, the result shows that natural river sand replacement is possible in mortar with manufactured sand at any level. River sand is also eliminated by the manufactured sand in mortar. This experimental work gives that manufactured sand is the best alternative of river sand in recent days.

References

1. Schneider M, Romer M, Tschudin M, Bolio H (2011) Sustainable cement production present and future. Cem Concr Res 41:642–650. https://doi.org/10.1016/j.cemconres.2011.03.019
2. Shi C, Qian J (2000) High performance cementing materials from industrial slags a review. Resour Conserv Recycl 29:195–207. https://doi.org/10.1016/S0921-3449(99)00060-9
3. Basheer PAM, Gilleece PRV, Long AE, McCarter WJ (2002) Monitoring electrical resistance of concretes containing alternative cementitious materials to assess their resistance to chloride penetration. Cement Concr Compos 24:437–449
4. Sudarvizhi M, Ilangovan R (2011) Performance of copper slag and ferrous slag as partial replacement of sand in concrete. Int J Civil 1(4):918–927. Retrieved from http://www.indianjournals.com/ijor.aspx?target=ijor:ijcse&volume=1&issue=4&article=021
5. Al-Otaibi S (2008) Durability of concrete incorporating GGBS activated by water-glass. Constr Build Mater 22(10):2059–2067. https://doi.org/10.1016/j.conbuildmat.-2007.07.023

Parametric Experimental Studies of Mortar Incorporating Ground Granulated Blast Furnace Slag (GGBFS) and Silica Fume

Sachin S. Raval and C. D. Modhera

Abstract Because of global warming and carbon emission, sustainable development has always been in demand for many decades. Different manufacturing industries are increasingly developing sophisticated technology even while dealing with waste disposal challenges. Environmental pollution is induced by multiple sectors' waste management problems. Concrete production is made possible by replacing cement with numerous manufacturing wastes, and efforts are made to mitigate environmental emissions and waste management concepts. The use of industrial waste in concrete is now being introduced to provide the best option for the environment and the infrastructure field to produce sustainable concrete. In present study, different percentage of industrial waste like ground granulated blast furnace slag (GGBFS) and silica fume is utilized for mortar production. Physical parameters like consistency, initial and final setting time, soundness, fineness, pozzolanic strength index and compressive strength of mortar were examined. To find out optimum replacement of wastes in place of cement, 10–50% GGBFS was used along with 5–20% silica fume in mortar preparation. The outcomes of this investigation were found to be satisfactory, showing that the mortar with the appropriate waste replacement enhances physical properties.

Keywords Ground granulated blast furnace slag (GGBFS) · Silica fume · Partial replacement · Pozzolanic strength index

1 Introduction

Mineral admixture in concrete is becoming more common as a result of increased socioeconomic awareness, conservation of resources and environmental consciousness, in addition to enhanced concrete engineering and reliability. However, due

S. S. Raval (✉) · C. D. Modhera
Civil Engineering Department, SVNIT, Surat 395007, India

C. D. Modhera
e-mail: cdm@amd.svnit.ac.in

B. Kondraivendhan et al. (eds.), *Sustainable Building Materials and Construction*,
Lecture Notes in Civil Engineering 222,
https://doi.org/10.1007/978-981-16-8496-8_21

to a lack of early strength gains, use of more supplementary cementitious content in concrete is limited. Up to 80% of the cement was substituted with GGBS, and compressive strength experiments were done at the mortar stage from the first to the ninetieth day under standard water curing. The compressive strength of mortar has been observed to decrease on all days, in general, and at young ages, especially with the increased use of GGBS. Silica-rich mineral admixtures have been mixed with GGBS in cement during the mortar mix preparation to mitigate for the strength loss. The compressive strength of silica-blended mortar mixes has increased substantially over the GGBS cement mix at an early age as compared to the GGBS cement mix [1].

For decades, researchers have been working in concrete technology around the world to find substitute materials that can be used in part of ordinary Portland cement (OPC) while still meeting the industrial by-products' power and durability specifications such as micro-silica, ground granulated blast furnace slag, fly ash, metakaolin, rice husk ash. The experiment is performed in the development of ternary-blended concrete using a ternary-blended cementitious process based on ordinary Portland cement (OPC), GGBS and micro-silica. At the ages of 7, 28, 60 and 90 days, the compressive strength of ternary-blended concrete was investigated for micro-silica and GGBS blends in various combinations. Micro-silica up to 15%, as well as GGBS, was substituted with up to 50%, respectively [2].

2 Experimental Work

Ordinary Portland cement 53 grade conforming to IS 269: 2015 [3] was used during the Study. GGBFS and silica fume were procured from Stallion Energy Pvt. Ltd., Rajkot, Gujarat, India. The basic components of the OPC, GGBFS and silica fume used for this study are presented in Table 1.

Table 1 Basic component of the OPC, GGBFS and silica fume

S. No.	Basic components	OPC (%)	GGBFS (%)	Silica fume (%)
1	Silica as SiO_2	21.45	35.47	92.80
2	Aluminum oxide as Al_2O_3	4.90	14.27	0.6
3	Iron oxide as Fe_2O_3	3.46	2.41	0.3
4	Calcium oxide as CaO	62.78	35.89	–
5	Magnesium oxide as MgO	1.62	8.06	0.6
6	Sulfur trioxide as SO_3	2.32	1.58	0.1
7	Sodium oxide as Na_2+ Potassium oxide as K_2O	0.63	0.2	1.17

3 Tests for Cement

The primary objective of the consistency test is to figure out the amount of water needed to make a standard consistency cement paste, as described by IS 4031(Part 4): 1988 [4] was conducted using Vicat apparatus. Temperature for molding room was maintained 27 ± 2 °C. The laboratory's relative humidity was maintained 65 ± 5%. To prepare mix, 10%, 20%, 30%, 40% and 50% of GGBFS along with 5%, 10%, 15% and 20% of silica fume were used as partial cement replacement as shown in following Fig. 1 denoted by mixes M1 to M20, respectively. Total 21 mixes including control mix denoted by PC were prepared for present study.

The initial and final setting time of all mixes were evaluated using Vicat apparatus as specified by IS 4031(Part 5): 1988 [5] and compared to ordinary Portland cement setting time. For the setting time test, cement paste was made by adding 0.85 times the amount of water required in the cement to make a paste of standard consistency. Portable water was used in preparing the paste. Soundness of all mixes was evaluated using Le-Chatelier mold as specified by IS 4031(Part 3): 1988 [6]. For the soundness test, the cement paste was made by gaging the cement with 0.78 times the amount of water required to achieve a normal consistency paste. To evaluate fineness of all mixes, 90 μm sieve was used as specified by IS 4031(Part 1): 1988 [7].

The compressive strength of GGBS and silica fume incorporated cement mortar was investigated under normal water curing at 7 and 28 days according to IS 4031(Part 6): 1988 [8]. The standard sand used in the test was conforming to IS 650: 1966 [9]. Mortar cube with edge length 70.6 mm × 70.6 mm was used for compressive strength test. One part of cement and three part of standard sand of Grades I, II and III each was mixed together to prepare dry mix for mortar. Amount of water added to prepare mortar mix was $\left(\frac{P}{4}+3\right)$ percent of combined mass of cement and sand, where P is the water percentage needed to render a paste of standard consistency as specified in IS 4031(Part 4): 1988 [5].

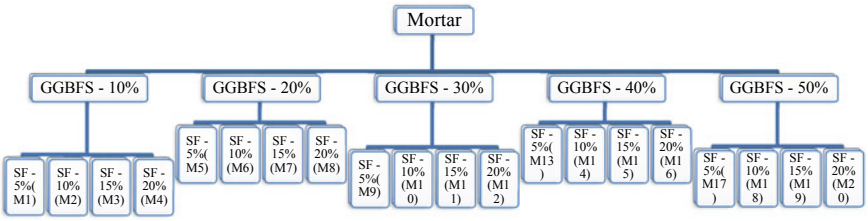

Fig. 1 Different percentage of GGBFS and silica fume used for all mixes

4 Results and Discussion

Figures 2 and 3 show results of consistency and setting time for all mixes. Result shows that consistency of all mixes was in the range of 30% to 35.9%. Initial setting time of all mixes was observed in range of 110 min to 149 min. Final setting time of all mixes in was observed in the range of 210 min to 256 min. Consistency, initial setting time and final setting time of all mixes increased as percentage of GGBFS and silica fume increased in mix as partial replacement with cement. Fineness of all mixes was observed in range of 1.10% to 2.45%. Soundness of all mixes was observed in range of 1 mm to 2 mm.

Figures 4 and 5 show results for 7 days and 28 days compressive strength of mortar respectively. As a result of the increased replacement rate of GGBFS and silica fume in cement, the compressive strength of cement mortar decreases as compared to the control mix PC. Compressive strength of 7 days mortar cubes was found in range 24.27 MPa to 45.43 MPa for all mixes. Compressive strength of 28 days mortar cubes was found in range 28.87 MPa to 64.29 MPa for all mixes.

To find out the influence of GGBFS and silica fume on the compressive strength mortar, pozzolanic strength index was evaluated for 7 days and 28 days by considering

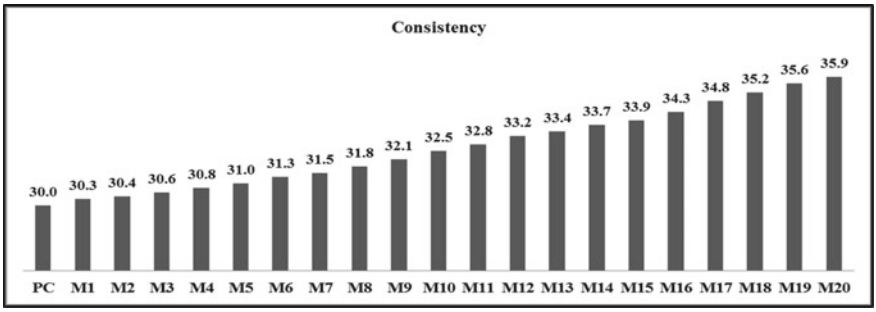

Fig. 2 Consistency for all mixes

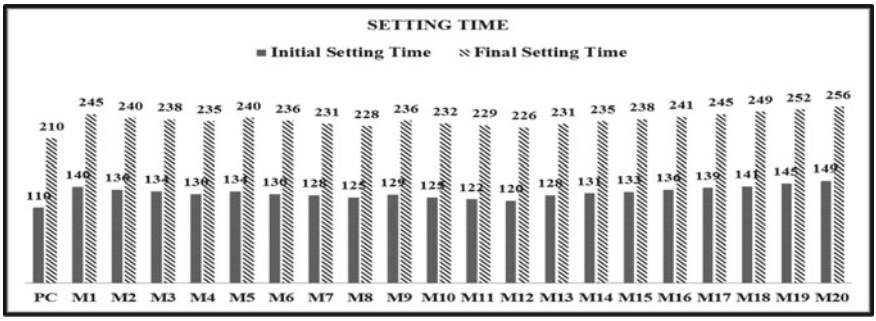

Fig. 3 Initial and final setting time for all mixes

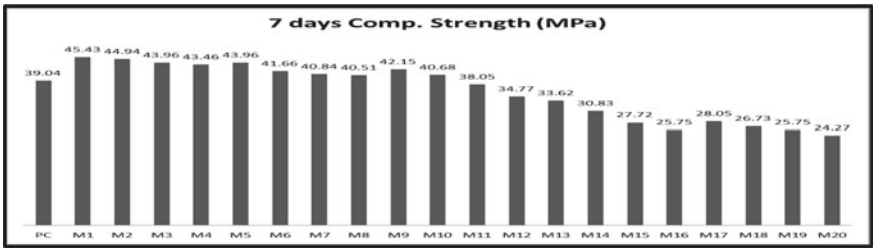

Fig. 4 Seven days compressive strength of mortar for all mixes

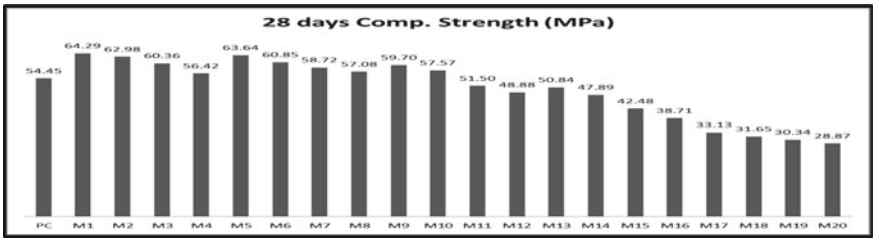

Fig. 5 Twenty-eight days compressive strength of mortar for all mixes

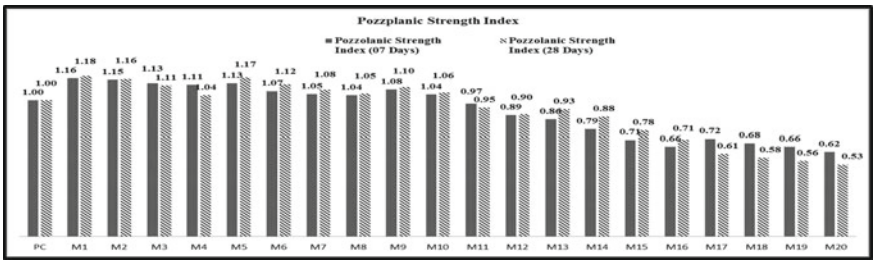

Fig. 6 Pozzolanic strength index for 07 days and 28 days mortar mixes

control mortar compressive strength as reference. Figure 6 shows pozzolanic strength index for 07 days and 28 days for mortar. Pozzolanic strength index of 7 days mortar cubes was found in range 0.62 to 1.16 for all mixes. Pozzolanic strength index of 28 days mortar cubes was found in range 0.53 to 1.18 for all mixes.

5 Conclusion

The following conclusions are drawn based on the experimental findings:

1. With the addition of GGBFS and silica fume, the cement's consistency and setting time (both initial and final) are improved. Water demands of blended cements were found higher than that of control cement paste. The increase in initial and final setting time of GGFBS and silica fume incorporated cement paste was higher than setting time of control cement paste. It indicates that the addition of GGFBS and silica fume retards the initial hydration of cements. The results of fineness and soundness of all mixes incorporated with GGBFS and silica fume satisfy codal provision.
2. Compressive strength of mortar mix M9 with 30% of GGBFS and 5% of silica fume as partial replacement of cement in mortar was found maximum as compared to control mix PC. After M9 mix, compressive strength of mortar decreased as combined percentage of GGBFS and silica fume increased in mortar.
3. Pozzolanic strength index of M9 mortar mix for 7 days and 28 days curing found 1.08 and 1.10, respectively, which indicates 8% and 10% growth in compressive strength of M9 mix compared to control mix PC.
4. By supplementing industrial waste for cement, carbon emission in the atmosphere caused by cement manufacturing can be reduced to some extent, making the environment more sustainable.

References

1. Mapa M, A R C M (2015) Investigation on Mechanical properties of silica and GGBS incorporated cement mortar, pp 30–34
2. Reddy SVB (2016) Influence of micro silica and GGBS on compressive strength of ternary blended concrete 5(03):688–695
3. IS 269-2015, Ordinary Portland cement specification. Bureau of Indian Standards, New Delhi. pp 1–10
4. IS 4031- Part 5 (1988) Methods of physical tests for hydraulic cement Part V- Determination of initial and final setting times. Bureau of Indian Standards, New Delhi, Reaffirmed in 2005.pp 1–3
5. IS 4031- Part 4 (1988) Methods of physical tests for hydraulic cement Part IV—determination of consistency of standard cement paste. Bureau of Indian Standards, New Delhi. pp 1–4
6. IS 4031-3 (1988) (Reaffirmed 2005) Methods of physical tests for hydraulic cement, part 3: determination of soundness. Bureau of Indian Standards, New Delhi, pp 1–10
7. IS 4031- Part 1 (1996) Method of physical tests for hydraulic cement: Determination of fineness by dry sieving. Bureau of Indian Standards, New Delhi, p. Reaffirmed in 2005. pp 1–5
8. IS: 4031- Part 6 (1988) Methods of physical tests for hydraulic cement part 6 determination of compressive strength of hydraulic cement other than masonry cement (First Revision). Bureau of Indian Standards, New Delhi, pp 1–3
9. IS 650:1991, Specification for standard sand for testing of cement. Indian Standards, pp 1–11

Study on Time—Viscosity Characteristics of Cement—Zeolite Grouts

Nazimali Chinwala, C. H. Solanki, S. R. Gandhi, N. H. Joshi, and A. V. Shroff

Abstract In the present study, zeolite was used to partially replace ordinary Portland cement at 10, 20, 40 and 60% by weight. Water to cementitious material ratio (w/c) was taken as 1 and 5 for preparing the grout. The results indicate that apparent viscosity, plastic viscosity and yield stress remains low up to limiting injection time and thereafter it increases rapidly reaching to gel time. For w/c 1 at 10% zeolite replacement minimum viscosity is observed and for w/c 5 at 40% zeolite replacement minimum viscosity is observed.

Keywords Ordinary Portland cement · Zeolite · Apparent viscosity · Plastic viscosity · Yield stress

1 Introduction

The rheological properties of grout are important in many applications including ground treatment, filling of cracks in concrete, reducing the permeability of soil/rocks, etc. The pumpability and ability of grout to penetrate inside voids are dependent on the rheological properties of grout in particular yield stress and viscosity [3]. The production of Portland cement contributes to about 10% of world carbon dioxide emission. There are many ongoing researches which are targeting a suitable replacement of Portland cement by supplementary cementitious materials in order to save the environment. Zeolites are hydrated aluminosilicate minerals made from interlinked tetrahedral of alumina (AlO_4) and silica (SiO_4) [6]. They have unique characteristics such as high specific surface area and cation exchange capacity as well

N. Chinwala (✉) · C. H. Solanki · S. R. Gandhi · N. H. Joshi · A. V. Shroff
Department of Civil Engineering, Sardar Vallabhbhai National Institute of Technology, Surat, Gujarat, India

C. H. Solanki
e-mail: chs@amd.svnit.ac.in

N. H. Joshi
e-mail: nhjoshi-appmech@msubaroda.ac.in

B. Kondraivendhan et al. (eds.), *Sustainable Building Materials and Construction*, Lecture Notes in Civil Engineering 222,
https://doi.org/10.1007/978-981-16-8496-8_22

Table 1 Chemical analysis of ordinary Portland cement

Loss of ignition (%)	3.15
Insoluble residue (%)	2.22
SO_3 (%)	2.55
MgO (%)	0.92
Total Alkalies as Na_2O (%)	0.53
Chloride (%)	0.035
Performance improver (Lime Stone) by (%)	1.38

as ability to store heat between hydration and dehydration cycles [2]. Zeolite is rich in reactive SiO_2 and Al_2O_3, and its substitution can improve the strength of concrete by pozzolanic reaction with $Ca(OH)_2$ [1]. Natural zeolite also prevents the undesirable expansion due to alkali aggregate reaction and sulphate attack [3]. Şahmaran [4, 5] through their study concluded that addition of natural zeolite modifies both the rheological and workability properties of grouts. The experimental studies indicated that the rheological properties of cement-based grouts were significantly affected by the replacement rate and fineness of natural zeolite [4, 5].

However, to the best knowledge of the authors, there is no systematic study about the rheological properties of grouts containing natural zeolites in India. Hence, it is important to quantify the effects of natural zeolite on the grout behaviour. For this reason, the main objective of this article is to assess the potential usage of natural zeolite in grouts and evaluate its effects on the rheological properties of grouts.

2 Methodology

2.1 Materials

2.1.1 Ordinary Portland Cement

Ordinary Portland cement of 53 grade was procured from Local Vendor of J. K Super Cement Ltd. The chemical composition as provided by the manufacturer are shown in Table 1.

2.1.2 Zeolite

Zeolite was procured from Local Vendor Nikunj Chemicals Pvt. Ltd. Vadodara. The chemical composition as provided by the manufacturer are shown in Table 2.

Table 2 Physical and chemical analysis of zeolite

SiO_2	52% Min
Al_2O_3	30–40%
Fe_2O_3	0.6% Min
TiO_2	0.65% Min
CaO	0.09% Min
MgO	0.03% Min
Na_2O	0.1% Min
K_2O	0.03% Min

2.2 Time—Viscosity Properties of Grout

2.2.1 Fluidity Test

Fluidity is a measure of ease of pumpability of a grout when it contains sufficient fluid to prevent dilation of the particle matrix during shear while injecting. For cement and cement bentonite grout, fluidity is measured by marsh cone test. In marsh cone test about 2000 cc of grout is to be poured in the marsh cone and time of afflux is noted to pour 1000 cc of grout in measuring cylinder.

2.2.2 Viscosity Test

Viscosity is the essential parameter for defining a grout since it determines the grout's ability to penetrate a given permeable porous medium. The viscosity of a grout in the present study is measured using Brookfield viscometer of rotational variety (RVT model). For calculating the yield stress of the grout Bingham model was used.

3 Results and Discussion

3.1 Time—Viscosity Properties of Grout

3.1.1 Fluidity Test

Figure 1 shows the time of afflux for grout at different zeolite % for w/c ratio 1 and 5.

3.1.2 Viscosity Test

Figures 2 and 3 shows apparent viscosity v/s time curves, Figs. 4 and 5 shows yield stress v/s time curves and Figs. 6 and 7 shows plastic viscosity v/s time curves.

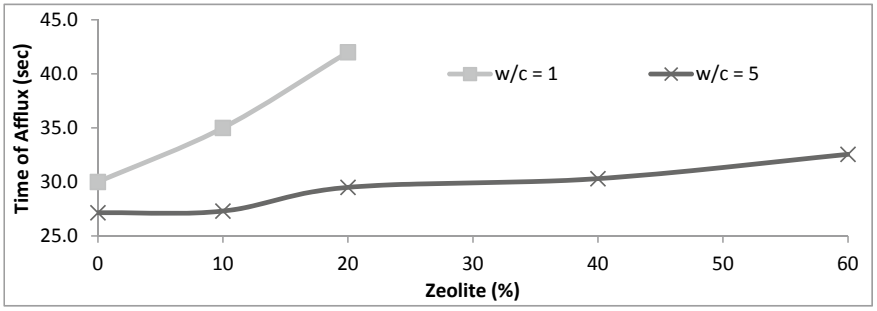

Fig. 1 Time of Afflux for grout at different zeolite % for w/c ratio 1 and 5

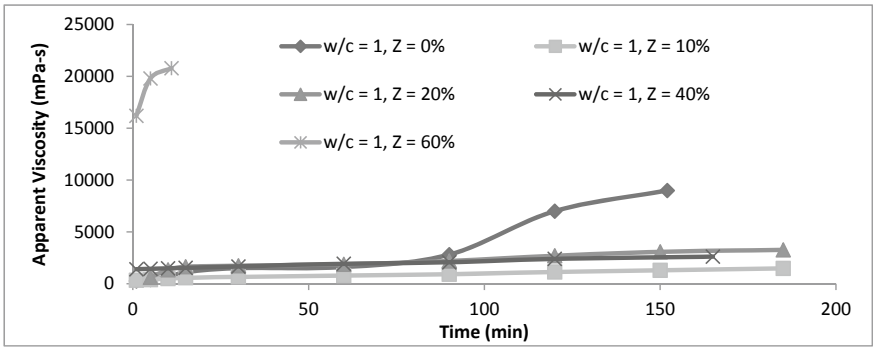

Fig. 2 Apparent viscosity versus time for grout at different zeolite % for w/c ratio 1

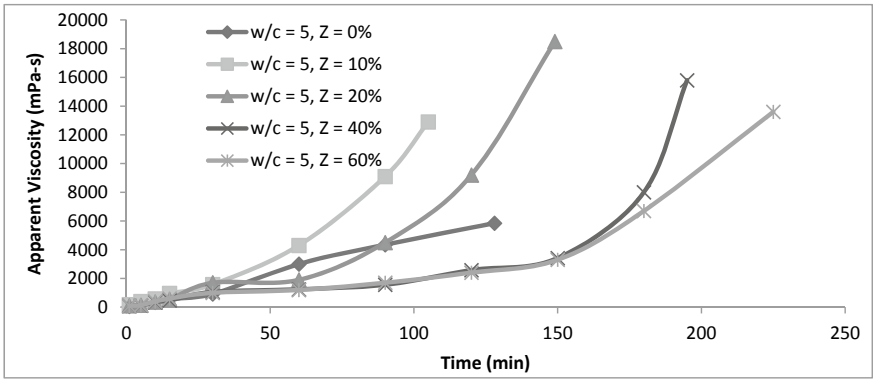

Fig. 3 Apparent viscosity versus time for grout at different zeolite % for w/c ratio 5

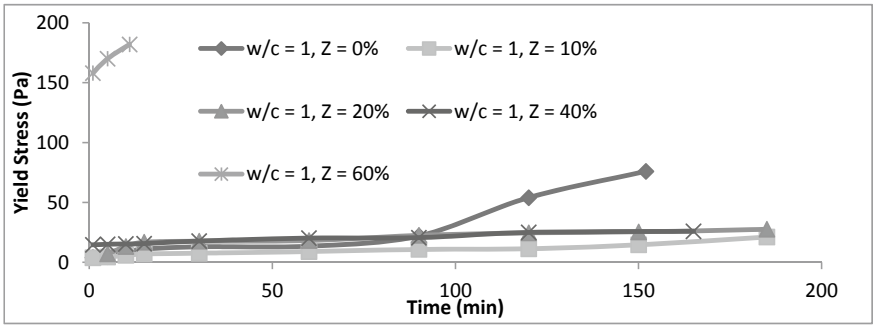

Fig. 4 Yield stress versus time for grout at different zeolite % for w/c ratio 1

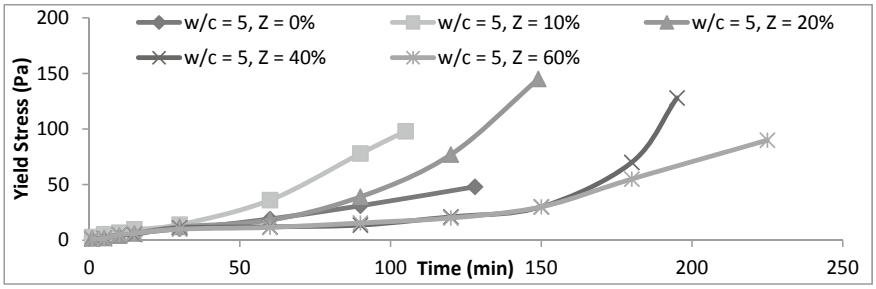

Fig. 5 Yield stress versus time for grout at different zeolite % for w/c ratio 5

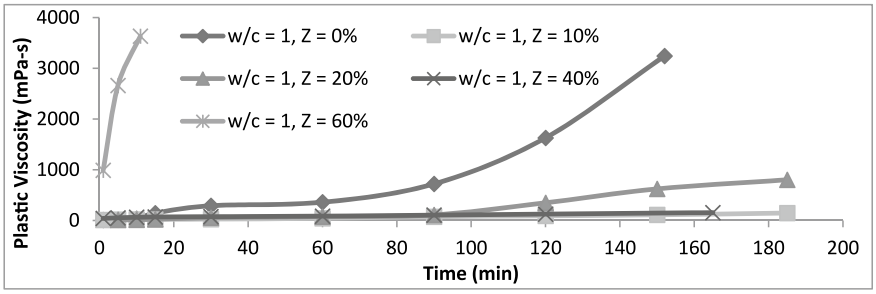

Fig. 6 Plastic viscosity versus time for grout at different zeolite % for w/c ratio 1

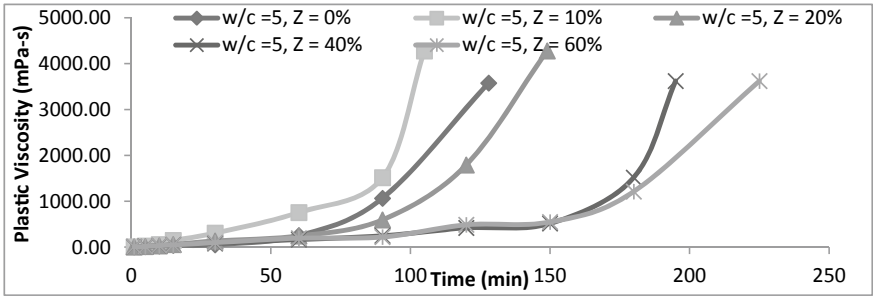

Fig. 7 Plastic viscosity versus time for grout at different zeolite % for w/c ratio 5

4 Conclusions

Following are some research findings from the above study.

- With increase in w/c ratio time of afflux decreases and addition zeolite from 10 to 60% time of afflux increases.
- Based on the time—yield stress, time—apparent viscosity and time—plastic viscosity curves it has been observed that viscosity and yield stress remains low up to limiting injection time and thereafter it increases rapidly reaching to geltime. The increased pseudo-plasticity response in the presence of zeolite may be due to the high water retention capacity of zeolite, which increases the agglomeration of particles.
- For w/c ratio 1 and 5, based on the curves it can be seen that at replacement of Z = 10% & Z = 40%, respectively, we get minimum value of viscosity.

References

1. Canpolat F et al (2004) Use of zeolite, coal bottom ash and fly ash as replacement materials in cement production. Cem Concr Res 34(5):731–735. https://doi.org/10.1016/S0008-8846(03)00063-2
2. Colella C, De Gennaro M, Aiello R (2001) Use of zeolitic tuff in the building industry. Rev Mineral Geochem 45(1996):551–587. https://doi.org/10.2138/rmg.2001.45.16
3. Ferraris CF, de Larrard F (1998) Testing and modelling of fresh concrete rheology, p 61
4. Şahmaran M et al (2008) Evaluation of natural zeolite as a viscosity-modifying agent for cement-based grouts. Cem Concr Res 38(7):930–937. https://doi.org/10.1016/j.cemconres.2008.03.007
5. Şahmaran M (2008) The effect of replacement rate and fineness of natural zeolite on the rheological properties of cement-based grouts. Can J Civ Eng 35(8):796–806. https://doi.org/10.1139/L08-039
6. Tsitsishvili GV (1992) Natural Zeolites, p 1976

Experimental Study on the Stress–Strain Behavior of Partially and Fully Wrapped Axially Loaded Square RC Columns Strengthened with BFRP

Tejash K. Patel, Sanjay R. Salla, S. A. Vasanwala, and Darshan Patel

Abstract This current research scenario focuses on strengthening and rehabilitation of RC columns by CFRP and GFRP. The ongoing study reveals a new class of natural composites made of basalt fiber reinforced polymer (BFRP) bonded to concrete specimens with epoxy resin as an alternative confinement material. The experimental study was conducted for strengthening by partially and fully wrapped square RC columns using BFRP unidirectional and bidirectional. The behavior of stress-strain curves and failure modes was observed. The experimental results show a substantial increment in the ultimate load-displacement capacity and ultimate stress-ultimate axial and lateral strains of BFRP failure. The fully wrapped square reinforced concrete (RC) column gives a better stress-strain behavior and displacement limit than the partially covered system. However, the strengthening with partial wrapped with BFRP is a promising and economical alternative compared to the fully wrapped. The test results exhibit that the CNR-DT-R1 model is more reliable compare to the Lam-Teng model.

Keywords Reinforced concrete · RC column · CFRP and GFRP · Wrapping

1 Introduction

The utilization of FRP is very convenient for the strengthening of the structural member. FRP material has excellent properties, strength, less stiffness, cost-effectiveness, ductility, and corrosion resistance. The use of FRP enhanced the compressive strength and ductility of the RC columns [6, 7, 11, 12]. Extensive experimental studies demonstrated the strengthened RC column specimens' load-displacement capacity to the best of the author's knowledge. It is governed by the significant, influential parameters, including the compressive strength, cross-section area, aspect ratio of the column specimens, different radius, the number of wrap layers, fiber alignment, longitudinal steel reinforcement ratio and orientation, and

T. K. Patel (✉) · S. R. Salla · S. A. Vasanwala · D. Patel
Civil Engineering Department, SVNIT, Surat 395007, India

B. Kondraivendhan et al. (eds.), *Sustainable Building Materials and Construction*,
Lecture Notes in Civil Engineering 222,
https://doi.org/10.1007/978-981-16-8496-8_23

the type of loading [5, 9, 14]. Saljoughian and Mostofinejad found that the corner radius of specimens investigated was 8 mm, significantly less than the indicated corner radius of 13 mm in ACI 440.2R-08 and 20 mm in FIB bulletin 14. [1, 13]. Basalt fibers were recently also used by melting basalt rock, and basalt fibers are later obtained by spinning the molten substance. In particular, the new manufacturing technologies for continuous BFRP are very similar to those used for GFRP production. The key difference is that GFRP is made of a diverse set of materials. At the same time, basalt filament is made without any other compounds from basalt melting minerals and hence has a cost advantage. In this, lower energy is essential due to the easiness of the industrial process [4]. This research explores the axial stress-strain behavior of square RC columns by applying fully and partially BFRP strengthened techniques. Various results were obtained, such as ultimate load, displacements, and axial stress in the concrete, whereas ultimate lateral strain in FRP wrapping.

Additionally, the study has tried to verify experimental data's reliability and accuracy with the theoretical models such as CNR-DT R1 and Lam and Teng [3, 10].

2 Experimental Program

In this present study, the effect of partial strengthened and fully strengthened of an axially loaded short RC column by using BFRP material with unidirectional and bidirectional wrapping, respectively, was evaluated. All square RC columns were designed based on IS-456-2000 [8]. The square column cross-section dimensions were 170 mm × 170 mm and height of 700 mm, as shown in Fig. 1. The different strengthened columns (B1X, B2X, B1Y, B2Y, B1Z, and B2Z) were prepared and the non-strengthened column (S1). B shows basalt fiber, 1 shows unidirectional wrapping, 2 for bidirectional wrapping, X for top strengthened, Y shows top-bottom strengthened, and Z shows fully strengthened.

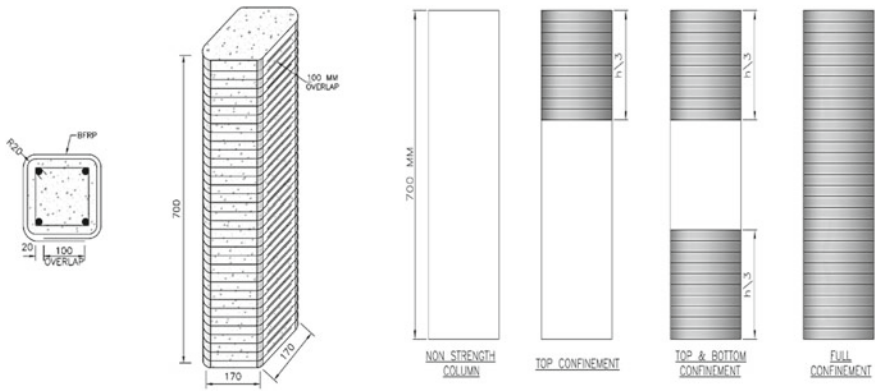

Fig. 1 Details of strengthing of columns

Table 1 Different property of BFRP and resin

FRP wraps	BFRP unidirectional	BFRP bidirectional	Resin
Thickness (mm)	0.115	0.32	–
Tensile strength (MPa)	2100	1950	30
E-modulus (GPa)	105	93	4500
Elongation (%)	2.6	2.3	1.5

This study was based on the Fe-500 grade locally accessible reinforcement bars. The maximum tensile strength of 12 and 8 mm bar was measured, respectively, with 587 MPa and 576 MPa. As per IS 1786: 2008, respectively, the percentage elongation was 21.66 and 29.25%. The concrete grade was M25, prepared according to IS 10262: 2009, and was a mixture of (1:1.90:3) and concrete. The properties of BFRP wraps, the flat coupon tensile test have been carried out. The BFRP materials test procedure was followed by the recommendations specified in the ASTM—D 3039: 2008 [2]. The elastic modulus of the tensile strength and the mean values of the rupture stress were determined, as shown in Table 1. The RC column specimens strengthened were carried out as per ACI 440.2R-2008 [1]. The strain gauges are placed on the column's surface to measure strains in the longitudinal and transverse directions, as shown in Fig. 2. All data for load, displacement, and strain measurements of concrete and FRP material were obtained by the data acquisition system (DAQ).

3 Results and Discussion

3.1 Load-displacement

The ultimate load-carrying capacity and displacement capacity of top strengthened BFRP unidirectional are more comparable to top strengthen BFRP bidirectional and non- strengthened columns in this experimental work. It was also found that the B1X gives more axial load-carrying capacity compared to B2X and S1, as shown in Fig. 3a. Similarly, in top-bottom strengthen, square RC columns B1Y and B2Y give more control on axial displacement to axial load-carrying capacity in BFRP unidirectional and BFRP bidirectional. Moreover, it was observed that the B1Y column initially load-carrying less compare to S1 and B2Y columns, as shown in Fig. 3b. Figure 3c shows that the square RC column's full wrapping increased the ultimate load-carrying capacity and displacement capacity compared to the non-strengthened column (S1). It was also observed that the B1Z and B2Z column ultimate load-carrying capacity and displacement capacity performance almost similar.

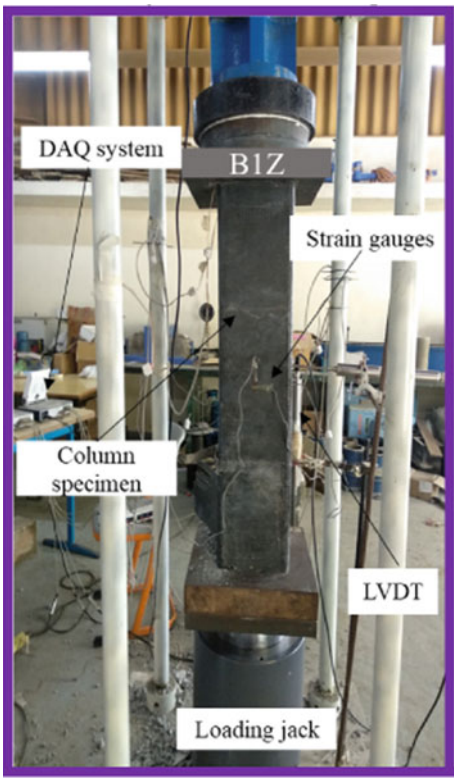

Fig. 2 Test setup

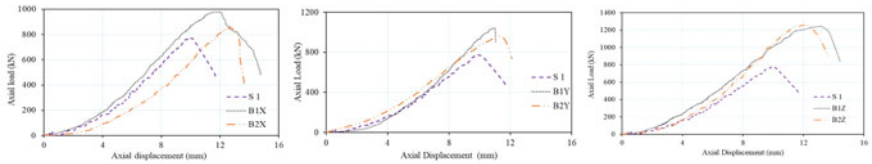

(a) Top (b) Top - Bottom (c) Full

Fig. 3 Axial load-displacement

3.2 Axial Stress-Strain Behavior

The stress-strain response of three groups of the RC column (top, top-bottom, and full strengthened), including the non-strengthened column, is presented in Fig. 4. The strain gauge on concrete was placed in the column specimen's mid-height, whereas the strain gauge on FRP wrapping was placed at the wrapping's mid-height. The concrete axial strain was considered positive, and the lateral strain of FRP wrapping was considered negative. The better stress-strain performance of BFRP wrapping is observed in Fig. 4a compared to the non-strengthened column specimen. The ultimate

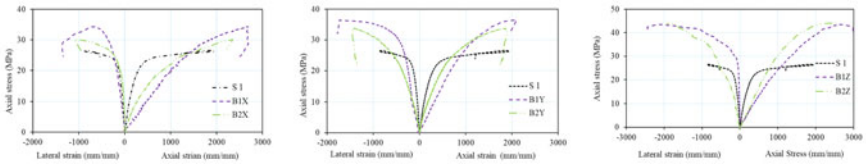

(a) Top (b) Top-Bottom (c) Full

Fig. 4 Axial stress-strain behavior

strain in the B1X and B2X column specimens was observed slightly higher than axial strain and lateral strains compared to the S1. It was also noted that the B1X in lateral strain had declined gradually, and B2X in lateral strain gas suddenly declined. The square RC columns top-bottom strengthened by BFRP uni and bidirectional show close to behavior against the axial and lateral strains in the elastic stage like the top strengthen column as shown in Fig. 4b.

The B1Y shows better performance than B2Y because BFRP bidirectional wrapping material was deboned with the column surface. The stress-strain behavior on BFRP wrapping in full strengthened column specimen was observed the most as concrete strain behavior shown in Fig. 4c. It is because of full FRP confinement on the concrete surface.

3.3 Comparison of Experimental Stress with a Different Model

The design of partially and fully FRP-confined RC column has been given in the CNR-DT 200 R1 [3], or some researchers had to use the theoretical model of Lam and Teng [10]. The experimental data were compared with the above two models to check the precision and reliability. The test results exhibit that the CNR-DT-R1 model is more reliable than Lam and Tang and provides reasonable and accurate predictions for the ultimate axial stress of partially and fully wrapped RC columns, as shown in Fig. 5.

3.4 Failure Mode

The non-strengthened and strengthened RC square column elements were tested until they arrive at their ultimate load. In the non-strengthened RC column specimens, vertical line-like cracks appear from the middle part to the top part of the square column, as shown in Fig. 6. The first crack was observed at around 45–55% of the ultimate load, at 70–80% of peak load.

Figure 7a shows the top strengthened RC column element's failure due to BFRP wrap rupture with severe core degradation in B2X. At the bottom corner of the

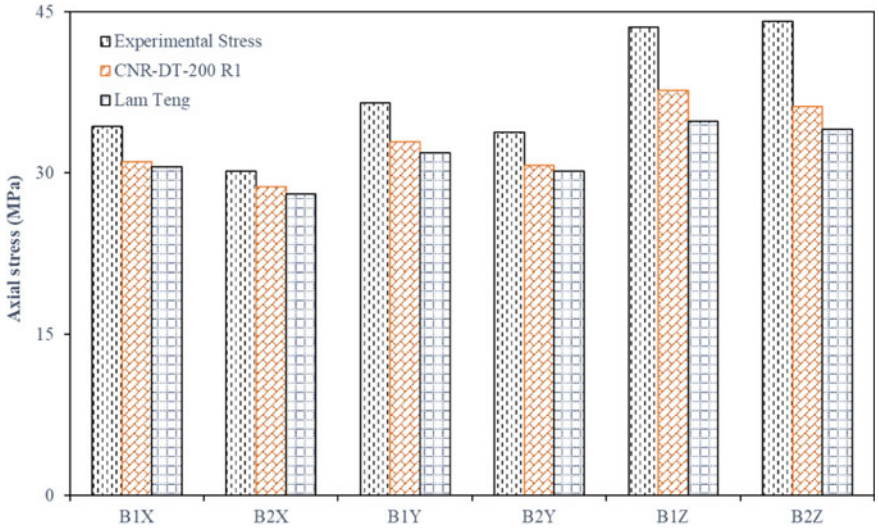

Fig. 5 Comparisons of axial stress for strengthened columns

Fig. 6 Failure of non-strengthened RC column elements

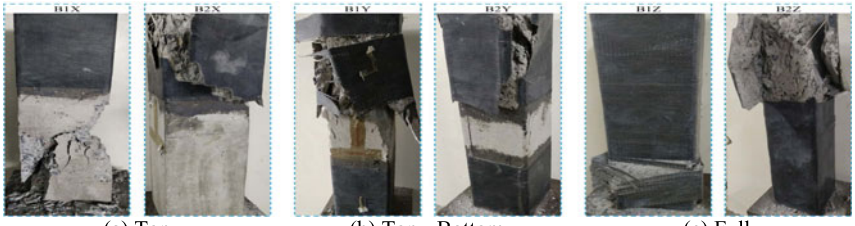

(a) Top (b) Top - Bottom (c) Full

Fig. 7 Failure of strengthened RC column elements

specimen, the cracking of the un-wrapped concrete cover originated and later spread over the specimen's entire circumference, as shown in B1X.

The specimens B1Yand B2Y were cracked internally at the yield axial load with snapping sounding. The top-bottom FRP confinement failure occurred due to the crushing of the concrete cover. An explosive sound was experienced during the failure of the specimen.

Failure of the fully confined RC column element occurred due to the crushing of concrete cover and rupture of BFRP wrap at the bottom side in B1Z and topside in B2Z, and the opposite of the overlap wrap zone shows in Fig. 7c. During the testing time of all full confined RC column crushed concrete after gradual failure at a bottom side in B1Z and topside in B2Z.

4 Conclusion

Based on the experimental results, the following conclusions are drawn:

1. The ultimate load-carrying capacity and displacement capacity of top strengthened BFRP unidirectional are more comparable to top strengthen BFRP bidirectional and non-strengthen columns.
2. The fully strengthened RC column gives more load-carrying capacity than partially top strengthened or top-bottom strengthened RC column. In addition to this, no more change in load-carrying capacity either uses unidirectional or bidirectional in fully strengthened RC column.
3. The fully strengthened RC column gives less ultimate displacement than partially top strengthened or top-bottom strengthened RC column. In addition to this, unidirectional has less ultimate displacement than or bidirectional in fully strengthened RC column.
4. The ability to carry the ultimate stress-strains behavior is more in BFRP unidirectional strengthened than bidirectional strengthened.

Thus, The BFRP unidirectional material shows better performance in all wrapping systems, and the experimental data were compared with CNR-DT-R1 and Lam-Teng models to check the precision and reliability. The test results exhibit that the CNR-DT-R1 model is more reliable than Lam-Teng.

References

1. 440, A. C. (2008) Guide for the design and construction of externally bonded FRP systems for strengthening concrete structures (ACI 440.2R-02), ACI 440.2R-08. https://doi.org/10.1061/40753(171)159
2. ASTM (2014) Astm D3039/D3039M, Annual Book of ASTM Standards, pp 1–13. https://doi.org/10.1520/D3039

3. CNR-DT 200 R1/2013 (2013) Guide for the design and construction of externally bonded FRP systems for strengthening existing structures, p 144
4. Fiore V, Di Bella G, Valenza A (2011) Glass-basalt/epoxy hybrid composites for marine applications. Mater Des 32(4):2091–2099. https://doi.org/10.1016/j.matdes.2010.11.043
5. Galal K, Arafa A, Ghobarah A (2005) Retrofit of RC square short columns. Eng Struct 27(5):801–813. https://doi.org/10.1016/j.engstruct.2005.01.003
6. Hadi MNS (2006) Comparative study of eccentrically loaded FRP wrapped columns. Compos Struct 74(2):127–135. https://doi.org/10.1016/j.compstruct.2005.03.013
7. Hadi MNS (2007) Behaviour of FRP strengthened concrete columns under eccentric compression loading. Compos Struct 77(1):92–96. https://doi.org/10.1016/j.compstruct.2005.06.007
8. IS 456 (2000) Concrete, plain and reinforced. Bureau of Indian Standards, New Dehli, pp 1–114
9. Karam G, Tabbara M (2005) Confinement effectiveness in rectangular concrete columns with fiber reinforced polymer wraps. J Compos Constr 9(5):388–396. https://doi.org/10.1061/(asce)1090-0268(2005)9:5(388)
10. Lam L, Teng JG (2003) Design-oriented stress-strain model for FRP-confined concrete. Constr Build Mater 17(6–7):471–489. https://doi.org/10.1016/S0950-0618(03)00045-X
11. Marques PF, Chastre C (2012) Performance analysis of load-strain models for circular columns confined with FRP composites. Compos Struct 94(11):3115–3131. https://doi.org/10.1016/j.compstruct.2012.04.036
12. Rocca S, Galati N, Nanni A (2009) Interaction diagram methodology for design of FRP-confined reinforced concrete columns. Constr Build Mater 23(4):1508–1520. https://doi.org/10.1016/j.conbuildmat.2008.06.010
13. Saljoughian A, Mostofinejad D (2016) Axial-flexural interaction in square RC columns confined by intermittent CFRP wraps. Compos B Eng 89:85–95. https://doi.org/10.1016/j.compositesb.2015.10.047
14. Wang YC, Hsu K (2008) Design of FRP-wrapped reinforced concrete columns for enhancing axial load carrying capacity. Compos Struct 82(1):132–139

Experimental Study on the Stress-Strain Behavior of Partially and Fully Wrapped Axially Loaded Square RC Columns Strengthened with GFRP

Tejash K. Patel, Sanjay R. Salla, S. A. Vasanwala, and Purvesh Patel

Abstract It is well recognized that the containment mechanism for reinforced concrete columns using glass fiber wraps is an economical solution for work rehabilitation and strengthening. This study aims to examine the partially and fully wrapped square RC columns strengthened by GFRP. The axial load-displacement, axial stress, axial and lateral strain behavior, and failure modes were observed. The experimental results show a substantial increment in ultimate load-displacement capacity and ultimate stress-ultimate axial and lateral strains of GFRP failure. The increase in load-carrying and displacement control capacity and stress-behavior was higher in the fully wrapped columns than in the partially wrapped columns. However, the strengthening with partial wrapped GFRP is a promising and economical alternative compared to the fully wrapped. The test results exhibit that the CNR-DT-R1 model is more reliable compare to the Lam-teng model.

Keywords Fiber-reinforced polymers · Reinforced concrete · RC column

1 Introduction

Fiber-reinforced polymers (FRPs) have evolved over the last several decades as effective materials for reinforcing damaged structural components. The FRP has been widely used to contribute to engineering qualities, including high tensile strength and rigidity, high strength-to-weight ratio, and high corrosion resistance [4, 5, 10, 13]. The lateral expansion of concrete is prevented by the transverse wrapping of concrete columns with FRP, leading to significant improvements in the strength and ductility of the columns [4, 7, 11]. The performance of fully FRP wrapped columns was investigated by most available research studies [3, 9, 12]. The experimental study of partially and fully strengthened systems can enhance the axial load-carrying capability and deformation performance and the axial stress-strain behavior of RC

T. K. Patel (✉) · S. R. Salla · S. A. Vasanwala · P. Patel
Civil Engineering Department, SVNIT, Surat 395007, India

B. Kondraivendhan et al. (eds.), *Sustainable Building Materials and Construction*,
Lecture Notes in Civil Engineering 222,
https://doi.org/10.1007/978-981-16-8496-8_24

columns of square cross sections. The technique's efficiency is compared to traditional C techniques that use GFRP wet layup wraps to confine the columns full or partial. Additionally, the study has tried to verify experimental data's reliability and accuracy with the theoretical models such as CNR-DT R1 and Lam and Teng [3, 8].

2 Experimental Program

The experimental study was designed to test the effects of partially and entirely strengthened square reinforced concrete column approaches. All columns had a height of 700 mm and a cross Sect. 170 mm × 170 mm as per IS 456: 2000, as shown in Fig. 1. The strengthened columns (G1X, G2X, G1Y, G2Y, G1Z, and G2Z) were prepared and the non-strengthened column (S1). G shows glass fiber, (1) shows unidirectional wrapping, (2) for bidirectional wrapping, X for top strengthened, Y shows top-bottom strengthened, and Z shows full strengthened.

2.1 Experimental Material

The Fe-500 grade of locally available reinforcement bars was used in this analysis. At 587 MPa and 576 MPa, respectively, the maximum tensile strength of 12 mm and 8 mm bars has been reached. As per IS 1786: 2008 [6], the measurement elongation was 22.06% and 30.25%, respectively. For the experimental work, the concrete grade of M25 was designed by IS 10262: 2009 [2], with the concrete design mix (1:1.88:3). The RC column specimens' strength was carried out as per ACI 440.2R-2008 [1]. At a radius of 20 mm, a smooth curvature at the corner of square columns

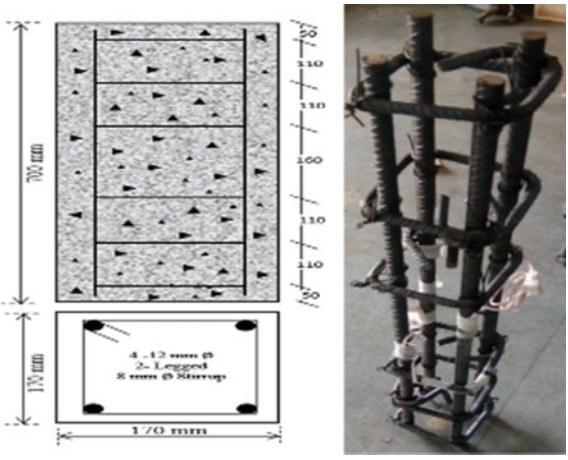

Fig. 1 Reinforcement detail of column

was provided to increase overall column confinement. To strengthen the column, the wet layup technique was implemented. Before placing the GFRP wraps, the surface of the specimen is impregnated with epoxy resin to adhere the GFRP wraps to the specimens. The unidirectional GFRP wraps were situated in the transverse direction, and bidirectional GFRP wraps were situated in the longitudinal and transverse directions. The specimens strengthened with one layer were enclosed with a 100 mm overlap based on ACI 440-2R-08.

2.2 Experimental Methodology

The column specimen was placed centrally on the floor of a loading frame with a capacity of 2500 kN. The specimens were put through their paces under a steadily increasing compressive load. A load cell at the top of the specimen was used to record the load. To evaluate the linear displacements, 100 mm gauge length LVDTs were held directly on the base plate ends of the specimen. The strain gauge was installed on column surface and FRP material mid-height at linear and lateral directions. The steel in strain gauges was placed on one in longitudinal and two on top and bottom stirrups. All the strain gauges, LVDT, and load cells were connected to the data acquisition system (DAQ) to get the reading during the testing. Before conducting the test, Fig. 2 illustrates the specimen under the compression testing machine.

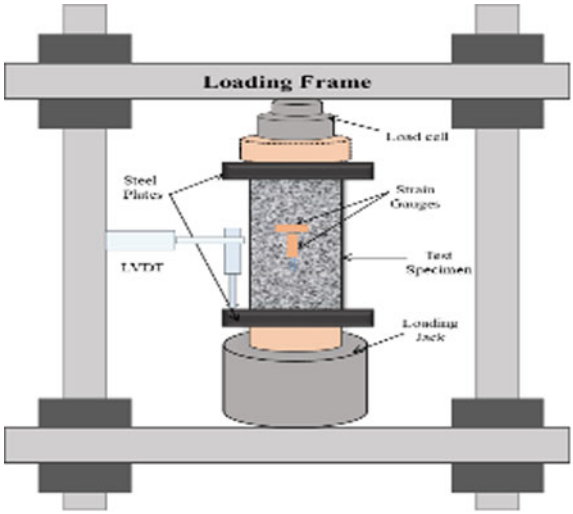

Fig. 2 Test setup and instruments

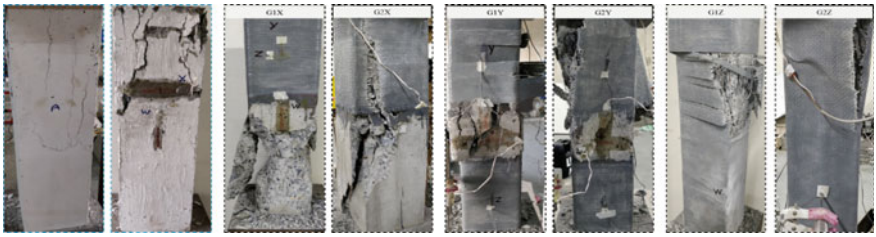

a) non-strengthened b) Top c) Top - Bottom d) Full

Fig. 3 Failure of RC column elements

3 Results and Discussion

3.1 Failure Mode

The non-strengthened RC columns were typically initially found to have cracks in the corner areas, usually as shown in Fig. 3a, and all sides of the column of the crushing failure at ultimate load from the top to the middle part. The failure of the top (h/3) strengthened RC column element occurred due to the rupture of FRP wrap with severe core degradation. At the bottom corner of the specimen, the cracking of the un-wrapped concrete cover originated and later spread over the entire circumference of the specimen. Subsequently, the small part (fibers) of G2X wraps at the end of the specimens was ruptured, as shown in Fig. 3b. The specimens G1Y and G2Y were cracked internally at the yield axial load with snapping sounding. An explosive sound was experienced during the failure of the specimen. Under the higher load, the concrete crack extended at mid-height to top and ultimately crushed in the GFRP wraps' ruptures at a top side as shown in Fig. 3c. Failure of the full confined RC column element occurred due to the crushing of concrete cover and rupture of FRP wrap at the top side and opposite of the overlap wrap zone shows in Fig. 3d. The failure of the specimens begins with a snap noise. The cracking of the concrete during test time was seen by visual inspection.

3.2 Ultimate Load-displacement

It can be observed from Fig. 4 that the ultimate displacement capacity of partially (G1X, G2X, G1Y, and G2Y) and fully (G1Z and G2Z) strengthened column is greater than the non-strengthened column. The axial displacement control of RC columns reinforced by GFRP bidirectional is larger than RC columns reinforced by GFRP unidirectional in this study. Moreover, it was noticed that the axial displacement control partially strengthened that the G1Y and G2Y are more than G1X and G2X. The G1Z exhibits the highest axial displacement at failure under the strengthened

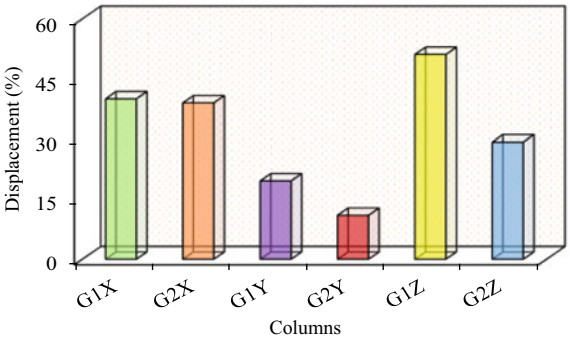

Fig. 4 Ultimate displacement in percentage

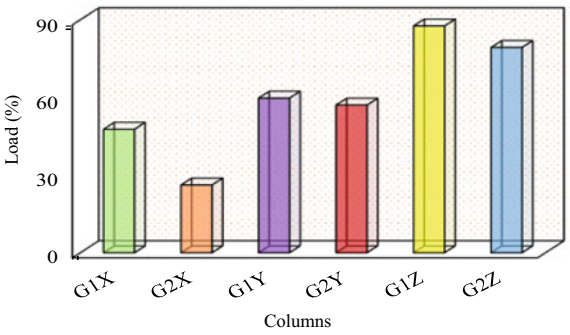

Fig. 5 Ultimate load in percentage

and non-strengthened column under axial loading mode. In comparison with non-strengthened RC columns, Fig. 5 indicates the percentage of axial load capability of strengthened square RC columns. The ultimate load-carrying capability of RC columns partially and entirely reinforced by GFRP is greater than that of RC columns that are non-strengthened. It was also found that the partially strengthened G1X and G1Z give more load-carrying capacity than G2X and G2Z. The fully strengthened RC column has load-carrying capacity G1Y and G2Y, almost the same as shown in Fig. 5.

3.3 Axial Stress-strain Behavior

Column specimens are divided into three different groups for ease of discussion. The stress-strain response of three RC columns, including the non-strengthened column, is presented in Fig. 6. The strain gauge on concrete was placed in the column specimen's mid-height, whereas the strain gauge on FRP wrapping was placed at the wrapping's mid-height. The positive axial strain of concrete was used, while the negative lateral strain of FRP wrapping was used. Figure 6a shows the ultimate strain in the G1X and G2X column specimens was observed slightly higher than

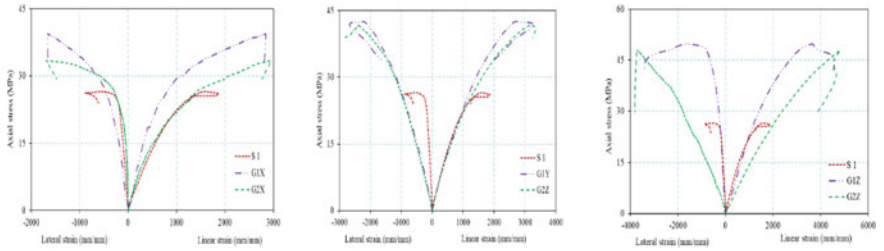

a) Top b) Top - Bottom c) Full

Fig. 6 Axial stress-strain behavior

axial strain and lateral strains compared to the S1. It was also noted that the G1X in lateral strain had declined gradually, and G2X in lateral strain gas suddenly declined. The top strengthens column in the stress-strain behavior initially elastic phase of the GFRP bidirectional peak performed well. The top-bottom strengthen columns axial and lateral strains slightly increase and lead to failure severely delayed as presented in Fig. 6b.

Additionally, the G1Y shows better performance than G2Y because GFRP bidirectional wrapping material was deboned with the column surface. The axial strain in G2Z shows better performance than G1Z, and lateral strain in G1Z shows better performance than G2Z. Figure 6c demonstrates the behavior of axial and lateral strains as they grow from the elastic to the plastic level. The load-carrying capacity of the column is increased, and failure occurs with a severe delay.

Table 1 also describes the normalized ultimate axial stress (*f'cc/f'co*) and normalized ultimate axial strains ($\varepsilon_{cu}/\varepsilon_{co}$). In the FRP confined column specimens, the stress ratio of *f'cc/f'co* was noted in the range of 0.92–1.73, whereas the strain ratio of $\varepsilon cu/\varepsilon_{co}$ was observed in the range of 1 to 2.64 and lateral strain ratio 0.07–0.19%.

Table 1 Test results summery

Specimen ID	$f'_{co,ave}$ (MPa)	$f'cc$ (MPa)	ε_{cu}	$\varepsilon_{h,ave}$	$f'cc/f'_{co}$	$\varepsilon_{cu}/\varepsilon_{co}$	$\varepsilon_{h,ave}/\varepsilon_f$
S 1	29.36	26.51	0.0018	0.0008	0.92	1.00	–
G1X	29.36	39.66	0.0028	0.00167	1.35	1.55	0.07
G2X	29.36	33.88	0.0030	0.00169	1.15	1.62	0.09
G1Y	29.36	42.89	0.0027	0.0022	1.46	1.46	0.10
G2Y	29.36	42.17	0.0032	0.00238	1.44	1.75	0.12
G1Z	29.36	50.34	0.0036	0.00156	1.71	1.97	0.07
G2Z	29.36	50.71	0.0048	0.00372	1.73	2.64	0.19

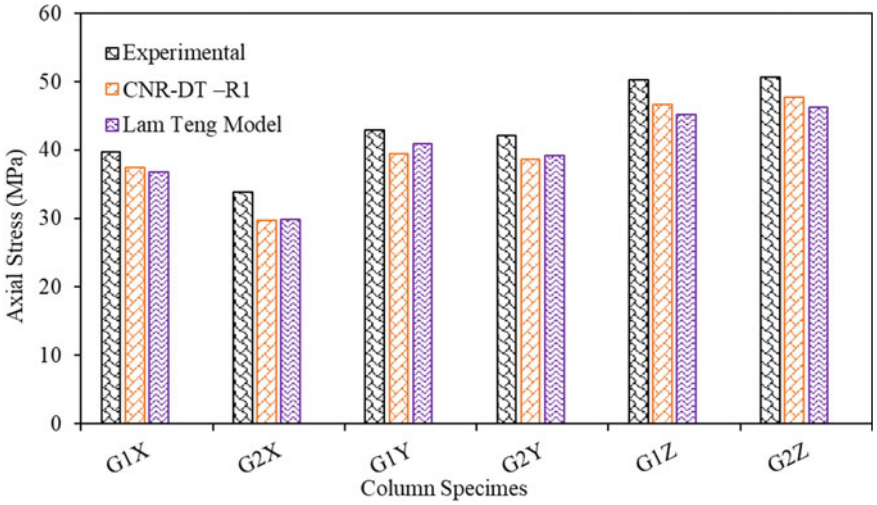

Fig. 7 Comparisons of axial stress for strengthened columns

3.4 Comparison of Experimental Stress with Different Model

The experimental data were compared with the two models to check the precision and reliability. The test results exhibit that the CNR-DT-R1 model is more reliable than Lam and Teng and provides reasonable and accurate predictions for the ultimate axial stress of partially and fully wrapped RC columns, as shown in Fig. 7.

4 Conclusion

Based on the experimental results, the following conclusions are drawn:

1. The partially top–bottom strengthened RC column gives more axial displacement control than the partially top strengthened RC column.
2. The unidirectional GFRP partially top and fully strengthened RC column give more load-carrying capacity than the bidirectional GFRP top and fully strengthened RC column.
3. The stress-strain behavior in unidirectional GFRP fully strengthened column lateral strain had declined gradually, and bidirectional GFRP fully strengthened column lateral strain gas suddenly declined.

Thus, the axial displacement control of RC columns strengthened by GFRP bidirectional is more than RC columns strengthened by GFRP unidirectional. The experimental data were compared with CNR-DT-R1 and Lam-Teng models to check the precision and reliability. The test results exhibit that the CNR-DT-R1 model is more reliable than Lam-teng.

References

1. 440, A. C. (2008) Guide for the design and construction of externally bonded FRP systems for strengthening concrete structures (ACI 440.2R-02), ACI 440.2R-08. https://doi.org/10.1061/40753(171)159
2. BIS:10262 (2009) Indian Standard Guidelines for concrete mix design proportioning, Bureau of Indian Standards, New Delhi, p New Delhi, India
3. CNR-DT 200 R1/2013 (2013) Guide for the design and construction of externally bonded FRP systems for strengthening existing structures, p 144
4. Hadi MNS (2006) Comparative study of eccentrically loaded FRP wrapped columns. Compos Struct 74(2):127–135. https://doi.org/10.1016/j.compstruct.2005.03.013
5. Hadi MNS (2007) Behaviour of FRP strengthened concrete columns under eccentric compression loading. Compos Struct 77(1):92–96. https://doi.org/10.1016/j.compstruct.2005.06.007
6. IS:1786-2008 (2008) High strength deformed steel bars and wires for concrete reinforcement—specification. Bureau of Indian Standards, New Delhi, pp 1–12
7. Karam G, Tabbara M (2005) Confinement effectiveness in rectangular concrete columns with fiber reinforced polymer wraps. J Compos Constr 9(5):388–396. https://doi.org/10.1061/(asce)1090-0268(2005)9:5(388)
8. Lam L, Teng JG (2003) Design-oriented stress-strain model for FRP-confined concrete. Constr Build Mater 17(6–7):471–489. https://doi.org/10.1016/S0950-0618(03)00045-X
9. Lin HJ, Liao CI (2004) Compressive strength of reinforced concrete column confined by composite material. Compos Struct 65(2):239–250. https://doi.org/10.1016/j.compstruct.2003.11.001
10. Rocca S, Galati N, Nanni A (2009) Interaction diagram methodology for design of FRP-confined reinforced concrete columns. Constr Build Mater 23(4):1508–1520. https://doi.org/10.1016/j.conbuildmat.2008.06.010
11. Saljoughian A, Mostofinejad D (2016) Axial-flexural interaction in square RC columns confined by intermittent CFRP wraps. Compos B Eng 89:85–95. https://doi.org/10.1016/j.compositesb.2015.10.047
12. Saljoughian A, Mostofinejad D (2016) Corner strip-batten technique for FRP-confinement of square RC columns under eccentric loading. J Compos Constr 20(3):04015077. https://doi.org/10.1061/(asce)cc.1943-5614.0000644
13. Shehata LAEM, Carneiro LAV, Shehata LCD (2002) Strength of short concrete columns confined with CFRP sheets. Mater Strucur 35(February):50–58

Performance of RC Beams Using CFRP, GFRP, and SSWM Subjected to Torsion: Numerical Study

Saloni V. Bhavsar, Sunil D. Raiyani, and Paresh V. Patel

Abstract The research on flexure, shear, and axial strengthening of reinforced concrete (RC) members has been conducted many times, but very few studies have been carried out on torsional strengthening of RC members. The main objective of the present study is to ascertain the better strengthening material in terms of torsional strength and damage patterns. A finite element (FE) study is carried out using ABAQUS software to understand the behavior of RC beam strengthened using different fiber reinforced polymers (FRPs), i.e., carbon fiber reinforced polymer (CFRP), glass fiber reinforced polymer (GFRP), and stainless-steel wire mesh (SSWM). Total sixteen beams are adopted from literature. One beam is kept as a control beam, while the other fifteen beams are strengthened using CFRP, GFRP, and SSWM with five different wrapping configurations. Torque-twist response, ultimate torque and corresponding twist, damage pattern, and maximum principal strain are measured and compared with experimental results from the literature. The study reveals that the effectiveness of SSWM as a strengthening material is as good as CFRP and GFRP in terms of torsional strength, failure pattern, and maximum principal strain.

Keywords Reinforced concrete beam · Glass fiber reinforced polymer · Stainless steel wired mess · Carbon fibre reinforced polymer

S. V. Bhavsar (✉) · S. D. Raiyani · P. V. Patel
Institute of Technology, Nirma University, Sarkhej-Gandhinagar Highway, Ahmedabad 382481, India
e-mail: 19mclc19@nirmauni.ac.in

S. D. Raiyani
e-mail: sunil.raiyani@nirmauni.ac.in

P. V. Patel
e-mail: paresh.patel@nirmauni.ac.in

B. Kondraivendhan et al. (eds.), *Sustainable Building Materials and Construction*,
Lecture Notes in Civil Engineering 222,
https://doi.org/10.1007/978-981-16-8496-8_25

1 Introduction

Torsion can appear in the structural elements when the load is applied away from the neutral axis. For the design of RC beams subjected to torsion, the number of stirrups can be increased up to a specific limit, but after that, it is tough to do the concreting. In that case, external strengthening of RC beams becomes essential. Strengthening of structural elements is necessary in case of an increase in loading, damage to the individual structural element, deterioration to the structural member, modification in the structural element and the cost of replacement of RC structural elements is very high. Structural elements subjected to torsion experience diagonal tension and compression and fail in a brittle manner. To avoid brittle failure, it is desirable to strengthen the element subjected to torsion. Ganganagoudar et al. [1] carried out an analytical and FE study to inspect the torsional behavior of FRP-strengthened RC elements to see the efficacy of FRP. The comparison was made between analytical results; FE results and experimental data from literature extracted that torsional strength of FRP strengthened beam is more than control specimen. Santhakumar et al. [2] presented FE study on retrofitted and non-retrofitted RC beams subjected to combined bending and torsion using CFRP. FE result was compared with experimental data published in the literature. Panchacharam and Belarbi [3] presented the behavior of RC members strengthened with GFRP subjected to pure torsion. Elwan [4] performed a parametric study using software ANSYS on the torsional strengthening of RC beams using CFRP and compared it with the previous experimental work by the author. Obaidat et al. [5] performed an experimental and FE studies on RC beams strengthened by near-surface-mounted CFRP strips subjected to pure torsion. From the results of the researchers [2–5], CFRP and GFRP can be used for torsional strengthening. Further, Jariwala et al. [6] performed an experimental study of RC beams using GFRP to enhance the torsional resistance. A beam having wrapping pattern corner and diagonal strip wrapping (CO&DS) exhibited a maximum (110%) increment in cracking torque and maximum (117%) increment in ultimate torque, compared to the control beam. Ameli et al. [7] presented an experimental and numerical study of RC beams using CFRP and GFRP for torsional strengthening. RC beams strengthened with CFRP showed better performance than GFRP-strengthened beams. Patel et al. [8] conducted an experimental study to interpret the behavior of RC beams strengthened with various wrapping configurations of SSWM subjected to pure torsion. Torque-twist behavior and failure modes for beams under pure torsion are obtained. The results obtained by the experimental study are further verified through numerical simulation using FE software ABAQUS [9]. Corner and diagonal strip (CO&DS) wrapping of SSWM on RC beam showed a maximum increase in cracking and ultimate torque compared to other wrapping patterns. FRPs or SSWM can upgrade the performance of existing RC structural elements as externally bonded materials. Researchers have selected CFRP, GFRP, and SSWM to strengthen the RC elements under torsional loading. Even though the experimental study presents very realistic results of RC elements under different types of loading and natural conditions, it is costly, time, and power-consuming, and experimental study on a full

scale is very difficult. At the same time, FE analysis provides results under various loading and boundary conditions.

The main objective of the present study is to understand the performance of RC beams with various wrapping configurations using CFRP, GFRP, and SSWM under pure torsion. The study is carried out using nonlinear FE-based software ABAQUS [9]. The results are obtained as torque–twist response, ultimate torque and corresponding twist, damage pattern and maximum principal strain. Results of CFRP and GFRP strengthened RC beams are compared with the experimental results of Ameli et al. [7]. It is further extended for SSWM-strengthened RC beams with the same wrapping configurations published by Ameli et al. [7].

2 Numerical Investigation

A nonlinear FE model is developed to predict the torsional behavior of RC beams strengthened using CFRP, GFRP, and SSWM using FE-based software ABAQUS. FE modeling of RC beam strengthened using FRP or SSWM is challenging as it should respond to the nonlinearity of the materials such as concrete, steel, and FRPs or SSWM in the form of cracking, crushing, concrete plasticity, yielding of reinforcement or SSWM, and FRP rupture. Concrete is modeled using 3D-eight-node solid brick elements (C3D8R).

The concrete damage plasticity model is used for nonlinear analysis. The compressive and tensile stress–strain relationship of concrete is derived from the literature by Jeng and Hsu [10]. Longitudinal and transverse reinforcements are modeled with 3D, three-node truss elements (T3D3). The stress–strain curve for reinforcement bars is derived from the literature by Jeng and Hsu [10]. CFRP, GFRP, and SSWM are modeled as 3D shell extrusion type of elements (S4R). The elastic properties of CFRP and GFRP are taken from the literature by Ameli et al. [7], and elastoplastic properties of SSWM are taken from the study of Patel et al. [8]. The damage parameters for compression and tension failure of concrete are adopted as described in ABAQUS manual [9].

For defining interaction between reinforcement and concrete, embedded constraint is used. Tie constraint is used to define the interaction between concrete and FRPs or SSWM. In tie constraint, perfect bonding is assumed between concrete and FRPs or SSWM. For that concrete surface is selected as master surface, and FRP or SSWM is selected as slave surface. Coupling constraint is used to provide twist about longitudinal axis. One end of the beam is kept as fixed. At another end, load is applied in the form of twist about member axis at reference point in terms of radian. Dynamic explicit analysis is used for the present study.

In this study, 11 specimens are adopted from the research presented by Ameli et al. [7]; out of which, one beam is kept as control beam, while other ten beams are strengthened with CFRP and GFRP. In addition to that, by keeping the same

five wrapping configurations, SSWM is used to strengthen the beam. All the cross-sectional, mechanical properties, reinforcement detailing, and five different wrapping patterns are taken from the literature by published Ameli et al. [7].

3 Results and Discussion

In this paper, only JS (U-Jacket, 7 strips of 100 mm spaced at 100 mm, one-layer of CFRP/GFRP/SSWM wrapping pattern) [7] is described for better understanding in terms of torque-twist behavior, ultimate torque and corresponding twist, damage pattern, and maximum principal strain. In addition, the torque-twist behavior of RC beams having remaining wrapping configurations is also presented in subsequent Sect. 3.1.

3.1 Torque-Twist Response

The torque-twist behavior of RC beams strengthened using CFRP and GFRP for JS wrapping pattern is compared with experimental results [7] as shown in Fig. 1a, b. The FE results for CFRP and GFRP strengthened beams are found in close agreement with experimental results [7]. The stiffness of the test specimen [7] at all ranges of response is well simulated using numerical analysis. The descending portion of the torque-twist response is also well predicted by the FE models, which reveal the precision of the material model adopted for the present study. Beside that, the torque-twist response of finite element analysis for RC beams strengthened with all three materials (i.e., CFRP, GFRP, and SSWM) are also presented in Fig. 1c to evaluate the capability of individual material for JS wrapping pattern. From Fig. 1, the ultimate torque for the beam strengthened using CFRP, GFRP and SSWM, i.e., CJS, GJS, and SJS, are 17.43 kN m, 17.22 kN m, and 17.24 kN m, respectively. The identical torque-twist behavior is observed for all three CJS, GJS and SJS cases.

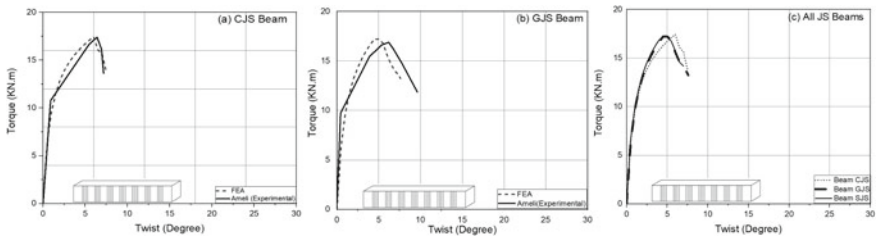

Fig. 1 **a** Comparison of torque-twist response for CJS (CFRP-JS) beam from experimental and FE study. **b** Comparison of torque-twist response for GJS (GFRP-JS) beam from experimental and FE study. **c** Comparison of torque-twist response for all JS beams from FE study

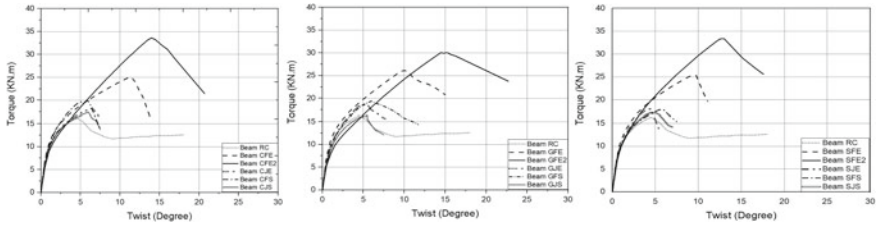

Fig. 2 FE results of torque versus twist behavior for CFRP, GFRP, and SSWM strengthened beams, respectively

As shown in Fig. 2, a comparison is made for all the beams strengthened using CFRP, GFRP, and SSWM with different wrapping patterns. It is noticed that torque-twist behavior is almost linear up to the first cracking of concrete for all the beams. After cracking, a sudden increase in the twist and the torque-twist response becomes nonlinear up to failure.

3.2 Ultimate Torque and Corresponding Twist

The ultimate torque and corresponding twist for all JS beams are shown in Fig. 3. The figure shows that the increase in ultimate torque for beam CJS is 6.93%, for the beam GJS 5.64% and for the beam SJS 5.77% regarding control specimen. Twist corresponding to ultimate torque for CFRP, GFRP, and SSWM strengthened beams also increases concerning the twist of control beam.

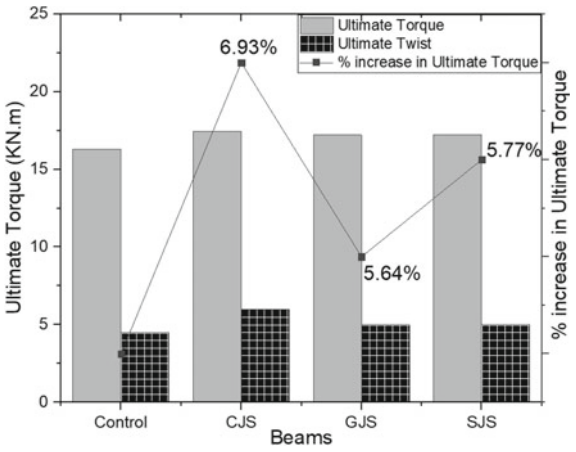

Fig. 3 Ultimate torque and corresponding twist for beams having JS wrapping pattern

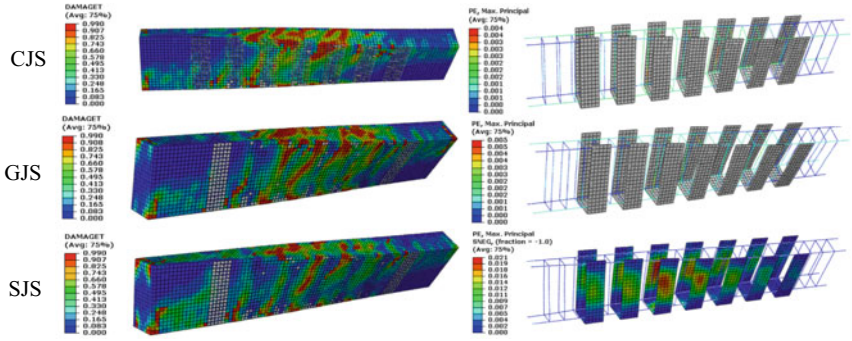

Fig. 4 Damage pattern and maximum principal strain for beams having JS wrapping pattern strengthened using CFRP, GFRP, and SSWM, respectively

3.3 Damage Pattern and Maximum Principal Strain

From Fig. 4, it is observed that the damage patterns for all the beams strengthened using CFRP, GFRP, and SSWM are almost identical for JS wrapping pattern. The maximum principal strain for beams CJS, GJS, and SJS is also shown in Fig. 4. It is observed that SSWM has contributed more effectively to strain distribution than CFRP and GFRP due to its elastoplastic nature.

4 Conclusions

A nonlinear FE model is developed in ABAQUS to register the torque-twist response and understand the failure progression, ultimate torque, corresponding twist and maximum principal strain. Major conclusions derived from the study can be summarized as below.

- The FE results are in good agreement with experimental results.
- The torque-twist response for all the beams having a similar strengthening pattern of FRPs, i.e., CJS, GJS, and SJS beams showed almost similar behavior up to the elastic region. A minor difference is observed in the post-cracking stage for all beams having the same wrapping pattern.
- It is observed that the ultimate torque for beam SJS is 1.15% lower than CJS beam and 0.13% more than GJS beam. Hence, the torsional strength of SSWM strengthened beam is almost similar to the beams strengthened using CFRP and GFRP.
- In all JS beams, diagonal torsional cracks occurred and widened in the unwrapped concrete part of the beams between FRP strips. Damage patterns derived from the numerical study replicate the experimental failure pattern.

- CFRP and GFRP have not contributed to strain distribution as effectively as SSWM due to their plastic properties, whereas SSWM has elastoplastic properties.

From the study, the behavior of RC beams under torsion using CFRP, GFRP, and SSWM can be identified. From the behavior, it can be understood that GFRP and SSWM are behaving more or equal to the same, whereas CFRP is giving better torsional resistance. So, either CFRP can be used to increase the torsional resistance, or GFRP can be replaced by SSWM because of its lower cost to strengthen the RC beam under torsion. Also, it is noticed that the performance of SSWM is as good as CFRP and GFRP in terms of torque-twist behavior, damage pattern, ultimate torque, and maximum principal strain to enhance the torsional behavior of RC beams. Hence, one can use SSWM for strengthening of RC beams subjected to torsion.

References

1. Ganganagoudar A, Mondal TG, Prakash SS (2016) Analytical and finite element studies on behavior of FRP strengthened RC beams under torsion. Compos Struct 153:876–885
2. Santhakumar R, Dhanaraj R, Chandrasekaran E (2007) Behaviour of retrofitted reinforced concrete beams under combined bending and torsion: a numerical study. Electron J Struct Eng 7:1–7
3. Panchacharam S, Belarbi A (2002) Torsional behavior of reinforced concrete beams strengthened with FRP composites. First FIB Cong 1:08–11
4. Elwan SK (2017) Torsion strengthening of RC beams using CFRP (Parametric study). KSCE J Civ Eng 21:1273–1281
5. Obaidat YT, Ashteyat AM, Obaidat AT (2020) Performance of RC beam strengthened with NSM-CFRP strip under pure torsion: experimental and numerical study. Int J Civil Eng 18:585–593
6. Jariwala VH, Patel PV, Purohit SP (2016) Torsional strengthening of RC beams using GFRP composites. Inst Eng (India) 93(30):313–322
7. Ameli M, Dux PF, Ronagh HR (2007) Behavior of FRP strengthened reinforced concrete beams under torsion. J Compos Constr 11(2):192–200
8. Patel PV, Raiyani S, Shah PJ (2018) Torsional strengthening of RC beams using stainless steel wire mesh-Experimental and numerical study. Struct Eng Mech 67(4):391–401
9. Dassault Systemes (2016) ABAQUS online user manual version 6.7-1. Dassault Systemes Waltham, MA, USA
10. Hsu TTC, Jeng CH (2009) A softened membrane model for torsion in reinforced concrete-members. Eng Struct 31(9):1944–1954

Studies on Seismic Safety of Hospital Structures

Kalesha Shaik and B. Ajitha

Abstract A large number of hospitals were damaged during the Bhuj earthquake of 2001, causing serious interruption in providing emergency medical services to injured people. Damage to hospital buildings resulted in not only deaths and injuries to people inside the hospital but also increased deaths due to non-availability of medical facilities after the earthquake, due to significant harm to medical equipment's and facilities during the earthquake. The necessity of working of hospitals after a major quake is obvious. It will be much appreciated, at least a few important medical necessities were facilitated for the injured. By using seismic protection by floor isolation, we can manage to provide emergency healthcare services post-earthquake. Seismic floor isolation is an ideal and economical method for protecting critical medical facility in hospital structures. The floor isolation uncouples the floor mass from the building framed structure, which results in minimum damage or disturbance, and in case of earthquake event, this eventually facilitates the chance, to the safe transfer of medical services in post-earthquake scenario. A case study is conducted on three floors building of the hospital, only a floor containing the operation theatre room is isolated using floor isolators then performed time history analysis using SAP2000 software. The reduction in seismic response of isolated floor is observed when compared to non-isolated hospital building, so that the reduced floor response can ensure the safety of the equipment and services on the isolated floor.

Keywords Seismic safety · Earthquake · Seismic protection · Commercial building

K. Shaik (✉) · B. Ajitha
JNTUA College of Engineering, Anantapur, AP, India

B. Ajitha
e-mail: ajitha123.civil@jntua.ac.in

B. Kondraivendhan et al. (eds.), *Sustainable Building Materials and Construction*,
Lecture Notes in Civil Engineering 222,
https://doi.org/10.1007/978-981-16-8496-8_26

1 Introduction

Earthquakes, floods, landslides, cyclones and tsunamis are the natural disasters which occur often in India. The country is being affected by many earthquakes of severe intensity in the recent decades. The working of hospitals during and after a major earthquake is necessary. Studies on hospital performance approximations and engineered retrofit methods may assist disaster mitigation efforts to provide appropriate treatment to the injured and ill. In base isolation, the key idea is achieving the decoupling with the use of an isolation scheme, which ensures the increase in effective fundamental period of the isolated structure compared to the structure above the isolation system. These techniques already became familiar in countries like US and Japan. In India, there are very few applications due to many factors like type of construction, economic considerations, etc., there is a massive demand for economically-viable safety systems, which can be implemented within new or existing structures.

2 Methodology

Seismic floor isolation is the method used to protect non-structural elements from the fixed base building structures. It is done by isolating the required floor systems from the preliminary structural floor using flexible components called as isolators, it is shown in Fig. 1. Thus, in floor isolation, decoupling of the floor portion is done by flexible isolators from the rest of the structure. Nowadays, floor isolation systems are observed to be more popular to protect critical structural elements/equipment in hospital.

3 Dynamic Seismic Analysis

To make the earthquake analysis and to design a structure, the genuine earthquake records are required which is to be constructed at the desired location. Also, it is impossible to consider such time history data at each and every place. Moreover, the analysis does not merely depend on the maximum value of the ground acceleration, it depends on the frequency and dynamic properties. Time history method and response spectrum method are basically two approaches for seismic dynamic analysis which are widely used to overcome the above difficulties; here, in this investigation, time history method is applied. Time history method of analysis computes the solution to dynamic equilibrium equation for the structural behaviour (acceleration, displacement, etc.) using the dynamic properties of the structure at an arbitrary time when dynamic load is applied. This technique represents the most advanced method of dynamic analysis for buildings. El Centro earthquake acceleration time history as shown in Fig. 3 and time history data generated compatible to 1893 spectrum for

Fig. 1 Floor isolation

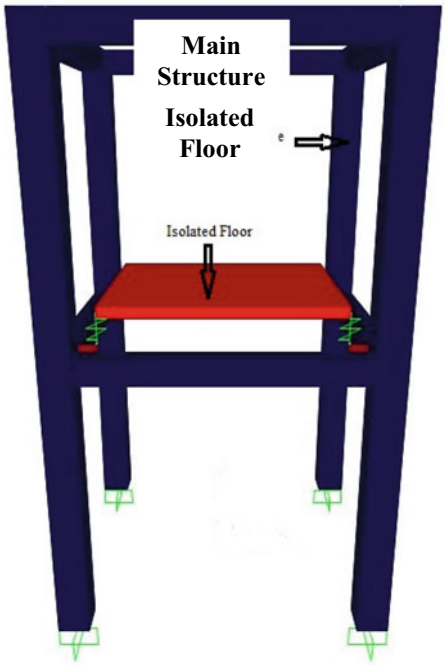

medium soil corresponding to 0.36 g peak value as shown in Fig. 4 are used as input time histories in this study. Both of these time history data files are uploaded in SAP2000 software for analysis.

4 SAP2000 Modelling

In order to find the floor isolation effectiveness, a case study is performed with three-storey hospital building in the SAP2000 tool. The three-storey building is a 30-bedded hospital with a total area covering around 2320 sq m. The hospital building contains eight bays in the direction of *X*-axis and four bays in the *Y*-direction. Each floor height in the hospital is taken as 3.6 m. The 3D model of the hospital is created in SAP2000 as shown in Fig. 2. Materials used for the construction are Fe415 grade steel and M30 grade concrete. The foundation is considered as fixed support. In SAP2000, columns and beams are designed as 3D frame elements, and the properties are assigned while modelling. In the analysis phase, a sample load of 2 KN/m^2 is considered. The modal analysis and dead load analysis are then performed to attain the reactions, moments and fundamental time period. Nonlinear modal time history analysis is made to analyse the building.

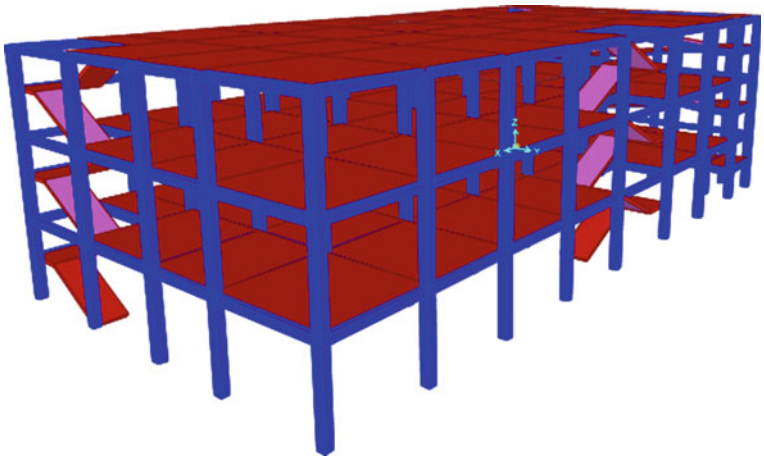

Fig. 2 Three-storey hospital building model

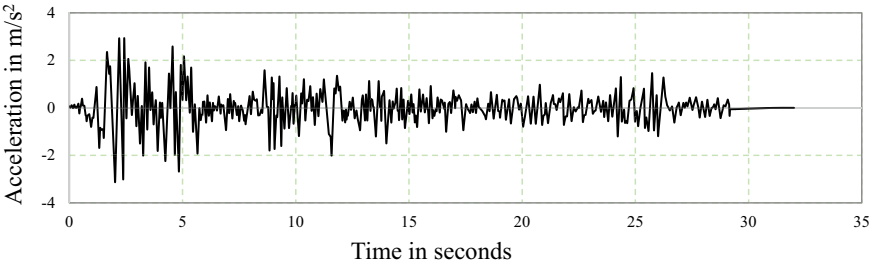

Fig. 3 El Centro earthquake time history input acceleration

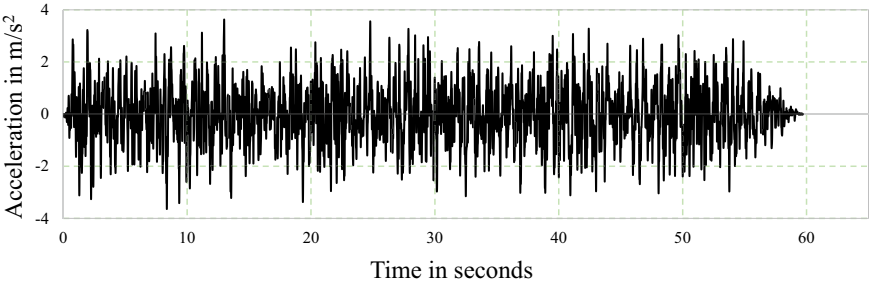

Fig. 4 IS:1893 [9] spectrum (0.36 g) time history input acceleration

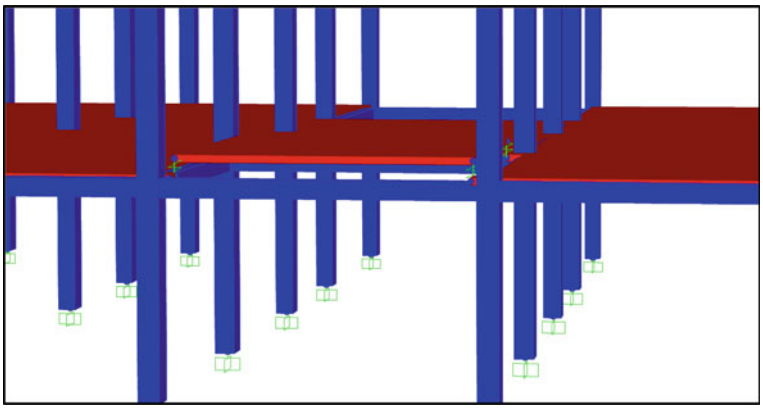

Fig. 5 Isolated floor in operating theatre of first floor

5 Floor Isolation in Hospital Building

See Fig. 5.

6 Results and Discussion

Nonlinear modal analysis with time history is made using the [9] spectrum compatible time history with 0.36 g and El Centro. Acceleration responses of isolated floor in first-floor level are compared with normal building without any isolated slab and observed the reduction in acceleration as shown in Figs. 6 and 7. The reduction of acceleration response is given in Table 1 for a given effective stiffness and corresponding damping values. This reduction in acceleration response is around **80%** observed for both El Centro and [9] earthquake time histories. Therefore, safe functionality is ensured during and after the earthquake for the operating theatre, which is isolated.

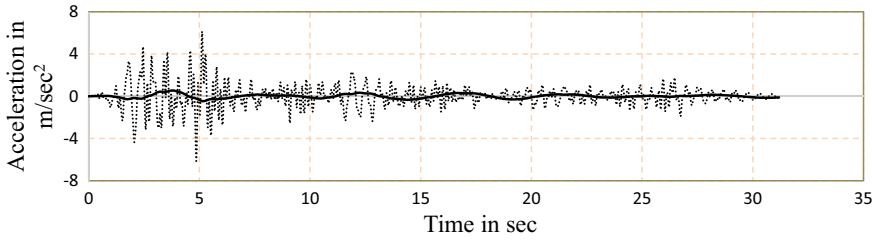

Fig. 6 Comparison of acceleration response of the first-floor level without floor isolation to the isolated floor for El Centro earthquake

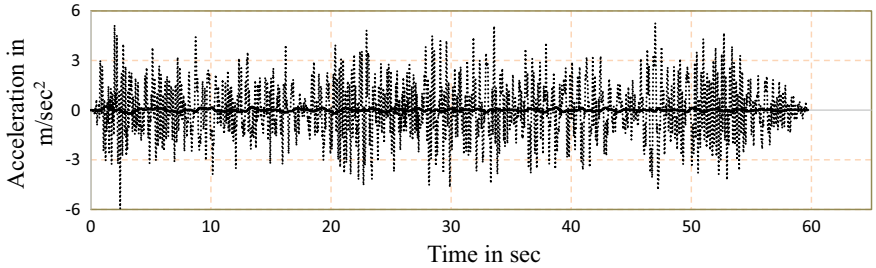

Fig. 7 Comparison of acceleration response of the first-floor level without floor isolation to the isolated floor for [9] (0.36 g)

Table 1 Acceleration reduction values

Effective stiffness Kh (Kf/4)	Effective damping for 20% damping ration	*X*-direction IS 1893			*Y*-direction IS 1893		
		PGA (g)	Isolated floor acceleration (g)	Reduction (%)	PGA (g)	Isolated floor acceleration (g)	Reduction (%)
3.134	87.504	0.36	0.06286	82.54	0.36	0.0597180	83.412
Effective stiffness Kh (Kf/4)	Effective damping for 20% damping ration	*X*-direction El Centro			*Y*-direction El Centro		
		PGA (g)	Isolated floor acceleration (g)	Reduction (%)	PGA (g)	Isolated floor acceleration (g)	Reduction (%)
3.134	87.504	0.31	0.05217	83.17	0.31	0.0547	82.355

7 Conclusions

- The principle of floor isolation recommends transmitted force to be least on the floor considered. From the observations made in this investigation, floor isolation helps in lowering the seismic responses like acceleration of the floor slab which is isolated.
- Around 80% of the reduction is observed between both the responses, which confirms the minimal interruption in facilitating the emergency medical services in the important wards like intensive care unit (ICU), emergency care unit, operation theatre, etc., whose functionality is important without during and post the earthquake without any interruption.
- For the chosen scheme of floor isolation, reduction in acceleration is predominant than reduction in displacement. Since two-storey building lies in velocity sensitive region of the time history spectrum, there is not much decrease in the displacement of isolated floor system compared to non-isolated floor system.
- This floor isolation system reduces the earthquake energy imparted. Hence, the equipment above isolated floor can be safe during earthquake.

- This floor isolation is an ideal solution whenever entire building is not possible or cost effective. Application of floor isolation is mostly found in data centres, high value laboratories and spaces having high-tech manufacturing equipment, medical equipment, etc.

References

1. Basu D et al (2005) Concept of floor isolation in reducing seismic demand. In: Proceedings of international conference on advances in concrete composites and structures. SERC, Chennai, India, pp 1057–1064
2. Filiatrault A et al (2017) Sustainable and low-cost room seismic isolation for essential care units in developing countries
3. Liu S, Warn GP (2012) Seismic performance and sensitivity of floor isolation systems in steel plate shear wall structures. Eng Struct 42:115–126
4. Mahmoud H, Chulahwat A (2015) Response of building systems with suspended floor slabs under dynamic excitations. Eng Struct 104:155–173
5. Pourmohammad H et al (2004) Analytic study of floor isolation system. In: Proceedings of 13th world conference on earthquake engineering, Vancouver, B.C., Canada. Paper No. 3372
6. Ziyaeifar M (2000) Method of mass isolation in seismic design of structures. In: 12th world conference on earthquake engineering, Auckland, New Zealand
7. Ziyaeifar M, Noguchi H (1998) Partial mass isolation in tall buildings. Earthquake Eng Struct Dyn 27:49–65
8. IS: 12433 Part-1: 1988 (R2003) Indian standard—basic requirements for hospital planning, Part 1 up to 30 bedded hospital
9. IS: 1893 (2016) Indian Standard—criteria for earthquake resistant design of structures, part-1, general provisions and buildings
10. Kasalanati A et al (2016) Seismic response case study of isolated floor system having special biaxial spring units
11. Anajafi H, Medina RA (2017) Robust design of a multi-floor isolation system
12. Cui S, Bruneau M (2008) Experimental study of isolated floor systems
13. Porcu MC Partial floor mass isolation to control seismic stress in framed buildings
14. Chopra AK Dynamics of structures theory and applications to earthquake engineering
15. Duggal SK Earthquake-resistant design of structures

Seismic Fragility Analysis of Base-Isolated Reinforced Concrete Frames Analysed by Direct Displacement-Based Design

Channabasaveshwar Chikmath, S. A. Vasanwala, and Veeresh Karikatti

Abstract Direct displacement-based design is performance-based design approach, and one has to check the suitability of the method against different types of ground motions, namely far field, near field fling step and near field forward directivity. The method is applied for the buildings with hysteretic isolation bearings. Fragility analysis is conducted on the buildings analysed by this method and is verified for maximum interstorey drift ratio (MIDR) and maximum isolator displacement (MID) as damage measures subjected to ground motions. The method is applied for eight- and twelve-storey reinforced concrete frame structures equipped with lead rubber bearing. The probability of exceedance was higher for near field forward directivity for all the buildings. Further, the base isolation was not much effective in twelve-storey building. The energy dissipation mechanism in the isolators controls the displacement of the structure within acceptable limits at the level of isolator.

Keywords Fragility analysis · Direct displacement-based design · Lead rubber bearings · Nonlinear time history analysis · Damage measures · Intensity measures

1 Introduction

According to statistics from 2011 Census of India, urban population of India is 377 million which is less than a third of the total. Due to the rapid increasing population and industrialization, the construction sector is spreading not only urban areas but also remote places. This is resulting the need for the construction of multi-storey structures even in severe seismic zones. Since major terrain in India falls under Seismic zone III and above, the designer must ensure that capacity of the building is greater than the

C. Chikmath (✉) · S. A. Vasanwala
Sardar Vallabhbhai National Institute of Technology, Surat, India

S. A. Vasanwala
e-mail: sav@amd.svnit.ac.in

V. Karikatti
KLE Institute of Technology, Hubballi, India

B. Kondraivendhan et al. (eds.), *Sustainable Building Materials and Construction*,
Lecture Notes in Civil Engineering 222,
https://doi.org/10.1007/978-981-16-8496-8_27

demand. The main objective of seismic isolation is to mitigate the potential damage caused by earthquake. Base isolation increases the damping, flexibility, time period of the system. Development of fragility functions and vulnerability functions form the major tools in seismic risk assessment after a major catastrophe. Fragility analysis helps all the stakeholders such as the owner, local authorities, insurance companies, contractors, structural consultant to be aware of the damage to the building after an earthquake event of certain intensity occurs. According to the performed studies, as the near fault records have pulses with long period, they have more impact on the structures in comparison to far fault records.

1.1 Direct Displacement-Based Design

Direct displacement-based design (DDBD) is predominantly displacement-based design method developed by Priestly [12] on reinforced concrete frame buildings. The development of first-generation displacement method procedures was given in 90 s [5, 13].

1.2 Fragility Functions

The fragility of a structure is defined as the conditional probability of failure for particular seismic response parameter which is a measure of deformation [4] such as maximum velocity, acceleration, displacement. In the present paper, fragility curves for maximum interstorey drift ratio (MIDR) and maximum isolator displacement (MID) are developed for eight- and twelve-storey seismically isolated RC frame structures analysed by DDBD proposed by Cardone et al. [3] for three different earthquake cases based on the source distance. Lead rubber bearing (LRB) is used as isolator.

2 Damage Measures and Damage States

Fragility curves are plotted for damage measures MIDR and MID. Slight, moderate, severe and complete are the four damage states. Defining the threshold values of the damage states is meaningful to the stakeholders in terms of causalities, retrofitting, downtime [7] and is given in Table 1.

Table 1 Damage measures and threshold values of damage states

Damage measures	Damage states			
	Slight	Moderate	Extensive	Collapse
MID (D_{max})	0.2	0.4	0.8	1.2
MIDR (%)	0.05	0.10	0.20	0.70

Note D_{max} = isolator design displacement

3 Analytical Procedure

Assuming that fragility curve follows lognormal distribution, only two parameters are sufficient to define them. The fragility curve can be expressed mathematically as lognormal cumulative density function [11] shown in Eq. (1).

$$P_f(\mathrm{d}s \geq \mathrm{d}si|\mathrm{IM}) = \varphi\left[\frac{1}{\beta_{total}} \ln\left(\frac{S_d}{S_c}\right)\right] \tag{1}$$

where

P_f = probability of exceeding the damage state ds for IM level of intensity,
S_d = seismic demand due to earthquake loads.
S_c = median value of structure's capacity with 50% probability being in a particular damage state [1],
$\varphi[]$ = standard normal (Gaussian) cumulative probability function, and
β_{total} reflects the total uncertainty or also called as randomness (by the engineers) associated with earthquake demand such as input motion β_d and structure capacity β_c in the form of resistance to particular damage measure in the fragility function and is given by Eq. (2) [2].

$$\beta_{\text{total}} = \sqrt{\beta_d^2 + \beta_c^2} \tag{2}$$

The demand models are formed by performing nonlinear time history analysis on the structures which is probabilistic in nature and relates the damage measure (DM) and intensity measures (IM) as in Eq. (3). The value of β_c is 0.3 [2]. The values of β_d, $\beta_c$and β_{total} are tabulated in Table 3.

$$\mathrm{DM} = a\mathrm{IM}^b \tag{3}$$

where the constants a and b are obtained by regression analysis of the demand model.

4 Numerical Example

The plan of a RC frame building is shown in Fig. 1. The height of each floor is 3 m. Eight- and twelve-storey buildings are considered for the study which form the midrise and high-rise buildings. The building is located in medium soil for Bhuj area which falls under Zone V according to Bureau of Indian Standards code for earthquakes [8]. The design is carried out using Bureau of Indian Standard code for concrete design [9]. Nonlinear time history analysis (NLTHA) is carried out to verify the interstorey drift ratio, isolator displacement for six set of each earthquake ground motions of far field, near field fling step and near field forward directivity, respectively. Isolator properties are shown in Table 2.

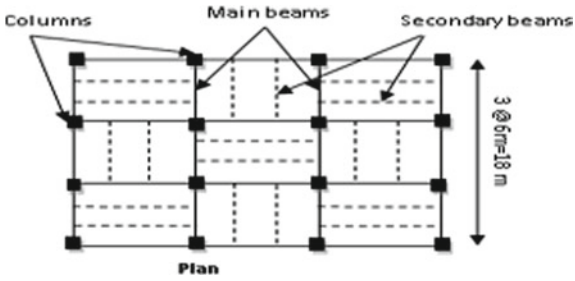

Fig. 1 Geometry of the building

Table 2 Isolator properties

	Eight storey	Twelve storey
Name of the isolator	LRB-S 550/200-120	LRB-S 600/204-130
Isolator displacement D_d (m)	0.4	0.4
Initial stiffness K_1 (kN/m)	7875	9250
Effective stiffness K_{eff} (kN/m)	810	950
Effective damping $\xi_{IS}(\%)$	26.65	26.85
Post-yield stiffness ratio γ	0.058	0.057
Yield force F_y (kN)	126	148
Vertical stiffness K_v (kN/m)	789,000	844,000

Table 3 Standard deviation of damage measures and earthquake types

No. of storeys	Damage measure	Type of earthquake	β_d	β_c	β_{total}
Eight	MIDR	FF	0.24	0.3	0.39
		NFD	0.40		0.50
		NFS	0.23		0.38
	MID	FF	0.28		0.41
		NFD	0.36		0.47
		NFS	0.42		0.51
Twelve	MIDR	FF	0.28	0.3	0.41
		NFD	0.42		0.52
		NFS	0.34		0.46
	MID	FF	0.30		0.42
		NFD	0.44		0.53
		NFS	0.52		0.60

5 Results and Discussions

The damage measures for different earthquake ground motions considered with standard deviation for demand and capacity are shown in Table 3. The fragility curves for maximum interstorey drift ratio (MIDR) and maximum isolator displacement (MID) for eight and twelve storeys are plotted from Figs. 2, 3, 4 and 5 for slight, moderate, severe and complete damage measures.

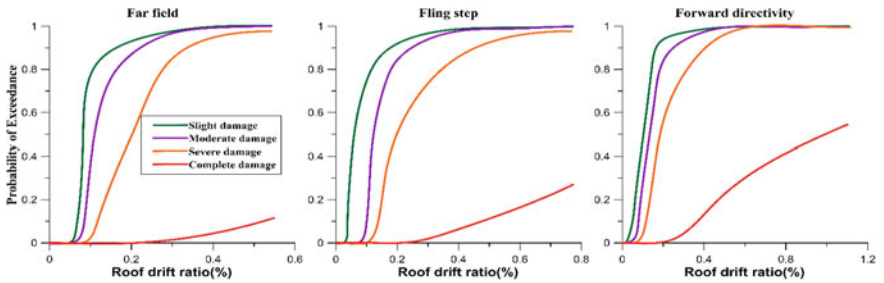

Fig. 2 Fragility curves for eight-storey maximum interstorey drift ratio

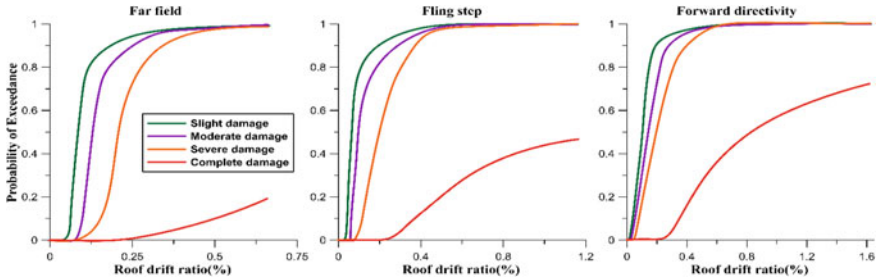

Fig. 3 Fragility curves for twelve-storey maximum interstorey drift ratio

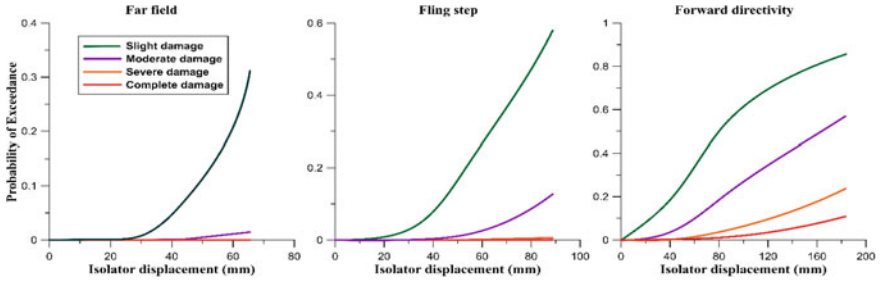

Fig. 4 Fragility curves for eight-storey maximum isolator displacement

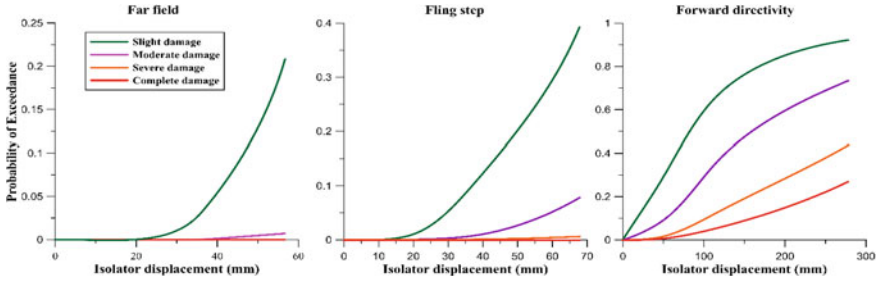

Fig. 5 Fragility curves for twelve-storey maximum isolator displacement

6 Conclusions

The fragility curves are developed for eight- and twelve-storey seismically isolated reinforced concrete frame structures located in Zone V according to Indian earthquake code of practice. The isolation allows the building to move elastically and dissipate the energy of the earthquake. These frames are analysed by direct displacement-based design subjected to six sets each of far field, near field fling step and near field forward directivity ground motions. Maximum interstorey drift ratio and maximum isolator displacement are taken as demand measures.

The base-isolated buildings are highly fragile to near field earthquakes. More than 90% of the structures were severely damaged in case of MIDR even for small change in drift. For MID, all the damage measures were slightly damaged up to 60% except twelve-storey forward directivity where it was nearly 92% for slight damage but less than design isolator displacement of 400 mm. The lowest probability of exceedance (POE) was given by far field earthquakes for all the damage measures and highest for near field forward directivity. The fragility analysis for the group of buildings at a given location helps to assess the damages occurring post-earthquake to all the stakeholders.

References

1. Barbat AH, Pujades LG, Lantada N (2008) Seismic damage evaluation in urban areas using the capacity spectrum method: application to Barcelona. Soil Dyn Earthq Eng 28(10–11):851–865. https://doi.org/10.1016/j.soildyn.2007.10.006
2. Bhandari M et al (2019) Seismic fragility analysis of base-isolated building frames excited by near- and far-field earthquakes. J Perform Constr Facil 33(3):1–16. https://doi.org/10.1061/(ASCE)CF.1943-5509.0001298
3. Cardone D, Palermo G, Dolce M (2010) Direct displacement-based design of buildings with different seismic isolation systems. J Earthquake Eng 14(2):163–191. https://doi.org/10.1080/13632460903086036
4. Ellingwood BR (2001) Earthquake risk assessment of building structures. Reliab Eng Syst Saf 74(3):251–262. https://doi.org/10.1016/S0951-8320(01)00105-3
5. FEMA 273 (1997) NEHRP guidelines for the seismic rehabilitation of buildings. Applied Technology Council, California
6. FIP Industriale (2016) Lead rubber bearings Series LRB. FIP Industriale, Italy. Available at https://www.fipindustriale.it/public/S03_LRB-eng.pdf
7. Gong W, Xiong S (2016) Probabilistic seismic risk assessment of modified pseudo-negative stiffness control of a base-isolated building. Struct Infrastruct Eng 12(10):1295–1309. https://doi.org/10.1080/15732479.2015.1113301
8. IS-1893 (2016) Indian standard criteria for earthquake resistant design of structures—Part 1 general provisions and buildings. Buereau of Indian Standards, New Delhi
9. IS-456 (2000) Indian standard code of practice for plain and reinforced concrete. Buereau of Indian Standards, New Delhi
10. Kalkan E, Kunnath SK (2006) Effects of fling step and forward directivity on seismic response of buildings. Earthq Spectra 22(2):367–390. https://doi.org/10.1193/1.2192560
11. Pitilakis K, Crowley H, Kaynia A (eds) (2014) SYNER-G: typology definition and fragility functions for physical elements at seismic risk, 1st edn. Springer, Netherlands
12. Priestley MJN, Pettinga JD (2005) Dynamic behaviour of reinforced concrete frames designed with direct displacement-based design. J Earthquake Eng 9:309–330
13. SEAOC Blue Book (1999) Recommended lateral force requirements and commentary. Structural Engineers Association of California, California

Seismic Investigation of Nuclear Reactor Containment Structure

Bhairav M. Thakur and Atul K. Desai

Abstract In the emerging industrial sectors, energy to sectors is predominant need. Compare to all other energy sources, the nuclear power plant (NPP) is considered versatile in compensating energy consumption needs. So, the behavior of nuclear containment structures (NCS) in natural calamities like seismic scenarios has prime importance. In the present study, the dynamic behavior of NCS is considered, and containment structure was analyzed for various shell thicknesses. At the same time, the linear time history analysis was employed for soil stiffness evolution. A software tool SAP2000v21 package was used to model the geometry of the nuclear reactor's (NR) containment structure. This research summarizes several guidelines and techniques related to soil–structure interaction (SSI) analysis of structures. The obtained results of different shell element thickness parameters suggested that the SSI should be considered for the detailed analysis of essential structures.

Keywords Soil-structure interaction · Nuclear power plant · Nuclear containment structures

1 Introduction

The seismic response of nuclear power plants (NPP's) is imperative as they are massive and stiff compared to traditional buildings. Power stations need to compensate for colossal power demand because observing a developing country's industrial sector; power demand increases rapidly. The overall consideration of the economy, human resources, and technology adoption for constructing the power plant with high capacity makes nuclear power an essential energy source. On March 03, 2011, the failure of the Fukushima Daiichi NPP created lots of awareness in NPP's constructional design and detailing [6]. The most critical uncertainties for failure are the reinforced concrete (RC) degradation mechanism, temperature effects, and soil–structure interaction (SSI).

B. M. Thakur (✉) · A. K. Desai
Civil Engineering Department, S.V. National Institute of Technology, Surat, India

B. Kondraivendhan et al. (eds.), *Sustainable Building Materials and Construction*,
Lecture Notes in Civil Engineering 222,
https://doi.org/10.1007/978-981-16-8496-8_28

SSI phenomenon affects the seismic response of an embedment structure. In seismic response studies, the analysis of NPP's with SSI is essential and necessary to avoid NPP failure [4]. The NPP's and subordinating structures, system and equipment (SS&E) needs to design for resisting the earthquake forces along with gravity, pressure, and thermal load effects.

In the present study, the two types of structural base systems are considered to evaluate the nuclear reactor (NR) response: NR with a fixed base and SSI base. The finite element software SAP2000 [3] was employed to generate the spectrum compatible linear time history compatible with IS 1893 [5] response spectra. Two types of seismic excitations were considered, i.e., long-duration earthquake (M 7.6 Bhuj and M 9.0 Japan earthquake) and short-duration earthquake (M 6.9 El-Centro and M 7.0 Koyna earthquake).

The primary research goal is to examine the seismic behavior of NR response with SSI and without SSI base. The performance of various shell element thicknesses in NR suggests that the SSI should be considered for a detailed analysis of important structures.

2 Research Significance

A massive complex structure like NPP is possessing challenges to structure fields. The presence of structures generally influences ground motions, and structural response to the ground motions is affected by the supporting subsoil's compliance. These tuned phenomena are due to an interaction called soil–structure interaction (SSI). These SSI effects are depending on the geometric constraints and the corresponding dynamic response of structures simultaneously. The NPP structure response associated with SS&E is more complex to analyze because of uncertainties in backfill and surrounding soil. The system and component of NPPs containment follow the environmental effects and possible load combinations. The dynamic method for simplifying an SSI effect must be capable of being solved by established approaches.

3 Numerical Modeling

An overview of containment structures details, properties of structures, concrete, soil, and numerical modeling approach for the structure-SSI is presented herein. Also, mention in point of ground motion selection and scaling criteria which are reported.

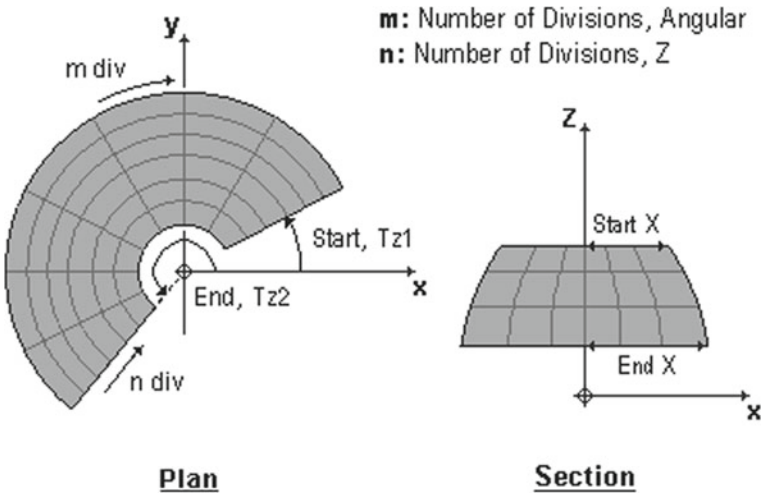

Fig. 1 Typical parabolic dome parameter [3]

3.1 Modeling of NR Containment Structures

A geometry of NR containment structure has been adapted from [2]. The main reactor building is situated on a raft element with a 5.5 m thickness, and the rectangular raft size is 52 m × 52 m. The cylinder and dome containment wall heights are 45.375 m and 7 m, respectively, the cylinder and parabolic dome radius is 21 m. The dome is lying on top of the cylindrical containment wall. The selected thicknesses for the dome and cylinder are 0.8, 0.9, 1.0, 1.1, and 1.2 m. For numerical modeling, a full-featured program named SAP2000 [3] has been employed. It can solve simple and major complicated problems like bridges, towers, industrial plants, dams, soil, and buildings [3].

The 3D NR containment model is shown in Fig. 2. A grid of cylinders was divided into Z-direction by 17 Nos for proper meshing, and individual grid height is 2.73 m. The grid in the radial direction was divided into 48 Nos. The particular grid radial length is 2.74 m; thus, the grid ratio nearly equal to 1:1, as shown in Fig. 1. In modeling input herein, the start *X*-direction value is 0, and the end *X* value is 21; the start angle, Tz_1 is 0°, and the end angle, Tz_2, is 360°.

3.2 Properties

The properties of the present scenario are taken into consideration and given in Table 1.

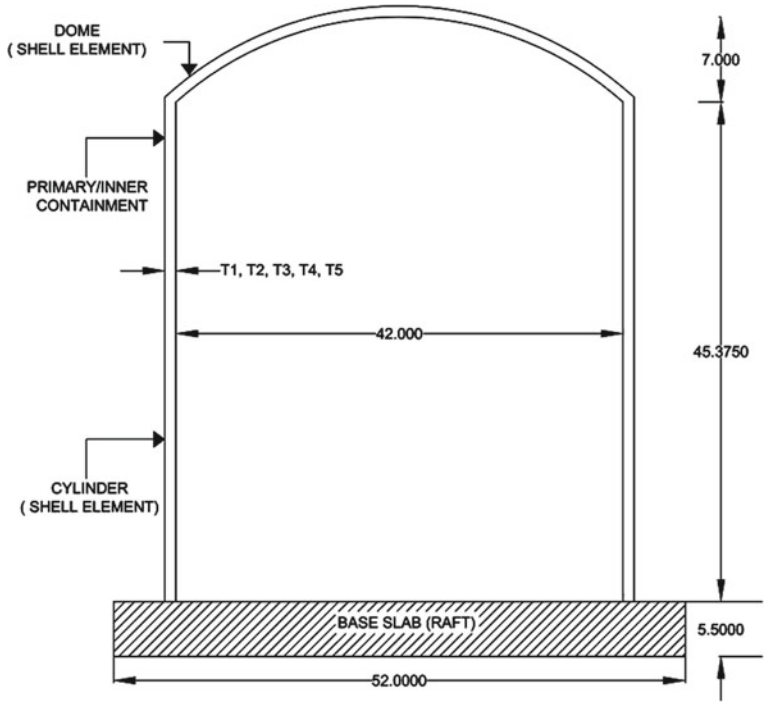

Fig. 2 Section of typical NR containment structure

Table 1 Material characteristics of the NR containment structures [2, 7]

Material characteristics	Value
Concrete Compressive strength, f_c (MPa)	57
Material type	High-Density Concrete (HDC)
Modulus of elasticity, E_c (GPa)	31.528559
Poisson's ration, μ	0.2
Mean mass density, ρ (kg/m^3)	5488
Soil	
Density of soil, ρ (gm/cc)	2.51
Dynamic modulus of elasticity, E_{dynamic} (kN/m^2)	124.54×10^4
Poisson's ratio (μ)	0.31
Shear modulus of soil, G (kN/m^2)	$\frac{E_S}{2(1+\mu)}$

Table 2 SSI springs stiffness equation for a rectangular base (ASCE 4-16)

Motion	Equivalent springs constant
Horizontal	$K_x = 2(1+\upsilon)G\beta_x\sqrt{BL}$
Rocking	$K_\psi = \frac{G}{1-\upsilon}\beta_\psi BL^2$
Vertical	$K_Z = \frac{G}{1-\upsilon}\beta_Z\sqrt{BL}$
Torsion	$R = \sqrt[4]{BL\left(B^2+L^2\right)/6\pi}[4]BL\left(B^2+L^2\right)/6\pi$

3.3 Modeling of SSI Springs

In the present study, SSI analysis by impedance function approach shall be used as per the ASCE standard of "Seismic Analysis of Safety-Related Nuclear Structures and Commentary" (ASCE 4-16). The SSI has been model as an array of closely-spaced-springs coupled with dashpots and gap elements (see Table 2).

3.4 Ground Motion Selection

Four real-time earthquake accelerogram records have been obtained from the pacific earthquake research center: strong ground motion database (PEER NGA database), and it was used to conduct a linear dynamic time history analysis. The selected ground motion database such as M7.6 Bhuj (January 26, 2001), M9.0 Japan (March 11, 2011), M6.9 El-Centro (May 18, 1940), and M7.0 Koyna (December 11, 1967) was selected for study and applied in *X*-direction to model. The time history records have been selected based on predominant frequency. A document of each earthquake is used for generating spectrum compatible time histories.

The artificially generated time history is compatible with the IS 1893 [5] response spectrum for medium soil type II, considering zone IV. The seismic zoning map of India was used as an input ground motion. Spectrum compatible time histories were generated for the maximum considered earthquake (MCE) condition, scaled by zone factor 0.24 for zone IV. In MCE condition, NPP will safely shut down during significant ground motion events. It means for MCE, the value of zone factor (Z) was entirely taken instead of the denominator, dividing by a factor of two as per IS1893 [5]. Spectrum compatible time history has been generated by using the computer program Seismomatch [8]. The dynamic method for simplifying an SSI effect must be capable of being solved by established approaches.

Table 3 Base shear for different time history with varying thickness of shell element

Time history	Type of base (kN)	Thickness, m				
		0.8	0.9	1.0	1.1	1.2
Bhuj	FB	275,311	284,881	294,251	306,004	317,581
	SSI	240,593	248,538	280,544	316,342	349,562
Japan	FB	289,976	299,251	308,398	322,529	337,637
	SSI	198,412	224,136	259,953	286,495	298,174
Koyna	FB	283,034	300,620	317,779	333,229	346,571
	SSI	197,314	219,929	237,436	261,062	289,154
El-Centro	FB	345,703	362,533	379,434	396,180	412,763
	SSI	247,105	281,056	295,890	311,325	318,399

4 Results and Discussion

As per the base shear and base moment, the four linear compatible time history was used to analyze nuclear reactors for different thicknesses of shell elements, fixed base, and flexible base.

4.1 Base Shear F_x (kN)

Table 3 shows the estimated maximum expected lateral force on the structure's base due to seismic activity.

As per the above results in all four time history cases, the maximum base shear is found in 1.2 m thickness of shell element, in both FB and SSI base, because the stiffer structure will attract more shear force. The maximum influence of SSI for base shear is to be noted in the Japan time history case of 32% lesser than FB.

4.2 Base Moment Mx (kN m)

Table 4 shows the estimated maximum base moment on the structure's base due to seismic activity.

From the above results in all four time history for the base moment, it appears that the maximum base moment in short and long duration will be in fixed base condition and flexible (SSI) base condition, respectively. In a long-duration earthquake, the maximum influence in a base moment due to SSI is to be noted as 25% more than a base moment in a fixed base condition.

Table 4 Base moment for different time history with varying thickness of shell element

Time history	Type of base (kN m)	Thickness, m				
		0.8	0.9	1.0	1.1	1.2
Bhuj	FB	5,728,577	6,454,190	7,185,777	7,923,864	8,666,244
	SSI	6,066,641	7,181,008	8,198,933	9,110,727	10,070,325
Japan	FB	6,006,188	6,761,867	7,517,152	8,270,807	9,024,567
	SSI	6,795,945	7,697,761	8,553,823	9,450,827	10,353,165
Koyna	FB	5,751,303	6,477,654	7,199,941	7,920,552	9,024,567
	SSI	5,669,851	6,303,039	6,928,797	7,670,367	8,412,660
El-Centro	FB	5,994,963	6,770,031	7,546,609	8,320,937	9,094,323
	SSI	5,917,530	6,714,108	7,487,061	8,272,910	9,076,620

5 Conclusions

The present study highlights the importance of SSI for NR containment structure subjected to four earthquake motions. The conclusion was drawn after comparing various nuclear reactor containment structures for efficient cases. The top portion structure was more in acceleration than the lower portion of the structure in both fixed and flexible bases. Short- and long-duration earthquake gives predominate acceleration in fixed-based and flexible-based conditions, respectively. The maximum base moment was selected based on the short duration of the earthquake. It was also observed the highest base shear. The highest base moment in the NR with flexible based for the earthquake's long duration represents maximum base shear too.

References

1. American Society of Civil Engineers (2016) Seismic analysis of safety-related nuclear structures and commentary. American Society of Civil Engineers
2. Bangash MYH (1981) Structures for nuclear facilities. J Chem Inform Model 53
3. CSI, S. v21 (2021) CSI, SAP2000 integrated software for structural analysis and design. Computer and structures Inc., Berkeley, California (USA)
4. Hoseyni SM, Yousefpour F, Aghaei Araei A, Karimi K, Hoseyni SM (2014) Effects of soil-structure interaction on fragility and seismic risk; a case study of power plant containment. J Loss Prev Process Ind 32:276–285
5. IS:1893 (Part1)-2002, Indian Standard, criteria for earthquake resistance design of structures, 5th addition, Part-1. Bureau of Indian Standard, New Delhi
6. Najafijozani M, Becker TC, Konstantinidis D (2020) Evaluating adaptive vertical seismic isolation for equipment in nuclear power plants. Nucl Eng Des
7. Shanmukhi K (2002) Seismic response study of nuclear reactor containment. Ph.D., thesis, Indian Institute of Technology, Kanpur
8. SeismoSoft (2021) SeismoMatch—a computer program for static and dynamic nonlinear analysis of framed structures
9. PEER Ground Motion Database. Pacific Earthquake Engineering Research Center. University of California, Berkeley, CA, USA (2020). http://ngawest2.berkeley.edu

Seismic Effect of CFG Pile Supported Building Structure in Soft Soil by Numerical Investigation

N. B. Umravia and C. H. Solanki

Abstract The CFG (Cement Flash and Gravel) pile, one technique, is widely used to efficiently provide the support and transfer load of structures overlaying on the soft soil ground. The application includes high-railway embankment, high-rise buildings, and many more to reduce the effect of structure overall settlement and enhance the bearing capacity of soft soil. This research paper covered the construction technology and structure engineering feature of CFG piles. It also introduced the CFG pile construction process mix and main points of attention. It demonstrated that the CFG pile treatment system is practical and feasible in combination with engineering practises. The main objective of the study the axial, lateral behaviours of CFG pile under the static and seismic loading in the soft ground by numerical approach. Therefore, this paper represents a full numerical comparison study of CFG piles with variable properties and no CFG piles. For the considered earthquake time history, the CFG piles in uneven soil strata layers in the soft ground significantly impact relative horizontal displacement. Moreover, the relative vertical displacement of the CFG piles toe, acceleration of ground motion at the CFG pile near ground level, and post-factor of treated ground. Furthermore, it concluded that the selection of time histories is necessary for seismic analysis.

Keywords CFG pile · Lateral load · Displacement

1 Introduction

Nowadays, four-lane expressways have been widely built in India for the last three decades. The logistics business and economic cooperation growth need the four-lane expressways; however, the need has surpassed their total capacity, so they cannot satisfy the need for increased traffic due to further economic progress. Many four-lane expressways widened to six lanes or eight lanes under these conditions. The lane expansion overcomes the traffic problem, but the embankment's differential

N. B. Umravia (✉) · C. H. Solanki
Civil Engineering Department, Sardar Vallabh Bhai National Institute of Technology, Surat, Gujarat, India

B. Kondraivendhan et al. (eds.), *Sustainable Building Materials and Construction*,
Lecture Notes in Civil Engineering 222,
https://doi.org/10.1007/978-981-16-8496-8_29

settlement effect continues and becomes a new problem in geotechnical engineering. The differential settlement has been found where the embankment is overlaying on soft ground. The impact of this differential settlement decreasing by procuring many ground improvement techniques like DM (deep Mixing), ESC (encased Stone column), CFG Pile, and many more. The CFG pile is one of the best techniques used in china to support the embankment [1]. Many heavy loads are moving express highway, high-rise building, and high-speed railway embankment project they have been used these techniques [3, 5, 7]. Moreover, these approaches are also effectively applicable at falling land mean silt area and coastal area.

Usually, pile foundation techniques are widespread to reduce damage due to earthquake excitation and vibration from the structure. The CFG piles behaviours are semi-rigid. In other words, they fail not as bulging or sudden collapse under the load. This technique is the ground improvement column technique [4, 6, 8]. The CFG piles interact with the soil under the dynamic analysis and seismic design of massive and composite foundations in different structures and are widely used in china country.

2 Methodology

The construction process of CFG piles with a composite foundation for ground improvement application in the soft ground is described in Fig. 1 [2, 5]. The soil CFG pile structure interaction (SCSI) has been effective under seismic load. In this present study, the Drucker-Prager model is used to soil plasticity nonlinearity and Plaxis-3D to a general-purpose finite element analysis in performing the nonlinear dynamic analysis of the CFG pile foundation system. Additional research on the dynamic calculation for structure-soil interaction impacts residential building 18 m height with 3 m basements with and without the CFG pile composite foundation. The defining free-field compliant base with confining boundary condition in earthquake

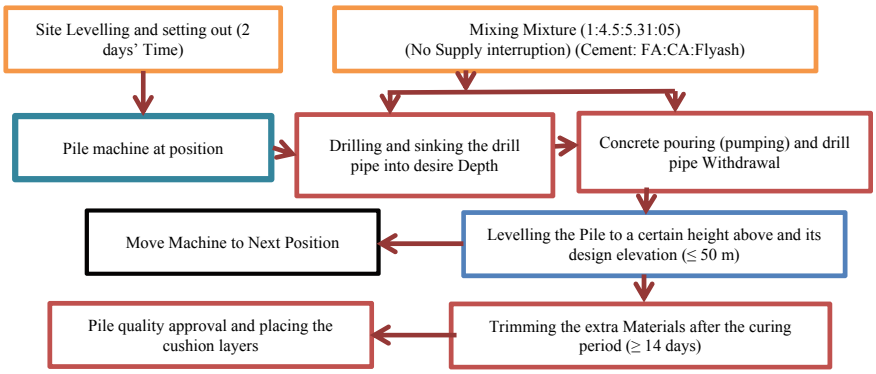

Fig. 1 Construction method of CFG pile and insolation

simulated model through displacement multiplies and EL Centro model has been used to study its behaviours on the structure and CFG pile foundation.

Hence, the soil consisted of two layers. The top layer consisted of soft clay up to 15 m from ground level, and the bottom layer consisting of 25 m below soft clay. The soils and CFG piles properties were considered as mention in Table 1. The boundary soil condition considered 160 m long and 5 m width for earthquake-dominated effect across the width. The geometry of the Plaxis model is shown in Fig. 2. The building lengths were 12 m and width 5 m, whilst the floor height 3 m, including the basement. In addition, wall and basement materials were assigned as plates, and a value of 4.5 kN/m^2 was taken as its weight. The Residential building and other input data have been considered, as shown in Table 2.

Table 1 Material properties

No	Parameter	Soft clay	Sandy soil	CFG pile
1	Material model	HS small	HS small	Linear elastic
2	Drainage type	Drained	Drained	Non-porous
3	Unsaturated unit weight (kN/m^3)	14	20	22
4	Saturated unit weight (kN/m^3)	17	20	22
5	Modulus of elasticity E (kN/m^2)	E-2.0e 4	E_{50}-35,000	22,000
6	Poison's ratio	0.2	0.2	0.25
7	Cohesion (kN/m^2)	10	5	–
8	Angle of internal friction (φ) (°)	18	28	35
9	Dilation angle ψ (°)	0	0	–
10	E_{oed}^{ref}	2.561×10^4	3.601×10^4	–
11	Unloading and loading	9.484×10^4	1.108×10^4	–
12	Shear strain at $G_s = 0.722\ G_0$ ($\gamma_{0.7}$)	1.2×10^{-4}	1.5×10^{-5}	–
13	Shear modulus at very small strains	2.7×10^5	1.0×10^5	–

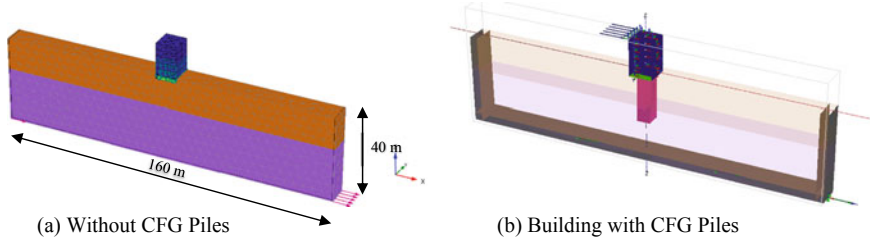

(a) Without CFG Piles (b) Building with CFG Piles

Fig. 2 Plaxis model **a** without CFG piles. **b** Building with CFG piles

Table 2 Building materials properties

Parameters	Name	Rest of building	Basement	Unit
Model types	Type	Elastic: Isotropic	Elastic: Isotropic	
Thickness	d	0.3	0.3	m
Material weight	γ	33.33	50	kN
Young's modulus	E1	3×10^7	4×10^7	kN
Passion's ratio	$\upsilon 12$	0	0	–
Rayleigh samping	α	0.232	0.232	
	β	8×10^3	9×10^3	–

3 Results and Discussion

Results presented here are based on nonlinear dynamic El Centro excitation analysis of CFG pile-supported building foundation interaction with the soil. When subjected to cyclic shear loading, the hardening soil model with small-strain stiffness shows typical hysteretic behaviour. Starting from the small-strain shear stiffness, G_0 ref, the actual stiffness decrease with increasing shear. Figures 3 and 4 show the 2 × 2 and 3 × 3 group CFG piles head response under the effect of young's Modulus (E_s), respectively. Figures 5 and 6 show the impact of pile head under the CFG pile spacing. Acceleration max obtains after entering the value of the earthquake. Details

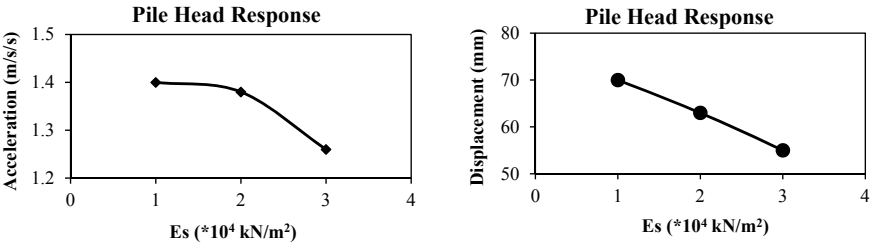

Fig. 3 Effects of Young's modulus on CFG pile head response in 2 × 2 pile foundation systems

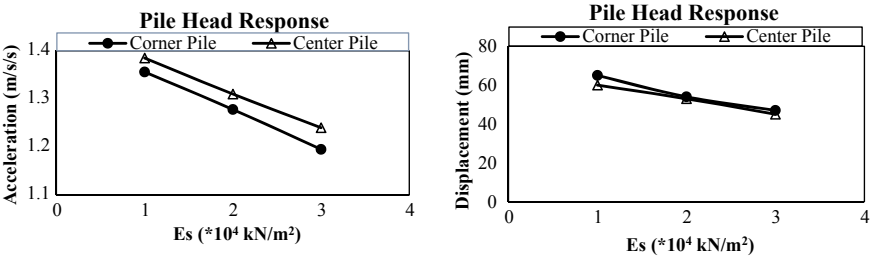

Fig. 4 Effects of Young's modulus on CFG pile head response in 3 × 3 pile foundation systems

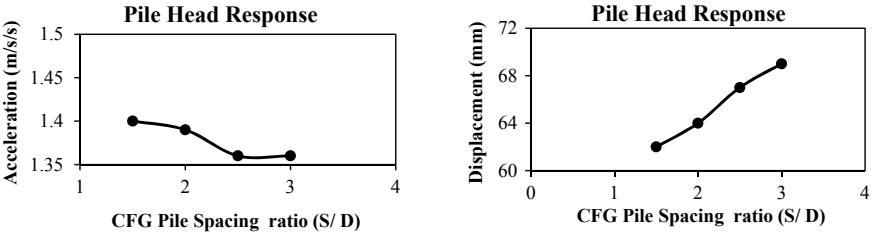

Fig. 5 Effects of spacing on CFG pile head response in 2 × 2 pile foundation systems

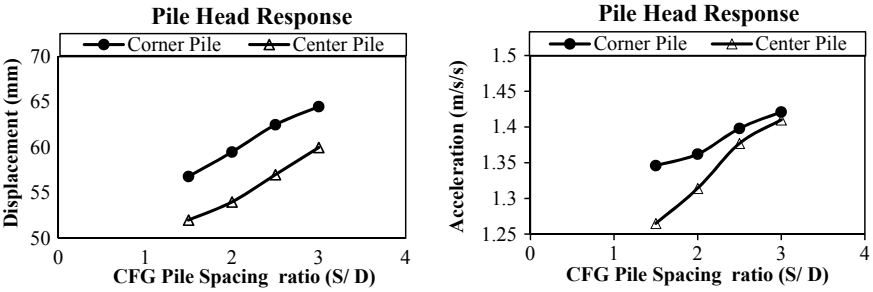

Fig. 6 Effects of CFG pile Spacing ratio on CFG pile head response in 3 × 3 pile foundation systems

results are analyses and concluding that deflected pile head with Young's modulus has been an increase.

4 Conclusion

- Results presented here based on three-dimensional FEM nonlinear dynamic analyses for the interaction of soil-pile group foundation systems.
- This present studies the effects of CFG pile group configurations on seismic soil-CFG pile kinematic interaction by investigating 2 × 2 CFG pile foundation systems and 3 × 3 CFG pile foundation systems with different soil properties and piles spacing ratios included. The compare relationship between the pile head and modulus of elasticity at the corner CFG pile, and the centre pile is linearly and increases 6% at each acceleration.
- The effect of CFG pile head deflection and acceleration decreased with the increasing the modulus of elasticity (E_s) because it is based on soil sharing parameter; therefore, soil resists the CFG pile lateral displacement.
- Comparing the 2 × 2 and 3 × 3 CFG pile-supported foundation, expected results found that if the S/D ratio at 3 defections is maximum and acceleration is near 2.5 S/D. Mean acceleration effect in soil overlap due to short S/D ratio.

- Optimum design application of CFG piles supported structure for ground improvement subjected to the vibration or earthquake load. It should prefer outer CFG piles diameter higher than the intermediate pile to reduce the lateral effect of the outer CFG pile.
- S/D ratio considered 2.5 for better performance of small groups pile-supported foundation.

References

1. Cao HY, Liu YF (2014) Optimum design of CFG pile compound foundation based on numerical simulation method. Appl Mech Mater 578–579:346–350. https://doi.org/10.4028/www.scientific.net/amm.578-579.346
2. Feng S, Liu X, Cui H (2017) Dynamical response of an elastic supporting pile embedded in saturated soil under horizontal vibration. Stavební obzor Civil Eng J 26(2):99–113. https://doi.org/10.14311/cej.2017.02.0010
3. Jiang DP, Wang BL (2012) An analysis on failure pattern of CFG pile-net composite foundation of high-speed railway. Adv Mater Res 594–597:1357–1362. https://doi.org/10.4028/www.scientific.net/amr.594-597.1357
4. Shen Y, Wang H (2016) Optimization design on CFG-pile foundation with different cushion thickness in Beijing-Shanghai high-speed railway. Transp Infrast Geotechnol 3(1):3–20. https://doi.org/10.1007/s40515-015-0026-7
5. Uge BU (2020) CFG pile composite foundation: its engineering applications and research advances
6. Umravia NB et al (2019) Recent study on the behaviour of CFG pile, DM (Deep Mixing) column and stone columns ground improvement technology, February, pp 241–246
7. Yang Y, Zhu L, Ma H (2017) Research on vertical bearing capacity of ram-compacted pile with vibrating gravel base in collapsible loess foundation. 123(Msmee):1062–1070. https://doi.org/10.2991/msmee-17.2017.207
8. Zhang C et al (2015) Lateral displacement of silty clay under cement-fly ash-gravel pile-supported embankments: analytical consideration and field evidence. J Central South Univ 22(4):1477–1489.https://doi.org/10.1007/s11771-015-2665-9

Influence of Geometric Variation on Seismic Fragility Assessment

Nirav K. Patel and Sandip A. Vasanwala

Abstract All planners are motivated to form structures in the best possible way to limit quakes in this time when sustainability is critical. Damages to the buildings during recent earthquakes in India lead to the need for seismic risk assessment, capable of predicting the probability of damage to the building. During analysis, seismic loads being implied is crucial to evaluate the provisional probability of structural response of the buildings considering realistic aspect by the generation of fragility curves to predict vulnerability index. Before an earthquake, fragility curves can be plotted to estimate losses, and after an earthquake, they can be used to assess seismic losses. Depending on the source of data and type of analysis, fragility curves may be derived using empirical or analytical methods and can be plotted to display the likelihood of any harm state being surpassed. For short-period, medium-period, and long-period structures, the work described here is compiled for building frame structures with deviations for 3, 6 and 12 storeys, respectively, each having variation in planar shape as a square shape, L-shape and T-shapes based on nonlinear static analysis, using SAP2000 as a software tool for analysing the structure and guidelines as per HAZUS technical manual for plotting fragility curves. The technique mentioned here is very useful for determining the seismic vulnerability of a building system using fragility analysis as an effective tool for risk and vulnerability assessment.

Keywords Seismic fragility assessment · Earthquake engineering · Damage analysis · Reinforced concrete

N. K. Patel (✉) · S. A. Vasanwala
Civil Engineering Department, Navrachana University, Vadodara, Gujarat, India

S. A. Vasanwala
e-mail: sav@amd.svnit.ac.in

B. Kondraivendhan et al. (eds.), *Sustainable Building Materials and Construction*,
Lecture Notes in Civil Engineering 222,
https://doi.org/10.1007/978-981-16-8496-8_30

1 Introduction and Background

Natural disasters such as earthquakes are regarded as one of the most serious threats, with severe consequences not only economically, but also socially. Earthquakes have a huge influence on both man-made and natural structures. Moreover, its after-effects tend to destroy additionally over successive months and years. Despite the fact that natural disasters are unavoidable, structural designers must create earthquake-resistant structures.

To assess the realistic seismic risk of reinforced concrete moment frame buildings, performance-based earthquake engineering (PBEE) is now used. This, however, does not indicate the likelihood of damage. As a result, the need for the development of a fragility curve has arisen in order to determine the damage probability. Current developments in the nonlinear structural analysis have enabled the development of fragility curves.

The fragility curve is specified as the probability distribution which exceeds the given limit state and used to assess a structure's seismic vulnerability. Fragility curves are amongst the critical component for assessing seismic hazard, correlating the intensity felt due to seismic activity to the likelihood of achieving or exceeding a damage state intensity (i.e. slight for minor, average as moderate, extreme and collapse about to fail) for all dangerous members. As a function of one or more seismic intensity measures (IM), fragility curves provide a graphical representation of exceeding a drift or damaged condition. The likelihood of reaching a specified limit state is projected against an IM, which is a reference ground motion parameter.

The availability of relevant fragility curves is required for the most of presently existing methodologies for evaluating probable damages. The field of seismic hazard assessment has seen noteworthy advancements over the last few decades. Calvi et al. [6] provided a thorough review of the various methods that can be used to develop fragility curves/function in the field of earthquake engineering. Empirical curves, curves based on expert opinion, analytical curves and hybrid curves are the four standard classes that are generally classified. Billah and Alam [3] summarised the benefits and drawbacks of each form. Analytical curves have been favoured over other approaches because they are derived from the results of static or dynamic analyses of structural models. Kircher et al. [11] introduced a framework and authentic viewpoint on the advancement of the seismic loss assessment techniques of the HAZUS methodology, delineated the distinctive modules of the HAZUS earthquake and abbreviates the critical thoughts of these procedures. D'Ayala and Meslem [7] highlighted a paper to direct users towards better quantification of uncertainties such as the impact regarding selecting of structure capability variables and their complexity may have on the derivation of risk and vulnerability functions. Porter [13] gave a briefing regarding fragility, vulnerability and risk specifically for the earthquake. Maske et al. [12] seismic vulnerability assessment of multi-storey buildings was carried out by them using pushover analysis. Barbat et al. [2] evaluated the seismic damage in urban areas focussing on Barcelona. Patel and Vasanwala [14]

gave the methodology for propagating fragility curves for reinforced concrete (RC) building using spectral displacement (S_d) as the intensity measure in this analysis.

A structure's seismic risk assessment includes hazard classification, building capacity assessment and the creation of fragility curves. This research focusses on the impact of geometric parameters such as building height and plan layout on the seismic vulnerability of reinforced concrete framed structures. As a result, its primary goal stands to compute the impact of the factors on seismic vulnerability.

2 Description and Design of RC Building

IS 456 [5] and IS1893 [4] were incorporated to design the building frame using SAP2000 as a tool. The buildings frames considered for the study are nine RC frame building having storey varying as 3, 6 and 12 storeys to represent short, medium and long-period structures having storey height as 3 m for all storeys and constant slab thickness as 150 mm. All selected buildings have three sets of plan arrangements; square shaped, L-shaped and T-shaped plan arrangement with six bays, 4 m each for an office building resting on medium soil type in seismic zone IV as per IS 1893 [4]. The base shear for a square-shaped building is calculated and presented in Table 1 along with the column and beam sizes considered.

2.1 Pushover Analysis

Applying constant gravity loads to a building model whilst gradually rising lateral forces or displacements is known as pushover analysis (POA). POA is a technique of incremental static analysis that evaluates the force-displacement relationship of a structure or structural feature, also known as the capacity curve. The designer must translate each output objective into a corresponding damage aim whilst using pushover analysis to assess a building's behaviour. Displacements and forces are the most common damage targets. As lateral loads or displacements are incrementally added to the building, the target displacement is compared to the displacement calculated at a roof-level control node. The analysis is terminated if the displacement at the control node exceeds the goal displacement of any performance stages, indicating

Table 1 Square shape building details

Storey (S)	H (m)	T_d (s)	S_a/g	W (kN)	A_h	V_d (kN)	Beam size (mm)	Column size (mm)
3	9	0.390	2.50	12,335	0.060	740.12	250 × 450	300 × 300
6	18	0.655	2.07	27,194	0.048	1305.29	250 × 450	400 × 400
12	36	1.102	1.234	62,516	0.030	1875.48	300 × 600	550 × 550

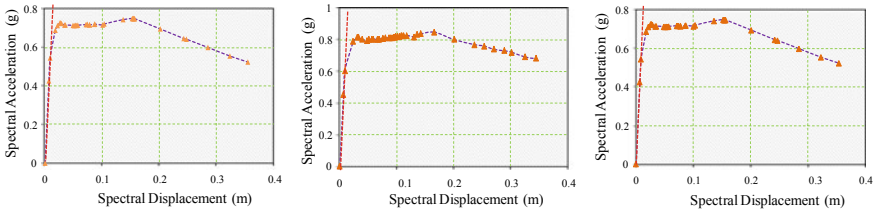

(a) 3 Storey Square (b) 3 Storey L (c) 3 Storey T

Fig. 1 Capacity curve indicating control points for 3 storey building model

that the performance objective has been surpassed. This form of analysis is known as displacement-based pushover analysis.

2.2 *Control Points*

The following principles and expert judgement are used to assess capacity curve control points from the capacity curve. The yield ability control point (D_y, A_y) is chosen as the location as soon as notable yield just starts to happen. The slope of the ability curve is constant till the yield point. The point of highest spectral acceleration is chosen as the ultimate power control point acceleration (D_u, A_u) (i.e. maximum building strength). It is worth noting that values should not exceed the spectral acceleration at which the structure has just reached its maximum plastic potential (i.e. at the point where the structure becomes a mechanism, ignore additional straining). A set of the capacity curve has been illustrated in Fig. 1 for 3 storey models, and Table 2 summarises the value of the control point of all building model considered.

2.3 *Damage State Threshold ($\widehat{S}_{d,ds}$) and Damage State Variability (β_{ds})*

Barbat et al. [2] estimated the value of the damage state threshold for different states, as slight at 70% of yield point, moderate at yield point, extensive as yield in addition to 25% of the difference of ultimate and yield and complete at ultimate point.

Table 4 displays the β_{ds} for different damage states taken from HAZUS. The damage state variability and capability variability are considered moderate for analysis since moderate damage applies to responses at or just above yield. Significance of degradation factor as 0.9, 0.5, 0.1 and 0.1; equivalent to slight, moderate, extensive and complete collapse damage state, respectively. Table 3 indicates that the overall β_{ds} decreases as the number of storeys rises, whilst β_{ds} increases for a constant storey

Table 2 Summary of control point

Storey (S)	Control points	Slab thickness in mm		
		Square	L-shape	T-shape
3	(D_y) m	0.010	0.010	0.010
	(A_y)	0.550	0.600	0.560
	(A_u)	0.730	0.300	0.730
	(D_u) m	0.050	0.030	0.025
6	(D_y) m	0.020	0.018	0.020
	(A_y)	0.250	0.250	0.270
	(A_u)	0.350	0.400	0.400
	(D_u) m	0.060	0.070	0.075
12	(D_y) m	0.030	0.020	0.020
	(A_y)	0.070	0.070	0.080
	(A_u)	0.160	0.170	0.170
	(D_u) m	0.150	0.160	0.160

Table 3 Fragility curve building parameters

Damage state (storey)	Shape	Slight		Moderate		Extensive		Collapse	
		$\widehat{S}_{d,\mathrm{ds}}$	β_S	$\widehat{S}_{d,\mathrm{ds}}$	β_M	$\widehat{S}_{d,\mathrm{ds}}$	β_E	$\widehat{S}_{d,\mathrm{ds}}$	β_C
C1L (3 storey)	S	07.00	0.80	10.00	0.95	20.00	1.05	50.00	1.05
	L	07.00	0.80	10.00	0.95	15.00	1.05	30.00	1.05
	T	07.00	0.80	10.00	0.95	13.75	1.05	25.00	1.05
C1M (6 storey)	S	14.00	0.75	20.00	0.85	30.00	1.00	60.00	1.00
	L	12.60	0.75	18.00	0.85	31.00	1.00	70.00	1.00
	T	14.00	0.75	20.00	0.85	33.75	1.00	75.00	1.00
C1H (12 storey)	S	21.00	0.75	30.00	0.85	60.00	1.00	150.0	1.00
	L	14.00	0.75	20.00	0.85	55.00	1.00	160.0	1.00
	T	14.00	0.75	20.00	0.85	56.25	1.00	165.0	1.00

height as the damage level increases commencing slight to collapse. In the Table 3, C1-concrete structures; L as low, M for medium and H for high rise [8].

2.4 Fragility Curve Development Using HAZUS

In Table 4, a lognormal probability distribution function based on HAZUS methodology (2009) is used and tabulated using Eq. (1). Furthermore, as per HAZUS MH MR1, attention must be paid because the distribution may not always be the best fit

Table 4 Cumulative damage probability of building

Model	Slight	Moderate	Extensive	Collapse
3 S	0.827	0.663	0.390	0.124
3 L	0.809	0.641	0.477	0.236
3 T	0.827	0.663	0.530	0.311
6 S	0.944	0.836	0.665	0.395
6 L	0.958	0.865	0.653	0.337
6 T	0.944	0.836	0.622	0.312
12 S	0.979	0.914	0.681	0.328
12 L	0.995	0.968	0.711	0.305
12 T	0.995	0.968	0.704	0.294

Note Here, 3, 6 and 12 are storeys; and S, L and T-shape in planar view

(2003).

$$P_f(d_s/S_d) = \varphi\left[\frac{1}{\beta_{\text{ds}}}.\ln\left(\frac{S_d}{\overline{S}_{d,\text{ds}}}\right)\right] \tag{1}$$

where ϕ = the standard normal cumulative distribution function; βds = standard deviation of the natural logarithm of spectral displacement for damage state, ds; *Sd* = spectral displacement; $S_{d,\text{ds}}$ = median value of spectral displacement at which the structure touches the damage state threshold, ds; $P_f(\cdot)$ = probability of being at or exceeding a particular damage state (ds). The fragility curves are being plotted in Fig. 2.

3 Conclusions

Using the guidance given in the HAZUS manuals, a fragility analysis was performed to establish a fragility curve that characterises potentially expected structural damage. Focussing on the effect of the no. of storeys of the structure; lesser no. of the storey is more liable to moderate damage. The probability of occurrence of all damage state rises due to the increase in the no. of storeys. Concerning the plan configuration, the buildings at significant risk are the L shape building as compared to T shaped ones. However, the variations are not overly large in the cases examined here, confirming the notion that a complex plan configuration is not the best option in seismic areas. This technique can be used to measure the amount of building damage associated with a given spectral displacement value. The HAZUS approach also creates a quick and simple method for assessing seismic risk for various types of structures. Fragility curves are used by researchers as well as construction engineers to forecast the overall

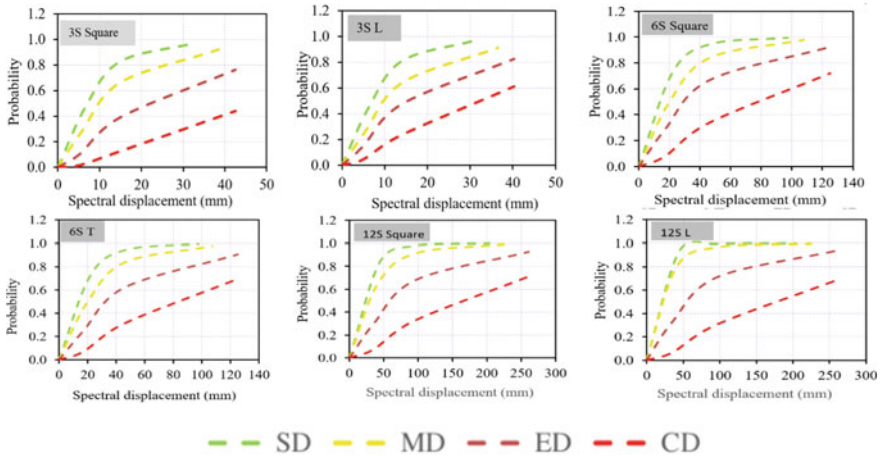

Fig. 2 Fragility curves for models

behaviour of a building in an event of a known earthquake, necessitating the need for structural retrofitting.

References

1. ATC-40 (1996) Seismic evaluation and retrofit of concrete buildings. Volume ATC-40 report, Applied Technology Council
2. Barbat A, Pujades LG, Lantada N, Moreno R (2008) Seismic damage evaluation in urban areas using a capacity spectrum based method: application to Barcelona. Soil Dyn Earthq Eng Urban Earthquake Hazard Damage Assess 28(10–11):851–865
3. Billah A, Alam M (2014) Seismic fragility assessment of highway bridges: a state-of-the-art review. Struct Infrastruct Eng 1–29
4. BIS IS 1893 (2002) Criteria for earthquake resistant design of structures, Part 1. New Delhi
5. BIS IS 456 (2000) Plain and reinforced concrete code of practice. New Delhi
6. Calvi GM, Pinho R, Magenes G, Bommer JJ, Restrepo-Velez LF, Crowley H (2006) Development of seismic vulnerability assessment methodologies over the past 30 years. J Earthquake Technol 472(3):75–104
7. D'Ayala D, Meslem A (2013) Sensitivity of analytical fragility functions to capacity-related parameters. GEM Foundation
8. Federal Emergency Management Agency (2003) Earthquake loss estimation methodology, HAZUS.®-MH MR1, Advanced Engineering Building Module, Technical and User's Manual. FEMA, Mitigation Division, Washington, DC
9. Federal Emergency Management Agency (2009) Multi-hazard loss methodology, Earthquake Model, HAZUS.®-MH MR4, Technical Manual. Department of Homeland security, emergency Preparedness and Response Directorate, FEMA, Washington, DC
10. Federal Emergency Management Agency (2000) Prestandard and commentary for seismic rehabilitation of buildings. FEMA-356, Washington, DC

11. Kircher CA, Whitmam RV, Holmes WT (2006) HAZUS earthquake loss estimation methods. Nat Hazards Rev 7:45–59
12. Maske A, Maske N, Shiras P (2014) Pushover analysis of reinforced concrete frame structures: a case study. (IJATES) 2:118–128
13. Porte K (2015). Beginner's guide to fragility, vulnerability, and risk. Encyclopedia Earthquake Eng 235–260
14. Patel N, Vasanwala SA (2020) Propagating fragility curve for RC buildings via Hazus methodology. Mater Today Proc 32(3):314–320

Pushover Analysis: Recent State of Art

Moksha A. Shah and Nirav K. Patel

Abstract Any building should be designed in such a way that it should withstand an earthquake. The damage to the building construction during the earthquake demonstrated the need for seismic risk assessment to predict the consequences of earthquakes and evaluate their vulnerability. Engineered and non-engineered buildings may collapse during seismic events is the foremost contributor which leads to the loss of lives and wounds to individuals. The building deforms inelastically during the seismic action. Performance-based seismic design is a modernized technique that is earthquake resistance that can predict the performance of structure using rigorous nonlinear static analysis. Pushover analysis is a nonlinear static analysis that is mostly used for assessing the performance of the structure. Pushover analysis was introduced in the 1970s, and it is a standardized design approach for structures to accomplish the predictable overall performance of the structure. During a seismic action, pushover analysis consists gravity loads and monotonically increasing lateral forces till the design displacement is achieved. The structure is pushed until the limit state or collapse condition and plotted the graph of shear force v/s lateral displacement at each increment. It shows the seismic performance of the structure and additionally gives clues of forwarding movement of destruction and the end failure of the structural component.

Keywords Pushover · Performance-based design · Nonlinear static analysis · Earthquake engineering

1 Introduction

Earthquakes are a natural disaster, and the impact of an earthquake on metropolitan conditions may be delivered uncountable misfortunes to society. Natural hazard like earthquakes is unpredictable and devastating which causes loss of human lives. Territory turns into high-risk areas when there is a high population and buildings

M. A. Shah (✉) · N. K. Patel
Civil Engineering Department, Navrachana University, Vadodara, Gujarat, India

B. Kondraivendhan et al. (eds.), *Sustainable Building Materials and Construction*,
Lecture Notes in Civil Engineering 222,
https://doi.org/10.1007/978-981-16-8496-8_31

and infrastructures are unprotected. This happens because the faulty and inadequate design and creation of structures in megacities are under serious hazard. Designers should be more concerned about constructing different load-resistant members by knowing their necessity and its overall performance within the structure [1].

The main reason for adopting dynamic seismic analysis because of lack of uniform standards, construction shortages, newly revised codes, change in design traditions, changes in building uses, etc. Many traditional buildings do not follow current design requirements. As a result, current buildings must be classified in terms of their ability to withstand expected earthquake response before retrofitting activities can begin [2].

Structures experienced inelastic deformation under huge earthquakes when it is designed by considering elastic behavior. The actual behavior of structures is decided on the basis of the overall performance of primarily based design techniques under such conditions. In the construction of both new and old buildings, nonlinear analysis can be extremely useful [11]. A nonlinear analysis is used to analyze and design retrofit possibilities for old buildings, as well as to construct a modern structure that uses structural materials, structures, and other characteristics that do not follow today's standards.

2 Performance-Based Design

The word "performance-based design" relates to a method of communicating systemic norms in terms of achieving a particular performance goal. The maximum appropriate damage state for a defined seismic risk is used to represent seismic efficiency. Deformation is taken into account in execution-based design, whereas strength is taken into account for forced-based design [15]. However, more significant is seismic performance deformation. Generally, the target displacement method is used for designing to achieve more strength for the nonlinear behavior of the structures. Potential damage in any structural member can figure out by displacement-based design, so that it tends to be retrofitted. This method is used for both existing as well as for new structures [3].

3 Pushover Analysis

Pushover analysis is an efficient and great option in contrast to dynamic time-history analysis, due to its simplicity [10]. It is equipped for giving significant underlying response data. Pushover analysis indicates the result of series of yielding and destruction of member and primary level. For developing a capacity curve of any building, a sequence of incremental static evaluations is to be performed. The load magnitude will increase till the building attains the target displacement.

The term 'pushover curve' or 'capacity curve' refers to any curve that depicts the correlation between base shear and roof displacement. The design's strength,

deformity limits, and how the structure carries beyond the elastic limit are defined by the pushover curve [2].

3.1 Limitation of Pushover Analysis

1. Estimation of deformity concluded from pushover analysis is that when the structure has higher mode effects, it might be inaccurate.
2. Displacement method is more accurate and performed well as compared to the force control method for analysis purposes.
3. Damage is only a function of primary deformation, according to nonlinear static pushover analysis. It takes into account period impacts, stress reversal participants, and the need for accumulated energy dissipation [14].
4. The forward-developing changes in modal properties of a system which is not taken into consideration when it is exposed to cyclic nonlinear yielding during earthquakes [14].

4 Building Performance Level

I Operational Building Performance Level: There is no destruction to the underlying and non-primary components in the structures. This level of performance is considered the most efficient level [12].

II Immediate Occupancy Building Performance Level: Damage to structural components is minimal, and damage to non-structural elements is restricted. After an earthquake, the building is absolutely safe to reoccupy. The member's strength and stiffness are virtually intact. There is no visible concrete crushing or a hairline fracture [12].

III Life Safety Building Performance Level: Extensive destruction to both the underlying and non-primary elements. Extensive damage is observed in beams. There might be spalling of concrete cover in columns. Major structural repair work can be done and partial repair before reoccupying [12].

IV Collapse Prevention Building Performance Level: Deep cracks have appeared, but the structure will not collapse. Repairs will not be recommended; in most situations, the structure will have to be dismantled. Degradation of lateral load resisting system. The vertical load system supports gravity load without any margin of safety against collapse [12].

5 Literature Review

Ahmed et al. [4] the study based on different types of shear walls is considered. Four shear walls are sided shear wall, edge double core shear wall, double middle core

shear wall, and single middle core shear wall for three, four, five, and six spans. The end result indicates that the placement of shear walls in different locations has a greater impact on the performance of buildings. The more accurate result is found in three and five span in the double middle core. In four-span building, better performance is found in the single and double middle core. For the six span, excellent performance is in single-core and double middle core buildings.

Deep and Raju [5] the researchers considered the G+9 residential high-rise RCC structure. Comparison is made for pushover analysis on four different seismic zones of India having the same structural properties. The analysis result shows that the base shear and displacement have been progressively increased in higher zones. Hinges were initially produced in the beam.

Oswal and Shinde [6] this study points out a nonlinear analysis of structures. The dynamic analysis and pushover analysis for a six-story reinforced concrete building are compared. It can be shown from the result that more hinges evolved in the beams than the columns. Pushover analysis revealed demand, capability, and plastic hinges, providing insight into the actual behavior of structures.

Anwar et al. [7] the literature is about the study of nonlinear static analysis on RCC buildings with having vertical irregularities. In this study, two types of vertical irregularities are considered. One is mass irregularities, and another is stiffness irregular for G+7 story in seismic zone V. Mass and stiffness irregularities considered at first, fifth, and eighth story. Story drifts increased at the bottom story are more. The heavier mass is experienced at the middle height of the building and has a significant effect on the story shear. Stiffness irregularities have a crucial effect on story displacement. The seismic capacity of the regular buildings falls under the "immediate occupancy" level and mass irregular buildings fall under the "collapse" level, whereas stiffness building falls under the "life of safety" level.

Shinde et al. [8] carried out a study of a pushover analysis of high-rise buildings to find out the effect of seismic reaction of G+10 RC structure. The result shows that the performance point of base shear from the pushover analysis is more as compared to the performance point of concept base shear.

Hakim et al. [2] the paper covers the seismic computation of an RC building using pushover analysis. A six-story building is analyzed using SAP2000 and considered displacement control method. Pushover analysis can predict the failure mechanism of the structure. It also shows the redistribution of the forces and classifies the vulnerable components of the building. It gives information for repairing work for elements. It cannot properly constitute dynamic phenomena.

Dinar et al. [1] the literature deals with the descriptive study pushover analysis of RCC structures considering rigid joints. Studies evaluate and compare the overall performance of a soft story and shear wall for seven-story buildings by considering six different infill percentage cases and shear wall in two opposite formats. The end result shows when the consideration of infill wall increases the overall performance of the structure will increase. Shear wall performed very well as compared to infill wall. It shows three times more resistance in opposition to any lateral loads. The position of the shear wall plays an important role in the seismic performance of the

structure. When the shear wall is located on the verge of structure, it might be a better option than a parallel shear wall configuration.

Anwaruddin and Saleemuddin [9] focused on a study on pushover analysis of medium-rise RCC frame with and without considering vertical irregularities. The study was carried out on five models with G+3 medium-rise RCC buildings situated in zone V and models having irregularities 200%–300%. Flexure and shear demand reduces as the vertical irregularities increased. The structure's lateral displacement is decreased when the percentage of irregularities increased. As the vertical irregularities increases, the story drift decreases and the value continues within allowable limits.

6 Conclusions

From the literature review, it can be concluding that pushover analysis is an important method for analyzing structural behavior in a nonlinear zone. It is a simple and less time-consuming method. Flexure, shear demand, lateral displacement, and story drift are reducing as the increase in vertical irregularity either in mass or in stiffness. If the structure is protected under earthquake loading, the performance point of base shear should be greater than the concept base shear. The placement of shear walls has a considerable effect on the overall performance levels of buildings. Double middle core shear walls are more effective as compared to other shear walls. Pushover analysis performed well for regular shape buildings, but due to some limitations of pushover analysis, new methods were developed for analyzing modern irregular shape buildings precisely and accurately. There is more scope for further study in this domain.

References

1. Dinar MY, Hossain I, Biswas RK, Rana MM (2014) Descriptive study of pushover analysis in RCC structures of rigid joint. IOSR J Mech Civil Eng 11:60–68
2. Hakim RA, Alama MS, Ashour SA (2014) Seismic assessment of an RC building using pushover analysis. Eng Technol Appl Sci Res 4(3):631–635
3. Rana N, Rana S (2015) Non-linear static analysis (pushover analysis) a review. Int J Eng Tech Res 3:7
4. Ahmed MM, Akter A, Roy S (2018) Pushover analysis of RCC buildings with different types of shear walls and different number of spans by frame elements based model method. Int J Sci Res 8
5. Deep VM, Raju PP (2017) Pushover analysis of RC building: comparative study on seismic zones of India. Int J Civil Eng Technol 8(4):567–578
6. Oswal N, Shinde VV (2016) A nonlinear analysis of structure: pushover analysis. Int J Innovations Eng Res Technol 3
7. Anwar SF, Firasath Ali MD, Malik SA (2016) Study on pushover analysis of RC frames with vertical irregularity. Global J Eng Sci Res 3:10

8. Shinde DN, Nair Veena V, PudaleYojana M (2014) Pushover analysis of multistory building. Int J Res Eng Technol 3:3
9. Akberuddin MAM, Saleemuddin MZ (2013) Pushover analysis of medium rise multi-story RCC frame with and without vertical irregularity. J Eng Res Appl 3(5):540–546
10. Mwafy AM, Elnashai AS (2001) Static pushover versus dynamic collapse analysis of RC buildings. Eng Struct 23:5. https://doi.org/10.1016/S0141-0296(00)00068-7
11. Ashwini KC, Manjunath YM (2017) Comparative study of pushover analysis on RCC structures. Int J Eng Res Technol 6
12. ATC-40 (1996) Seismic evaluation and retrofit of concrete buildings, vol ATC-40 Report, Applied Technology Council
13. FEMA. FEMA 356 (2000) Nehrp prestandard and commentary for the seismic rehabilitation of buildings
14. Krawinkler H, Seneviratna GDPK (1998) Pros and cons of a pushover analysis of seismic performance evaluation. Eng Struct 20:4–6. https://doi.org/10.1016/S0141-0296(97)00092-8
15. Kassem MM, Mohamed Nazri F, NoroozinejadFarsangi E (2020) The seismic vulnerability assessment methodologies: A state-of-the-art review. Ain Shams Eng J. https://doi.org/10.1016/j.asej.2020.04.001

Incremental Dynamic Analysis of Geometrically Irregular RCC Buildings

Nidhi J. Sitapra, Kunal P. Shukla, Chirag M. Asodariya, and Amit J. Thoriya

Abstract Focussed on parametric analysis of irregular building, the paper encompasses a study of seismic behaviour of RCC multi-storey framed structures, comprising of different plan and vertical geometric irregularities, using incremental dynamic analysis. The frame design was meant to incorporate the effective moment of inertia clause prescribed in the latest revision of IS 1893 (part-1) 2016. Frames, when subjected to far-field, near-field and fling-step ground motions, revealed a wide range of difference between behaviour of regular and irregular buildings in terms of inter-storey drift demands at increasing ground acceleration values. Shape and behaviour of IDA curves were used to assess acceleration and deceleration experienced by the buildings. For far-field ground motions, buildings possessing less or no geometric irregularity were affected less as compared to buildings possessing more geometric irregularities. For near-field ground motions with and without fling-step characteristics, buildings possessing more geometric irregularities were affected less as compared to buildings possessing less or no geometric irregularity.

Keywords Irregular buildings · Incremental dynamic analysis · IDA · Seismic performance

N. J. Sitapra (✉) · K. P. Shukla · C. M. Asodariya · A. J. Thoriya
Department of Civil Engineering, Marwadi Education Foundation Group of Institutions, Faculty of PG Studies, Rajkot, Gujarat 360003, India

K. P. Shukla
e-mail: kunal.shukla@marwadieducation.edu.in

C. M. Asodariya
e-mail: chirag.asodariya@marwadieducation.edu.in

A. J. Thoriya
e-mail: amitkumar.thoriya@marwadieducation.edu.in

B. Kondraivendhan et al. (eds.), *Sustainable Building Materials and Construction*,
Lecture Notes in Civil Engineering 222,
https://doi.org/10.1007/978-981-16-8496-8_32

1 Introduction

As per FEMA 356 [1], due to the dynamic and non-linear nature of the earthquake, non-linear dynamic analysis is the only method that describes the actual behaviour of a structure during an earthquake and depicts more realistic results, as compared to other analysis methods. Incremental dynamic analysis (IDA) has emerged as an accurate tool to estimate the capacity of the structure and its non-linear behaviour. IDA involves performing multiple non-linear dynamic analyses of a structural each scaled to several levels of seismic intensity to force the structure through the entire range of behaviour, from elastic to inelastic and finally to global dynamic instability, where the structure reaches its ultimate capacity and essentially experiences collapse [2].

2 IDA Procedure

IDA involves a series of dynamic non-linear runs performed under scaled accelerogram time histories, whose IMs are selected to cover the whole range from elastic to non-linear and finally to collapse of the structure.

The steps followed in IDA [3] have been listed here:

1. A set of earthquake time histories are selected to be applied on the structure under consideration.
2. Selecting appropriate scalable IMs and DM.
3. Accelerograms of the selected time histories are scaled using a set of increasing scale factors.
4. The resultant scaled accelerograms are then used to perform a series of non-linear runs of time history analysis on the structural model.
5. DMs of the structural model at each level IM of the scaled ground motion are used to plot IDA curves.
6. Limit states are applied on the IDA curves, by appropriate DM-based rule or IM-based rule, to know the regions in curve where the structure exceeds limits prescribed in guidelines.
7. Behaviour of IDA curves are interpreted.

3 Modelling Assumptions and Ground Motion Records

A ground motion database of time histories listed in Table 1 was compiled to include three suits of ground motions to cover a range of frequency content, duration and amplitude, considering single direction component.

A ten-storey regular bare frame, with bay width of 3 m in both directions and 3 m storey height, was modelled as the reference frame. All the irregular building

Table 1 Time-history records

	Earthquake	Magnitude	Recording station	PGA (g)
Far-field	Loma Prieta, 1989	6.9	Capitola (capx)	0.42
	Chamoli, 1999	6.4	Gopeshwar (chamoli)	0.36
	Imperial Valley, 1940	6.95	El Centro Array #9 (elcx)	0.31
	Superstition Hills, 1987	6.7	El Centro Imp. Co. Centre (iccx)	0.51
	Northridge, 1994	6.7	Northridge-Saticoy St. (stcx)	0.53
Near-field	Imperial Valley, California, 1979	6.6	El Centro Array #5 (EQ11)	0.37
			El Centro Array #7 (EQ21)	0.46
	Northridge, California, 1994	6.7	Newhall (EQ31)	0.72
			Rinaldi (EQ51)	0.89
			Sylmar (EQ61)	0.73
Fling-step	Chi-chi, 1999	7.6	TCU052_NS	0.44
			TCU068_EW	0.50
			TCU074_EW	0.58
			TCU084_NS	0.42
			TCU129_NS	0.61

configurations were derived by eliminating certain bays from the reference frame as shown in Fig. 1. Beams and columns were modelled to possess effective moment of inertia for cracked section as prescribed in the latest revision of IS 1893:2016 [4]. All frames were assumed to be located in zone-V as per seismic zones defined in IS 1893. All members were designed in SAP2000 software as per IS 456:2000 considering loads and load combinations complying to IS 875 parts 1, 2 and 5 and considering M25 grade concrete.

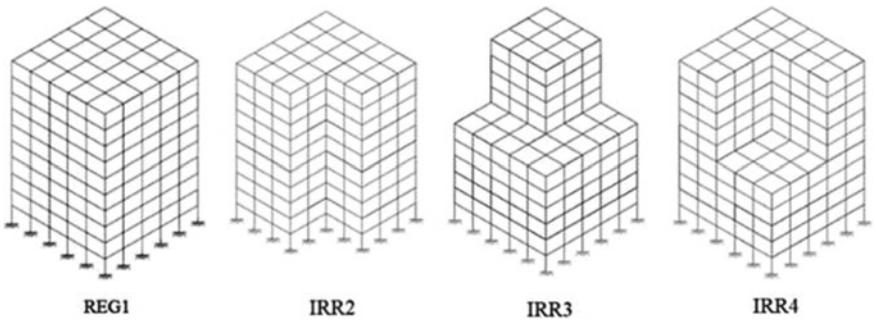

Fig. 1 Models considered for the analysis

4 Performing the Analysis

The scope of IDA performed was limited to the following control parameters [5] for plotting the IDA curves:

1. Intensity measures (IM): Out of various scalable IMs, peak ground acceleration (PGA) was selected to plot the IDA curves.
2. Damage measures (DM): Maximum inter-storey drift-ratio % was selected as the damage measure (DM) as it relates well to joint rotations and both global and local storey collapse.
3. Scale factors: All far-field and near-field time-history accelerograms were scaled using scale factors 0.1–2.0 and all fling-step time histories using scale factors 0.1–1.5, at equal increments of 0.1 for each.

One model for each building subjected to one time-history function at a time were prepared and analysed in SAP2000 v21.2.0. Thus, for 4 buildings and 15 time histories, a total of 60 models were prepared in tool. All the models were subjected to a series of non-linear direct-integration time-history analysis runs for each of the scaled time-history accelerograms, resulting into a total of 1100 NLTHA runs.

5 Results and Post-Processing

For the critical frames, where the members reach their yield capacities first as compared to other frames of the building, inter-storey drift ratio was calculated from the displacement values at storey levels pertaining to the first mode obtained via the analyses. IDA curves were plotted for PGA versus maximum inter-storey drift-ratio %.

Using the results of simulation, time history-wise combined IDA curves showing behaviour of four buildings for one time-history record at a time were plotted (Fig. 2).

Similarly, building-wise multi-record IDA plots showing behaviour of each building when subjected to multiple time histories from different suits of ground motions were also plotted (Fig. 3).

Limit states applied on the IDA curves include onset of collapse at initial yielding as per hinge rotation capacities defined in FEMA 356, and the design basis earthquake (DBE) and maximum considered earthquake (MCE) limits are defined as per IS 1893.

6 Discussion of Results

Overall, the IDA curves for far-field records showed a hardening behaviour; curves for near-field records showed a softening behaviour, and curves for fling-step records showed an initial weaving behaviour with eventual softening.

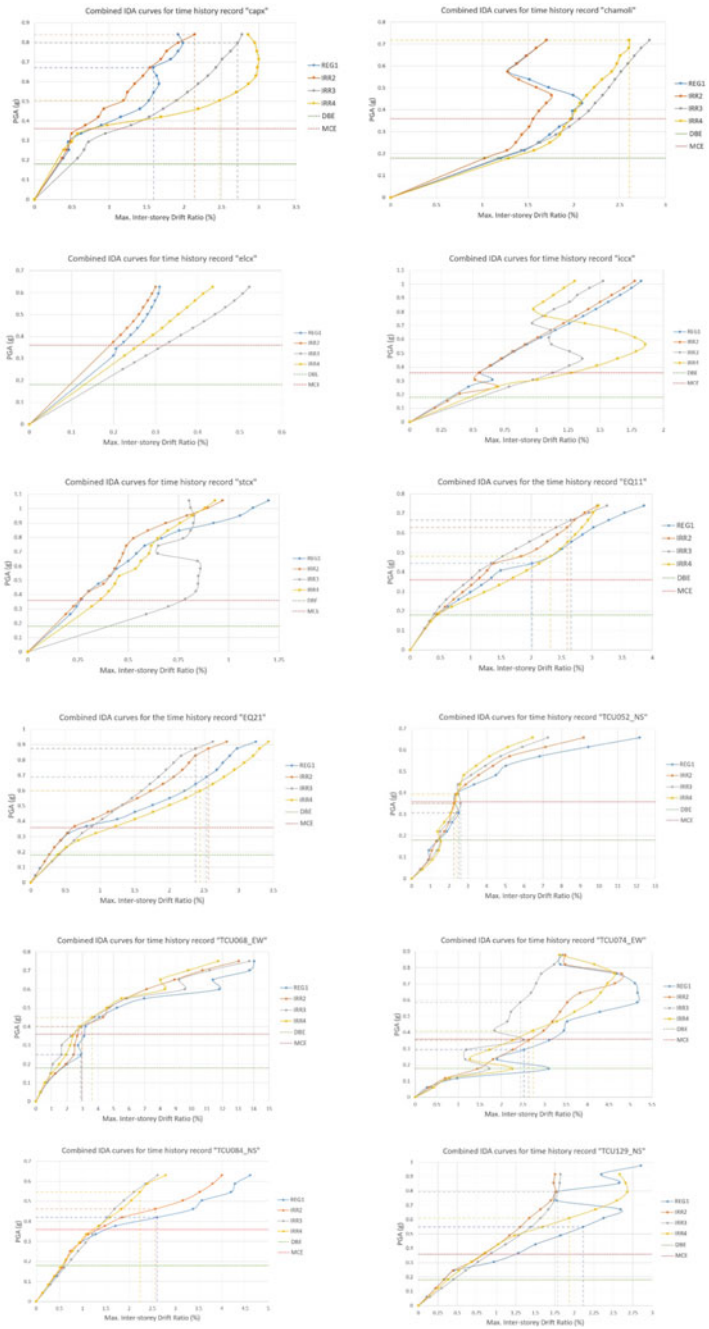

Fig. 2 Time history-wise IDA plot comparing behaviour of all four buildings for time history record

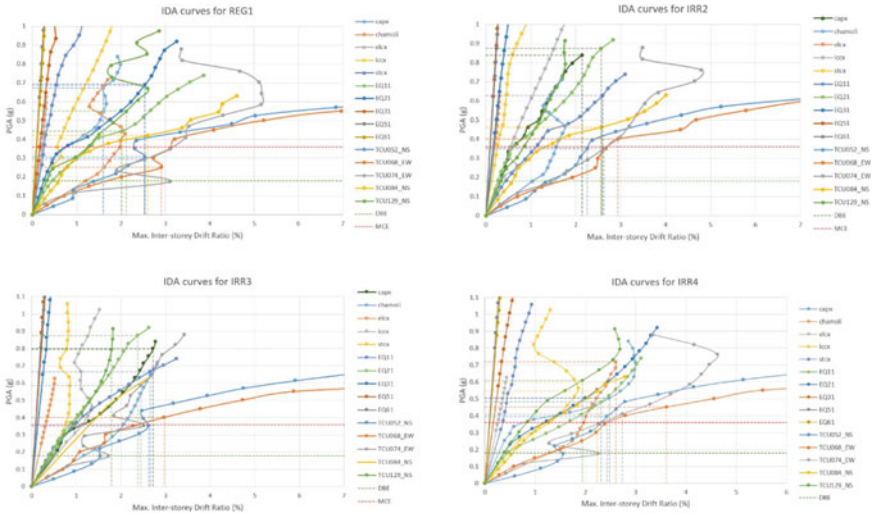

Fig. 3 Building-wise multi-record IDA plots for each building subjected 15 ground motions

The multi-record IDA curves for each building showing comparison of behaviour due to different time histories showed that buildings when subjected to far-field ground motions and near-field ground motions without fling component reached the collapse limits at PGA values well above the PGA of maximum considered earthquake (MCE) PGA = 0.36 g, and the same buildings when subjected to fling-step ground motions reached the collapse limit at PGA values below that of MCE but above the PGA of design basis earthquake (DBE) PGA = 0.18 g.

From the combined IDA curves comparing time history-wise behaviour of different buildings for every time history, it was observed that for far-field ground motions, the buildings REG1 and IRR2 were affected less as compared to IRR3 and IRR4. Which means, the buildings possessing less or no geometric irregularity were affected less as compared to the buildings possessing more geometric irregularities. For near-field ground motions with and without fling-step characteristics, it was observed that the buildings IRR3 and IRR4 were affected less as compared to REG1 and IRR2. Which means, the buildings possessing more geometric irregularities were affected less as compared to the buildings possessing less or no geometric irregularity.

7 Conclusions

The work represents the use of incremental dynamic analysis (IDA) method to extensively analyse the seismic behaviour of irregular RCC multi-storey framed structures, comprising of different plan and vertical geometric irregularities, when subjected to

far-field, near-field and fling-step ground motions. The effective moment of inertia clause prescribed in the latest revision of IS 1893 (part-1) [6] was incorporated in the design of the frames. Shape and behaviour of IDA curves were used to assess the acceleration and deceleration experienced by the buildings. Comparison of behaviour of different buildings for a particular time history as well as the behaviour of every particular building when subjected to different time histories reveals a wide range of difference in behaviour of regular and irregular buildings in terms of inter-storey drift demands of the structures at increasing ground acceleration values.

It was observed that buildings, when subjected to far-field ground motions and near-field ground motions without fling component, reached the collapse limits at PGA values well above the PGA of MCE, and the same buildings, when subjected to fling-step ground motions, reached the collapse limit at PGA values below that of MCE but above the PGA of DBE. It was observed that for far-field ground motions, the buildings possessing less or no geometric irregularity were affected less as compared to the buildings possessing more geometric irregularities. For near-field ground motions with and without fling-step characteristics, it was observed that the buildings possessing more geometric irregularities were affected less as compared to the buildings possessing less or no geometric irregularity.

Acknowledgements The research described in this paper was guided by Prof. Kunal P. Shukla, Prof. Chirag M. Asodariya and Prof. Amit J. Thoriya from Department of Civil Engineering, Marwadi Education Foundation Group of Institutions, Morbi Road Gauridad Rajkot 360003, Gujarat, India.

References

1. FEMA 356 (2000) Prestandard and commentary for the seismic rehabilitation of buildings. Federal Emergency Management Agency, Washington, D.C. https://law.resource.org/pub/us/code/bsc.ca.gov/sibr/gov.fema.fema356.pdf
2. Vamvatsikos D, Jalayer F, Cornell CA (2003) Application of incremental dynamic analysis to an RC-structure. In: FIB symposium on concrete structures in seismic regions, Athens. https://www.researchgate.net/publication/228578842
3. Vamvatsikos D, Cornell CA (2002) Incremental dynamic analysis. Earthquake Engg Struct Dyn 31:491–514. https://doi.org/10.1002/eqe.141
4. Prajapati SK, Amin JA (2019) Seismic assessment of RC frame building designed using gross and cracked section as per Indian standards. Asian J Civil Eng 20:821–836. https://doi.org/10.1007/s42107-019-00147-9
5. Shimpi V, Bhat G (2017) Performance evaluation of RC frame structure through incremental dynamic analysis. Indian J Sci Technol 10(3):1–8. https://doi.org/10.17485/ijst/2017/v10i3/94891
6. IS 1893 Part-1 (2016) Criteria for earthquake resistant design of structures. Bureau of Indian Standard s; Manak Bhavan, 9 Bahadur Shah Zafar marg, New Delhi, India. https://law.resource.org/pub/in/bis/S03/is.1893.1.2002.pdf

Cable Supported Bridges for Long to Superlong Spans

J. H. Gabra and A. K. Desai

Abstract Since ages, bridges are pivotal and maintained to be the lifeline in the area transportation and allied services; beaming in demand of long to superlong bridges owing to modernization, globalization and increased population; leading to erection of numerous fascinating, mesmerizing bridges. For optimization, owing to their structural behaviour, cable supported bridges have been preferred nomenclatured as **cable-stayed** type of **bridges** (CSBs), **suspension** type of **bridges** (SBs), **composite bridges** (CBs), **Cable-stayed-suspension hybrid bridges** (CSSHBs). CSSHB should inherently be preferred owing to the fact that it incorporates advantages of both CSBs and SBs for bridges having longer spans. The analysis of bridges is highly needed, as its failures may/can be catastrophic, thereby generating necessity to conceptualize the basic mechanism of loading and/or failures and incorporate them in the design/analysis—the possible reason(s) for such failures and possible remedial measures thereon. Some of the possible profile/arrangement/system of the cable supported bridges for very long-span are illustrated in this paper; wherein, models are prepared has using SAP2000 software. This study includes the response of the bridge(s) modelled (towards MTHA), with variation in cable system is adopted.

Keywords Cable-stayed-suspension hybrid bridge (CSSHB) · Modal time history analysis (MTHA) · SAP2000

1 Introduction

With growing infrastructure, globalization, recent advancement technology, need of bridges spanning long to superlong spans has immensely increased. And, owing to their structural behaviour, cable supported bridges have been preferred, which as

J. H. Gabra (✉)
H.A.M.D, G.P., Himatnagar, Gujarat, India

SVNIT, Surat, Gujarat, India

A. K. Desai
Civil Engineering Department, SVNIT, Surat, Gujarat, India

B. Kondraivendhan et al. (eds.), *Sustainable Building Materials and Construction*,
Lecture Notes in Civil Engineering 222,
https://doi.org/10.1007/978-981-16-8496-8_33

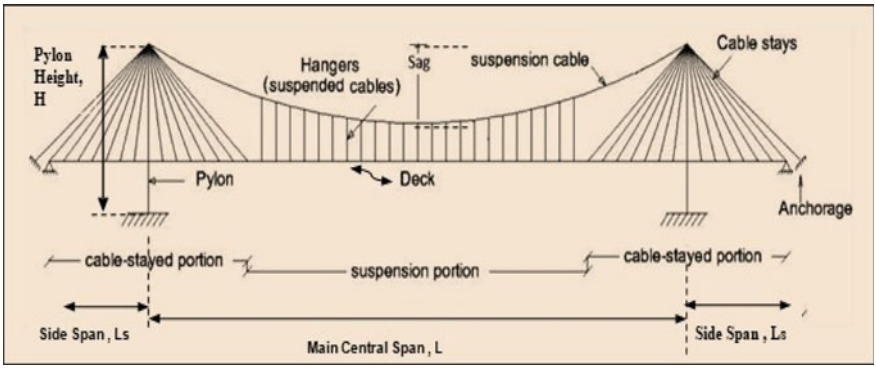

Fig. 1 CSSHB

any structure is subcategorized, respectively, into two categories of "super-structure" and "sub-structure", respectively. Depending upon the cable system adopted, it may result into cable-stayed bridge (CSB, hereafter) or suspension bridge; herein, CSB has comparative higher structural stiffness whilst the suspension bridge has better feasibility whilst offering longer span. It has been, therefore, obviously suggested/claimed that incorporating advantages of these two structural systems evolves meticulously, a hybrid/combined system, viz., Cable-stayed-suspension hybrid bridge (CSSHB, hereafter).

Components formulating the superstructure, as illustrated in Fig. 1, comprises of ed as

1. Cables (main cables—cable-stayed and suspension cable, stay cables and hanger cables)
2. Pylon tower and 3. deck.

Herein, the stay cables made of steel (stranded or solid) can be arranged in a fan type, radial, harp pattern (system); the spatial arrangement of cables spatial arrangement of cable system adopted may be in a vertical plane or an inclined plane, single or double plane system. Similarly, tower can be of steel and/or RCC bearing geometry/shape which resembles twin frame or door shaped or H type shape, A shape, inverted Y, diamond shaped, etc. The deck can be constructed using steel and/or RCC or its combination and can be solid or box girder in c/s.

2 Literature Survey

An birds eye view regarding some of literature for CSBs can be categorized subsequently as development and description; static analysis procedures; dynamic analysis; seismic analysis; analysis of CSSHBs. However, brief of the research work carried out on CSSHB in particular can be illustrated as

- Zhang and Sun [1], in 2005, presented his work on "aerodynamic stability of CSSHBs"
- Zhang and Stern [2], in 2008, submitted his research on "wind-resistant design of CSSHBs"
- EGON KIVI [3], in 2009, presented his thesis on "structural Behaviour of CSSB"
- Bruno et al. [4], in 2009, presented A parametric study on the dynamic behaviour of combined cable-stayed and suspension bridges under moving loads
- Konstantakopoulos et al. [5], in 2010, proposed "A mathematical model for a combined cable system of bridges"
- Qiu et al. [6], in 2011, evaluated "analysis of structural parameters of CSSBs"
- Lonetti [7], in 2014, submitted "optimum design analysis of hybrid cable-stayed suspension bridges"
- Sevalia [8], in 2016, submitted his research thesis on "effect of geometrical aspects on static and dynamic behaviour of CSSHB".

3 Problem Statement

3.1 Introduction to the Software

Overhere for study, SAP2000 v 19.2.1, by CSI, Berkely, USA is used which is a FEM-basedtool enriched by various characteristics multiple coordinate system; powerful graphical display; frame, cable and shell structural elements; frequency dependent link and support properties; wide range and variety of loading and analysis options including loading functions of time history, response spectrum, etc.; Geometric nonlinearity and many more.

3.2 Modelling of CSSHB with 319 m + 1400 m + 319 m as Span Configuration

Figure 2 illustrates extruded 3D model of CSSHB generated of the problem considered, which is similar to *Bridge of East channel of Lingding Strait in China.*

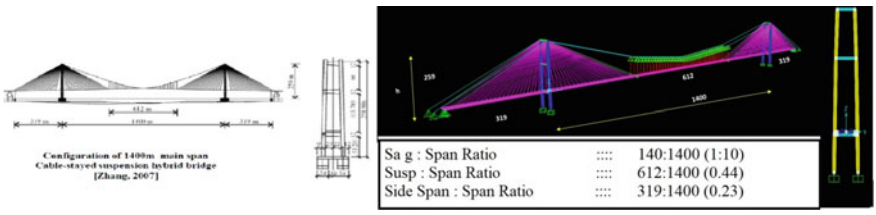

Fig. 2 Problem statement: CSSHB

It is an earth-anchored CSSHB with 319 + 1400 + 319 m as span configuration, (side span to main span ratio of 0.23); wherein, the main span of 1400 m consists of 788 m and 612 m as the cable-stayed portion and suspension portion, respectively. The two main cables are spaced is 34 m apart laterally maintaining a cable sag to span ratio of 1/10, such that the vertical hangers follow a c/c spacing of 18 m along longitudinal direction whereas The anchorage of stay cables to the girder is after every 18 m in the central span and 14 m in the side spans, respectively, following **fan type** geometric profile/pattern.

The **deck c/s** provided is a streamlined box girder (c/s 36.8 m × 3.8 m), made up of steel. The towers, made up of M45 concrete, are door shaped (H shaped pylon) frames with three transverse beams along its height, wherein height above ground is about 259 m. Table 1 entabulates the properties of the material used and various cross sectional parameters adopted. **Girder** was modelled as frame element, **pylon tower (H type)** modelled, as frame element using concrete with 6 m × 5.0 m c/s, 258.786 m high, (to note that height of pylon tower is slightly less than 1/5 of main central span) with 3 **transverse beams** (4 m × 2.5 m in c/s) along its height. The deck is subjected to DL of nearly 98 kN/m, LL of 50 kN/m in addition to side imposed dead load (parapet) of approx. 38 kN/m. Seismic time history details of Bhuj Earthquake of 30 Jan 2000, recorded at Ahmedabad, having magnitude of 7.7 on Ritcher scale, lasting for a duration of approx. 134 s, with a PGA of nearly 1.04 m/s^2 is considered for the study (far field EQ). Fixed condition (support) is adopted for the pylon footings.

Table 1 Material and c/s properties bridge

Property	Material	
	Fe345 steel	M45 concrete
Modulus of elasticity (E), kN/m^2	2.0×10^8	3.354×10^7
Unit weight (Υ) kN/m^3	76.973	24.993
Poisson's ratio (μ)	0.3	0.20
Shear modulus (G) kN/m^2	1.115×10^6	1.397×10^7
Coeff. of thermal expansion (α)	1.17×10^{-5}	0.55×10^{-5}

Particulars	Diameter (mm)	Area (mm^2)
Vertical hanger	90.3	6400
Main cable (SS)	635	367×10^3
Main cable (CS)	672	354,700
Stay cable (1)–(9)	100.9–135.4	8.00 to 14.41×10^3

Table 2 Validation: modal time period (MTHA)

Modes		Zhang, 2006		Sevaliya, 2015		Our results, 2018 (SAP2000 v19.2)		Difference, (%) Wrt to Sevaliya	
Type	Shape	T (sec)	F (Hz)	T (sec)	F (Hz)	T (sec)	F (Hz)	T	F
Lateral bending	1-S	14.51	0.0689	13.14	0.0761	13.09	0.0764	−0.38	+0.39

4 Results and Discussion

4.1 Validation

The bridge is analyzed to validate the software, SAP2000, and as such MTHA is carried out to study/understand the behaviour of bridge, in terms of evaluation of a set of modal properties in form of structural frequencies /time periods. Table 2 shows the comparison of our results and research paper results.

4.2 Other Geometrical Configurations Studied as Parametric Studies

4.2.1 Effect of Pylon Shape

After applying far fault ground motions on CSSHB for different pylon shapes, it is concluded that the H type tower gives minimum axial force and least displacement is in A-frame. In case of inverted Y and diamond type of shape almost same observations are noted for analysis for base reaction, axial force, in main cable (cs) and cable stay (c8) against dead load. Also the pylon top displacement along 3–3 axis is observed to be the same. However, lateral and longitudinal displacement of pylon top are observed not to be the same. (U1 is max in H type and least in A type) as can be illustrated in Fig. 3.

4.2.2 Effect of Sag to Span Ratio

Generally, it is observed that the catenary profile directly governs the angles of inclination the stay cables makes with girder and/or pylon and thereby the axial forces exerted in/on the cables; thus affects ultimately the stiffness and/or dynamic behaviour of the bridge on a whole. Table 3, illustrates the cable sag to the main span ratio considered and subsequently the behavioural aspects observed after analyzing the results of MTHA, When sag to main ratio is reduced from 1/10 to 1/12.6, time period reduces by about 2%. Pylon top displacement increases by 17% and axial

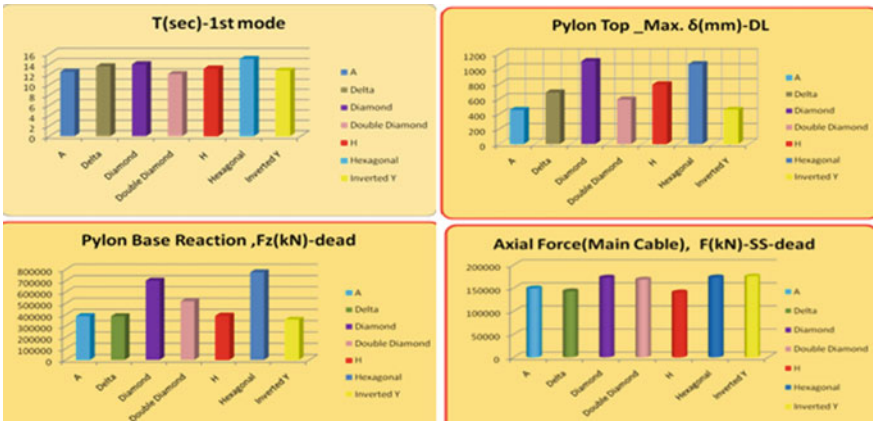

Fig. 3 Effect of pylon shape: CSSHB

Table 3 Study for cable sag to span ratios

Sag to span ratio	T(sec)-1st mode	Pylon top-max. δ(mm)-dead	Pylone base reaction Fz(kN)-dead	Main cable-axial force F(kN)-SS-dead
01:07.6	13.0796	778.73	388,917.7	138,181.67
01:10	13.0895	840.05	386,056.7	140,183.39
01:12.4	12.8341	990.72	404,724.1	167,081.33

force in main cable enhanced by 17%. Similarly, when sag to span ratio is increases from 1:10 to 1:7.6, time period is almost same.

5 Conclusion

- In this study, MTHA for 7 different types of pylon's shape as figured in Fig. 3 using SAP2000 software was carried out. H type tower gives optimal design as it induces least axial force amongst the group analyzed seconded by A type or inv. Y type of shape; owing to the fact that, H type provides probably more enhanced (torsional) stability and thenceforth more stiffness even though A shaped pylon results in least pylon top displacement in longitudinal direction. Modal time period of the bridge with double diamond shape pylon followed by A shaped pylon is less when compared to other two pylon shapes, owing to possible tripod effect.
- Sag_span ratio of 1:10 has yielded to be more optimal as compared to lower or higher ratios, however, the variation in modal time period, (after, MTHA) is minimal.

References

1. Zhang X, Bing-nan S (2005) Aerodynamic stability of cable-stayed-suspension hybrid bridges. J Zhejiang Univ Sci 6:869–874
2. Zhang X, Stern DA (2008) Wind-resistant design of cable-stayed-suspension hybrid bridges. In: Transportation and development innovative best practices (TDIBP2008), pp 444–449
3. EGON KIVI (2009) Structural behaviour of CSSB: thesis. ISSN 1406-4766
4. Bruno et al (2009) A parametric study on the dynamic behavior of combined cable-stayed and suspension bridges under moving loads. https://doi.org/10.1080/15502280902939452
5. Konstantakopoulos TG et al (2010) A mathematical model for a combined cablesystem of Bridges. Eng Struct 32:2717–2728
6. Qiu J et al (2011) Analysis of structural parameters of cable-stayed suspension bridges. Adv Mater Res 163–167:2068–2076
7. Lonetti P, Pascuzzo A (2014) Optimum design analysis of hybrid cable-stayed suspension bridges. Adv Eng Softw 73(2014):53–66
8. Savaliya G et al (2016) Effect of geometrical aspects on static and dynamic behaviour of CSSHB. Thesis, SVNIT Surat

Development of Fragility Curves for Performance Evaluation of R.C. Moment Resisting Frames Using Nonlinear Static Analysis

Khushali Y. Desai and Rutvik K. Sheth

Abstract Dreadful scenario of loss of life and assets are witnessed during unpredictable earthquake due to unintended structural failure. Hence, assessment of seismic vulnerability is required. To portray a realistic structural behaviour, performance evaluation using nonlinear analysis is carried out here with fragility curve development. Regular and plan irregular reinforced concrete (RC) moment resisting frames with 5 and 10 storeys are analysed for seismic zone III and V using ETABS software and designed as per IS code. The performance evaluation of frames is done with nonlinear pushover analysis using SeismoStruct. A probabilistic study of vulnerability is carried out in form of fragility curves with an assumption of lognormal distribution. Results are shown in terms of capacity curve profile and fragility curves considering performance levels as per ATC 40. It was observed that frames designed for seismic zone III has higher over-strength compared to its corresponding frame designed for zone V. It was also seen that there is negligible probability of exceedance of collapse prevention limit state for PGA corresponding to design basis earthquake.

Keywords RC frame · Nonlinear static analysis · Seismo struct · Reinforced concrete

1 Background

The fresh trend for development in the International Standards is to outline the codes for alternative design methods which are better representative of the performance of the structures rather than strength. Performance assessment methods for evaluating seismic demand and capacity of the structures can be broadly classified into: nonlinear static and dynamic analysis. Here, nonlinear static analysis is carried out under permanent vertical loads and gradually increasing lateral loads in order to estimate damage of structure as nonlinear dynamic analysis is highly computationally

K. Y. Desai (✉) · R. K. Sheth
Dharmsinh Desai University, Nadiad, Gujarat, India

B. Kondraivendhan et al. (eds.), *Sustainable Building Materials and Construction*,
Lecture Notes in Civil Engineering 222,
https://doi.org/10.1007/978-981-16-8496-8_34

intensive in nature. The behaviour of the structure is described by capacity curve that represents the relation amid the base shear and the peak displacement.

Vulnerability evaluations of structures are normally carried out for arbitrating the strengthening requirement for vital members against earthquakes. The best way to accomplish such assessments is fragility curves. It demonstrates the conditional probability that a response of a particular structure may exceed the performance limit at a given ground motion intensity. Fragility curve provides knowledge regarding the extent of damage, by which one can figure out the appropriate mitigation method as per possible damage.

2 Methodology of Fragility Curve Development

Fragility curves are the probability of failure in the form of damage state (DS) as a function of ground motion intensity measure (IM). For the present study, DS is taken as interstorey drift ratio (IDR) and IM is peak ground acceleration (PGA). If at a certain time instant, demand exceeds the capacity, safety is at stake. All permutations of capacity-demand variations during lifetime can hardly be predicted accurately. Hence probability distribution is to be done. Process of fragility curve development using nonlinear static analysis is as shown in Fig. 1.

- ADRS = Acceleration displacement response spectra
- Performance point is attained using equivalent linearization method from FEMA 440 [2].
- Fragility parameters of median and dispersion for immediate occupancy (IO), life safety (LS) and collapse prevention (CP) are computed. In the study, regression analysis is done using least square formulation [6]. Equation 1 shows the probability of exceedance of DS w.r.t IM [5]

$$P(\mathrm{DS} \geq \mathrm{ds}_i \,|\mathrm{IM}) = \varphi\left(\frac{\ln(\mathrm{IM}) - \lambda_{\mathrm{DS|IM}}}{\beta_{\mathrm{ds}_i}}\right) \tag{1}$$

where,

$\lambda_{\mathrm{DS|IM}}$ Lognormal mean of the generic structural response conditioned on the ground motion intensity (IM)

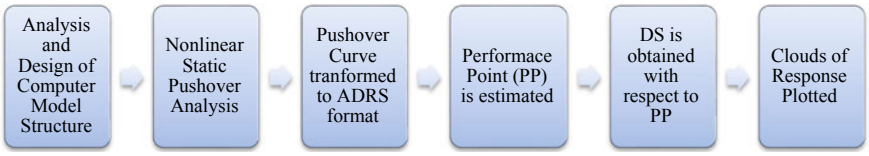

Fig. 1 Flow chart for fragility curve development

β_{ds_i} Total dispersion defined as the lognormal standard deviation of DS|IM
φ Standard normal cumulative distribution function.

3 Illustrative Problem

Reinforced concrete moment resisting regular and plan irregular (L-shape) frames with 5 and 10 storey are analysed using ETABS-2016 and designed as per IS code provisions [3]. The frames are considered to be resting on hard soil and lying in seismic zone III and zone V [4]. Each storey height is considered as 3.2 m. The floor area of both the frames are near to 150 m^2 with maximum bay width of 6 m. Dead load assumed, includes self-weight of members like column-beam, slabs and wall and the imposed load assumed was 4.00 kN/m^2. Concrete grade M25 and steel grade Fe415 was used for design. For envelop of load combinations, the design of each frame is carried out distinctly. For irregular frame, provision is made for increase in shear force on the lateral force resisting elements resulting from twisting about the vertical axis of the frame, arising due to eccentricity between the centre of mass and centre of resistance at the floor levels.

3.1 Nonlinear Modelling

SeismoStruct software is used for nonlinear analysis. The uniaxial nonlinear confinement concrete model and uniaxial bilinear stress–strain model were used for concrete and steel reinforcement, respectively. Inelastic force-based plastic hinge frame type is taken featuring distributed inelasticity and forced based formulation.

4 Results

4.1 Results from Nonlinear Static Analysis

Pushover curve is the plot between base shear v/s. roof displacement. In this study, structural performance levels, i.e. IO, LS and CP are defined as per ATC 40 guidelines [1]. Capacity curves of regular (R) and irregular (L) frame with 5 and 10 storeys in zone III and zone V are plotted in Fig. 2a–h. **Notations:** Frame type (R or L)-storey (5 or 10)-seismic zone (III or V).

Ratio of base shear at CP to design base shear is stated as over-strength ratios which are given in Table 1 for each frame as mentioned nomenclature. Here V_b is design base shear and V_b(CP) is base shear at CP limit state.

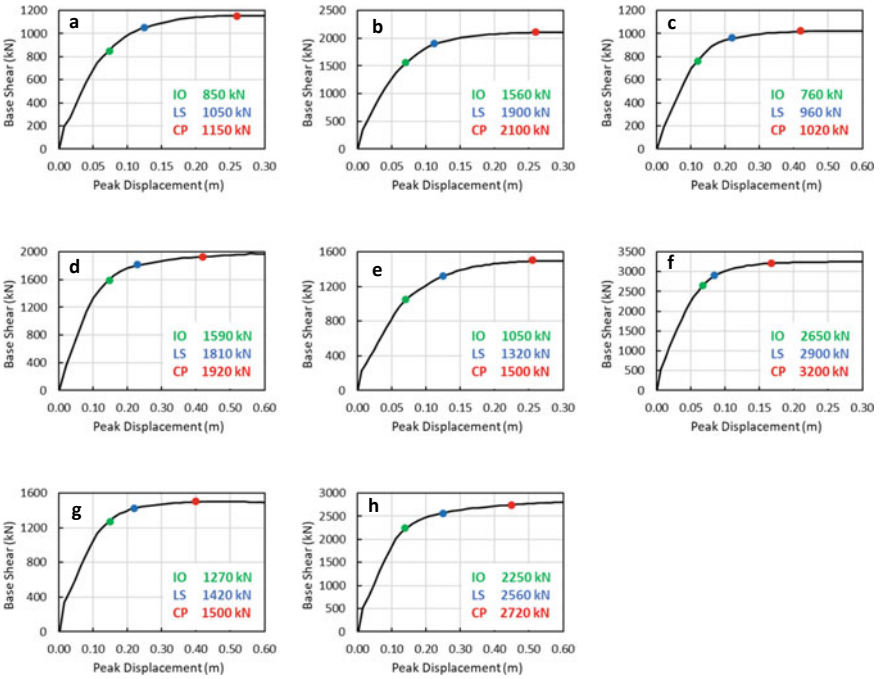

Fig. 2 Capacity curves for **a** R-5-III, **b** R-5-V, **c** R-10-III, **d** R-10-V, **e** L-5-III, **f** L-5-V, **g** L-10-III, **h** L-10-V

Table 1 Over-strength ratio

	R-5-III	R-5-V	R-10-III	R-10-V	L-5-III	L-5-V	L-10-III	L-10-V
V_b (kN)	420	1009	461	1166	382	904	425	970
$\frac{V_b(\text{CP})}{V_b}$	2.75	2.08	2.21	1.64	3.92	3.53	3.52	2.80

The over-strength of irregular frames are more compared to corresponding regular frames as it is designed for torsional eccentricity and analysed using static pushover analysis in first mode.

4.2 Results from Fragility Curves

Threshold IDR values were derived from performance criteria of ATC 40 chord rotations and capacity curve of individual frame. After obtaining clouds of responses, they are arranged in ascending order. The procedure of fragility curve development is followed using logarithmic plots of IM and DS, i.e. ln(PGA) versus ln(IDR) for

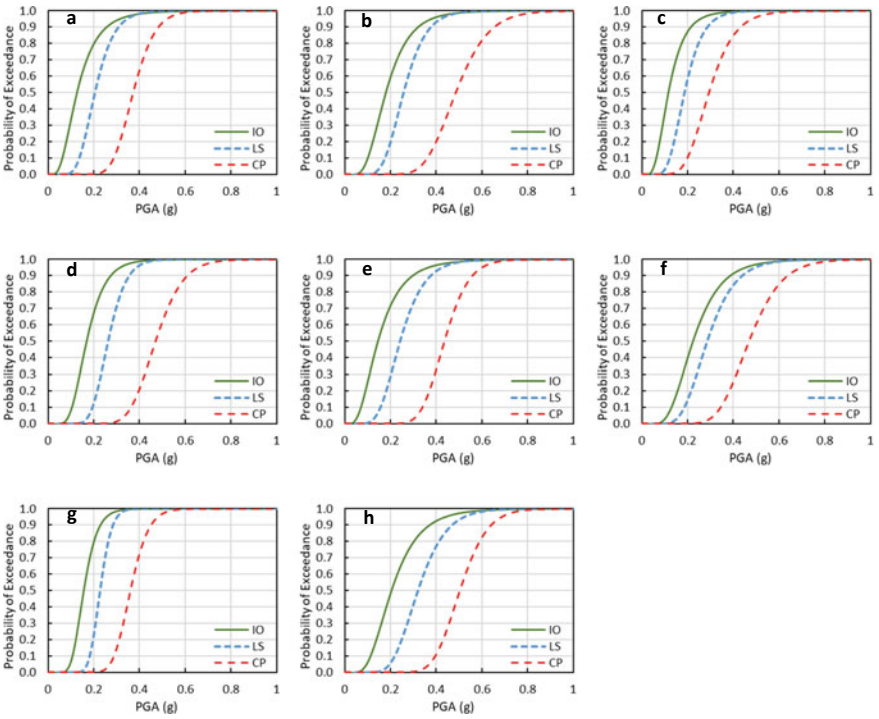

Fig. 3 Fragility curves for **a** R-5-III, **b** R-5-V, **c** R-10-III, **d** R-10-V, **e** L-5-III, **f** L-5-V, **g** L-10-III, **h** L-10-V

regression analysis and normal distribution of fragility parameters using median and dispersion. Figure 3a–h shows the fragility curve plots.

4.3 Summary of Fragility Curves

Frames are designed for design basis earthquake (DBE), i.e. Z/2 peak ground acceleration (PGA). Frames designed for zone III and V have maximum considered earthquake (MCE) at 0.16 g PGA and 0.36 g PGA, respectively.

Table 2 shows the summary of fragility curve results using nonlinear static analysis.

Table 2 Probability of exceedance

	R-5-III		R-5-V		R-10-III		R-10-V		L-5-III		L-5-V		L-10-III		L-10-V	
	DBE	MCE	DBE	MCE	DBE	MCE	DBE	MCE	DBE	MCE	DBE	MCE	DBE	MCE	DBE	MCE
IO (%)	25	64	50	95	21	75	51	98	17	56	32	87	2	51	40	89
LS (%)	1	21	15	87	0	33	7	89	0	13	10	75	0	3	4	62
CP (%)	0	0	0	10	0	2	0	9	0	0	0	14	0	0	0	4

5 Conclusions

The objective of the present study is to evaluate the structural response when subjected to range of potential levels of ground motion record and assessment of probability of exceedance of damage state under the effect of various PGA. Fragility curves are obtained for probabilistic assessment of vulnerability by means of lognormal distribution using results of nonlinear static pushover analysis. The following conclusions have been drawn from this study:

- From nonlinear static analysis, it has been observed that frames designed for seismic zone III has higher over-strength compared to its respective frame designed for seismic zone V.
- From fragility curve development, it is observed that there is negligible probability of collapse prevention limit state for PGA corresponding to design basis earthquake (Z/2), i.e. 0.08 g and 0.18 g for zone III and zone V, respectively.
- The probability of exceedance of given limit state is in the same range for regular and L-shaped frames. It can be said that additional torsional moment considered in analysis by calculating design eccentricity compensates effects of plan irregularity.
- From fragility curves, it is observed that probability of reaching collapse prevention limit is less than 15% when MCE is considered (0.16 g and 0.36 g for zone III and zone V, respectively).
- As the fragility curves are developed using nonlinear static analysis, conservative performance of irregular frame is observed.

References

1. Applied Technology Council, ATC 40. Seismic evaluation and retrofit of concrete buildings, vol 1, California
2. FEMA440 (2005) Improvement of nonlinear static seismic analysis procedures, Washington D.C
3. IS 456 (2002) Indian standard for plain and reinforced concrete-code of practice. Bureau of Indian Standard, New Delhi
4. IS 1893 Part 1 (2016) Indian standard for criteria for earthquake resistant design of structures-general provision and building. Bureau of Indian Standard, New Delhi
5. Kirc MS, Polat Z (2006) Fragility analysis of mid-rise R/C frame buildings. Eng Struct 28:1335–1345
6. Lallemant D et al (2015) Statistical procedures for developing earthquake damage fragility curves. J Int Assoc Earthq Eng 44:1373–1389

An Assessment of Efficiency Factors of Recycled Aggregate Concrete Bottle-Shaped Struts

Abhishek Devidas Chaudhari and Shiwanand R. Suryawanshi

Abstract The efficiency factors of bottle-shaped struts have been reanalysed using strut-and-tie models based on shear test data published in the literature. A total of 80 beam specimens made of recycled aggregate concrete, as well as control beam specimens of purely natural aggregate concrete, were considered in this study. The strut efficiency factor is the measure of performance of deep beams when they are analysed using strut-and-tie models. The measured values of efficiency factors of the recycled aggregate concrete bottle-shaped struts have been compared with those made of natural aggregate concrete and with the predictions of current design codes like the ACI 318-14, Eurocode2 and the AASHTO LFRD Bridge Design Specifications. The comparison of code recommendations has been made in order to make sure is the strut-and-tie modelling provisions of current design codes to evaluate strut efficiency factors of natural aggregate concrete bottle-shaped struts can conservatively be used for recycled aggregate concrete bottle-shaped struts or not. The results of the reanalysis indicate that the efficiency factors of natural as well as recycled aggregate concrete bottle-shaped struts are highly conservative when figured out against the predictions of AASHTO-2014, whereas both ACI 318-14 and Eurocode 2 gave predominantly unconservative efficiency factor predictions.

Keywords Bottle-shaped strut · Efficiency factor · RCA-concrete

1 Introduction

In order to reduce the effect of concrete construction on environment utilization of recycled concrete aggregate (i.e. RCA) sourced from construction and demolition (C&D) waste for the production of fresh concrete (i.e. RCA-concrete) is being continuously stirring up. Despite of the many economical as well as environmental benefits of RCA concrete production, the construction sector has not utilizing it, especially

A. D. Chaudhari (✉) · S. R. Suryawanshi
Department of Civil Engineering, Sardar Vallabhbhai National Institute of Technology, Surat, Gujarat, India

B. Kondraivendhan et al. (eds.), *Sustainable Building Materials and Construction*,
Lecture Notes in Civil Engineering 222,
https://doi.org/10.1007/978-981-16-8496-8_35

for structural applications. Very few information is available in the context of structural applications of RCA-concrete, especially on the shear behaviour of reinforced RCA-concrete. On the basis of the outcomes of Choi et al. [1] RCA can be replaced directly upto 50% for making concrete with current code provisions, beyond 50% replacement strength in shear reduced as much as 30%. Fathifazl et al. [2, 3] disagreed with this and argued that reason for the reduction of strength in shear is mainly due to the use of conventional mixture proportioning method, which is unsuitable for RCA concrete. With this Gonzalez and Martinez [4] were in the opinion that with 50% replacement of production of RCA concrete is possible but with that to maintained required W/C ratio, there is a need to add 6.2% more quantity of cement than conventional concrete.

Over the past years shear-critical regions of structural concrete are analysed and designed with the help of strut-and-tie models (STMs) which is relatively simple and effective method for design of discontinuous regions. In this method, the combined effect of the shear, flexural and torsional resistance is considered and modelled in terms of axial force paths represented by truss members. Concrete portion that are in compression represented by struts, whilst tensile reinforcement represented by tie member and point of intersection between struts and ties is called node.

A strut represents the resultant of a compression field and, as per ACI 318-14 [5], when extra width is available for the compressive stress trajectories to spread laterally near the mid-length of the strut it is called as a bottle-shaped strut. In bottle-shaped strut due to direct compression, indirect tension induced in normal direction to the axis of strut which reduces the effective compressive strength of concrete. The factor which indicates this reduction in effective compressive strength of concrete is called as strut efficiency factor (β_s). Consequently, questions have been raised with respect to the applicability of existing codal provisions, i.e. ACI 318-14 [5], AASHTO [6] and Eurocode 2 [7] for the efficiency factors of the RCA concrete bottle-shaped strut which are originally intended for NA-concrete.

Towards an appraisal of strut efficiency factors in current design codes in the context of RCA-concrete, from the reported test results [1–3, 8, 9] on shear behaviour of reinforced RCA concrete and the respective companion control specimens made of NA-concrete are reanalyzed using STMs in order to calculate the strut efficiency factors of bottle-shaped struts from the experimental results and to compare it with the current code provisions.

2 STM Analysis

A wide range of data of RCA concrete short as well as deep beams experimental results of past research papers which were originally designed using sectional method or using empirical formulae were collected from reputed journal and reanalysed by using STM method to evaluate the strut efficiency factor and shear capacity of deep

beams, these results were compared and validated with various codes like ACI 318-14 [5], AASHTO [6], and Eurocode 2 [7] conservatism of above-mentioned codes are studied.

2.1 STM Analysis of Typical Beam Specimen Tested by Han et al. [8]

Han et al. [8] tested total 12 reinforced concrete (RC) beam specimens out of which 2 specimens were control specimens casted using natural aggregate, whilst remaining 10 specimens casted using RCA using conventional method of mixture proportioning. The variables considered for study were the shear span to depth ratio (a_v/d), type of coarse aggregate and shear reinforcement ratio (ρ_v). Six beams composed without web reinforcement and six with web reinforcement along the entire beam length. Sufficient longitudinal reinforcement was provided (1.11% in specimens with no web reinforcement and 2.21% in those having web reinforcement). The geometry and strut-and-tie model of a typical beam specimen tested by Han et al. [8] is as shown in Fig. 1. It was assumed in the analysis that in all the beams the load transfer took place through direct strut action. This assumption was supported by the fact that all the beams, which failed by shear, exhibited diagonal cracks more or less aligned along the axis of the diagonal bottle-shaped strut. The width of the tie, t_w, may be taken twice the difference of the overall depth and effective depth of the beam, as the main reinforcement assumed to be provided at the effective depth of the beam. ACI318 suggests equal depth of top horizontal prismatic strut, s_w, and bottom horizontal main tie. However, the top width was calculated equating compressive force in top prismatic strut and tensile force in bottom tie, which is the product of area of steel and its yield strength provided in main tie. This procedure is well established in practise and conservative. Using width of prismatic strut-and-tie member, lever arm, j_d, was calculated as the difference between overall death, D, and half the sum of width

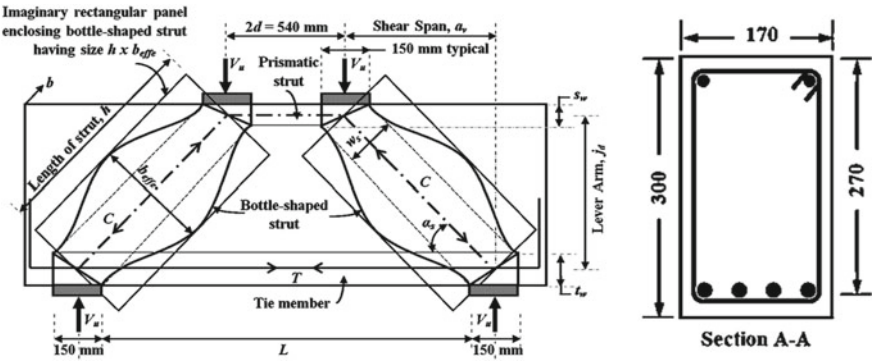

Fig. 1 Strut-and-tie model superimposed on a beam specimen tested by Han et al. [8]

of bottom tie member and width of top prismatic strut. Inclination of bottle-shaped strut, α_s, was estimated knowing the shear span to depth ratio reported by author and the estimated lever arm.

As depicted in Fig. 1, the width of diagonal bottle-shaped strut at the strut and node interface, w_s, was taken as the minimum of the values obtained from the expressions $w_s = l_b.\sin\alpha_s + t_w.\cos\alpha_s$ and $w_s = l_b.\sin\alpha_s + s_w.\cos\alpha_s$. The effective transverse reinforcement ratio, ρ_T, of the diagonal struts was calculated using the corrected version of the ACI code transformation Eq. 23.5.3 of ACI 318-14 [5] proposed by Sahoo et al. [10]. From the reported shear stress (v_u) values, ultimate shear resisting capacity (V_u) was estimated. Similarly, all the beam specimens reported in the literature were reanalysed using STM method as shown in Fig. 1, and the capacity of the diagonal bottle-shaped struts and the tension resisted by tie member was calculated from statics as $C = V_u / \sin\alpha_s$ and $T = C.\cos\alpha_s$, respectively. Knowing the capacity of strut, the experimental strut efficiency factor, $\beta_{s,\text{expt}}$, of the diagonal bottle-shaped struts were calculated using the following equation,

$$\beta_{s,\text{expt}} = \left(\frac{C \times 10^3}{w_s b_s f'_c}\right) \tag{1}$$

Efficiency factor suggested by ACI was calculated using Table 23.4.3 of ACI 318-14 [5]. According to AASHTO strut efficiency factor is calculated using Cl.5.6.3.3.3 of AASHTO [6]. Eurocode assumes bottle-shaped strut which classifies as partial discontinuity and full discontinuity, for this study bottle-shaped strut with partial discontinuity is assumed and efficiency factor was calculated with reference to Cl. 6.5.2 of Eurocode 2 [7].

3 Results and Discussion

The various parameters affecting struts efficiency factors identified as compressive strength of concrete, shear span to depth ratio, replacement ratio and transverse reinforcement ratio. The effect of these parameters on measured and predicted efficiency factor is shown in Fig. 2. From Fig. 2a, it has been observed that increase in compressive strength of concrete increases the shear strength of beam but may not be the strut efficiency factor. Effective transverse reinforcement is one of the main parameters found controlling the strut efficiency factor. The strut efficiency was improved on increased amount of effective transverse reinforcement ratio upto certain limit only, thereafter, it improves the deformation characteristics as shown in Fig. 2b. Measured strut efficiency factor found to be reduced at higher values of shear span to depth ratio as depicted in Fig. 2c. If the shear span to depth ratios goes on increasing, shear transfer mechanism is changing from strut action to beam action which is an agreement with the observations reported in literature. As shown in Fig. 2d, reported test results do not indicate any significant effect of replacement of natural aggregate with

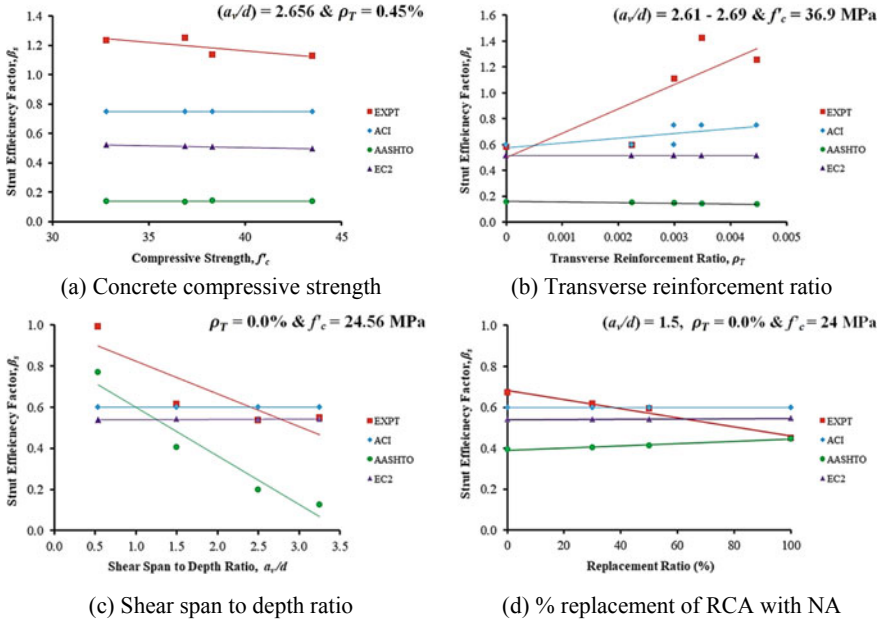

(a) Concrete compressive strength (b) Transverse reinforcement ratio

(c) Shear span to depth ratio (d) % replacement of RCA with NA

Fig. 2 Effect of different parameters on measured and predicted efficiency factors

recycled aggregate on measured strut efficiency factors. There is marginal reduction in strut efficiency factor with increased replacement ratio.

As shown in Fig. 3, the ACI 318 [5] predicts unconservative results in many cases because it recommends empirical strut efficiency factor values, whereas the AASHTO [6] predicts highly conservative results, possibly due to the higher and seemingly non-realistic estimated ε_1 value. The use of EC2 [7] STM provisions yields nearly consistent forecasts.

4 Conclusion

Based on the reanalysis of reported beam specimens, it has been concluded that the comparison of the different code predictions indicate that the ACI 318-14 [5] gives unconservative results in many cases as it recommends the empirical values of strut efficiency factor for the provided transverse reinforcement (i.e. β is 0.6 when ρ_T is zero and β is 0.75 when ρ_T is more than 0.3%) whereas the AASHTO [6] yields highly conservative results, may be due to the higher and seeming non-realistic estimated value of average tensile strain in concrete (i.e. ε_1). Use of Eurocode 2 [7] provisions results into practically constant predictions as it is the function of only compressive strength of concrete. It also be noted that strut efficiency factor provided by ACI 318-14 [5] and Eurocode 2 [7] are insensitive to inclination of strut. Higher level of

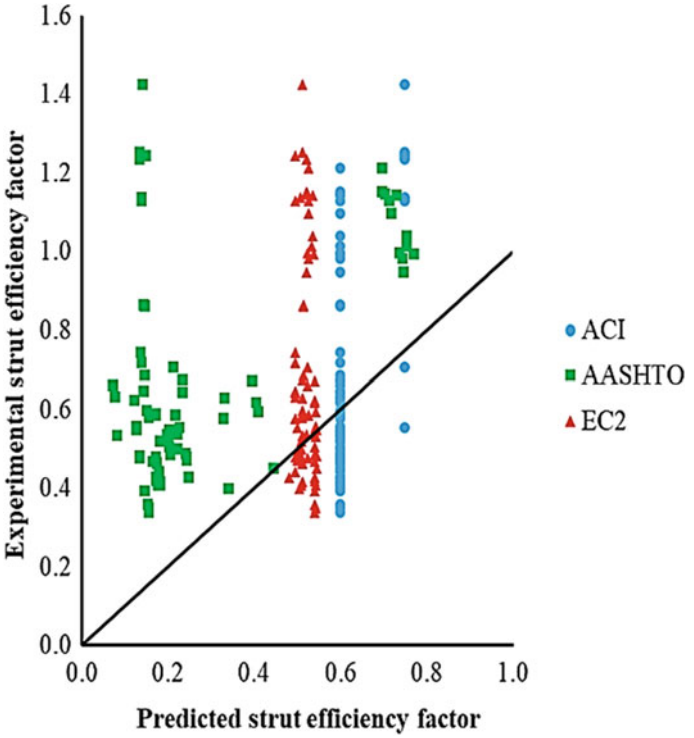

Fig. 3 Comparison of measured and predicted strut efficiency factors

replacement of natural aggregate in a concrete do not affect the relative efficiency much, however, the deformation characteristics may be affected and needed to be addressed.

References

1. Choi HB, Yi CK, Cho HH, Kang KI (2010) Experimental study on the shear strength of recycled aggregate concrete beams. Mag Concr Res 62(2):103–114
2. Fathifazl G, Razaqpur AG, Isgor OB, Abbas A, Fournier B, Foo S (2009) Shear strength of reinforced recycled concrete beams without stirrups. Mag Concr Res 61(7):477–490
3. Fathifazl G, Razaqpur AG, Isgor OB, Abbas A, Fournier B, Foo S (2010) Shear strength of reinforced recycled concrete beams with stirrups. Mag Concr Res 62(10):685–699
4. Gonzalez B, Martinez F (2007) Shear strength of recycled concrete beams. Constr Build Mater 21(4):887–893
5. ACI Committee 318 (2014) Building code requirements for structural concrete and commentary (ACI 318-14/318R-14). American Concrete Institute, Farmington Hills, MI
6. American Association of State Highway and Transportation Officials (2014) AASHTO LRFD bridge design specifications (7th edn). American Association of State Highway and Transportation Officials Washington, DC, USA

7. European Committee for Standardization (2004) Eurocode 2 design of concrete structure: part 1-general rules and rules for buildings (BS EN 1992-1-1) Brussels
8. Han BC, Yun HD, Chung SY (2001) Shear capacity of reinforced concrete beams made with recycled-aggregate. In: Proceeding of the fifth CANMET/ACI international conference on recent advances in concrete technology ACI SP-200, pp 503–515
9. Singh B, Jacob NM, Sahoo DK (2013) Efficiency factors of recycled aggregate concrete bottle-shaped struts. Mag Concr Res 65(14):878–887
10. Sahoo DK, Singh B, Bhargava P (2011) Minimum reinforcement for preventing splitting failure in bottle-shaped struts. ACI Struct J 108(2):206–216

Assessment of Stress–Strain Relationship for Recycled Aggregate Concrete

Akshay J. Pawar and Shiwanand R. Suryawanshi

Abstract The stress–strain relationship provides basis for analytical and numerical analysis of the structures. It is especially important in engineering designs. Material indices such as elastic modulus, peak-strain (ε_0), peak-stress (f_0 or f'_c), ductility index and normalized toughness are being evaluated from the measured stress–strain relationships. The measured stress–strain relationship of recycled aggregate concrete, reported in the literature, was compared with the predictions of typical constitutive models for meant natural aggregate concrete. Moreover, to ascertain the efficacy of considered stress–strain relationships for normal strength natural aggregate concrete were revisited for normal strength recycled aggregate concrete in terms of toughness and normalized ductility. It has been observed that the predictions of reported stress–strain equations for natural aggregate concrete significantly differ especially in the post-peak region of measured stress–strain curves of recycled aggregate concrete.

Keywords Recycled aggregate concrete · Stress-strain relationship · RCA concrete

1 Introduction

The production of concrete in the world due to rapid industrialization is around 6 billion tonnes per year [4]. As the concrete is made up of 70% aggregates and the earth is a source of natural aggregates, thus acquiring these quantities from the earth has an averse influence on the environment. Moreover, dismantling the concrete structures and discarding the concrete waste at dumping area would worsen the problem [7]. Therefore, recycling C and D waste plays an important role to promote the sustainable development programme; it may also help to conserve natural resources and decreases the disposal problem.

A. J. Pawar (✉) · S. R. Suryawanshi
Department of Civil Engineering, Sardar Vallabhbhai National Institute of Technology, Surat, India

S. R. Suryawanshi
e-mail: ssr@amd.svnit.ac.in

B. Kondraivendhan et al. (eds.), *Sustainable Building Materials and Construction*,
Lecture Notes in Civil Engineering 222,
https://doi.org/10.1007/978-981-16-8496-8_36

The consumption of recycled concrete aggregate (RCA) in structural application gives opportunities in which recycled materials can be used for making such a new concrete and it may help to support sustainable development programme. Any new material which is used for engineering purpose requires their stress–strain relationship for the understanding of their behaviour under load [5]. Thus, a whole understanding of the stress–strain relationships of this new material is very important and so that its potential can be checked in structural applications. The recycled concrete aggregate had been used for long time but it is restricted to non-structural applications such as filling, roadwork, earth work. The use of recycled aggregate in structural applications is scarcely reported [8].

The instantaneous axial deformation of the specimen under load can be described conveniently by a stress–strain diagram. The stress–strain diagram represents the strength and deformation characteristics, which is a very essential material characteristic of concrete when it is used in the design structural element [9]. The behaviour of concrete, an estimate of the elastic modulus (E), which is defined as the ratio of the applied stress and strain (ε) at that particular stress ($for f_c$) within an assumed proportional limit, is very useful for defining the stresses caused by strains associated with environmental effects. It is also used in the calculation of design stresses in simple elements under load, as well as moments and deflections in complicated structures. There have been many attempts to formulate the stress–strain curve mathematically for natural aggregate concrete (NAC). However, due to various influencing factors and various experimental conditions, the proposed curve gives dissimilar results. Therefore, for durability and service life of the structure a complete knowledge about the behaviour of concrete members at an early age is essential. The primary object of this study is to ascertain the applicability of recycled aggregate concrete (RAC) in structural applications.

2 Review on Existing Stress–Strain Constitutive Models for Natural Aggregate Concrete

Following typical constitutive models for natural aggregate concrete have been considered to predict the test results reported by Xiao et al. [9].

Hognestad [3] proposed a second-degree parabola stress–strain equation as represented by the following mathematical form.

$$f'c = fc\left[2\left(\frac{\varepsilon}{\varepsilon_0}\right) - \left(\frac{\varepsilon}{\varepsilon_0}\right)^2\right] \tag{1}$$

In 1964 Desayi and Krishnan proposed a stress–strain equation for concrete in compression under short time loading.

$$f = \left[\frac{E\varepsilon}{1 + \left(\frac{\varepsilon}{\varepsilon_0}\right)^2} \right] \tag{2}$$

Popovics [6] proposed a model for unconfined normal-weight concrete for an estimation of the complete stress–strain relationship under short-term loading.

$$\frac{f}{f_0} = \left(\frac{\varepsilon}{\varepsilon_0}\right) \left[\frac{n}{n - 1 + \left(\frac{\varepsilon}{\varepsilon_0}\right)^n} \right] \tag{3}$$

In 1985, Carreira and Chu were developed a model for the stress–strain relation of plain cement concrete in compression. The equation is represented as:

$$\frac{fc}{f'c} = \left[\frac{\beta\left(\frac{\varepsilon}{\varepsilon_0}\right)}{\beta - 1 + \left(\frac{\varepsilon}{\varepsilon_0}\right)^\beta} \right] \tag{4}$$

Suryawanshi et al. [8] proposed the simple stress–strain relationship model for NAC as well as RCA-concrete using a fourth-degree polynomial equation is as follows:

$$\overline{\sigma} = a(\overline{\varepsilon}) + b(\overline{\varepsilon})^2 + c(\overline{\varepsilon})^3 + d(\overline{\varepsilon})^4 \tag{5}$$

In Eq. 5, the coefficient 'a' is expressed in terms of the RCA replacement level, R. Equation 5 can be used to represent the stress–strain behaviour of natural as well as recycled aggregate concrete by using the appropriate value of coefficient 'a' for certain level of replacement ratio. Other coefficients in Eq. 5 are related to coefficient 'a' [8]. The stress–strain equation for natural aggregate concrete can be transformed into stress–strain relationship for fully or partially replaced natural aggregate concrete by adopting suitable values of coefficients *a*, *b*, *c* and *d*. In this study, Eq. 5 corresponding to NAC by considering replacement level 0%, was used to compare the behaviour of recycled aggregate concrete as the objective of this study to assess the suitability of constitutive models of natural aggregate concrete for recycled aggregate concrete.

3 Measured Stress–Strain Behaviour of RCA-Concrete

In order to examine the validity of the stress–strain relationship models, the experimental data was extracted from the literature [9]. This is termed as the measured data and for typical replacement levels say for example 0%, 50% and 100% designated

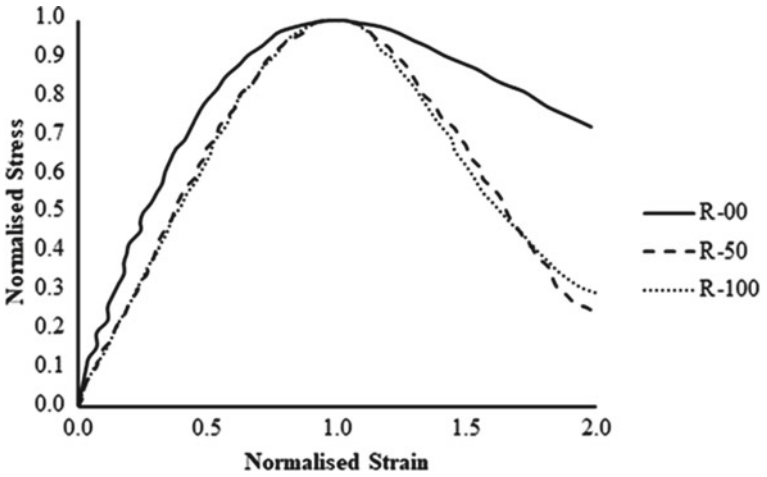

Fig. 1 Comparison of measured stress–strain relationship (for 0%, 50% and 100% replacement levels)

as R-00, R-50 and R-100, respectively, have been considered for validation purpose. Using this measured data the validation of natural aggregate concrete constitutive models was done. Figure 1 shows the measured stress–strain curves for natural aggregate concrete and RCA-concrete specimens. The slopes of the stress–strain curve in pre-peak region, as well as the peak-stress, both decreased as the replacement level of RCA increased, with the former indicating a reduction in the elastic modulus with increasing RCA content in the concrete. It was also observed that as the RCA content increased; the slope of stress–strain curve in post-peak region became sharper, indicating increase in brittleness compared to natural aggregate concrete.

4 Assessment of Applicability of Existing Natural Aggregate Concrete Stress–Strain Models to Recycled Aggregate Concrete

The analysis of the available selected stress–strain models for normal strength natural aggregate concrete was applied to RAC measured data. From the measured data of stress–strain curve; various models were applied to check whether current NAC models are applicable to RCA-concrete in their present form or not and also investigate the prediction accuracy of the equation with the measured data. Figures 2 and 3 illustrate the comparison of measured stress–strain relationships with the predictions of models proposed by Desayi and Krishnan [2], Popovics [6], Honestad [3] Carriera and Chu [1] and Suryawanshi et al. [8]. From Figs. 2b and 3 it is clearly observed that the applicability of various NAC models give greater area under curve than that

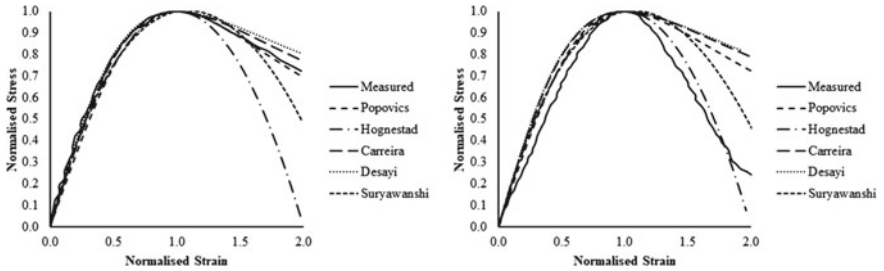

(a): For R-00 (b): For R-50

Fig. 2 Comparison of measured stress–strain relationship for recycled aggregate concrete with the predictions of various models for natural aggregate concrete

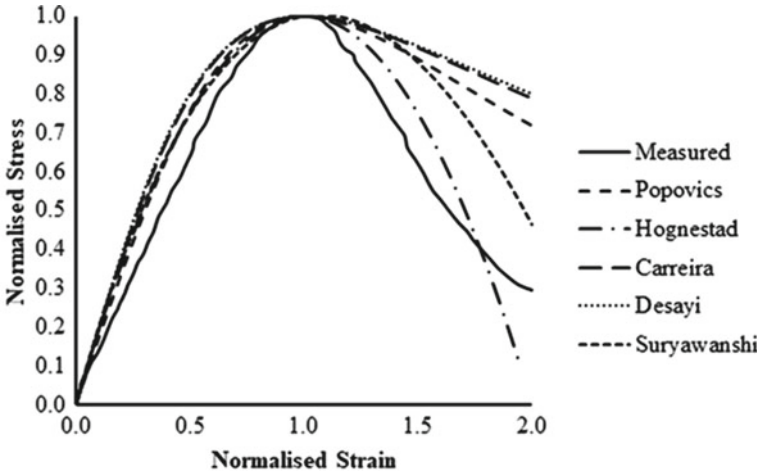

Fig. 3 Comparison of measured stress–strain relationship for recycled aggregate concrete with the predictions of various models for natural aggregate concrete (for R-100)

of measured data of RCA-concrete which shows the toughness of natural aggregate concrete is greater than that of the recycled aggregate concrete. In case of Popovic's [6] model it gives nearly accurate results for the pre-peak region of RCA-concrete stress–strain curve however post-peak region is not predicted accurately. The equation proposed by Hognestad [3] gives approximately accurate results particularly for the post-peak region of RCA-concrete stress–strain curve as compared to other analytical models. In the case of Carriera and Chu [1] and Desayi and Krishnan [2] both are giving nearly same results for the pre-peak as well as post-peak branch of RCA-concrete stress–strain curve, which is not predicted accurately. Equation 5 Suryawanshi et al. [8] which is used as a natural aggregate concrete stress–strain

model gives good prediction upto peak-stress but in post-peak region the predictive efficacy found marginally decreased. In short, it can be said that the predictions of reported stress–strain models for natural aggregate concrete significantly differ especially in the post-peak region of measured stress–strain relationship of RCA-concrete.

5 Conclusions

On the basis of analysis of various constitutive models it has been observed that the usage of recycled concrete aggregate in concrete may not significantly affect the compressive strength but it certainly affects the deformation characteristics. The material indices such as peak-strain, ultimate strain, elastic modulus, normalized toughness and ductility index have been significantly reduced when the natural aggregates in the concrete was replaced by recycled concrete aggregates. It should be noted that no quantification is done for above index properties. It was also observed that the predictions of reported stress–strain models for natural aggregate concrete significantly differ especially in the descending branch of measured stress–strain relationship of recycled aggregate concrete. Therefore, the current NAC models cannot be applied directly to RCA-concrete. If these models are to be used for RCA-concrete, suitable modification in these equations are required or better to develop a separate stress–strain relationship for recycled aggregate concrete. Thereafter use of RAC is possible in structural applications.

References

1. Carreira DJ, Chu KH (1985) Stress-strain relationship for plain concrete in compression. J Am Concr Inst 82(6):797–804
2. Desayi P, Krishnan S (1964) Equation for the stress-strain curve of concrete. J Am Concr Inst 61(3):345–350
3. Hognestad E (1951) A study of combined bending and axial load in reinforced concrete members. Engineering Experimental Station, University of Illinois, Urbana, Bulletin No. 399(49)
4. Marinkovic S, Ignjatovic I (2010) Recycled aggregate concrete for structural use-an overview of technologies, properties and applications. In: Proceedings of the ACES workshop innovative materials and techniques in concrete construction Corfu
5. Ozbakkaloglu T, Saatcioglu M (2004) Rectangular stress block for high-strength concrete. ACI Struct J 101(4):475–483
6. Popovics S (1973) A numerical approach to the complete stress-strain curve of concrete. Cem Concr Res 3(5):583–599
7. Rao MC, Bhattacharyya SK, Barai SV (2010) Recycled aggregate concrete: a sustainable built environment. In: International conference on sustainable built environment (ICSBE), pp 227–232
8. Suryawanshi S, Singh B, Bhargava P (2017) Equation for stress-strain relationship of recycled aggregate concrete in axial compression. Mag Concr Res 70(4):163–171
9. Xiao J, Li J, Zhang C (2005) Mechanical properties of recycled aggregate concrete under uniaxial loading. Cem Concr Res 35(6):1187–1194

Comparative Study of Diagrid Steel Building with Conventional Steel Braced Building

Tushar P. Kakadia, C. D. Modhera, K. N. Sheth, and Sagarkumar Naik

Abstract Diagrid structural system is widely used for tall steel buildings due to its structural efficiency, architectural design, interior design point of view due to column free area and aesthetic potential provided by the unique geometric configuration of the system. This paper provides comparative study of diagrid steel building of different five inclinations with horizontal and conventional steel building with inverted V-bracing. Also comparison made of varying inclination throughout the height for G + 36 storey steel structure considering earthquake forces and wind load, having plan dimensions of 40 m × 40 m and keeping storey height 3.6 m. The models are exported to structural engineering software such as ETABS for design and analysis. Results comparison made for storey displacement, storey drift, storey shear, steel quantity consumed.

Keywords Diagrids · Tall building · Convectional steel structure · Etabs · Response spectrum analysis

1 Introduction

Enhancement in construction technology, evolution of efficient structural system and scarcity of urban land caused the development of the high rise buildings around the world. Structural design of high rise buildings is governed by lateral loads due to wind or earthquake. Usually shear wall core, braced frame and their combination with frames are interior system where lateral load is resisted by centrally located elements. While framed tube, braced tube structural system resist lateral loads by

T. P. Kakadia (✉) · K. N. Sheth
Department of Civil Engineering, Dharmsinh Desai University, Nadiad, Gujarat, India

C. D. Modhera (✉)
Department of Civil Engineering, S.V.N.I.T, Surat, Gujarat, India
e-mail: cdm@amd.svnit.ac.in

S. Naik
Department of Civil Engineering, S.V.N.I.T, Surat, Gujarat, India

B. Kondraivendhan et al. (eds.), *Sustainable Building Materials and Construction*,
Lecture Notes in Civil Engineering 222,
https://doi.org/10.1007/978-981-16-8496-8_37

elements provided on periphery of structure. It is very important that the selected structural system is such that the structural elements are utilized effectively while satisfying design requirements.

In rigid frame system; tall building should be limited to 20 stories as it leads to shear racking of deflection due to bending of columns and beams which causes storey drift too great. To reduce this storey drift in tall building an additional diagonal or braces within the frame is created to eliminate the bending of columns and beams.

It is a form of space truss consists of multiple diagonal inclined elements to form a diagonal grid on the periphery of structure and perimeter grid form series of triangulation truss system. Almost all the conventional vertical peripheral columns are eliminated. Diagonal member in diagrid structure act as both inclined column and bracing element and also carry gravity loads as well as lateral forces due to triangulation configurations [2].

2 Methodology

2.1 Building Configurations

Diagrid steel building with different inclination taken for the study such as 55.22°, 65.16°, 70.85°, 74.47° and 76.96°. Horizontal spacing kept between two diagrid is 5 m. The physical properties and data of the building considered for the present study is as Tables 1 and 2:

Table 1 Properties and data of building taken for study [5]

Height of building	Plan size	Typical Storey height	Location	Seismic zone	Slab thickness	Frame material except slab	Floor Finish
135.6 m	40 × 40m	3.6 m	Surat (wind speed = 44 m/s)	III	125 mm	Structural steel	1 kN/m^2

Table 2 Properties and data of building taken for study [3]

Wall load	Glass load	Live load	Zone factor	Importance factor	Response reduction factor	Damping ratio
7 kN/m	0.601 kN/m of 6.5 mm thick having density of 0.167kN/m^2	4 kN/m^2	0.16	1.5	4	2%

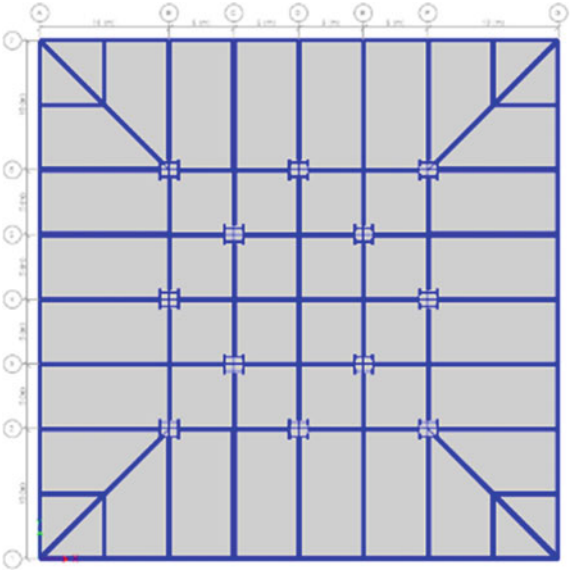

Fig. 1 Typical floor plan of diagrid steel structure

2.2 Diagrid Buildings

The structural elements like beams and columns in the model are analysed and designed as a beam elements and external diagrid structures which are placed at the periphery of the steel building are analysed and design as a truss elements to resist gravity as well as lateral loads due to wind and earthquake which is acting on the structure [6]. Type of section used for modelling of beams and columns is done by using I-section and built-up section, respectively. Diagrid system is provided by using pipe sections. All the sections in buildings are optimized for design sections (Figs. 1, 2 and 3).

2.3 Conventional Steel Braced Building

For lateral load resistance conventional steel building with inverted v- bracings are taken for the comparison. Beam elements are provided at 4 m in both the x-direction and y-direction. Beams and columns are analysed and designed as a beam element and external bracings which are placed at the periphery of the steel building are analysed and designed as a truss element for resisting all the lateral loads due to wind and earthquake which is acting on the structure [7]. Type of sections used for beam and column elements in braced building is done by using Indian standards I-sections and Universal sections [6]. Tubular sections are used for the bracing system (Figs. 4, 5 and 6) and (Tables 3 and 4).

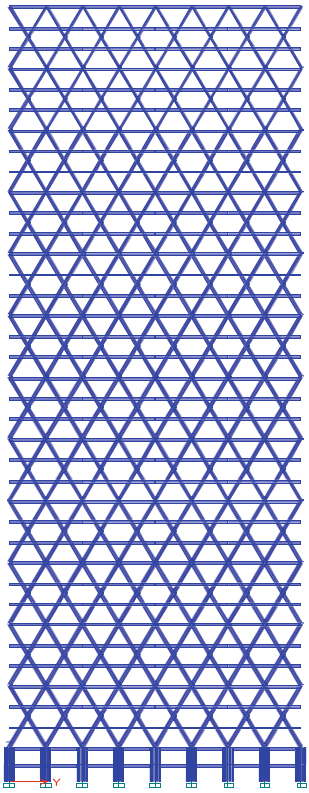

Fig. 2 Elevation of G + 36 storey diagrid building with diagrid 65.16 degree inclination

3 Results and Discussion

3.1 Displacement Comparison

It is observed that earthquake forces are predominant at lower storey but as height increases wind forces are comparatively higher. Therefore displacement and drift values are higher in case of wind forces.

Displacement comparison for RS-X, RS-Y, wind-X and wind-Y are shown in Figs. 7, 8, 9 and 10. We can see that conventional steel building with inverted V-bracing shows highest value of top storey displacement while diagrid steel building with mixed angle type A shows the lowest value of top storey displacement. Here, mixed angle type A is nothing but the varying angle starts from higher degree at bottom and reduces as height increases. While for mixed angle type B is vice versa.

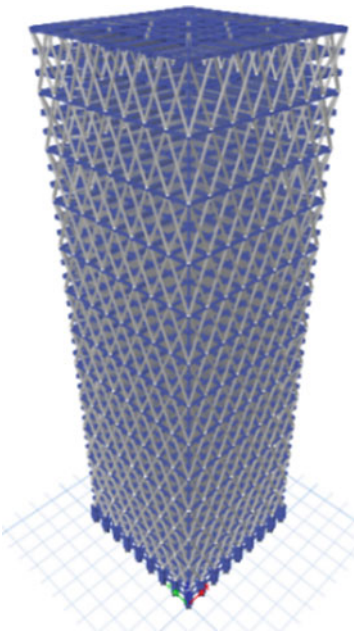

Fig. 3 3D View of G + 36 storey diagrid building with diagrid 65.16 degree inclination

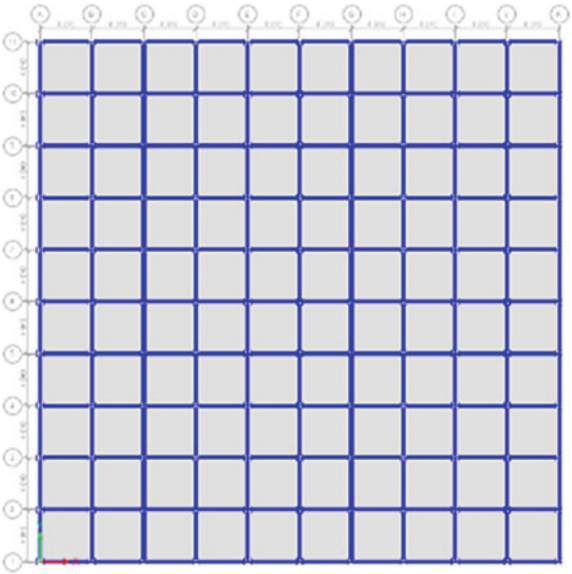

Fig. 4 Typical floor plan of conventional steel structure with inverted V-bracing

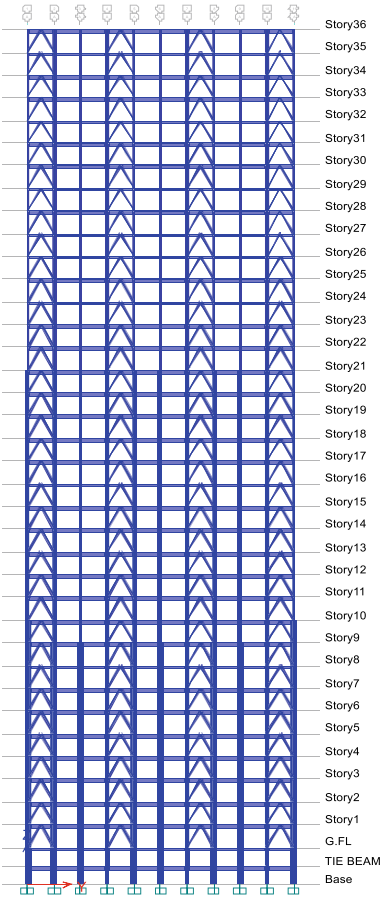

Fig. 5 Elevation of G + 36 storey conventional steel structure with inverted V-bracing

3.2 Drift Comparison

Storey drift is displacement of one level relative to the other level above or below. Storey drift comparison for RS-X, RS-Y, wind-X and wind-Y are shown in Figs. 11, 12, 13 and 14. We can see that conventional steel building with inverted V-bracing shows highest value of storey drift while diagrid steel building with mixed angle type A shows the lowest value of storey drift.

3.3 Storey Shear Comparison

Storey shear is the sum of design lateral forces at all levels above the storey under consideration. The storey shear comparison of G + 36 storey steel building is shown

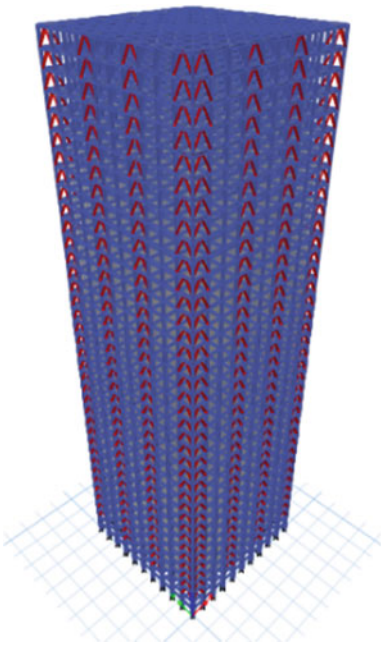

Fig. 6 3D View of G + 36 storey conventional steel Structure with inverted V-bracing

Table 3 Peripheral diagrid sections used in diagrid steel building with inclination 65.16 degree [4, 11]

Diagrid steel building with 65.16 degree				
Diagrid sections				
Storey height	6–49.2 m	49.2–70.8 m	70.8–114 m	114–135.6 m
Sections	Pipe Sect. 600 × 25mm	Pipe Sect. 508 × 16mm	Pipe Sect. 457 × 16mm	Pipe Sect. 406.4 × 10mm

Table 4 Bracings used at different heights for conventional steel building with inverted V-bracing [4, 11]

Inverted V-braced steel building			
Storey height	Up to 52.8 m	52.8 m to 99.6 m	99.6–135.6 m
Bracing	ISNB 300H	ISNB 250 H	ISNB 150 H

in Fig. 15. It is observed that storey shear due to wind load is higher than earthquake load and vice versa so the design is done by using both wind and earthquake load combination.

Steel quantity consumed by all the structure shown in Fig. 16. From Fig. 16 it is observed that steel quantity consumed by all the diagrid structures is shown reduction about 13–30% compared to conventional steel structure with inverted V-bracing. diagrid steel structure with diagrid angle 65.16 degree consumes comparatively lower amount than other all the cases.

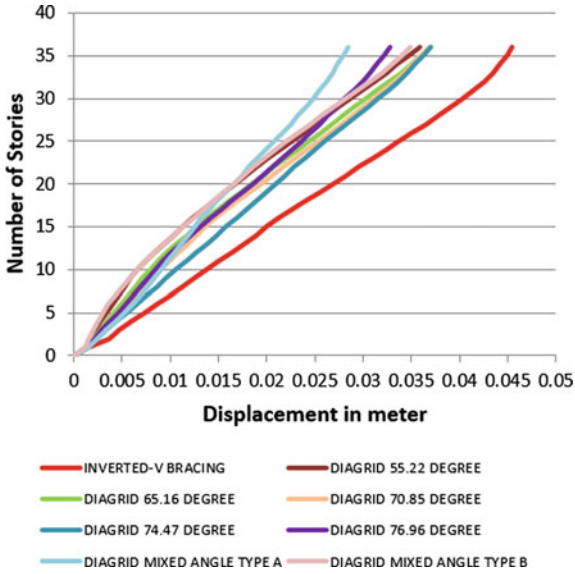

Fig. 7 Displacement comparison for RS-X

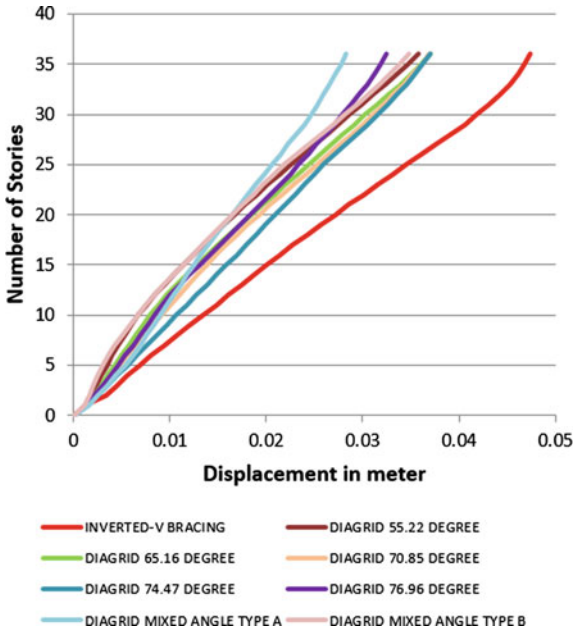

Fig. 8 Displacement comparison for RS-Y

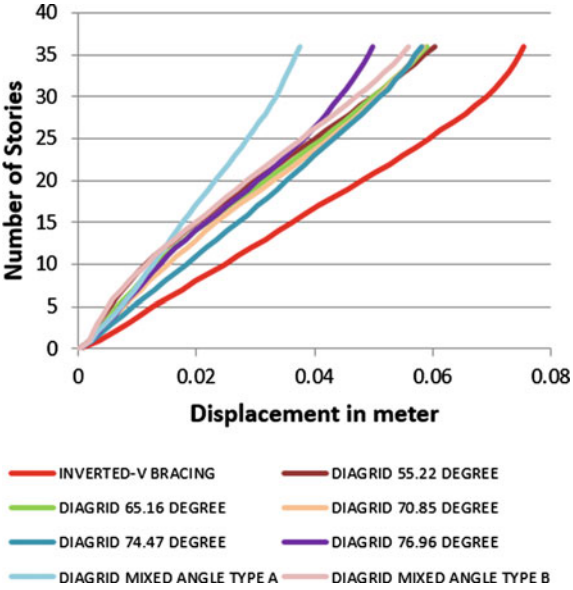

Fig. 9 Displacement comparison for wind-X

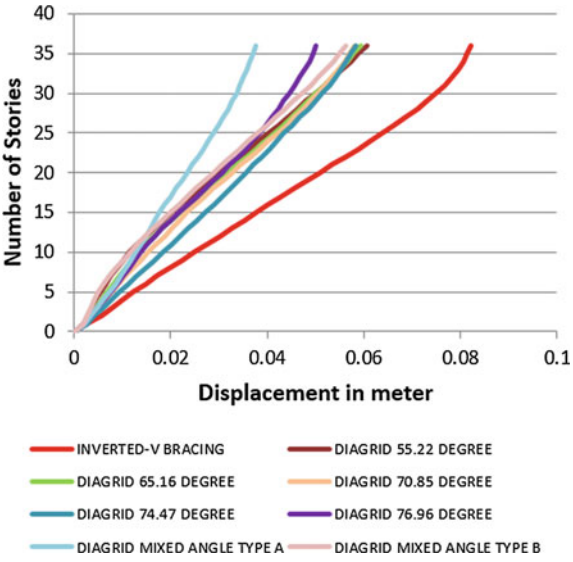

Fig. 10 Displacement comparison for wind-Y

4 Conclusions

From material consumption point of view, diagrid structure with diagrid angle 65.16 degree consumes lowest amount of steel compared to other cases and also it is lower than the conventional steel structure with inverted v-bracing. Steel quantity

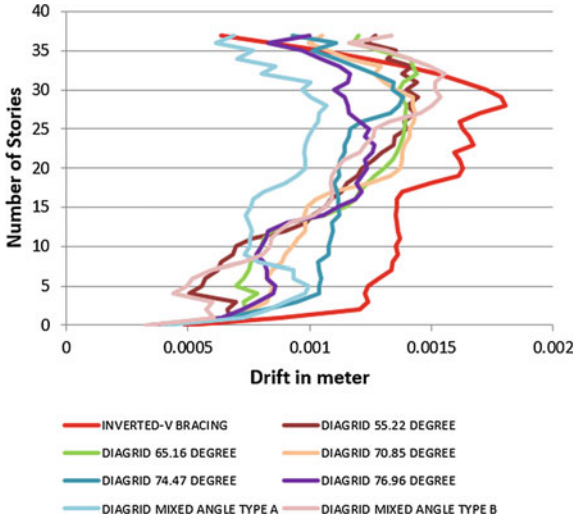

Fig. 11 Storey drift comparison for RS-X

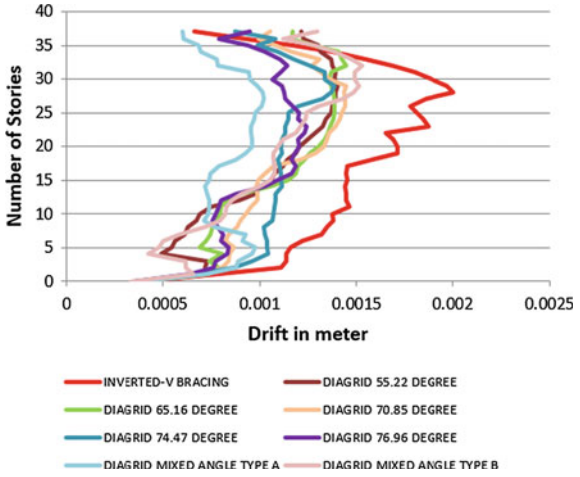

Fig. 12 Storey drift comparison for RS-Y

consumed by all the diagrid structures is shown reduction about 13–30% compared to conventional steel structure with inverted V-bracing. Displacement value due to wind for all the buildings taken for study have the higher value than displacement due to earthquake. Storey drift due to wind for all the buildings taken for study has the higher value than storey drift due to earthquake. Conventional steel structure gives higher displacement compared to diagrid steel structure for all cases. Conventional steel structure gives higher storey drift compared to diagrid steel structure for all cases. At lower storey conventional steel structure gives lower storey shear compared to diagrid steel structure, however there is no clear cut trend between angle of diagrid and storey shear. Storey shear due to wind is predominant as compared to storey shear

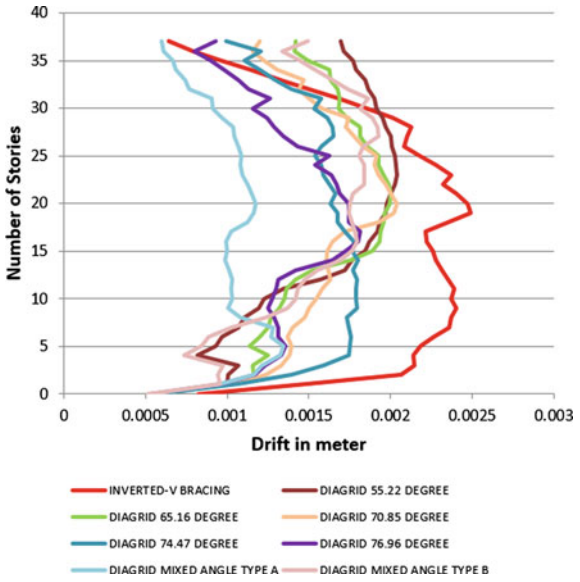

Fig. 13 Storey drift comparison for wind-X

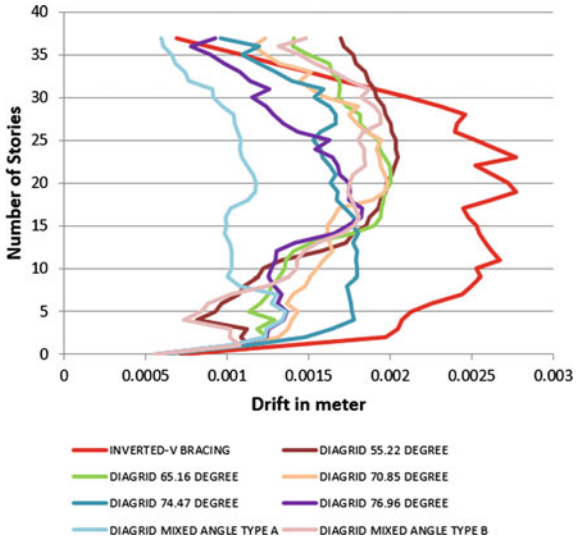

Fig. 14 Storey drift comparison for wind-Y

due to earthquake. Mixed angle type A has the lower value of top storey displacement compared to other inclination for both wind and earthquake load.

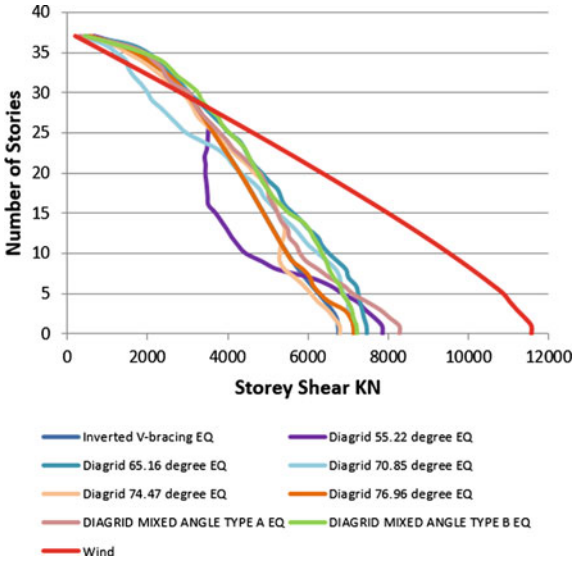

Fig. 15 Story shear comparison for earthquake and wind

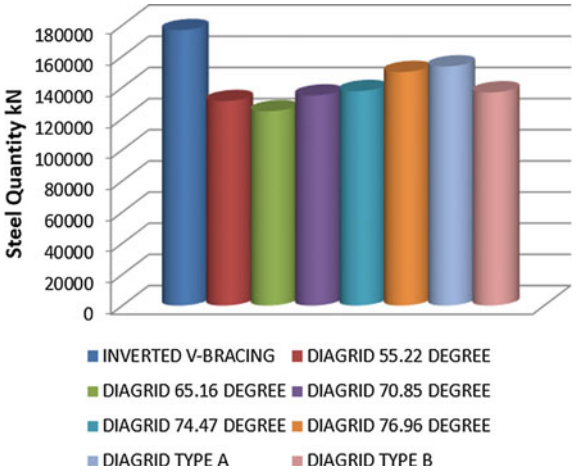

Fig. 16 Steel quantity comparison in kN for all the considered cases

References

1. Ali MM, Moon KS (2007) Structural developments in tall buildings: current trends and future prospects. Archit Sci Rev 50(3):205–223
2. Boake TM (2014) Diagrid structures: systems, connections, details. Walter de Gruyter
3. Bureau of Indian Standards (2016) IS 1893:2016—Indian Standard Criteria for Earthquake Resistant Design of Structures, Part 1-General Provisions and Buildings.Bureau of Indian Standards(1893 December)
4. Bureau of Indian Standards (2007) IS 800: 2007—General Construction in Steel-Code of Practice. 3rd Revision, Bureau of Indian Standard, New Delhi, India

5. Bureau of Indian Standards (2015) IS 875: 2015—Code of practice for Design of Wind loads for buildings and Structures, Part-3. Bureau of Indian Standards (2015)
6. Jani KD, Patel PV (2013) Design of diagrid structural system for high rise steel buildings as per indian standards. In Structures Congress (2013): Bridging Your Passion with Your Profession, pp 1070–1081
7. Kim JS, Kim YS, Lho SH (2008 March) Structural schematic design of a tall building in asan using the diagrid system. In: CTBUH 8th World congress (2008). Dubai, CTBUH
8. Leonard J (2007) Investigation of shear lag effect in high-rise buildings with diagrid system. Doctoral dissertation, Massachusetts Institute of Technology
9. Moon KS (2008) Practical design guidelines for steel diagrid structures. In: AEI (2008): Building Integration Solutions, pp 1–11
10. Moon KS, Connor JJ, Fernandez JE (2007) Diagrid structural systems for tall buildings: characteristics and methodology for preliminary design. Struct Design Tall Spec Build 16(2):205–230
11. Taranath BS (2004) Wind and earthquake resistant buildings: Structural analysis and design. CRC Press

Dynamic Response of RC Wall Panel Subjected to Air Blast Loading

Palak J. Shukla, Atul K. Desai, and Chetankumar D. Modhera

Abstract Parametric sensitivity study of reinforced concrete (RC) wall panel under air blast loading was conducted using finite element analysis software ABAQUS. The RC wall was modelled using three-dimensional solid elements and the steel reinforcements were modeled as 3-D truss elements. The stress–strain response of concrete was simulated using concrete damaged plasticity model while the metal plasticity with isotropic linear elasticity material model was used for steel reinforcements. The blast load was simulated using inbuilt CONWEP blast function available with ABAQUS. After validating the numerical analysis model, the effect of different parameters such as thickness of RC wall panel, standoff distance, charge weight and boundary conditions were investigated. It was observed from the study that displacement and axial stress in reinforcement are considerably reduced by increasing thickness of RC wall panel and standoff distance of blast charge. It was also observed that displacement and axial stresses were increased with increase in charge weight. Out of other support conditions studied, cantilever boundary condition indicated higher displacement of the panel and higher axial stress in reinforcements.

Keywords Finite element analysis · Concrete damaged plasticity · Standoff distance · Charge weight

1 Introduction

The behaviour of concrete under blast loading is quite different from static or quasi-static load condition due to short duration effects. Hence, RC wall panel shall be

P. J. Shukla (✉)
Applied Mechanics, Shri K. J. Polytechnic, Bharuch, Gujarat, India

A. K. Desai · C. D. Modhera
Department of Civil Engineering, Shri K. J. Polytechnic, Bharuch, Gujarat, India
e-mail: cdm@amd.svnit.ac.in

P. J. Shukla · A. K. Desai · C. D. Modhera
Department of Civil Engineering, SVNIT, Surat, Gujarat, India

B. Kondraivendhan et al. (eds.), *Sustainable Building Materials and Construction*,
Lecture Notes in Civil Engineering 222,
https://doi.org/10.1007/978-981-16-8496-8_38

designed with proper understanding of structural response under blast loading. Such response can be studied by (1) analytical approach which includes use of theoretical model for dynamic analysis [7, 10], (2) experimental approach includes small scale or prototype experimental setups [2, 8] and (3) numerical analysis using finite element method [3, 5]. However reviewed literature provides different results of RC panels under blast loading, the detailed numerical analysis of RC wall panel under air blast loading is required for better understand its dynamic behaviour under air blast loading. Hence the present study is carried out using nonlinear finite element application ABAQUS considering varying wall thicknesses, boundary conditions and the effect of explosive characteristics, i.e. standoff distance and charge weight.

2 Methodology

2.1 Three-Dimensional (3-D) Finite Element Modelling

3-D dynamic analysis of RC wall under free air burst scenario has been performed in present study using ABAQUS [1]. Figures 1 and 2 show the details of finite element (FE) model and elements used to model square RC wall panel (percentage of reinforcement 1.58% for 100 mm thick wall and 1.06% for 150 mm thick wall provided in two layers with 25 mm cover as per IS 456: 2000).

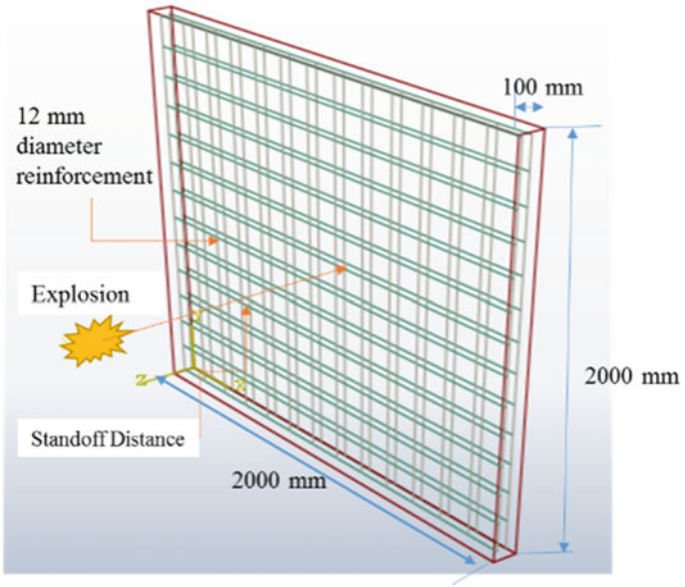

Fig. 1 FE model of RC wall panel

Fig. 2 Elements used in present analysis

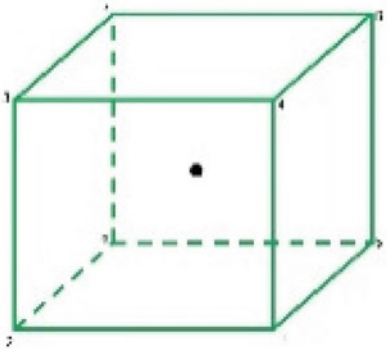

(a) 3-D solid element(8 node brick element with reduced integration)(C3D8R) (For wall)

(b) 3-D truss element (T3D2)(for reinforcement)

The stress–strain response of concrete is modelled using concrete damaged plasticity model while steel reinforcement is modelled using metal plasticity with isotropic linear elasticity. The methodology of modelling material and blast load has been adopted from [6].

2.2 Validation with Experimental Data

The experimental data available from Wang et al. [9] is simulated by adopting identical geometry, boundary condition and material properties in order to validate the results. Table 1 indicates the comparison of results in terms of normalized peak deflection vs scale down factors. The results of simulation carried out for present study indicated close agreement with experimental results providing further confidence over the adopted simulation technique.

Table 1 Comparison of the results: experimental with numerical modelling

Slab	Dimension (mm) ($l \times b \times h$)	Scale distance m/(kg$^{1/3}$)	Central deflection δ (mm)		Normalized peak deflection (δ/*h*)		Difference (%)
			Experimental	Simulation	Experimental	Simulation	
A	750 × 750 × 30	0.591	9	9.8	0.3	0.32	6.67
B	750 × 750 × 30	0.518	26	24.81	0.87	0.83	4.59
C	1000 × 1000 × 40	0.591	15	16.36	0.375	0.409	9
D	1000 × 1000 × 40	0.518	35	35	0.875	0.875	0
E	1250 × 1250 × 50	0.591	19	19.31	0.38	0.386	1.57
F	1250 × 1250 × 50	0.518	40	41	0.8	0.82	2.5

3 Results and Discussion

Table 2 shows different case of analysis considered in the current study. Blast pressure time histories are generated using CONWEP blast function for different charge weight and different standoff distance and presented in Fig. 3. For comparison purpose deformation in the direction of applied blast load and axial stresses in reinforcement are monitored for the given time.

3.1 Effect of Charge Weight

To study effect of charge weight, the typical case of 150 mm thick simply supported (SS) RC wall panel with explosion at 2 m standoff distance is considered. For standoff distance of 2 m, charge weight 1, 3 and 5 kg indicates blast pressure of 0.63, 1.84 and 3.04 MPa, respectively, (Fig. 3). The maximum displacement 4.29 mm, 0.99 mm is observed in case of 5 kg and 1 kg charge weight, respectively (Fig. 4). It is also

Table 2 Different cases of analysis

Various cases for parametric studies	Thickness of panel	Boundary condition	Charge wt (W; kg)	Standoff distance (R; m)
Values of parameters	100 mm, 150 mm	SS, Cantilever	1,3,5	1,1.5,2
Other values	W = 3 kg, 5 kg, R = 1 m, SS	W = 1 kg, t = 100 mm, R = 1.5 m	t = 150 mm, R = 2 m, SS	W = 5 kg, 100 mm Cantilever

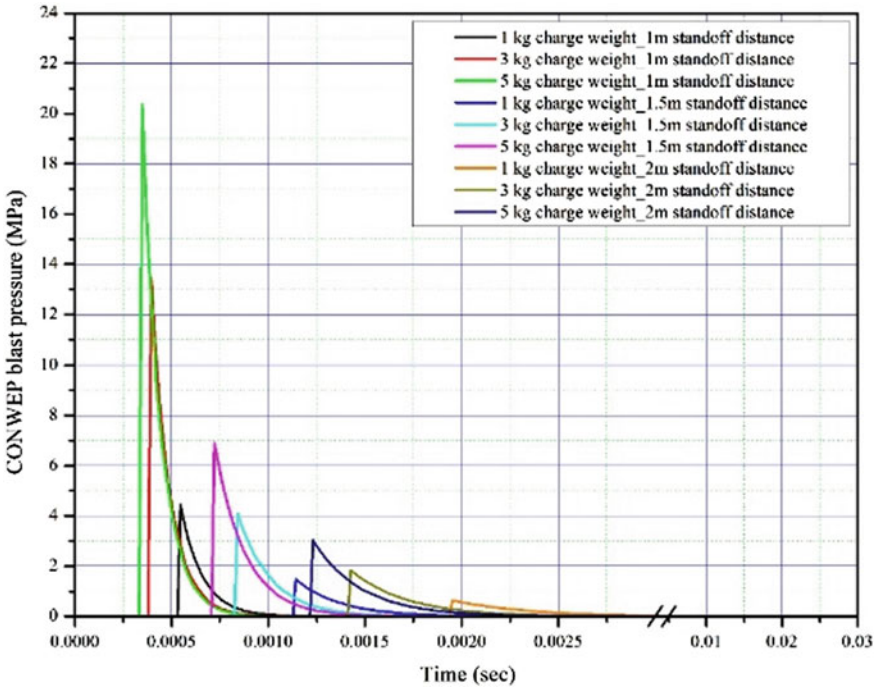

Fig. 3 Pressure time histories for parametric study of RC wall panel

observed that due to the explosion maximum axial stress of 52 and 250 MPa were developed in the reinforcement of 150 mm thick RC wall panel for 1 and 5 kg charge weight, respectively, weight (Fig. 5).

3.2 Effect of Standoff Distance

It is observed from Fig. 3 that the maximum pressure 20.37 MPa due to 5 kg charge weight at 1 m standoff distance while it is reduced by 66% for 1.5 m standoff distance and 85.2% for 2 m standoff distance with same charge weight. The displacement time histories are plotted considering cantilever boundary condition under 1 kg TNT charge weight (Fig. 6). Maximum displacement of 50.5 mm is observed for 1 m standoff distance which is reduced to 38.59 mm for 1.5 m and 29.38 mm for 2 m standoff distance.

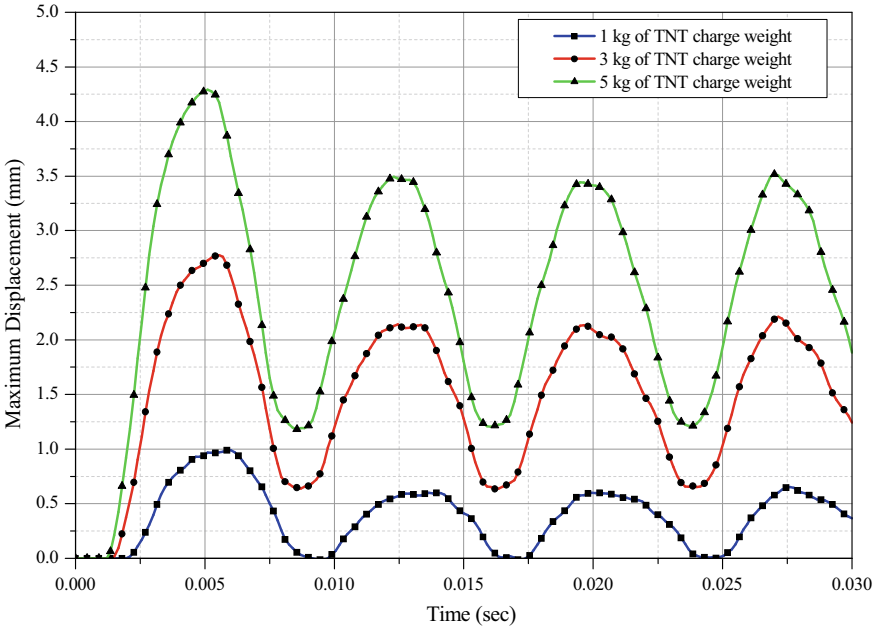

Fig. 4 Displacement time history (comparison of effect of charge weight)

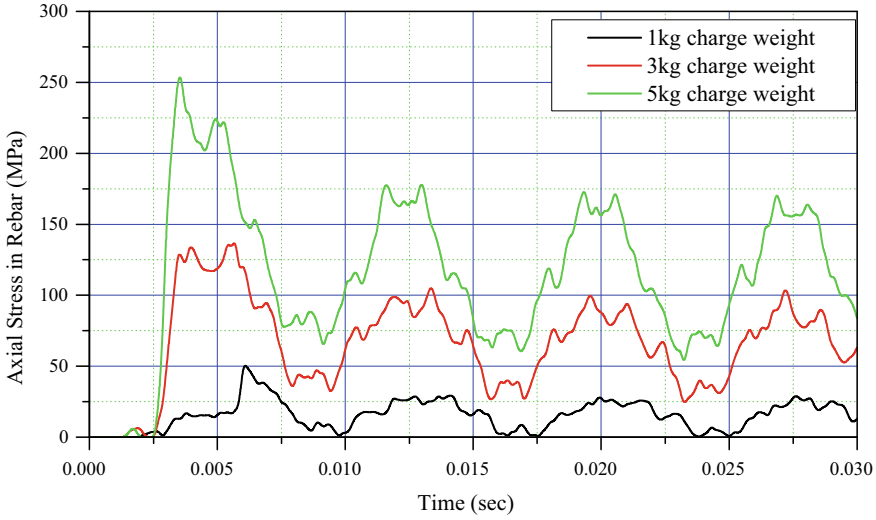

Fig. 5 Variation in axial stress in reinforcement for 150 mm thick SS panel under explosion at 2 m standoff distance

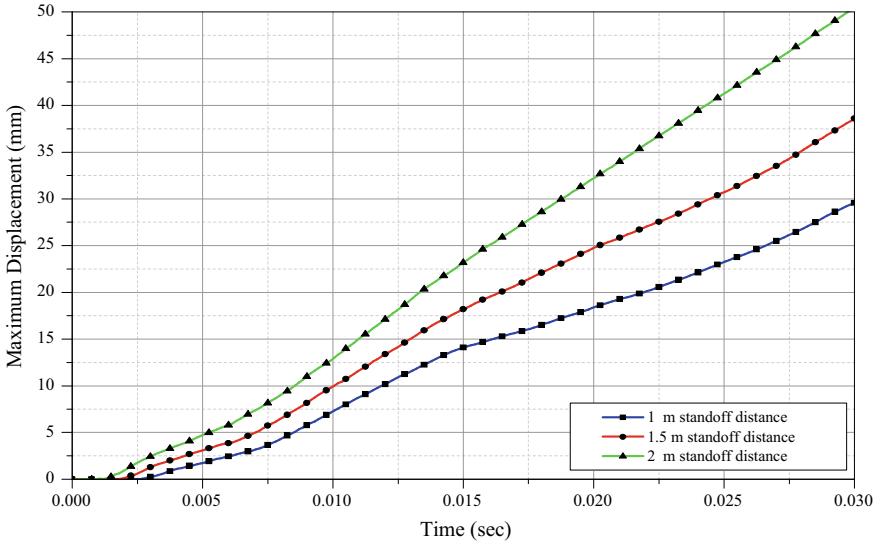

Fig. 6 Displacement time history (comparison of effect of standoff distance)

3.3 Effect of Thickness of Panel

The maximum stress in reinforcement under blast load due to 3 kg explosive weight is 434 MPa in case of 100 mm thick panel, while it is reduced to 267 MPa in 150 mm thick wall panel. Hence the axial stress in reinforcement decreases due to an increase in the thickness of the panel (Fig. 7). The effect of thickness of RC wall panel under blast loading was investigated for typical case of simply supported RC wall panel under blast load due to 3 kg and 5 kg explosive charge. The maximum displacement of RC wall panel under 3 kg explosive charge is noted as 16.75 mm which is reduced by 5.96 mm due to increase in thickness of panel to 150 mm. The 100 mm thick RC wall panel experience maximum displacement of 49.8 mm under 5 kg explosive charge which is reduced to 10.1 for 150 mm thick RC wall panel (Fig. 8).

3.4 Effect of Boundary Condition

150 and 100 mm thick RC wall panel subjected to 1 kg explosive charge at 1.5 m standoff distance was consider to study effect of two different boundary conditions, i.e. simply supported (SS) and cantilever. It can be observed that 100 mm thick panel with SS boundary condition deflects to 2.83 mm while cantilever panel have more deflection, i.e. 38.59 mm (Fig. 9). In same behaviour also observed in case of 150 mm thick panel, i.e. maximum displacement 1.48 mm is noted in case if SS panel while maximum displacement 25.16 mm is noted in case of cantilever panel. It is observed

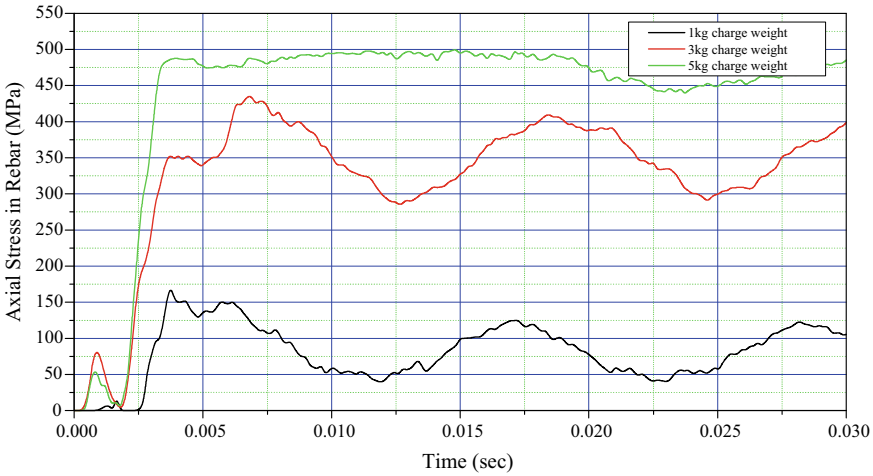

(a) 100 mm thickness of panel

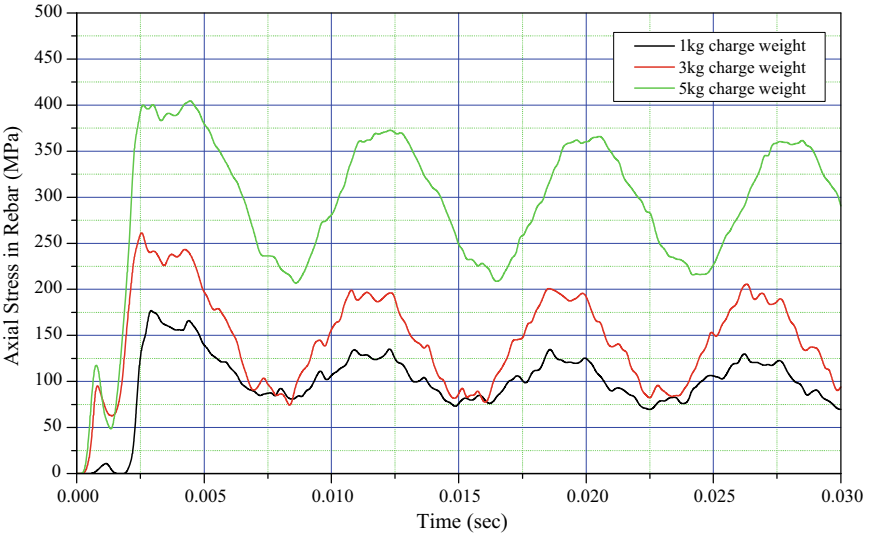

(b) 150 mm thickness of panel

Fig. 7 Comparison of axial stress in reinforcement for different thickness of simply supported RC wall panel under explosion at 1 m standoff distance

from the variation of rebar stress that the axial stress in rebar reaches up to maximum, i.e. up to yield value for smaller standoff distance in both the boundary condition. However, in the cantilever boundary condition that the maximum tensile stress in reinforcement remains constant throughout applied blast time history (Fig. 10).

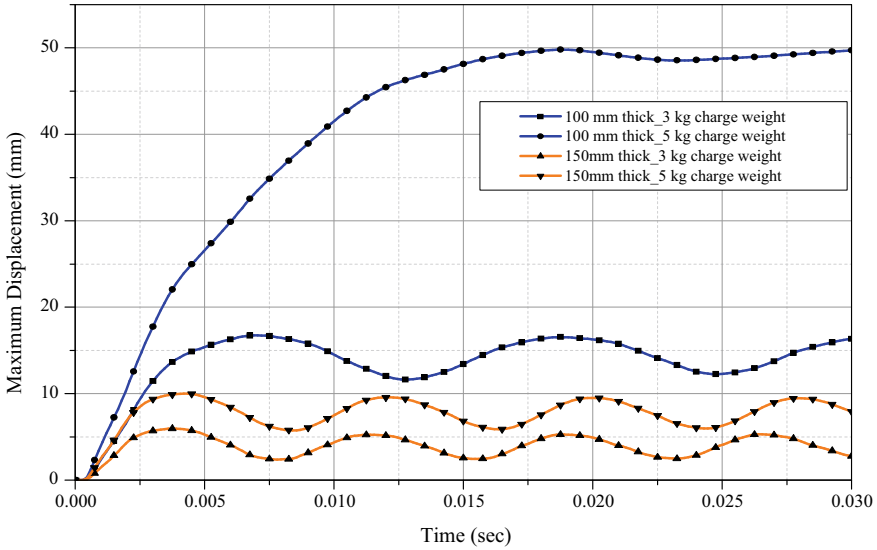

Fig. 8 Displacement time history (comparison of different panel thickness)

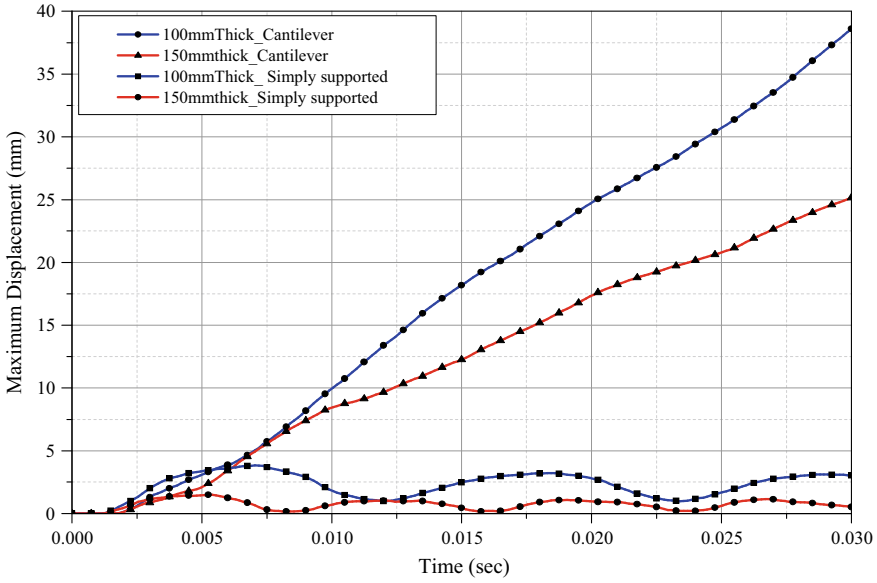

Fig. 9 Displacement time histories (different boundary condition)

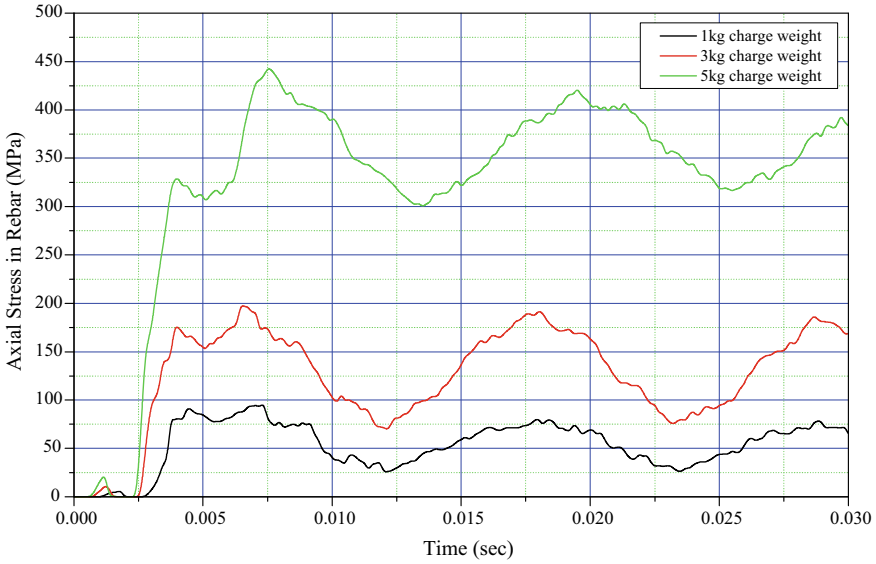

(a) Simply supported boundary condition

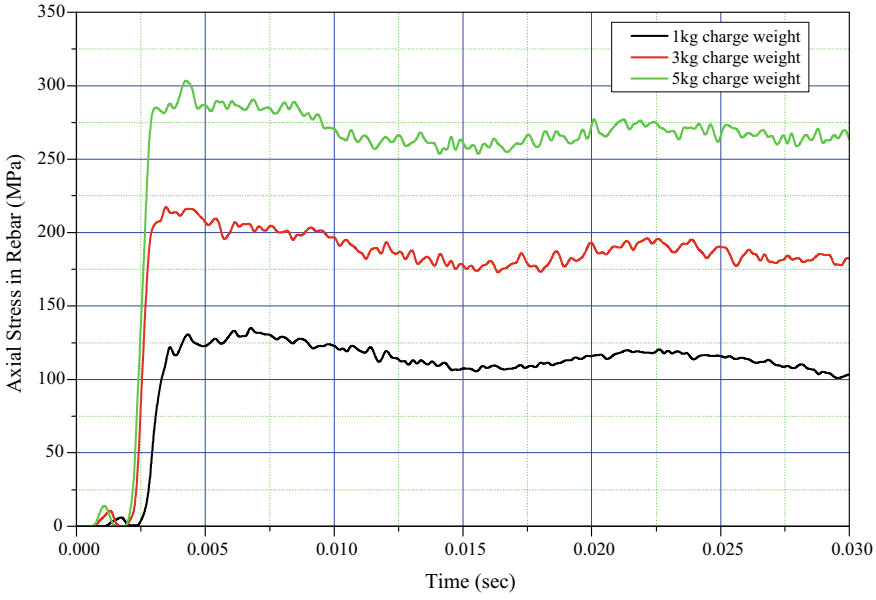

(b) Cantilever boundary condition

Fig. 10 Variation in axial stress in reinforcement (comparing different boundary condition)

4 Conclusions

The present study employed the finite element analysis software ABAQUS to investigate dynamic response of RC wall panel under blast load. The results are summarized as follows:

1. The applied blast pressure increases due to increase explosive charge. However, if standoff distance of explosive can be increased the applied blast pressure on the RC wall panel is considerably reduced.
2. The results of analysis indicates that increase in standoff distance of explosive and thickness of RC wall panel is effective in reduction of maximum displacement of RC wall panel. However, higher value of charge weight of explosion and cantilever boundary condition indicates increased maximum displacement of RC wall panel.
3. It is observed from the variation of reinforcement stress that the axial stress in reinforcement reaches up to maximum, i.e. up to yield value for smaller standoff distance in both the boundary condition. However, in the cantilever boundary condition that the maximum tensile stress in reinforcement remains constant throughout applied blast time history (Fig. 10).

References

1. Abaqus/CAE User's Manual, Version 6.11 (2012) Dassault Systems Simulia Corporation, Providence, Rhode Island, USA
2. Luccioni B, Isla F, Codina et al (2017) Effect of steel fibers on static and blast response of high strength concrete. Int J Impact Eng 107:23–37
3. Matsagar VA (2016) Comparative performance of composite sandwich panels and non-composite panels under blast loading. Mater Struct 49:611–629
4. Shukla P, Desai A, Modhera C (2018) The current practices of analysis of reinforced concrete panels subjected to blast loading. Int J StructConstrEng 12(10):935–943
5. Shukla P, Desai A, Modhera C (2019) Transient response of RC panel protected with slurry infiltrated micro reinforced concrete jacket under blast loading. Inter J Recent Techno Eng 8(2):1196–1210
6. Shukla P, Desai A, Modhera C (2021) Dynamic response of cut and cover tunnel section under blast loading. InnovInfrastructsolut 6(1):1–23
7. Tai Y, Chu T , Hu et al (2011) Dynamic response of a reinforced concrete slab subjected to air blast load, Theor Appl Fract Mech 56:140–147
8. Thiagarajan G, Kadambi A, Robert et al. (2015) Experimental and finite element analysis of doubly reinforced concrete slabs subjected to blast loads. Inter J Impact Eng 78:162–173
9. Wang W, Zhang D, Lu et al. (2012) Experimental study on scaling the explosion resistance of a one way square reinforced concrete slab under a close-in blast loading. Int J Impact Eng. 49:158–164. https://doi.org/10.1016/j.ijimpeng.2012.03.010
10. Wang Y, Liew Richard JY, Lee SC (2015) Theoretical models for axially restrained steel-concrete-steel sandwich panels under blast loading. Int J Impact Eng 76:221–231

Experimental and Numerical Modal Analysis of Cantilever Beam

A. J. Shah and G. R. Vesmawala

Abstract Modal analysis is the study of dynamic properties of a system such as natural frequency, mode shape and damping. This paper presents a numerical and experimental analysis of a cantilever beam. The experimental procedure is carried by means of ambient vibration testing which involves applying random vibrations on the cantilever beam and capturing them using accelerometer. The dynamic properties of cantilever beam are extracted using enhanced frequency domain decomposition method (EFDD) and stochastic subspace identification (SSI) method in frequency and time domain, respectively, with the help of software ARTeMIS modal. The numerical results obtained using ABAQUS software are compared with the experimental results and a good agreement is found between the obtained modal parameters.

Keywords Cantilever beam · Numerical model · Frequency domain decomposition method (EFDD) · Stochastic subspace identification (SSI)

1 Introduction

Modal analysis is the process of evaluating the dynamic properties of a system such as natural frequencies, mode shapes and damping [1]. There are mainly two types of approaches for determining dynamic parameters namely, numerical and experimental. The finite element method is widely used for performing numerical analysis. The accuracy of a finite element model depends on number of factors which includes element type and size, geometry information, material property and boundary conditions. The theoretical concepts used for calculations incorporate certain simplification with many of these factors due to which the numerical model often differs from the experimental structure. Hence, it is imperative that the finite element analysis results should be correlated with the actual structure using experimental tests.

There are primarily two different approaches to identify the dynamic properties of the structure experimentally namely, forced vibration testing and ambient vibration

A. J. Shah (✉) · G. R. Vesmawala
S.V. National Institute of Technology, Surat, India

B. Kondraivendhan et al. (eds.), *Sustainable Building Materials and Construction*,
Lecture Notes in Civil Engineering 222,
https://doi.org/10.1007/978-981-16-8496-8_39

testing. In forced vibration testing, the known input forces such as impulse hammer and electrodynamic shaker are used to excite the structure, while measuring the responses whereas in ambient vibration testing, the unknown input forces such as wind, wave and traffic excite the structure during the response measurement. Forced excitations is expensive due to use of impulse hammer or electrodynamic shaker and may possibly cause damage to the structure. However, ambient excitations occur naturally and do not cause any damage during testing [2]. In past two decades, ambient vibration-based testing has received a lot of attention which has enabled engineers and researchers to gain better knowledge of the dynamic properties of structure which enables better performance monitoring and condition assessment [3].

In the present study, the dynamic properties of a cantilever beam determined numerically with the help of ABAQUS software are compared with the results obtained experimentally using ambient vibration testing. The dynamic properties are obtained from measured vibration data using Enhanced frequency domain decomposition (EFDD) method [4] and stochastic subspace identification (SSI) method [5] in frequency and time domain, respectively

2 Experimental analysis

A cantilever beam is used for experimental investigation. The sectional properties of beams are specified in Table 1. Two and three dimensional views of the beam are shown in Fig. 1.

For measuring acceleration low cost uniaxial piezoelectric accelerometer PCB 603C01 with locally prepared magnet mounting having a total weight of 98 gms was

Table 1 Properties of cantilever beam

Length (mm)	Width (mm)	Thickness (mm)	Young's modulus (GPa)	Poisson's ratio	Density (kg/m^3)
800	50	25	200	0.3	7700

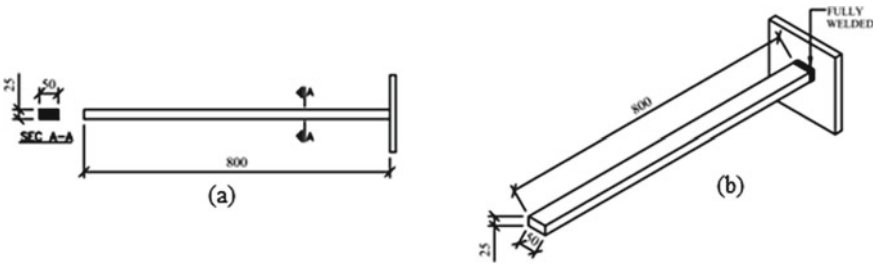

Fig. 1 Cantilever beam **a** 2-D-view and **b** 3-D-view

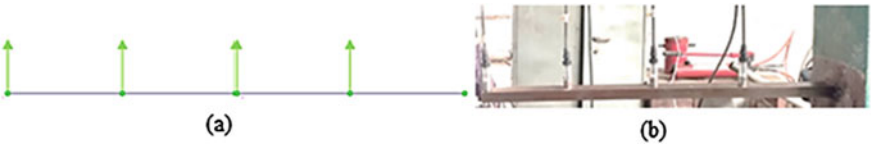

Fig. 2 Accelerometer location in (**a**) Artemis modal (**b**) In laboratory

used. The accelerometers were placed at four equidistant points in the beam. Ambient vibration was applied for 10 min and data was collected from accelerometer in NI-cDAQ-9174 data acquisition system with NI-9234, a four channel series module. The signal captured was acquired as well as processed in software ARTeMIS modal. Figure 2 shows the location and direction of accelerometer in laboratory as well as in software ARTeMIS modal [6]. The results obtained from EFDD method and SSI-UPC are shown in Fig. 3. The values of natural frequency obtained for both methods are shown in Table 2. Values obtained from both the methods are in agreement with each other.

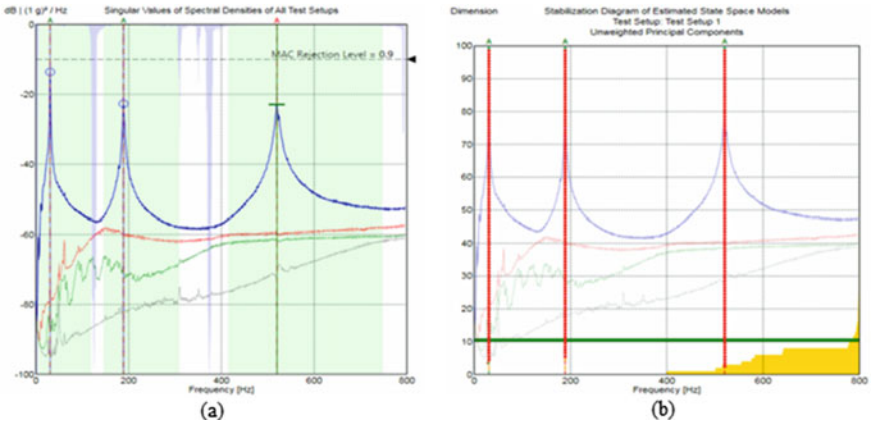

Fig. 3 Results obtained in ARTeMIS Modal (**a**) EFDD method (**b**) SSI method

Table 2 Experimentally obtained natural frequencies of cantilever beam

Modes	Natural frequency EFDD method (Hz)	Natural frequency SSI method (Hz)
1	30.67	30.56
2	188.85	188.91
3	519.74	520.10

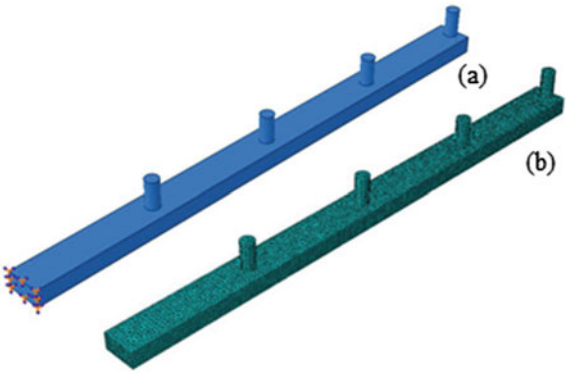

Fig. 4 ABAQUS model (**a**) Assembly view and (**b**) Meshing view

Table 3 Numerical natural frequency

Modes	Natural frequency (Hz)
1	31.1
2	193.62
3	536.49

3 Finite Element Modelling

The 3-D finite element model of beam using solid elements with geometric properties as specified in Table 1 was constructed in ABAQUS [7] and then computational modal analysis was done to determine the first three natural frequency and mode shape in vertical direction. In finite element analysis, the steel beam to be tested is idealized as homogenous material and modelled with eight-node solid (brick) elements, which are identified as C3D8R in software ABAQUS. After a thorough mesh sensitivity analysis, a size of 5 mm was chosen. The accelerometer each of weight 98gms were modelled at 200, 400, 600 and 800 mm as solid element to account for added mass (Fig. 4). The natural frequency for the cantilever beam obtained in bending mode using ABAQUS is shown in Table 3. The corresponding numerically obtained mode shape is shown in Fig. 5.

4 Comparison of results

The natural frequencies which are determined using experimental and numerical method are shown in Table 4. It is observed in Table 4 that the frequency results obtained are practically identical with a maximum difference of 3.12%. Figure 6 shows the normalised mode shapes obtained at accelerometer locations using numerical and experimental methods. The modal assurance criteria (MAC) establishes

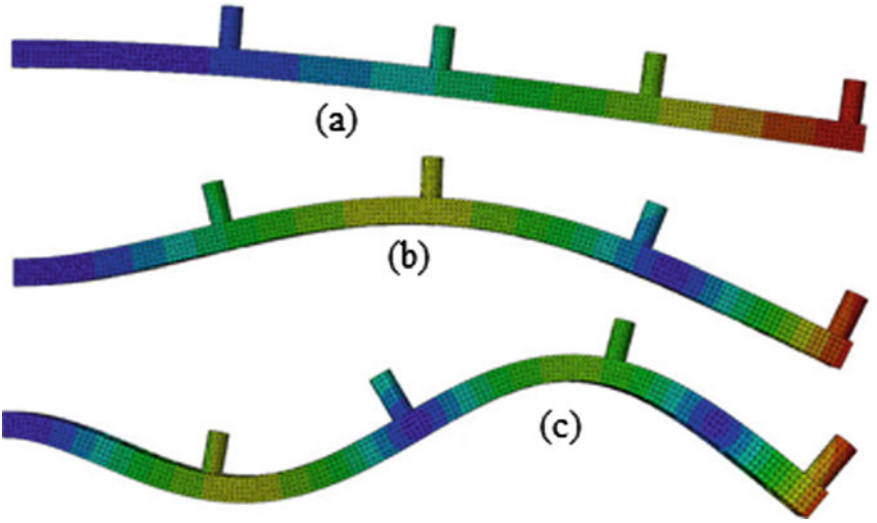

Fig. 5 Mode shape for cantilever beam **a** Mode 1 **b** Mode 2 and **c** Mode 3

Table 4 Comparison between numerical and experimental frequency of beam

Modes	Numerical natural frequency (Hz)	Natural frequency EFDD method (Hz)	Natural frequency SSI Mmethod (Hz)	Difference (%)
1	31.1	30.67	30.56	1.39
2	193.62	188.85	188.91	2.46
3	536.49	519.74	520.10	3.12

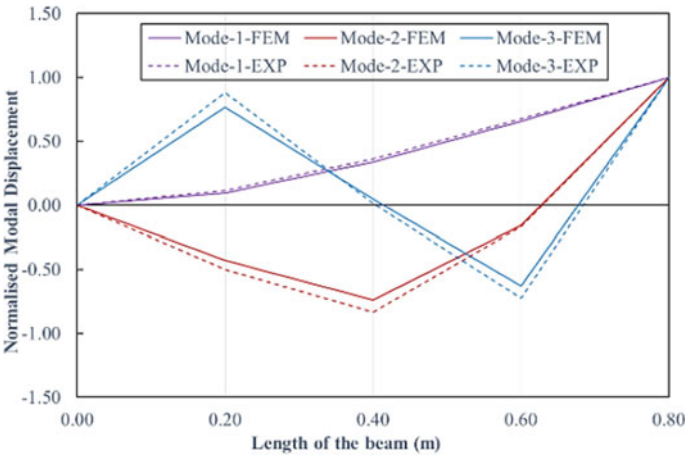

Fig. 6 Numerical and experimental modal vectors obtained

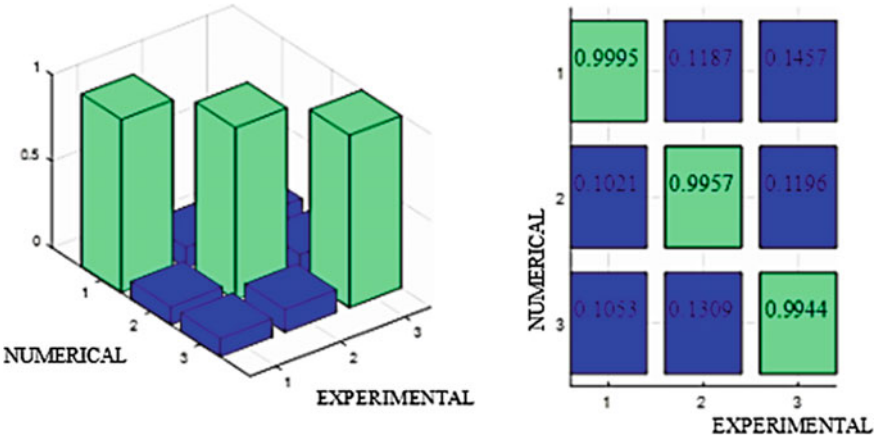

Fig. 7 MAC values between numerical and experimental modes

a correlation between numerical and experimental modes. The MAC value varies between 0 and 1, where 1 indicates high degree of correlation [8]. The MAC values for numerical and experimental mode shapes are shown in Fig. 7. MAC values are greater than 0.99 indicating a good correlation between the mode shapes.

5 Conclusions

In the present work, modal analysis of a cantilever beam was performed numerically using finite element method and experimentally under ambient random vibration conditions. The comparison of the dynamic properties, i.e. frequency and mode shape obtained showed overall a very good agreement. MAC factors obtained from the numerical and experimental mode shapes shows a good correlation. Overall, the modal characteristics were successfully obtained experimentally under ambient vibration conditions.

References

1. He J, Fu ZF (2001) Modal analysis. Butterworth-Heinemann, Boston, MA
2. Cantieni R (2005) Experimental methods used in system identification of civil engineering structures. In: Proceedings of the 1st international operational modal analysis conference (IOMAC05), Copenaghen, Denmark, pp 249–260
3. Reynolds P (2008) Dynamic testing and monitoring of civil engineering structures. Exp Tech 32(6):54–57
4. Jacobsen A, Brincker D (2007) Using EFDD as a robust technique to deterministic excitation in operational modal analysis. In: Proceedings of ISMA2006: international conference on noise

and vibration engineering, Leuven, Belgium
5. Peeters B, De Roeck G (1999) Reference-based stochastic subspace identification for output-only modal analysis. Mech Syst Signal Process 13(6):855–878
6. ARTeMIS Pro 6.1 (2019)Structural vibration solutions A/S, NOVI Science Park, Aalborg
7. Abaqus V (2013) 6.13 Documentation. DassaultSystemesSimulia Corporation
8. Allemang RJ, Brown DL (1982) Correlation coefficient for modal vector analysis. In: Proceedings of the 1st international modal analysis conference (IMAC-1), Orlando, Florida, USA

Strengthening of Multistory Steel Moment-Resisting Frame Building by Providing Chevron Bracings

Parthav P. Patel and Digesh D. Joshi

Abstract Progressive collapse is one of the failure mechanisms, in which the failure of a few critical structural elements leads to the collapse of large parts of a structure disproportionate to original failure. In the present study, the progressive collapse potential of a 9-story steel moment-resisting frame building strengthened by providing a combination of vertical and horizontal arrangement chevron bracings is assessed using the Alternate Path Method (APM) as specified by U. S. General Services Administration (GSA 2016) guidelines. Linear static, nonlinear static, and nonlinear dynamic analyzes are performed using SAP2000 software under the different column and/or brace removal scenarios from the ground floor of the exterior frame. Demand Capacity Ratio (DCR) of columns adjoining to the removed column are calculated from linear static analysis. The nonlinear analyzes are carried out to understand the failure mechanism and to obtain the vertical displacement time history at the column removal location. Linear static analysis results indicate that the provision of chevron bracing effectively limits the DCR value of critical columns within the acceptance criteria. Nonlinear dynamic analysis results advocate effective redistribution of additional loads to the adjoining members upon column removal.

Keywords Alternate path method (APM) · Moment resisting frame · Providing chevron bracings · Demand capacity ratio

1 Introduction

Progressive collapse of a structure occurs due to loss of primary load-bearing element-like column which leads to a partial or full collapse of the structure. It is a dynamic failure mechanism that generally occurs due to abnormal loading which

P. P. Patel (✉) · D. D. Joshi
Institute of Technology, Nirma University, Sarkhej Gandhinagar Highway, Ahmedabad 382481, India
e-mail: 19mclc13@nirmauni.ac.in

D. D. Joshi
e-mail: digesh.joshi@nirmauni.ac.in

B. Kondraivendhan et al. (eds.), *Sustainable Building Materials and Construction*,
Lecture Notes in Civil Engineering 222,
https://doi.org/10.1007/978-981-16-8496-8_40

can cause catastrophic failure of the structure, significant economic losses as well as loss of human lives. Altogether, the progressive collapse of any structure will ultimately adversely affect sustainability. The collapse of the Ronan Point Apartment (London 1968) draws attention to protect the structure against progressive collapse. After the collapse of the World Trade Center (New York 2001), many government and private agencies started to work upon the development of guidelines for the design of progressive collapse-resistant structures. Among these guidelines, the U. S. General Services Administration (GSA) (2016) and Unified Facility Criteria (UFC) published by the Department of Defense (DoD) [7] employ the Alternate Path Method (APM) to ensure structure's safety against progressive collapse.

Chen et al. [2] presented the effectiveness of chevron bracings provided in all the bays of the top story in all the directions, for strengthening of the steel building. Progressive collapse.

The potential of a 9-story steel moment-resisting frame building was evaluated by Marjanishvili et al. [5] along with a comparison of the results of various analysis methods. Khandewal et al. [4] analyzed the building for progressive collapse by providing concentric (X-type) and eccentric bracings by using UFC guidelines. The progressive collapse potential of building with the concentric and eccentric braces was evaluated by Naji and Zadeh [6] using SAP2000 software following GSA guidelines. The authors studied the effect of different sizes of bracing sections and different link beam lengths on the progressive collapse resistance of the building. Asgarian and Rezwani [1] evaluated the progressive collapse potential of a 10-story braced frame building through the calculation of the progressive collapse Impact Factor.

Even though several studies have been conducted to evaluate the effect of different types of bracings on the progressive collapse of steel structures, limited literature is available presenting the influence of combined arrangement of vertical and horizontal bracing members on progressive collapse resistance of steel structures. In this paper, the effectiveness of chevron bracings provided vertically and horizontally is assessed as a strengthening measure for the 9-story steel moment-resisting frame building. Linear static, nonlinear static, and dynamic analyzes are carried out by following GSA 2016 guidelines under the different column and/or brace removal scenarios from the ground floor of the exterior frame.

2 Methodology

The 9-story regular steel building is considered for the present study. The braced frame structural system is used to strengthen the existing moment-resisting frame building. The design of various structural members like beams, columns, and braces are carried out as per IS 800: 2007. The progressive collapse potential of the moment frame and braced frame building is evaluated by following GSA 2016 guidelines using SAP2000 software. For progressive collapse analysis, three column and/or brace removal scenarios are considered which include a middle column from the

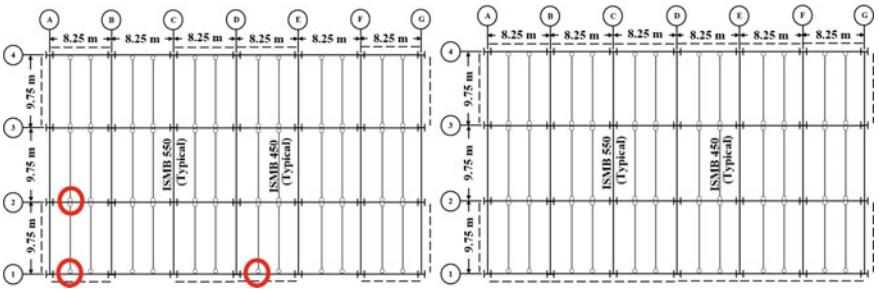

(a) First Floor Plan (b) Top Floor Plan

Fig. 1 Plan of braced frame building

longitudinal bay (Scenario 1), corner column (Scenario 2), and adjacent to corner column from the transverse bay (Scenario 3).

2.1 Description of Model

The 9-story steel building considered for the study is having 6-bays in the longitudinal direction and 3-bays in the transverse direction. Chevron bracings (also known as inverted V bracings) are designed to enhance the progressive collapse resistance of the steel building. The plan and elevation of the braced frame building are shown in Figs. 1 and 2, respectively. The column and/or brace removal locations for different scenarios are highlighted as shown in Fig. 1a.

2.2 Loading on Building

The Dead Load (DL) includes 2.25 kN/m^2 slab load on all floors and 19.7kN/m wall load on periphery beams except on the roof. The Live Load (LL) of 3.5 kN/m^2 and 1 kN/m^2 is considered on the typical floor and roof, respectively. Earthquake and wind loads are considered as per IS 1893:2016 (Part 1) and IS 875–2015 (Part 3), respectively. The section of braces is designed as Square Hollow Section (SHS) and columns are designed as a built-up column. The designed section of the brace is SHS 220 × 220 × 10 and SHS 180 × 180 × 8 in the longitudinal direction and transverse direction, respectively. The yield stress of steel material is considered as 310 N/mm^2.

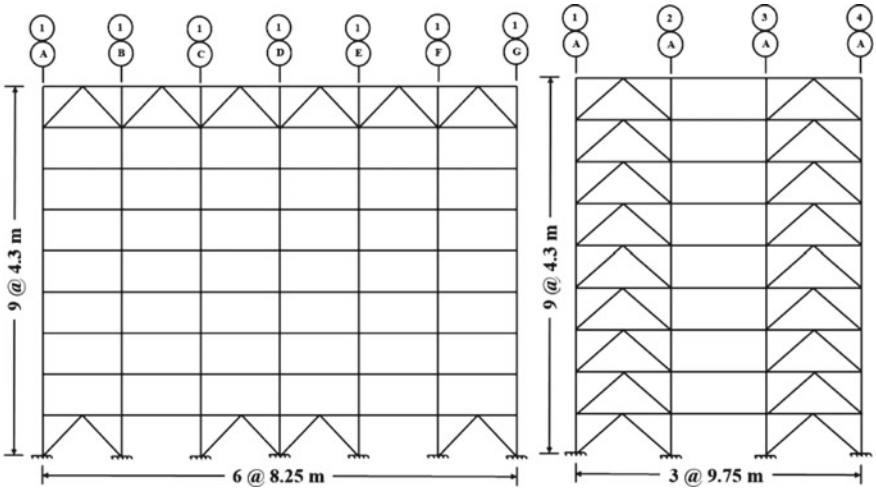

(a) Longitudinal Elevation (b) Transverse Elevation

Fig. 2 Elevation of braced frame building

3 Linear Static Analysis

The load combination is used as specified by GSA [3] guidelines for linear static analysis and load factor for deformation-controlled (G_{LD}) action and Force-Controlled (G_{LF}) action is calculated and shown in Eqs. 1 and 2, respectively.

$$G_{LD} = 3.773(1.2DL + 0.5LL) \tag{1}$$

$$G_{LF} = 2.0(1.2DL + 0.5LL) \tag{2}$$

From the linear static analysis, Demand Capacity Ratio (DCR) for columns adjoining to the removed column are calculated for three different column removal scenarios. The DCR for columns is presented in Fig. 3. The nomenclature represents the location of columns, i.e., C1 represents the column at the intersection of grid C and grid 1, which is adjoining to middle column removal considered in scenario 1.

Results of DCR for columns as shown in Fig. 3 indicate that the configuration of chevron bracings considered in the present study significantly reduces and limits the DCR value within acceptance criteria and safeguard the building against progressive collapse.

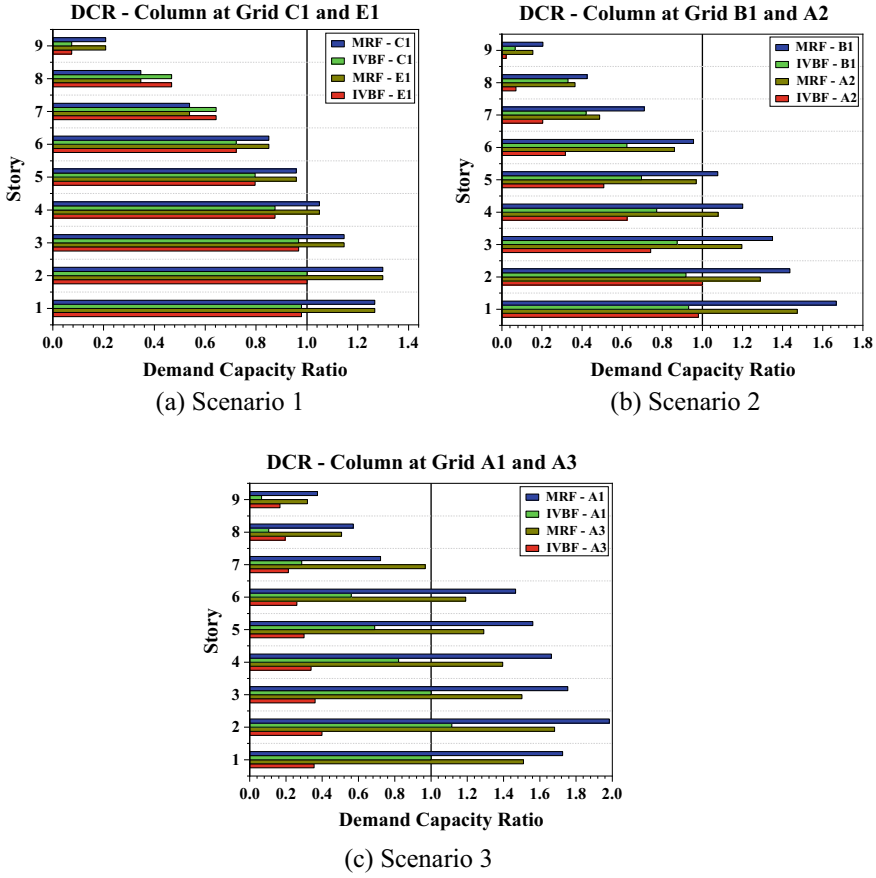

Fig. 3 Demand capacity ratio (DCR) for column

4 Nonlinear Static Analysis

The failure mechanism and collapse load of the building are evaluated using nonlinear static (Pushdown) analysis. This method of analysis is more accurate than linear static analysis because it includes the material and geometric nonlinearity. The load combination used for nonlinear static analysis (G_N) and calculation of load factor is carried out according to GSA 2016 guidelines as presented in Eq. 3.

$$G_N = 1.36(1.2DL + 0.5LL) \tag{3}$$

From the nonlinear static analysis, a graph of the percentage of Total Load versus Vertical Displacement at the location of column removal location is developed and

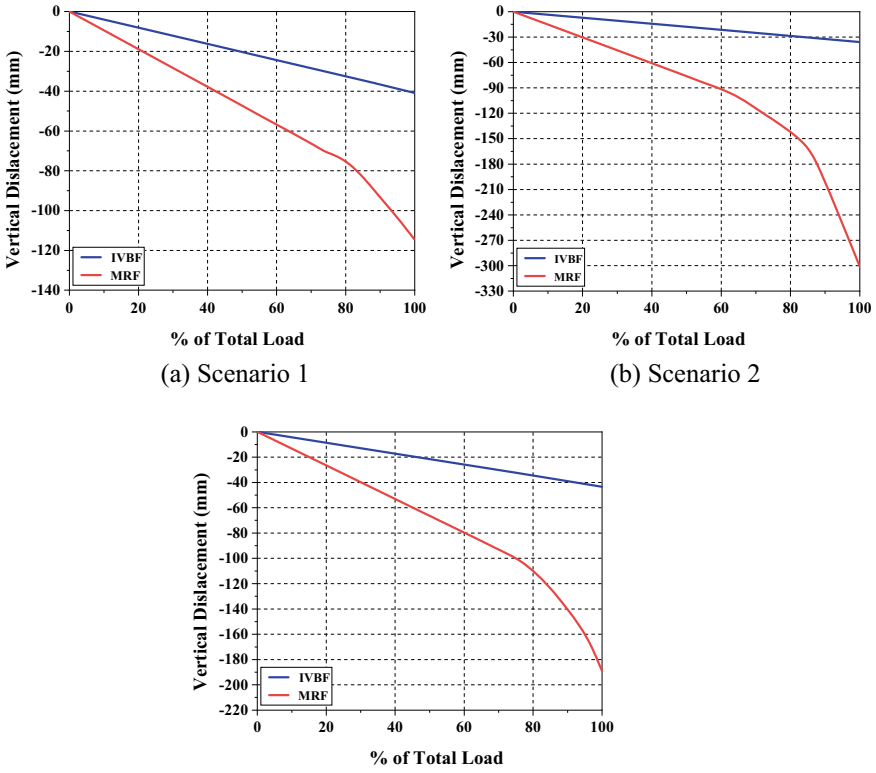

Fig. 4 Nonlinear static curve at column removal location

presented in Fig. 4 for different column removal scenarios. From these graphs, the load capacity of the building after column removal is evaluated.

From Fig. 4, it is evident that maximum static displacement at column removal location reduces significantly in braced frame building compared to moment frame building. Also, the braced frame building is in the elastic stage under the different column and/or brace removal scenarios, which indicates the superior performance of the building against progressive collapse.

5 Nonlinear Dynamic Analysis

Nonlinear dynamic analysis is an important method to evaluate the progressive collapse potential of a building, as it includes nonlinearity as well as the dynamic condition of a building due to column removal. In this method, the column is removed

suddenly by ramping down its axial force after all the gravity load reaches the equilibrium condition. The load combination used for nonlinear dynamic analysis (G_{ND}) is given in Eq. 4. In the present study, only the gravity loads are considered for the occurrence of progressive collapse and lateral loads are not considered as specified by the U.S. General Services Administration [3] guidelines.

$$G_{ND} = 1.2DL + 0.5LL \tag{4}$$

From this analysis, displacement time history at column removal location is plotted for all column and/or brace removal scenarios as shown in Fig. 5. The Rayleigh Damping is considered in the analysis with a 2% damping ratio (ξ). The displacement time history graphs indicate that maximum dynamic displacement at column removal location in braced frame building reduced drastically compared to displacement in moment frame building.

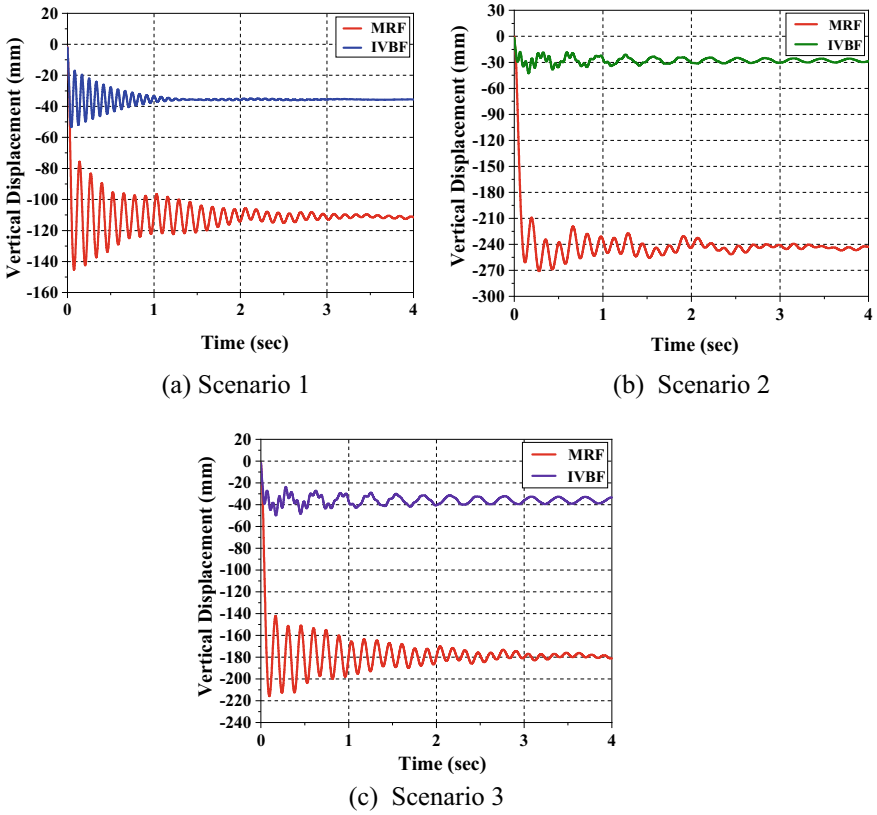

Fig. 5 Displacement time history plot at column removal location

6 Conclusions

In the present study, the 9-story steel Moment-Resisting Frame (MRF) building is strengthened by providing chevron bracings (also referred to as inverted V bracings) provided horizontally and vertically. Based on results obtained following conclusions are derived:

- Demand Capacity Ratio of columns under the different column and/or brace removal scenarios satisfies acceptance criteria in braced frame building, which indicates that present bracing configuration effectively enhances progressive collapse of building considered.
- Nonlinear static and nonlinear dynamic analysis results show that both moment-resisting frame and braced frame building resists 100% load without significant failure, however, most of the beams in moment-resisting frame building enter into the nonlinear stage, while all beams and columns in braced frame building remain in the elastic stage.
- The displacement time history curve obtained from nonlinear dynamic analysis at the location of column removal shows that the maximum dynamic displacement in braced frame building is reduced by 63.3, 84.2, 76.9% for scenario 1, scenario 2, and scenario 3, respectively.
- The axial force demand in columns increases due to the presence of bracing but it reduces bending moment drastically and safeguards the building against the progressive collapse.

References

1. Asgarian B, Rezvani HF (2010) Determination of progressive-collapse impact factor of concentric braced frames. In: Paper presented at 14th european conference on earthquake engineering, Ohrid, Macedonia, August 2010
2. Chen J, Peng W, Ma R, He M (2012) Strengthening of horizontal bracing on progressive collapse resistance on multistory steel moment frames. J Perform Constr Facil 26(5):720–724
3. General Services Administration (2016) Alternate path analysis and design for progressive collapse resistance. 1st Revision, United States, January 28, 2016
4. Khandewak K, El-Tawil S, Sadek F (2009) Progressive collapse analysis of seismically designed braced frames. J Constr Steel Res 65(3):699–708
5. Marjanishvili S, Agnew E (2006) Comparison of various procedures for progressive collapse analysis. J Perform Constr Facil 20(4):365–374
6. Naji A, Zadeh MK (2019) Progressive collapse analysis of steel braced frames. Practice Periodical Struct Design Construct 24(2)
7. Unified Facilities Criteria (UFC 4–23–03) (2016) Design of buildings to resist progressive collapse. Department of Defense (DoD), Change 3, 1 November 2016

Structural Analysis of Heritage Timber Structure

Jofina Elsa Raji and N. Senthil Kumar

Abstract Heritage buildings in Kerala is known for its architectural and aesthetic uniqueness, whose main materials of construction were sustainable goods like wood, stone, sand, etc..... This paper is concerned with the structural analysis of timber joineries of Aranmula Parthasarathy Temple, which is one among the Divya Desams situated on the banks of river Pampa. It was constructed during 16A.D and is made of teak wood as well as granite which is elevated from the normal ground level approximately by 40ft. The noticeable feature about the structure is that even though the banks of the temple were affected by natural calamities (i.e., flood in 2018 and also the frequent wind loads as it is located on river banks), the structure still stays strong without any damage. It is believed that this can be due to the material characteristics of the structure as well as the joints and connections provided within the structure. In this paper, we will go through the finite element analysis of the different types of timber joints as well as the material tests of timber. The main focus of this work will be to incorporate these joints in the modern construction practices in order to make the structure more stable.

Keywords Timber structure · Heritage building

1 Introduction

Heritage buildings are those structure that possess architectural, aesthetic, historic or cultural values. Heritage Architecture is a term that refers to the buildings of historic or cultural importance, which are a vital part of the country's heritage and require conservation. The heritage structures provide a sense of identity of culture and history of the society. Heritage buildings are a unique piece of art of our ancestors. It is very interesting to note that the ancient structures are strong enough to resist the loads and

J. E. Raji (✉) · N. S. Kumar
VIT, Vellore, India

N. S. Kumar
e-mail: n.senthilkumar@vit.ac.in

B. Kondraivendhan et al. (eds.), *Sustainable Building Materials and Construction*,
Lecture Notes in Civil Engineering 222,
https://doi.org/10.1007/978-981-16-8496-8_41

forces acting upon them since ages. Also, if we compare both heritage and modern buildings, it is evident that modern buildings are designed for a maximum period of 50 years; whereas the ancient structures still stay strong even after thousands of years. So, there comes the need of the structural analysis of heritage structures.

Kerala is a state where extensive ancient architectural master pieces are found especially in timber. Aranmula Parthasarathy Temple is one among the heritage structures in Kerala. It is a temple constructed on stone and timber masonry, which is situated on a high platform from the normal ground level. Since the temple is situated on the banks of the river Pampa, and also the structure is situated on a high level, it undergoes wind loads continuously. Also, the banks of the river Pampa were affected by the severe floods caused in 2018. These are the major loads the structure has faced during its lifetime till now. The main attraction, or the thing that makes the temple structurally unique is that even though the structure undergoes a lot of loads and forces, it stays strong. In this project, I am focusing on the wind load analysis of the structure.

We all know that the timber masonry involves a lot of timber joineries, which help them to adhere together and thus provide strength to the structure. A joint is simply a combination of two or more pieces to be held together. In this project, I am also focusing on the finite element modelling and analysis of certain types of joineries involved in timber masonry that were discovered by the ancient people. This is to find out the individual capacities of each type of joints.

2 Literature Review and Gap of Study

Kim et al. [1] utilizing top ordinary burdens in sections of a four-segment reference model, blend decides were suggested that can be applied to abnormal supertall structures dependent on the idea of mix factors, which are characterized for various stacking conditions. The blend factor for the square model is roughly 0.5, and those for abnormal models vary contingent upon building shape.

Foo et al. [2] done in situ testing of a wood Warren support building and research centre testing of four bracket joints normal of those found in a Warren support building are completed over a range of five years. Tests were directed on supports with old and new wood. It was discovered that the inflexibility of a joint is identified with the quantity of connectors in the joint zone.

Schmidt and Miller [3] examined collar-tied rafters convey the biggest bowing minutes in the rafters and furthermore the biggest ductile powers in the ties. Reformist breakdown load was opposed simply by statically determinate eave and edge joint and vague purlin rafters. Collar swaggers enormously lessen the twisting second in rafters without the utilization of purlin upholds yet additionally require a solid and solid bind to the mating eave.

Fig. 1 Visible part

3 Timberjoineries

A joint is the portion where two or more timber pieces are held together or joined together. It is that crucial point, which determines the overall strength and performance of the structure. A joint is said to have two aspects after joining. They are the visible and the invisible. The visible part is known as the portion which is seen to our naked eyes even after joining and the invisible is the portion which is hidden inside the joint. There are almost twelve joineries of timber mentioned in Kerala architecture which comes within the wall plate, floor plate, sill, etc.…The twelve joineries are ardhapani, sukaragrahana, vajrasannibha, jhasadantakam, meshayuddha, adharapattika in floor plate and elevated sill, three types of floor plate joints and birds mouth joint. The detailed analysis of two among the above-mentioned joints are done in the following sections using finite element analysis by the software Abaqus CAE (Figs. 1 and 2).

4 Analysis of Timberjoineries

4.1 Meshayuddha Joint

It is commonly known as Mortise- Tenon Joint. In Sanskrit, mesha- a ram (sheep); yuddha- fight. It tries to replicate the interlocking of horns of two rams involved in fight. The central tenon is of a width of a third that of the pillar and the length is twice or two and a half times its width. This joinery generally happens at the top of columns and also sometimes at the bottom of the columns too (Fig. 3).

The analysis was carried out using the finite element software Abaqus CAE. The dimensions of the joint taken are:

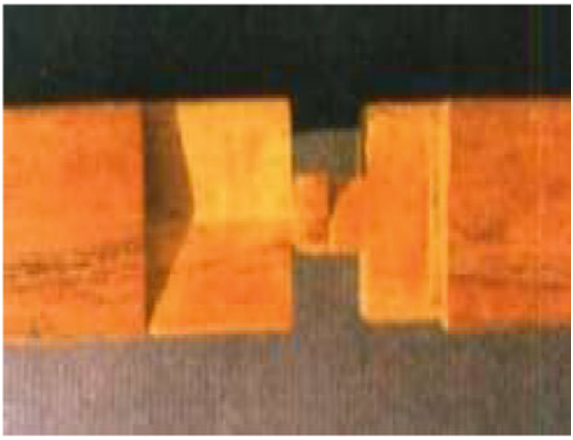

Fig. 2 Invisible part

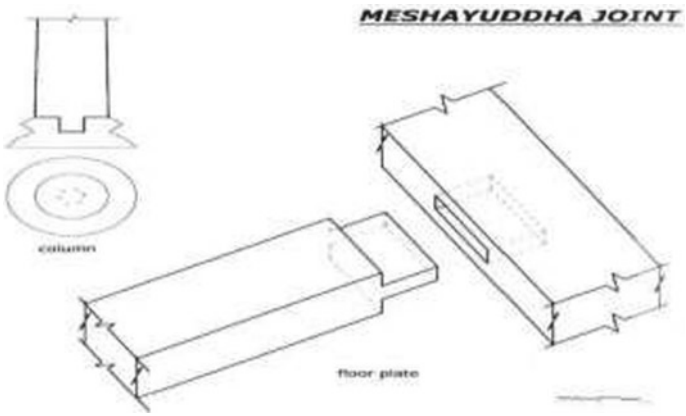

Fig. 3 Meshayuddha joint

- **MORTISE**: L = 1 m, B = 0.4 m, D = 0.3 m, Slot: 40 × 15 × 20mm
- **TENON**: L = 1 m, B = 0.4 m, D = 0.3 m, Tenon: 40 × 15 × 20mm

Both the parts were modelled, given properties, BC, load and meshed. The properties taken were as per IS:883-1994 and is mentioned in the Table 1. The boundary

Table 1 Material properties taken from IS code

Parameters	Values
Modulus of elasticity	99.7 N/mm^2
Density	660 kg/m^3
Poissons ratio	0.4
Coefficient of friction	0.25

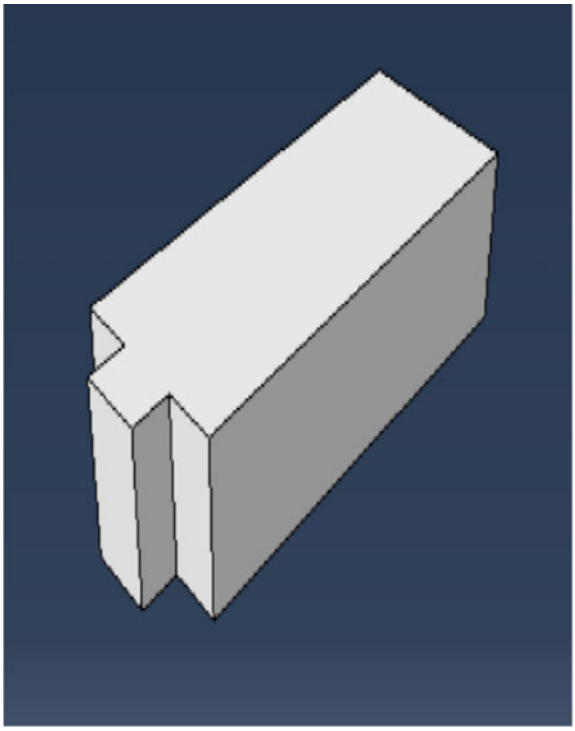

Fig. 4 Mortise

condition was given as both ends hinged. And the load considered was only gravity load (Figs. 4 , 5, 6, 7 and 8).

4.1.1 Results of Analysis of MeshayuddhaJoint

The joint can take up a max. stress of 0.0097 MPa with a max. displacement of 0.001609 cm when gravity load was applied. It is also clear that the critical stress occurs at the ends of the tenon part, while the critical displacement occurs at the joint. Thus, it can be inferred that, due to a stress happening at the end of the joinery, the joint was subjected to a displacement (Figs. 9 and 10).

4.2 Adharapattika Joint

Adharapattika joint is the one found in the floor plates (Fig. 11).

The dimensions were taken as mentioned below. Also, the material properties were specified as per Table 2. The BC and load conditions were mentioned as in clause 3.1 (Figs. 12, 13, 14, 15 and 16).

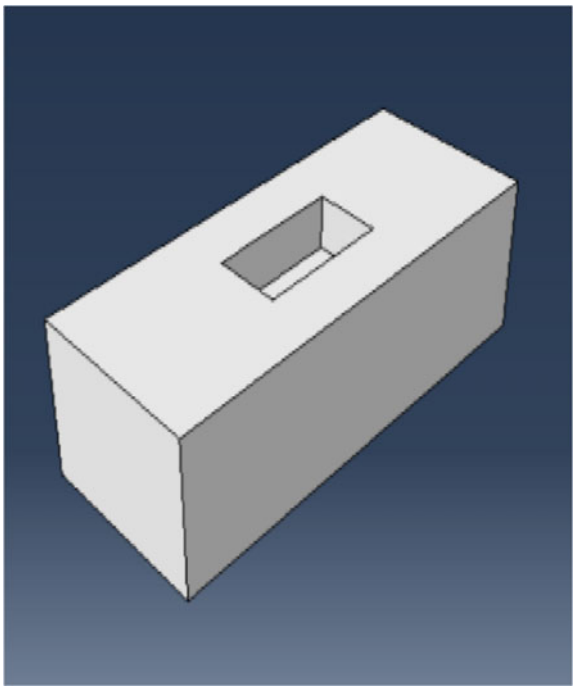

Fig. 5 Tenon

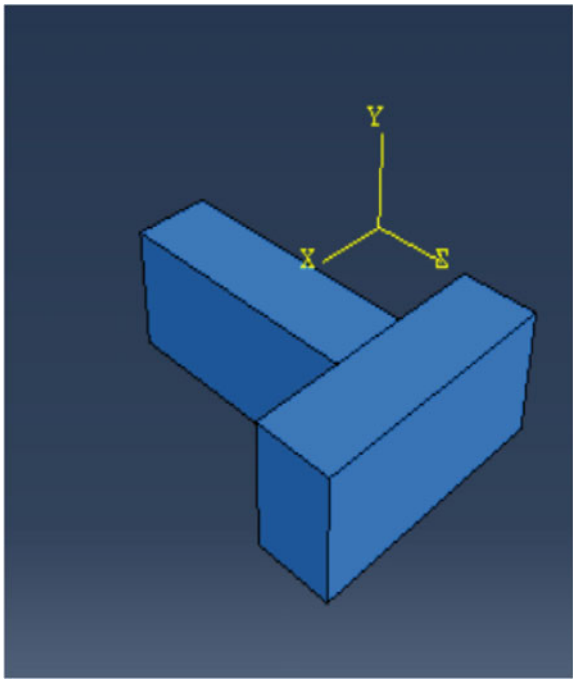

Fig. 6 Modelled meshayuddha joint

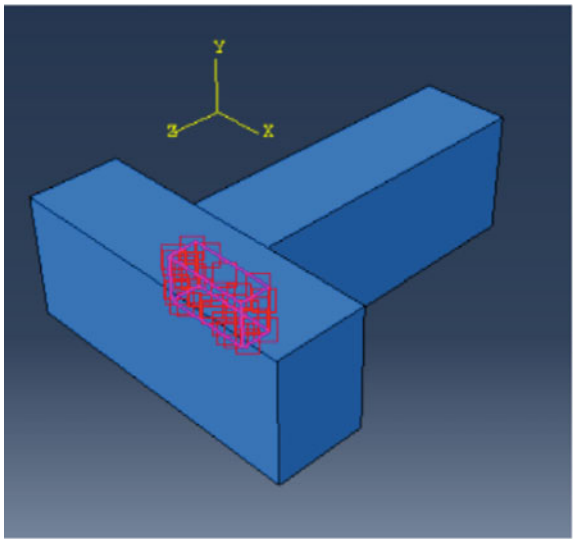

Fig. 7 Applied boundary conditions

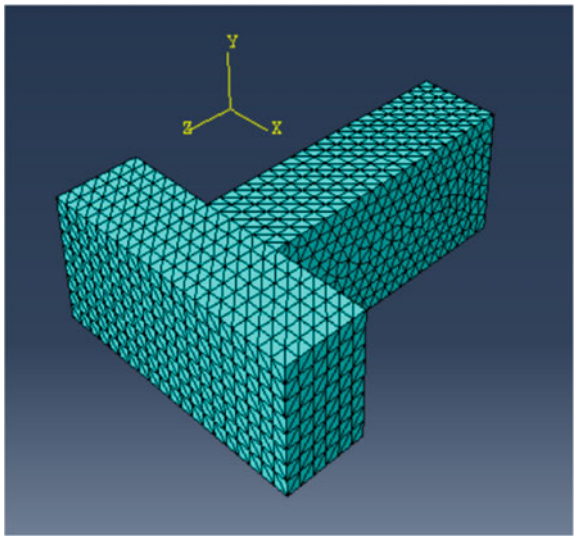

Fig. 8 Meshed joint

- Length = 1.3 m
- Breadth = 0.4 m
- Width = 0.4 m

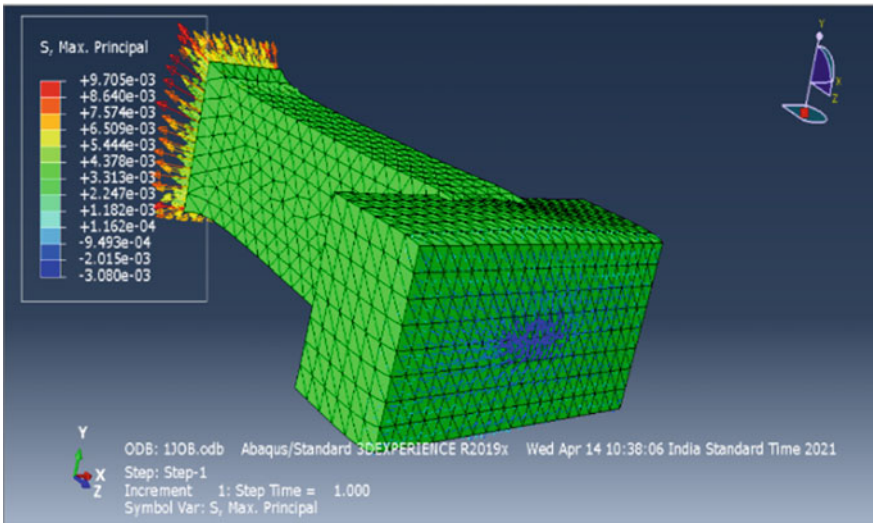

Fig. 9 Maximum principal stress contour

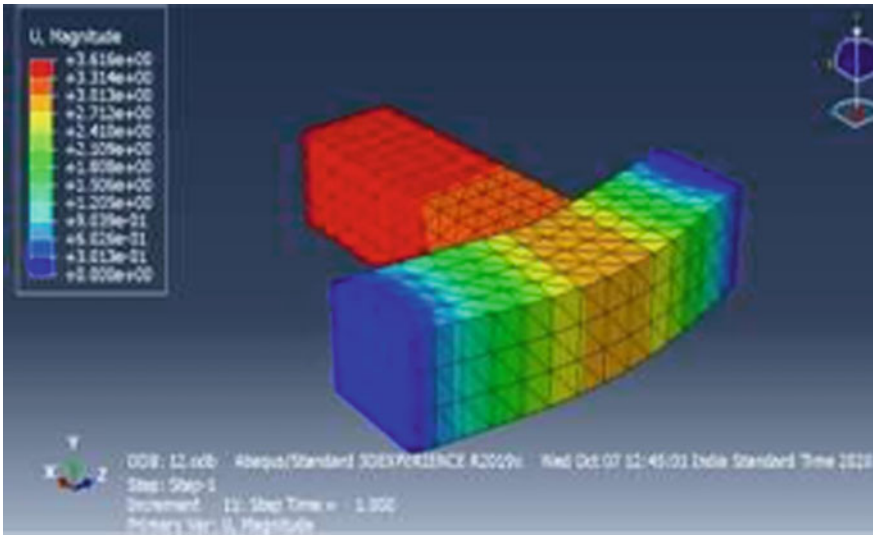

Fig. 10 Displacement contour

4.2.1 Results of Analysis of Adharapattika Joint

The joint can take up a max. stress of 0.05865 MPa with a max. displacement of 0.05816 cm when gravity load was applied. It is clear that the critical stress occurs at the ends of both the parts, while the critical displacement occurs at the joint. Also,

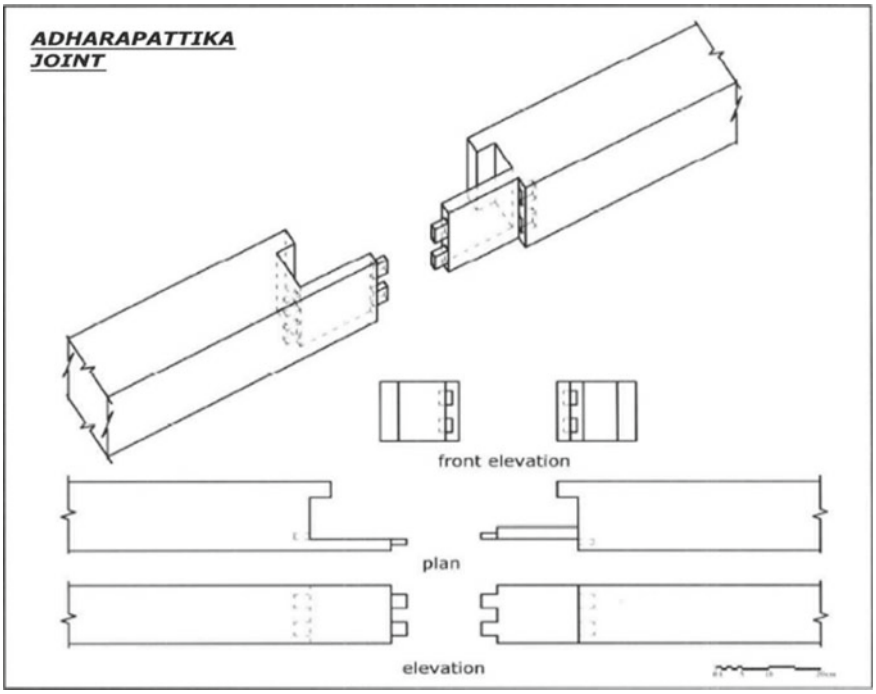

Fig. 11 Adharapattika joint

Fig. 12 Modelled part-1

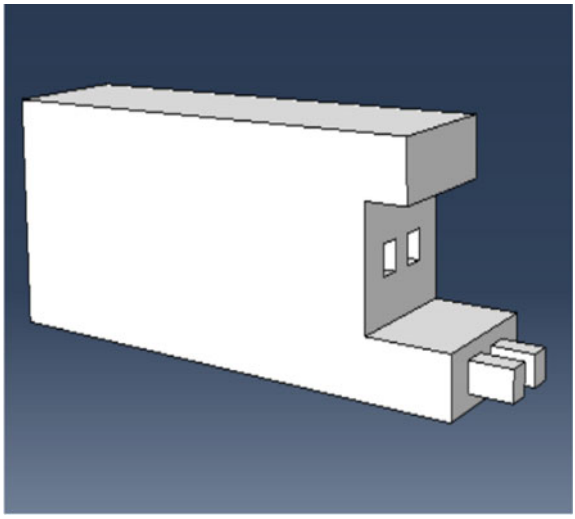

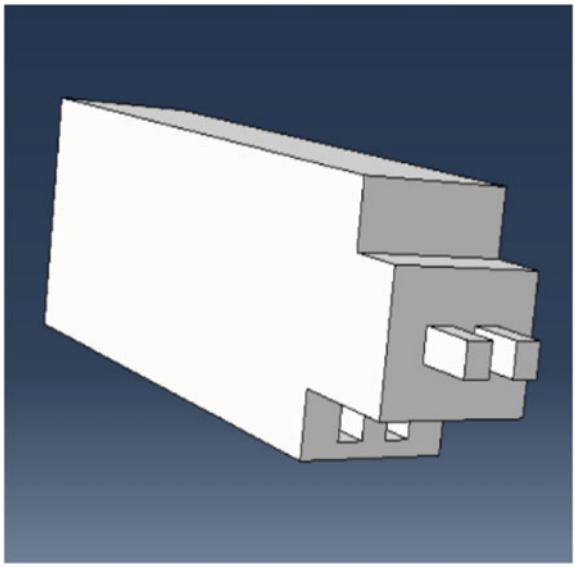

Fig. 13 Modelled part-2

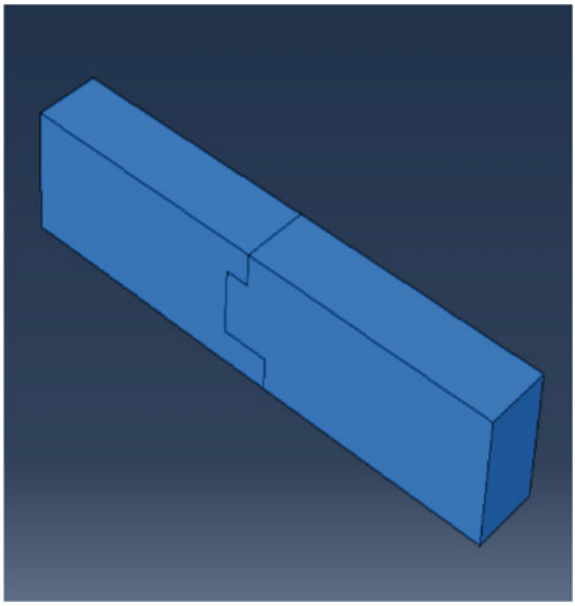

Fig. 14 Modelled adharapattika

when a small portion of the parts were removed from the model, and analysed, the stress (0.05865 < 0.08118 MPa) as well as the displacement (0.05816< 0.07901 cm) values were higher than the other results. Thus, it can be concluded that, even a small projection plays a crucial role in the strength of the structure (Figs. 17 and 18).

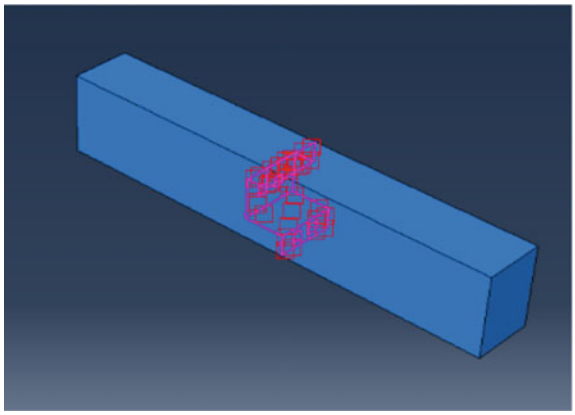

Fig. 15 Applied BC

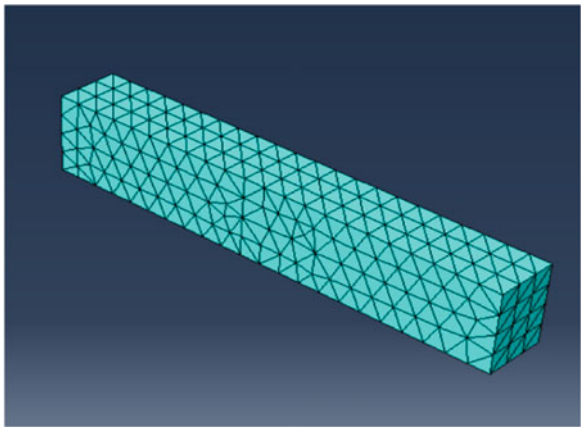

Fig. 16 Meshed joint

5 Conclusions

The finite element analysis of two types of timber joints, i.e. meshayuddha joint and adharapattika joint were done. The analysis results shows that both of the joints are able to withstand stress as well as displacements, even for a small cross-section of joint. Meshayuudha joint was able to carry a stress of upto 0.0097 N/mm^2 and adharapattika joint was able to carry a stress of 0.0586 N/mm^2. Also, they could displace through 0.01 and 0.5 mm respectively. So, we can infer that heritage buildings stay strong due to these kinds of special types of joints. So, if we incorporate these kinds of joints in modern constructional practices, we can make them stay stronger, along with the modern era of constructional practices.

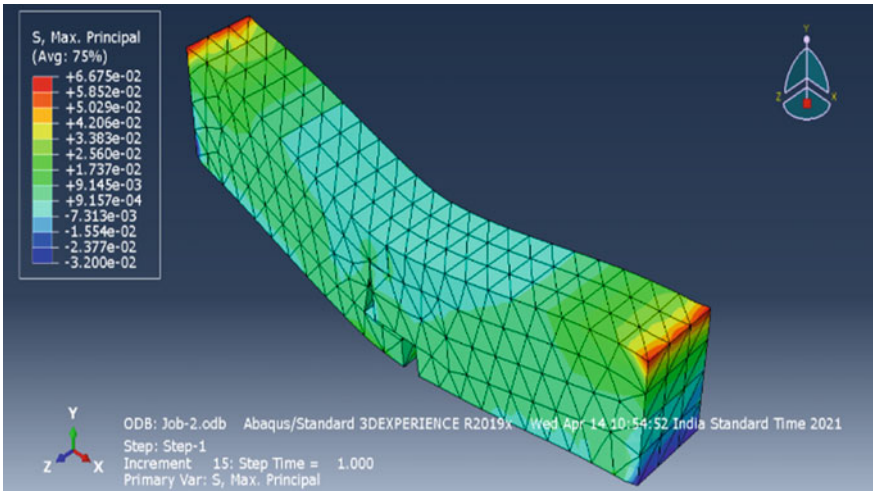

Fig. 17 Stress contour

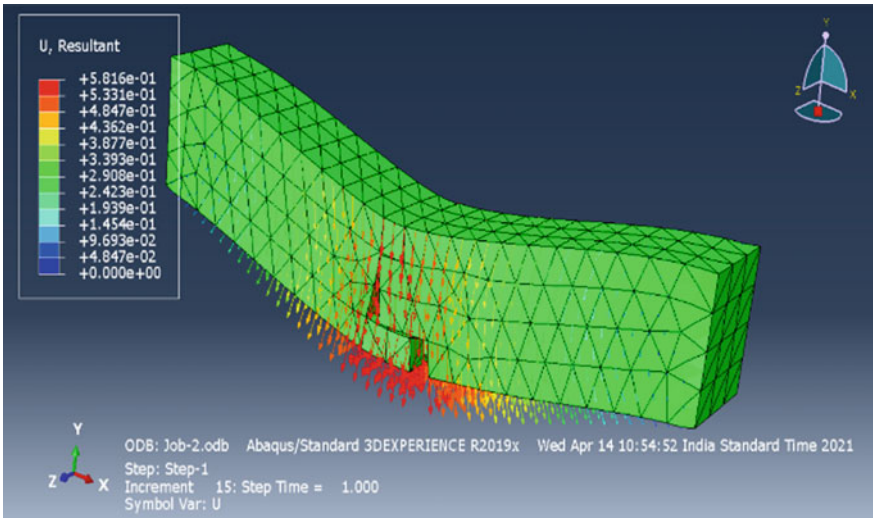

Fig. 18 Displacement contour

References

1. Kim YC, Tamura Y, Kim S (2015) Wind load combinations of atypical supertall buildings. ASCE-J Str Engg 04015103–1–8
2. Foo HC (1993) Experimental study of timber trusses and joints. ASCE- J. Str Engg 119:1283–1296

3. Schmidt RJ, Miller JF (2012) Considerations for design of rafters in timber buildings. In: ASCE-practice periodical on structural design and construction, August 1, vol 17(3), pp 127–132

Variation in Governing Wind Loads on RC Chimney—Parametric Study

Megha Bhatt, Amey Gadkari, and Sandip A. Vasanwala

Abstract This paper deals with the study of variation in governing wind loads based on variation in dimensional parameter like H/Db ratio and tapered height of chimney. The analysis is carried out as per IS 4998: 2015. Parametric study has been carried out to study the wind force effects for total of 96 cases by varying parameters, namely basic wind speed, ratio of height to outer diameter at the bottom (H/Db), and tapered section height of the chimney. From the 96 cases, the case for basic wind speed of 47 m/s with H/Db ratios 10, 12, and 14 and tapering ratios 0, 1/3, and 1 has been discussed with the help of result tables and graphical output portraying the effects of above mentioned parameters on requirement of across wind load analysis, first mode frequency, second mode frequency, and governing wind loads on the chimney along its height. This study helps in identifying the range of dimensional parameters that are feasible for the analysis through comparison.

Keywords RC chimney · Wind load · Design parameters

1 Introduction

There is invariable co-dependency of threshold factor for dynamic analysis requirement on the dimensional parameters, i.e., as per the IS 4998: 2015 [1, 2], the across wind analysis requirements are based on the critical wind speed V_{cr} falling in to the region of 0.5 V (z_{ref}) to 1.3 V (z_{ref}), where $V(z_{ref})$ is design hourly mean wind speed at (5/6) of H in m/s, and H is total height of chimney above ground in meters. The ascertained dependency of dimensional parameters can be cited directly based on the empirical formulae provided in the code, but few secondary parameters also influence the threshold factor for dynamic analysis requirement. The objective of this paper is to carry out a parametric study considering one of the both direct and indirectly influencing dimensional parameters.

M. Bhatt (✉) · A. Gadkari · S. A. Vasanwala
LDRP–ITR, Gandhinagar, Gujarat, India

B. Kondraivendhan et al. (eds.), *Sustainable Building Materials and Construction*,
Lecture Notes in Civil Engineering 222,
https://doi.org/10.1007/978-981-16-8496-8_42

2 Literature Review

The analytical methods depicted in the IS 4998 have been sophisticated over time, yet not to be put out of consideration; the Vickery–Basu "simplified" model has been a strong influence and has been adopted in the code after modification and simplification. The earlier revision of IS 4998 had incorporated the modified version of the Vickery–Basu "simplified" model with two separate formulae for chimney classified based on taper ratio. The ideology of taper was in congruence of slope in the elevation of the tower, i.e., it should not involve the "taper ratio" Dt/Db, but also slenderness ratio H/Db of the chimney. There were studies carried out by Vickery that denoted strong influence of tower geometry on the response. The paper by Devdas Menon and P. S. Rao [2] has discerned the influence of dimensional parameters on geometry and discussed about the disparities in codal estimates of across wind moments; this paper essentially denotes that parametric study is desideratum for understanding the analytical veracity and reliability of the proposed code.

3 Methodology

3.1 Problem Formulation

Parametric study has been carried out to study wind force effects for total of 96 cases by varying parameters, namely basic wind speed, ratio of height to outer diameter at bottom (H/Db), and tapered section height. The chimneys with tapering ratio 0, ¼, 1/3, and 1 are analyzed for H/Db ratios 10, 12, 14, 16 for all the basic wind speeds as per IS: 875 (Part 3)—2015 [3] that are 33, 39, 44, 47,50, and 55 m/s. The chimney has height of 126 m above ground and is considered to be unlined and does not have any opening in the shell. Only wind load effects are considered, i.e., the temperature stresses and earthquake forces are not considered. Table 1 shows the considered dimensional parameters for the comparative analysis, which includes outer diameter at base D_b, thickness at base t_b, outer diameter at top D_t, and thickness at top t_t. As wind force is considered to be predominant and more critical lateral load as compared to seismic force in the design of RC chimney [4, 5, 6] the parametric study is carried out only for wind forces.

Table 1 Diameter and thickness of shell for various H/D

H/D_b	D_b (m)	t_b (m)	D_t (m)	t_t (m)
10	12.6	0.63	4	0.2
12	10.5	0.525	3.3	0.17
14	9	0.45	2.8	0.14

3.2 Analytical Procedure

The analysis has been carried out as per the guidelines given in IS 4998: 2015 [1, 2]. The following steps are followed to carry out the analysis and finally the comparison.

Step 1: Carry out the static analysis using gust factor.

Step 2: Calculate critical wind speed for across wind loads for first and second mode.

Step 3: Compute moments corresponding to the specific case of wind speed and dimensional parameters.

Step 4: Calculate combined moments for cases where across wind load analysis is required.

Step 5: Plot and compare the analysis outcomes in order to draw inferences.

3.3 Comparison

A comparative study is carried out to justify the dependency of across wind load analysis requirement on dimensional parameters under study and clearly define thresholds based on these dimensional parameters. Another purpose of comparative study is to clearly outline the feasible range of dimensional parameters that can be utilized while trying to gage the behavior with the preliminary calculations.

4 Results and Discussion

The selective results for the case of basic wind speed $Vb = 47$ m/s, H/Db ratios 10, 12, and 14 and tapering ratios 0, 1/3, and 1 have been depicted in Tables 2, 3 and 4.

Tables 3 and 4 have the computed values of natural frequency of the chimney for first mode and second mode, respectively, which are used for determining the critical wind speed and then verifying with the threshold range for across wind analysis specified in the IS 4998: 2015 [1, 2].

Table 4 depicts the requirement for the across wind load analysis based on the criteria specified in the code.

Table 2 Natural frequencies for first mode

H/D_b	Un-tapered height		
	0H (m)	1/3H (m)	1H (m)
10	0.817	0.822	0.573
12	0.677	0.68	0.477
14	0.587	0.59	0.429

Table 3 Natural frequencies for second mode

H/D_b	Un-tapered height		
	0H (m)	1/3H (m)	1H (m)
10	3.078	3.084	3.441
12	2.554	2.559	2.861
14	2.194	2.198	2.496
H/D_b	Un-tapered height		
	0H (m)	1/3H (m)	1H (m)
10	3.078	3.084	3.441
12	2.554	2.559	2.861
14	2.194	2.198	2.496

Table 4 Across wind load analysis requirement comparison

H/D_b	Un-tapered height		
	0H (m)	1/3H (m)	1H (m)
10	1st mode	Not required	1st mode
12	Not required	2nd mode	1st mode
14	2nd mode	2nd mode	Not required

The dependency of natural frequency for both first mode (f_1) and second mode (f_2) on the dimensional parameters in study, i.e., D_t and D_b indicate the interdependency of critical wind speed (V_{cr}) on them too which governs the possibility of critical wind speed (V_{cr}) falling into the range of 0.5 V (z_{ref}) to 1.3 V (z_{ref}) and thus demonstrating the requirement for dynamic or across wind load analysis (Fig. 1).

The graph illustrates that for the case of fully tapered shell the along wind load governs throughout the height of the chimney (Fig. 2).

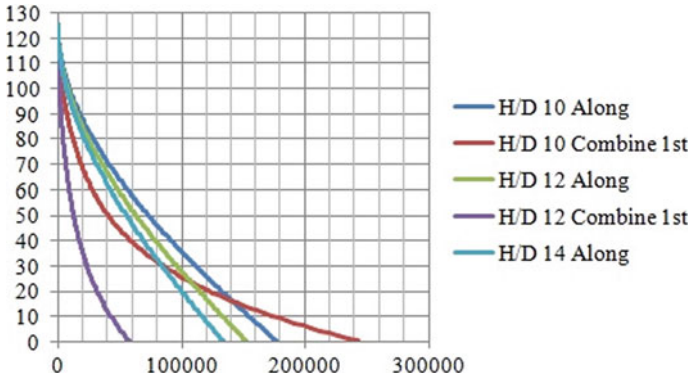

Fig. 1 Height of RC chimney (m) versus moments (kN.m) for fully tapered

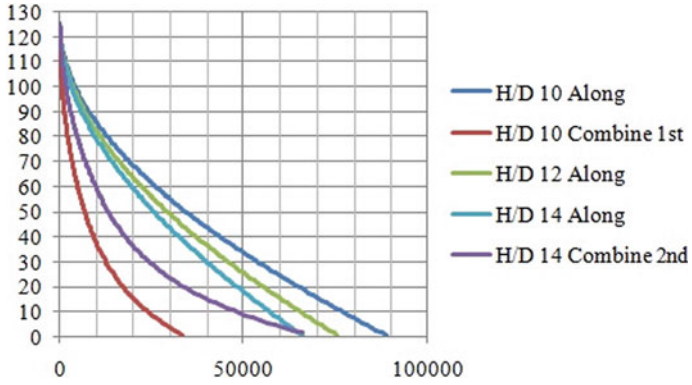

Fig. 2 Height of RC chimney (m) versus moments (kN.m) for 1/3 tapered

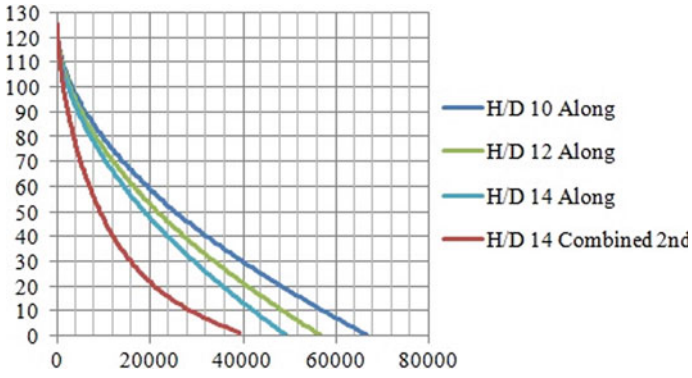

Fig. 3 Height of RC chimney (m) versus moments (kN.m) for fully un-tapered case

The graph illustrates that for the case of 1/3 tapered shell the along wind load governs throughout the height of the chimney (Fig. 3).

The graph illustrates that for the case of fully un-tapered shell the along wind load governs for nearly top 5/6H of the height of the chimney, while for the remaining height, first mode combined effect is significant. For H/D 12 and 14, the along wind load governs for the total height of chimney above the ground.

5 Ambiguities in the Code

In the code IS 4998: 2015 [1, 2], there are three parametric coefficients whose range have been mentioned, but the condition to be considered in a case when the value falls out of the required range has not been specified.

The three parametric coefficients identified are as follows:

F_{1A} = Strouhal number parameter;	F_{1B} shall be between 0.2 and 1;
F_{1A} shall be between 0.6 and 1;	β_s = Structural damping as a fraction of critical damping for across wind load;
F_{1B} = Lift coefficient parameter;	β_s shall be between 0.01 and 0.04;

According to the code IS 4998: 2015 [1, 2], clause 5.5.7-page no. 6 V* is to be varied between 0.8 V_{cr} and 1.2 V_{cr} (at least 10 intervals shall be considered). The maximum value of V* shall be limited to 1.3 V (Z_{ref}). Considering, if we take 10 intervals, we will have 10 values of $\overline{V}_*$ which value has to be taken for $F_{al}(z)$ computation has not been specified.

6 Conclusions

i. The tapered height variation for same H/Db does not affect the calculated natural frequency significantly and thus does not change Vcr.
ii. The un-tapered chimney has reduced frequency compared to other tapering cases due to elimination of (t_b/t_t) and second mode frequency becomes six times f_1.
iii. The H/D_b ratio variation has significant effect on natural frequency.
iv. First mode across wind load analysis requirement arises as the H/Db ratio, and basic wind speed is decreased, i.e., as the chimney becomes slender, at lower basic wind speed frequency for first mode decreases, and thus, V_{cr} falls into range of 0.5 V(z_{ref}) to 1.3 V(z_{ref}).
v. The case of fully un-tapered shell showed significant deviation in the qualitative response observations than the other three tapering cases. The straight cylindrical geometry, with decrease in H/Db ratio along with subsequent decrease in basic wind speed had combined moments governing over the bottom sections.

The exclusion of taper ratio from the expression based on empirical information has made this dimensional parameter almost insignificant. The earlier depiction of strong influence of aspect ratio by Vickery throughout the model experiments, and simplification has been standing contradictory to the current analytical approach. The inferences by Devdas Menon and P. S. Rao are discordant to current observations, thus portraying the significant variation in the incorporation of dimensional parameters in the recent revision of the IS 4998: 2015 [1, 2]. The effect of taper obtained from analytical computation has to be in conformity to practical response; this gives a scope to study and adopt semi-empirical method developed by Vickery.

References

1. IS 4998: (2015)—Design of reinforced concrete chimneys—criteria
2. Menon G, Devdas, Srinivasa Rao P (1997) Uncertainties in codal recommendations for across-wind load analysis of R/C chimneys. J Wind Eng Indus Aerodynam 72:455–468
3. IS 875 (Part 3): (2015)–Wind loads "Design loads (Other than Earthquake) for buildings and structures—code of practices"
4. Baiju A, Geethu S (2016) Analysis of tall RC chimney as per indian standard code. IJSR 5(9)
5. Siva Rama Prasad CV, Vijaya Simha Reddy Y, Prashanth Kumar J et al. (2018) Earthquake and wind analysis of a 100m industrial RCC chimney. IJTIMES 4(02)
6. Reddy KRC, Jaiswal OR et al. (2011) Wind and earthquake analysis of tall RC chimneys. IJESE 04(06) SPL

Structural Assessment of Banashankari Temple, Badami, Karnataka

S. Tejas and N. Senthil Kumar

Abstract This dissertation work is concerned with a case study on 'Banashankari temple, Badami, Bagalkot, Karnataka', which is an ancient temple constructed during seventh century. The study involves detailed assessment and investigation of the Sandstone specimen, taken from the site, which was then used material for construction of this temple. The sample was examined under optical microscopy, SEM analysis and XRD analysis in order to determine the mineralogical composition and morphology. Further, compression test, non-destructive tests and also thermal conductivity test were conducted on the specimen in order to determine the structural and thermal properties. The physical properties of the sample were thus studied.

Keywords Structural assessment · Optical microscopy · SEM and XRD

1 Introduction

Assessment of heritage structures is a very important and frequent engineering task as they always contribute to a great historical, social and economic value. The heritage structures of any region are replica of the culture and tradition of that region. The structural behaviour of ancient structures in this era are given priority and several architects and structural engineers are conducting case studies on various monuments, performing detailed assessments and also comparing their behaviour with modern structures. India, a nation known for its beautiful ancient heritage structures and monuments require regular inspections, assessments and maintenance to be carried out in order to preserve them. The structure under case study is a typical stone masonry structure, the predominant construction material being used is Sandstone. As it is very much essential to preserve the aesthetics and architecture of our ancient

S. Tejas · N. Senthil Kumar (✉)
School of Civil Engineering, VIT University, Katpadi, Vellore, Tamil Nadu 632014, India
e-mail: n.senthilkumar@vit.ac.in

S. Tejas
e-mail: tejas.s2019@vitstudent.ac.in

B. Kondraivendhan et al. (eds.), *Sustainable Building Materials and Construction*,
Lecture Notes in Civil Engineering 222,
https://doi.org/10.1007/978-981-16-8496-8_43

Fig. 1 16-pillared mandapam structure

monuments, this work aims at analysis of an ancient temple of Badami, a heritage city in Karnataka, India. We shall also be identifying the defects and failures in the structure and suggest suitable remedial measures (Fig. 1).

2 Methodology

The objective of this project is to make a detailed structural assessment on the stone lamp tower. Detailed information about the temple, required for the project were collected from the temple officials after visiting the temple. The information thus collected included historical background, then used materials for constructing the temple, methods and techniques adopted during construction, etc. All the measurements of the key structural elements were taken at the site with prior permission from the authorities.

As Sandstone was the predominant material used for the construction of this temple, the specimens were collected at a nearby quarry site and were further examined. The examination involves assessment of mineralogical properties of the specimen by performing XRD analysis, studying the specimen's morphology by

Fig. 2 Sandstone samples collected at the quarry site (Bagalkot, Karnataka) and cut as per standard dimensions

performing SEM analysis. Strength related properties of the specimen can be determined and cross verified by conducting both compression tests and non-destructive tests.

Further, thermal properties of the specimen were determined by guarded heat flow method as per ASTM-1530. The results thus obtained from the above tests, are the input data for the analysis, which shall be carried out by finite element approach using ABAQUS FEM software. The structural behaviour can therefore be assessed with these analytical results.

2.1 Material Test

Sandstone, a member of sedimentary rocks family, is the predominant material used for the construction of this temple. After collecting detailed information about the material and its availability, few of the Sandstone specimens were later collected from a quarry near to the temple site. The collected parental stone samples have to be cut to the standard dimensions (150 × 150 × 150 mm or 100 × 100 × 100 mm cubes) before testing (Fig. 2).

The Sandstone specimens collected at the temple's site were tested for compressive strength, thermal conductivity, water absorption, porosity, specific gravity, etc. in order to assess the mechanical, thermal and mineralogical properties. The mineral and chemical composition and the morphology of the Sandstone were studied through X-ray diffraction (XRD) analysis, XRF analysis and SEM analysis.

2.1.1 FE-SEM Analysis of Sandstone.

scanning electron microscopy (SEM) is a test method that uses an electron beam to scan a sample and create a magnified image for analysis. SEM analysis, also known as SEM microscopy, is a technique for microanalysis and failure analysis of

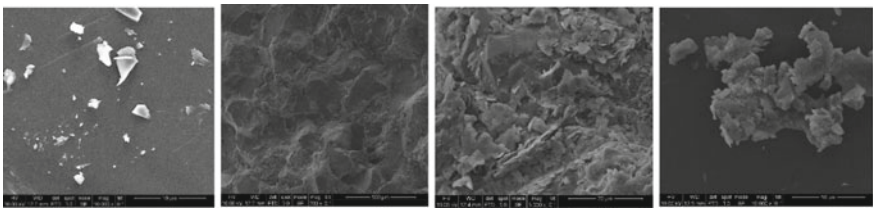

Fig. 3 FE-SEM pictures of the sandstone specimen

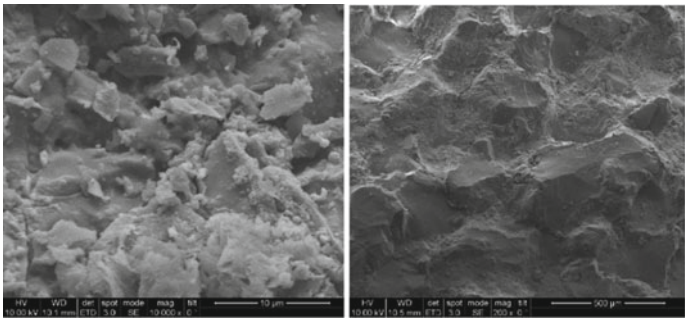

Fig. 4 FE-SEM images showing less porous matrix

solid inorganic materials that is very accurate. The focussed electron probe extracts the structural and chemical information point-by-point from a region of interest in the sample. The scanning electron microscope is the most versatile and simplified technique for describing the structure and morphology of manufactured and natural materials.

Figures 3 and 4 manifest the FE-SEM images of the Sandstone specimen. It is obvious that the amount of pores are less in the images and hence, very fine particles are found in the specimen. Thus, the SEM examination of the specimen showed that the Sandstone specimen at the site has a compact microstructure with a well embedded aggregate matrix.

2.1.2 Thermal Conductivity Test (ASTM-1530)

Thermal conductivity is an intensive physical property of a specimen that relates the heat flow over a unit area of the specimen to the temperature gradient across the specimen. A material's thermal conductivity represents the ability of the material to conduct heat. GHFM-02 samples should be preferably 70 × 70 × 12 mm or 2 inches in diameter. The top and bottom surfaces should be flat and parallel (Fig. 5, Table 1).

Therefore, it can be seen that for the given Sandstone specimen of size 70 × 70 × 12 mm, the thermal conductivity yielded at a temperature of 136.41 °C or 410 K is found to be 4.29 W/m K.

Fig. 5 Sandstone specimens (70 × 70 × 12 mm) for thermal conductivity test

Table 1 Results of thermal conductivity test on sandstone specimens (70 × 70 × 12 mm)

Test report	
Temperature (°C)	Thermal conductivity (W/m °C)
	Sample: sandstone (70 × 70 × 12 mm)
−13.68	6.047
11.48	5.733
36.68	5.33
61.64	5.33
86.6	5.008
111.5	4.307
136.41	4.29

Validation of thermal conductivity test results:

The above results of thermal conductivity test are validated by using the results of porosity of Sandstone, i.e. 0.1545 or 15%.

$$\begin{aligned}\text{Solidity of Sandstone} &= 1 - \text{Porosity}\\ &= 1 - 0.1545\\ &= \mathbf{0.845}.\end{aligned}$$

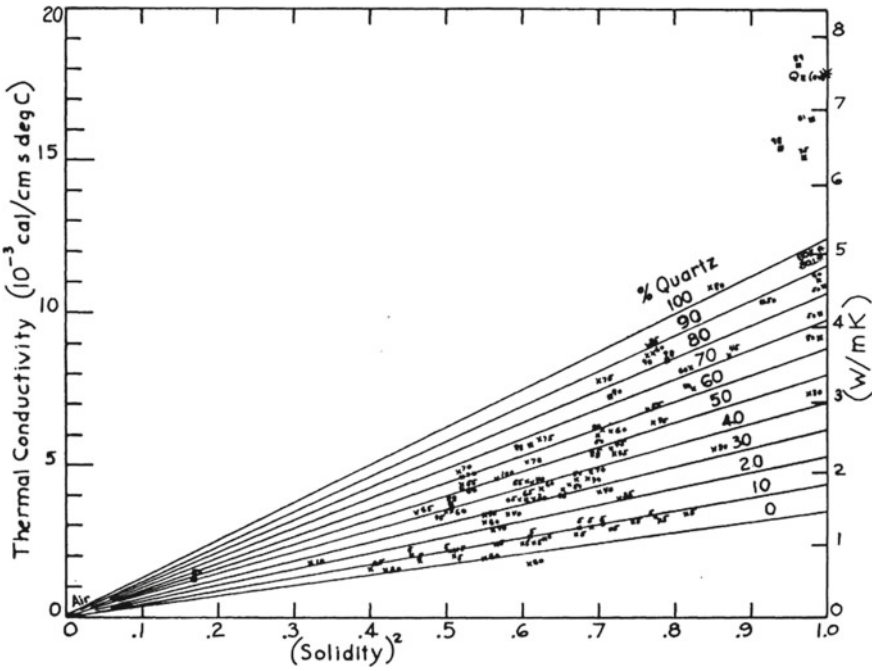

Fig. 6 Solidity verses thermal conductivity curve for a given percentage of quartz for sandstone

Or

$$\text{Therefore, Solidity} = \mathbf{84.5}\%.$$

With the solidity value of Sandstone in hand, referring to the solidity vs thermal conductivity curve for a particular percentage of Quartz (SiO_2), i.e. 92% (as obtained from FE-SEM and EDX results), we have the thermal conductivity of Sandstone as shown below (Fig. 6),

From the above figure, it can be seen that for 92% of Quartz as obtained by XRD and SEM analysis and for a solidity of 84.5%, we have the thermal conductivity value for the Sandstone 4.3 W/m K. Therefore, we can infer that the thermal conductivity results thus obtained from guarded heat flow technique is valid and acceptable.

2.1.3 Compression Test on Sandstone

From the compression test, the average compressive strength of Sandstone was found to be **95 MPa**. The above stress–strain curve was derived from the results of compressive test of Sandstone specimen (No.1.) which failed at a load of **926.45 kN**. Based on this result, the slope of the curve, i.e. the modulus of elasticity of Sandstone was found to be as follows (Fig. 7),

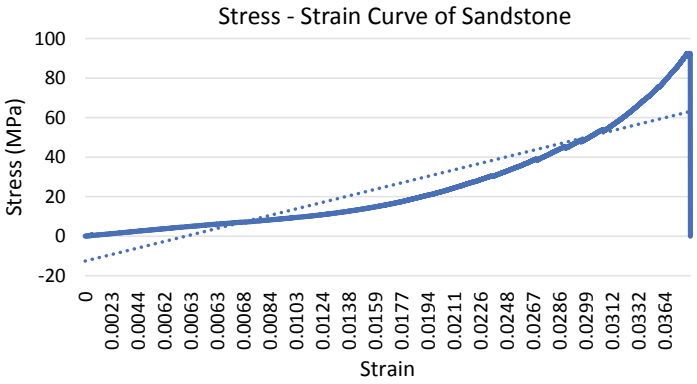

Fig. 7 Stress–strain curve obtained from compression test for sandstone

$$E_{Sandstone} = \frac{(60 - 40)MPa}{(0.0326 - 0.280)} = 4347.826MPa \quad (1)$$

Thus, from the above two figures, we can infer that, the results of nodal temperature distribution on the ribs of the stone lamp tower as obtained from both steady-state and transient heat transfer analysis are same and matching.

References

1. Ali S, Page A (1988) Finite element model for masonry subjected to concentrated loads. J Struct Eng 114(8):1761–1784
2. Ronald JA, Menon A, Prasad AM, Menon D, Magenes G (2018) Modelling and analysis of South Indian temple structures under earthquake loading. Indian Acad Sci
3. Ahmadizadeh M, Shakib H (2016) Experimental study of the in-plane behavior of confined stone masonry walls. J Struct Eng 142(2):04015145
4. Vasconcelos G, Lourenço P (2009) In-plane experimental behavior of stone masonry walls under cyclic loading. J Struct Eng 135(10):1269–1277

5. Lourenço P, Oliveira D, Roca P, Orduña A (2005) Dry joint stone masonry walls subjected to in-plane combined loading. J Struct Eng 131(11):1665–1673
6. Roca P, Cervera M, Gariup G, Pela L (2010) Structural analysis of masonry historical constructions. Class Adv Appr
7. Sun Q, Lu C, Cao L, Li W, Geng J, Zhang W (2016) Thermal properties of Sandstone after treatment at high temperature. Int J Rock Mech Min Sci
8. Shen Y-J, Zhang Y-L, Gao F, Yang G-S, Lai X-P (2018) Influence of temperature on the microstructure deterioration of sandstone. Energies
9. Pal P (2019) Dynamic poisson's ratio and modulus of elasticity of pozzolana Portland cement concrete. Int J Eng Technol Innov 9(2):131–144

Reference Books and Codes

10. Woodhead Publishing series in civil and structural engineering) Ghiassi, Bahman_ Milani, Gabriele—Numerical modeling of masonry and historical structures_from theory to application—Woodhead Publication
11. [RILEM State-of-the-Art Reports 20] Masayasu Ohtsu (eds.)—Innovative AE and NDT Techniques for On-Site Measurement of Concrete and Masonry Structures_ State-of-the-Art Report of the RILEM Technical
12. [Springer Series in Solid and Structural Mechanics 9] Mario Como (auth.)—Statics of Historic Masonry Constructions (2017, Springer International Publishing)—libgen.lc
13. National Building Code—2016
14. IS : 1124—1974. Method Of Test For Determination Of Water Absorption, Apparent Specific Gravity And Porosity Of Natural Building Stones
15. IS : 1121—1974 Part 1. Methods Of Test For Determination Of Strength Properties Of Natural Building Stones

Usage of Waste Marble Powder for the Manufacture of Limestone Calcinated Clay Cement (LCCC)

S. M. Gunjal and B. Kondraivendhan

Abstract Day by day, the production of cement is increasing with the increase in demand for construction industries. In the process of cement manufacturing, a lot of carbon dioxide (CO_2) is released into the environment, which creates a global warming problem. Limestone calcinated clay cement (LCCC) can be used to partially solve this problem. In the present paper, the use of waste marble powder to manufacture calcinated limestone clay cement has been discussed. LCCC is an advanced ternary mixed cement made from a low grade mixture of 30% calcined clay, 15% limestone, 5% gypsum, and 50% cement clinkers. This means that 50% of cement clinkers are to be replaced by additional cementitious substances, which are beneficial for reducing CO_2emissionsduringcement production. In the present study, two types of cements were prepared, one contains LCCC, and another contains marble stone calcined clay cement MCCC (Marble Stone-15%, Calcined clay-30%, Gypsum-5% and Clinker-50%) and these cements are compared to fly ash-based pozzolanic portland cement (PPC) and grade 53 ordinary portland cement (OPC).Characteristics of the prepared cement samples such as physical and chemical were carried out and compared with OPC and PPC. Similarly, prepared cement's compressive strength (CS) was taken on cubes of 70.7 mm and tested after 3, 7, and 28 days, and results are compared with OPC and PPC.

Keywords Waste marble powder · Limestone powder · Calcined clays · Standard consistency test · Compressive strength

S. M. Gunjal (✉) · B. Kondraivendhan
Department of Civil Engineering, S.V.N.I.T, Surat 395007, India

S. M. Gunjal
Department of Structural Engineering, Sanjivani College of Engineering, S.P.P.U, Kopargaon, Maharashtra 423603, India

B. Kondraivendhan et al. (eds.), *Sustainable Building Materials and Construction*,
Lecture Notes in Civil Engineering 222,
https://doi.org/10.1007/978-981-16-8496-8_44

1 Introduction

With the accelerated industrial and infrastructural growth, the requirement of concrete has been increased in last decade. In the economically growing countries, massive amount of concrete is required for construction. It is a varied combination of cement, water, coarse and fine aggregate. At the time of preparation of 1 t cement, almost 1 t carbon dioxide (CO_2) is emitted into the climate [5]. India is among the top two cement manufacturing countries in the world, just behind China producing 280 million tons of cement annually [12]. A significant amount of greenhouse gas is released into the air during the cement manufacturing process. Therefore, it is essential to lessen cement consumption by using new cementitious constituents. A novel ternary mixed cement [14] called limestone calcined clay cement (LCCC) is formed in this regard. It's made up of OPC50%, calcined clay 30%, ground limestone 15% and gypsum 5%.

In comparison to all other mixes, 30% metakaolin and 15% limestone in portland cement produce superior results [2]. With increase in kaolin clay, CS was almost similar to ordinary portland cement and when kaolin content decreases it was similar to PPC [3]. When fly ash is located faraway than the clay, the creation of LCCC is economical compared to portland pozzolana cement [10]. At all stages, the more remarkable fineness of calcined clay and cement can dramatically improve compaction consistency, whereas the fineness of calcined clay only works at an early stage [1]. Calcined concrete made from LCCC cement has achieved equivalent strength development than PPC and enhances the advancement [4]. The study of Shah and Bishnoi [15] has reported that the strength achieved by LCCC is similar to a 43 grade of OPC at 28 days. In the production of LCCC, 15% limestone is required, and also the chemical composition of limestone is nearly equal to the marble stone. Therefore, in the present study, limestone has been substituted by the marble powder.

In India, 17 MT marble is manufactured on yearly basis [11] which is produced from the metamorphic rocks. During the process of polishing, dressing and cutting, huge amount of dust is generated which is hazardous for the environment and may leads to several health problems. However, marble contains higher calcium oxide, and therefore, it is beneficial to use marble stone to create calcinated clay marble stone cement (MCCC). Marble is used only as a filler material in self-compacting concrete made using natural sand, course aggregate, marble powder and fly ash at w/c of 0.35 [6]. The purpose of this research is to examine either waste marble powder can be used to prepare marble stone calcined clay cement as an alteration of limestone. Similarly, calcinated clay marble stone cement (MCCC) is manufactured to verify the characteristics (physical and chemical) of this cement by using 50% ordinary portland cement, 30% calcined clay, 15% marble stone powder, and 5% gypsum.

2 Material

OPC of grade 53 in compliance to IS 12269-2013 [9] and portland pozzolana cement (PPC) with fly ash based confirming to IS 1489-1991 part-1 [8] were used for comparison with cement developed using clinker, limestone powder, calcined clay, gypsum, and marble stone powder. Table 1 displays the chemical properties of these materials as defined by an X-ray fluorescence test. Using LCCC and MCCC, two types of cement systems were developed. As seen in Figs. 1 and 2 on limestone powder and waste marble powder, an X-ray diffraction (XRD) test was conducted. The pozzolanic reactivity of calcinated clay was 9.11 MPa, which follows the specifications of IS 1727-1967 (Indian Standard, 1967). The specific gravity of calcined clay is reported as 2.6. It was detected that the materials (calcined clay, limestone powder, and marble powder) used for the preparation of LCCC and MCCC systems contain finer particles as compared to OPC. As a fine aggregate, nearby Pravara river sand with a fineness modulus of 2.69 was used. In the ratio of 70:30 verifying IS 383-1970, as coarse aggregate, basalt crushed stone aggregate with minimum sizes of 12.5 and 20 mm was used.

2.1 Development of Cement Systems

Two cement viz. OPC and PPC were used as a reference to check the suitability of two cement systems developed in the laboratory as indicated by marble stone calcinated clay cement and limestone calcinated clay cement. The characteristics of all these cement systems are mentioned in Table 2. The CS of OPC, PPC, LCCC, and MCCC was calculated using mortar cubes of side 70.7 mm with a water to cement ratio of 0.415, 0.422, 0.45, and 0.456, respectively, on the basis of standard consistency as per IS 4031-1988 [7]. For the preparation of mortar cubes, 1:3 proportion was taken in which one part refers to cement system, and three parts of standard sand were taken as per IS 650-1991.The mix proportion of prepared cement in LCCC was OPC 50, 30% calcined clay, 15% limestone powder and 5% gypsum and in MCCC system 30% calcined clay, waste marble powder 15, 5% gypsum, and 50% OPC was used. In OPC system, 100% OPC cement and in PPC system 100% PPC cement was used to prepared cement systems.

Table 3 shows the strength results of cubes over a specified period of curing. It is seen that at the initial age of 3 and 7 days, mortar prepared from LCCC and MCCC has less CS, but as the curing time increased, LCCC and MCCC cement system were comparable to ordinary portland cement and slightly more than PCC. This is because of the pozzolanic behavior of the material identified at the later ages.

Table 1 Oxides constituent of materials

Chemical oxide (%)	Al_2O_3	SiO_2	K_2O	CaO	TiO_2	Na_2O	MgO	P_2O_5	MnO	Fe_2O_3	Loss of ignition
Calcined clay	44.32	53.75	0.004	0.483	1.707	0.447	0.19	0.078	0.004	0.415	0.30
Marble waste	3.37	3.76	0.45	47.5	0.15	0.38	1.99	0.28	0.16	2.78	39.0
OPC	3.6	22.07	0.7	63.25	0.007	0.3	1.08	0.008	-	4.69	1.140
Limestone powder	2.15	11.42	0.82	44.82	0.11	0.13	2.10	0.03	0.11	1.97	36.14

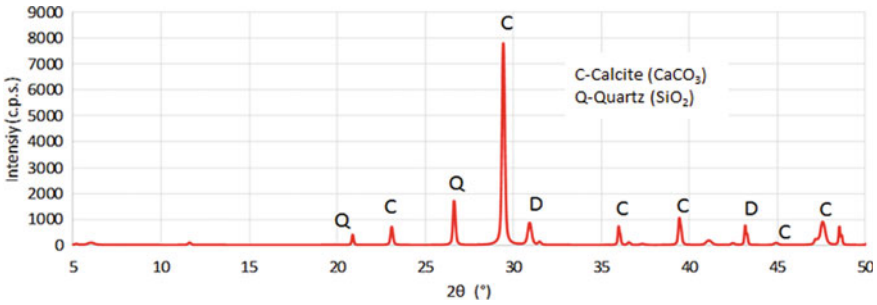

Fig. 1 Limestone powder (XRD) pattern

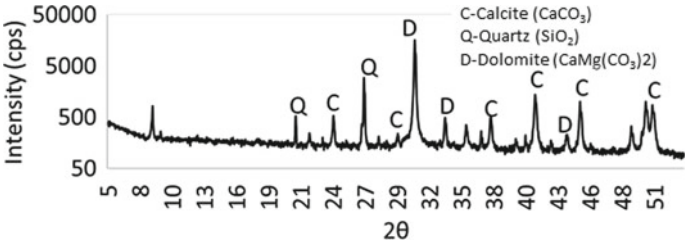

Fig. 2 Marble powder (XRD) pattern

Table 2 The characteristics of prepared materials

Description	LCCC	MCCC	OPC
Standard consistency (%)	34.5	34.0	29.5
Initial period of setting (minutes)	90	96	100
Final period of setting (minutes)	250	260	270
Soundness (mm)	2.0	2.2	2
Specific gravity (g/cc)	2.80	2.90	3.15
Fineness (%)	4.2	4.5	5.2

Table 3 CS of OPC, PPC, LCCC, and MCCC blends for different curing period

S No.	Mix	CS (N/mm^2)			
		3 days	7 days	28 days	56 days
1	OPC	18.2	36.44	54.6	55.8
2	PPC	13.6	30.22	45.5	51.2
3	LCCC	16.3	33.4	53.2	55.1
4	MCCC	16.5	34.2	53.6	55

3 Results and Discussions

3.1 The Physical Characteristics

Physical characteristics viz. consistency of LCCC and MCCC cement system were higher than OPC. As the material used for the preparation of both the cement systems is finer than OPC and the calcined clay particle has high surface area, the water demand increases [16]. The initial and final setting time (in minutes) of LCCC and MCCC cement system satisfied requirement of IS 4031-1988 part-5.

3.2 Compressive Strength

Compressive strength of LCCC and MCCC cement system at initial days (i.e., 3 and 7 days) has slightly less than the OPC however more than PPC. As curing period increases, the strength of LCCC and MCCC cement system is also increases. This may be the case because of the pozzolanic behavior of calcined clay which gives later age strength. Marble powder and limestone contain carbonate source which reacts with aluminates present in calcined clay to produce carbo aluminate hydrates. This hydrate fills the pore space and contributes to the development of strength in LCCC and MCCC cement system [14]. Compressive strength of LCCC clays containing more than 40% Kaolin are equivalent to plain portland cement [13]. With higher percentage of kaolin clay addition in LCCC system, higher compressive strength may be obtained at an early age. Calcium aluminum silicate hydrate forms when calcinated clay reacts with water (C-A-S-H) as suggested by Scrivener [14]. The study conducted by Joseph et al [10] on calcined clay cement system has also observed the same trend.

4 Conclusions

- Physical properties of the LCCC and MCCC cement systems such as standard consistency is slightly more because of finer material particles, Initial and final setting period satisfied IS requirement.
- At all curing stages, the CS of the LCCC and MCCC cement systems are greater than that of PPC but less than OPC system at initial ages. This is because of the pozzolanic reaction between binders at a later age.

References

1. Anders L et al (2015) Effect of fineness in clinker-clacined clay-limestone cements. Adv Cem Res 27(9):546–556. https://doi.org/10.1680/jadcr.14.00095
2. Antoni M et al (2012) Cement substitution by a combination of metakaolin and limestone. Cem Concr Res 42(12):1579–1589. https://doi.org/10.1016/j.cemconres.2012.09.006
3. Bishnoi S et al (2014) Pilot scale manufacture of limestone calcined clay cement: The Indian experience. Indian Concr J 88(7):22–28
4. Dhandapani Y et al (2018) 'Mechanical properties and durability performance of concretes with Limestone Calcined Clay Cement (LC^3).' Cem Concr Res 107:136–151. https://doi.org/10.1016/j.cemconres.2018.02.005
5. Gartner E (2004) Industrially interesting approaches to "low-CO_2" cements. Cem Concr Res 34(9):1489–1498. https://doi.org/10.1016/j.cemconres.2004.01.021
6. Gesoğlu M et al (2012) Fresh and hardened characteristics of self compacting concretes made with combined use of marble powder, limestone filler, and fly ash. Constr Build Mater 37:160–170. https://doi.org/10.1016/j.conbuildmat.2012.07.092
7. Indian Standard (1988) 'Methods of physical tests for hydraulic cement, part 4,5,6,7', in IS 4031-1988, Bureau of Indian Standard
8. Indian Standard (1991) 'Specification for Portland pozzolana cement, Part 1: Flyash based', in IS 1489-1, pp 1–19
9. Indian Standard (2013) 'Ordinary Portland Cement,53 Grade-Specification', in IS 12269, Bureau of Indian Standard (BIS), pp 1–17
10. Joseph S, Bishnoi S, Maity S (2016) An economic analysis of the production of limestone calcined clay cement in India. Indian Concr J 90(11):22–27
11. Krishnan S et al (2018) Hydration kinetics and mechanisms of carbonates from stone wastes in ternary blends with calcined clay. Constr Build Mater 164:265–274. https://doi.org/10.1016/j.conbuildmat.2017.12.240
12. Planning Commission (2011) Low carbon strategies for inclusive growth, Government of India
13. Scrivener K et al (2017) Calcined clay limestone cements (LC^3). Cem Concr Res December:49–56. https://doi.org/10.1016/j.cemconres.2017.08.017
14. Scrivener KL (2014) Options for the future of cement. Indian Concr J 88(7):11–21
15. Shah V, Bishnoi S (2015) Use of marble dust as clinker replacement in cement. Indian Concr J 89:27–32. https://doi.org/10.1007/978-81-322-2181-6_130
16. Snelson D, Wild S, Farrell MO (2011) Setting times of portland cement-metakaolin-fly ash blends. J Civ Eng Manag 17(1):55–62. https://doi.org/10.3846/13923730.2011.554171

A Literature Review Identifying the Scope for Utilization of Waste Polyethylene Terephthalate Bottle Fibers in Concrete for Enhancing Structural Properties

Sudhir Bhaskarrao Gayake and Atul K. Desai

Abstract Concrete is a paramount construction material, consuming naturally occurring ingredients such as fine aggregates, coarse aggregates and mainly, cement as binding material. Therefore, heed is required in order to understand optimum usage and application of these ingredients as it affects the environmental and ecological balance. Concrete is an excellent construction material when handled appropriately, but it has poor tensile, flexural, and toughness strength, which may be enhanced by adding fiber to it, resulting in fiber-reinforced concrete (FRC). Whereas, many waste materials have shown good capabilities of its utilization in concrete with enhancement in structural behavior. Polyethylene terephthalate (PET) is the most widely used thermoplastic polymer in the beverages and mineral water bottle packaging industries. These bottles have less residence time and have chances of being recycled and reused in concrete. Previous research has demonstrated that PET plastic may be used as a fibrous material or as a substitute for inert material in constructive and practical ways for concrete making. In this paper, a review of the literature is presented with applications, effects, and influence of PET fiber on concrete for mechanical behavior, as well as future research possibilities employing varied aspect ratios (AR), fiber topologies, and fiber volume (FV) are suggested. The utilization of PET showed improvement in tensile, bending, and impact strength also revealed decrement in thermal conductivity.

Keywords Polyethylene terephthalate fibers · Aspect ratio · Fiber volume · Flexural strength · Impact strength · Thermal conductivity

S. B. Gayake (✉) · A. K. Desai
Department of Civil Engineering, S.V.N.I.T, Surat 395007, India

S. B. Gayake
Department of Civil Engineering, Sanjivani College of Engineering, S.P.P.U, Kopargaon, Maharashtra 423603, India

B. Kondraivendhan et al. (eds.), *Sustainable Building Materials and Construction*,
Lecture Notes in Civil Engineering 222,
https://doi.org/10.1007/978-981-16-8496-8_45

1 Introduction

Concrete has proven to be one of the most important materials in the construction sector, with direct and indirect environmental implications. Therefore, kind attention should be given on the use of raw material for preparing concrete which will have less adverse effects on environment and will lead to sustainable infrastructural development with some green credits to the construction sector [16]. Use and application of waste material have shown greater impact on the consumption of raw material in concrete making and hence saving the mother earth and environment. The strength of FRC depends on pull-out strength of fiber from matrix which affects ductility also. Recent research and trials have revealed that combining recycled fibres in concrete to produce crack-free concrete with high tensile strength, strong bending strength, and improved structural features might be a feasible solution for the green concrete revolution [15].

The main demand of construction sector is to have unceasing developments having a goal of balanced environment, social, and economic needs for present and upcoming generations without sacrificing to the structural properties of concrete [19]. To achieve the said goals for sustainable and green solutions in concrete construction industry, conventional and traditional ways of concrete production and consumption should be reduced, and new techniques shall be implemented for better life cycle assessment of concrete.

New techniques that mainly comprise at reducing raw materials usage through adoption of waste and recycled materials as an inert or fibrous ingredient of concrete. Ordinary concrete has certain flaws, namely low tensile strength, low ductility, less energy absorption, low crack resistance, and shrinkage cracking [18]. Many recent studies have shown potentialities to overthrow these defects, by integrating the concrete mixture with different forms of fibers [5]. If the fiber is made from recyclable waste, such as PET, it will have a lower environmental effect, produce fewer waste streams, and will be less likely to end up in landfills, thereby lowering land pollution and saving aquatic life in water. Every year, millions of tons of plastic trash accumulate in the globe after its initial use, the majority of which is not reused and dumped into landfills or water and is therefore not recyclable [1, 8, 9].

Even if adopted for recycling, it consumes energy and increases more pollution to environment in terms of air, water, or land. This disposal of waste material is difficult, not environmental friendly or costlier matter, and therefore, use of these materials for manufacturing of concrete is somewhat economical alternative. Recent studies have shown polyethylene scrap being used successfully as restricted replacement for fine aggregates in concrete, or it can be utilized as a fiber in concrete [8, 9, 17]. Using waste material for concrete production can be an alternative method for reducing waste and adding positive fresh and harden properties to concrete. Since the green concrete industry is progressing rapidly, a close and detailed prospective is necessary to identify the aspects of concrete that contains waste material and its effectiveness after adoption [12]. With this aim, a comprehensive literature-based

study is presented with various experimentation adopted on PET FRC and scope for the future work is advertised.

2 Experimental Analysis of Pet FRC

The goal of mixing concrete with randomly oriented fibers to increase fracture resistance, tensile strength, bending behavior, and impact strength of concrete was originally researched in the early 1960s. Many different types of fibers have been adopted in concrete making, namely in the form of natural fibers, with organic origin and synthetic fibers with inorganic origin. There have been various experimental, theoretical studies, and investigations performed on use of PET plastic in concrete.

Some of the studies in the area are presented here as literature review considering the raw material consideration, PET bottle collection and fiber extraction, effect on structural properties of FRC with PET fibers, effect on thermal conductivity, heat flux of FRC, experimental study on impact strength of FRC, and pull-out behavior of PET fibers etc.

2.1 Effect of PET Fiber on Workability of FRC

The ability of easy placement and well compaction are the properties of fresh concrete, leading to its better strength. The incorporation of PET fibers has shown reduction in the workability of concrete as the fibers are flakey and gets decussate with each other forming a cluster [1]. It also reduces if the fiber volume content is increased beyond 0.3% [20].

2.2 Effect of PET Fiber on Compressive Strength of FRC

The effect of ultra-fine palm oil fuel ash and PET fibers on concrete demonstrates that the compressive strength of PET FRC does not increase [1]. Also the fiber volume (FV) does not have much effect on the reduction in compressive strength of FRC. But this added FV has improved the tensile strength of concrete. Therefore, the addition of fibers will not hamper the design target compressive strength of FRC but additionally will improve the tensile strength with given dosage of FV [8, 9, 17]. Increment in compressive strength was observed for self-compacting concrete with 1.5% of fiber ratio due to homogeneity [14]. Surfactant particles of recycled aggregates on the surface of PET fiber showed a 3–9% increase in compressive strength [4].

2.3 Effect of PET Fiber on Splitting Tensile Strength of FRC

Experimental result shows that the splitting tensile strength depends on fiber volume percentage in the matrix and showed optimum dosage of 30% for PET; beyond this, there is no such improvement in strength [17]. Results also indicate that irregularly shaped PET fibers caused no increase in the splitting tensile strength when compared with regular pattern fibers which showed enhancement in strength [8, 9].

2.4 Effect of PET Fiber on Flexural Behavior

Although the load carrying capability of PET FRC has not improved significantly, specimen ductility has improved for the 'O' kind of fiber as compared to ordinary flakey fibers due to good bonding [5, 6]. The deflection carrying capacity and ductile nature is seen for fibers with higher aspect ratio (AR) [11]. In terms of structural member behavior, it was discovered that PET FRC beams had higher ultimate strength and ductility than accompanying specimens without fiber reinforcement, as well as it exhibits high elastic activity, making the specimen more ductile [10].

2.5 Effect on Pull-Out Strength of PET Fiber

The embedded length of fiber also plays a vital role in defining the fiber pattern for FRC. Different material fibers with similar embedded lengths and widths exhibit contrary behavior in pulling strength. The width of fiber and embedded length are directly proportional to pull-out strength of fiber from concrete matrix with some limitations on width [8, 9]. A wider surface contact area of fiber exhibits high tensile strength attainment and reduces debonding of fiber.

2.6 Effect of PET Fiber on Impact Strength of FRC

The energy absorption and impact strength of FRC is proven to be enhanced by use of PET fiber above 1.25% fiber volume; below this, there is not much improvement in strength [2]. Ordinary concrete begins fractures at fewer blows of impact than FRC built with metalized plastic waste (MPW), and small fibers are incapable of contributing to impact resistance due to insufficient anchoring in the hardened matrix [3, 13].

2.7 Effect of PET Fiber on Heat Transfer and Thermal Conductivity of FRC

Low thermal conductivity and less heat exchanging material are nowadays adopted for making green building solutions. Thermal conductivity for normal prepared concrete from all plastic fiber concrete decreased with increasing volume fractions of PET fibers, and their thermal conductivity was lower than that of the conventional concrete [17]. An experimentation undertaken by replacing aggregates by PET waste showed reduction in thermal conductivity up to 60% replacement of aggregates [7, 12].

3 Results and Conclusions

Based on the literature studied and reviewed, it is observed that the fresh properties of PET FRC is hampered with increase with fiber volume ratio. The compressive strength is not enhanced nor decreased with PET fiber addition but showed improvement in tensile strength of FRC with increase in aspect ratio and fiber volume ratio. The maximum flexural strength has been found for the 'O' kind of fiber.

Also, the change in aspect ratio and dosage rate has impact on bending strength of FRC. Fiber pull-out strength is affected by fiber volume ratio, embedded length, and surface area of fiber formations, which increases FRC ductility also. The impact and toughness strength of PET FRC vary according to the fiber volume percentage and the even dispersion of fibers in the matrix. The spalling is reduced due to the presence of fibers in the hard mass. PET material has good thermal resistance and can be used as a green building material in concrete which lowers the rate of heat transfer to the given thickness of member.

4 Future Scope for Research

Incorporation of fibers to the normal concrete contributes ductile behavior to it, which will be crack resistance and ultimately will have good durability aspects. It also improves the fracture behavior, and there are less chances of brittle type of failure in specimens. Adopting alternative aspect ratios, fiber patterns, length and surface treatment to fibers, coating of fibers with adhesive materials, hybrid fiber combination, and durability features of FRC may all be used for further research and experimentation. Study can also focus on the feasibility and viability of using PET bottle trash as fibers or inert material in FRC to improve structural characteristics while also saving the environment and pollution caused by non-biodegradable trash.

References

1. Alani AH, Bunnori NM, Noaman AT, Majid TA (2019) Durability performance of a novel ultra-high-performance PET green concrete (UHPPGC). Constr Build Mater 209:395–405
2. Al-Hadithi AI, Noaman AT, Mosleh WK (2019) Mechanical properties and impact behavior of PET fiber reinforced self-compacting concrete (SCC). Compos Struct 224(2018):111021
3. Bhogayata AC, Arora NK (2018) Impact strength, permeability and chemical resistance of concrete reinforced with metalized plastic waste fibers. Constr Build Mater 161:254–266
4. Bui NK, Satomi T, Takahashi H (2018) Recycling woven plastic sack waste and PET bottle waste as fiber in recycled aggregate concrete: an experimental study. Waste Manage 78:79–93
5. Foti D (2011) Preliminary analysis of concrete reinforced with waste bottles PET fibers. Constr Build Mater 25(4):1906–1915
6. Foti D (2013) Use of recycled waste pet bottles fibers for the reinforcement of concrete. Compos Struct 96:396–404
7. Fraternali F, Ciancia V, Chechile R, Rizzano G, Feo L, Incarnato L (2011) Experimental study of the thermo-mechanical properties of recycled PET fiber-reinforced concrete. Compos Struct 93(9):2368–2374
8. Khalid FS, Irwan JM, Ibrahim MHW, Othman N, Shahidan S (2018) Performance of plastic wastes in fiber-reinforced concrete beams. Constr Build Mater 183:451–464
9. Khalid FS, Irwan JM, Wan Ibrahim MH, Othman N, Shahidan S (2018) Splitting tensile and pullout behavior of synthetic wastes as fiber-reinforced concrete. Constr Build Mater 171:54–64
10. Kim SB, Yi NH, Kim HY, Kim JHJ, Song YC (2010) Material and structural performance evaluation of recycled PET fiber reinforced concrete. Cement Concr Compos 32(3):232–240
11. Meza A, Siddique S (2019) Effect of aspect ratio and dosage on the flexural response of FRC with recycled fiber. Constr Build Mater 213:286–291
12. Misri Z, Ibrahim MHW, Awal ASMA, Desa MSM, Ghadzali NS (2018) Review on factors influencing thermal conductivity of concrete incorporating various type of waste materials. In: IOP conference series: earth and environmental science, vol 140(1)
13. Mohammadhosseini H, Tahir MM, Sam ARM (2018) The feasibility of improving impact resistance and strength properties of sustainable concrete composites by adding waste metalized plastic fibres. Constr Build Mater 169:223–236
14. Noroozi R, Shafabakhsh G, Kheyroddin A, MohammadzadehMoghaddam A (2019) Investigating the effects of recycled PET particles shredded recycled steel fibers and Metakaolin powder on the properties of RCCP. Constr Build Mater 224:173–187
15. Pelisser F, Neto ABDSS, La Rovere HL, Pinto RCDA (2010) Effect of the addition of synthetic fibers to concrete thin slabs on plastic shrinkage cracking. Constr Build Mater 24(11):2171–2176
16. Pereira EL, de Oliveira Junior AL, Fineza AG (2017) Optimization of mechanical properties in concrete reinforced with fibers from solid urban wastes (PET bottles) for the production of ecological concrete. Constr Build Mater 149:837–848
17. Poonyakan A, Rachakornkij M, Wecharatana M, Smittakorn W (2018) Potential use of plastic wastes for low thermal conductivity concrete. Materials 11(10):1–17
18. Rai A, Joshi YP (2014) Applications and properties of fibre reinforced concrete. J Eng Res Appl 4(1):123–131. www.ijera.Com
19. Rostami R, Zarrebini M, Mandegari M, Sanginabadi K, Mostofinejad D, Abtahi SM (2019) The effect of concrete alkalinity on behavior of reinforcing polyester and polypropylene fibers with similar properties. Cem Concr Compos 97(2018):118–124
20. Wiliński D, Łukowski P, Rokicki G (2016) Application of fibres from recycled PET bottles for concrete reinforcement. J Build Chem 1(March):1–9

Experimental Investigation on the Combined Effect of Fly Ash and Eggshell Powder as Partial Replacement of Cement

Palla Charan Kumar, T. Shanthala, Kamarthi Aparna, and Sake Vinay Babu

Abstract The use of industrial products is the main confront in India since it causes environmental problems. In this aspect, this current work has been carried out to utilize the eggshell powder and fly ash as a partial replacement of cement. In this study, concrete mixtures were prepared with the replacement of cement with fly ash of 20%, and the eggshell powder varied from 0 to 15%. The effect of cementitious material has been evaluated with the parameters, namely compressive strength, split tensile strength, rebound hammer test and electrical resistivity test. The effect of fly ash and egg shell powder on above parameters has been evaluated at the ages of 1, 7 and 28 days. From the results, it has been observed that the replacement with cementitious material with eggshell up to 10% and the 20% fly ash shown better performance as compared to reference mixture.

Keywords Fly Ash · Eggshell powder · Mechanical properties

1 Introduction

Concrete adaptability, sturdiness and economy have made it the world's most utilized development materials. Concrete has played main role for binding the materials. At the present days, the raise in environmental pollution causes the decrement for the building life span [1]. However, the emissions from cement industry also contribute for the environmental pollution. In this view, most of the researchers [1–3] are searching for the alternative of cement, namely supplementary cementitious materials, industrial waste utilization, to decrease the cement production and thus reduces the pollution caused by carbon dioxide emissions [4].

P. C. Kumar (✉) · T. Shanthala · K. Aparna
Civil Engineering Department, SRIT, Ananthapuramu, India

S. V. Babu
Civil Engineering Department, GPCET, Kurnool, India

B. Kondraivendhan et al. (eds.), *Sustainable Building Materials and Construction*,
Lecture Notes in Civil Engineering 222,
https://doi.org/10.1007/978-981-16-8496-8_46

Table 1 Properties of different aggregates

Property	Fine aggregate	Coarse aggregate	Cement
Water absorption	0.32	0.01	–
Specific gravity	2.6	2.8	3.06

2 Materials

2.1 Materials

The research was performed with OPC, fine aggregate, coarse aggregate and water to characterize the results of this study (Table 1).

Here, egg shell powder and fly ash were used as a partial cement replacement, apart from other constituents. From nearby bakeries and food stalls, egg shells were obtained. The raw egg shells contained yellowish fluid which was washed using clean water.

Once washed properly, the egg shells were oven dried for 24 h at a temperature of 105 ± 5°C to remove the moisture that may have been gained during the cleaning. After the egg shells were oven dried, the egg shell was grinded using a blender. The grinded egg shell was then sieved through the sieves 50 and 100 μm.

Fly ash as a concrete mixture not only improves the technological advantage over particular properties but also reduces the pollution from the environment. We generate about 75 million tons of fly ash per year in India alone, which is now a major environmental problem [4]. As a result, concrete engineers and government departments are paying close attention to the efficient use of fly ash in the production of concrete [5].

2.2 Mix Proportion

Consider the constant water and cement ratio as 0.55 and the density of concrete as 240 kg/m^3. However, 20% of cement is replaced with fly ash and 0, 5 and 10% of cement is replaced with egg shell powder [6] (Table 2).

Table 2 Nomenclature of various mixtures

Mixes	Cement (%)	Fly ash	Egg shell powder
M1	100	–	–
M2	80	20%	0%
M3	75	20%	5%
M4	70	20%	10%

3 Experimentation

3.1 Compressive Strength Test

The test affirming to IS: 516-1953 was used in this study. In a 2000 kN compression testing press, all concrete samples are tested. Effective cubes of 150 × 150 × 150 mm were tested to assess the crushing intensity by loading the cubes at 1400 N/Cm^2 /min until the cubes cracked and maximum load was noted. Compressive strength was calculated with the obtained rupture load and cross-section area of cube.

3.2 Split Tensile Strength Test

The test is conducted in a 2000 KN capacity compression testing machine by placing the cylindrical specimen. The plywood is placed between the plates and cylinder, the load was continuously applied until a breakdown takes place on the vertical axis. Note the force at which the specimen fails and the split stress is obtained by using formula in IS: 5816-1970.

$$Ft = \frac{2P}{\pi \mathrm{DL}}$$

3.3 Rebound Hammer Test

Schmidt's rebound hammer is one of the typical equipments for measuring surface hardness. It consists of a spring hammer that fits on a plunger into the tube housing. The mass recovers from shower head as the plunger is pushed into the surface of the concrete. The concrete hammer and the spring trigger are rebound and the rider is passed over the lead scale along with them. The rider can be sustained to allow reading by pressing a button. The rebound number is the distance traveled by the mass and is indicated by the rider which moves over a scale which consists of graduations. Testing may be performed at any specific angle, horizontally, vertically, either upward or downward. At each stage, the rebound number is similar for the same concrete and separate validation or correction charts are necessary.

3.4 Electrical Resistivity Test

Electric resistivity of concrete can be achieved through the application of the current in the concrete and the measurement of the response voltage. There are various methods for concrete resistivity measurements. Current is passed to two electrodes connected to ends of a uniform cross-section specimen, and the concrete electrical resistance can be analyzed. Electric resistivity from the equation can be obtained.

$$P = \frac{\mathrm{RA}}{L}$$

The ratio of voltage to current is the electrical resistance of the specimen in ohms.
L is the length of the material in meters.
A is the cross-sectional area of the specimen in square meters.

4 Results

4.1 Compressive Strength Test

In Fig. 1, the graphical representation shows the strength changes in all mix proportions of concrete with time. The observation shows that the replacement of 5% of egg

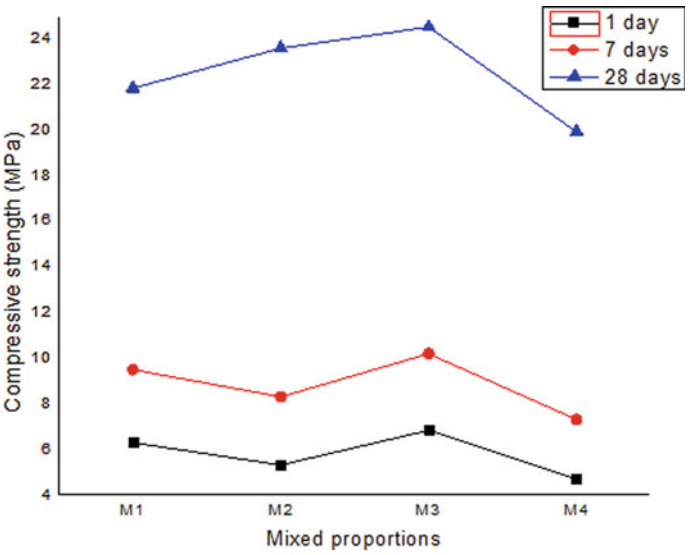

Fig. 1 Comparison of compressive tensile strength verses mix proportions

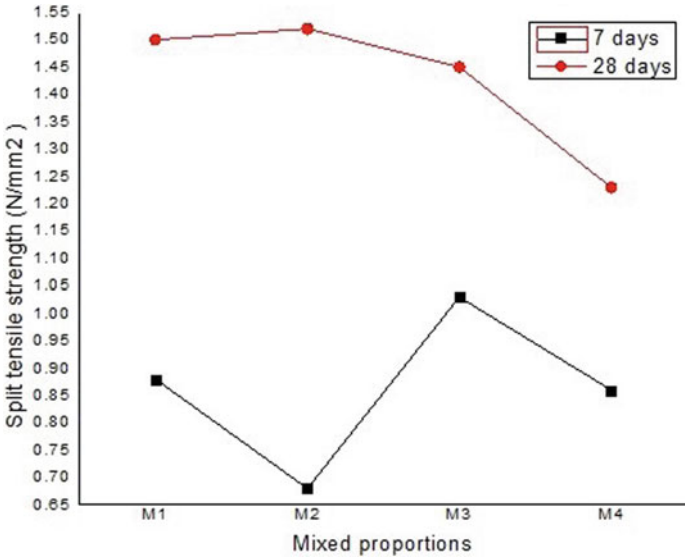

Fig. 2 Comparison of split tensile strength verses mix proportions

shell powder attained higher strength. However, the compressive strength decreases with the rise in egg shell powder.

4.2 Split Tensile Test

Figure 2 represents the results of split tensile strength for all concrete mix proportion concretes with age. The observation shows that the replacement of 5% of egg shell powder will provide greater strength than conventional concrete. However, when the egg shell powder is increased the split tensile strength will decrease.

4.3 Rebound Hammer Strength Test

Figure 3 depicts the results of rebound hammer strength for all mix proportions of concretes with age; it clearly shows that 5% ESP replacement has greater strength than other concrete mixes. The rebound hammer strength decreases with the increase of eggshell powder (Table 3).

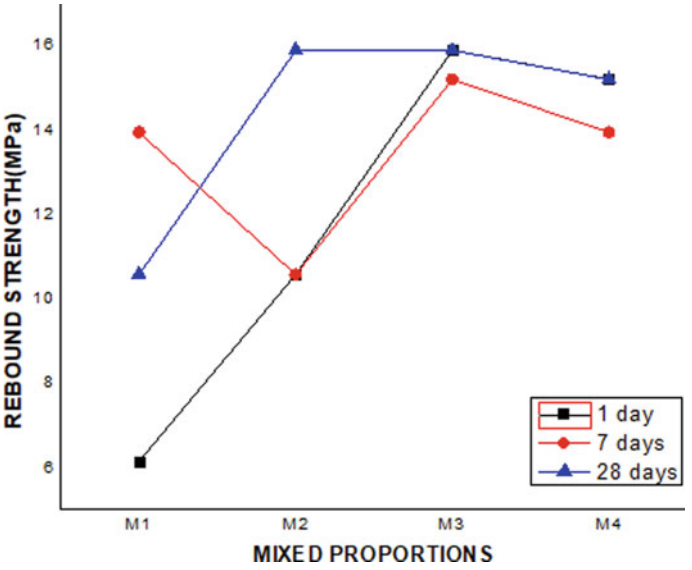

Fig. 3 Comparison of rebound hammer strength test verses mix proportions

Table 3 Rebound hammer strength test results

Mixes	Rebound strength(MPa)		
	1 day	7 days	28 days
M1	6.15	13.94	10.57
M2	10.57	10.57	15.88
M3	15.88	15.19	15.88
M4	15.19	13.94	15.19

4.4 Electrical Resistivity Test

Figure 4 depicts the change in electrical resistivity value for all mix proportion concretes with age. ESP replacement by 5% has received higher strength than other concrete mixtures. However, the electrical resistant value decreases with the increase in the egg shell powder (Table 4).

Slightly higher strength up to a 5% ESP replacement in M1 and M2 specimens is due to chemical processes between ESP and concrete paste. The particles are increased at higher limestone replacement and strength decreases as a result [7]. Concrete strength decreased in this study with higher ESP percentages. The improved strength due to fly ash addition along with ESP in M4 when compared to corresponding ESP-replaced concrete M3 may be due to improved particle packing along with pozzolanic activity. Evidently, M4 has a higher density than M3. As already discussed, it is considered that the calcium ESP may respond with cement and thus

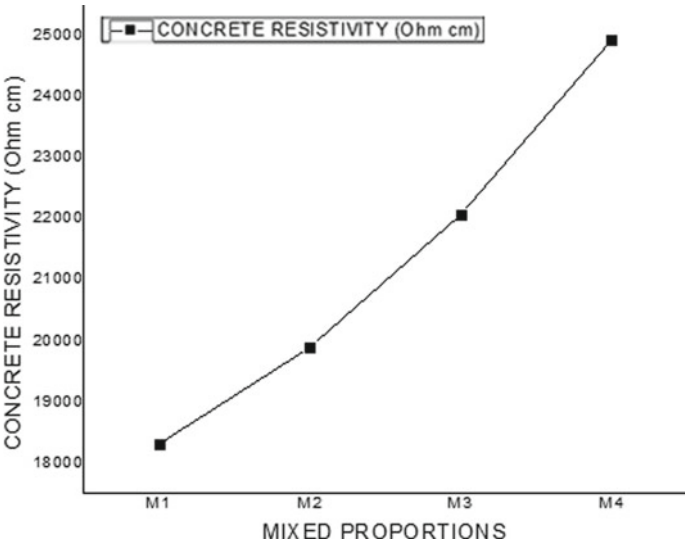

Fig. 4 Comparison of electrical resistivity verses mix proportions

Table 4 Electrical resistivity test values

Mixes	Concrete resistivity (Ohm-Cm)	Likely corrosion rate
M1	18,315	Low
M2	19,890	Low
M3	22,065	Negligible
M4	24,915	Negligible

have assistance in a compacted structure, producing similar performance in terms of electrical conductivity to the conventional concrete. The research on the impact of ESP particle size on concrete may, therefore, also improve.

5 Conclusions

At 7 and 28 days of curing, 20% fly ash and 5% replacement of ESP had higher compression strength and split tensile strength than conventional concrete. More than 10% of ESP replacements had lower strength than nominal concrete. Fly ash addition increased the corresponding ESP concrete compressive power. The Cao properties in cement and eggshell powder are almost the same in this research. During this experiment, it was discovered that a specific limit of Cao properties enhances compressive strength. It can be utilized for any form of construction work, both nominal and normal. This research work is suitable for earth quake areas [1, 2, 5, 6, 8].

References

1. Dhanalakshmi M, Sowmya NJ, Chandrashekar A (2015) A comparative study on egg shell concrete with partial replacement of cement by fly ash. Int J Eng Res 4(05):1532–1538. https://doi.org/10.17577/ijertv4is051303
2. Gowsika D, Sarankokila S, Sargunan K, et al (2014) Experimental investigation of egg shell powder as partial replacement with cement in concrete. In J Eng Trends Technol 14(2):65–68. http://www.ijettjournal.org
3. Mtallib MOA, Rabiu A (2009) Effects of eggshells Ash (Esa). Effects of Eggshells Ash (ESA) On The Setting Time Of Cement, (Nigerian Journal of Technology) 28(2):29–38
4. Okonkwo UN, Odiong IC, Akpabio EE et al (2012). The effects of eggshell ash on strength properties of cement-stabilized lateritic. Int J Sustain Construc Eng Technol 3(1):18–25. ISSN: 2180-3242
5. Rice F, Ash H (2020) ISSN NO : 0022–1945 An experimental investigation on mechanical properties of M25 Concrete using egg shell powder and volume XII , Issue VII , July/2020 Page No : 1332 Journal of Interdisciplinary Cycle Research ISSN NO : 0022–1945 Page No : 1333. XII(1332):1332–1347
6. Yerramala A (2014) Properties of concrete with eggshell powder as cement replacement. Indian Concr J 88(10):94–102
7. Guemmadi Z, Resheidat M, Chabil H et al (2009) Modeling the Influence of Limestone Filler on Concrete: A Novel Approach for Strength and Cost. Jordan J Civ Eng 3(2):158–196
8. Malhotra VM, Mehta PK (2002) High-performance. High-volume fly ash concrete. Supplementary cementing materials for sustainable development, inc., Ottawa, Canada, p 101

An Investigation of the Mechanical Properties of Recycled Aggregate Concrete with Silica Fume

Nilesh Masne and Shiwanand Suryawanshi

Abstract This study aimed to investigate the sustainable replacement of aggregates and cement in concrete. Recycled coarse aggregate (RCA) was added as a natural coarse aggregate (NCA) substitute to 50% and silica fume (SF) as a cement substitute in 5, 10, and 15%. This has the potential to reduce material costs and at the same time have a positive impact on the environment. A single size of recycled coarse aggregates was used and four sets of concrete mixes were made. A constant water/binder ratio of 0.40 was used in all concrete mixes. The mechanical properties, including compressive strength, tensile strength, and flexural strength of concrete, have been investigated and compared to those of natural aggregate concrete (NAC). Test results showed that the SF has a positive effect on the compressive strength, tensile strength, and flexural strength if the RCA content in the recycled aggregate concrete (RAC) is approximately 50%. It was found that the use of SF 5 to 10% as a cement substitute for RAC improved the performance of concrete.

Keywords RCA · RAC · SF · Replacement ratio · Sustainable environment

1 Introduction

Wealth from waste is the need of today's sustainable environment. Concrete is the greatest engineering material consume in the world. The coarse aggregates and cement is the main ingredient of concrete. Now a day's many researchers show a wide interest to find alternative materials for conventional materials in concrete. Ordinary portland cement is one of the key constituents used in the manufacture of concrete. Numerous ecological problems lead to their lease of an enormous extent of CO_2 into the atmosphere, a chief influence on greenhouse consequences and global warming. To solve these problems, therefore, supplementary cementing material such as SF is used as a partial replacement of cement. Numeral studies are underway in India and other countries to study the influence of these materials as substitute

N. Masne (✉) · S. Suryawanshi
Department of Civil Engineering, S.V. National Institute of Technology, Surat 395007, India

B. Kondraivendhan et al. (eds.), *Sustainable Building Materials and Construction*,
Lecture Notes in Civil Engineering 222,
https://doi.org/10.1007/978-981-16-8496-8_47

materials. SF is a mineral admixture and a precise reactive pozzolan and it results in high resistance and durability. SF is a by-product of the manufacture of silicon metal alloys or ferrosilicon. There is a too vast demand for natural aggregates in the construction sector, with a large gap between supply and demand, which can be reduced to a certain amount by recycling construction and demolition (C & D) waste. Practitioners must be aware of the properties and benefits of using C & D waste. In India, the quantity of C & D waste represents between 25 and 30% of total urban solid waste CPCB [1]. In many countries, regulations and procedures for the reuse of waste in construction applications have been put in place. In January 2016, the standard for coarse and fine aggregates was revised, made it possible to use RCA up to 20% in reinforced concrete specified in CPCB:2016 and IS-383:2016. The performance of RCA has recently been investigated in India. As a result, research on concrete recycling is very limited. Investigators in other countries researched the mechanical properties and additional characteristics of RAC to determine C and D waste in concrete. The empirical expression for RAC was developed by Suryawanshi et al. [2] and that has been agreed with the experimental results. As the increase in the level of replacement of the RCA, the toughness and ductility index of the RAC decreased according to Suryawanshi et al. [3].

Zhou and ping Chen [4] studied the mechanical properties of recycled concrete and revealed that different varieties of RCA have significant variance in mechanical properties of RCA concrete. Matias et al. [5] concluded that the splitting tensile strength was influenced by the replacement ratio of natural aggregate (NA) by recycled aggregate (RA). Dilbas et al. [6] and Kou et al. [7] found that the mixtures of SF, RA, and NA, increased the performance of RAC. By the addition of 10% SF in RAC, the required compressive and flexural strength of RAC were achieved by Huot et al. [8]. According to Uddin and Shaikh [9], the sluggish pozzolanic response of slag led to the enduring compressive and tensile strengths of RAC with 10% SF. The objective of this work was to explore the mechanical properties of concretes containing SF at different proportions and to substitute the NCA with RCA. For this purpose, four concrete mixtures of 50% RCA with 0, 5, 10, and 15% SF were produced, and the mechanical properties such as compressive strength, splitting tensile strength, flexural strength, and workability of RAC were inspected.

2 Material and Mix Proportion

Ordinary Portland Cement (OPC) 53-grade cement conforming to the requirements of IS: 12269-2013 and SF conforming to ASTM C 1240–05 were used in this experimentation. Table 1 shows the chemical and physical properties of cement and SF. Fine Aggregate (FA) of zone II and Crushed natural coarse aggregate having maximum nominal size 20 mm conforming to IS 383: 2016 [10], was used to cast the concrete.

Table 1 Properties of cement and silica fume

Contents	SiO_2 (%)	CaO (%)	SO_3 (%)	Al_2O_3 (%)	Fe_2O_3 (%)	MgO (%)	Specific Gravity	Bulk Density (kg/m^3)	Loss on Ignition %	Specific Surface (m^2/kg)
Cement	25	62	3	5	3	2	3.14	1440	11.2	370
SF	93.47	0.5	2	–	–	0.6	2.40	770	3.82	22,280

2.1 Recycled Coarse Aggregates (RCA)

In this study, the debris of a demolished structural element of a building in the Nashik, Maharashtra (India) was used as shown in Fig. 1. The structural element was broken with the help of a mechanical breaker into small pieces and brought to the laboratory. Then by using a steel hammer, manually the debris was broken into small pieces and pick up only fewer mortar aggregates. Then sieved from 20 mm sieve and retained on 4.75 mm conforming to IS 383:2016 was used to cast the concrete in replacement of 50% to the NCA. Table 2 showed the physical properties of NCA, RCA, and fine aggregate (FA). According to the IS 456:2000, portable tap water was used to mix and cure concrete.

To maintain the workability of concrete mix the polycarboxylic ether-based super-plasticizer conforming to IS 9103:1999 and ASTMC494/C494M -13 was used in the experimental work.

Fig. 1 Recycled coarse aggregates acquired from the demolished structure

Table 2 The properties of NCA, RCA, and FA

Type	Density (kg/m^3)	Water absorption (%)	Fineness modulus	Specific gravity	Impact Test (%)	Crushing test (%)
NCA	1750	1.02	6.54	2.66	14.80	18.20
RCA	1650	2.58	6.76	2.48	19.60	23.38
FA	1600	3.20	2.75	2.65	–	–

Table 3 Concrete mix proportion

Mixture	% replacement of silica fume	Cement (Kg/m^3)	Silica fume (Kg/m^3)	Coarse Aggregate (Kg/m^3)	Recycled Coarse Aggregate (Kg/m^3)	Fine Aggregate (Kg/m^3)	Super Plasticizer (Kg/m^3)
M_{00}	0	400	0	1130	0	670	4.5
M_{05}	5	380	20	565	565	670	4.5
M_{10}	10	360	40	565	565	670	4.5
M_{15}	15	340	60	565	565	670	4.5

2.2 Concrete Mixtures

Four sets of concrete mixes of grade M30 that contain the earlier stated aggregates and SF were produced in the laboratory according to concrete mix proportioning-Guidelines IS10262:2009. Table 3 presented the mixed proportions of concrete design by the absolute volume method. In all the mixes, the water/binder ratio (w/b) was a constant value of w/b = 0.40. A pan mixer was used to mix the concrete in a test lab. The coarse, fine aggregates and sand were mixed for one minute. The cement and SF were then added, and the mixture was dry mixed for another minute. Two-thirds of water were added in the third minute, and steady mixing was maintained. After that the remaining water and Superplasticizer were added, and the total mixing time was five minutes. Concrete was cast according to IS456:2007 and vibrated until large air bubbles emerged and blow at the surface.

2.3 Specimens and Curing

To evaluate the splitting tensile strength 150ø × 300 mm cylinder specimens were manufactured. 150 × 150 × 150 mm cube specimens were also cast to know the compressive strength and 100 × 100 × 500 mm prism was produced for flexural strength. The samples were cast in metal molds and compacted with the aid of a vibrating table. After remolding, all samples were cured in a water-curing tank, until 7 and 28 days.

3 Results and Discussions

3.1 Compressive Strength

After 7 and 28 days of curing the specimens were tested by a compression testing machine. Figure 2 and Table 4 exposed the results of the compressive strength of the concrete. The cube strength was evaluated according to IS 516:2004.

Every existing value is the average of the test results of the three samples. The strength of concrete depends on the strength of the aggregate, whereby the cement matrix and the interfacial transition zone (ITZ) were differentiated between the matrix and the aggregates. Since the recycled aggregates are more porous, some of the cement and SF may penetrate the aggregate, which increases the bond strength between the aggregates and the hydrated cementitious matrix. In the presence of SF, the cracks in the RCA were reduced due to the healing effect of cement paste mixed

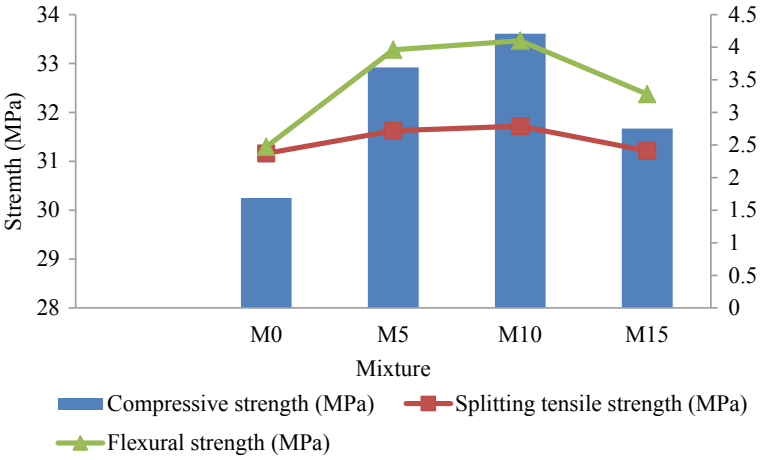

Fig. 2 Correlation between mixtures and strength

Table 4 The test result of the concrete mixtures at 7 and 28 days

Mixture	SF (%)	Slump		Compressive strength (MPa)		Splitting tensile strength (MPa)		Flexural strength (MPa)	
		Slump cone (mm)	Compaction factor	7 day	28 day	7 day	28 day	7 day	28 day
M_0	0	98	0.91	18.00	30.25	1.49	2.37	1.85	2.47
M_5	5	102	0.94	19.90	32.92	1.67	2.72	2.28	3.96
M_{10}	10	105	0.95	21.03	33.61	1.76	2.79	2.32	4.10
M_{15}	15	95	0.91	18.23	31.67	1.41	2.41	2.10	3.28

with SF after curing. This indicates that the SF content has a positive effect on the compressive strength if the RCA content in the RAC is approximately 50%.

3.2 Splitting Tensile Strength

The splitting tensile strength of the sample was determined at the age of 7 and 28 days curing. The outcomes of the splitting tensile strength present in Table 4 and Fig. 2. The proportions of the splitting tensile strength to the compressive strength are given in Table 5. The tensile strength was evaluated following IS 5816–2004.The splitting tensile strengths of the sample containing 5–10% SF and RCA were superior to the strengths of the conventional concrete sample. Another interesting result from Table 4 is that the use of the SF in RAC has a slightly increasing effect on tensile strength, i.e., the tensile splitting strength was found as 2.72, and 2.79 for the M_5 and M_{10}concrete blend. A drastic decrease in tensile strength for the M_{15} concrete mix was also observed. Figure 3 shows that RCA had broken in the concrete after the tests conducted on the sample. Therefore, the weakest point in this RAC was the RCA itself. In other words, the cracks in the RCA structure were caused by crushing operations, and the higher porosity was caused by the properties of adhered old mortar, which reduced the strength of the RAC.

The effect of SF contents on the ratios of the splitting tensile strength to the compressive strength at 28 days is shown in Table 5. It was seen that from Table 5 the ratios of the M_5 and M_{10} mixture (i.e., 0.082, 0.083)at 28 days were greater than those of M_0 and M_{15} (i.e., 0.078, 0.076). This rise in the ratios is due to the use of

Table 5 The ratio of splitting tensile strength to compressive strength at 28 day

Mixture	M_0	M_5	M_{10}	M_{15}
SF (%)	0	5	10	15
Ratio	0.078	0.082	0.083	0.076

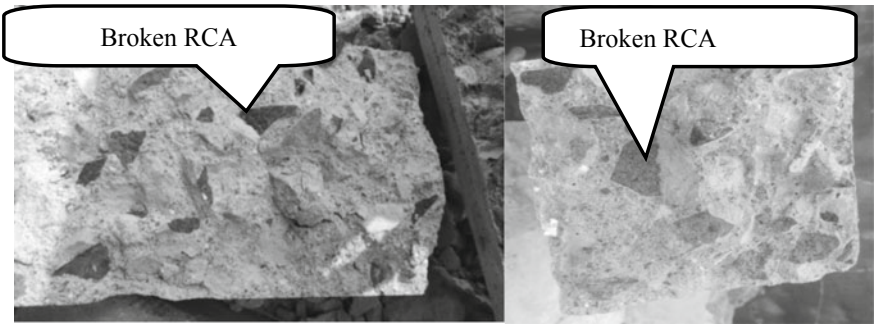

Fig. 3 Samples after splitting tensile strength and flexural test containing RCA

5 and 10% SF content. The RAC ratio, on the other hand, was reversed when the percentage of SF was increased from 10 to 15%, as shown in Table 5.

3.3 Flexural Strength

According to IS 516:2004, this test was performed on beams measuring 100 × 100 × 500 mm, taking into account that the material was homogeneous. The results of flexural strength of the concrete are shown in Table 4 and Fig. 2. The RCA in the concrete was found broken after the tests on the sample, as was the case with the splitting tensile test of concrete, as shown in Fig. 3.

4 Conclusions

The addition of 5 to 10% silica fume considerably enhanced the compressive strength, splitting tensile strength, and flexural strength of concrete containing 50% RCA. SF comprising 5 to 10% is an alternate method to increase the compressive strength of RAC for the consumption of concrete in the construction industry. The splitting tensile strength of the sample with 5 to10% SF contents improves by replacing the NCA with 50% RCA. The flexural strength of the mixture of the sample with 5 to 10% SF contents increases by replacing the NCA with 50% RCA. The ratio of the splitting tensile strength to the compressive strength of RAC decreases as the percentage of SF material is increased from 10 to 15%. The final SF is a mineral additive that improves RAC efficiency.

References

1. Guidelines On Environmental Management of C & D Wastes(2016) (Prepared in compliance of Rule 10 sub-rule 1(a) of C & D Waste Management Rules, 2016) Central Pollution Control Board
2. Suryawanshi S, Singh B, Bhargava P (2018) Equation for the stress-strain relationship of recycled aggregate concrete in axial compression. Mag Concr Res 70(4):163–171. ISSN 0024-9831, E-ISSN 1751-763X
3. Suryawanshi SR, Singh B, Bhargava P (2015) Characterization of recycled aggregate Concrete. In: Advances in structural engineering. Springer India
4. Zhou C, Chen Z (2017) Mechanical properties of recycled concrete made with different types of coarse aggregate. Constr Build Mater 134:497–506
5. Matias D, de Brito J, Rosa A, Pedro D (2013) Mechanical properties of concrete produced with recycled coarse aggregates—influence of the use of superplasticizers. Constr Build Mater 44:101–109
6. Dilbas H, Simsek M, Cakır O (2014) An investigation on mechanical and physical properties of recycled aggregate concrete with and without silica fumes. Constr Build Mater 61:50–59

7. Kou S-C, Poon C-S, Agrela F (2011) Comparisons of natural and recycled aggregate concrete prepared with the addition of different mineral admixtures. Cem Concr Compos 33(8):788–795
8. Huot P, Suntharavadivel TG, Duan K (2014) Effect of silica fume on recycled aggregate concrete. In: 23rd Australasian conference on the mechanics of structures and materials (ACMSM23). Byron Bay, Australia, pp 9–12
9. Uddin F, Shaikh A (2017) Mechanical properties of recycled aggregate concrete containing ternary blended cementitious materials. Int J Sustain Built Environ 6:536–543
10. BIS IS383-1970 (2016) Specification for coarse and fine aggregates from natural sources for concrete. Bureau of Indian Standards, New Delhi (India)

Performance Evaluation of Pongamia Pinnata Shell-Waste for the Treatment of Toxic Congo-Red Dye Bearing Wastewater

Tripti B. Gupta and Khalid S. Ansari

Abstract This current study was completed to analyze the adsorption limit of the Pongamia pinnata shell-waste for the expulsion of toxic Congo-red dye containing wastewater. The impact of *pH*, dosage, contact span, concentration, and temperature on adsorption was considered. The Langmuir, Freundlich, and Temkin adsorption isotherm models were applied to investigate adsorption information and were discovered to be relevant to this adsorption cycle. The mechanism of adsorption is researched by considering pseudo 1st and 2nd order kinetics. The adsorption study revealed that the ideal dosage for Pongamia pinnata shell-waste was discovered to be 2.5 gm/50 ml. Percent seizure of Congo-red dye increases with the increase in ideal dosage up to a specific breaking point and afterward remains practically steady. Adsorption is greatest in acidic pH range ($pH = 6.88$). The equilibrium time was discovered to be 3 h. The isotherm investigation shows that the Langmuir isotherm is best-fitted. Thermo-dynamic parameters show adsorption has unconstrained, arbitrary, and endothermic nature. The usage of Pongamia pinnata shell-waste as an adsorbent for the genuine wastewater containing dye can be the response for actuated carbon.

Keywords Congo-red · Dye · Pinnata · Pongamia · Shell-waste

1 Introduction

Water (H_2O) is one among the crucial liquid on which every bit of existence depends. Its pollution has become overall concern. We should observe water as it is the significant normal asset on the sphere. Litter as water and its emergencies are the main

T. B. Gupta (✉)
Department of Civil Engineering, Shri Ramdeobaba College of Engineering and Management, Nagpur 440013, India
e-mail: guptatb@rknec.edu

K. S. Ansari
Department of Civil Engineering, Yeshwantrao Chavan College of Engineering, Nagpur 441110, India

B. Kondraivendhan et al. (eds.), *Sustainable Building Materials and Construction*,
Lecture Notes in Civil Engineering 222,
https://doi.org/10.1007/978-981-16-8496-8_48

difficulty. Because of uneconomical and inadequate basic debased water purifying ways, a ton of assembling and creation ventures let go their polluted water to nearby territory or water sources without any handling and treatment [1]. Physico-chem adsorption is one among most of valuable handling framework. This framework turns out to be more beneficial if the adsorbent is cost proficient. Incalculable examinations have yielded out to comprehend the capability of rotating assets. A sensibly evaluated and with less grieved available adsorbent would make reasonable alternative. In this examination, clump measures were dropped to investigate the possibility of Pongamia pinnata shell-waste (PPS) as a sorbent for seizure of the debased water.

2 Resources and Methodologies

Pongamia pinnata shell-waste (PPS) is chosen as an adsorbent in the current undertaking. The basic classification for this plant is "Su-babul." General imprint reagents are used in this present work. Congo-red dye (C-R dye) is bought from Standard Scientific Company, Nagpur. The expert supply of 1000 mg/L (ppm) and ensuing stock for each arrangement was made by taking particular measure of reagent in refined water.

3 Results and Discussion

3.1 Arrangement of Adsorbent and Character Investigations of PPS

This examination researched the employment of Pongamia pinnata shell-waste as a bio-adsorbent for shading expulsion of colors from watery arrangement. Pongamia pinnata is the logical name of a locally reachable ever-green sort of plant. The nearby name of this plant is "Karanja." The phloem-xylem was basically utilized as an adsorbent material for this examination. The plant material was obtained from Nagpur. New parts of the plant were cut then the external bark was eliminated. The inward part was then squashed and crushed to get the necessary molecule size. The material so acquired (PPS) was then washed with triple distilled water for 4–5 times. After washing, the material was sun dried for 4–5 h. The handled adsorbent material was then at long last put to testing. Characters of PPS include parametric investigations. Billed to presence of unpredictable substance, PPS might be considered as natural and burned in conduct. Parametric character investigations of PPS as per Indian norms code 1350:1984 [5] show that moisture-content, ash-content, volatile-content, and fix-carbon-content are observed to be 8.4, 10, 76.6, and 5%, respectively.

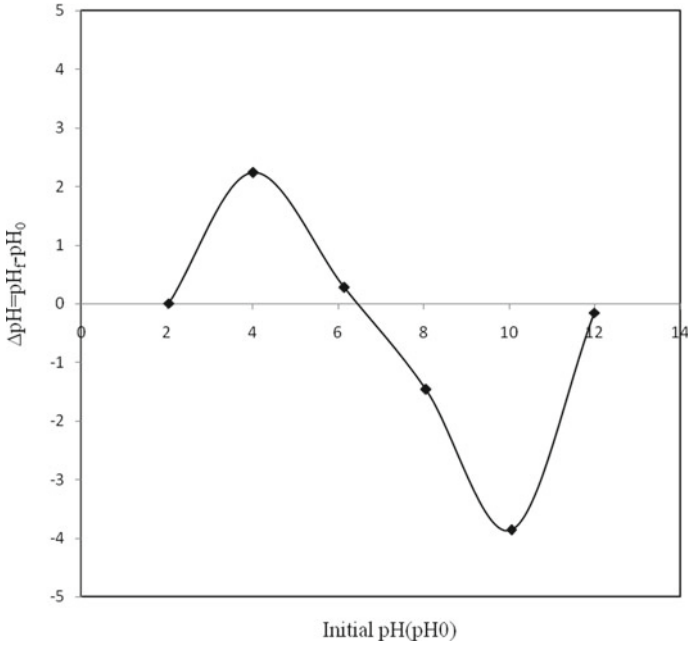

Fig. 1 Mark of zero charge

3.2 Mark of Zero Charge

In present investigation, the mark of zero charge for the adsorbent material is discovered. It was resolved utilizing strong expansion technique [6]. The mark of zero charge for the PPS was discovered to be 6.32. During the adsorption interaction, it was seen that the pH of the arrangement was diminished subsequent to adding the PPS dose. The underlying pH of the arrangement was 6.88 which has become < 6.88. The pH declines because surface becomes negatively charged due to adsorbing OH-particles from the arrangement [8]. Figure 1 shows the mark of zero charge chart for PPS.

3.3 Scanning Electron Microscopic (S-E-M) Analysis

SEM investigation of the PPS test was completed to contemplate the surface morphology of the adsorbent material. Tests were tried at 500 × amplification to notice the distinction in the surface morphology of the virgin and stacked PPS. The SEM testing was finished utilizing JEOL (JSM 6380 A) makes scanning electron microscope. As the examples were non-directing sort, they were covered with platinum covering utilizing JEOL JFC sixteen hundred coater. Figure 2a and b show the

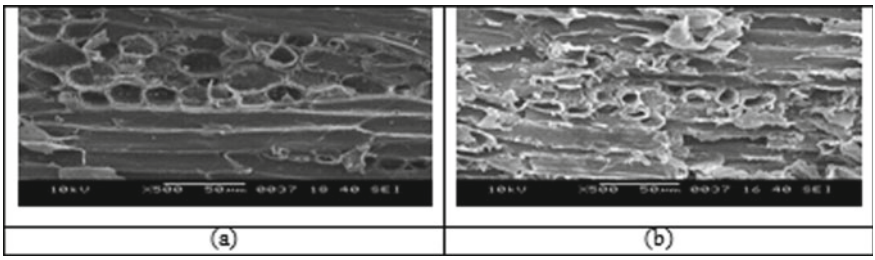

Fig. 2 SEM of **a** virgin PPS, and **b** stacked PPS at 500 × amplification

SEM pictures of virgin and stacked PPS tests. It can be clearly seen from the pictures that there is twisting of pores and scale like statement on the outside of the stacked PPS tests.

3.4 Batch Investigations

In exhibit of understanding the impact of assorted boundaries, the group lab tests were directed.

3.4.1 PPS Dosage Impact

The PPS dosage (m) impact on the seizure of C-R dye by PPS at $C_O = 50$ mg/L is shown in Fig. 3. It can be seen that the C-R dye seizure grows up to some esteem followed by roughly steady. Most good m was discovered to be 50 g/L for PPS. Figure 3 shows that the q_e decreases with support in estimation of m. This is due to exhaustness of adsorption region and the contact term of PPS, which outcomes into firm accumulation [2].

3.4.2 Solute-Dissolvable *pH* Impact

pH changes the shell estimation of the adsorbed material just as the particle development measure of the solute-solvents [8]. It is an observation from the Fig. 4 that the shell adsorbs negative particles at less fortunate *pH* because of rate of H^+ ionized substances, while the shell is dynamic for the adsorption of positive particles at raised *pH* because of the testimony of OH^- ionized substances [2]. The C-R dye is generally firm at around normal $pH = 6.88$ for PPS, all advantageous research facility tests were considered at nature *pH* of 6.88.

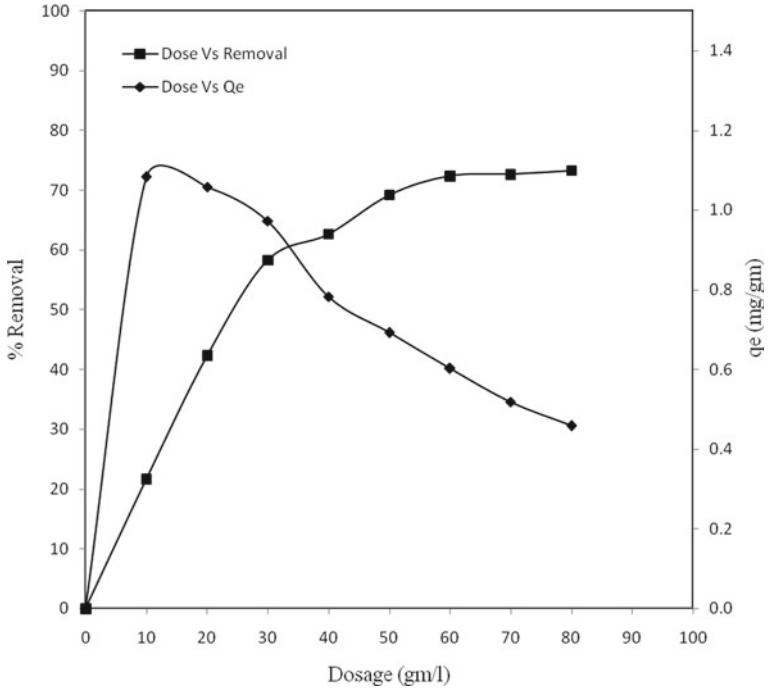

Fig. 3 Dosage impact of C-R dye by PPS

3.4.3 Congo-Red Dye Concentration Impact

The C_0 impact on the seizure of C-R dye by PPS shows that the measure of C-R dye adsorbed per part mass of PPS (q_e) broadened with the lift in C_0, despite the fact that % C-R seizure falls with the lift in C_0. Similarly, Fig. 5 portrays that the adsorption of the C-R dye support up concerning temperature that shows the endo-thermal instrument mechanism.

3.4.4 Contact Span Impact

The contact span (t) plots appeared in Fig. 6 gives a thought regarding fast adsorptive instrument of C-R in the most punctual 30 min. At that point, the adsorptive component waterfall bit by bit and the adsorption procures even harmony in 3 h. Figure 6 additionally expresses the independently, constant, smooth, and flat diagrams mixing toward dissemination. These diagrams specify a feasible single layer of C-R on the PPS seal [3]. The % seizure is most prominent at 3 h of contact span.

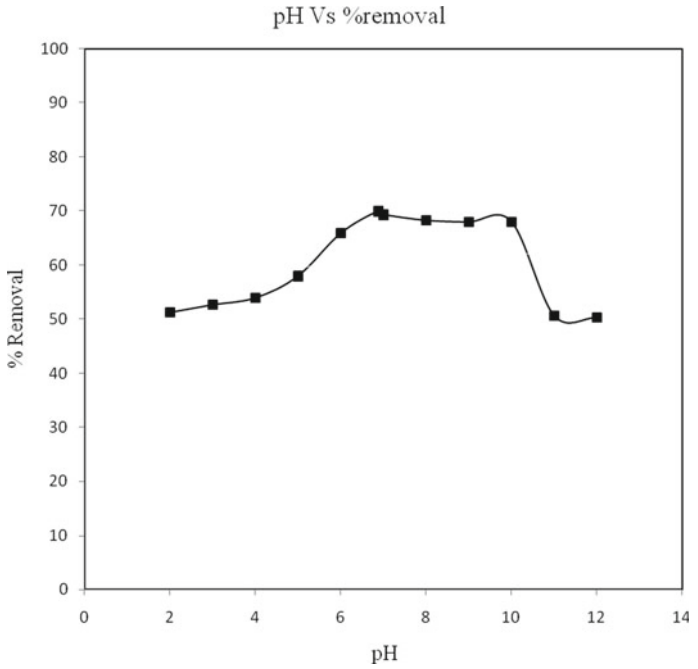

Fig. 4 Solute-dissolvable pH impact of C-R dye by PPS

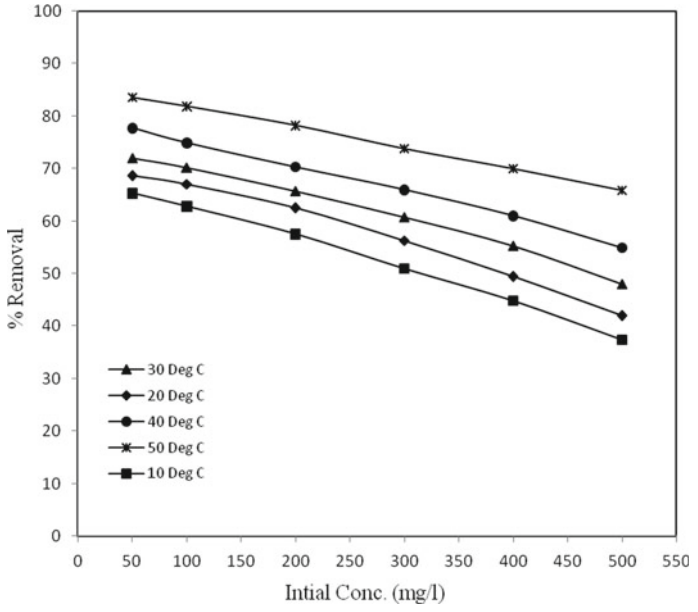

Fig. 5 Concentration impact of C-R dye by PPS at 10–50 °C

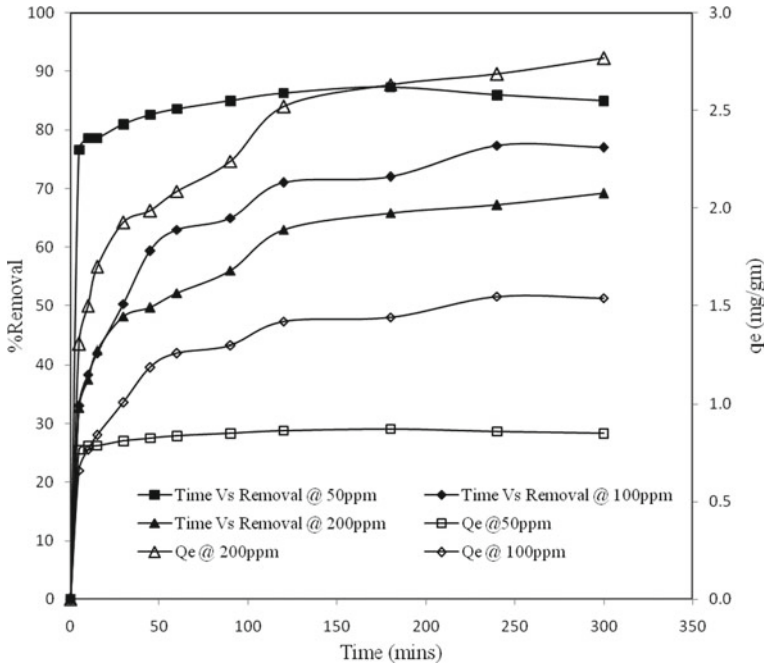

Fig. 6 Contact span impact onto C-R dye by PPS

3.4.5 Adsorption Temperature Impact

Figure 7 address that the adsorptive system of C-R dye support up with the raise in temperature. This raise describes that the adsorptive instrument may be because of chemisorbs [7]. This Fig. 7 also portray that at more unfortunate C-R dye fixations, q_e raises piercingly.

3.5 Best Fit Equilibrium Analysis

Best fitting connections for the equilibrium charts are broke down to do enhancement of adsorption instrument. It is applied to isotherm models like Langmuir, Freundlich, and Temkin to communicate the steadiness and even characters of adsorption measure.

By doing appraisal of the results of the principles through assorted error functions and from Fig. 8, it is set up that Langmuir model is best-most-fitted isotherm for seizure of C-R dye onto PPS at around each temperature.

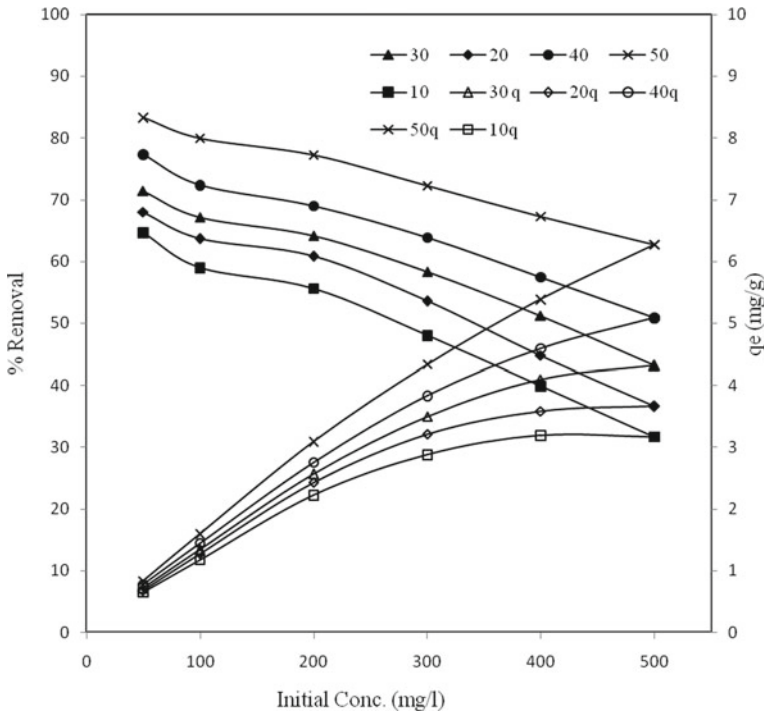

Fig. 7 Temperature impact of C-R dye by PPS at 10–50 °C

3.6 1st and 2nd Order Kinetic Energy Investigation

The active examination administers the dissolvable solute adsorption rate that go adjusts and portrays the leftover contact span of take-up [4]. The adsorptive instrument of C-R under an ideal condition adjusts switching first active request, after a sole class is chosen on a hetero-grouped territory. In present work, 1st and 2nd order kinetic energy investigations yielded out in group's mode in order to get the procedure of take-up. 1st order Fig. 9a and 2nd order Fig. 9b active diagrams have been plotted and noticed.

Figure 9a imagines that the estimation of take-up (q_e) drops down with the raise in C-R dye concentration. The 1st order kinetic energy investigation is exhibiting more unfortunate connections correspondence esteems with lower fits. The 2nd order kinetic energy investigation Fig. 9b of C-R by PPS visualizes that the estimation of take-up (q_e) ascends with the augmentation in C-R dye concentration. The relationship correspondence esteems are in the area of close up to one connoting the 2nd order kinetic energy investigation fine into the entire research center tests framework.

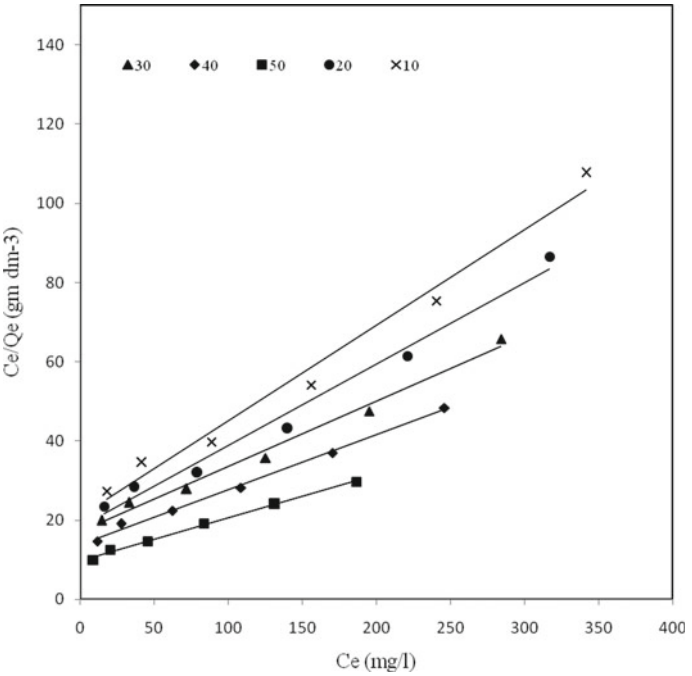

Fig. 8 Langmuir chart for the exclusion of C-R dye at 10–50 °C by PPS

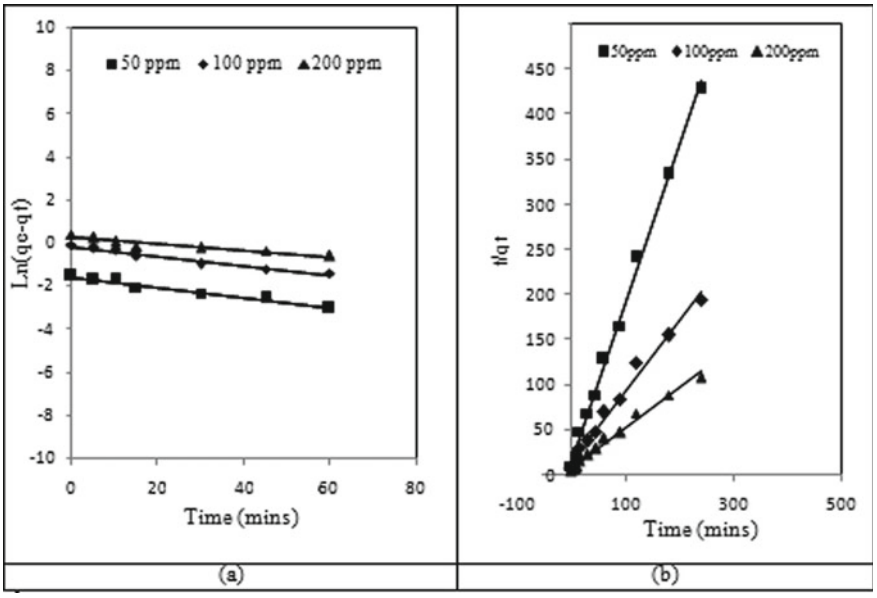

Fig. 9 **a** 1st order and **b** 2nd order kinetic energy investigation of C-R dye by PPS

3.7 Thermo-Dynamic Investigation

The Van't Hoff's condition and its plot for Langmuir isotherm model are considered in thermo-dynamic investigation. The Gibbs free energy change (ΔG), enthalpy change (ΔH), and entropy change (ΔS) are determined from Langmuir model for sorption of C-R dye onto PPS. The positive worth ΔH, i.e., 1.571 kJ/mol affirms the endothermic idea of the generally sorption measure. The C-R dye particles need to dislodge more than one water atom for their adsorption and these outcomes in the endothermicity of the adsorption interaction. The positive estimation of ΔS, i.e., 0.0689 kJ/mol K proposes expanded irregularity at the strong/arrangement interface for certain underlying changes in the adsorbate and adsorbent and a proclivity of PPS toward C-R dye. Additionally, positive estimation of ΔS compares to an expansion in the level of opportunity of the adsorbed species [7]. The ΔG estimations were negative, i.e., -17.919 kJ/mol K at 10 °C up to -20.674 kJ/mol K at 50 °C showing the attainability and suddenness of the adsorption cycle.

4 Conclusions

The most ideal PPS dosage and contact span for the existing research work were distinguished to be 50 gm/L and 3 h individually. Percent seizure of C-R dye support up with the raise in PPS dosage up to a persuaded reach and afterward relics pretty much unvarying. Then again, percent seizure lets down with the raise in C-R dye concentration. Adsorptive investigation of C-R dye on PPS is most prominent in normal pH ($pH = 6.88$). The isotherm equilibrium study portrays that the Langmuir model is best-most fit model for C-R dye sorption onto PPS under ideal conditions. The 1st and 2nd order kinetic energy investigation guarantees that the 2nd order kinetic energy plot is relevant for the entire movement. Thermo-dynamic parameters show adsorption process is unconstrained, arbitrary, and endothermic in nature. The usage of pinnata shell-waste is affordable choice against the other sorption substances or activated carbons. It can be easily disposed of by burning, which may give good calorific value.

References

1. Gupta TB, Lataye DH (2018) Adsorption of indigo carmine and methylene blue dye: Taguchi's design of experiment to optimize removal efficiency. Sadhana, Indian Acad Sci 43(170):1–13. https://doi.org/10.1007/s12046-018-0931-x
2. Gupta TB, Siddh SP, Khungar HP (2019) Adsorptive removal of Direct-red-28 dye from contaminated water using Subabool timber wood waste. Helix 9(6):5691–5695. https://doi.org/10.29042/2019-5691-5695

3. Gupta TB, Lataye DH (2017) Adsorption of indigo carmine dye onto acacia nilotica (Babool) sawdust activated carbon. ASCE J Hazardous Toxic Radioactive Waste 21(4):1–11. https://doi.org/10.1061/(ASCE)HZ.2153-5515.0000365
4. Gupta TB, Lataye DH (2019) Removal of crystal violet and methylene blue dyes using Acacia Nilotica sawdust activated carbon. Ind J Chem Tech 26(1):52–68 http://nopr.niscair.res.in/handle/123456789/46985
5. Lataye DH, Mishra IM, Mall ID (2008) Adsorption of 2-picoline onto bagasse fly ash from aqueous solution. Chem Eng J 138(1–3):35–46
6. Lataye DH, Mishra IM, Mall ID (2006) Removal of pyridine from aqueous solution by adsorption on bagasse fly ash. Ind Eng Chem Res 45(11):3934–3943
7. Srivastava VC, Swamy MM, Mall ID, Prasad B, Mishra IM (2006) Adsorptive removal of phenol by bagasse fly ash and activated carbon: Equilibrium, kinetics and thermodynamics. Colloids Surf A Physicochem Eng Asp 272(2):89–104
8. Uddin MT, Islam MA, Shaheen M, Rukanuzzaman M (2009) Adsorptive removal of methylene blue by tea waste. J Hazard Mater 164(1):53–60

Experimental Investigation on Geopolymer Concrete Containing Recycled Plastic Waste Aggregates

Gaurav Jagad, C. D. Modhera, and Dhaval Patel

Abstract The increasing rate of plastic waste generated in the world day by day is alarming for humans. The illegal burning plastic waste result into the releasing of hydrocarbons is stringent pollutants. The amount of plastic waste is generated 0.4 kg per capita per day which is tremendously high as per GPCB and CPCB. In order to control the rate of the generation and disposal along with illegal burning, the pollution control board laid strong emphasis on utilization of the waste into the road construction and in other construction industry. This research presents the strength properties of geopolymer concrete (GPC) containing recycled waste plastic aggregate as one of the constituents. Waste plastic products recycled into granules. The conventional constituents of GPC namely grit was partially replaced with recycled plastic granules in varying proportions. All the mechanical properties were obtained and test results revealed that inclusion of recycled plastics in GPC significantly improved the compression, tension and flexural strength and compared to the conventional GPC mixes.

Keywords Geopolymer concrete · Recycled plastic waste aggregate · Compressive strength

1 Introduction

Plastic exhibits outstanding properties. These days, lots of garbage plastic are generated all over the planet and resulting in waste material which is proving unsafe to environment. Safe disposal and management of plastic waste is a global challenge. Utilization of plastic waste in construction material as a constituent could be one of the best steps toward ecofriendly and nutritive environment and eco-friendly construction.

GPC is formed by the reaction of raw materials rich in silica and alumina with alkaline liquids [1]. GPC is made from large amounts of industrial waste to produce

G. Jagad (✉) · C. D. Modhera · D. Patel
Sardar Vallabhbhai National Institute of Technology, Surat, India

B. Kondraivendhan et al. (eds.), *Sustainable Building Materials and Construction*,
Lecture Notes in Civil Engineering 222,
https://doi.org/10.1007/978-981-16-8496-8_49

low energy, low-carbon footprint, sustainable concrete without Portland cement [2]. Alkaline liquids can be used to react with silicon (Si) and aluminum (Al) in materials of geological origin or by-product materials (such as fly ash and rice husk ash) to form a binder. The most commonly used alkaline liquid in geopolymerization is the combination of sodium hydroxide (NaOH) or potassium hydroxide (KOH) and sodium silicate or potassium silicate [3, 4]. Geopolymer concrete has demonstrated potential as sustainable material as its base ingredients are fly ash or rice husk ash which are by products and hazardous to environment. By mixing GPC with recycled plastic waste aggregate is a step forward toward green concrete [5, 6].

In this paper an experimental data is represented based on experimental study conducted on the utilization of RPWA (Recycled Plastic Waste Aggregate) as a partial replacement of the 10 mm aggregates as 5, 10, and 15% by weight in geopolymer concrete to identify the different mechanical properties compression, tension, and flexural test have been carried out with and without RPWA which parade a good strength improvement in RPWAC.

2 Material and Mix Proportions

2.1 Plastic Waste

Plastic waste in form of recycled granules was collected from plastic pipe industry nearby shapar (Dist. Rajkot, Gujarat, India). Following figure shows waste plastic aggregate collected from pipe industry (Fig. 1).

Fig. 1 Grinded material from base material

Table 1 Physical properties of recycled plastic waste aggregate

Specific gravity	Abortion	Color	Shape	Surface	Size
0.9	<0.5%	White	Irregular	Rough	10–12 mm

Table 2 Chemical composition of GGBS and Fly ash by XRF Test

Particulars	(SiO_2)	(Al_2O_3)	(Fe_2O_3)	(CaO)	(MgO)	(K_2O)	(Na_2O)	(TiO_2)
Fly Ash	50	28	12	6.5	6	1.5	0.2	0.1
GGBS	32.19	8.59	2.8	38.09	5.5	0.4	0.26	8.89

2.1.1 Different Properties of Plastic Waste

A physical property is any measurable property whose value describes the state of the physical system. As shown in Table 1, the following performance tests were performed on the crushed particles.

2.2 GGBS and FLY ASH

GGBS is created by the method of quenching, which is the method of sudden ion slag cooling from a blast furnace using water or flux. A glassy, granular substance, is obtained at the end of the process, and then dried and grinded into fine powder. GGBS is a form of off-white cement. It's often referred to as slag cement by the United Kingdom which used in Europe, United States and Asia. GGBS is a binding material which is used mainly in ready-mix concrete with a ratio of 30–70% to create an eco-friendly concrete. GGBS used as the main binder material in this article and the chemical composition of GGBS is as below.

In the present experimental work, along with GGBS, Class F fly ash was used as secondary base material. Earlier only Fly Ash used as a binder material but, while using only Fly ash Temperature curing needed for polymerization process. Incorporating GGBS in geopolymer concrete eliminate temperature curing from research. The chemical composition of Fly ash is mentioned in Table 2.

2.3 Alkaline Solution

For the geopolymerization process alkaline solution play central role. The combination of NaOH and Na_2SiO_3 was used as an Alkaline Liquid. 16 M NaOH used in entire research work. The sodium silicate (Na_2SiO_3) solution was purchased from Sadguru Chemicals, Veraval, Rajkot.

2.4 Aggregate

Aggregates that were locally available has been used for the experiment work. Properties of aggregate is mentioned in following Table 3.

3 Experimental Program

RPWA used as replacement of 10 mm natural aggregates. The concrete mixture is prepared using GGBS and Class-F fly ash and Alkaline liquid. It is recommended to prepare an alkaline liquid by mixing the two solutions together at least one day before use. It is recommended to use a solution with a Na2O/SiO2 mass ratio of about 2 (for example, SiO2 = 29.4%, Na2O = 14.7%, water = 55.9%). Use palates form of sodium hydroxide with a purity of 98%. Dissolve the solid in water to make a solution of 16 M concentration. The mixture is then placed in a mold and vibrated on a bench shaker. The casting process, alkaline solution, machine mixing and testing of Geopolymer Concrete have described in Fig. 2.

Table 3 Mechanical properties of an aggregate

Size	Specific gravity	Impact value (%)
20 mm	2.75	20
10 mm	2.65	24

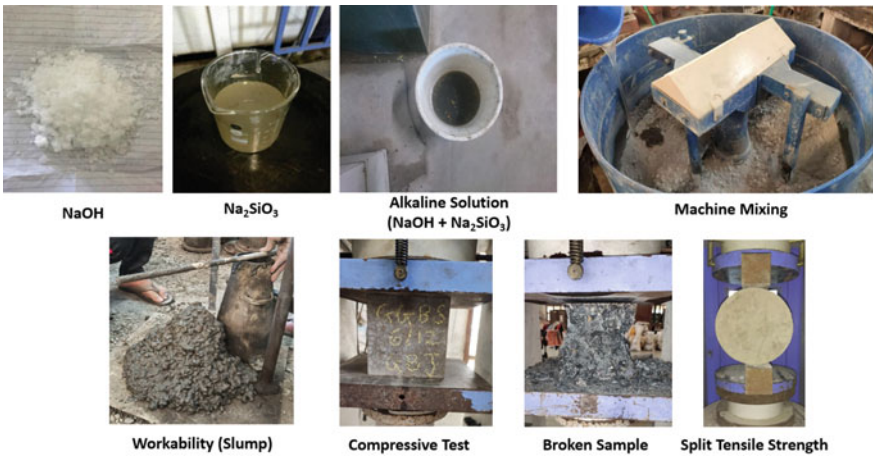

Fig. 2 Casting procedure and testing

Table 4 Mix proportion

Constituent	GGBS	Fly ash	Sand	Coarse aggregate	NaOH solution	Na_2siO_3	Extra water
Quantity (kg/m^3)	184	184	554.4	1293	46	138	29.44

Table 5 Recycled plastic waste aggregate content

Mix specification	Control mix	GPC 1	GPC 2	GPC 3
Proportion of PVC granules	0%	5%	10%	15%

3.1 Mix Design

The mix design and percentage replacement of coarse aggregate by recycled plastic waste aggregate have tabulated in Tables 4 and 5 respectively.

4 Results and Discussion

The mechanical properties of with and without plastic waste aggregate have been carried out. The discussion of the mechanical properties is as under.

- Compression test of control concrete observed 25 MPa at the age of 24 h and about 40 MPa at 7 days. Recycled plastic waste aggregate concrete gave better result, while 10% partially replaced by natural aggregate as shown in Fig. 3
- Split tensile strength of control concrete was observed 2.46 MPa at the age of 24 h and about 2.66 MPa at the age of 7 days. Along with recycled plastic waste

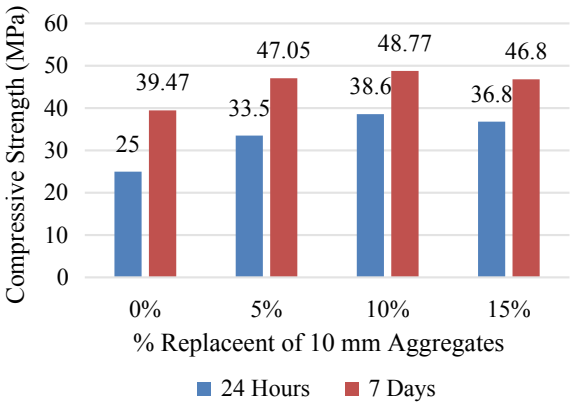

Fig. 3 Compressive strength result at 24 h and 7 Days

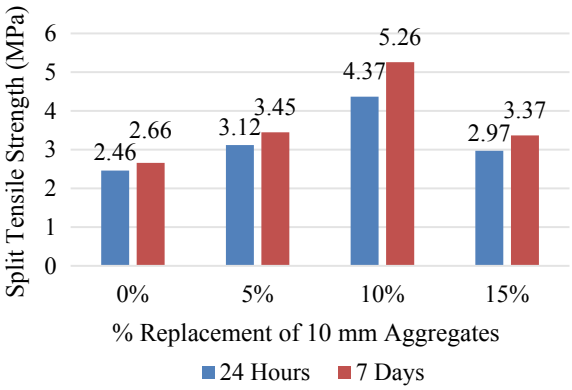

Fig. 4 Split tensile strength results at 24 h and 7 Days

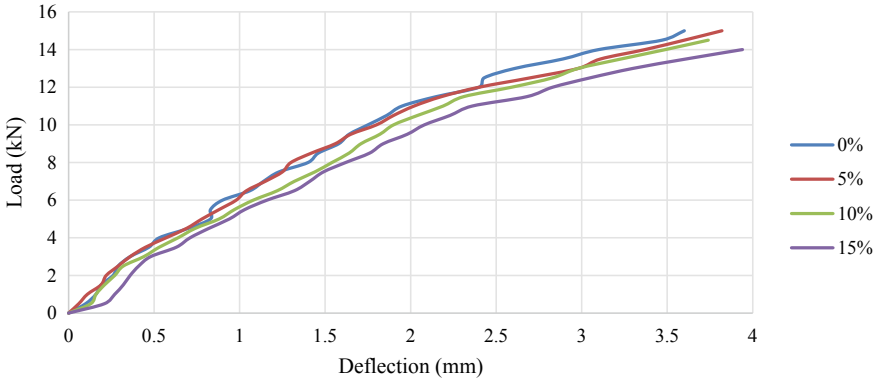

Fig. 5 Flexural strength results at 7 Days

aggregate 10% replacement by weight resulted the highest split tensile strength as shown in Fig. 4.

- The load versus deflection graphs has been shown in figure to find the flexural strength of the control and recycled plastic waste aggregate concrete. The flexural strength or the load carrying capacity of all beams is almost same (Fig. 5).

5 Conclusions

According to experimental study following conclusions could be drawn.

- The incorporation of recycled plastic waste aggregate in geopolymer concrete as replacement as coarse aggregate by 10% improved mechanical strength of the Concrete.

- In flexural test the plastic aggregate increases the fracture properties of the concrete and prevent sudden failure.
- The experimental study showed the potential of the utilization of RPWA in geopolymer concrete.

References

1. Davidovits J (1989) Geopolymers and geopolymeric materials. J Therm Anal 35:429–441
2. Hardjito D, Rangan BV (2005) Fly ash-based geopolymer concrete development and properties of low-calcium fly ash based geopolymer concrete. Research Report GC 1
3. Hardjito D, Rangan BV, Wallah SE (2010) Geopolymer concrete: turn waste into environmentally friendly concrete. In: International Conference on Recent Trends in Concrete Technology and Structures (INCONTEST), pp. 10-11, Sep 2010
4. Dave SV, Bhogayta AC, Arora NK (2015) Utilization of plastic waste in Geopolymer concrete: State of the art review. Int J Adv Eng Res Develop 2(12), Dec 2015
5. Prajapati HR, Bhogayta A, Arora NK (2013) Few aspects of durability of Geopolymer concrete containing metallized plastic waste. Int J Adv Eng Res Studies, E-ISSN2249-8974, July-Sept 2013
6. Bhogayata A, Shah KD, Arora NK (2013) Strength properties of concrete containing postconsumer metalized plastic wastes. International Journal of Engineering Research & Technology (IJERT) 2(3), March 2013

Utilization of Steel Slag for Wastewater Treatment: A Review

Chaitali Solanki

Abstract Steel dross will accumulate year after year owing to the steel industry's rapid expansion, occupying an excessive amount of farmland and presenting environmental and safety risks. India's current comprehensive steel slag usage rate is appallingly low, lagging well behind developed countries. Steel slag has got a lot of coverage lately as a result of its new applications. Since slag is used in so many different ways, its properties have a significant effect on how it is used. For addressing these concerns and maintaining the steel industry's long-term survival, rising the high usage rate of steel slag is important. Steel dross has a porous texture and a large surface area, as well as a high density that allows it to absorb water. Slag is manufactured in a variety of furnaces of differing operating conditions. Recent advances in well-known steel slag applications are examined in this article. This paper presented a consistent analysis of steel slag resource usage as waste water absorbent materials, as well as the important improved technique and challenging issues for steel slag as absorbent materials. In water and drainage, it is effective in the treatment of supplements, heavy metals, and polluted stream/stormwater.

Keywords Steel slag · Wastewater treatment · Environmental risk.

1 Introduction

The blast furnace slag is a solid waste formed from the iron industries, and hence, the major challenge facing such industries is the disposal of huge quantities of ferrous slag [1]. Steel slag weighs 125–140 kg for every tons of steel made. Steel slag stored in storage yards totaled more than 1.8 billion tons between the early 90 s and the end of 2018. The most popular way to dispose of steel slag is to deposit it in a landfill, but this takes up a lot of farmland. Furthermore, unplanned and irrational landfill practices pose significant environmental risks. In India, the consumption rate of steel slag is currently about 30%.

C. Solanki (✉)
Bhagwan Mahavir College of Engineering and Technology, Surat, Gujarat, India

B. Kondraivendhan et al. (eds.), *Sustainable Building Materials and Construction*,
Lecture Notes in Civil Engineering 222,
https://doi.org/10.1007/978-981-16-8496-8_50

Nowadays, the blast furnace slag is not considered as a waste material, whereas it could be viewed as a by-product which finds its potential reuse as a source of fine aggregate in place of natural river sand [2, 3]. Since over-exploitation of river sand ultimately results in the ecological imbalance of the environment, slag can be utilized in place of sand for various environmental engineering applications. Now, the blast furnace slag has located capability which makes use of like treatment of acid mine drainage, stabilization of sewage sludge and natural soil, polluted resources of water and wastewater which include nutrients and heavy metals, and consequently is not considered a waste [4, 5].The steel slag mainly consists of CaO, SiO_2, P_2O_5, FeO, Fe_2O_3, MgO, MnO, and Al_2O_3.

2 USE of Steel Slag for Water and Wastewater Treatment

There are various types of adsorbents for phosphate, nitrate, and heavy metals. Mercado-

Borrayo et al. [6] describe the practice of using iron slag as sorbents or reagents for the co-precipitation of contaminants. The by-products of industries can be used as adsorbents for removing nutrients and heavy metals from water and wastewater [7, 8].

Gao et al. [9] investigated the adsorptive ability of treated water quenched blast furnace slag in three different forms for eliminating methyl orange from aqueous solutions.

In current years, increasingly researchers be aware of the software of metallic slag in wastewater remedy. Metallic slag is a promising absorption fabric. But, the absorption overall performance of steel slag is suffering from many factors, collectively with lattice aperture duration, channel dredging, cation function and ratio of Si and Al, and so on., the absorption performance remains low, so it needs to be changed. Composite exchange refers to at the least one or more substances combined with metallic slag and then thru inorganic trade or excessive temperature amendment technique. At present, changed metal slag is especially used to adsorb heavy steel ions and natural pollution in wastewater.

The absorption effect of steel slag with particular pretreatment and exchange techniques on Pb2+ is different. Take a look at accomplished on electroslag, which had a better capability to remove Pb2+ , and its absorption capability grows to be higher than 20 mg/g. Used steel slag modified by H_2SO_4 to adsorb Pb2+ in waste water, and the removal rate was increased from 60% of the original steel slag to 96.94%. It has end up speculated that the absorption mechanism of modified steel slag on lead changed into specially primarily based mostly on chemical precipitation and ion alternate. Ma Yan et al. determined that the elimination charge of Cr6+ adsorbed through metallic slag has grown to be as excessive as 99.9%. With the decrease of slag particle size, the increase of the reaction time and slag dosage, the removal rate of Cr6+ of steel slag increased significantly. The removal of Cr6+ via the use of steel slag particularly is predicated upon the reducing rate of metal slag.

Jiang et al. dealt with Cr6+ in leachate with excessive temperature modified metal slag and determined that the changed metal slag adsorbed nicely most effective for below acidic conditions [10].

The high pH could be attributed to the presence of lime, iron, and calcium silicates [11]. The role of ferrous slag in water and wastewater treatment is manifold. It has a significant role in pollutant removal [12]. Because of its high alkaline pH, iron slag can be used to neutralise acidic wastes and mine drainage, as well as for agricultural purposes such as soil remineralization and conditioning, as a liming agent, fertiliser, etc. [13]. Several studies have demonstrated that it could be used as media for removing nutrients [14, 15, 16]. Many studies described phosphorus sorption capacity of slag from wastewater. The earlier research was mainly done for removing phosphate from synthetic wastewater. Phosphorous recycling was also possible by growing barley seeds in mixed media consisting of blast furnace slag, limestone, polonite, opaka, and sand and reed beds planted with Phragmites australis in composite media using gravel, blast furnace slag, and sand [17]. Thus, it is obvious that phosphate removal from wastewater could be achieved using either blast furnace slag alone or in combination with other materials such as hydrated lime as pointed out by Gong et al. [18]. Nilsson et al. [19] compared the removal of phosphorous and bacteria using polonite and blast furnace slag separately. There are several treatment technologies for removing heavy metals from industrial wastewater, including cation exchange materials [20, 21]. The blast furnace slag could be used for eliminating heavy metals such as copper, zinc, nickel, and a combination of these metals along with cadmium and chromium from wastewater. The study conducted by Nehrenheim and Gustaffon [22] showed its efficiency as a sorbent for nickel, zinc, lead, and chromium at higher concentrations which is in contrast to the previous study. Apart from the pure form, an activated slag has been made and used as a filter media for removing lead and chromium [23]. Wetlands are well known for their effective wastewater treatments. High BOD and suspended solids could be removed using a bed containing sand, gravel, organic matter, and minerals. The application of slag in constructed wetlands makes a low-cost and energy-efficient technology [24]. The factors influencing the operation of various treatments and in the design of filters using slag are particle size [19], pH (Johansson and Gustafsson 2000), [12, 23], porosity [17], hydraulic conductivity and calcium content [17] of the media, pH of wastewater [25, 19] agitation rate in the reactor, temperature [25, 23], and hydraulic retention time [19, 16, 23].

The untreated disposal of sewage, overuse of fertilizers, detergents, stormwater runoff, animal husbandry, etc., contribute surplus amounts of nutrients in water bodies. The accumulated nutrients may enhance the eutrophication phenomenon. The blast furnace slag prevents eutrophication by making phosphorus insoluble in water and absorbs a part of the insoluble phosphorus [26].

Fine amorphous and crystalline slag and coarse crystalline slag were found to be efficient or removing small amounts of phosphorous according to the study conducted using fine and coarse amorphous and crystalline slag and opoka (Johansson and Gustafsson 2000). It was reported that phosphorus might be removed by absorption or precipitation in the form of calcium phosphates. The experimental results for

phosphate removal from synthetic wastewater in a batch reactor showed more than 99% efficiency [25]. The minimum dosage of blast furnace slag was 60 g/L, for removing 180 ppm phosphate in 50 ml wastewater.

The removal of phosphorus is difficult in subsurface flow wetlands with sand, gravel, and improved site soil, and hence, there is a need for alternative media. The slag-based wetland system was found to be efficient for removing phosphate, phosphorus, total-P, total suspended solids, coliform bacteria, and COD from domestic wastewater and also for nitrate nitrogen production or nitrification [24]. Besides phosphorous, removal of other parameters such as total organic carbon and bacteria, Enterococci were possible using blast furnace slag. Column experiments are performed for high and low BOD_7 values, 120 mg/L and 20 mg/L (mean) for an average hydraulic residence time of 535 h showed 22% and 18% phosphorous removal, 21% and 19% TOC removal, and 81% and 16% bacteria removal, respectively.

In a study on effluent from a waste stabilization pond using a filter column filled with slag, phosphorus removal was declined logarithmically with hydraulic retention time [16]. Zuo et al. [27] noticed a decrease in phosphorus removal efficiency from 100 to 6.6% due to the inhibition of Ca-P precipitation caused by the presence of dissolved organic carbon. Gong et al. [18] conducted batch experiments for phosphorous absorption, but it was very less for the combination of blast furnace slag-hydrated lime than hydrated lime alone. The suitability of granulated blast furnace slag, cement kiln dust, zeolite, coconut shell, and silica sand for phosphorus sorption was studied by Agrawal et al. [28]. The performance evaluation of a roughing filter consisting of blast furnace slag yielded 63%, 55%, 69%, 72%, and 71% removal for chlorophyll 'a' content, green algae, blue-green algae, diatoms, and total algal count, respectively [29]. It was further supported by Nilsson et al. [19]. Turbidity and iron removal using the roughing filter were 37% and 57%, respectively. Abdolahnejad et al. [30] studied the water softening behavior of low sand filter the use of Iranian natural zeolite and blast furnace slag and confirmed higher results.

3 Conclusions

The applications of slag as a construction material or filter media are manifold in water and wastewater treatment plant construction. The essential characteristics find its use as a filter media, and thus, it is an excellent alternative source for replacing sand.

- Even though the laboratory-scale and field trials show positive results, its implementation on a largescale needs to be studied.
- The absorption and chemical precipitation may sometimes encounter physical clogging.
- The recovery or regeneration technologies are found to be effective only for a small duration.

- Innovative researches are being done in constructed wetlands using slag as media, but its longevity is to be determined.
- Since the slag is disposed of in large quantities around the premises of ferrous industries, its effective utilization in pollution remediation technology should be strongly appreciated.
- The literature strongly recommends the need for developing an appropriate technology for reusing ferrous slag in water/wastewater treatment which would be effectively, efficiently, and environmentally managed for a long duration.

References

1. Lim JW, Chew LH, Choong TS, Tezara C, Yazdi MH (2016) Overview of steel slag application and utilization. In: MATEC web of conferences, EDP sciences, vol 74, pp 00026
2. Asish DK, Singh B, Verma SK (2016) The effect of attack of chloride & sulphate on ground granulated blast furnace slag concrete. Adv Concrete Construct 4(2):107–121
3. Patra RK, Mukharjee BB (2018) Influence of granulated blast furnace slag as fine aggregate on properties of cement mortar. Adv Concrete Construct 6(6):611–629
4. Anjali MS, Sunil BM (2019) Potential valorisation of ferrous slag in the treatment of water and wastewater: A review. Adv Environ Res 8(1):55–69
5. Kaya Z (2016) Effect of slag on stabilization of sewage sludge and organic soil. Geomech Eng 10(5):689–707. https://doi.org/10.12989/gae.2016.10.5.689
6. Mercado-Borrayo BM, González-Chávez JL, Ramírez-Zamora RM, Schouwenaars R (2018) Valorization of metallurgical slag for the treatment of water pollution: an emerging technology for resource conservation and re-utilization. J Sustain Metall 4(1):50–67
7. Singh NB, Nagpal G, Agrawal S (2018) Water purification by using adsorbents: A review. Environ Technol Innov 11:187–240
8. Yasipourtehrani S, Strezov V, Evans T (2019) Investigation of phosphate removal capability of blast furnace slag in wastewater treatment. Sci Rep 9:7498
9. Gao H, Song Z, Zhang W, Yang X, Wang X, Wang D (2017) Synthesis of highly effective absorbnets with waste quenching blast furnace slag to remove Methyl Orange from aqueous solution. J Environ Sci China 53:68–77
10. Jiang YH, Liu MM, Qiu MD (2012) Safety and environmental engineering, vol 19
11. Bowden LI, Johnson KL, Jarvis AP, Robinson H, Ghazireh N, Younger PL (2006) The use of basic oxygen steel furnace slag (BOS) as a high surface area media for the removal of iron from circum neutral mine waters. In: Proceedings of the 7th international conference on acid rock drainage (ICARD). St. Louis, Missouri, U.S.A., Mar 2006
12. Ge Y, Wang X, Zheng Y, Dzakpasu M, Zhao Y, Xiong J (2015) Functions of slags and gravels as substrates in large-scale demonstration constructed wetland systems for polluted river water treatment. Environ Sci Pollut Res 22(17):12982–12991
13. Proctor DM, Fehling KA, Shay EC, Wittenborn JL, Green JJ, Avent C, Bigham RD, Connolly M, Lee B, Shepker TO, Zak MA (2000) Physical and chemical characteristics of blast furnace, basic oxygen furnace, and electric arc furnace steel industry slags. Environ Sci Technol 34(8):1576–1582. https://doi.org/10.1021/es9906002
14. Ballantine DJ, Tanner CC (2010) Substrate and filter materials to enhance phosphorus removal in constructed wetlands treating diffuse farm runoff: a review. New Zealand J Agricult Res 53(1):71–95
15. Johansson WL (2010) The use of blast furnace slag for removal of phosphorus from wastewater in Sweden—a review. Water 2(4):826–837

16. Shilton A, Chen L, Elemetri I, Pratt C, Pratt S (2013) Active slag filters: rapid assessment of phosphorus removal efficiency from effluent as a function of retention time. Environ Technol 34(2):195–200
17. Korkusuz EA, Beklioğlu M, Demirer GN (2007) Use of blast furnace granulated slag as a substrate in vertical flow reed beds: field application. Bioresour Technol 98(11):2089–2101
18. Gong G, Ye S, Tian Y, Wang Q, Ni J, Chen Y (2009) Preparation of a new sorbent with hydrated lime and blast furnace slag for phosphorus removal from aqueous solution. J Hazard Mater 166(2):714–719
19. Nilsson C, Renman G, Westholm LJ, Renman A, Drizo A (2013) Effect of organic load on phosphorus and bacteria removal from wastewater using alkaline filter materials. Water Res 47(16):6289–6297
20. Carolin CF, Kumar PS, Saravanan A, Joshiba GJ, Naushad M (2017) Efficient techniques for the removal of toxic heavy metals from aquatic environment: a review. J Environ Chem Eng 5(3):2782–2799
21. Naushad M, AL-Othman ZA (2015) Separation of toxic Pb2+ metal from aqueous solution using strongly acidic cation-exchange resin: analytical applications for the removal of metal ions from pharmaceutical formulation. Desalin Water Treat 53:2158–2166
22. Nehrenheim E, Gustafsson JP (2008) Kinetic sorption modelling of Cu, Ni, Zn, Pb and Cr ions to pine bark and blast furnace slag by using batch experiments. Bioresour Technol 99(6):1571–1577. https://doi.org/10.1016/j.biortech.2007.04.017
23. Srivastava SK, Gupta VK, Mohan D (1997) Removal of lead and chromium by activated slag—a blast-furnace waste. J Environ Eng 123(5):461–468
24. Korkusuz EA, Beklioğlu M, Demirer GN (2004) Treatment efficiencies of the vertical flow pilotscale constructed wetlands for domestic wastewater treatment. Turk J Eng Environ Sci 28(5):333-344
25. Oguz E (2004) Removal of phosphate from aqueous solution with blast furnace slag. J Hazard Mater 114(1):131–137. https://doi.org/10.1016/j.jhazmat.2004.07.010
26. Horii K, Tsutsumi N, Kitano Y, Kato T (2013) Processing and reusing technologies for steelmaking slag. Nippon Steel Technical Report 104:123–129
27. Zuo M, Renman G, Gustafsson JP, Klysubun W (2018) Dual slag filters for enhanced phosphorus removal from domestic wastewater: Performance and mechanisms. Environ Sci Pollut Res 25:7391–7400
28. Agrawal SG, King KW, Fischer EN, Woner DN (2011a) PO43- removal by and permeability of industrial by products and minerals: Granulated blast furnace slag, cement Kiln dust, coconut shell activated carbon,silica sand, and Zeolite. Water Air Soil Pollut 219(1–4):91–101. https://doi.org/10.1007/s11270-010-0686-4
29. El-Taweel GE, Ali GH (2000) Evaluation of roughing and slow sand filters for water Treatment. Water Air Soil Pollut 120(1):21–28. https://doi.org/10.1023/A:1005252900175
30. Abdolahnejad A, Ebrahimi A, Jafari N (2014) Application of Iranian natural zeolite and blast furnace slag as slow sand filters media for water softening. Int J Environ Health Eng 3(2):58–63

Evaluation of Adhesion Factor Between Clay and Steel Slag

V. M. Vasiya and C. H. Solanki

Abstract The main characteristics of the clayey soil are poor shear strength, swelling potential, and excess settlement. Such soil always poses challenges for the development of infrastructure. The study of enhancing the strength of weak soil is an ongoing process. One of them is the utilization of industrial waste, which reduces waste management and is cost-effective. This paper presents experimental work on three different clayey soil, stabilized with a steel slag column. The height of steel slag columns was kept constant (150 mm), and the diameter of steel slag columns was adjusted so that the L/D ratio of 10, 6, 5, 4, 3 can be obtained. Clayey soil was stabilized with steel slag column as non-displacement in floating condition. Loading was applied through a 10 mm thick circular plate with a diameter equals to the diameter of a steel slag column. Load versus settlement curves were obtained for each soil with all L/D ratios. Experimental results were verified through a conventional mathematical equation. Adhesion factor between clay and steel slag was determined for each L/D ratio. An empirical correlation was established between the adhesion factor and the L/D ratio.

Keywords Adhesion factor · Clayey soil · L/D ratio · Steel slag

1 Introduction

Clay deposits can be found in many areas. They have high compressibility and low strength. Different improvement techniques are used in a wide range of situations. Lime, cement, bitumen, etc., are the conventional materials applied for the same. Natural sand has been also used in different ways for enhancing the load-carrying capacity of the clayey soil.

Akinwumi [1] modified lateritic soil with pulverized steel slag and found a reduction in plasticity index and improvement in uncured strength at optimal content of steel slag at 8%. A laboratory test on colluvial soil with hydrated lime and steel slag

V. M. Vasiya (✉) · C. H. Solanki
Civil Engineering Department, SardarVallabhbhai National Institute of Technology, Surat, Gujarat, India

B. Kondraivendhan et al. (eds.), *Sustainable Building Materials and Construction*,
Lecture Notes in Civil Engineering 222,
https://doi.org/10.1007/978-981-16-8496-8_51

was performed by Indraratna [2]. The blend shows a friction angle of 42 °, which natural colluvial soil gives 25 °. Koteswara, et al. [3] reinforced the marine clay with steel slag. Laboratory test showed 13% steel content reduced the plasticity index by 5.4%, improvement in plate load test by 270% comparing untreated marine clay. Lim et al. [4] reviewed the application of steel slag in various engineering fields and found its suitability instead of disposal off. Steel slag and lime mixed with sandy soil at various proportions by Mohammed and Elsageer [5]. Experimental results show at 25% steel slag and 15% lime maximum dry unit weight obtained through compaction. Onda et al. [7] examined steel slag for the replacement in a sand pile. Equivalent improvement was found comparing the sand pile. Poh et al. [8] stabilized English China clay with electric arc furnace slag and basic oxygen steel slag fines (BOS) and found that 15–20% of BOS fines improves the mineral evolution. The treated soil was used in the embankment construction as a test result shows improvement in cementation of the steel slag. Zumrawi and Babikir [9] stabilized expansive soil with steel slag. Experimental results show a 33% reduction in liquid limit and55% reduction in the free swell index at 30% steel slag. 10% steel gives a 10% improvement in MDD with a considerable reduction in OMC and 1.5 times improvement in UCS value.

This paper describes a model plate load test with different L/D ratios to stabilize clay with a steel slag column.

2 Methodology

2.1 Materials

2.1.1 Steel Slag

Essar steel plant at village Hazira, District Surat, Gujarat, India, is producing high-quality steel. Steel slag is collected from the Essar plant. Basic tests were performed on the oven-dried steel slag. The unit weight and specific gravity found 19.8 kN/m^3 and 2.87, respectively. Impact and abrasion values were found at 11.85% and 12.05%.

2.1.2 Clay Soil

Clayey soil was collected from village Bhatpore near the bank of river Tapi, District Surat, Gujarat, India. The soil was collected at depth of 4–5 m from the existing ground level with three different distances from the river Tapi, at 500 m, 0.9 km, and 1.4 km. Collected soil sealed in the polythene bag to maintain the moisture content and transfer to the laboratory. All preliminary tests were performed to confirming to Indian standard. Laboratory results are listed in Table 1.

Table 1 Properties of the three different soil

No	Description	Soil A	Soil B	Soil C
1	Field moisture content	49%	42%	37%
2	Specific gravity	2.53	2.56	2.58
3	Plasticity index	56	50	38
4	MDD (kN/m^3)	14.45	15.58	16.12
5	OMC	25%	24%	22%
6	Unit weight (kN/m^3)	14	15.2	16.7
7	Classification (ISC)	CH	CH	CH
8	Cohesion (kg/cm^2)	0.15	0.216	0.327
9	Clay content	70%	66%	65%

2.1.3 Hollow Steel Pipe

Hollow steel pipe of thickness less than 1 mm, with outer diameter 15, 25, 30, 37.5, and 50 mm, were taken. The height of all the pipes was kept at 150 mm to maintain different L/D ratios of 10, 6, 5, 4, and 3.

2.2 Model Test

Model tests were performed in a steel tank cylindrical in shape with 300 mm diameter and 600 mm height. The soil (clay) was placed in the 5 cm thickness layer at field moisture content to established ground condition. To make room for the steel slag, a hollow steel pipe was lowered into the clay. Clay was removed with great care. Steel slag was poured in five equal lifts, each with a thickness of 30 mm. Weight of the steel slag was determined for each lift concerning the diameter of the steel slag column. For air expulsion, normal compaction was used at each lift. As the height of the steel slag column of 150 mm is placed, the steel pipe was withdrawn from the clay bed. The steel slag column was covered with a 10 mm thick MS plate. The diameter of the MS plate was kept the same as the steel slag column's diameter. At a rate of 1 mm per minute, the load was applied to the steel slag column through the MS plate. An LVDT was attached to the plate to record the settlement. Load versus settlement curves were obtained for all three soil and each L/D ratio.

3 Result and Discussion

The load-carrying capacity of the steel slag column found increases as the L/D ratio decreases. The steel slag shows the replacement of natural aggregates [7]. Figures 1,

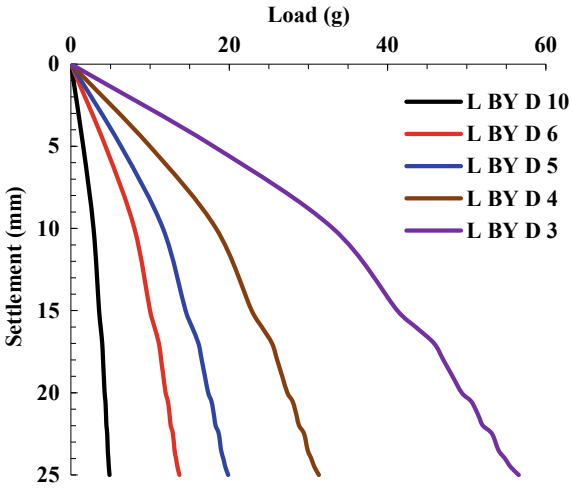

Fig. 1 Load versus settlement curve for soil A

2 and 3 revealed load versus settlement characteristics of clay treated with steel slag column. All these figures also demonstrate that as the cohesion value increases steel slag column is more responsive. Each L/D ratio of steel slag column resists higher load with a higher shear strength of the clay. A similar pattern was obtained by Naseer et al. [6].

A traditional equation was applied to evaluate the adhesion factor between clay and steel slag.

$$P = C \times N_c \times A_c + \alpha \times C \times A_s \tag{1}$$

where,

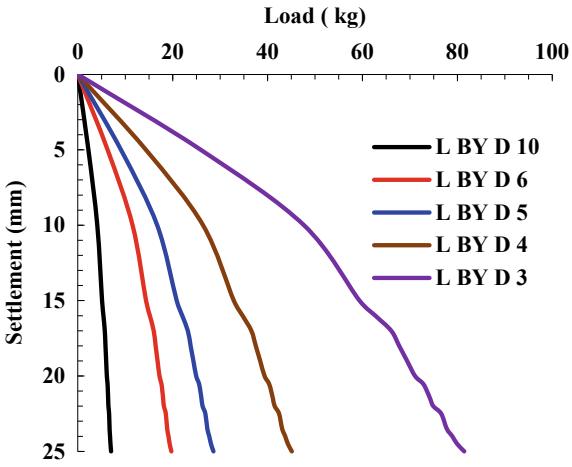

Fig. 2 Load versus settlement curve for soil B

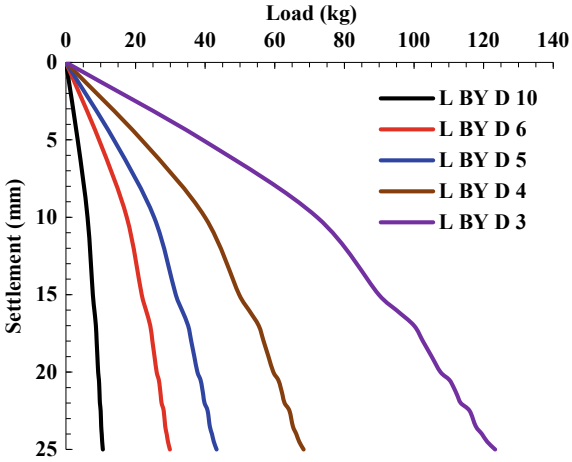

Fig. 3 Load versus settlement curve for soil C

P = Load taken by steel slag column.
C = Cohesion of clay.
N_c = Bearing capacity factor.
A_c = Area of steel slag column.
α = adhesion factor.
A_s = Surface area of steel slag column.

Applying Eq. (1) for L/D ratio 10, for soil A soil B, and soil C, we will get Eqs. 2, 3, and 4 as below.

$$4.87 = 0.15 \times N_c \times 1.77 + \alpha \times 0.15 \times 26.52 \tag{2}$$

$$7.01 = 0.216 \times N_c \times 1.77 + \alpha \times 0.216 \times 26.52 \tag{3}$$

$$10.61 = 0.327 \times N_c \times 1.77 + \alpha \times 0.327 \times 26.52 \tag{4}$$

Solving Eqs. (2) and (3), we may get $N_c = 9$ and $\alpha = 0.624$. Equation (4) will also satisfy these values. Following the same mathematical procedure, the bearing capacity factor and adhesion factor were evaluated for each L/D ratio, as 3 equations available for 2 unknowns. The model test results and evaluated factors are listed in Table 2.

Equation (5) can be developed for the evaluation of the adhesion factor between steel slag and clay for any L/D ratio using all of the above model test results and regression analysis.

$$\alpha = 0.6\left[1 + \frac{0.4}{\frac{l}{d}\text{ratio}}\right] \tag{5}$$

Table 2 Summary of model test results

L/D Ratio	P in kg (Load taken by steel slag column)			Bearing capacity factor (N_c)	Adhesion factor (α)
	Soil A	Soil B	Soil A		
10	4.87	7.01	10.61	9	0.624
6	13.70	19.73	29.87	9	0.64
5	19.86	28.59	43.29	9	0.648
4	31.32	45.11	68.29	9	0.66
3	56.57	81.46	123.33	9	0.68

4 Conclusion

A total of 15 model tests were conducted on clayey soil stabilized with a steel slag column in floating conditions. Response of clayey soil with steel slag column with different L/D ratios was studied. The adhesion factor between clay and steel slag is evaluated through a conventional equation. The results of the experimental studies can be used to reach the following conclusions:

- Steel slag possesses natural aggregate characteristics.
- The steel slag can be used for the replacement of the natural aggregate.
- Adhesion factor increases as the L/D ratio decreases.
- The adhesion factor between clay and steel slag follows an empirical mathematical equation.

References

1. Akinwumi I (2014) Soil modification by the application of steel slag. Periodica Polytechnica Civil Engineering 58(4):371–377. https://doi.org/10.3311/PPci.7239
2. Indraratna B (1996) Utilization of lime, slag and fly ash for improvement of a colluvial soil in New South Wales, Australia. Geotech Geol Eng 14(3):169–191. https://doi.org/10.1007/BF00452946
3. Koteswara R, Sravani G, Naga B (2014) A laboratory study on the affect of steel slag for improving the properties of marine clay for foundation beds. International Journal of Scientific & Engineering Research 5(7):253–259
4. Lim JW, Chew LH, Thomas SY, Tezara C, Yazadi MH (2016) Overview of steel slag application and utilization. MATEC Web of Conferences 74(26):3–7. https://doi.org/10.1051/matecconf/20167400026
5. Mohammed AA, Elsageer MAA (2018) The effect of adding steel slag and lime on the engineering properties of a Sandy soil. AIJR publishers CEST 2:563–570. https://doi.org/10.21467/proceedings.4.23
6. Naseer S, Sarfraz M, Jamil S (2019) Laboratory and numerical based analysis of floating sand columns in clayey soil. International Journal of Geo-Engineering 10(1):1–16. https://doi.org/10.1186/s40703-019-0106-6

7. Onda K, Honda H, Yoshitake H (2014) Examination of application of steel slag to sand compaction pile method. JFE Technical Report 19(19):41–48
8. Poh HY, Ghataora GS, Ghazireh N (2006) Soil stabilization using basic oxygen steel slag fines. Journal of Materials in Civil Engineering 18(2):229–240. https://doi.org/10.1061/(asce)0899-1561(2006)18:2(229)
9. Zumrawi MME, Babikir A (2017) Laboratory study of steel slag used in stabilizing Expansive soil. Asian Engineering Review 4(1):1–6. https://doi.org/10.20448/journal.508.2017.41.1.6

Alkali-Activated Binders Using Industrial Wastes Applications in Geotechnical Engineering: Review

Hiral Modha and Shruti Shukla

Abstract There are abundant amount of industrial wastes produced every year globally. These waste materials are stock piled on the earth surface and create problems related to the pollution of air, water and land. Industrial wastes like low- and high-calcium fly ash, slag, red mud, calcium carbide residue, mine tailings, copper slag and construction and demolition wastes need to be utilized in a systematic way for various applications in civil engineering. The alkali-activated binder, popularly known as geopolymer, is one of such emerging methodologies in a development stage, which can effectively utilize these industrial wastes and convert it to a valuable final product which can be comparable with cement (binder) like properties. The present review focuses on the various design parameters, and recent research work has been done in the geotechnical engineering field using these alternative binders. The review covers the various factors affecting the design of alkali-activated binders, their development study in the geotechnical engineering applications and future scope of work in the said domain. This presented study helps the prospect researchers to explore this new potential binders and work on the unexplored area of applications in the field of geotechnical engineering.

Keywords RC Frame · Nonlinear static analysis · Seismo struct · Reinforced concrete

1 Introduction

Alkali-activated binders (geopolymers) are inorganic aluminosilicate materials formed by polycondensation of silica and alumina which have excellent physical and chemical properties. Geopolymer terminology was given by Davidovits [5], consists of alkaline activators and silica alumina-rich precursors which are available from a wide range of waste materials like fly ash and slag. It is developing

H. Modha (✉) · S. Shukla
Geotechnical Engineering, Nirma University, Ahmedabad, India
e-mail: hiral.modha@nirmauni.ac.in

B. Kondraivendhan et al. (eds.), *Sustainable Building Materials and Construction*,
Lecture Notes in Civil Engineering 222,
https://doi.org/10.1007/978-981-16-8496-8_52

class of cementitious material which increased response from construction material research community. There are several areas of applications of these binders which includes precast structures and non-structural elements, concrete pavements and products, containment and immobilization of toxic, hazardous and radioactive wastes, advanced structural tooling and refractory ceramics and fire-resistant composites used in buildings, aeroplanes, shipbuilding, racing cars and nuclear power industry. Provis [20] explained that alkali-activated binders are not one fits to all solution like OPC. The application of an alkali-activated binder in the geotechnical engineering field is not explored yet in detail. The major objective of using geopolymers is the environment concern regarding the emission of CO_2 during the production of cement which is approximately 7% at global level. Another important aspect of search for alternative binders is systematic utilization of industrial wastes. Therefore, many researchers have explored the geopolymer applications in geotechnical engineering and compared the results with the traditional binders. The main objective of the study is to review the applications of geopolymers in soil stabilization in terms of design parameters, mechanical strength behaviour, microstructure and future scope of study.

2 Design Mix of Alkali-Activated Binder for Soil Stabilization

The geopolymers performance is affected due to design various parameters such as the wide range of waste based of precursor and their proportion, alkaline medium and their concentration (molarity), modulus ratio SiO_2/Na_2O, alkaline solution to binder ratio, curing conditions and time period for curing (ambient curing, elevated temperature curing and relative humidity conditions).

2.1 Precursor and Mix Proportion

Sharma and Kumar [26] concludes that the 5–20% of proportion of alkali-activated binders/geopolymers are optimum range which can improve the geotechnical properties of soil. Various literature study reported the use of precursor based on industrial waste for developing alkali-activated binders such as volcanic ash, ggbs, fly ash, silica fume, rice husk ash [2, 13], red mud [8, 11], palm oil fuel ash [22], copper mine tailings, glass powder, marble powder, low calcium slag, metakaolin, red gypsum [2, 13], ground coal bottom ash [6], calcium carbide residue and mine tailings, Fe-rich clays [15], clay-rich sludges resulting from water treatment [10], agricultural waste ashes [3] and kaolin purification [14].

2.2 Modulus Ratio: SiO_2/Na_2O

The properties of the geopolymer system are subtle to ratio of SiO_2/Na_2O (Jiaren et al., 2020). The compressive strength of alkali-activated binders depends on the ratio of SiO_2/Na_2O and alkaline solution concentration (Bakharev et al., 1999). The highest strength of fly ash-based geopolymer activated by sodium silicate reported by Provis et al. [21] in the range of 1.0–1.5 of modulus ratio. The similar result reported by (Jiaren et al., 2020) which gave higher strength development for with ggbs-stabilized soil with at 28 days with ASM (anhydrous sodium metasilicate).

2.3 Alkaline Medium

Alkaline activator is in the form of solution, which activates the alumina and silica source material, and reaction ended with forming a gel. The various alkaline activators used in the previous study were reported as sodium silicate, potassium hydroxide, calcium oxide, sodium sulphate, anhydrous metasilicate, calcium hydroxide, sodium carbonate and manganese oxide. The range of alkalinity for alkaline activator was reported by researchers between 8 and 14 M by Sharma and Kumar [26]. Sodium hydroxide with sodium silicate was chosen as alkali activator more commonly as it is cheaper than other alkali activators and it maintains higher capacity to detach the silicate and aluminate monomers. The higher concentration of NaOH requires careful handling because of its classified as a dangerous material as well its storage, handling and management on the site is difficult due to its corrosive nature. Due to these limitations, the use of NaOH for large-scale applications are difficult. (Jiaren et al., 2020) reported the use of anhydrous sodium metasilicate (ASM) powder as solid alkaline activator of a one part geopolymer for soil stabilization study of soft soil for its strength development. The most effective activator providing the best performance for high strength and other advantageous properties is a mixture combining sodium hydroxide (NaOH) and sodium silicate (Na_2SiO_3) [25].

2.4 Water (Alkaline Solution) to Binder Ratio

The water content strongly affects the strength improvement of the stabilized soil, and it is desirable to use a binder to water ratio low. The water to binder ratio is an important parameter for alkali-activated materials and their strength development. Sharma and Kumar [26] reported to have 0.35–0.85 range as a ratio of water to binder for geopolymer use in case of soil stabilization.

3 Types of Soil Mixed with Alkali-Activated Binder for Stabilization

The literature reported the soil stabilization using geopolymer binders are majorly fine-grained types of soil. The various types of soil which are stabilized using the geopolymer technology are reported by Zhang et al. [31] lean clay, [12] Pb-contaminated clay soil, [9] low compressible clay soil (CL type), [32] sulphate-rich soil, [23] soft marine clay soil (CL and CH type), [24] lateritic soil, [13] loess, [7], silty sand type of soil (SM type), [4] high-plasticity clay (CH type soil), [1] Dune sand, [19] expansive soil (CH type soil).

4 Application of Geopolymer in Geotechnical Engineering

Many researchers reported about the use of geopolymers for the application of soil stabilization, protective coating, concrete and waste encapsulation. The application of geopolymers at shallow depth for pavements, subgrade and shallow foundation reported by [23, 24, 31]. Zhang et al. [31] reported about the feasibility of using geopolymer as a soil stabilizer. Yaghoubi et al. [30] reported the study for application of slag-based alkali-activated binder for stabilization using deep soil mixing and concluded that the minimum requirements of strength development were achieved. Wong et al. [27] summarize the work done with of geopolymers for soil stabilization and deep soil mixing. Mohammadinia et al. [18] utilized the fly ash and slag-based alkali-activated binder in loose sand for deep mixing soil projects. Modha and Rangwala [16] checked the feasibility of slag and fly ash geopolymer-based grout considering the compressive strength and setting time as a design parameter. Alkali-activated material mix was successfully applied to form a brick by Modha et al. [17].

5 Mechanical Performance of Geopolymer Stabilized Soil

Murmu et al. [19] reported that UCS increases significantly in case of expansive soil using fly ash-based geopolymer. The UCS increased and it fulfils the condition of IRC 37, 2012 stabilized subbase material must achieve 750 kPa strength at the end of 28 days curing. Liu et al. [13] studied about the compressive strength of loess which stabilized with fly ash-based geopolymer, and the result that UCS of potassium hydroxide is more compared to sodium hydroxide-activated sample. Pourakbar et al. [22] performed model study of alkaline-activated binder using palm oil fuel ash (POFA) as precursor and UCS was reported with NaOH- and KOH-based mixture as 900 kPa and 1200 kPa at 28 days of curing. The UCS strength depends on the molarity of alkaline activator, modulus ratio and alkaline solution to binder ratio.

Sharma and Kumar [26] reviewed the UCS strength of various types of geopolymer stabilized soil under the effect of various parameters ranges from 1 to 12 MPa.

6 Microstructure of Geopolymer Stabilized Soil

Sharma and Kumar [26] reviewed that using various microstructural characterization method such as SEM-EDX, XRD and FT-IR proves about the development of binding gel which creates the compact structure. The gel formed is responsible for the binding phase.

7 Future Scope of Study

The soil stabilization with geopolymer is still at development stage, so the more simple mixture technique (one part geopolymer or powder-based) need to be developed. The long-term strength of geopolymer stabilized soil should be checked. There are many parameters in design of geopolymer for soil stabilization need to be control. The formation of gel and its nature should be explored in detail. The cost analysis of geopolymer-stabilized soil should be explored. The dynamic properties of soil using geopolymer as stabilizer are not explored yet.

8 Conclusion

The main advantage of the geopolymer is compared with cementious binder, so it has potential to replace the cement as a binder for soil stabilization purpose. There are various materials including natural clay, aluminosilicate minerals and agro-industrial by-products that can be utilized through alkaline activation technique, so it has potential to be compared with OPC. With increase in the binder to soil ratio, the compressive strength of stabilized soils are improved considering the time and curing condition. Also, increasing the sodium silicate/sodium hydroxide ratio or higher alkali activator concentration, increases the mechanical strength of the alkali-activated soil-treated specimens, however, they reduce the workability. Alkali-activated material application for geotechnical engineering depends on various parameters like raw materials, alkaline solution, molarity of alkaline solution, curing condition and alkaline solution to binder ratio.

References

1. Arab M, Junaid MT, Omar M, Zeiada W, Shanableh A, Rammal R (2019) Using alkali-activated binders to improve UAE dune sand. In: Proceedings of the 4th world congress on civil, structural, and environmental engineering, pp 1–8. https://doi.org/10.11159/icgre19.179
2. Bahmani SH, Orense RP (2017) Review on recent developments in alkali-activated materials. pp 1–8
3. Bernal SA, Rodríguez ED, Kirchheim AP, Provis JL (2016) Management and valorisation of wastes through use in producing alkali-activated cement materials. J Chem Technol Biotechnol 91:2365–2388
4. Cristelo N, Glendinning S, Pinto AT (2011) Deep soft soil improvement by alkaline activation. Proc Inst Civ Eng Gr Improv 164:73–82. https://doi.org/10.1680/grim.900032
5. Davidovits J (1994) Properties of geopolymer cements. In: Presented at the first international conference on alkaline cements and concretes. Scientific Research Institute on Binders and Materials Kiev State Technical University pp 131–149
6. Donatello S, Maltseva O, Fernandez-Jimenez A, Palomo A (2014) The early age hydration reactions of a hybrid cement containing a very high content of coal bottom ash. J Am Ceram Soc 97:929–937
7. Dungca JR, Codilla EET (2018) Fly-ash-based geopolymer as stabilizer for silty sand embankment materials. Int J GEOMATE 14:143–149. https://doi.org/10.21660/2018.46.7181
8. Gong C, Yang N (2000) Effect of phosphate on the hydration of alkali-activated red mudslag cementitious material. Cem Concr Res 30:1013–1016
9. Ghadir P, Ranjbar N (2018) Clayey soil stabilization using geopolymer and Portland cement. Constr Build Mater 188:361–371. https://doi.org/10.1016/j.conbuildmat.2018.07.207
10. Guo XL, Shi HS, Dick W (2010) Use of heat-treated water treatment residuals in fly ash based geopolymers. J Am Ceram Soc 93:272–278
11. Kumar S, Kumar A (2013) Development of paving blocks from synergistic use of redmud and fly ash using geopolymerization. Constr Build Mater 38:865–871
12. Li YY, Zhang TT, Jia SB, Liu J, Quan XH, Zheng W (2019) Mechanical properties and leaching characteristics of geopolymer-solidified/stabilized lead-contaminated soil. Adv Civil Eng. https://doi.org/10.1155/2019/6015769
13. Liu Z, Cai CS, Liu F, Fan F (2016) Feasibility study of loess stabilization with fly ash-based geopolymer. J Mater Civ Eng 28(5):1–8
14. Longhi MA, Rodríguez ED, Bernal SA, Provis JL, Kirchheim AP (2016) Valorisation of a kaolin mining waste for the production of geopolymers. J Clean Prod 115:265–272
15. McIntosh SEM, Lawther J, Kwasny MN, Soutsos D, Cleland S, Nanukuttan S (2015) Selection and characterization of geological materials for use as geopolymer precursors. Adv Appl Ceram 114:378–385
16. Modha H, Rangwala H (2021) Feasibility of geopolymer grout for granular soil. In: Sitharam et al (eds) Ground improvement techniques, lecture notes in civil engineering. Springer, Singapore. https://doi.org/10.1007/978-981-15-9988-0 (in press)
17. Modha H, Sharma N, Singh S (2021) Alkali activated material brick. In: Sanjay Kumar Shukla et al (eds) Advances in geotechnics and structural engineering, 978-981-33-6968-9, 495951_1_En (13) Lecture Notes in Civil Engineering, vol 143. (in press)
18. Mohammadinia A, Disfani MM, Conomy, D, Arulrajah A, Horpibulsuk S, Darmawan S (2019) Utilization of alkali-activated fly ash for construction of deep mixed columns in loose sands. J Mater Civ Eng 31. https://doi.org/10.1061/(ASCE)MT.1943-5533.0002878
19. Murmu AL, Jain A, Patel A (2019) Mechanical properties of alkali activated fly ash geopolymer stabilized expansive clay. KSCE J Civ Eng 23(9):3875–3888. https://doi.org/10.1007/s12205-019-2251-z
20. Provis JL (2018) Alkali-activated materials. Cem Concr Res 114:40–48. https://doi.org/10.1016/j.cemconres.2017.02.009
21. Provis JL, Rees CA (2009) Geopolymer synthesis kinetics. https://doi.org/10.1533/9781845696382.1.118

22. Pourakbar S, Huat BBK, Asadi A, Fasihnikoutalab MH (2016) Model study of alkali-activated waste binder for soil stabilization. Int J Geosynthetics Ground Eng 2(4):1–12
23. Phetchuay C, Horpibulsuk S, Arulrajah A, Suksiripattanapong C, Udomchai A (2016) Strength development in soft marine clay stabilized by fly ash and calcium carbide residue based geopolymer. Appl Clay Sci 127–128:134–142. https://doi.org/10.1016/j.clay.2016.04.005
24. Phummiphan I, Horpibulsuk S, Phoo-ngernkham T, Arulrajah A, Shen SL (2016) Marginal lateritic soil stabilized with calcium carbide residue and fly ash geopolymers as a sustainable pavement base material. https://doi.org/10.1061/(ASCE)MT.1943-5533.0001708
25. Rashad AM (2013) A comprehensive overview about the influence of different additives on the properties of alkali-activated slag—a guide for civil engineer. Constr Build Mater 47:29–55
26. Sharma K, Kumar A (2020) Utilization of industrial waste based geopolymers as a soil stabilizer a review. Innov Infrastruct Solut 5. https://doi.org/10.1007/s41062-020-00350-7
27. Wong BYF, Wong KS, Phang IRK (2019) A review on geopolymerisation in soil stabilization. IOP Conf Ser Mater Sci Eng 495. https://doi.org/10.1088/1757-899X/495/1/012070
28. Yu J, Chen Y, Chen G, Wang L (2020) Experimental study of the feasibility of using anhydrous sodium metasilicate as a geopolymer activator for soil stabilization. Eng Geol 264:105316. https://doi.org/10.1016/j.enggeo.2019.105316
29. Yi Y, Li C, Liu S (2015) Alkali-activated ground-granulated blast furnace slag for stabilization of marine soft clay. J Mater Civ Eng 27:1–7. https://doi.org/10.1061/(ASCE)MT.1943-5533.0001100
30. Yaghoubi M, Arulrajah A, Miri M (2020) Compressibility and strength development of geopolymer stabilized columns cured under stress. Soils Found 60:1241–1250. https://doi.org/10.1016/j.sandf.2020.07.005
31. Zhang M, Guo H, El-Korchi T, Zhang G, Tao M (2013) Experimental feasibility study of geopolymer as the next-generation soil stabilizer. Constr Build Mater 47:1468–1478
32. Zhang M, Zhao M, Zhang G, Nowak P, Coen A, Tao M (2015) Calcium-free geopolymer as a stabilizer for sulfate-rich soils. Appl Clay Sci 108:199–207. https://doi.org/10.1016/j.clay.2015.02.029

Use of Sugarcane Bagasse Ash and Ground-Granulated Blast-Furnace Slag in Cementitious System for Sustainable Development

Satish Palaskar and Gaurang Vesmawala

Abstract This research paper presents the performance of binary and ternary concrete prepared using sugarcane bagasse ash (SCBA) and ground-granulated blast-furnace slag (GGBFS), which are agriculture and industrial waste, respectively. Two parameters were taken into account (a) binary concrete containing SCBA replacement percentage (i.e., 0, 15, 20, 25, and 30%) (b) ternary concrete containing SCBA and GGBFS replacement percentage (i.e., 0, 15, 20, 25, and 30%). Standard cube, cylinder, and beam specimens were made. The mechanical properties (compressive strength, flexure strength, and split tensile strength) and microstructural properties were then determined and discussed. Test result reveals that compressive strength increases in binary concrete up to 15% replacement, whereas in ternary concrete, up to 25% replacement (SCBA 20% and GGBFS 05%). Flexure strength increases for 15% replacement in binary concrete, whereas for ternary concrete, decreases for all mixes. Split tensile strength decreases for all mixes.

Keywords Sugarcane bagasse ash · GGBFS · Sustainable development

1 Introduction

Cement is a fundamental building material that is widely used in urban housing and infrastructure construction. The cement industry is one of the top sources among manufacturing industries responsible for carbon dioxide emission, which are considered the main culprit in climate change. The utilization of cement replacement material possessing pozzolanic ability is found to be one of the steps toward the concern for sustainable development. For the generation of steam in sugar factories, sugarcane bagasse is used, which yields 3–5% ash. This is the unwanted product that is deposited in open land, causing contamination [1].GGBFS, which is a result of iron-producing blast furnaces. The average production of one ton of steel outcome is a byproduct of 200–400 kg, including slag, dust, sludges, and other material [2].

S. Palaskar (✉) · G. Vesmawala
SVNIT, Surat, India

B. Kondraivendhan et al. (eds.), *Sustainable Building Materials and Construction*,
Lecture Notes in Civil Engineering 222,
https://doi.org/10.1007/978-981-16-8496-8_53

Production of more amount of waste highlights a scope to the researcher for waste management.

Amin et al. [3] used activated SCBA at 900 °C and found that SCBA activated at that temperature becomes highly amorphous [3]. Arif et al. [4] used SCBA as a filler in concrete and noted a substantial improvement in compressive strength and acid resistance measured by both mass loss and compressive strength test [4]. Moraes et al. [5] used blast furnace slag and sugarcane straw ash along with alkaline solution composed of sodium hydroxide and sodium silicate. Result shows that alkaline solution affect the compressive strength development [5]. Cordeiro et al. [6] investigated the pozzolanic activity of SCBA by grinding and noted the quartz content decreased significantly which increases amorphous content and subsequently, the pozzolanic activity also observed good relation between amorphous content and SCBA reactivity [6]. A Bahurudeen et al. [7] used SCBA as supplementary cementitious material and found enhanced performance in terms of low heat of hydration, additional strength gain, and substantial decrease in permeability [7]. Rerkpiboon et al. [8] examined the strength and durability properties of concrete, incorporating 50% SCBA and found that 90% strength, as compared with control concrete, increases in chloride resistance [8]. Fernando et al. [9] used SCBA sand in concrete and reported maintained mechanical properties along with micropore clogging, whereas improvement in the durability [9]. Rattanashotinunt et al. [10] introduced SCBA and calcium carbide residue as new cementitious material and found use of these SCM's to reduce OPC consumption by 70% [10]. Khodair and Bommareddy [11] investigated the outcome of fly ash, slag, and recycled concrete aggregate. It shows an adverse impact on compressive strength at 28 days, whereas improvement in resistance to chloride permeability [11]. Cheng et al. [12] noted lesser strength in compression, higher drying shrinkage, and carbonation depth when fly ash, GGBFS, and metakaolin are used [12].

The use of SCBA and GGBFS was reported by many researchers in the production of binary concrete; however, no one published work related to ternary concrete made by using OPC, SCBA, and GGBFS. In this investigation, binary and ternary concrete is prepared using SCBA and GGBFS to study mechanical and microstructural properties. The aim is to use agriculture and industrial waste to develop a sustainable cementitious system.

2 Methodology

The Ordinary Portland cement of 53 grade confirming to IS12269-1987 [13] was used in this work. SCBA was obtained from Prasad Sugar and Allied Agro Products Ltd. Ahmednagar, Maharashtra. The SCBA obtained is heated in a muffle furnace at 700 ºC for 2 h and then allowed to cool at room temperature. Before using, it was ground to make it fine. GGBFS is obtained from Guru Corporation, Ahmedabad, Gujarat. The chemical properties of SCBA and GGBFS are shown in Table 1. Natural sand having a maximum size of 4.75 mm was used as fine aggregate, whereas coarse

Table 1 Chemical properties of SCBA and GGBFS

Material	Property					
	SiO_2	Al_2O_3	Fe_2O_3	CaO	MgO	SO_3
SCBA	82.53	12.62	0.60	2.34	1.04	0.001
GGBFS	34.12	18.95	0.23	35.46	8.2	0.45

Table 2 Mix proportion

Material (%)	Mix id							
	P	B15	B20	B25	B30	B10G05	B10G10	B10G15
Cement	100	85	80	75	70	85	80	75
SCBA	0	15	20	25	30	10	10	10
GGBFS	0	0	0	0	0	05	10	15
Material (%)	Mix id							
	B10G20	B15G05	B15G10	B15G15	B20G05	B20G10	B25G05	
Cement	70	80	75	70	75	70	70	
SCBA	10	15	15	15	20	20	25	
GGBFS	20	05	10	15	05	10	05	

aggregate of maximum size 20 and 12.5 mm in the proportion of 60:40 was used in the concrete mix. For the M25 grade of concrete, a mix design was done concerning IS10262-2009 [14].

The replacement percentage used for the experiments is given in Table 2. Experiments were done to check the performance of binary and ternary concrete by using compressive, flexure, and split tensile strength at 28 days. Scanning electron microscopy (SEM) was undertaken for microstructural exploration of selected concrete specimens which was carried out using Field Emission-Scanning Electron Microscope (FE-SEM) laboratory of college of Engineering, Pune.

3 Results and Discussion

OPC strength at curing age 7 and 28 days was determined as 22.16 and 33.18 N/mm^2, respectively (Fig. 1). Compressive strength was discovered to drop with rise in SCBA amount for binary concrete of a particular curing period. Compressive strength was found to rise for 15% SCBA from 20.38 to34.00 N/mm^2. Improvement in strength results with SCBA can be initiated by the filler effect and the pozzolanic reaction among calcium hydroxide from cement hydration and reactive SiO_2 from SCBA. A reduction in strength in compression may be caused by the dilution effect. Previous studies observed similar behavior [15]. OPC concrete performs well compared to

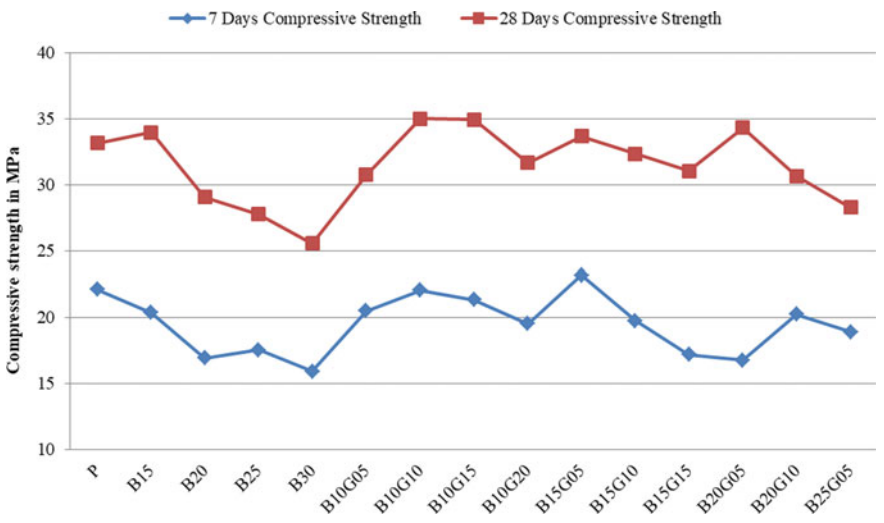

Fig. 1 Compressive strength for various binary and ternary mixes of SCBA and GGBFS

SCBA concrete for the initial 7 days of curing, but at 28 days, curing concrete containing 15% SCBA performed well.

The above test result confirms that concrete with SCBA amount up to 15% develops comparable strength in compression to that of control concrete specimen. The causes for the improvement of strength in compression of SCBA concrete might be attributed to silica content, fineness, and pozzolanic reaction between calcium hydroxide and reactive silica in SCBA. Similar behavior was reported by previous work [7, 16]. At 20, 25, and 30% SCBA content, strength in compression decreases. Therefore, binary concrete containing 15% SCBA appears to be the optimum substitution giving higher strength output. In ternary concrete containing SCBA and GGBFS, the compressive strength increases for B10G10, B10G15, B15G05, and B20G05. The lime present in GGBFS reacts with water, developing complex C–S–H and C–H, which occupies more void space. Both in binary and ternary concrete, reduced compressive strength was acquired at an early age. Similar behavior was reported by previous work [17, 18]. The 28 days strength of cylinder and beam was found to be decreasing by incorporating SCBA and GGBFS for all mixes except the B15 blend (Fig. 2). Flexure strength for B15 mix was found to be 12.93 N/mm^2 which was more as compared with control concrete. The increase in flexure strength can be associated with the increase in compressive strength.

Figure 3 demonstrates SEM images of P, B20, B30, and B20G10 specimens cured for 28 days.

Images highlight change caused due to incorporation of SCBA and GGBFS in binary and ternary concrete. SEM image for B20 and B30 mix highlights the presence of voids and micropores, which are mainly responsible for the change in structure quality and overall properties. Void fraction and untreated particles present in the B30

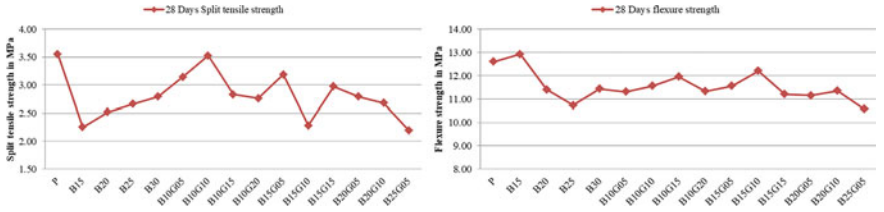

Fig. 2 Split tensile and flexure strength for various binary and ternary mixes of SCBA and GGBFS

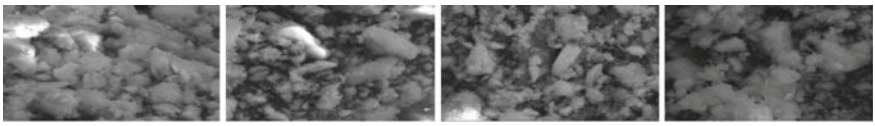

Fig. 3 SEM evaluation of the concrete specimen

blend were higher than the B20 blend, which is responsible for reducing strength. SEM image for B20G10 combination shows the dense internal structure and C–S–H gel exist in the form of a continuous block; these result in higher strength. Similar behavior was reported by previous work [19].

4 Conclusions

Through the experimental research on the concrete modified with SCBA and GGBFS, the following conclusions are drawn:

- Compressive strength enhanced in binary concrete containing SCBA (SiO_2 content was 82.53%) for B15, and in ternary concrete containing SCBA (Cao content was 2.34%), and GGBFS (CaO content was 35.64%) for B20G05 mix.
- Flexural strength is enhanced for B15 mix; for all other replacements, it decreases both in binary and ternary concrete.
- Split tensile strength decreases for all replacement levels both in binary and ternary concrete.

References

1. Mulay S, Vesmawala G, Patil Y, Gholap V (2017) Experimental investigation of sugarcane bagasse ash concrete under sodium hydroxide solution of bagasse ash. Int J Am J Civil Eng 5(1):1–8. https://doi.org/10.11648/j.ajce.20170501.11

2. World steel in figures (2017) World steel association
3. Amin N, Faisal M, Muhammad K, Gul S (2016) Synthesis and characterization of geopolymer from bagasse bottom ash, waste of sugar industries and naturally available china clay. Int J Cleaner Prod 129: 491–495. https://doi.org/10.1016/j.jclepro.2016.04.024
4. Arif E, Clark MW, Lake N (2017) Sugarcane bagasse ash from a high-efficiency co-generation boiler as filler in concrete. Int J Constr Build Mater 151:692–703. https://doi.org/10.1016/j.conbuildmat.2017.06.136
5. Moraes JCB, Tashima MM, Akasaki JL, Melges JLP, Monzo J, Borrachero MV, Soriano L, Paya J (2017) Effect of sugar cane straw ash (SCSA) as solid precursor and the alkaline activator composition on alkali-activated binders based on blast furnace slag (BFS). Int J Constr Build Mater 144:214–224. https://doi.org/10.1016/j.conbuildmat.2017.03.166
6. Cordeiro GC, Tavares LM, Filho RDT (2016) Improved pozzolanic activity of sugarcane bagasse ash by selective grinding and classification. Int J Cem Concr Res 89:269–275. https://doi.org/10.1016/j.cemconres.2016.08.020
7. Bahurudeen A, Kanraj D, Dev VG, Santhanam M (2015) Performance evaluation of sugarcane bagasse ash blended cement in concrete. Int J Cem Concr Compos 59:77–88.https://doi.org/10.1016/j.cemconcomp.2015.03.004
8. Rerkpiboon A, Tangchirapat W, Jaturapitakkul C (2015) Strength, chloride resistance, and expansion of concretes containing ground bagasse ash. Int J Constr Build Mater 101:983–989. https://doi.org/10.1016/j.conbuildmat.2015.10.140
9. Almeida FCR, Sales A, Moretti JP, Mendes PCD (2015) Sugarcane bagasse ash sand (SBAS): Brazilian agroindustrial by-product for use in mortar. Int J Constr Build Mater 82:31–38. https://doi.org/10.1016/j.conbuildmat.2015.02.039
10. Rattanashotinunt C, Thairit P, Tangchirapat W, Jaturapitakkul C (2013) Use of calcium carbide residue and bagasse ash mixtures as a new cementitious material in concrete. Int J Mater Design 46:106–111. https://doi.org/10.1016/j.matdes.2012.10.028
11. Khodair Y, Bommareddy B (2017) Self-consolidating concrete using recycled concrete aggregate and high volume of fly ash, and slag. Int J Constr Build Mater 153:307–316. https://doi.org/10.1016/j.conbuildmat.2017.07.063
12. Cheng S, Shui Z, Sun T, Yu R, Zhang G, Ding S (2017) Effects of fly ash, blast furnace slag and metakaolin on mechanical properties and durability of coral sand concrete. Int J Appl Clay Sci 141:111–117. https://doi.org/10.1016/j.clay.2017.02.026
13. IS 12269-1987: Specification for ordinary Portland cement. Bureau of Indian Standards, New Delhi, India
14. IS 10262-2009: Recommended guidelines for concrete mix design. Bureau of Indian Standards, New Delhi, India
15. Embong R, Shafiq N, Kusbiantoro A, Nuruddin MF (2016) Effectiveness of low-concentration acid and solar drying as pre-treatment features for producing pozzolanic sugarcane bagasse ash. Int J Cleaner Prod 112:953–962. https://doi.org/10.1016/j.jclepro.2015.09.066
16. Chu I, Kwon SH, Amin N, Kim J-K (2012) Estimation of temperature effects on autogenous shrinkage of concrete by a new prediction model. Int J Constr Build Mater 35:171–182. https://doi.org/10.1016/j.conbuildmat.2012.03.005
17. He T, Zhang YX (2016) The influence of bagasse fibre and fly ash on the long-term properties of green cementitious composites. Int J Constr Build Mater 111:237–250. https://doi.org/10.1016/j.conbuildmat.2016.02.103
18. Hwang CL, Chandra S (1996) The use of rice husk ash in concrete. Int J Waste Mater Concrete Manuf 1:184–234. https://doi.org/10.1016/b978-081551393-3.50007-7
19. Zheng W, Li H, Wang Y (2012) Compressive behaviour of hybrid fiber-reinforced reactive powder concrete after high temperature. Int J Mater Design 41:403–409. https://doi.org/10.1016/j.matdes.2012.05.026

Utilization of Potential of PET Resin and Pond Ash in Cement Mortar

Satish Waysal, Yogesh D. Patil, and Bharathkumar Z. Dholkiya

Abstract Polyethylene terephthalate (PET) is a widely used plastics in the packaging industry because of its advantages. However, PET waste slowly decomposes and needs hundreds of years to return to the cycle of nature. It can be managed by recycling PET and using it as resin in concrete for waste plastics management. It would save up to 15% of cement consumptions. The thermal power plant is producing pond ash as waste during the combustion of coal. The management of pond ash is another environmental threat. The used PET and pond ash in concrete would provide relief for the environment and sustainable development. In this work, PET resin is prepared and used as a cement substitute at 5, 10, and 15%, and pond ash is added in 10, 20, and 30% replacement to fine aggregate. The effect of PET resin on properties of cement paste was studied in this work. The effect on mortar properties with the replacement of pond ash and PET resin is studied. It is observed that 10% resin content and 20% replacement of pond ash have satisfactory slump flow, compressive strength, tensile strength, and water penetration resistance. PET resin and pond ash can effectively utilize in sustainable material production.

Keywords PET resin · Pond ash · Compressive strength · Tensile strength and Sustainability

1 Introduction

The world around us is constantly changing, and new innovative materials are developed; one such material is polyethene terephthalate (PET). A PET has outstanding qualities such as non-reactive to substance, gas tapping capacity, light in weight, and no volume change on varying temperature conditions [11]. It increases the demand of PET for the packaging of mineral water, beverages, etc. These advantages increased the consumption of PET, and another problem arise with the management of post consumed PET. The PET is not suitable for reuse, it is injuries to health. PET can

S. Waysal (✉) · Y. D. Patil · B. Z. Dholkiya
SVNIT, Surat, Gujrat, India

B. Kondraivendhan et al. (eds.), *Sustainable Building Materials and Construction*,
Lecture Notes in Civil Engineering 222,
https://doi.org/10.1007/978-981-16-8496-8_54

be used as fiber in concrete, enhances the flexural strength, reduces the compressive strength and workability [12]. The shape and arrangement of PET fibers alter the properties of concrete [5, 9]. The toughness of the material increases and reduces the first crack strength when PET is used as reinforcement [4]. The durability and mechanical properties of concrete enhance after the addition of polymer [1]. The addition of waste glass and PET flakes as aggregate in the production of concrete blocks gains early strength and reduces water absorption [3].

A country like India majorly depends on the thermal power plant for the need of electricity. The thermal power plant generates energy after the combustion of coal; during this, the coal ash is generated. The generated ash is categorized as fly ash and pond ash. The fly ash over the years is being used to produce pozzolanic cement and fly ash bricks. The pond ash consists of the unburnt coal slurry transported into ponds. The pond ash is stored in huge quantity and still demanding land for disposal. The non-availability of land for disposal establishes the need of using pond ash as resource material. The fine aggregate can be replaced by coal bottom ash up to 30% which increases concrete strength [6]. Due to porosity, it reduces the workability of concrete [2]. The durability and strength of concrete increases with addition of bottom ash and micro silica [7]. The 30% replacement of washed bottom ash as fine aggregate gives the optimum results in all parameters [13].

The bottom ash can be used in high-strength concrete, which enhances the mechanical property up to 25% replacement and reduces concrete's dead weight [8].

Considering the problem of PET and pond ash in this research, cement was replaced with PET resin at 5%, 10%, 15%, and fine aggregate replaced by pond ash replacement at 10%, 20%, and 30%. The effect of this replacement on properties of cement and cement morter are studied.

2 Materials

2.1 Fine Aggregate

Fine aggregate used for this work was brought from Sarangkheda, Maharashtra

2.2 Pond Ash

The pond ash is collected from the thermal power plant, Eklhare, Nashik Maharashtra.

Table 1 Material properties (Physical)

Sample	Specific gravity	Water absorption	Fineness
Fine aggregate	2.62	1.10	Confirms the Zone I of BIS 383
Pond ash	1.69	19.68	Confirms the Zone I of BIS 383

2.3 Cement

Ultratech brand's ordinary Portland cement (OPC) 53-grade cement is used.

2.4 Polyethene Terephthalate (PET) Resin

PET glycolysis is carried out in polypropylene glycol (PPG), with a PET to glycol ratio of 40:60, and zinc acetate was used as a catalyst. The mixture of PET and PPG is heated for 180 °C for one hour, and then, the temperature is raised to 210 °C until all solids of PET will disappear and resin obtained [10]. The styrene monomer is added in a 50:50 ratio to increase the viscosity.

2.5 Methyl Ethyl Ketone Peroxides (MEKPo)

MEKPo was used as a curing agent for PET resin; it is added as 7.5% of PET resin content.

2.6 Physical Properties

Table 1 shows the physical properties.

2.7 Testing Program

The effect on fresh properties of the binder upon the addition of PET resin is determined as per IS 4031-1968 and IS 269-1976. The 1:3 (Cement: Sand) mix proportion and water according to consistency are added for this work. The cube of size 70.7 cm × 70.7 cm × 70.7 cm are cast and tested for compressive strength as per IS 4031-1968, IS 269-1976, and IS 650-1966. The tensile test conforming BIS: 269-1958 was

Table 2 Mix proportion for mortar (1:3) in kg/m^3

Cement	PET resin%	Weight of PET resin	Fine aggregate	Pond ash %	Weight of pond ash
788	0	–	1965	0	–
748	5	12.5	1769	10	127
714	10	25.0	1572	20	254
674	15	37.5	1376	30	381

performed on the briquette specimen with minimum cross Sect. 25.4 mm × 25.4 mm. The compressive strength and tensile strength were determined at the curing age of 1, 7, and 28 days. A flow table test measured the flowability. The water penetration resistance was carried out as per DIN 12,390 part 8. The test specimens were cast and cured using potable water.

2.8 Mix Proportion

The normal mortar mix was prepared according to the guidelines given in IS 4031-part 6, at the mix ratio of 1:3 and is given in Table 2

3 Result and Discussion

3.1 Soundness

The cement paste should not be subject to volume change, particularly when cement is replaced by other binding material. The soundness of cement occurs due to excess lime, magnesia, and calcium sulfate in the cement mix. The soundness remains unaffected for PET resin specimen with and without MEKPo curing agent, as given in Table 3.

3.2 Standard Consistency

The standard consistency is as given in Table 3 and measured for 5% to 15% resin content at an increment of 5%. The standard consistency for normal cement mix was 32%. It was the same for 5% resin content. The specimen of 10% and 15% resin contents indicates a reduction in standard consistency by 2% and 3.5%, respectively. This reduction in consistency is because at higher percentage of PET

Table 3 Properties of cement

Sr. no	PET resin content	Standard consistency in %	Soundness in mm	Setting time in min	
				Initial setting	*Final setting*
1	0%	32	2	50	495
2	5% PET	32	1	170	650
3	10% PET	30	1	210	690
4	15% PET	29	1	275	755
5	5% PET + MEKPo	32	1.5	145	430
6	10% PET + MEKPo	30	2	165	395
7	15% PET + MEKPo	28	2	180	380

resin content increases the plasticity of cement paste contributes in reducing the consistency cement paste.

3.3 Soundness

Cement paste must not be subject to volume change, particularly when cement is replaced by other binding material. The soundness of cement occurs due to excess lime, magnesia, and calcium sulfate in the cement mix. The soundness remains unaffected for PET resin specimen with and without MEKPo curing agent, as given in Table 3.

3.4 Setting Time

The setting time variation is given in Table 3, the initial setting time is 50 min, and the final setting time is 495 min for a normal cement specimen. The addition of PET resin shows the increment in setting time, but it reduces after the curing agent's addition. The initial setting time increased by 120, 160, and 225 min. The final setting time increased by 155, 195, and 260 min, respectively, for 5% to 15% resin content at an increment of 5% without MEKPo compared to normal specimen. The setting time depends upon the hydration of cement paste, and it is temperature-dependent property. The initial setting time increased by 95, 115, and 130 min. The final setting time is reduced by 65, 100, and 115 min, respectively, for 5% to 15% at an increment of 5%, compared to normal cement specimen after addition of curing agent.

3.5 Slump Flow

The variation in slump flow is as given in Table 4. The slump flow is measured for PET resin with a curing agent. The higher water absorption of pond ash reduces the slump flow at 30% replacement as fine aggregate. The addition of PET resin increases the flow by 15, 55, and 60 mm for 5, 10, and 15% resin content. The increase in a slump is because of styrene in PET resin. The presence of voids in pond ash reduces the slump flow in comparison with PET resin slum flow. The increase in slum flow for 10% pond ash content is 25, 40, and 45 mm and for 20% pond ash 10, 25, and 30 mm, respectively, for 5% to 15% at an increment of 5% resin content as compared to normal cement paste the 30% pond ash content the minimal variation in slump flow.

3.6 Compressive Strength

Table 4 shows the compressive strength at 1, 7, and 28 days of curing. The one-day strength for PET resin content specimen with and without pond ash is higher than normal cement paste because of PET resin and MEKPo as curing agent. It will act as a polymer in cement mortar. The one-day compressive strength is 80% of the targeted strength of the specimen. The one-day curing compressive strength for 0% pond ash is 39.38, 40.81, and 39.76 N/mm^2; for 10% pond ash is 37.88, 41.42, and 40.77 N/mm^2; for 20% pond ash 37.77, 41.69, and 41.42 N/mm^2; for 30% pond ash 39.69, 42.32, and 42.80 N/mm^2 higher than normal specimen, respectively, for 5% to 15% at increment of 5% resin content. The compressive strength gain at 7 days varies from 15.99 to 20.66 N/mm^2 for all specimens compared to normal mix specimen. The compressive strength at 28 days curing shows a small variation in compressive strength compared to the one-day curing strength. The increment in 28 days compressive strength lies between 1.5 and 4.42 N/mm^2 for PET resin content specimen as compared to normal specimen. The strength gaining is depended upon the hydration of cement paste. The addition of PET resin and MEKPo as curing agent raises cement paste temperature because this hydration process accelerates, and early strength gain is possible. The early strength leads to cracking because of the temperature rise, but the polymer's presence arrested it.

3.7 Tensile Strength

Table 4 shows the variation in tensile strength of cement mortar at 1, 7, and 28 days of curing. The tensile strength was increased as PET resin content and pond ash content increase. The increase in one-day tensile strength for 0% pond ash content is 3.72, 4.63, and 3.60 N/mm^2, for 10% pond ash is 3.98, 4.93, and 3.93 N/mm^2, for

Table 4 Properties of cement mortar

Pond ash content (%)	Resin content in percentage	Slump flow in mm	Compressive strength in N/mm^2			Tensile strength in N/mm^2			Water penetration in mm
			1 day	7 day	28 day	1 day	7 day	28 day	
0	0	80	10.47	39.27	57.67	0.71	2.15	3.19	28
0	5	95	49.85	55.26	59.17	4.43	4.79	4.98	22
	10	135	51.28	56.89	60.19	5.34	5.72	5.89	19
	15	140	50.23	57.28	61.59	4.31	4.42	4.76	18
10	5 + MEKPo	105	48.35	56.31	58.14	4.69	5.1	5.69	19
	10 + MEKPo	120	51.89	57.34	60.78	5.64	5.92	6.23	18
	15 + MEKPo	125	51.24	58.36	62.18	4.64	5.06	5.43	17
20	5 + MEKPo	90	49.24	57.15	58.25	4.96	5.49	5.89	18
	10 + MEKPo	105	52.16	59.13	61.23	5.65	6.09	6.53	16
	15 + MEKPo	110	51.89	59.23	62.89	4.73	5.39	5.76	18
30	5 + MEKPo	75	50.16	57.35	59.14	4.36	4.59	4.98	23
	10 + MEKPo	85	52.79	60.12	61.26	5.24	5.29	5.94	19
	15 + MEKPo	90	53.27	59.93	62.09	4.23	4.39	4.69	18

20% pond ash is 4.25, 4.94, and 4.02 N/mm^2, and for 30% pond ash is 3.65, 4.53, and 3.52 N/mm^2, respectively, for 5% to 15% at increment of 5% resin content as compared to normal cement mortar specimen. The gain in tensile strength is noticed for one-day curing and 7 and 28 days of curing. The growth for 7 days curing varies from 2.24 to 3.94 N/mm^2, and for 28 days curing, it varies from 1.50 to 3.34 N/mm^2 as compared to the normal mix. The gain in strength is because of the polymer chain of PET resin in the mix. The polymer chain acts as a link and increases the resistance under tension. It enhances the flexibility of material.

3.8 Water Penetration Resistance

Water penetration resistance is as given in Table 4. The water penetration resistance was determined on cube at 28 days of curing; the specimen was tested. The water penetration resistance was increased as the percentage of PET resin and pond ash increases. The resistance is increased because of PET polymer and the fitness of pond ash. The maximum water penetration was 28 mm for normal cement specimen and for the minimum is 16 mm for 20% pond ash 10% PET resin content. The reduction lies between 5 and 12 mm.

4 Conclusion

(1) The addition of PET resin reduces the water required for consistency. There was no effect of MEKPo on the standard consistency of cement.
(2) The setting time increased as the percentage of PET resin was increased, and there was a reduction in setting time when MEKPo is added in PET resin
(3) Soundness was unaffected by the percentage of PET resin present in the mix.
(4) The slump flow was increased as the increase in PET resin and pond ash content.
(5) The compressive strength at one-day curing equals to 80% of the targeted strength with PET resin and MEKPo. Compressive strength at 10% PET resin and 20% of pond ash is the highest among all mixes.
(6) The tensile strength of mortar was increased with an increase in PET resin with and without pond ash.
(7) The penetration to water resistance is increased as the increase in PET resin with and without pond ash

Overall, the 30% pond ash and 10% resin content satisfy all the requirements compared to the normal mix. The PET and pond ash can be suitably used in cement mortar.

References

1. Agavriloaie L, Oprea S, Barbuta M, Luca F (2012) Characterisation of polymer concrete with epoxy polyurethane acryl matrix. Constr Build Mater Elsevier Ltd 37:190–196. https://doi.org/10.1016/j.conbuildmat.2012.07.037
2. Andrade LB, Rocha JC, Cheriaf M (2009) Influence of coal bottom ash as fine aggregate on fresh properties of concrete. Constr Build Mater Elsevier Ltd 23(2):609–614. https://doi.org/10.1016/j.conbuildmat.2008.05.003
3. Chidiac SE, Mihaljevic SN (2011) Performance of dry cast concrete blocks containing waste glass powder or polyethylene aggregates. Cement Concr Compos. https://doi.org/10.1016/j.cemconcomp.2011.05.004
4. Fraternali F, Farina I, Polzone C, Pagliuca E, Feo L (2013) On the use of R-PET strips for the reinforcement of cement mortars. Compos B Eng. https://doi.org/10.1016/j.compositesb.2012.09.070
5. Ghernouti Y, Rabehi B, Bouziani T, Ghezraoui H, Makhloufi A (2015) Fresh and hardened properties of self-compacting concrete containing plastic bag waste fibers (WFSCC). Constr Build Mater 82:89–100. https://doi.org/10.1016/j.conbuildmat.2015.02.059
6. Kadam MP, Patil DYD (2013) Effect of coal bottom ash as sand replacement on the properties of concrete with different W/C ratio. Int J Adv Technol Civil Eng 21:2231–5721. https://doi.org/10.12691/ajcea-2-5-2
7. Kadam MP, Patil YD (2017) Strength, durability, and micro structural properties of concrete incorporating MS and GCBA as sand substitute. 76(Oct), pp 644–653
8. Kim HK, Lee HK (2011) Use of power plant bottom ash as fine and coarse aggregates in high-strength concrete. Constr Build Mater Elsevier Ltd 25(2):1115–1122. https://doi.org/10.1016/j.conbuildmat.2010.06.065
9. Marthong C (2015) Effects of PET fiber arrangement and dimensions on mechanical properties of concrete. IES J Part A: Civil Struct Eng 8(2):111–120. https://doi.org/10.1080/19373260.2015.1014304
10. Purohit J, Chawada G, Choubisa B, Patel M, Dholakiya B (2012) Polyester polyol derived from waste poly (ethylene terephthalate) for coating application on mild steel polyester polyol derived from waste poly (thylene terephthalate) for coating application on mild steel. Chem Sci J (CSJ-76) 1–7
11. Reis JML, Carneiro EP (2012) Evaluation of PET waste aggregates in polymer mortars. Constr Build Mater 27(1):107–111. https://doi.org/10.1016/j.conbuildmat.2011.08.020
12. Saikia N, De Brito J (2014) Mechanical properties and abrasion behaviour of concrete containing shredded PET bottle waste as a partial substitution of natural aggregate. Constr Build Mater 52:236–244. https://doi.org/10.1016/j.conbuildmat.2013.11.049
13. Syahrul M, Sani M, Muftah F, Muda Z (2010) The properties of special concrete using washed bottom ash (WBA) as partial sand replacement. Int J Sustain Constr Eng Technol 1(2):65–76